

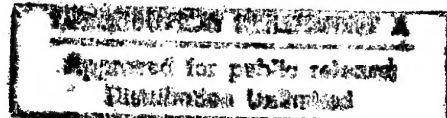


## 1998 IEEE Sixth International Conference on Terahertz Electronics Proceedings



Weetwood Hall, The University of Leeds  
3rd and 4th September 1998

19981013 058



IEEE Catalog Number: 98EX171

4Q F99-01-0050

**1998 IEEE Sixth International Conference on Terahertz Electronics Proceedings**

Responsibility for the contents of the papers published in these proceedings rests upon the authors and not upon IEEE or any of its members.

*Additional copies of these proceedings are available from,*

The Institute of Electrical and Electronic Engineers, Inc.  
Publication Order Department,  
445 Hoes Lane,  
Piscataway,  
NJ 08855-1331  
USA.

---

Copyright and Reprint Permission: Abstracting is permitted with credit to the source. Libraries are permitted to photocopy beyond the limit of U.S. copyright law for private use of patrons those articles in this volume that carry a code at the bottom of the first page, provided the per-copy fee indicated in the code, is paid through Copyright Clearance Center, 222 Rosewood Drive, Danvers, MA 01923. For other copying, reprint or republication permission, write to IEEE Copyrights Manager, IEEE Service Center, 445 Hoes Lane, P. O. Box 1331, Piscataway, NJ 08855-1331. All rights reserved. Copyright © 1996 by the Institute of Electrical and Electronic Engineers, Inc.

---

IEEE Catalog Number:	98EX171
ISBN:	0-7803-4903-2
	Softbound Edition
	0-7803-4904-0
Library of Congress Number:	98-85025
	Microfiche Edition

---

# REPORT DOCUMENTATION PAGE

Form Approved OMB No. 0704-0188

Public reporting burden for this collection of information is estimated to average 1 hour per response, including the time for reviewing instructions, searching existing data sources, gathering and maintaining the data needed, and completing and reviewing the collection of information. Send comments regarding this burden estimate or any other aspect of this collection of information, including suggestions for reducing this burden to Washington Headquarters Services, Directorate for Information Operations and Reports, 1215 Jefferson Davis Highway, Suite 1204, Arlington, VA 22202-4302, and to the Office of Management and Budget, Paperwork Reduction Project (0704-0188), Washington, DC 20503.

1. AGENCY USE ONLY (Leave blank)		2. REPORT DATE	3. REPORT TYPE AND DATES COVERED
		18 September 1998	Conference Proceedings
4. TITLE AND SUBTITLE		5. FUNDING NUMBERS	
The Sixth IEEE International Conference on Terahertz Electronics		F61775-98-WE110	
6. AUTHOR(S)		7. PERFORMING ORGANIZATION NAME(S) AND ADDRESS(ES)	
Conference Committee		University of Leeds, Institute of Microwaves and Photonics School of Electronic and Electrical Engineering Leeds LS2 9JT United Kingdom	
8. PERFORMING ORGANIZATION REPORT NUMBER		9. SPONSORING/MONITORING AGENCY NAME(S) AND ADDRESS(ES)	
N/A		EOARD PSC 802 BOX 14 FPO 09499-0200	
10. SPONSORING/MONITORING AGENCY REPORT NUMBER		11. SUPPLEMENTARY NOTES	
CSP 98-1072			
12a. DISTRIBUTION/AVAILABILITY STATEMENT		12b. DISTRIBUTION CODE	
Approved for public release; distribution is unlimited.		A	
13. ABSTRACT (Maximum 200 words)			
<p>The Final Proceedings for The Sixth IEEE International Conference on Terahertz Electronics, 3 September 1998 - 4 September 1998</p> <p>This is an interdisciplinary conference, providing a forum for the exchange of information on the theory, technology and application of the emerging and interdisciplinary field of terahertz electronics. Specific topics will include Antennas and Arrays, Detectors and Receivers, Imaging, Measurements, Modeling of Active and Passive Components, New Fabrication &amp; Integration Technologies, Opto/Terahertz interactions, Quasi-Optical Design, and sources.</p>			
14. SUBJECT TERMS		15. NUMBER OF PAGES	
terahertz electronics, Antennas, Detector Technology, Modelling & Simulation		248	
		16. PRICE CODE N/A	
17. SECURITY CLASSIFICATION OF REPORT	18. SECURITY CLASSIFICATION OF THIS PAGE	19. SECURITY CLASSIFICATION OF ABSTRACT	20. LIMITATION OF ABSTRACT
UNCLASSIFIED	UNCLASSIFIED	UNCLASSIFIED	UL

NSN 7540-01-280-5500

Standard Form 298 (Rev. 2-89)  
Prescribed by ANSI Std. Z39-18  
298-102

# 1998 IEEE Sixth International Conference on Terahertz Electronics Proceedings

edited by

**P. Harrison**

*Institute of Microwaves and Photonics,  
School of Electronic and Electrical Engineering,  
University of Leeds, LS2 9JT.  
United Kingdom*



## Preface

Interest in utilising the frequency range between 100 GHz and 10 THz is increasing rapidly. Traditional applications such as radio astronomy and remote-sensing are being supplemented by commercial and military interest in imaging, broadband communications, tagging, sensors and other higher volume products. Recent technological developments in the area of semiconductor devices, solid-state lasers and micromachining herald an era where the opportunities to explore this frequency region will become more widely available. This broad frequency region lies at the transition from electronics to optics and is therefore of interest to microwave engineers and physicists alike.

This volume contains the proceedings of the sixth meeting in the series of conferences on terahertz electronics. This year's meeting follows the successful meeting held in Grenoble, France in September 1997. The conference, which is sponsored by the IEEE, has become the premier European meeting for terahertz electronics research and draws experts in this field from across the world. It provides a forum for the exchange of ideas and information on the theory, technology and application of terahertz electronics. It is also intended to foster an appreciation of the capabilities and potential of this technology for future applications.

The Technical Programme Committee, chaired by Martyn Chamberlain, selected 70 papers for presentation at this year's conference. The papers span a wide range of important topics, dealing with antennas and arrays; detectors and receivers; imaging; measurements; modelling; fabrication and integration technologies; opto-terahertz interaction; quasi-optical design and finally the key issue of sources. The proceedings consist of invited and contributed papers. We are particularly grateful to the invited speakers for their contributions, which help to set the scene for each topic area. The organisers are very grateful to the reviewers and committee members for their time and to the authors for making this conference a success. I would also like to express my appreciation to the organising committee for their many hours of hard work. We are confident that readers will find this a useful volume for future reference and that conference delegates will be stimulated by the many ideas and techniques described in the proceedings.

Christopher M. Snowden  
Conference Chairman  
University of Leeds, August 1998.

---

We wish to thank the following for their contribution to the success of this conference:

United States Air Force European Office of Aerospace Research and Development



## Organizing Committee

<b>Chairman</b>	Prof. Christopher M. Snowden, <i>Institute of Microwaves and Photonics, University of Leeds</i>
<b>Secretary</b>	Dr Stafford Withington, <i>Department of Physics, University of Cambridge</i>
<b>Treasurer</b>	Prof. Roger D. Pollard, <i>Institute of Microwaves and Photonics, University of Leeds</i>
<b>Local Arrangements</b>	Dr Robert E. Miles, Lyn A. Cookman <i>Institute of Microwaves and Photonics, University of Leeds</i>
<b>Publicity</b>	Dr Stavros Iezekiel, <i>Institute of Microwaves and Photonics, University of Leeds</i>
<b>Technical Programme Chair</b>	Dr Martyn Chamberlain, <i>Department of Physics, University of Nottingham</i>
<b>Publication Chair</b>	Dr Paul Harrison, <i>Institute of Microwaves and Photonics, University of Leeds</i>

## Technical Programme Committee

Dr Don Arnone, <i>Toshiba Cambridge Research Centre</i>
Prof Nigel Cronin, <i>School of Physics, the University of Bath</i>
Prof Harold Fetterman, <i>Department of EE, University of California, Los Angeles</i>
Dr J R Gao, <i>Department of Applied Physics, University of Groningen</i>
Prof P S Hall, <i>School of Electrical &amp; Electronic Engineering, The University of Birmingham</i>
Prof Tatsuo Itoh, <i>Department of EE, University of California, Los Angeles</i>
Prof Linda Katehi, <i>Radiation Laboratory, University of Michigan, Ann Arbor</i>
Prof Erik Kollberg, <i>Department of Microwave Technology, Chalmers University of Technology</i>
Prof Michael Shur, <i>Department of Electrical Computer and Systems Engineering, Rensselaer Polytechnic Institute</i>
Prof Michael Steer, <i>Centre for Advanced Computing &amp; Communications, NC State University, Raleigh</i>
Prof Mark Sherwin, <i>Department of Physics, University of California, Santa Barbara</i>
Dr Charly Unterrainer, <i>Solid State Electronics, Technical University of Vienna</i>
Prof Tom Wenckebach, <i>Faculty of Applied Physics, Delft University of Technology</i>



## Contents

### 1. DETECTORS AND RECEIVERS

---

B. S. Karasik, A. Skalare, R. A. Wyss, W. R. McGrath, B. Bumble, H. G. LeDuc, J. B. Barner, and A. W. Kleinsasser, 'Low-noise and wideband hot-electron superconductive mixers for THz frequencies'	1
O. Harnack, S. Beuven, M. Darula, H. Kohlstedt, M. Tarasov, E. Stephantsov, and Z. Ivanov, 'Characterisation of millimeter and submillimeter wave mixers based on high- $T_c$ superconductor structures'	5
D. Wilms Floet, E. Miedema, J. R. Gao, and T. M. Klapwijk, 'Hotspot mixing: a new principle of heterodyne mixing in a superconducting hot-electron bolometer'	9
M. C. Gaidis, H.M. Pickett, P. H. Siegel, C. D. Smith, R. P. Smith, and S. C. Martin, 'A 2.5 THz receiver front-end for spaceborne applications'	13
R. Blundell, J. H. Kawamura, C. E. Tong, D. C. Papa, T. R. Hunter, G. N. Gol'tsman, S. I. Cherednichenko, B. M. Voronov, and E. M. Gershenson, 'A hot electron bolometer mixer receiver for the 680-830 GHz frequency range'	18

### 2A. ANTENNAS AND QUASI-OPTICS

---

M. B. Steer, M. Ozkar, and C. E. Christoffersen, 'Circuit-level modelling of spatially distributed mm and sub mm-wave systems'	21
P. Arcioni, M. Bozzi, G. Conciauro, L. Perregrini, and A. R. Ruiz Laso, 'Accurate modeling of quasi-optical frequency multipliers excited by a Gaussian beam'	26
I. A. Ehtezazi, C. Letrou, and G. Beaudin, 'Radiation patterns from substrate-lens antennas: a method of analysis for THz application'	30

### 2B. TERAHERTZ IMAGING

---

V. Agrawal, T. Bork, S. Kee, and D. W. van der Weide, 'Electronic THz reflection spectroscopy for detecting energetic materials'	34
M. Hangyo, S.-I. Shikii, M. Yamashita, T. Kondo, M. Tonouchi, M. Tani, and K. Sakai, 'Imaging of supercurrent distribution in YBCO thin films using THz radiation excited by femtosecond laser pulses'	38

### 3. NEW CONCEPTS IN DESIGN & FABRICATION OF PASSIVE & ACTIVE COMPONENTS

---

Y. Qian, R. Cocciali, F.-R. Yang, and T. Itoh, 'Passive and active component design using PBG'	42
C. Mann, 'Fabrication technologies for Terahertz waveguide'	46
J. Carbonell, J. Danglot, X. Mélique, O. Dupuis, E. Lheurette, P. Mounaix, O. Vanbésien, and D. Lippens, 'Electromagnetic analysis of micromachined devices'	50
J. R. Thorpe, P. Steenson, and R. E. Miles, 'Non-linear transmission lines for millimeter-wave frequency multiplier applications'	54

#### 4. SOLID STATE SOURCES I

---

T. W. Crowe, 'Multiplier technology for Terahertz applications'	58
V. Duez, X. Mélique, R. Havart, F. Podevin, P. Mounaix, F. Mollot, O. Vanbésien, and D. Lippens, 'Heterostructure barrier quantum well varactor'	62
H. Eisele, A. Rydberg, G. I. Haddad, 'Recent advances in the performance of InP Gunn devices for the 100-300 GHz frequency range'	66
M. Krach, J. Freyer, and M. Claasen, 'Doping-barrier varactors for frequency-multipliers'	69
A. Simon, C.-I. Lin, M. Rodriguez-Gironés, H. L. Hartnagel, P. Zimmermann, R. Zimmermann, and R. Henneberger, 'High efficiency frequency multipliers using substrateless Schottky diodes'	72

#### 5. INTERSUBBAND SOURCES

---

P. Harrison, R. W. Kelsall, P. Kinsler, and K. Donovan, 'Quantum well intersubband transitions as a source of terahertz radiation'	74
C. Y. L. Cheung, P. Rees, and K. A. Shore, 'Quantum well structures for THz bandwidth near-infrared unipolar semiconductor lasers'	79
P. D. Buckle, P. Dawson, M. A. Lynch, C.-Y. Kuo, M. Missous, and W. S. Truscott, 'An inter-subband device with THz applications'	82
R. C. Strijbos, A. V. Muravjov, C. J. Fredricksen, W. Trimble, S. H. Withers, S. G. Pavlov, V. N. Shastin, and R. E. Peale, 'Mode locking of far-infrared p-Ge lasers'	86
J. N. Hovenier, M. C. Diez, T. O. Klaasen, W. Th. Wenckebach, A. V. Muravjov, S. G. Pavlov, and V. N. Shastin, 'The p-Ge THz laser in low B-field: properties under pulsed and mode locked operation'	90

#### 6A. OPTICAL GENERATION AND DETECTION OF TERAHERTZ

---

Z. Jiang, F. G. Sun, and X.-C. Zhang, 'Spatio-temporal imaging of THz pulses'	94
J. Shikata, K. Kawase, K. Karino, and H. Ito, 'Tunable THz-wave generation from $LiNbO_3/MgO:LiNbO_3$ optical parametric oscillators'	98

#### 6B. OPTICAL CONTROL OF TERAHERTZ ELECTRONICS

---

H. Fetterman, A. Udupa, D. Bhattacharya, H. Erlik, M. Ali, Y. Chang, W. Steier, L. Dalton, and B. Tsap, 'Photonic control of Terahertz systems'	102
R. M. De La Rue, M. R. S. Taylor, K. Li, M. Sasaki, T. Hori, and M. Izutsu, 'Terahertz frequency regime waveguide photonic microstructures for electro-optic modulation'	106

## 7. MEASUREMENTS

---

R. J. Collier, 'Measurements of impedance above 110 GHz'	110
O. Wohlgemuth, B. Agarwal, R. Pullela, D. Mensa, Q. Lee, J. Guthrie, M. J. W. Rodwell, R. Reuter, J. Braunstein, M. Schlectweg, T. Krems, and K. Köhler, 'An integrated circuit for network analysis within 50-200 GHz'	113
D. W. van der Weide, F. Keilmann, V. Agrawal, and J. Murakowski, 'Gas absorption spectroscopy with electronic Terahertz techniques'	117
P. Goy, S. Caroopen, M. Gross, J. Mallar, J. Tuovinen, F. Mattiocco, 'Quasi-optics vector measurements of dielectrics from 8 GHz to the THz'	120

## 8. SOLID STATE SOURCES II

---

E. Schomburg, M. Haeussler, K. Hofbeck, K. F. Renk, J. M. Chamberlain, D. G. Pavel'ev, Yu. Koschurinov, V. Ustinov, A. Zhukov, A. Kovsch, and P. S. Kop'ev, 'Narrowband microwave emission by a frequency-locked current oscillation in a GaAs/AlAs superlattice'	124
M. S. Shur, J.-Q. Lu, and M. I. Dyakonov, 'Plasma wave electronics: Terahertz sources and detectors using two dimensional electronic fluid in high electron mobility transistors'	127

## 9. RECEIVERS AND RELATED TOPICS

---

G. Rehm, K. Huber, S. Martius, 'Excess noise in Schottky diodes for THz applications'	131
C.-I. Lin, A. Simon, M. Rodriguez-Gironés, H. L. Hartnagel, P. Zimmermann, Rüdiger Zimmermann, and R. Henneberger, 'Planar Schottky diodes for submillimeter wave applications'	135
R. Nitsch and K. Jacobs, 'A planar SIS mixer for 400-500 GHz'	139
Y. Gousev and H. Olsson, 'Niobium Nitride hot-electron mixer for THz frequencies'	141
H. Merkel, P. Yagoubov, P. Khosropanah, and E. Kollberg, 'An accurate calculation method of the absorbed LO power in hot electron bolometric mixers'	145
P. Yagoubov, M. Krug, H. Merkel, E. Kollberg, J. Schubert, H.-W. Hübers, G. Schwaab, G. Gol'tsman, and E. Gershenson, 'Performance of NbN phonon-cooled hot-electron bolometric mixer at Terahertz frequencies'	149
J. Grajal, V. Krozer, F. Maldonado, E. Gonzalez, C.-I. Lin, and H. L. Hartnagel, 'Tripler circuit design with Schottky varactors'	153
J. Vazquez, C. G. Parini, P. De Maagt, and P. J. B. Clarricoats, 'Full wave modelling of integrated submmw receivers by using the FDTD/lumped element method'	157

## 10. MEASUREMENTS; NOVEL TECHNIQUES FOR PASSIVE DEVICES

---

C. W. Rella, M. Drabbels, and L. D. Noordam, ' <i>Long wavelength infrared streak camera</i> '	161
D. Thompson, R. E. Miles, and R. D. Pollard, ' <i>Complex permittivity measurements using a quasi-optical multistate reflectometer</i> '	163
J. Weinzierl, Ch. Fluhrer, and H. Brand, ' <i>Dielectric waveguides at submillimeter wavelengths</i> '	166
J. W. Bowen and S. Hadjiloucas, ' <i>The precision of quasi-optical null-balanced bridge techniques for S-parameter measurement</i> '	170
D. Budimir, ' <i>Design of air-filled rectangular waveguide bandpass filters by DBFILTER code for Terahertz applications</i> '	173
C. E. Collins, R. E. Miles, J. W. Digby, G. M. Parkhurst, R. D. Pollard, J. M. Chamberlain, and D. P. Steenson, ' <i>Micro-machined 'Snap together' rectangular waveguide for Terahertz circuits</i> '	176

## 11. TERAHERTZ-OPTO INTERACTIONS AND APPLICATIONS

---

J. W. D. Chi, K. A. Shore, and J. Le Bihan, ' <i>Calculation of THz frequency conversion by HNDFWM in <math>\lambda/4</math>-shifted DBF lasers</i> '	179
J. M. Tang and K. A. Shore, ' <i>Multiwave mixing of terahertz detuned optical pulses in semiconductor optical amplifiers</i> '	183
J. M. Tang and K. A. Shore, ' <i>Analysis of terahertz optical asymmetric demultiplexers subject to picosecond control and signal optical pulses</i> '	187
A. J. Vickers, S. B. Alleston, M. Hassan, P. O. Müller, and D. Erasme, ' <i>A gain switched semiconductor laser pump-probe source</i> '	191
M. Schall, H. Helm, and S. R. Keiding, ' <i>THz time-domain spectroscopy of electro-optic crystals</i> '	194
C. Winnewisser, F. Lewen, J. Weinzierl, and H. Helm, ' <i>Frequency-selective surfaces analyzed by THz-time-domain spectroscopy</i> '	196
M. Ryzhii, I. Khmyrova, V. Ryzhii, and M. Willander, ' <i>Terahertz operation of GaAs/AlGaAs metal-semiconductor-metal photodetectors</i> '	199
H. Ohtake, S. Izumida, S. Ono, Z. Liu, and N. Sarakura, ' <i>THz-radiation from InAs under magnetic field and its spectrum control</i> '	201
Jaehoon Lee, Heeseok Lee, Woopoung Kim, Jongjoo Lee, and Joungho Kim, ' <i>&gt;100 GHz time domain measurement using photoconductive sampling</i> '	204
Heeseok Lee, Jaehoon Lee, and Joungho Kim, ' <i>Transient response of terahertz emitter using finite-difference time-domain (FDTD) method</i> '	208
I. Scherbatko, A. Herukh, and S. Iezekiel, ' <i>Terahertz double-doppled wavelength shifting of infrared optical pulses in excited semiconductor medium</i> '	211

---

## 12. SOLID STATE SOURCES AND RELATED TOPICS

---

R. Judaschke and K. Schünemann, ' <i>Modulated impurity-concentration InP-TEDs for second-harmonic oscillators at 260 GHz</i> '	215
P. See, C. E. Collins, D. D. Arnone, D. P. Steenson, E. H. Linfield, P. D. Rose, D. A. Ritchie, and G. A. C. Jones, ' <i>Millimetre wave/microwave power combining from arrays of resonant tunnelling diodes defined by in-situ focussed ion beam lithography</i> '	219
K. Donovan, P. Harrison, R. W. Kelsall, and P. Kinsler, ' <i>A theoretical study of quantum well terahertz lasers</i> '	223
R. Zobl, M. Fuchshuber, G. Strasser, K. Unterrainer, E. Gornik, K. D. Maranowski, and A. C. Gossard, ' <i>THz emission from parabolically graded quantum wells in tilted magnetic fields</i> '	227
G. Samsonidze, S. Rudin, and M. S. Shur, ' <i>Large signal theory of plasma electronics terahertz detectors</i> '	231

---

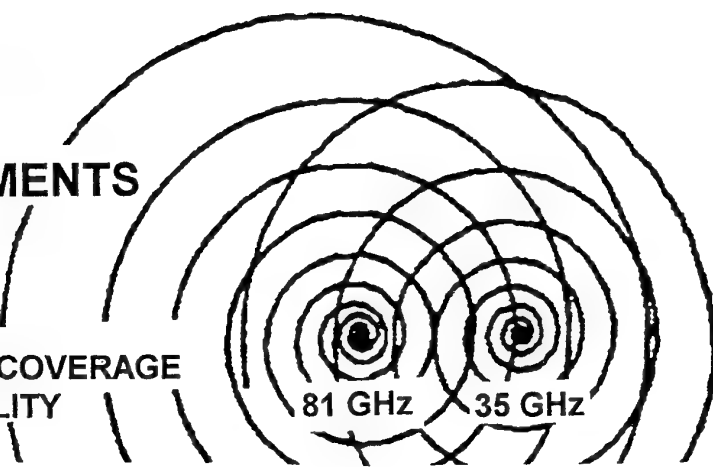
## 13. OTHER TOPICS

---

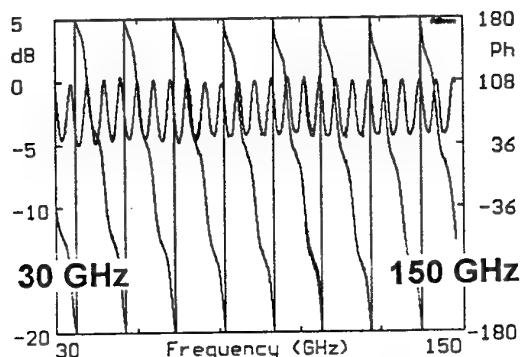
M. G. Kong, ' <i>Enhanced harmonic generation at terahertz frequencies with a two-frequency wiggler</i> '	234
M. Raum and K. Huber, ' <i>Standard design of SMMW laser ring resonators with optical pump beam guiding</i> '	238
R. Martini, F. Hilbk-Kortenbruck, P. H. Bolivar, and H. Kurz, ' <i>Inversionless amplification of coherent THz radiation</i> '	242
R. Blundell, C.-Y. E. Tong, S. Paine, C. Papa, J. W. Barrett, R. L. L. Leonbruno, R. Kimber, R. W. Wilson, and T. R. Hunter, ' <i>Receivers for the sub-millimeter array</i> '	246

# 8-1000 GHz VECTOR MEASUREMENTS ON YOUR TABLE

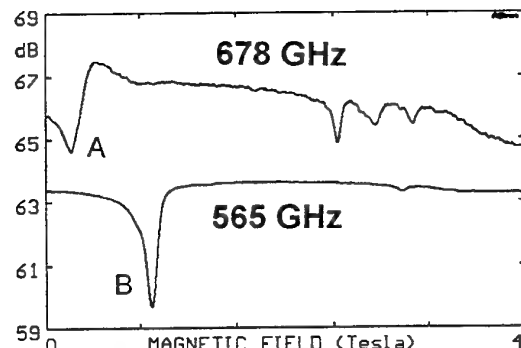
MVNA 8-350  
CONTINUOUS FREQUENCY COVERAGE  
DUAL-FREQUENCY CAPABILITY



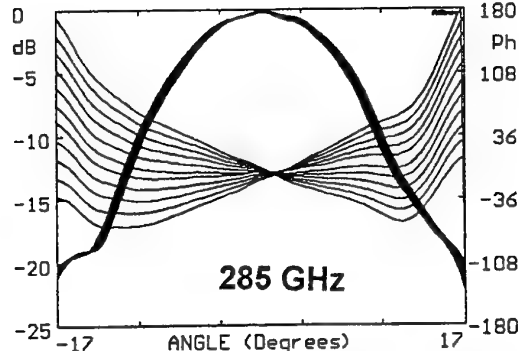
More than thirty Millimeter Vector Network Analyzers MVNA 8-350 have been produced and installed in over ten different countries since 1989. They are used by industry and universities in electrical engineering departments. Physics departments also, working for instance on plasma physics, radioastronomy, atomic physics, condensed matter physics, have found MVNA 8-350 invaluable. Various applications include measurements on waveguide and quasi-optical devices, radar modeling and propagation studies, active and passive components, antennas, dielectric, superconductive or magnetic materials, spectroscopy of atoms, molecules or radicals. MVNA 8-350 has proved to be reliable and in the past ten years no major intervention has ever been necessary on the part of the manufacturer. The figure above shows a polar plot of helicon waves observed by 35 and 81 GHz transmission across InSb at room temperature, submitted to a 0-17T magnetic field sweep (University of Nijmegen, The Netherlands). See other examples below.



Amplitude (oscillatory line, given in dB) and phase (decreasing line, given in degrees) observed by transmission across a 10mm thick slab of sapphire where the measured permittivity is  $\epsilon'=9.40$  and the loss  $\tan\delta$  is below 0.001.



Magnetic resonances as dips in transmission across a FeI<sub>2</sub> sample at 5K (Riken Institute, Japan). Top line (678 GHz) and bottom line (565 GHz) are recorded simultaneously, during the same magnetic field sweep (dual-frequency MVNA configuration). The phase acquisition, not shown, resolves lineshape problems. Its variations indicate that the resonances A (at top left) and B (at bottom left) belong to upwards and downwards branches, respectively, in the frequency/field diagram. Line B appears to be a single Lorentzian. Line A (quality factor close to unity) is a double Lorentzian, with a splitting of one third of the linewidth.



H-Plane antenna pattern of a conical horn at 285 GHz, where the horn is laterally moved by 0.2mm steps for the phase center determination, at which the observed phase variation becomes stationary.

E-mail: [abmm001@ibm.net](mailto:abmm001@ibm.net)  
[www.abmillimetre.com](http://www.abmillimetre.com)

**ABmm**

AB MILLIMETRE  
 52 RUE LHOMOND  
 75005 PARIS FRANCE  
 TEL:33 1 4707 7100  
 FAX:33 1 4707 7071

# Low-noise and Wideband Hot-Electron Superconductive Mixers for THz Frequencies

B.S. Karasik\*, A. Skalare, R.A. Wyss, W.R. McGrath, B. Bumble, H.G. LeDuc, J.B. Barner, and A.W. Kleinsasser

Center for Space Microelectronics Technology, Jet Propulsion Laboratory,  
California Institute of Technology, Pasadena CA 91109, USA

**Abstract**—Superconductive hot-electron bolometer (HEB) mixers have been built and tested in the frequency range from 1.1 THz to 2.5 THz. The mixer device is a 0.15–0.3  $\mu\text{m}$  microbridge made from a 10 nm thick Nb film. This device employs diffusion as a cooling mechanism for hot electrons. The double sideband noise temperature was measured to be  $\leq 3000$  K at 2.5 THz and the mixer IF bandwidth is  $\sim 9$ –10 GHz for a 0.1  $\mu\text{m}$  long device. The local oscillator (LO) power dissipated in the HEB microbridge was 20–100 nW. Further improvement of the mixer characteristics can be potentially achieved by using Al microbridges. The advantages and parameters of such devices are evaluated. The HEB mixer is a primary candidate for ground based, airborne and spaceborne heterodyne instruments at THz frequencies. HEB receivers are planned for use on the NASA Stratospheric Observatory for Infrared Astronomy (SOFIA) and the ESA Far Infrared and Submillimeter Space Telescope (FIRST). The prospects of a submicron-size  $\text{YBa}_2\text{Cu}_3\text{O}_{7-\delta}$  (YBCO) HEB are also discussed. The expected LO power of 1–10  $\mu\text{W}$  and SSB noise temperature of  $\sim 2000$  K may make this mixer attractive for various remote sensing applications.

## I. INTRODUCTION

Low noise heterodyne receivers are needed for astrophysical and earth remote-sensing observations at frequencies between about 100 GHz and 3 THz (3 mm to 100  $\mu\text{m}$  wavelength). Niobium (Nb) SIS quasiparticle mixers provide excellent performance up to about the bulk superconductive energy gap frequency  $f_g$  of 750 GHz, but are unlikely to work well much above 1 THz (see Fig. 1 [1]). A unique superconducting transition-edge hot-electron bolometer (HEB) mixer has been proposed [2,3] as an alternative to address the THz-regime applications. The HEB mixer is expected to operate up to at least several 10's of THz, due to the relatively frequency independent absorption of rf radiation in a superconductor above the gap frequency. The rf impedance of a superconducting microbridge is expected to be real and independent of frequency from about  $f_g$  up to frequencies of visible light. Theory [4] predicts the HEB mixer noise temperature due to the intrinsic thermal-fluctuation noise mechanisms to be very low, so it would be most likely quantum limited at THz frequencies. Also the required local oscillator (LO) power is independent of frequency and can be made very low (the coupled LO power is less than 100 nW for Nb *diffusion-cooled* devices) for appropriate choice of transition temperature  $T_c$  and film sheet resistance. Our approach utilizes  $\sim 100$  Å thick low-resistivity, high quality Nb films, in which out-diffusion of electrons to normal metal contacts serves as the

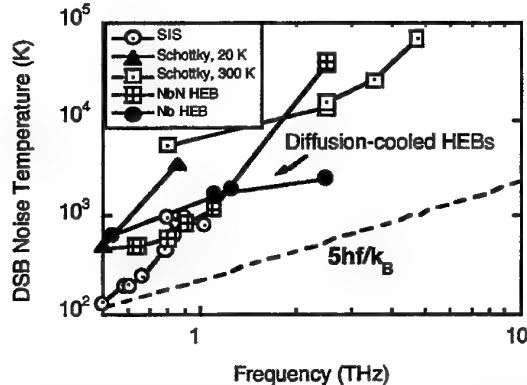


Fig. 1. Diffusion-cooled HEB receiver performance compared to state-of-the-art heterodyne receiver performance at submillimeter wavelengths.

dominant electron cooling mechanism [3].

## II. NOISE PERFORMANCE OF Nb HEB MIXERS

We have successfully developed and tested quasi-optical *diffusion-cooled* HEB mixers at 1.1 THz and 2.5 THz in heterodyne receivers. Record sensitivity and IF bandwidth were obtained demonstrating the advantages of diffusion-cooled HEB mixers at THz frequencies. These results are described here (see recent publications [5,6] for additional details).

The bolometer devices used in these experiments consist of a 0.30  $\mu\text{m}$  long by 0.15  $\mu\text{m}$  wide microbridge made of a 12 nm thick sputtered-deposited Nb film. The length of the bridge was defined by the gap between the 150 nm thick gold contact pads using a unique self-aligned fabrication process [7]. The surrounding mixer embedding circuit and planar antenna are fabricated from 300 nm thick gold. This process gives automatic registration of the Nb under the gold to provide dependable electrical and thermal contact. This fabrication process produced excellent device parameters: critical temperatures  $T_c$  up to 6.5 K, transition width  $\leq 0.3$  K; and sheet resistance 10–20  $\Omega/\text{sq}$ . The critical current density at 4.2 K was as high as  $1.5 \times 10^7$  A/cm<sup>2</sup>.

Two different quasi-optical mixer designs were developed. For 1.1 THz, the mixer consisted of double-dipole antenna with coplanar strip transmission lines located at the focus of a quartz hyperhemispherical lens [5]. The mixer embedding circuit for 2.5 THz used a twin-slot antenna and coplanar waveguide transmission line located at the second focus of an elliptical silicon lens [6] (see Fig. 2). The receiver test system employed either a backward wave oscillator operating at 1105 GHz as a local oscillator (LO) source, or a CO<sub>2</sub>-pumped FIR gas laser to generate LO power at 2522 GHz using methanol vapor. A vacuum box containing two blackbody loads with similar emissivities was designed and built for Y-factor measurements of the receiver noise temperature. The box

\*Address: JPL, M/S 168-314, 4800 Oak Grove Drive, Pasadena, California 91109-8099, USA. E-mail: Boris.Karasik@jpl.nasa.gov

The valuable contribution to this work made by M. Gaidis and M. Burns is greatly appreciated. This research was performed by the Center for Space Microelectronics Technology, Jet Propulsion Laboratory, California Institute of Technology under a contract with the National Aeronautics and Space Administration.

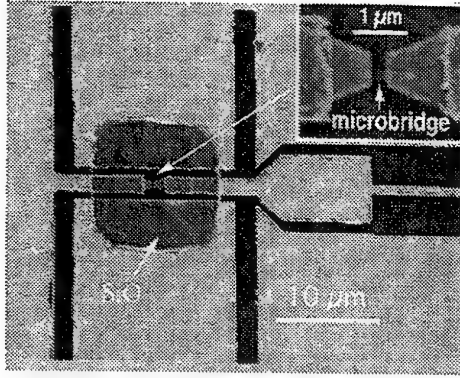


Fig. 2. 2.5 THz Planar mixer circuit consisting of the twin-slot antenna and coplanar waveguide transmission line. To the right are the IF and dc lines with an integrated rf choke filter.

is connected to the LHe vacuum cryostat, allowing operation without a pressure window in the signal path. The box and cryostat are evacuated to remove the effect of atmospheric absorption which is significant above 1 THz. The 1.1 THz receiver used a cooled HEMT IF amplifier centered at 1.5 GHz, and the 2.5 THz receiver used a similar amplifier centered at 2.1 GHz.

### III. IF BANDWIDTH IN Nb HEB DIFFUSION-COOLED MIXERS

Since these bolometer mixers use outdiffusion of hot electrons as the cooling mechanism, the thermal relaxation  $\tau_T$  time should vary as  $L^2$ , where  $L$  is the microbridge length, for devices shorter than about 0.5  $\mu\text{m}$  [8]. The thermal response time can be estimated from the expression:  $\tau_T \sim L^2/(\pi^2 D)$ , where  $D$  is the thermal diffusivity of the film. Thus the 3-dB IF bandwidth  $f_{3\text{dB}} = 1/(2\pi\tau_T)$  should vary as  $L^2$ .

The IF bandwidth of several devices varying in length between 0.3  $\mu\text{m}$  and 0.1  $\mu\text{m}$  was measured in mixing experiments at frequencies  $\sim 500$ -600 GHz. As shown in Fig. 3, the bandwidth did indeed vary as  $L^2$ , with the largest bandwidth greater than 9 GHz for a device 0.1  $\mu\text{m}$  long. The mixer noise bandwidth however is generally greater than the signal bandwidth [4,9]. This is the highest bandwidth ever measured for a low-noise bolometer mixer.

### IV. RF COUPLING AND LOSSES IN THE MIXERS

The mixer antenna frequency response was measured

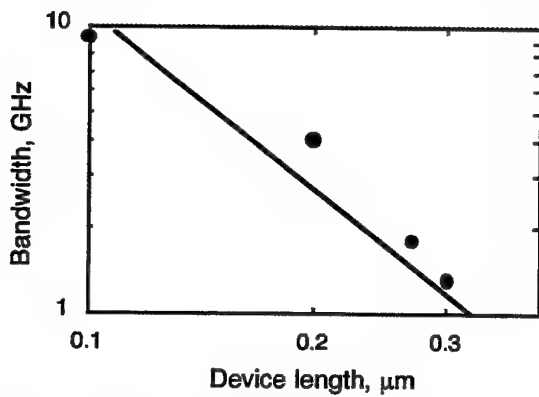


Fig. 3. Bandwidth vs length for devices with different lengths. Solid line is the  $L^{-2}$  dependence for the diffusion cooled case. The devices with  $L = 0.2 \mu\text{m}$  was twice less resistive as the other two. That was likely the reason that the bandwidth for this device was somewhat larger than expected.

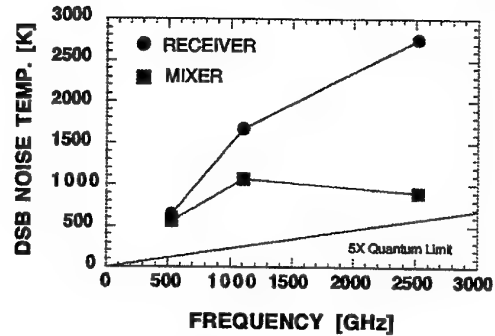


Fig. 4. HEB receiver (circles) and mixer (squares) noise temperature versus frequency for 3 different receivers. The mixer noise is essentially flat over a 2 THz frequency range.

using a Fourier Transform Spectrometer (FTS). For this measurement, the HEB device operating temperature was set to a value near  $T_c$ , and the bias voltage was adjusted to obtain a large direct-detection response in the bolometer. For the double-dipole antenna the center frequency is about 980 GHz and the rf bandwidth is 730 GHz. For the twin slot antenna, the center frequency is about 1900 GHz and the 3-dB bandwidth is approximately 1.1 THz. These results agree with the expected performance for double-dipoles and twin-slots and demonstrate that these antennas still function well up to 2.5 THz.

Y-factor measurements give a noise temperature of 1670 K DSB for the 1.1 THz receiver [5]. To calculate the mixer noise, only the simplest and best measured corrections were made. Removing the amplifier noise and small off-resonant antenna loss would imply a mixer noise of  $\leq 950$  K. For the 2.5 THz receiver, a best noise temperature of 2500-3000 K was obtained for an IF near 1.4 GHz. Doing similar corrections the mixer noise temperature of about 900 K can be obtained. The LO power absorbed in the 2.5 THz device was about 80 nW, and the total mixer LO requirement is estimated to be 420 nW (this accounts for the  $\sim 7.2$  dB of optical and embedding circuit losses [6]). These results at 2.5 THz are 5-times lower noise and 10-times lower LO power than competing technologies. Figure 4 summarizes these results along with our previous measurements at 530 GHz [10] and demonstrates that the HEB mixer noise is nearly independent of frequency over a range of at least 2 THz.

Straightforward improvements in antenna design, device impedance match, and use of anti-reflection coatings should result in at least a factor 2 improvement in receiver noise. Thus receiver noise temperature less than about 1000 K should be readily possible up to 3 THz using Nb devices.

The HEB mixer fixed-tuned rf bandwidths of  $\sim 50\%$ , discussed above, are many times larger than SIS mixers since the rf impedance of the HEB device is almost purely resistive up to frequencies over 100 THz. The HEB thus provides a broadband resistive match to the broadband planar antennas (using spiral antennas, mixer bandwidths of several octaves should be possible).

### V. ADVANTAGES OF MATERIALS WITH LOWER CRITICAL TEMPERATURE FOR HEB MIXERS

Currently LO source technology is not as well developed as mixer technology and this puts further demands for improvement of HEB mixers in terms of decreasing the LO power requirements and increasing the IF bandwidth. Also, since theoretically the HEB mixers can achieve quantum limited noise performance, it is of practical interest to find a way to achieve this limiting performance. A proper choice of the device material can create a more optimal combination of mixer parameters.

The diffusion cooling regime can be achieved in most

materials as long as the device is made sufficiently short. As seen in Fig. 5, Nb, NbC, and Al all have  $D \geq 1 \text{ cm}^2/\text{s}$ . For  $D \sim 10 \text{ cm}^2/\text{s}$  (a typical value for aluminum) and  $L = 0.1 \mu\text{m}$ , the calculated diffusion time is  $\sim 1 \text{ ps}$  which corresponds to an effective mixer bandwidth of 160 GHz. Even taking into account the difference between the theory and experiment, a bandwidth of several tens GHz seems to be quite possible.

A large range of diffusion constants gives flexibility in adjusting the mixer resistance to a desirable value. Indeed, if one tries to increase the bandwidth by using a very clean film, it may happen that the resistivity will be so low that the mixer device will be mismatched with the planar antenna impedance. Such a situation is more likely in Nb which has a higher density of electron states  $N_e$  ( $\rho^{-1} = N_e e^2 D$ ) than Al and NbC where the density of states is three times lower than in Nb (see Fig. 5). Therefore one can use cleaner films (= larger bandwidth) of these materials, while maintaining at the same time a suitable resistance for matching to rf embedding circuits.

According to theory [4] the best HEB mixer performance takes place when the thermal fluctuation noise dominates over the Johnson noise. Under these circumstances assuming that the device operates at temperature  $T \ll T_c$ , the SSB mixer noise temperature for diffusion-cooled mixer,  $T_M$ , is given by the following expression:  $T_M = 2T_c$ . These limits are shown in Fig. 6 (horizontal lines). One can see that the theoretical limit for Al is many times lower than that for higher critical temperature materials. The theory [4] does not consider any quantum phenomena though the quantum noise limit will be important at THz frequencies. A simplistic empirical correction can be made by adding one quantum contribution,  $h\nu/k_B$ , to the limit of theory [4]. As a result the difference in  $T_M$  between Al and other HEB mixers becomes smaller but is still significant.

Another advantage of low- $T_c$  materials is the small required LO power. For  $T^2 \ll T_c$ ,  $P_{LO} \propto T_c$ , and one can see that Al with its low  $T_c$  ( $\sim 1.6 \text{ K}$  in thin films) requires very low LO power ( $\leq 20 \text{ nW}$ ) compared to other materials with  $T_c \sim 6-10 \text{ K}$ . The bandwidth does not suffer however since it is temperature independent, in contrast to that in phonon-cooled devices. Due to the latter circumstance the diffusion-cooled mixer provides more flexibility in optimization for a particular application.

## VI. HIGH- $T_c$ HEB MIXER

Sensitive and tunable terahertz heterodyne receivers are required for several important remote-sensing and in-situ applications, including spectroscopic mapping of the earth's atmosphere, other planetary atmospheres, as well as

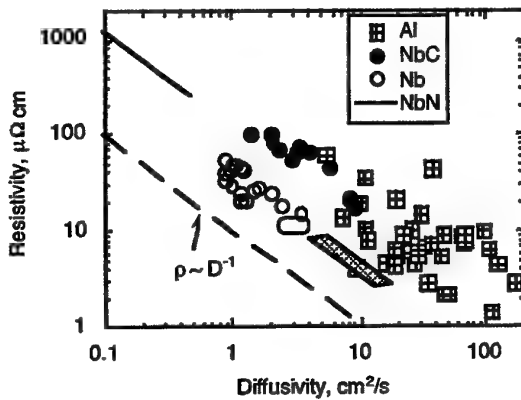


Fig. 5. The resistivity vs diffusivity data for different superconducting films. The shaded tetragonal is an extrapolation for some low-resistive Nb film (diffusivity was not measured), the oval represents the range for Nb films used at JPL.

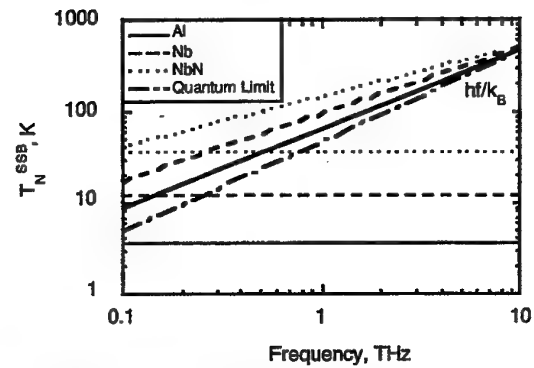


Fig. 6. Theoretical noise temperature limits for different mixer materials. The dash-and-dot line is the quantum limit.

the gases and chemical composition of comets. Today the only heterodyne instrument available for such long-duration space missions is based on a Schottky-diode mixer (see Fig. 1). The fixed-tuned RF bandwidth is less than 20%, and the required LO power is 1-3 mW which can be provided only by a bulky and power consuming FIR laser at terahertz frequencies.

During the last few years preliminary heterodyne mixing experiments have been performed with large area ( $\sim 20 \times 10 \mu\text{m}^2$ ) high- $T_c$  devices made from a 50-60 nm thick YBCO film [11]. These experiments demonstrated that (a) the mixing mechanism is bolometric (b) the mixing performance does not depend on the radiation frequency (the measurements were done between 30 THz and 300 THz), and (c) the conversion efficiency bandwidth can be as wide as  $\sim 100 \text{ GHz}$  and is determined by the intrinsic electron-phonon relaxation time in the material.

Our theoretical calculations [12] show that  $\text{YBa}_2\text{Cu}_3\text{O}_{7-\delta}$  (YBCO) HEB mixers operating at 66-77 K can perform better than Schottky-diode mixers in terms of both noise temperature and LO power requirements. A consideration of the phonon diffusion from the device into the normal metal contacts significantly increases the thermal conductance between the electron and phonons when the device length  $L \sim 0.1 \mu\text{m}$ , allowing for larger amount of the LO power per unit of volume and lower noise temperature of the mixer. Figure 7 shows the size dependence of the noise temperature and the required LO power for an optimized high- $T_c$  mixer device operated at 66 K for an intermediate frequency  $f_I = 2.5 \text{ GHz}$ . One can see that the noise temperature as low as  $\sim 2000 \text{ K}$  along with the LO power of a few  $\mu\text{W}$  might be possible for a  $0.1 \mu\text{m}$  long device fabricated from a 10 nm thick YBCO film.

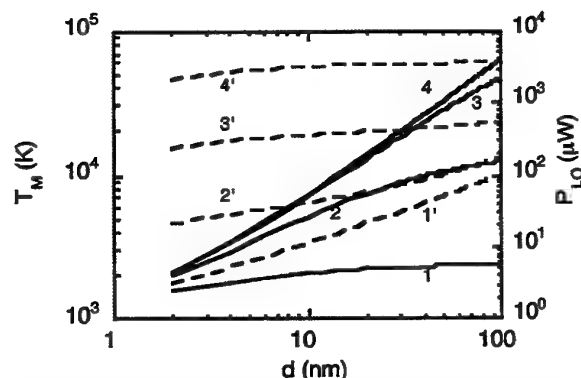


Fig. 7. Size dependence of the mixer noise temperature (solid lines) and optimal LO power (dashes). 1 and 1',  $L = 0.1 \mu\text{m}$ ; 2 and 2',  $L = 0.3 \mu\text{m}$ ; 3 and 3',  $L = 1.0 \mu\text{m}$ ; 4 and 4',  $L = 3.0 \mu\text{m}$ .

Recently we have fabricated relatively large,  $1 \times 1 \mu\text{m}^2$ , antenna-coupled devices from a 20 nm thick YBCO film on an  $\text{YAlO}_3$  substrate. Very thin high-quality films,  $\leq 20$  nm, are required to minimize the phonon escape time from the film and hence improve the thermal conductance which improves the mixer performance. Such films were produced by laser ablation on an  $\text{YAlO}_3$  substrate with a 20 nm  $\text{PrBa}_2\text{Cu}_3\text{O}_{7-\delta}$  (PBCO) buffer layer. The superconducting transition in our devices occurs at  $\sim 85$  K and the transition width is less than 2 K. A more detailed description of the whole process is given in [13].

Using a  $\text{CO}_2$ -pumped far-infrared laser, we performed RF tests of the high- $T_c$  devices at 77 K. The amount of LO power needed to maximize the mixing signal as well as the position of the optimal operating point were close to those predicted by theory [12]. However the overall RF coupling to the device was poor. The improvement of optical coupling and tests of submicron-sized devices must be performed to provide a fully convincing "proof of concept" test of this new technology.

## VII. SUMMARY

Excellent performance of diffusion-cooled Nb HEB receivers has been demonstrated at 1.1 THz and 2.5 THz with noise temperatures of 1670K and 2750K respectively. The mixer noise performance is shown to be independent of frequency from 0.5 THz to 2.5 THz. The absorbed LO power is 80 nW or less. The ultra-wide rf bandwidths (up to 1 THz) of these HEB mixers if combined with a broadband photomixer LO would allow for the first time the possibility of a single-channel heterodyne receiver with 700 to 1000 GHz of easily-tunable frequency range.

The further development of HEB mixers is seen to go both to lower and to higher temperatures. At subkelvin temperatures HEB devices for radioastronomy applications made from low- $T_c$  materials, such as Al, can demonstrate a quantum limited performance with  $\sim 10$  nW of required LO power dissipated in the device. At  $\sim 70$  K submicron size YBCO devices can outperform Schottky-diode mixers since they would require only a few  $\mu\text{W}$  of LO power. The natural niche for such mixers would be long duration atmospheric and planetary missions aimed at spectral surveys and mapping of chemical species in atmospheres.

## VIII. REFERENCES

[1] These data are taken from different sources: Schottky diode data are taken from the *Proc. of the 7th Int. Symp. on Space Terahertz Technology* (STT-7), University of Virginia, Charlottesville, VA, March 1996; SIS data are from STT-7; NbN HEB data are from STT-7, STT-8, STT-9, J. Kawamura et al., *J. Appl. Phys.* **80**, pp. 4232-4234 (1996); *Appl. Phys. Lett.* **70**, 1619-1621 (1997), and A.D. Semenov et al., *Appl. Phys. Lett.* **69**, 260-262 (1996). G.W. Schwab, *1998 SPIE Int.Symp. Astronomical Telescopes and Instrum.* (communications); Nb HEB data are from Refs. 5, 6 & 10.

[2] E.M. Gershenson, G.N. Gol'tsman, I.G. Gogidze, Y.P. Gusev, A.I. Elant'ev, B.S. Karasik, and A.D. Semenov, "Millimeter and submillimeter range mixer based on electronic heating of superconducting films in the resistive state," *Sverkhprovodimost'* (KIAE), 3(10), 2143-2160 (1990) [*Sov.Phys. Superconductivity*, 3(10), 582-1597 (1990)].

[3] D.E. Prober, "Superconducting terahertz mixer using a transition-edge microbolometer," *Appl. Phys. Lett.* **62**(17), 2119-2121 (1993).

[4] B.S. Karasik and A.I. Elant'ev, "Noise temperature limit of a superconducting hot-electron bolometer mixer," *Appl. Phys. Lett.* **68**, 853-855 (1996); "Analysis of the noise performance of a hot-electron superconducting bolometer mixer," *Proc. of the 6th Int. Symp. on Space Terahertz Technology*, 21-23 March 1995, Caltech, Pasadena, pp. 229-246.

[5] A. Skalare, W.R. McGrath, B. Bumble, H.G. LeDuc, "Measurements with a diffusion-cooled Nb hot-electron bolometer mixer at 1100 GHz", *Proc. 9th Int. Symp. on Space Terahertz Technology*, 17-19 March 1998, Hilton Hotel, Pasadena, pp. 115-120.

[6] B.S. Karasik, M.C. Gaidis, W.R. McGrath, B. Bumble, H.G. LeDuc, "Low noise in a diffusion-cooled hot-electron mixer at 2.5 THz", *Appl. Phys. Lett.* **71**, 1567-1569 (1997).

[7] B. Bumble and H.G. LeDuc, "Fabrication of a diffusion cooled superconducting hot electron bolometer for THz mixing applications", *IEEE Trans. Appl. Supercond.*, Vol. AS-7, pp. 3560-3563 (1997).

[8] P.J. Burke, R.J. Schoelkopf, D.E. Prober, A. Skalare, W.R. McGrath, B. Bumble, and H.G. LeDuc, "Length scaling of bandwidth and noise in hot-electron superconducting mixer," *Appl. Phys. Lett.* **68**, 3344-3346 (1996).

[9] R.J. Schoelkopf, P.J. Burke, D.E. Prober, B. Karasik, A. Skalare, W.R. McGrath, M.C. Gaidis, B. Bumble, H.G. LeDuc, "Noise bandwidth of diffusion-cooled hot-electron bolometers", *IEEE Trans. Appl. Supercond.*, Vol. AS-7, pp. 3576-3579 (1997).

[10] A. Skalare, W.R. McGrath, B. Bumble, H.G. LeDuc, P.J. Burke, A.A. Verheijen, R.J. Schoelkopf, and D.E. Prober, "Large bandwidth and low noise in a diffusion-cooled hot-electron bolometer mixer," *Appl. Phys. Lett.* **68**, 1558-1560 (1996).

[11] M. Lindgren, M.A. Zorin, A. Trifonov, M. Danerud, D. Winkler, B.S. Karasik, G.N. Gol'tsman, and E.M. Gershenson, "Optical mixing in a patterned  $\text{YBa}_2\text{Cu}_3\text{O}_{7-\delta}$  thin films," *Appl. Phys. Lett.* **65**, 3398-3400 (1994); V.A. Trifonov, B.S. Karasik, M.A. Zorin, G.N. Gol'tsman, E.M. Gershenson, M. Lindgren, M. Danerud, and D. Winkler, "9.6  $\mu\text{m}$  wavelength mixing in a patterned  $\text{YBa}_2\text{Cu}_3\text{O}_{7-\delta}$  thin films," *Appl. Phys. Lett.* **68**, 1418-1420 (1996).

[12] B.S. Karasik, W.R. McGrath, and M.C. Gaidis, "Analysis of a high- $T_c$  hot-electron mixer for terahertz applications," *J. Appl. Phys.* **81**(3), 1581-1589 (1997).

[13] M.J. Burns, A.W. Kleinsasser, K.A. Delin, R.P. Vasquez, B.S. Karasik, W.R. McGrath, and M.C. Gaidis, "Fabrication of high- $T_c$  hot-electron bolometric mixers for terahertz applications", *IEEE Trans. Appl. Supercond.*, Vol. AS-7, pp. 3564-3567, June 1997.

# Characterisation of Millimeter and Submillimeter Wave Mixers based on High-T<sub>C</sub> Superconductor Structures

Oliver Harnack<sup>1</sup>, Stephan Beuven<sup>1</sup>, Marian Darula<sup>1</sup>, Hermann Kohlstedt<sup>1</sup>, Michael Tarasov<sup>2</sup>  
Evgeni Stephanov<sup>2</sup>, Zdravko Ivanov<sup>2</sup>

**Abstract**—We report on our experimental studies of noise properties and conversion efficiency of high-T<sub>C</sub> Josephson mixers and high-T<sub>C</sub> hot-electron bolometric (HEB) effect mixers at frequencies between 90 GHz and 550 GHz. Noise measurements using a Josephson mixer at 90 GHz gave noise temperatures of 2900 K at 20 K. Measurements in a quasi-optical setup at 430 GHz and 546 GHz showed mixer noise temperatures of 1200 K and 1100 K at 4.2 K, respectively. Heterodyne mixing experiments using high-T<sub>C</sub> HEB mixers have been performed at temperatures around 78 K and at frequencies between 78 GHz and 119 GHz. The uncorrected conversion efficiency at an intermediate frequency of 3 GHz was measured to be -30 dB.

**Index terms**—High-T<sub>C</sub> superconductor, Josephson mixer, hot-electron bolometer mixer

## I. INTRODUCTION

Low-temperature superconductive mixers for millimeter and submillimeter wave receivers utilizing quasiparticle tunneling are known to have a high sensitivity and low power consumption. Mixers, based on high-temperature superconductors (HTS) could be attractive candidates for applications where operation temperatures above 20 K are required. All attempts to fabricate mixers based on quasiparticle tunneling in HTS junctions failed. Several reasons, such as short coherence length, nonconventional pairing mechanism, and sensitivity to processing, made it impossible to fabricate high quality tunnel junctions from HTS materials. The presently possible HTS mixers can utilize the Josephson effect or the Hot-Electron Bolometric (HEB) effect. We have investigated both types of mixers. After describing the RF setup and the calibration which was used for conversion and noise measurements, we are present the fabrication process and the characterisation of HTS Josephson and HEB mixers.

## II. RF SETUP AND CALIBRATION

The RF setup consists of a mixer block receiver system for 80 GHz to 120 GHz, assembled inside a cryostat. An external diplexer or a simple beam splitter was used to combine the signal and the local oscillator (LO) signal. For experiments at frequencies between 430 GHz and 550 GHz the junctions were mounted into a quasi-optical setup using an extended hyperhemisphere MgO lens. The down-converted intermediate frequency (IF) signal was amplified by an internal cooled amplifier or by an external room-temperature amplifier at 1.4 GHz. The ouput signal was amplified by 65 dB and limited by a bandpass with a bandwidth of 400 MHz. We calibrated the noise temperature of the IF chain by using a heatable 50  $\Omega$  load attached to the cold plate as a thermal noise source and a coaxial switch for connecting the mixer or the load to the IF system. Using the Y-factor method we calculated IF noise temperatures ( $T_{\text{if}}$ ) of 5 K for the cooled amplifier and 130 K for the room-temperature amplifier.

## III. THEORETICAL PREDICTIONS FOR THE JOSEPHSON MIXER NOISE PERFORMANCE

It is known that the sensitivity of Josephson mixers is limited by excess noise, which includes intrinsic junction noise and noise generated by internal Josephson oscillations. Theoretical studies by Likharev et al. [1] predict a minimum noise temperature of  $T_n = 10.5T(\omega/\omega_c)^2$  for normalised frequencies  $\Omega > 1$ , where  $\Omega = \omega/\omega_c$ ,  $\omega_c = 2I_cR_n e/\hbar$  is the characteristic frequency,  $I_c$  is the critical current, and  $R_n$  is the normal-state resistance. A more optimistic prediction of  $T_n = 6T$  was given for signal frequencies  $\omega$  equal to  $\omega_c$  ( $\Omega = 1$ ). Schoelkopf et al. [2] have showed that the linewidth of the internal Josephson oscillation is comparable with that frequency at bias points close to the critical current. This results in an excess noise floor at low voltages. This model predicts a minimum double side band (DSB) mixer noise temperature of  $T_n = 20T$  for  $\Omega = 0.5$

<sup>1</sup>Institut fuer Schicht- und Ionentechnik, Forschungszentrum Juelich GmbH, D-52425 Juelich, Germany

<sup>2</sup>Institute of Applied Physics, Chalmers University of Technology, Sweden

assuming a fluctuation parameter  $\gamma = 0.01$ , which is defined by  $\gamma = 2k_B T / \hbar I_c$ , the ratio of the thermal energy,  $k_B T$ , to the Josephson coupling energy,  $\hbar I_c / 2e$ . In general, the noise temperature of a Josephson mixer increases with increasing  $\gamma$ .

#### IV. CHARACTERISATION OF HIGH- $T_c$ JOSEPHSON MIXERS

##### A. Fabrication

Grain boundary junctions (GBJ) are specific for high- $T_c$  superconductors and not known for conventional metallic superconductors. This class of junctions includes step-edge junctions (SEJ) and bicrystal junctions (BCJ). The former junction type can be realized by fabricating GBs at steep substrate steps. In the latter case, a grain boundary which is present in a bicrystal substrate grows through the epitaxial HTS film during deposition.

We have fabricated SEJs and BCJs on (100) MgO substrates ( $\epsilon_r = 9.6$ ). Pulsed laser deposition method was used for growing thin YBCO films with different thickness between 50 nm and 100 nm. In order to have a low-loss antenna material, an approximately 50 nm thick gold layer was deposited in-situ on top of the YBCO film. We used standard photolithographic processes and ion beam etching (IBE) with an etching rate of 1 nm/min to define the junction and the antenna structure. The junctions were integrated into bow-tie and logarithmic-periodic antenna layouts for measurements in the waveguide and the quasioptical setup, respectively. A Josephson junction consists of a 1  $\mu\text{m}$  wide bridge which crosses a 24° grain boundary (BCJ) or a 250-nm-high substrate step (SEJ). In order to remove the shunting gold layer from the top of the bridge we defined a window across the bridge and applied IBE with an etching rate of 4 nm/min. In order to passivate the HTS bridges we evaporated a  $\text{SiO}_x$  layer of about the same thickness as the YBCO layer.

##### B. Receiver and mixer noise measurements

The noise performance and conversion efficiency of the fabricated HTS Josephson mixers have been studied at frequencies between 90 GHz and 550 GHz. All noise measurements were done by using the Y-factor method and 300 K (hot) / 77 K (cold) absorber loads. From the related IF power levels we can directly determine the receiver noise temperature  $T_{\text{rec}}$  which is connected to the mixer noise temperature  $T_m$ , the conversion efficiency  $\eta$ , and  $T_{\text{if}}$  by  $T_{\text{rec}} = T_m + \eta^{-1} T_{\text{if}}$ .

##### 1) W-band noise and conversion measurements

IF power measurements in the waveguide setup with external pumping at 90 GHz showed noise temperatures of

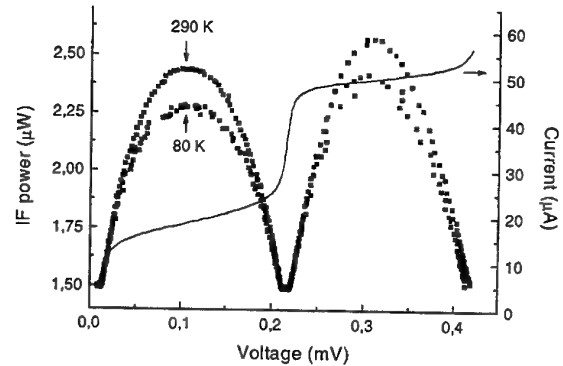


Fig. 1: IF power measurement at 90 GHz (LO) and 20 K using the standard hot/cold technique. The lowest receiver noise temperature was 2900 K.

about 2900 K at physical temperatures of 20 K and at an IF of 1.4 GHz (Fig. 1). In this case the mixer was a bicrystal junction on MgO with a critical current of 50  $\mu\text{A}$  at 20 K and a normal resistance of 14  $\Omega$ . The conversion efficiency, not corrected for the IF impedance mismatch, was approximately -10 dB. Since we have used the room-temperature amplifier, the contribution of the IF noise to  $T_{\text{rec}}$  was relatively high (about 1300 K). We estimate a mixer noise temperature of about 1600 K.

##### 2) Quasioptical measurement

Similar measurements were performed in a quasioptical setup. A 1  $\mu\text{m}$  wide bicrystal junction with a current voltage characteristic without any excess current at 4.2 K was used. The mixer noise temperature at 4.2 K and 430 GHz measured in the fundamental mixing mode was 1200 K for the junction shunted by a low-inductance resistive shunt, and 1400 K for the junction with no shunt [3]. Measurements at 546 GHz gave noise temperatures of about 1100 K (Fig. 2).

##### C. Temperature dependence of $T_N$ and $\eta$

In Fig. 3 the measured dependence of the receiver noise

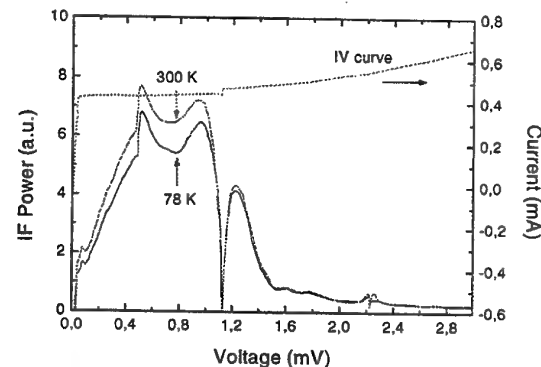


Fig. 2: IF power measurement at 546 GHz (LO) and 4.2 K using the standard hot/cold technique. The formally calculated receiver noise temperature was 1100 K.

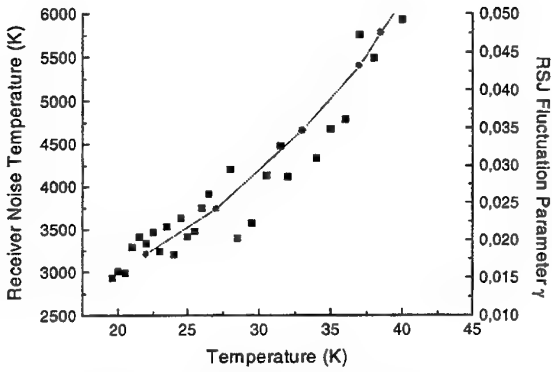


Fig. 3: The receiver noise temperature in dependence of the physical temperature at 90 GHz. The mixer was the same device as in B) 1. The curve (line) displays the RSJ fluctuation parameter  $\gamma$  at different temperatures.

Temperature of a BCJ mixer on MgO is shown between 20 K and 40 K. From the receiver output signal difference related to 77 K and 300 K input signals we calculated the uncorrected conversion efficiency  $\eta$  of the mixer using the calibration described in section II.  $\eta$  was -10.4 dB at 20 K, -11.5 dB at 30 K, and -13.5 dB at 40 K.  $\gamma(T)$  (right axis in Fig. 3) was extracted from  $I_c(T)$ . The temperature dependence of  $\gamma$  is the same as that of  $T_{rec}$  so that the increase of the noise can be well explained by the increase of  $\gamma$ . The influence of the temperature dependence of  $\eta$  seems to be less significant in this temperature range.

#### D. Optimum local oscillator power level

An optimum LO power level exists for a lowest  $T_{rec}$ , since the conversion efficiency and the mixer noise depend strongly on the level of pumping of the mixer. Fig. 4 displays the measured  $T_{rec}$  versus the suppression of  $I_c$ . The lowest  $T_{rec}$  was measured at a suppression of 75 % of the  $I_c$ . The absorbed LO power can be calculated from the height of the zeroth Shapiro step by using the resistively shunted junction (RSJ) model [4]. In this experiment the absorbed LO power was about 4 nW at the optimum point.

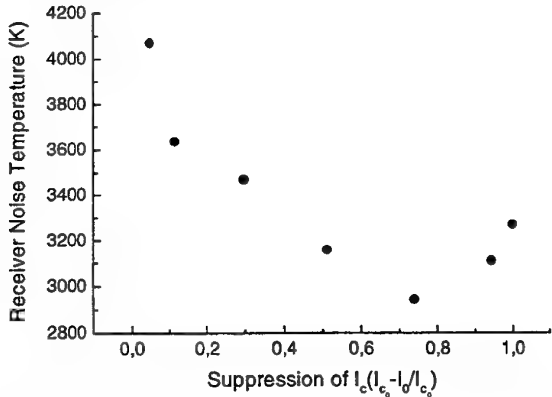


Fig. 4: Dependence of the noise temperature on the suppression of  $I_c$ . The LO frequency was 90 GHz and the operation temperature was 20 K.  $I_0$  is the height of the zeroth step,  $I_{c_0}$  is the critical current without LO.

## V. CHARACTERISATION OF HIGH-T<sub>C</sub> HOT-ELECTRON BOLOMETRIC MIXERS

Another type of mixer, which is most promising for operation in the THz regime, is the superconductive hot-electron bolometer (HEB) [5],[6]. Some of the advantages of HEB mixers are the real device impedance and the insensitivity against magnetic noise. HEB devices usually consist of a thin film microbridge which is connected to two normal metal electrodes. Absorbed rf power generates non-equilibrium „hot“ electrons, which result in an increase of the resistance of the device and a related voltage response. Depending on intrinsic relaxation mechanisms, HEB devices can be fast enough to follow the intermediate frequency oscillation of several GHz. In contrast to the Josephson mixer, HEB mixer are not limited by the energy gap. Karasik et al. published a detailed theoretical analysis of the performance of HEB mixers based on YBCO [7].

#### A. Fabrication

For the fabrication of HEB effect mixers, thin YBCO films of thickness of about 30-50 nm have been grown on MgO and sapphire substrates using the laser deposition method. In the case of sapphire we applied a 30 nm thin CeO<sub>2</sub> buffer layer between the substrate and the YBCO film. The thin YBCO films have been protected by a in-situ sputtered gold layer. Inductive  $T_c$ -measurements showed critical temperatures of 89-90 K for YBCO films on sapphire substrates and 84-86 K for films on MgO substrates. The transition widths were in the range between 0.5 and 1 K. After patterning of 1  $\mu$ m wide microbridges, integrated into bow-tie antennas for waveguide measurements, a small-area window (1  $\mu$ m by 2  $\mu$ m) was opened in the gold layer and a protection layer was applied (see IV. A.) We observed no significant degradation of the critical current density ( $J_c$ ) by using this technique.

#### B. DC characteristics

Fig. 5 shows the current-voltage characteristics of four different microbridges at 73 K. The bridges were integrated into bow-tie antennas. We used a current stabilized source for biasing the devices. The thickness  $d$  of the YBCO film was in the range 30 to 35 nm, the width  $w$  of the microbridges was 1  $\mu$ m, and the in-plane distance  $L$  between the gold electrodes was about 2  $\mu$ m. The critical current density for these devices was relatively high, in the range between  $1.9 \times 10^7$  A/cm<sup>2</sup> and  $9.6 \times 10^6$  A/cm<sup>2</sup> at 73 K. For the devices with the highest  $J_c$ , the curves show the typical thermal hysteresis which is related to the generation of hot spots along the microbridge. The normal state resistance was about 22 Ohm for all tested devices.

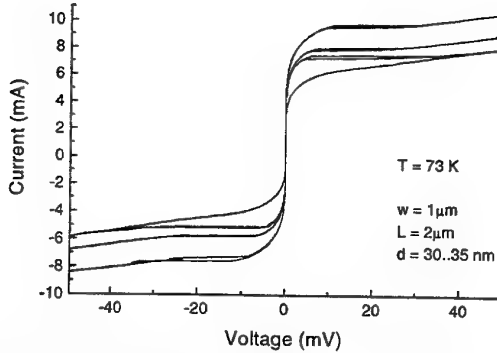


Fig. 5: DC characteristics of four microbridges on sapphire at 73 K.

### C. Heterodyne mixing and conversion efficiency

Heterodyne mixing experiments have been performed at temperatures close to the transition temperature of the bridges of 85-88 K and at frequencies between 78 GHz and 119 GHz. Fig. 6 displays the result of a mixing experiment using two monochromatic sources at 90 GHz (signal) and 91.38 GHz (LO). The physical temperature of the mixer on MgO was 78 K. Strong down-converted signals at intermediate frequencies up to 9 GHz have been obtained by using a spectrum analyser, which was directly connected to the mixer. The conversion efficiency at 3 GHz was measured to be -30 dB, including all impedance mismatch losses and front-end losses.

We attribute the IF signal to a non-equilibrium hot-electron mixing effect, since the corresponding time constant is about 110 ps. The process of electron-phonon scattering followed by phonon escape from the film into the substrate is most likely the dominant relaxation mechanism, because the in-plane dimensions of the active area are above 1  $\mu$ m. Phonon diffusion will contribute to the relaxation process as soon as the distance between both normal metal electrodes will be smaller than a few hundred nanometers [7]. Hot/cold noise measurements showed only a non-reproducible, very weak response of these HEBs. We be-

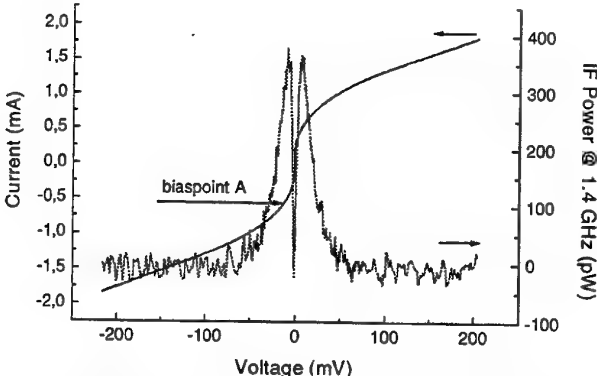


Fig. 6: Heterodyne mixing experiment at 90 GHz and 77 K using a microbridge on MgO. We also measured the IF spectrum in the current biaspoint A and obtained a strong signal at 1.38 GHz.

lieve that the conversion efficiency is too low to get a measurable down-conversion of the input noise signal. Further decrease of the in-plane dimension and the film thickness should increase the sensitivity of YBCO HEBs.

### VI. CONCLUSION

We demonstrated for the first time that low-noise mixing is possible with high- $T_c$  Josephson mixers at temperatures above 20 K. The dependence of the noise temperature on the physical temperature can be well explained by the RSJ model. The required LO power was 4 nW at 90 GHz. We measured mixer noise temperatures at 90 GHz of about 1600 K and at submillimeter waves in the range between 1100 K and 1200 K. We successfully fabricated HEB mixers on MgO and sapphire substrates and demonstrated heterodyne mixing at 90 GHz with large IF bandwidths at liquid nitrogen temperatures.

### VII. ACKNOWLEDGMENT

This work is supported by the German Ministry of Education and Research (BMBF, 13N7321/6) and in part by the European Community under Grant No. IC15-CT96-0806 (INCO-Copernicus project). We would also like to thank D. Diehl and P. Zimmermann from Radiometer Physics GmbH, K. Jacobs from KOSMA/University of Cologne, and E. Tong for useful help and fruitful discussions. We also are grateful for comments by B. Karasik and R. W. McGrath from JPL. B. Vowinkel from KOSMA provided us with the 1.4 GHz cooled amplifier.

### VIII. REFERENCES

- [1] K. K. Likharev, V. V. Migulin, *Josephson effect millimeter range receivers*, Radio Engineering and Electron Physics, v. 25, June 1980, pp. 1-18
- [2] R. J. Schoelkopf, Ph.D. dissertation, California Institute of Technology, 1995 (unpublished)
- [3] M. Tarasov, E. Stepanov, Z. Ivanov, O. Harnack, M. Darula, S. Beuven, H. Kohlstedt, in preparation for the Applied Superconductivity Conference, 1998
- [4] K. K. Likharev, *Dynamics of Josephson Junctions and Circuits*, Gordon and Breach Science Publishers, New York, 1986
- [5] E. M. Gershenson, G. N. Gol'tsman, I. G. Gogidze, Y. P. Gusev, A. I. El'ant'ev, B. S. Karasik, and A. D. Semenov, 'Millimeter and Submillimeter Range Mixer based on Electronic Heating of Superconducting Films in the Resistive State', *Sverkhprovodimost'* (KIAE), vol. 3(10), pp. 2143-2160, October 1990 [*Sov. Phys. Superconductivity*, vol. 3(10), pp. 1582-1597, 1990]
- [6] D. E. Prober, 'Superconducting Terahertz Mixer using a Transition-edge Microbolometer', *Appl. Phys. Lett.*, vol. 62(17), pp. 2119-2121, 1993
- [7] B. S. Karasik, W. R. McGrath, and M. C. Gaidis, *Analysis of a high- $T_c$  hot-electron superconducting mixer for terahertz applications*, *J. Appl. Phys.* 81 (3), 1997

# Hotspot mixing: a new principle of heterodyne mixing in a superconducting hot-electron bolometer

D. Wilms Floet, E. Miedema, J.R. Gao, and T.M. Klapwijk

**Abstract**—We present the hotspot mixing as a new principle of heterodyne mixing in a superconducting hot-electron bolometer. Applying DC and LO powers to a superconducting bridge generates a hotspot within the bridge. The size of the hotspot, thus the resistance of the bridge, oscillates with the heating power at intermediate frequency. By solving heat-conducting equations, we can predict the mixer performances, such as the conversion efficiency, as a function of *dc* bias voltage, LO power, or the bath temperature.

The experimental demonstration of heterodyne mixing with superconducting hot electron bolometer (HEB) opens a new opportunity in THz detection technology. Currently, superconducting HEB mixers are considered to be the most sensitive heterodyne detectors at frequencies far above 1 THz. The core of a HEB mixer is simply a narrow superconducting strip in contact with normal metal pads. Roughly speaking, heterodyne mixing in a superconducting HEB takes advantage of a resistance change due to the superconducting-normal phase transition. This transition is induced by radiation heating. There are several superconductors suitable for HEB mixers. Depending on the cooling mechanisms of hot electrons, one can have diffusion-cooled Nb or phonon-cooled NbN HEB mixers. Both are being intensively studied. Other superconductors, such as high- $T_c$  YBCO and low- $T_c$  Al, can also be potential useful detectors fulfilling some special applications. This is because the former, using phonon-cooling, allows a high operating temperature and the latter may give extremely low intrinsic noise.

Until we proposed a so-called hotspot mixing model<sup>1</sup>, the heterodyne mixing in a superconducting HEB was interpreted as a superconducting transition-edge<sup>2</sup>. The electron temperature in a microbridge at a bath temperature much lower than  $T_c$  is raised to near mid-point of the superconducting transition by *dc* and LO power ( $P_{LO}$ ) heating. Applying a second rf (weak) signal  $P_s$  will cause a further change of the temperature and consequently the resistance. An output voltage at the intermediate frequency can be produced if the device is biased with a current. Implicitly, the transition-edge model assumes that a change of electron temperature due to *dc* and rf heating takes place homogeneously within a bridge, in the same way as the bath temperature is elevated. However, in reality, the heating process in a superconducting microbridge does not fulfill this assumption.

It has been demonstrated by Skocpol, Beasley and Tinkham<sup>3</sup> (SBT) both theoretically and experimentally that *dc* current heating creates a local hotspot in a superconducting bridge, giving rise to a resistive state. The temperature of phonons (electrons) within this spot is higher than  $T_c$  and also higher than the bath temperature. As long as a hotspot does not exceed the bridge, its length can increase with increasing *dc* power, and thus the resistance. The existence of a hotspot is manifested by hysteresis in the *IV* curve of a superconducting bridge at temperatures much lower than  $T_c$ .

Based on the SBT model of the *IV* curve, we recently develop a new concept of heterodyne mixing for superconducting HEB<sup>1</sup>. Although here we focus our discussion on Nb diffusion-cooled HEB, this model can in principle be used to describe any type of superconducting HEBs, such as Al, NbN and even YBCO. The essence of this concept is that, two coupled rf signals ( $P_{LO}$  and  $P_s$ ) together with *dc* self-heating can generate a hotspot in a superconducting bridge. The length of the hotspot, thus the corresponding resistance, oscillates with the heating power at intermediate frequency (IF), provided that diffusion cooling is fast enough. The hotspot mixing principle is schematically illustrated in fig. 1. As usual, it is impossible for the hotspot to follow rf signals because their frequencies are too high with respect to the thermal response time.

This work is presented in 6<sup>th</sup> IEEE International Conference on Terahertz Electronics, 3-4 September, 1998, Leeds, UK.

The authors are with the Department of Applied Physics and Materials Science Center, University of Groningen, Nijenborgh 4, 9747 AG Groningen, The Netherlands.

One of the authors, J.R. Gao, is also with Space Research Organization of the Netherlands, PO Box 800, 9700 AV Groningen, The Netherlands

It is important to note that in the hotspot model the voltage responsivity  $S$  is determined by  $dL_H/dP$  and is given by:

$$S = \frac{\rho I}{dW} \left( \frac{dL_H}{dP} \right) \quad (1)$$

where  $L_H$  is the length of a hotspot,  $P$  heating power,  $I$  dc current,  $W$  the bridge width,  $d$  the thickness, and  $\rho$  dc resistivity in the normal state. In contrast to the superconducting transition-edge model<sup>2</sup>,  $dR/dT$  in the transition region (or  $\Delta T_c$ ) is no longer relevant, where  $R$  is the resistance of a bolometer.

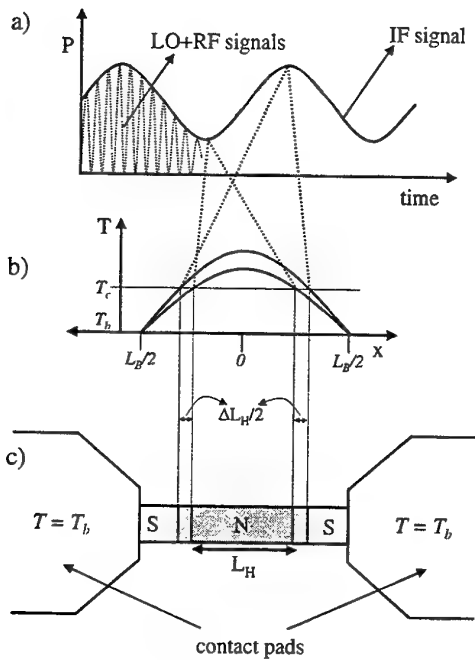


Figure 1 A schematic illustration of the hotspot mixing concept in a superconducting microbridge. (a) Two rf signals ( $P_{LO}$  and  $P_s$ ) coupled to a superconducting bridge generate a heating power at intermediate frequency. (b) and (c) The rf powers together with dc current heating produce a hotspot in the resistive state. The length of the hotspot can oscillate with ac heating power at intermediate frequency (beating frequency) assuming the thermal response is fast enough. As a result, the resistance of the bridge oscillates and a mixing output signal is generated.

To model a superconducting hotspot mixer, we write two one-dimensional heat-conduction equations, developed from the SBT model. One describes the temperature of

electrons  $T(x)$  inside a hotspot  $|x| < L_H/2$ , where the hotspot is assumed to be in the middle of a bridge.

$$-K_N \frac{d^2 T}{d x^2} + \frac{c_e}{\tau_{e-p}} (T - T_b) = \left( \frac{I}{wd} \right)^2 \rho + p_{LO} \quad (2a)$$

Here  $K_N$  is the thermal conductivity in the normal state,  $K_S$  the thermal conductivity in the superconducting state,  $T_b$  the bath temperature.  $c_e$  the electron-heat capacity,  $\tau_{e-p}$  the electron-phonon interaction time, and  $p_{LO}$  absorbed LO power density (per unit volume).

In comparison with the SBT model, we have made two modifications: i) one heat transfer process is via electron-phonon scattering. To derive an analytical solution, we further assume that this heat transfer has simple temperature dependence  $T - T_b$ ; ii) we include the heating of LO signal.

The other equation describes the temperature outside a hotspot  $|x| > L_H/2$ ,

$$-K_S \frac{d^2 T}{d x^2} + \frac{c_e}{\tau_{e-p}} (T - T_b) = p_{LO} \quad (2b)$$

To solve these two equations, we assume that:

- the incoming rf signals have frequencies higher than the Nb gap frequency. Thus  $p_{LO}$  is independent of  $x$ ;
- $K_S = K_N$  although in reality  $K_S < K_N$ . Also, the value is independent of  $x$ ;
- sharp interfaces between hotspot region and superconducting region. This means the superconducting transition width  $\Delta T_c \rightarrow 0$ . A hotspot can be formed if  $T > T_c$ ;
- we take  $T|_{x=\pm L/2} = T_b$ , where  $L$  is the bridge length. For simplicity, we solve these equations in the diffusion-cooling limit, namely that a thermal healing length  $(D\tau_{e-p})^{1/2}$  being much longer than the length of a bridge. Here  $D$  is the diffusion constant.
- We neglect the charging-imbalance effect<sup>1</sup> near the interface between the superconducting and hotspot regions.

By calculating a relation between  $I$  and  $L_H$ , we are able to determine the properties of a superconducting HEB mixer, such as, electron temperature profile, the voltage responsivity  $S$ , and the conversion efficiency  $\eta$  ( $= P_{IF} / P_s$ ) using dc bias voltage, LO power, or the bath temperature as a variable parameter.

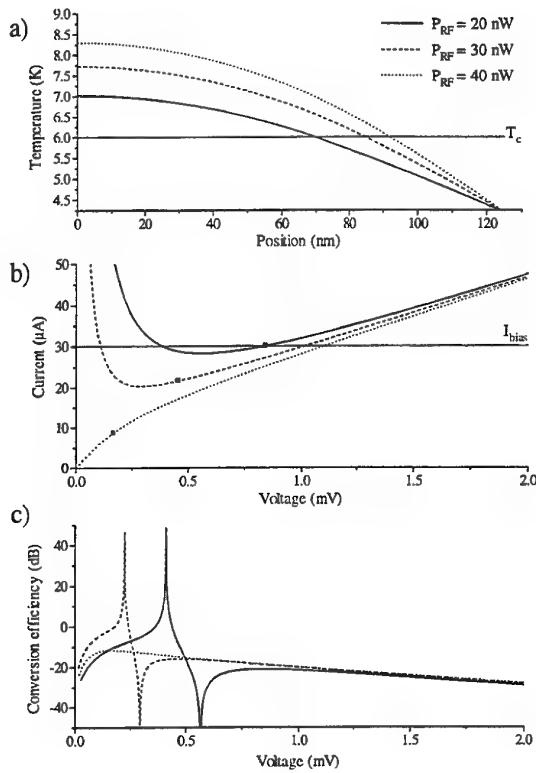


Figure 2 (a) Calculated electron temperature as a function of position within a bridge, where  $x=0$  corresponds to the mid-point of the bridge. Different profiles and thus different hot-spot lengths correspond to the rf heating power. Here  $dc$  bias current is fixed. The bridge length  $L=250$  nm, the bath temperature  $T_b=4.2$  K, and the LO power  $P_{LO}=20$  nW, 30 nW, and 40 nW. (b) The corresponding  $IV$  curves. (c) Calculated conversion efficiency as a function of  $dc$  bias voltage.

As an example, Fig. 2 shows calculated the temperature profile, the  $IV$  curves, the conversion efficiency  $\eta$  (single sideband) as a function of  $dc$  bias voltage with variable LO power  $P_{LO}$ . The HEB is a Nb bridge with  $d=10$  nm,  $L=250$  nm, and  $L/W=2$ . The normal state resistance equals  $50\ \Omega$  in this case. The bath temperature is 4.2 K.

For the calculation of the mixer conversion efficiency, as usual, we first calculate the voltage responsivity  $S$  and derive subsequently the conversion efficiency. We also take IF impedance matching into account by using a model described in ref. 4. We use the dynamical resistance of the bolometer, which is calculated from the  $IV$  curve, as the output impedance at IF and choose  $50\ \Omega$  for the load impedance.

The electron temperature profile of the microbridge is given in fig2 (a), calculated for three different LO power values,  $P_{LO}=20$ , 30, and 40 nW, but with a fixed bias current of 30  $\mu$ A. Varying  $P_{LO}$  results in the different temperature profiles. It is clear from this result that the hotspot lengths

correspond to rf heating levels. The importance of this result is that, firstly, the temperature of electrons is not constant along the bridge. Therefore, a superconducting HEB can not be simply treated as a lumped element. When dealing with mixer noise, one has to take the electron temperature distribution into account. To our knowledge, how to describe the mixer noise for such a distributed device is still an open question. Secondly, the electron temperature as indicated by the calculation can be considerably higher than the  $T_c$ . Thus, the model<sup>2</sup> using a  $T_c$  as a typical electron temperature for the determination of the mixer noise temperature has to be reconsidered.

For the  $IV$  curves with different  $P_{LO}$ , our calculations suggest that with a relatively low  $P_{LO}$ , to form a hotspot,  $dc$  heating power is needed. This explains why there is a negative dynamical resistance region at low  $dc$  bias. This negative dynamical resistance region disappears when the pumping level increases and becomes 40 nW. This is because the  $P_{LO}$  is higher enough to generate a hotspot within the bridge, even without  $dc$  heating.

The conversion efficiencies under different pumping levels are plotted in Fig. 2 (c). For the low pumping levels ( 20 nW and 30 nW), the oscillations of the conversion efficiency start when  $dc$  bias voltage becomes low and the dynamical resistance becomes negative, as a result of the IF impedance matching. However, this is not the case when the  $P_{LO}=40$  nW. since there is no negative dynamical resistance region in this case. To quantify  $\eta(\max)$ , we list the maximal value of  $\eta$  (SSB) for each  $P_{LO}$  at the bias voltages before the oscillations occur. These are -21 dB for  $P_{LO}=20$  nW and  $V_{DC}=0.85$  mV, -16 dB for  $P_{LO}=30$  nW and  $V_{DC}=0.46$  mV, and -12 dB for  $P_{LO}=40$  nW and  $V_{DC}=0.17$  mV. These values are consistence with a measured value in a Nb diffusion-cooled HEB mixer<sup>5</sup>, which is -14.4 dB (SSB).

**ACKNOWLEDGEMENT:** The authors would like to thank P. de Korte for his support and discussions. We also thank W. F. M. Ganzevles and G. de Lange for their useful discussions on this subject. This work is financially supported partly by the Stichting voor Technische Wetenschappen which is part of the Nederlandse Organisatie voor Wetenschappelijk Onderzoek and partly by ESA under contract No. 11738/95/NL/PB.

## References

1. D. Wilms Floet, J.J. Baselmans, J.R. Gao, and T.M. Klapwijk, in Proc. 9th Int. Symp. on Space Terahertz Technology, 17-19 March, 1998, Pasadena, USA , p63.
2. D.E. Prober, *Appl. Phys. Lett.* **62**, 17 (1993); B.S. Karasik and A.I. Elantev, *Appl. Phys. Lett.* **68**, 853(1996).
3. W.J. Skocpol, M.R. Beasley, and M. Tinkham, *J. Appl. Phys.* **45**, 4054(1974).

4. E.M. Gershenzon, G.N. Gol'tsman, I.G. Gogidze, Y.P. Gusev, A.I. Elant'ev, B.S. Karasik, and A.D. Semenov, Sov. Phys. Superconductivity 3, 1582(1990).
5. A. Skalare, W.R. McGrath, B. Bumble, H.G. LeDuc, P.J. Burke, A.A. Verheijen and D.E. Prober, *Appl. Phys. Lett.* **68**, 1558(1996).

# A 2.5 THz Receiver Front-End for Spaceborne Applications

M.C. Gaidis<sup>a</sup>, H.M. Pickett, P.H. Siegel, C.D. Smith<sup>b</sup>, R.P. Smith, S.C. Martin  
*Jet Propulsion Laboratory, California Institute of Technology, Pasadena, CA 91109*

**Abstract**— The OH radical is an important player in known ozone depletion cycles; however, due to its location in the atmosphere, it must be studied from either a balloon or spaceborne platform. For long-term mapping over large portions of the earth, a spaceborne platform is the most desirable. NASA's Earth Observing System Microwave Limb Sounder instrument is slated to house a 2.5 THz Schottky-diode receiver for such measurements. Here we describe the design, fabrication, and testing of the engineering model receiver front end. This is the precursor to the first terahertz heterodyne receiver to be flown in space.

## I. INTRODUCTION

The OH radical plays a significant role in a great many of the known ozone destruction cycles, and has become the focus of an important radiometer development effort for NASA's Earth Observing System (EOS) Chem I satellite, which will monitor and study many tropospheric and stratospheric gases and is scheduled for launch in 2002 [1]. The Microwave Limb Sounder (MLS) instrument on this satellite is the only near-term opportunity to obtain global measurements of this important radical.

The lowest order OH doublets at 2510 and 2514 GHz fall fortuitously close to a strong methanol laser line at 2522 GHz. A receiver noise of 20,000 K, SSB provides enough sensitivity for daily global stratospheric maps of OH above 35 km and weekly zonal maps above 18 km from a limb-sounding satellite in polar orbit. These requirements are consistent with the performance that can be obtained from state-of-the-art room-temperature Schottky diode mixers. The molecular oxygen line at 2502 GHz can also be monitored as a pressure/altitude indicator.

The challenges of producing such sensitive mixers are numerous, but for this application, there is the added challenge of designing a robust receiver which can withstand the environmental extremes of a rocket launch and five years in low earth orbit. In this presentation, we discuss the design and implementation of the first terahertz heterodyne receiver scheduled to be flown in space.

## II. RECEIVER FRONT END DESIGN

The receiver front-end used to detect the OH radical at 2.5 THz consists of the following components and is schematically outlined in Figure 1:

<sup>a</sup> E-mail: gaidis@merlin.jpl.nasa.gov

<sup>b</sup> C.D. Smith is with Swales Aerospace, Pasadena, CA 91107.

We would like to acknowledge the many valuable contributions of the following people: J. Apodaca, P. Bruneau, T. Cox, T. Crawford, A. Deslis, V. Ford, R. Kovac, T. Lee, C. Mann, E. Mueller, J. Oswald, A. Pease, J. Podosek, P. Stimson, R. Tsang, J. Voeltz, and U. Zimmerman.

This research was performed at the California Institute of Technology, Jet Propulsion Laboratory, under contract with the National Aeronautics and Space Administration's Office of Advanced Concepts and Technology and the Earth Observing System Microwave Limb Sounder Project Office.

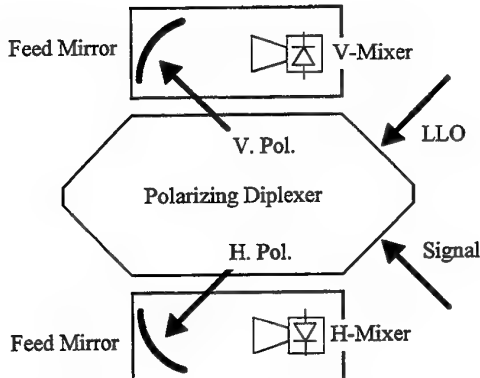


Fig. 1. Schematic diagram of the quasi-optical components in the 2.5 THz receiver front end.

- A diplexer to combine the OH signal and the laser local oscillator (LLO)
- Elliptical feed mirrors to shape the beams of the mixer feedhorns
- Fundamental Schottky-diode mixers for horizontal and vertical polarizations
- Support structures allowing simple, rugged alignment
- Low noise IF amplification chain (not pictured) from 7 to 22 GHz.
- Mixer bias circuitry (not pictured).

Note that the space-qualified LLO is a complex subsystem in itself, and is not included here as part of the front-end. However, it should be mentioned that the LLO technology is quite well developed, and will deliver more than 20 mW of 2.5 THz power for only  $\square$  125 W of spacecraft power. The LLO is  $75 \times 30 \times 10$  cm in size, and 20 kg in mass [2].

Shown in Figure 2, the engineering model (EM) diplexer is a dual-polarization Martin-Puplett type. The diplexer's dual-polarization operation serves to lower the system noise by  $\square 2$  and provide the redundancy so important to space flight missions. The design has been optimized for stand-alone use, ruggedness, mass, volume, and thermal stability. It receives 45° linear polarization from the laser local oscillator and the signal, and generates two output beams: one with horizontal and one with vertical polarization. The two 45 mm free-aperture wire grid polarizers incorporate 5  $\mu\text{m}$  diameter gold-coated tungsten wire on 12.5  $\mu\text{m}$  centers [3]. The path difference responsible for constructive interference at both LO and signal frequencies is nominally set at 9.972 mm with invar spacers on one of the rooftop mirror mounts. This path length offers ideally 94% LO coupling, 84% coupling at 8.4 GHz IF, 99% at 12.8 GHz IF, and 46% at the less-critical 20.4 GHz oxygen line IF band. To allow for machining tolerances, a mechanism is used to give  $\pm 200 \mu\text{m}$  in fine adjustment of this path length. The adjustment is accomplished with a circular "adjuster wheel" which rotates about a shoulder bolt 200  $\mu\text{m}$  off-center. The

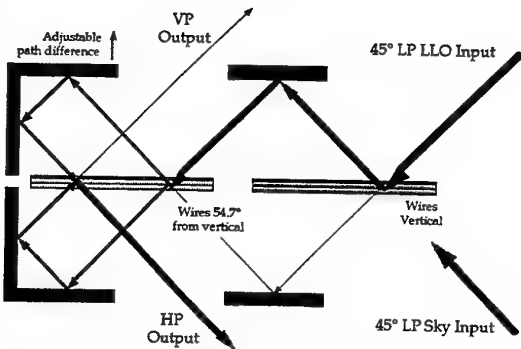


Fig. 2. Diplexer principle of operation. The right most grid splits the two input signals into two components (each). The heavy line follows the reflected half of the LLO input. The left most grid splits this into two components, and interferometrically combines them after these two components are subjected to slightly different path lengths. The path length difference is adjusted such that the vertical portion of the LLO appears horizontal at the "HP Output" port. The horizontal portion of the LLO travels through the right most grid, and appears as vertical at the "VP Output" port. The inverse is true for the sky input.

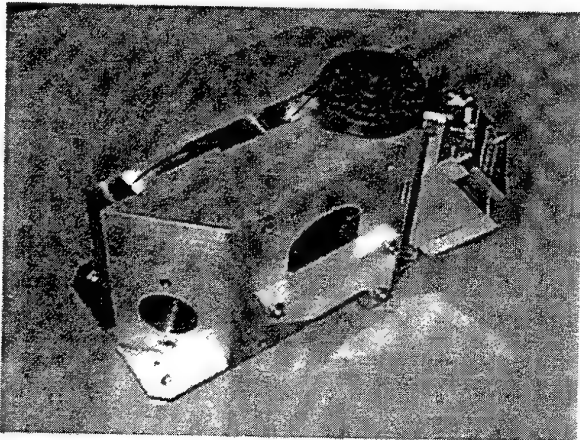


Fig. 3. 2.5 THz diplexer. One can see the LO input port at bottom left, the vertical-polarization output in the center, and the adjuster wheel with tilting roof mirror at the top right. For volume and shape concerns, the diplexer has been fashioned into a "3-D" version of that diagrammed in Figure 2.

wheel contacts an invar spacer, and is eccentrically rotated to tilt the rooftop mirror mount, causing a change in path length with a negligible effect on beam location. This mechanism is secured with epoxy before flight, and the rooftop mirror mount is spring-loaded to withstand vibration. Figure 3 shows the engineering-model diplexer and its adjustment mechanism.

The feed mirrors are diamond-turned off-axis ellipsoids which convert the rapidly diverging feedhorn beam to a well-collimated beam suited for best diplexer performance. All mirrors are optically accurate, allowing the difficult receiver alignment to include the use of a HeNe laser and an optical autocollimating alignment telescope.

We use a dual-mode Pickett-Potter conical feedhorn [4] to collect the radiation into a single-mode 2.5 THz rectangular waveguide which in turn feeds a mixer. The mixers we are presently implementing are GaAs Schottky monolithic membrane diodes (MOMEDs), designed and fabricated at the Jet Propulsion Laboratory [5]. The mixers utilize a new fabrication technique which offers more robust construction than existing whisker-contact corner-cube designs, while maintaining state-of-the-art noise performance.

The LO power requirements of these mixers ( $< 5$  mW) is modest enough to permit use of a low-power laser LO.

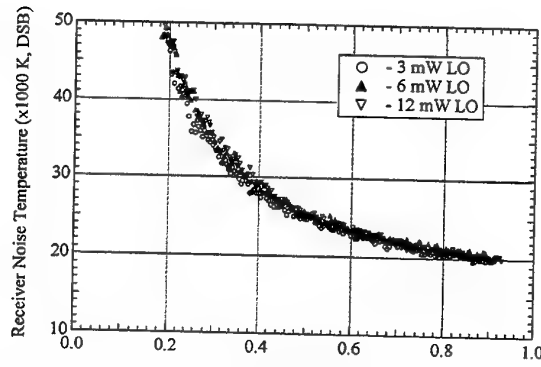


Fig. 4. Receiver noise vs. current at an IF of 8.4 GHz, demonstrating the use of current bias to reduce sensitivity to LO fluctuations. A factor of  $\square$  4 in LO power results in virtually no input noise temperature change.

Fluctuations of laser power will be minimized through the use of three feedback loops, one of which uses the mixer DC signal to eliminate standing wave variations created by thermal changes as the spacecraft orbits the earth. Future work will also implement novel planar-whisker contacted waveguide mixers from the Rutherford Appleton Laboratory [6].

A resistive bias-tee arrangement has been chosen to offer protection to the mixers, while providing a DC bias path for the Schottky diode with minimal impact on the IF throughput. We have designed and implemented a differential feedback circuit to provide a stiff current bias with good immunity to noise pickup. The current bias also serves to reduce sensitivity of the device to LLO power fluctuations. As shown in Figure 4, a factor of 4 change in LO power results in virtually no change of input noise temperature. Conversion gain behaves similarly. Other devices we have tested exhibit somewhat more sensitivity to LO power. Our thinking at present is that the IF transformer match is not as good for these other devices, and the LO power fluctuations result in device impedance changes which have non-negligible effect on the receiver characteristics. The IF transformer is a 7 - 22 GHz quartz suspended-substrate stripline step transformer, typically  $250 \square$  at the mixer end, and  $50 \square$  at the amplifier. Recent measurements suggest a lower impedance transformer may improve the match on these devices. Low-noise (150 K) IF amplifiers with AC-coupled inputs [7] handle the downconverted mixer output before sending the signal to the spacecraft's second amplification stage and spectrometer modules. Figure 5 shows the assembled front end

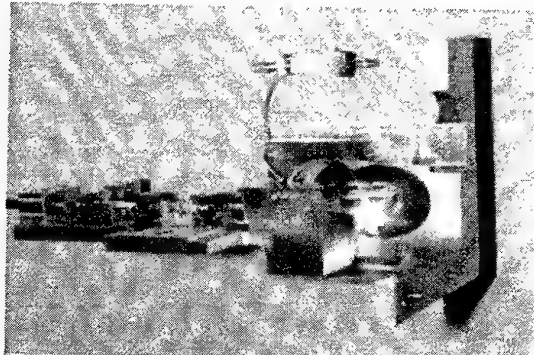


Fig. 5. Closeup of receiver front end components. The chain includes an off-axis elliptical feed mirror, the mixer, a 7 to 22 GHz IF amplifier, a clamped attenuator, and a clamped semi-rigid coax. DC bias for the mixer is presently fed through the connector at top. The face to the right bolts to a long edge of the hexagonal diplexer.

components.

### III. 2.5 THZ MIXER TEST SYSTEM

Accurate RF noise measurements at 2.5 THz are complicated by several factors: high mixer noise temperatures, variable atmospheric attenuation, poorly calibrated "absolute power" detectors, unavailability of matched attenuators, "gray" body loads, and imperfect Gaussian beams. The measurement test system used here to overcome these difficulties is schematically shown in Figure 6. At this time, relatively few measurements have been made in demonstrating the successful operation of the flight-type diplexer, as a more flexible Martin-Puplett type diplexer [8] was used for earlier receiver measurements.

The noise temperatures are measured using the standard Y-factor technique on the full receiver only (that is, including the diplexer and atmospheric losses, and the addition of noise by the bias tee and the IF amplifier). A chopper switches the signal beam between a hot and a cold load during the measurement. A lock-in detector at the  $\square$  100 Hz chopper frequency extracts a hot/cold load power output variation from a crystal diode detector. A filter is placed in front of the crystal diode detector to select the IF band of interest: 8.4 GHz, 12.8 GHz, or 20.4 GHz. The filter bandwidth is  $\square$  700 MHz.

After converting the lock-in signals from RMS to peak-to-peak values, we combine with the average DC output power to give the hot and cold powers needed for an accurate Y-factor calculation. This technique can be used to evaluate receivers with noise in excess of 500,000 K, DSB. It has

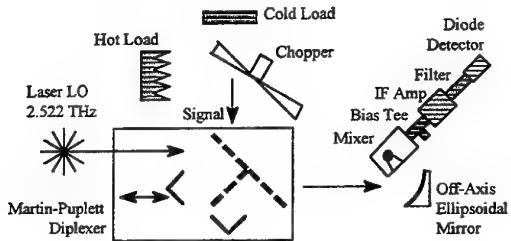


Fig. 6. Schematic of the 2.5 THz mixer test system. It is designed for sensitive measurement of high-noise devices, flexibility, and rapid computer-controlled measurements.

been demonstrated that the noise temperature measured with the test system is consistent with that measured on the actual EM diplexer.

### IV. MOMED SCHOTTKY DIODE MIXERS

The Schottky-diode mixers and the mixerblock housings have been previously described [5]. To date, we have extensively RF tested 13 different devices of varying designs. Seven of these devices have given receiver noise temperatures of better than 22,500 K, DSB at 8.4 GHz IF. This group has nominal anode sizes of 0.2  $\mu$ m by 1  $\mu$ m. Three of the poorer performers had 0.1 by 1  $\mu$ m anodes, and the others suffered design or mounting problems. Figures 4, 7, and 8 show data from three different devices of the low-noise group.

Figure 7 plots receiver noise versus DC diode bias voltage, for LO power levels between  $\square$  2 and 5 mW. The receiver performance measured here is competitive with that of the best reported in the literature [9], particularly when one considers the fine quality of the beam from the Pickett-Potter horn. Another device (that of Figure 4) showed the

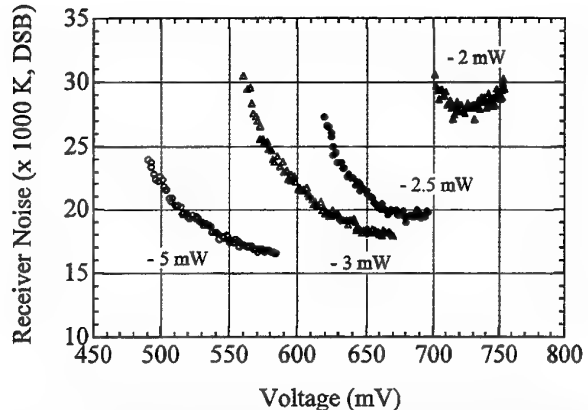


Fig. 7. Measured receiver noise temperature for a JPL MOMED device, with LO power levels between 5 mW and  $\square$  2 mW. The best receiver (system) noise temperature obtained was 16,500 K, DSB, with the maximum available LO power of  $\square$  6 mW.

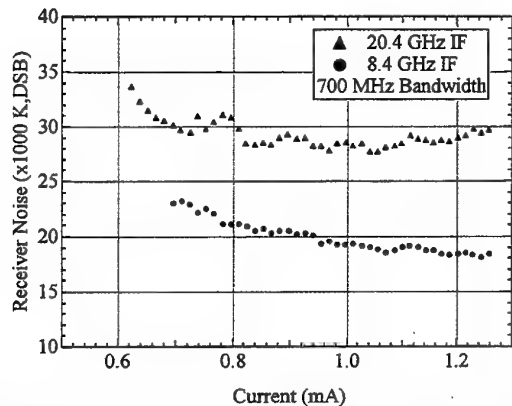


Fig. 8. Receiver noise vs. current at intermediate frequencies of 8.4 GHz and 20.4 GHz. Note the minimum in the 20.4 GHz curve, presumably due to better IF match at moderate currents.

same noise temperature vs. current curve for LO power levels of  $\square$  3 mW and  $\square$  22 mW. It appears the IF match is responsible for variations in noise with LO power, and we are actively testing this theory at the present time.

In support of this idea, Figure 8 compares receiver performance at 8.4 and 20.4 GHz. The 8.4 GHz curve suggests that the combined RF and IF match is best at high current (low dynamic resistance). However, the 20.4 GHz curve exhibits a minimum in noise temperature at an intermediate current. Because the 20.4 GHz IF is such a small fraction of the 2.5 THz LO frequency, it is unlikely that the difference in noise temperature and in the shape of the curves is due to an RF effect. Rather, higher loss and sensitivity to structures with mixer block dimensions make the 20.4 GHz channel more difficult to treat at IF. Network analyzer return loss measurements on this mixer indicate that at 20.4 GHz, the IF transformer is indeed best matched for intermediate DC bias current. Straightforward modifications in the transformer and the mixerblock housing are expected to improve the IF match for all three frequency bands.

Also interesting to note is the return loss measurements for 8.4 GHz predict a best IF match at a relatively low current ( $\square$  0.5 mA). The behavior in Figure 8 would then suggest that the RF match would improve if the diode impedance were lower (e.g., at higher bias). In addition, the poor performance of the smaller 0.1 x 1  $\mu$ m anode devices (typically  $\square$  50,000 K rather than 20,000 K) provides

support for lower impedance diodes. We are in the process now of testing  $0.4 \times 1 \mu\text{m}$  anode devices and expect to have results in the very near future.

## V. QUALIFICATION FOR SPACEFLIGHT

Although it is possible to create a low noise terahertz receiver in the laboratory, a serious challenge exists in making it robust enough for practical use. Much effort has gone into the design of the receiver front end so that it will withstand the environmental extremes of vibration during launch. The nature of the device and its mounting fixtures make the other environmental effects less difficult to deal with: thermal, vacuum, and radiation effects are not a serious problem in the EOS-MLS spacecraft. It is yet another chore to ensure the 5 year lifetime of the mission.

The spaceflight qualification of the front end began with a balloon flight of a breadboard model front end. The front end performed without a problem, and some useful OH data was retrieved.

To further establish the reliability of the mixers, the mixer blocks were subjected to thermal testing. Rapid thermal cycling (4 cycles from  $-50^\circ\text{C}$  to  $+100^\circ\text{C}$ , 20 min dwell times at each extreme) was performed on 6 devices, and found to have no noticeable effect on the DC device characteristics. As thermally-induced damage is potentially the most difficult problem to circumvent, the test results offer a good deal of reassurance that the JPL MOMED mixers will perform well in a flight environment. The predicted flight survival temperature range for the EOS-MLS THz receiver front end is from  $-20^\circ\text{C}$  to  $+55^\circ\text{C}$ .

The small size of the MOMED mixers makes them relatively insensitive to the low-frequency vibration experienced during launch. The rest of the front end is quite susceptible to damage. To test the robustness of the design, the assembled front end was subjected to the following random vibration, for 3 minutes each in x, y, and z axes (expected to mimic the launch environment):

20 - 50 Hz	+6 dB/octave
50 - 500 Hz	0.2 g <sup>2</sup> /Hz
500 - 2000 Hz	-6 dB/octave
Overall	13.0 g (rms).

Figure 9 shows the assembled front end on the z-axis

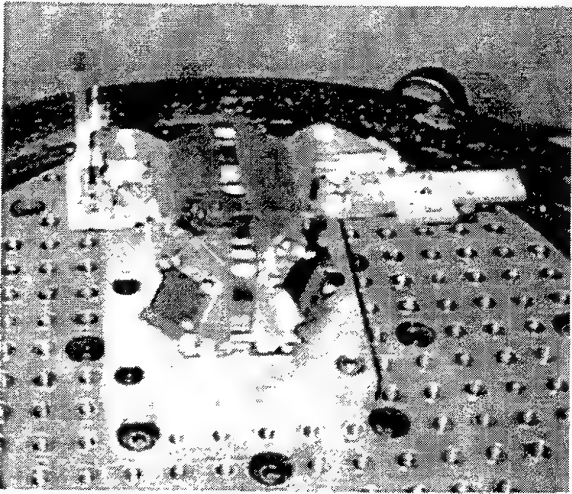


Fig. 9. Assembled receiver front end, mounted on the electrodynamic shake table. Note the "vertical" mixer on the left, and the "horizontal" mixer on the right. The diplexer adjuster wheel is atop the roof mirror on the left.

shake table. The front end survived vibrational testing quite well, with the only defect noted to be the cracking of an epoxy joint used to secure the horizontal mixer block SMA connector. RF coupling, noise temperature, and DC I-V characteristics were otherwise identical before and after the test. We do not plan to use epoxy in such a manner for the flight receiver.

The burden of operation in a vacuum environment primarily places requirements on the types of epoxies allowed, and on the thermal difficulties due to lack of convection. Simulations have been performed to estimate temperatures around the receiver front end, and predict no problems. The diplexer is designed to be insensitive to temperature, and harmful thermal gradients are minimized.

The predicted total radiation dose over the 5 year mission life is 60 krad (Si). Proton irradiation of the device will not be an issue because it is surrounded by  $\square 5$  mm of brass mixerblock. In addition, GaAs diodes are known to be relatively immune to total-dose effects resulting from the deposition of ionizing energy [10].

To ensure mixer lifetimes in excess of the 5 year mission, accelerated lifetests with fit to an Arrhenius-lognormal degradation are planned to begin in early 1999. Parameters used to define a device failure are expected to include  $I_{\text{sat}}$ ,  $R_s$ ,  $\eta$ , as well as the low-frequency noise signature of the device. It is hoped that one can use the low frequency noise as a diagnostic as well as a measure of degradation [11].

## VI. SUMMARY

Excellent performance of fixed-tuned Schottky-diode receivers in a robust, stand-alone receiver configuration has been demonstrated. Such performance is required for monitoring of atmospheric chemistry, as well as several important remote-sensing and in-situ applications [12]. With the concurrent development of low-power, compact THz laser local oscillators, this technology is realizable in a spaceborne platform. Work in the near future will concentrate on noise temperature reduction, environmental testing, and device lifetime testing.

## VII. REFERENCES

- [1] J.W. Waters, "The Chlorine Threat to Stratospheric Ozone," *Engineering and Science*, 3 - 13 (Summer, 1993), and H.M. Pickett and D.B. Peterson, "Comparison of Measured Stratospheric OH with Prediction," accepted for publication in the *Journal of Geophysical Research*.
- [2] E.R. Mueller, W.E. Robotham, Jr., R.P. Meissner, R.A. Hart, J. Kennedy, and L.A. Newman, "2.5 THz Laser Local Oscillator for the EOS Chem 1 Satellite," *Proc. 9th Int'l Symp. on Space THz Tech.*, Pasadena, CA, 563 - 572 (1998).
- [3] Graseby Specac, 500 Technology Court, Smyrna, GA 30082
- [1] H.M. Pickett, J.C. Hardy, and J. Farhoomand, "Characterization of a Dual-Mode Horn for Submillimeter Wavelengths," *IEEE Trans. Micr. Theory Tech.*, 32, 936 - 937 (1984).
- [2] P.H. Siegel, R.P. Smith, M.C. Gaidis, and S. Martin, "2.5 THz GaAs Monolithic Membrane-Diode Mixer," submitted to *IEEE Trans. Micr. Theory Tech.*, June 1998.
- [3] B.N. Ellison, B.J. Maddison, C.M. Mann, D.N. Matheson, M.L. Oldfield, S. Marazita, T.W. Crowe, P. Maaskant, and W.M. Kelly, "First Results for a 2.5 THz Schottky Diode Waveguide Mixer," *Proc. of the 7th Int'l Symposium on Space THz Tech.*, Charlottesville, VA, 494 - 502 (1996).
- [4] Miteq model JSD2-00010, Miteq Inc., 100 Davids Drive, Hauppauge, NY 11788
- [5] Thomas Keating, Ltd., Station Mills, Billingshurst, West Sussex, RH14 9SH, England
- [6] H.P. Roser, H.W. Hubers, T.W. Crowe, and W.C.B. Peatman, "Nanostructure GaAs Schottky Diodes for Far-Infrared Heterodyne Receivers," *Infrared Phys. Technol.*, 35, 451 - 462 (1994).

- [7] S. Kayali, G. Ponchak, and R. Shaw, "GaAs MMIC Reliability Assurance Guidelines for Space Applications," JPL Publication 96-25 (1996).
- [8] L.K.J. Vandamme, "Noise as a Diagnostic Tool for Quality and Reliability of Electronic Devices," *IEEE Trans. Electron. Devices*, **41**, 2176 - 2187 (1994).
- [9] E.R. Mueller, personal communication.

# A Hot-Electron Bolometer Mixer Receiver for the 680 - 830 GHz Frequency Range

Raymond Blundell, Jonathan H. Kawamura, C. Edward Tong, D. Cosmo Papa, Todd R. Hunter, Gregory N. Gol'tsman, Sergei I. Cherednichenko, Boris M. Voronov and Eugene M. Gershenson

**Abstract**— We describe a heterodyne receiver designed to operate in the partially transparent atmospheric windows centered on 680 and 830 GHz. The receiver incorporates a niobium nitride thin film, cooled to 4.2K, as the phonon-cooled hot-electron mixer element. The double sideband receiver noise, measured over the frequency range 680 - 830 GHz, is typically 700 - 1300 K. The instantaneous output bandwidth of the receiver is 600 MHz. This receiver has recently been used at the SubMillimeter Telescope, jointly operated by the Steward Observatory and the Max Planck Institute for Radioastronomy, for observations of the neutral carbon and CO spectral lines at 810 GHz and at 806 and 691 GHz respectively. Laboratory measurements on a second mixer in the same test receiver have yielded extended high frequency performance to 1 THz.

are two classes of this type of mixer. The first, proposed by Gershenson [4], relies on a strong electron-phonon interaction to cool the excited electrons. The second, subsequently proposed by Prober [5], relies on cooling the electrons through normal metal sinks at either end of the mixer element. For radioastronomy, the main factors that characterize a heterodyne receiver system are the receiver noise, input frequency range and instantaneous operating bandwidth. Other factors such as cryogenic requirements and ease of operation are often considered secondary. To date, a number of groups have demonstrated relatively low-noise mixer performance using the NbN phonon-cooled mixer [6,7,8]. Whereas, groups working with the diffusion-cooled mixer have largely concentrated on improving the instantaneous operating bandwidth.

## I. INTRODUCTION

In the frequency range 100 - 1000 GHz niobium based superconductor-insulator-superconductor (SIS) mixer receivers currently offer the lowest noise performance, and so are the preferred choice for radioastronomy spectral line observations. Above about 1000 GHz however the noise performance of these receivers significantly degrades due to fundamental limitations in the superconducting material. A potentially promising SIS mixer material for higher frequency use is NbN. Unfortunately, early experiments with NbN SIS mixers yielded significantly poorer performance [1] than the technologically more developed Nb mixers at the same frequency, 205 GHz. More recently experiments with NbN SIS mixers have been made at 700 GHz [2], and NbTiN) films show promise in low-loss tuning circuits for SIS mixers [3]. It is, however, and with minimal experimental justification, the superconducting hot electron mixer that has become the mixer element of choice for development in the 1 - 3 THz frequency range. There

## II. INSTRUMENT DESIGN

### A. Mixer Design

The mixer design is essentially a scaled version of our earlier HEB mixers [8]. These were based on SIS mixers we developed [9,10,11] for the Sub-Millimeter Array of the Smithsonian Astrophysical Observatory. The mixer is of the waveguide type and is made in two sections. The front section carries the integrated corrugated horn feed, which is electroformed and press-fit into a copper block. The back section houses a short length of waveguide, 0.28 mm x 0.07 mm, the length of which is chosen so as to provide a reasonable input match to the mixer element over the signal input frequency band. The IF output from the mixer is taken from one end of a quartz substrate that supports the HEB element which is suspended between the two halves of the mixer block.

### B. Hot electron bolometer elements

The mixer elements are made from high purity NbN films, deposited on crystalline quartz substrates, and are defined using electron beam lithography. Although higher quality NbN films, and hence wider bandwidth films, have been deposited on both sapphire and silicon substrates, we use crystalline quartz as the supporting substrate as this simplifies the overall mixer design. The key parameter in achieving wide IF bandwidth with the phonon-cooled mixer

Raymond Blundell, Cheuk-yu Edward Tong, D. Cosmo Papa and Todd Hunter are with the Harvard-Smithsonian Center for Astrophysics, 60 Garden Street, Cambridge, MA 02138, Jonathan H. Kawamura is with the California Institute of Technology, 320-47, Pasadena, California, 91125, Gregory N. Gol'tsman, Sergei I. Cherednichenko, Boris M. Voronov and Eugene M. Gershenson are with the Moscow State Pedagogical University, Moscow, Russia

is the quality of the NbN film. In general, for a given superconductor, the film quality is related to its transition temperature: the higher the  $T_c$  the better the film. However, the film thickness is also critical for efficient phonon cooling of the electrons, to achieve efficient cooling we use 4 nm thick films.

### C. Test Receiver System

For test purposes the receiver is housed in a liquid-helium filled cryostat equipped with a liquid nitrogen cooled radiation shield. This type of cryostat has a liquid helium hold time in excess of 12 hours and is well-suited for laboratory use. Local oscillator (LO) and signal inputs are combined in a Martin-Puplett polarizing interferometer placed directly in front of the cryostat vacuum window, a 0.2 mm thick Teflon sheet. The mixer block is bolted directly to the cryostat cold-plate and is cooled to 4.2 K. IF output from the mixer passes via a bias tee and an isolator to an IF amplifier, also bolted to the cryostat cold-plate. This amplifier has a center frequency of 1.5 GHz and a noise temperature of about 5 K. Signal output from the receiver then passes through a filter, 600 MHz wide, and is then further amplified by room-temperature stages.

## III. LABORATORY TESTS

A number of different mixer elements covering a wide range of parameter space in normal state resistance, critical current, critical temperature and physical size have been tested in the above set-up. A typical current-voltage (I-V) curve for a mixer element cooled in the mixer block to 4.2 K is shown in figure 1. Also shown in the figure is the I-V curve with optimum LO power applied for low-noise mixing. The receiver output, measured using the full 600 MHz IF bandwidth, in response to alternating hot (295 K) and cold (77 K) loads placed at the receiver input is used to determine the receiver noise temperature. The receiver noise has been measured in this way at frequencies across the receiver operating bandwidth, from 680 GHz to 830 GHz. We should note that the receiver's response is relatively flat in noise temperature across the operating bandwidth, rising from about 700 K at the lowest frequency to about 1,300 K at 830 GHz. Since hot electron mixers are known to have limited instantaneous bandwidth, we have also measured the receiver noise performance across its IF bandwidth, we see no degradation in performance across the IF band.

## IV. TEST OBSERVATIONS

The test HEB mixer receiver has been installed at the Sub-Millimeter Telescope Observatory, a joint operation of the University of Arizona, Steward Observatory, and the Max Planck Institute for radioastronomy. In order to test the

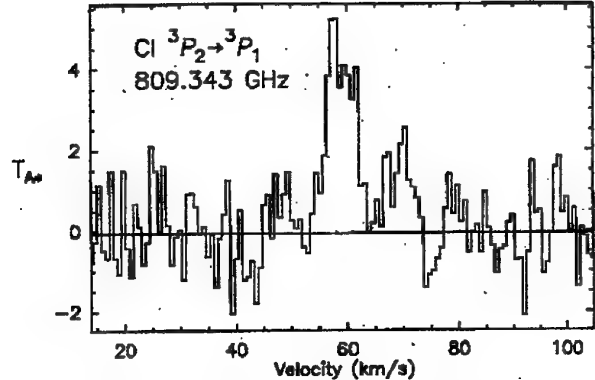


Figure 1: The  $^3P_2 \rightarrow ^3P_1$  fine structure transition of neutral carbon, towards G34.3+2.

receiver's performance, a series of test observations were made on astronomical sources in the frequency range 690 - 830 GHz. Initial experiments focussed on continuum observations of Venus; these were used to estimate the telescope efficiency and to provide a rough check on the beam shape of the antenna. These measurements were also used to update the telescope-pointing model required so that other astronomical data could be obtained. A number of spectral line observations were then made on several astronomical sources. Initially we looked at the ultracompact HII region G34.3+02. This source was chosen as it is known to contain lines of many species including the  $^3P_2 \rightarrow ^3P_1$  fine structure transition of neutral carbon and, being extended in size, is less subject to telescope pointing errors. Figure 1 shows the spectrum obtained after integrating for about one hour. In this case the receiver noise temperature was about 1400 K DSB, giving a system temperature of about 60,000 K with an atmospheric opacity of 1.8. We subsequently made measurements of the CO (7→6) at 806 GHz and (6→5) at 691 GHz transitions in the evolved star IRC+10216.

## V. FUTURE WORK

We are currently developing a facility version of this hot electron mixer receiver system for installation at the Sub-Millimeter Telescope in time for the next winter observing season. The main improvements between this system and the test version will be an increase in IF bandwidth and an increase in cryogen hold-time. We are preparing an IF amplifier chain and autocorrelator to provide 800 MHz instantaneous bandwidth, and are currently transferring the cold receiver components into a hybrid cryostat that has a 1-week hold time between liquid helium fills and should allow for easier telescope operation. Since high frequency waveguide mixer chips are quite delicate and easily broken, we have produced a second mixer block in which HEB mixer elements can be tested.

Using the second mixer block, we have also tested the receiver at 1 THz. In figure 2 we show the mixer I-V curves with and without optimum LO power applied and the receiver output in response to hot and cold input loads. Referring to the figure, we calculate the receiver noise temperature to be about 2,100 K at an LO frequency of 1.002 THz.

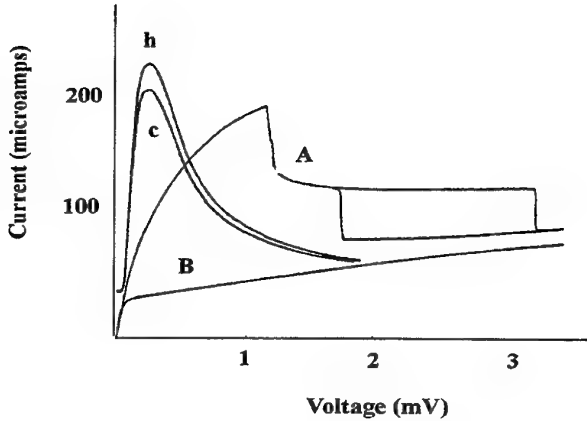


Figure 2: Measured current-voltage characteristic of HEB mixer: (A) without LO power, and (B) with optimum LO power at 1.002 THz. Also shown is the receiver output (on a linear scale) in response to (h) hot, 295 K, and (c) cold, 77 K loads placed at the receiver input.

## VI. CONCLUSION

We have developed a hot electron mixer test receiver for the frequency range 650 - 850 GHz. We have demonstrated the first use of the superconducting hot electron mixer receiver: we have detected the spectral lines of CI at 809 GHz and CO at 691 GHz and 806 GHz at the Sub-Millimeter Telescope Observatory (SMTO). Finally, initial measurements on a second mixer block yield superior noise performance at 800 GHz and extended frequency coverage to 1 THz.

## ACKNOWLEDGEMENT

We thank Peter Strittmatter of the Steward Observatory for his interest in this work, and for allocating valuable observing time to us at the SMTO. We also thank Tom Wilson of the SMTO for supporting this work, and for providing logistical support for our observations. A special thanks to Ferdinand Patt who provided technical support and helped interface the receiver to the telescope, and to the staff of the SMTO for assisting in our observations. Finally, we are indebted to Michael Smith for the care and

skill with which he prepared many receiver components, most notably the machining of the mixer blocks.

## REFERENCES

1. W. R. McGreath *et al.*, "Low-noise 205 GHz SIS Mixers using High Current Density Nb and NbN Tunnel Junctions," *Proceedings of the 2nd Int. Symp. on Space Terahertz Technology*, Pasadena, CA, PP. 423-438, 1991.
2. Y. Uzawa, Z. Wang, and A. Kawakami, "All NbN quasi-optical SIS mixers at terahertz frequencies," *Proceedings of the 8th Int. Symp. on Space Terahertz Technology*, Cambridge, MA, pp. 301-309, 1997.
3. J. W. Kooi, J. A. Stern, G. Chattopadhyay, H. G. LeDuc, B. Bumble, and J. Zmuidzinus, "Low-Loss NbTiN Films for THz Mixer Tuning Circuits," *Proceedings of the 8th Int. Symp. on Space Terahertz Technology*, Cambridge, MA, pp. 310-318, 1997.
4. E. M. Gershenzon, *et al.*, "Millimeter and Sub-millimeter Range Mixer based on Electronic Heating of Superconducting Films in the Resistive State," *Sov. Phys. Superconductivity*, 3, pp. 1582-1597, 1990.
5. D. E. Prober, "Superconducting Terahertz Mixer using a Transition-Edge Microbolometer," *Appl. Phys. Lett.* 62, pp. 2119-2121, 1993.
6. H. Ekstrom, E. Kollberg, P. Yagubov, G. Gol'tsman, E. Gershenzon, and S. Yngvesson, "Gain and Noise Bandwidth of NbN Hot Electron Bolometric Mixers," *Appl. Phys. Lett.*, 70, pp. 3296-3298, 1997.
7. C. Rosch, T. Lehnert, C. Schwoerer, M. Schicke, K. H. Gundlach, K. F. Schuster and F. Schafer, "Low-noise NbN Phonon-Cooled Hot Electron Bolometer Mixers at 810 GHz," *Proceedings of the 9th Int. Symp. on Space Terahertz Technology*, Pasadena, CA, pp. 53-61, 1998.
8. J. Kawamura, R. Blundell, C. E. Tong, G. Gol'tsman, E. Gershenzon, B. Voronov, and S. Cherendichenko, "Phonon-Cooled NbN HEB Mixers for Submillimeter Wavelengths," *Proceedings of the 8th Int. Symp. on Space Terahertz Technology*, Cambridge, MA, pp. 23-28, 1997.
9. R. Blundell, *et al.*, "A Wideband Fixed-Tuned SIS Receiver for 200 GHz Operation," *IEEE Trans. Microwave Theory Tech.* 43, pp. 933-937, 1995.
10. C. E. Tong, *et al.*, "Design and Characterization of a 250-350 GHz Fixed-Tuned Superconductor - Insulator - Superconductor Receiver," *IEEE Trans. Microwave Theory Tech.* 44, pp. 1548-1556, 1996.
11. C. E. Tong, R. Blundell, B. Bumble, J. A. Stern, and H. G. LeDuc, "Sub-Millimeter Distributed Quasiparticle Receiver Employing a Non-Linear Transmission Line," *Proceedings of the 7th Int. Symp. on Space Terahertz Technology*, Charlottesville, VA, pp. 47-62, 1996.

# Circuit Level Modelling of Spatially Distributed mm and sub mm-Wave Systems

Michael B. Steer, Mete Ozkar and Carlos E. Christoffersen

**Abstract**—Modelling of millimeter-wave and submillimeter-wave systems have generally been developed from a circuit perspective with the effect of the electromagnetic environment modeled essentially as lumped elements. Recent developments in steady-state and transient analyses integrating circuit and electromagnetic modeling are presented.

## I. INTRODUCTION

In millimeter-wave and submillimeter-wave circuits the electromagnetic environment has a crucial effect on system performance. Generally design proceeds with a very large amount of intuition and limited modeling. The pioneering work of Eisenhart and Khan [1] exemplifies an approach to modeling the effect of waveguide-based structures. In this work described it was shown for the first time that quite sophisticated and accurate models could be developed for a three-dimensional waveguide system. This model has been used extensively in the design of post mounted waveguide components. The model developed is compatible with simple nonlinear circuit simulation. Millimeter-wave and submillimeter wave circuits are becoming ever more commercially viable and along with the large scale production design practices must evolve to be more sophisticated.

Millimeter-wave and submillimeter wave circuits are generally simple consisting of single-ended active circuits driving a one-port “electromagnetic” environment. Recently a new family of millimeter-wave circuits has been proposed and are being explored. These are the active spatial or quasi-optical power combining structures. Most spatial power combining systems can be illustrated by the configurations in Figure 1 [2], [3], [4], [5], [6]. Here a waveguide horn spreads the energy from an input waveguide over a surface that could be several wavelengths on a side. This spatially distributed signal impacts an array of amplifiers perhaps arranged in a grid, or an array of coupled slots, etc. The reverse function is implemented on the obverse side where the output from the individual amplifiers is combined to produce a single coherent output beam.

Recent advances in the new technology of two-dimensional quasi-optical power combining promise significant progress in bringing the advantages of solid

state monolithic technology to moderate and high power millimeter-wave applications. A major characteristic of the conventional quasi-optical circuits is the use of three-dimensional free space for the power combining. In [8], [9] and [10] this concept is extended leading to the development of a quasi-optical system which combines power in two dimensions such as shown in Figure 2. The 2D geometry can lead to circuits which are less sensitive to instabilities and are easier to optimize for efficiency as well as being smaller and lighter.

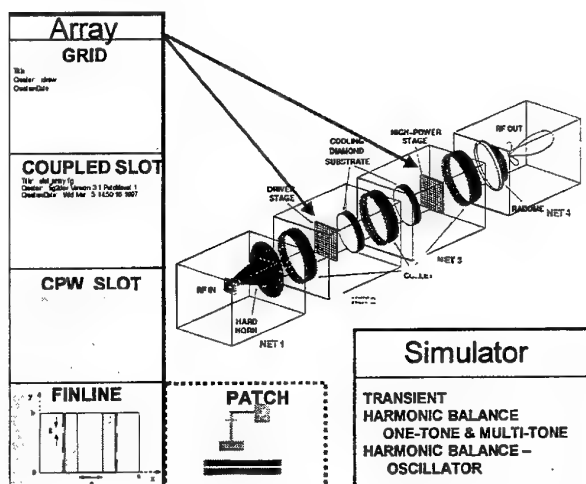


Figure 1. A three dimensional transmission-mode spatially distributed amplifying system.

Spatial power combining systems are complex the electromagnetic environment is crucial to the operation of the system. In this paper necessary strategies for analyzing such structures are discussed. Modeling and simulation are important for their own right. Just as importantly characterization serves the purpose of increasing the understanding of the intrinsic behaviour of these systems and can serve to isolate effects that can then be addressed one by one to achieve desired performance.

The authors are with the department of Electrical and Computer Engineering, North Carolina State University, Raleigh, NC 27695-7911, U.S.A. [m.b.steer@ieee.org](mailto:m.b.steer@ieee.org).

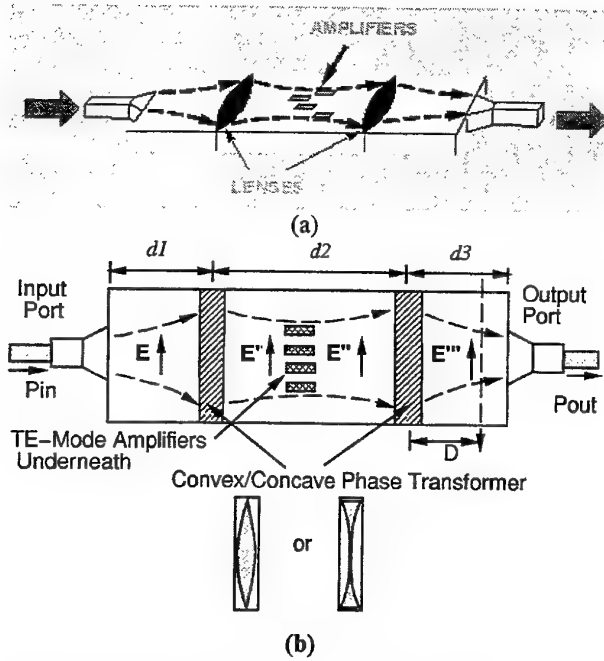


Figure 2. A two dimensional travelling wave mode spatially distributed amplifying system.

## II. DEVELOPMENT

The major obstacle to integrating electromagnetic analysis with circuit analysis and hence conventional simulation is that circuits represent a very high level of abstraction. The reverent appreciation of this quickly evolves when trying to merge disparate forms of modeling. A circuit is essentially a simple graphical construct for coupling together algebraic and first order differential equations. These various equations arise from the constitutive relations of the individual elements and Kirchoff's current law specifies what form these individual equations must be in, and how the equations are coupled. Circuits do get a bit more sophisticated than this but this is the essential abstraction. The analysis thus described is called nodal admittance analysis. It is important to note that circuits have no sense of space – a circuit is defined as though it existed at point. How then is an electromagnetic structure which inherently is distributed in space to be inserted in to this system? Two approaches are being pursued. One of these is to insert the device equations into an appropriate electromagnetic simulator such as a finite difference time domain (FDTD) simulator [12], [13]. This approach reduces the level of abstraction of the “circuit” and embeds the constitutive relations of the conventional circuit elements in the analysis grid of the FDTD method. An alternative is to retain the high-level circuit abstraction and incorporate the results of a field analysis (the spatially distributed circuit) into a circuit structure [11], [14], [15], [16], see Figure 3. Thus the problem is one of taking an electromagnetic solution and using a physically consistent approach to inserting the field solution into a circuit solution. At this point it is useful to review modified nodal admittance (MNA) analysis. MNA analysis was developed to handle elements that do not have admittance descriptions. For these offending elements additional

equations are added to the nodal admittance equations and these equations become additional rows and columns in the evolving matrix system of equations. A similar approach can be followed for the electromagnetic elements. The process is a little more sophisticated, it is no longer sufficient to add additional rows. Instead the concept of local reference nodes was developed [7] based on the earlier compression matrix approach [16]. This concept provides another way to incorporate alternate equations in the evolving MNA matrix. However, rather than adding additional constitutive relations, the local reference node concept changes the way the port-based parameters are used. The process begins by dividing and conquering. The first decision is that the nonlinear circuit should be the point of integration. Figure 4 shows a circuit with a spatially distributed circuit and with a global reference node indicated by the conventional inverted triangle symbol. In a conventional circuit only one reference node (ground) is possible so that KCL is applied to the currents in the red dotted oval of Figure 4. This global reference node introduces one additional redundant row in the indefinite form of the MNA matrix. With the local reference node concept shown in Figure 5 with the local reference nodes indicated by the diagonal symbol, KCL is applied to one locally referenced group at a time. The local reference nodes are not electrically connected and so KCL applied to each of the locally referenced groups, here M, results in M redundant rows in the MNA matrix. Modifications to standard circuit theory are required to handle this situation [7]. The local reference node concept is the nodal equivalent of the reference terminal of a group of ports.

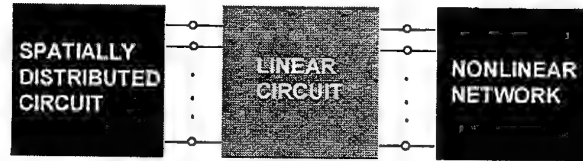


Figure 3. Partitioning of a system into a spatially distributed part, a linear circuit part and a nonlinear network part.

## III. STEADY-STATE CASE STUDY: A GRID AMPLIFIER

One of the benefits of modelling and characterization is the physical insight that is gained. An example will be presented in this section. Figure 6 shows a quasi-optical grid amplifier with input and output horns and here 4 unit amplifiers located at the intersection of horizontal and vertical grid lines. (Correlation of measured and simulated nonlinear performance was presented previously [15].) The horizontal lines act as the input antennas of the amplifiers and the vertical lines are the output radiators. In the originally constructed amplifier, Figure 7(a), the simulated field profile of Figure 7(b) was found. In the modified amplifier of Figure 9(a) with closer attention paid to circuit symmetry the field profile of Figure 9(b) was calculated. Note that the beam is not centered in the original circuit but is centered in the modified circuit. Similar beam centers were also found experimentally. Simulation of larger grid structures

indicated another cause of non-ideal performance resulting from geometric (or grid) symmetry and circuit symmetry which are incompatible with each other. The solution is to embed groups of unit cells in larger unit structures to more closely approximate common grid and circuit symmetries.

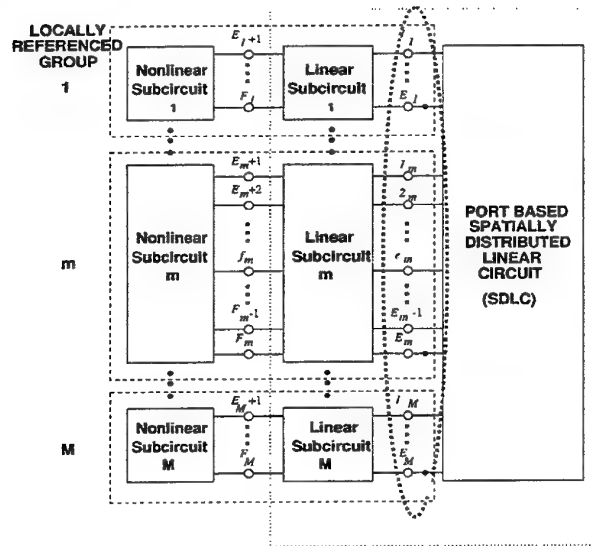


Figure 4. A conventional circuit with a single global reference node.

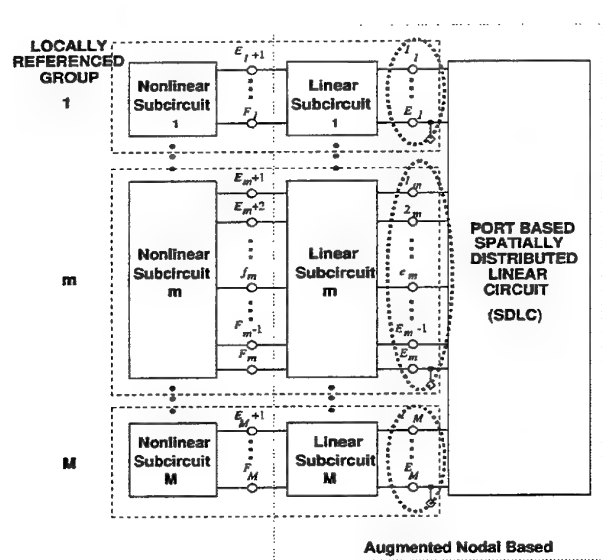


Figure 5. A circuit with local reference nodes.

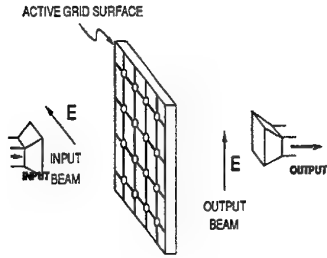
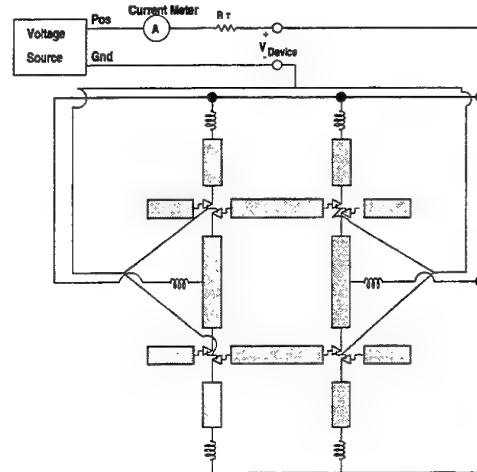


Figure 6. A quasi-optical grid amplifier between an input and output horns.



(a)

BEAM  
CENTER

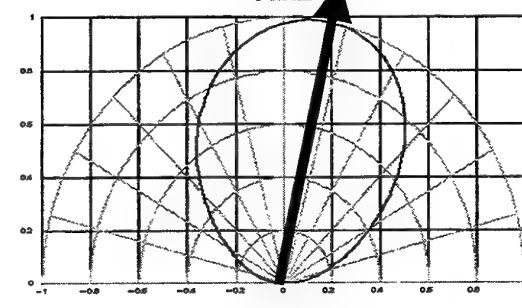
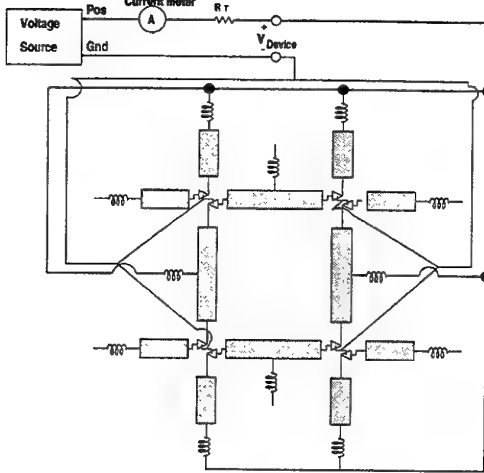
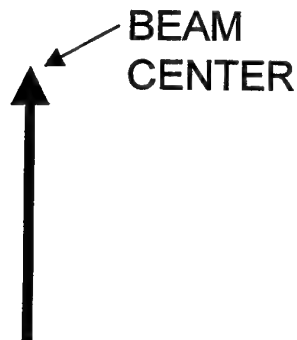


Figure 7. Calculated field profile of a 2x2 grid amplifier with "non-ideal" symmetry.



(a)



(b)

Figure 8. Calculated field profile of a  $2 \times 2$  grid amplifier with corrected symmetry: (a) circuit schematic and (b) calculated field profile.

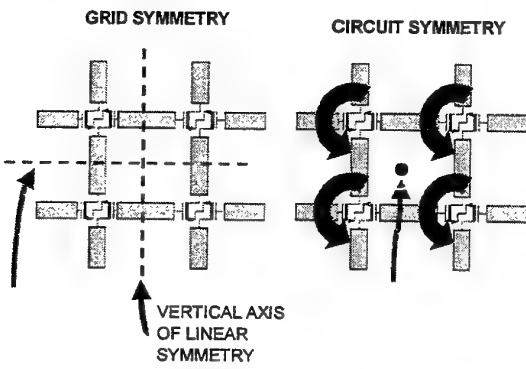


Figure 9 . Grid and circuit symmetry in a grid amplifier.

#### IV. TRANSIENT CASE STUDY: NONLINEAR TRANSMISSION LINE

In the previous example a method of moments field solver was used to characterize the electromagnetic

environment. Method of moments analysis is attractive as it naturally produces port-based parameters. Integration of the port-based parameters works, in general if state-variables are implemented as unknowns in the circuit solver. This has been achieved in steady-state (harmonic balance) solvers for some time but only recently has this been implemented in a transient solver. In our analysis of quasi-optical systems and nonlinear transmission lines we use a convolution of the impulse response of the linear network parameters with the current-voltage relations of an active device. The impulse response is obtained as the inverse Fourier transform of the frequency domain parameters. It is crucial that the this domain-to-domain conversion be physical. This means that the response be frequency limited (in the frequency domain linear circuit characterization) and time-limited (in the equivalent time-domain characterization). One way of achieving this is shown in Figure 10, where absorbing elements (resistors) are used to damp the transient response, and reactive elements are used to bandlimit the frequency domain response. Furthermore delay modification is required to zero the imaginary response at  $F_{MAX}$  (or use Hilbert transforms) so that aliasing is controlled [17]. The effect of the lossy elements and of the additional delay is removed during subsequent transient iteration. Measured and calculated responses of a 47 diode nonlinear transmission line are shown in Figure 11.

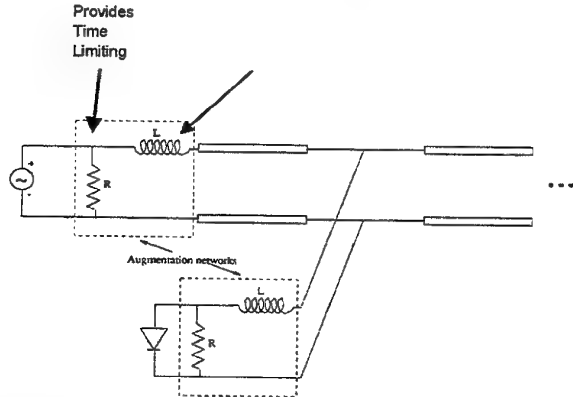


Figure 10. Strategies for controlling domain-to-domain transformation.

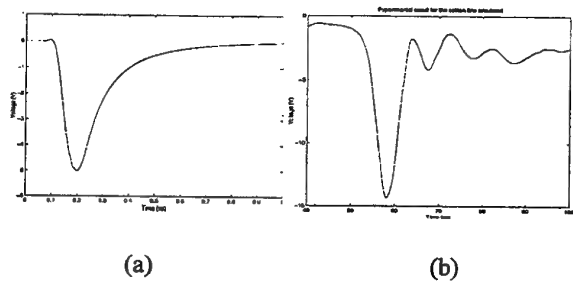


Figure 11. Response of a nonlinear transmission line at diode number 47 : (a) simulated results and (b) measured result.

## V. CONCLUSION

The modeling of high frequency systems integrating electromagnetic field characterization with circuit characterization has been shown to be entirely do-able. Considerable attention must be paid to the interface to ensure that the connection of different solution domains is physically correct. The same is true of domain-to-domain conversions. Several key concepts have been developed to facilitate the integrated analysis: 1) the local reference node concept; 2) impulse response/convolution using state variables; 3) frequency limiting using physical elements for aliasing control; 4) time limiting and 5) delay modification.

## VI. ACKNOWLEDGEMENTS

This work was supported in part by the Defense Advanced Research Projects Agency (DARPA) through the MAFET Thrust III program as DARPA agreement number DAAL01-96-K-3619.

## VII. REFERENCES

- [1] R.L. Eisenhart and P.J. Khan, "Theoretical and experimental analysis of a waveguide mounting structure," *IEEE Trans. Microwave Theory Tech.*, vol. 19, pp. 706-719, Aug. 1971.
- [2] T. Ivanov, S. Ortiz, A. Mortazawi, E. Schlecht, and J. Hubert, "A Passive Double-Layer Microstrip Array for the Construction of Millimeter-Wave Spatial Power-Combining Amplifiers," *IEEE Microwave and Guided Wave Letters*, vol. 7, pp. 365-367, Nov. 1997.
- [3] S. Hollung, A. E. Cox, and Z. B. Popovic, "A Bi-Directional Quasi-Optical Lens Amplifier," *IEEE Trans. on Microwave Theory and Techn.*, pp. 2352-2357, Dec. 1997.
- [4] A. Alexanian and R. A. York, "Broadband waveguide-based spatial combiners," *IEEE MTT S Int. Microwave Symp. Digest*, pp. 1139-1142, June 1997.
- [5] C.-M. Liu, M. P. De Lisio, Member, IEEE, A. Mousessian, and D. B. Rutledge, "Stability of grid amplifiers *IEEE Trans. Microwave Theory Tech.*, vol. 46, pp. 779-784, June. 1998.
- [6] M. P. De Lisio, S. W. Duncan, D.-W. Tu, C.-M. Liu, A. Mousessian, J. J. Rosenberg, and D. B. Rutledge, Modeling and performance of a 100-element pHEMT grid amplifier, *IEEE Trans. Microwave Theory Tech.*, vol. 44, pp. 2136-2144, Dec. 1996.
- [7] A. I. Khalil and M. B. Steer, "Circuit theory for spatially distributed microwave circuits," *IEEE Transactions On Microwave Theory and Techniques*, Oct. 1998.
- [8] C. W. Hicks, H.-S. Hwang and M. B. Steer, J. W. Mink, and J. Harvey, "Spatial power combining for two dimensional structures," *IEEE Transactions On Microwave Theory and Techniques*, pp. 784-791, June, 1998.
- [9] A. R. Perkins, Y. Qian and T. Itoh, "TM Surface-Wave Power Combining by a Planar Active-Lens Amplifier," *IEEE Trans. on Microwave Theory and Techn.*, pp. 775-773, vol. 46, June 1998
- [10] H.-S. Hwang, C. W. Hicks, M. B. Steer, J. Harvey and J. W. Mink, "A quasi-optical dielectric slab power amplifier with a large amplifier array," *Proc. 1998 IEEE Antennas and Propagation Symposium*, June 1998, pp 482-485.
- [11] E. Larique, S. Mons, D. Baillargeat, S. Verdeyme, M. Aubourg, P. Guillon, and R. Quere, Electromagnetic Analysis for microwave FET modeling *IEEE microwave and guided wave letters* Vol 8, pp. 41-43, Jan. 1998.
- [12] S. M. S. Imtiaz, and S. M. El-Ghazaly, Global Modeling of millimeter-wave circuits: electromagnetic simulation of amplifiers, *IEEE Trans. on Microwave Theory and Tech.*, vol 45, pp. 22082217. Dec. 1997.
- [13] C.-N. Kuo, R.-B. Wu, B. Houshmand, and T. Itoh, Modeling of microwave active devices using the FDTD analysis based on the voltage-source approach, *IEEE Microwave Guided Wave Lett.*, vol. 6, pp. 199-201, May 1996.
- [14] T. W. Nuteson, H. Hwang, M. B. Steer, K. Naishadham, J.W.Mink, and J. Harvey, "Analysis of finite grid structures with lenses in quasi-optical systems," *IEEE Trans. Microwave Theory Techniques*, pp. 666-672, May 1997.
- [15] M. B. Steer, M. N. Abdullah, C. Christoffersen, M. Summers, S. Nakazawa, A. Khalil, and J. Harvey, "Integrated electro-magnetic and circuit modeling of large microwave and millimeter-wave structures," *Proc. 1998 IEEE Antennas and Propagation Symp.*, pp. 478-481, June 1998.
- [16] J. Kunisch and I. Wolff, "Steady-state analysis of nonlinear forced and autonomous microwave circuits using the compression approach," *Int. J. of Microwave and Millimeter-Wave Computer-Aided Engineering*, vol. 5, No. 4, pp. 241-225, 1995
- [17] P. Perry and T. J. Brazil, "Hilbert-Transform-Derived Relative Group Delay," *IEEE Transactions on Microwave Theory and Techniques*, vol. 45, pp. 1214-1225, Aug. 1997.

# Accurate Modelling of Quasi–Optical Frequency Multipliers Excited by a Gaussian Beam

P. Arcioni, *Member, IEEE*, M. Bozzi, *Student Member, IEEE*, G. Conciauro, *Member, IEEE*,  
L. Perregini, *Member, IEEE*, A. R. Ruiz Laso

**Abstract**—This paper presents an accurate full-wave method for the calculation of the voltages induced on the elements of a planar antenna array by an incident electromagnetic field with gaussian amplitude distribution. The gaussian beam is expanded on a finite number of plane waves, and the voltage induced on each element is obtained as a superposition of the voltages induced by each plane wave. These voltages are evaluated under the infinite array approximation, i.e. considering only the elementary unit cell of the array. A similar approach can be applied also to the calculation of the impedance matrix of the array. This method proves advantageous both for the evaluation of the conversion efficiency of quasi-optical frequency multipliers and for the synthesis of planar arrays with a gaussian radiated field.

**Index terms**—Quasi-optical frequency multiplier, gaussian beam, planar array, infinite array approximation.

## I. INTRODUCTION

In the past years many efforts have been made in the design and fabrication of quasi-optical frequency multipliers, operating in the millimetre and sub-millimetre wave range [1]. A quasi-optical frequency multiplier consists of a planar antenna array, integrated with non-linear devices (Schottky diodes, Heterostructure Barrier Varactors, etc.) [2]. The antenna array is embedded in a quasi-optical gaussian system, together with input/output filters and dielectric matching slabs. A system

of mirrors is used to focus the input beam at the fundamental frequency on the multiplier chip and, similarly, to focus the output beam at the output harmonic. An accurate evaluation of the multiplier conversion efficiency requires a precise modelling of the non-linear devices as well as of the antenna system. The model of the non-linear device can be either extracted from the measured S-parameters of test structures or theoretically calculated using analytical models, while the modelling of the antenna requires a full-wave analysis of the whole structure.

Recently, we presented a simplified approach for the analysis of quasi-optical frequency multipliers, based on the approximation of an infinite array excited by a uniform plane wave incident from the broadside direction [3]. Although the approximation of a uniform plane wave is widely used for the modelling of quasi-optical frequency multipliers [4], a more precise representation of the incident beam is required in order to obtain an accurate evaluation of the overall efficiency. In fact, under the assumption of a broadside plane wave, all the non-linear devices are connected to the same embedding impedance, and are pumped with an identical power at the fundamental frequency. Therefore, they perform the frequency conversion with the same efficiency. On the other hand, the conversion efficiency of a non-linear device strongly depends on the pump power level and on the load impedance [5,6]. For this reason, to increase the analysis accuracy, the determination of a more realistic distribution of the open circuit voltage, as well as the calculation of the impedance matrix of the array, are required.

In this work, we present a rigorous theory for the evaluation of the voltages induced on the elements of an array excited by a gaussian beam, focused on the plane of the array. Moreover, we briefly discuss how a similar algorithm can be applied to the calculation of the impedance matrix.

P. Arcioni, M. Bozzi, G. Conciauro and L. Perregini are with the Dept Electronics, University of Pavia, Via Ferrata 1, 27100, Pavia, Italy. A. R. Ruiz Laso is with the Dept Communications, University of Cantabria, Av. los Castros s/n, 39005, Santander, Spain.

The work has been supported by the European Commission under the TMR Programme contract n. ERBFMRXCT960050 and by the University of Pavia under F.A.R. 1997/98 Funding.

## II. GAUSSIAN BEAM EXCITATION

Let us consider a planar array of arbitrarily shaped apertures, excited by an incident field with a gaussian distribution on the plane of the array (Fig. 1,2). The beam waist  $w_0$  of the gaussian beam is smaller than the dimension  $T$  of the array. On the focal plane  $z=0$ , the electric field has the following expression

$$\mathbf{E}^{inc}(x, y, 0) = A e^{-\frac{x^2+y^2}{w_0^2}} \mathbf{u}_y \quad (1)$$

In order to calculate the voltage induced by the non-uniform beam (1) on a planar array, the beam and its spatially shifted replicas are combined [7], thus obtaining the pseudo-periodic excitation shown in Fig. 3.

With this assumption, the incident electric field can be expressed as a summation of a finite number of uniform plane waves, incident from different directions

$$\mathbf{E}^{inc}(x, y, z) = \sum_{m,n=-N}^N \mathbf{F}_{mn} e^{j(\kappa_{x_m} x + \kappa_{y_n} y)} e^{-\gamma_{mn} z} \quad (2)$$

where

$$\mathbf{F}_{mn} = \frac{A \pi w_0^2}{T^2} e^{-\frac{w_0^2(\kappa_{x_m}^2 + \kappa_{y_n}^2)}{4}} \left( \mathbf{u}_y + j \frac{\kappa_{y_n}}{\gamma_{mn}} \mathbf{u}_z \right) \quad (3)$$

$$\kappa_{x_m} = \frac{2\pi}{T} m = k \sin \vartheta_{mn} \cos \varphi_{mn} \quad (4)$$

$$\kappa_{y_n} = \frac{2\pi}{T} n = k \sin \vartheta_{mn} \sin \varphi_{mn} \quad (5)$$

$$\gamma_{mn} = \sqrt{(\kappa_{x_m}^2 + \kappa_{y_n}^2) - k^2} \quad (6)$$

Moreover,  $k = \omega / \epsilon \mu$  is the wavenumber at the operation frequency, and  $(\vartheta_{mn}, \varphi_{mn})$  represents the direction of the  $(m, n)$ -th incident plane wave.

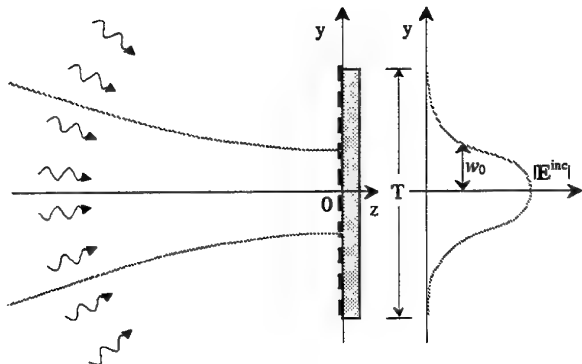


Fig. 1 – Side view of a planar array excited by a gaussian beam expanded on a set of uniform plane waves incident from different directions.

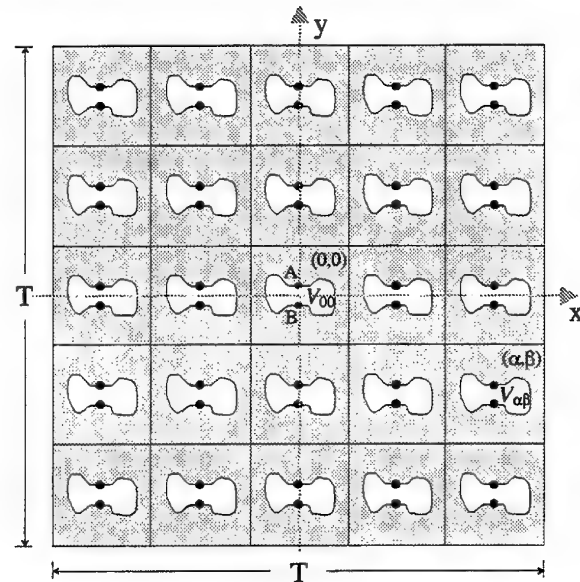


Fig. 2 – Front view of a planar array of arbitrarily shaped apertures.

It is evident that, the larger the ratio  $T/w_0$ , the higher the number  $(2N+1) \times (2N+1)$  of plane waves required to obtain a good accuracy in the field representation. As an example, in the case  $T=6w_0$ , an accuracy better than 2% in the approximation of the gaussian field can be achieved with  $N=3$ .

## III. CALCULATION OF THE OPEN CIRCUIT VOLTAGES

The calculation of the voltages induced on all the array elements by each plane wave in (2) can be performed under the infinite array approximation. With this assumption, the analysis of the array reduces to the investigation of a single unit cell, which is a rectangular waveguide with periodic boundary conditions [8], possibly filled by a layered medium (Fig. 4).

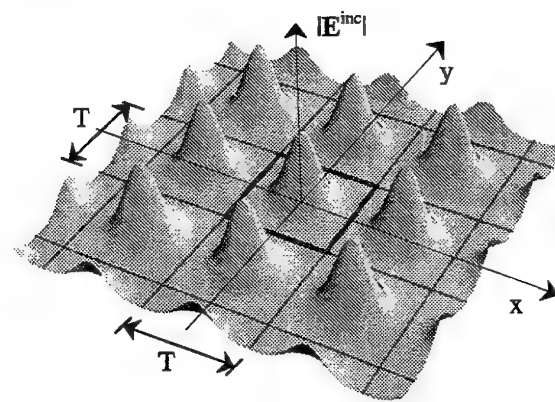


Fig. 3 – Periodic replicas of the gaussian beam.

Once the voltages  $V_{00}^{mn}$  induced by the  $(m,n)$ -th plane wave across the terminal A-B are known (see Fig. 2), the total voltage  $V_{\alpha\beta}$  induced by the gaussian beam on the generic  $(\alpha,\beta)$ -th element can be readily obtained.

In fact, the elementary voltages  $V_{\alpha\beta}^{mn}$  have the same amplitude, with a periodic phase shift depending on the angle of incidence and on the position of the element (i.e., on  $\alpha$  and  $\beta$ ). Applying the superposition of the effects, i.e., summing up with the proper phases all the contributions arising from each plane wave, the voltage  $V_{\alpha\beta}$  results

$$V_{\alpha\beta} = \sum_{m,n=-N}^N V_{\alpha\beta}^{mn} = \sum_{m,n=-N}^N V_{00}^{mn} e^{j(\alpha \kappa_{x_m} a + \beta \kappa_{y_n} b)} \quad (7)$$

where  $a$  and  $b$  are the dimensions of the rectangular waveguide (Fig. 4).

In this way, the computational effort translates into the evaluation of the voltage  $V_{00}^{mn}$  and this task is accomplished using the full-wave method presented in the following Section.

#### IV. ANALYSIS OF THE ELEMENTARY UNIT CELL

For the calculation of the voltage  $V_{00}^{mn}$ , we apply the equivalence theorem, replacing the aperture S by an ideal metal sheet. In such a way, the problem is divided in two parts, the former concerning the half-space  $z < 0$ , the latter  $z > 0$ . The fields in the two regions are related by the continuity condition of the tangential component of the fields across the aperture S. Considering two surface distributions of magnetic current M on the two sides of the aperture, equal in amplitude and opposite in phase (Fig. 5), the continuity of the tangential component of the electric field is automatically guaranteed. The continuity of the tangential component of the magnetic field across the aperture S is enforced by the following relationship

$$\mathbf{H}_{mn}^{inc}(x, y, 0^-) \Big|_{tan} + \mathbf{H}^-(x, y, 0^-) \Big|_{tan} = \mathbf{H}^+(x, y, 0^+) \Big|_{tan} \quad (8)$$

where  $\mathbf{H}_{mn}^{inc}$  is the magnetic field of the  $(m,n)$ -th incident plane wave, and  $\mathbf{H}^-$  ( $\mathbf{H}^+$ ) is the field scattered in the regions  $z < 0$  ( $z > 0$ ) sustained by the unknown current M.

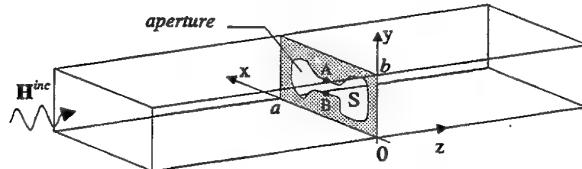


Fig. 4 – Elementary unit cell of the array.

The incident field  $\mathbf{H}_{mn}^{inc}$  can be expressed as a combination of the modes of the rectangular waveguide with periodic boundary conditions (Fig. 4). More in details we have

$$\mathbf{H}_{mn}^{inc} \Big|_{tan} = \begin{cases} I_{mn}^0 \mathbf{h}_{mn}^0 & \text{if } m = n = 0 \\ I_{mn} \mathbf{h}'_{mn} + I''_{mn} \mathbf{h}''_{mn} & \text{otherwise} \end{cases} \quad (9)$$

where  $\mathbf{h}_{mn}^0$ ,  $\mathbf{h}'_{mn}$  and  $\mathbf{h}''_{mn}$  are the magnetic modal fields of the TEM, TM and TE modes, respectively, and  $I_{mn}^0$ ,  $I_{mn}$  and  $I''_{mn}$  represent the expansion coefficients of the plane waves on the modal fields.

The magnetic fields  $\mathbf{H}^-$  in the regions  $z < 0$  and  $\mathbf{H}^+$  in  $z > 0$ , due to the incident field  $\mathbf{H}_{mn}^{inc}$ , are given as a function of the unknown current sheet M by the following Green's integral

$$\begin{aligned} \mathbf{H}^\pm(x, y, z) = & \\ & \pm \int_S \mathbf{G}^\pm(x, y, z, x', y', 0) \cdot \mathbf{M}(x', y', 0) dS' \end{aligned} \quad (10)$$

where  $\mathbf{G}^\pm(x, y, z, x', y', z')$  represents the Green's function of a section of the waveguide with the periodic boundary conditions and containing the layered medium. The eigenfunction expansion of the Green's function is given in [9]. In our approach, we are interested only in the transverse components  $\mathbf{G}_T$  of the dyadic Green's function

$$\begin{aligned} \mathbf{G}_T(x, y, z, x', y', z') = & \\ & = \sum_p \mathbf{h}_p(x, y) \mathbf{h}_p(x', y') \mathbf{Y}_p(z, z') \end{aligned} \quad (11)$$

where  $\mathbf{h}_p$  is the magnetic modal fields of the TEM, TM or TE modes of the periodically bounded waveguide. Moreover,  $\mathbf{Y}_p(z, z')$  is related to the transmission matrix of the layered medium for the  $p$ -th mode.

The integral problem resulting from (8) is solved using the Method of the Moments. The magnetic current M is expanded on a set of roof-top basis functions  $f_j$  (see, for instance, [4], pp. 41–42)

$$\mathbf{M}(x, y, 0) = \sum_j x_j f_j(x, y, 0) \quad (12)$$

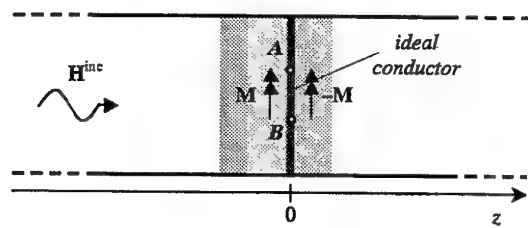


Fig. 5 – Magnetic current distributions on the aperture S.

By applying the Galerkin method, the problem is formulated in the following matrix form

$$[\mathbf{A}][\mathbf{X}] = [\mathbf{B}] \quad (13)$$

where

$$\mathbf{A}_{ij} = \iint_S f_i(x, y, 0) \cdot [\mathbf{G}_T^+(x, y, 0, x', y', 0) + \mathbf{G}_T^-(x, y, 0, x', y', 0)] \cdot f_j(x', y', 0) dS' dS \quad (14)$$

$$\mathbf{B}_i = \int_S f_i(x, y, 0) \cdot \mathbf{H}_{mn}^{inc}(x, y, 0) dS \quad (15)$$

and the unknown vector  $\mathbf{X}$  contains the expansion coefficients  $x_j$  introduced in (12).

The solution of the problem (13) leads to the evaluation of the magnetic current  $\mathbf{M}$  due to the  $(m, n)$ -th plane wave, which, in turn, permits the calculation of the voltage  $V_{00}^{mn}$ , given by

$$V_{00}^{mn} = \int_A^B \mathbf{E} \cdot d\mathbf{l} = \int_A^B \mathbf{M} \times \mathbf{u}_z \cdot d\mathbf{l} \quad (16)$$

This procedure is repeatedly applied to all the incident plane waves, leading to the calculation of the elementary contributions appearing in (7).

## V. CALCULATION OF THE IMPEDANCE MATRIX

As well known, the impedance matrix  $\mathbf{Z}$  of an array relates the voltages and the currents on the elements of the array. The generic element of  $\mathbf{Z}$  is given by

$$Z_{\alpha\beta, \xi\zeta} = \left. \frac{V_{\alpha\beta}}{i_{\xi\zeta}} \right|_{i_{\nu\tau}=0} \quad \forall (\nu, \tau) \neq (\xi, \zeta) \quad (2)$$

where  $i_{\xi\zeta}$  is the test current applied to the terminals A-B of the  $(\xi, \zeta)$ -th element of the array—being all the other elements open circuited—and  $v_{\alpha\beta}$  is the corresponding voltage induced on the  $(\alpha, \beta)$ -th element.

Also in this case, in order to calculate the voltage induced by the current  $i_{\xi\zeta}$  on a periodic array, we consider a pseudo-periodic excitation and we represent  $i_{\xi\zeta}$  as a summation of a finite number of periodic excitation  $i_{\xi\zeta}^{(m)}$ . Considering the elementary unit cell of the infinite array with the impressed current  $i_{\xi\zeta}^{(m)}$ , and enforcing the right discontinuity of the magnetic field across the aperture S, an integral problem similar to (8) is obtained. Solving this problem by the Galerkin procedure, the unknown magnetic current  $\mathbf{M}$  due to  $i_{\xi\zeta}^{(m)}$  is evaluated, and, by mean of a variational formula (see [3], for instance) the elements of the impedance matrix are calculated.

## VI. CONCLUSION

We presented a full-wave method for the accurate evaluation of the voltages induced on the element of a planar array by an incident gaussian beam. The method could also be applied to any spatially limited non-periodic excitation. Moreover, we briefly discussed on the evaluation of the impedance matrix that can be accomplished using an algorithm that differs only slightly from the one used in the voltage calculation.

## REFERENCES

- [1] Special Issue on Terahertz Technology, *Proc. IEEE*, Vol. 80, No. 11, pp. 1659–1860, Nov. 1992.
- [2] C. F. Jou *et al.*, “Millimeter-Wave Diode-Grid Frequency Doubler,” *IEEE Trans. Microwave Theory Tech.*, Vol. MTT-36, n. 11, pp. 1507–1514, Nov. 1988.
- [3] P. Arcioni *et al.*, “A Novel CAD-Tool for the Optimization of Quasi-Optical Frequency Multipliers,” *Proc. of ESA Workshop on MM Wave Technology and Applications*, Espoo, Finland, May 27–29, 1998.
- [4] T. K. Wu, *Frequency Selective Surface and Grid Array*, John Wiley and Sons, 1995.
- [5] T. J. Tolmunen, A. V. Räisänen, “An Efficient Shottky Varactor Frequency Multiplier at Millimeter Waves. Part I: Doubler,” *Int. Journal of Infrared and Millimeter Waves*, Vol. 8, n. 10, pp. 1313–1336, 1987.
- [6] P. Arcioni *et al.*, “A 430.5 GHz Quasi-Optical HBV Frequency Tripler,” *Proc. of the 9th Intern. Symposium on Space Terahertz Technology*, Pasadena, California, USA, March 17–19, 1998.
- [7] M. Shahabadi and K. Schunemann, “Excitation of Periodic Structures by Non-Uniform Electromagnetic Beams,” *Proc. of 20th ESTEC Antenna Workshop*, June 18–20, 1997, ESA-ESTEC, Noordwijk, The Netherlands.
- [8] N. Amitai, V. Galindo and C. P. Wu, *Theory and Analysis of Phased Array Antennas*, John Wiley and Sons, Inc., 1972.
- [9] L. B. Felsen and N. Marcuvitz, *Radiation and Scattering of Waves*, Prentice-Hall, Inc., Englewood Cliffs, N.J., 1973.

# Radiation Patterns from Substrate-Lens Antennas: A Method of Analysis for THz Application

Iraj A. Ehtezazi, Christine Letrou, and Gérard Beaudin

**Abstract**—This paper summarizes a spectral domain ray tracing (SRT) method for modeling substrate-lens antennas radiation patterns. An original rigorous and 3-D combination of Plane Wave Spectrum (PWS) decomposition of fields and Geometrical Optics is performed and implemented to model quasi-optical devices and in particular substrate-lens based antennas. Basic advantages of this method are: 1- Internal reflections inside the lens are taken into account, 2- The lens surface can be either in the near field or in the far field of the antenna, and 3- The method can be applied to model a given structure for a very wide frequency range. It is shown that results converge as the number of internal reflections is increased. The simulation results are compared with Physical Optics (PO) results in the case where the lens surface is in the far-field of the antenna (the only acceptable case for the PO analysis).

**Index terms**— quasi-optics, geometrical optics, ray tracing.

## I. INTRODUCTION

Substrate-lens antennas have found an increasing range of applications during the last years in the millimetric and submillimetric frequency range. They allow for an easy integration of circuits at the back of the lens, though avoiding substrate modes generation usually encountered in classical planar antennas configurations. Integration also makes multi-element arrays easier to realize than with waveguide and horns technology. Very wide band capabilities, as well as very low dissipative loss make substrate-lens antennas of general use for Terahertz applications such as far-infrared time-domain spectroscopy or Hot Electron Bolometer mixers testing.

This communication proposes a method of modeling substrate-lens antennas radiation patterns which does not rely on the usual assumption that the surface of the lens be in the far field of the printed antenna, and which takes internal reflections into account. This method thus does not introduce any limitations concerning either the respective sizes of the printed antenna and lens, the shape of the lens and its dimensions compared to the wavelength, or

I. A. Ehtezazi and C. Letrou are with the Institut National des Télécommunications, EPH, 9 rue Charles Fourier, 91011 EVRY cedex, FRANCE.

G. Beaudin is with the Observatoire de Paris, DEMIRM, 61 Avenue de l'Observatoire, 75014 PARIS, FRANCE.

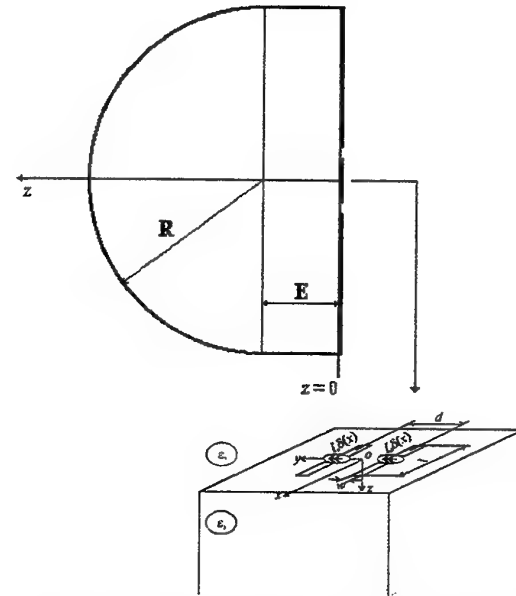


Fig. 1. Hybrid substrate-lens backed with a double-slot printed antenna.

the position of the antenna at the back of the lens. Such a method can prove especially useful for very wide band applications, where antireflection coatings cannot be efficient for the whole frequency band, and where the surface of the lens may be in the far field of the antenna at the lower end of the band, but not at higher frequencies.

## II. SUBSTRATE-LENS ANTENNAS DESCRIPTION AND PERFORMANCE

A substrate-lens antenna (cf. Fig. 1) is made of a planar antenna printed at the back of a lens which may be either elliptical (the most directive), hyperhemispherical (the most Gaussian) or hybrid (hemispherical with a cylindrical extension). The lens focuses the printed antenna pattern and the extension length of extended hemispherical lenses can be chosen so as to make them diffraction-limited (quasi-elliptical configuration). The printed antennas are most usually double dipoles for far-infrared spectroscopy, wide band antennas (bow-tie, logarithmic spiral...) for HEB substrate-lens antennas to a Gaussian beam, including the

testing, and double slot or annular slot for low noise focal millimetric or submillimetric receivers.

The higher the dielectric index, the lower the backward radiation. High resistivity silicon ( $\epsilon_r=11.7$ ) which is almost transparent in the THz range, is thus the preferred material for high performance applications. When no antireflection treatment can be used, the choice of such a high index is at the expense of internal reflections.

The radiation patterns are close to Gaussian beams, especially when the lens is hyperhemispherical and the radiation pattern of the printed antenna has a good symmetry. This is an important feature for focal receivers as well as for antennas which are used within a quasi-optical system. Evaluation of the coupling efficiency of substrate-lens antennas to a Gaussian beam, including the different loss contributions, and calculations of the parameters of the beam best coupling to the lens have been performed in the case of double dipole, double slot and annular slot antennas [1].

The analysis of substrate-lens configurations is usually performed through Physical Optics (PO) integration at the surface of the lens. The equivalent sources on that surface are obtained from the far field of the printed antenna, transformed at the interface through the usual Fresnel coefficients [2]. Such a method is well suited for high performance narrow band configurations, where the lens is large enough compared to the wavelength and the printed antenna. We propose here a method of modeling which can be applied to a broader range of configurations.

### III. PRINCIPLE OF THE METHOD

Our method is based on a Plane Wave Spectrum (PWS) representation of the fields radiated by the planar antenna. We explain the method for two essential cases: free space propagation, and propagation through the lens surface.

#### A. Free Space Propagation

In this case, if the back plane of the lens is the  $xy$ -plane at  $z = 0$ , and the antenna polarization is assumed in  $x$ -direction, the PWS representation yields for the  $x$ - and  $z$ -component of the radiated field :

$$E_x(x, y, z) = \int_{-\infty}^{+\infty} \int_{-\infty}^{+\infty} \tilde{E}_x(k_x, k_y) e^{-j(k_x x + k_y y + k_z z)} dk_x dk_y \quad (1)$$

$$E_z(x, y, z) = \int_{-\infty}^{+\infty} \int_{-\infty}^{+\infty} \tilde{E}_z(k_x, k_y) e^{-j(k_x x + k_y y + k_z z)} dk_x dk_y \quad (2)$$

where  $\tilde{E}_x(k_x, k_y)$  and  $\tilde{E}_z(k_x, k_y)$  are respectively the two-dimensional Fourier transform of the  $x$ - and  $z$ -component of the antenna field at  $z = 0$  plane.

The following step of the method consists in discretizing the PWS integrals (1) and (2) and considering each differential spectral contribution

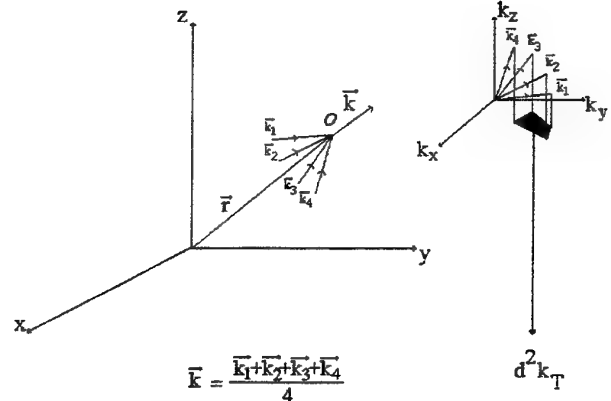


Fig. 2. Differential spectral surface  $d^2 \bar{k}_T$  obtained for a single ray at point  $O$  in the case of free space propagation.

$$[\tilde{E}_x(k_x, k_y) dk_x dk_y \hat{x} + \tilde{E}_z(k_x, k_y) dk_x dk_y \hat{z}] \times \exp[-j(k_x x + k_y y + k_z z)] \quad (3)$$

at point  $O(x, y, z)$  as a complex field carried by a  $\bar{k}$  directed ray, with  $\bar{k} = k_x \hat{x} + k_y \hat{y} + k_z \hat{z}$  and  $|\bar{k}| = 2\pi/\lambda$ . By adding up over all the ray contributions for all possible directions we get the electric field at the point  $O$  :

$$E_x(x, y, z) = \sum_{m=-\infty}^{+\infty} \sum_{n=-\infty}^{+\infty} \tilde{E}_x(mdk_x, ndk_y) \times e^{-j(mdk_x x + ndk_y y + k_{m,n} z)} dk_x dk_y \quad (4)$$

$$E_z(x, y, z) = \sum_{m=-\infty}^{+\infty} \sum_{n=-\infty}^{+\infty} \tilde{E}_z(mdk_x, ndk_y) \times e^{-j(mdk_x x + ndk_y y + k_{m,n} z)} dk_x dk_y. \quad (5)$$

Fig. 2 shows a differential spectral surface  $d^2 \bar{k}_T$  (which is equal to  $dk_x dk_y$  in the free space propagation case) obtained for a  $\bar{k}$ -directed ray at point  $O$  by using four rays  $\bar{k}_1$ ,  $\bar{k}_2$ ,  $\bar{k}_3$  and  $\bar{k}_4$  surrounded the ray. The notion of this four-ray tube is essential to find the corresponding  $d^2 \bar{k}_T$  when there are several interfaces between the  $z = 0$  plane and the observation point.

#### B. Propagation Through the Lens Surface

In the case of substrate-lens modeling, each plane wave in PWS is then represented by parallel ray tubes, which are refracted and reflected at the lens surface, and can be tracked by applying geometrical optics laws and Fresnel coefficients [3-5]. The contributions of all possible rays arriving at a point give the complex electric field radiated at that point: we have thus proposed to call this method the Spectral Ray Tracing (SRT) method.

To find the electric field at an observation point  $O$  we sweep the lens surface with three dimensional rays

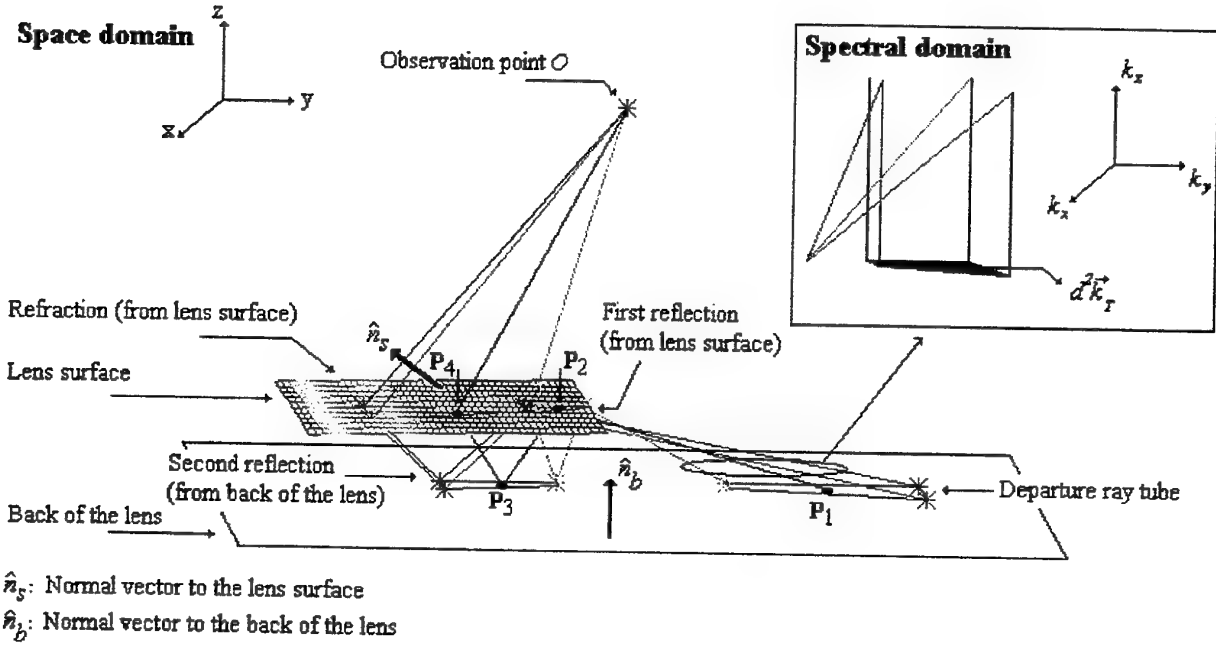


Fig. 3. Differential spectral surface  $d^2\bar{k}_T$  obtained for a single differential ray tube after two reflections and one refraction.

launched backward from the observation point  $O$ . For each ray direction towards the  $z = 0$  plane within the lens, the corresponding differential spectral surface  $d^2\bar{k}_T$  is determined by launching a backward four-ray tube surrounding the ray. (as in Fig. 2 in free space case) This tube is tracked according to Snell's law. The transversal differential surface on the  $k_x k_y$ -plane, obtained by projecting the directions of tube's rays within the lens on the  $k_x k_y$ -plane, gives the corresponding differential spectral surface.

Fig. 3 shows a multi-reflected ray tube which reaches the observation point  $O$  after two reflections and one refraction. Multi-reflected rays play an important role to determine high-order lobes of substrate-lens antennas radiation patterns. The field amplitude induced at the point  $O$  in Fig. 3 due to the single differential ray started from point  $P_1$  on the back of the lens is

$$|d\bar{E}| = \left| \tilde{E}(\bar{k}_{P_1 P_2}) \times \bar{R}_{P_2} \times DF_{P_2 P_3} \times \bar{R}_{P_3} \times DF_{P_3 P_4} \times \bar{T}_{P_4} \times DF_{P_4 O} \right| \times d^2\bar{k}_T \quad (6)$$

where  $\tilde{E}(\bar{k}_{P_1 P_2})$  is the PWS of the planar antenna in the direction  $P_1 P_2$ ,  $\bar{R}_{P_2}$  are Fresnel reflection coefficients for parallel and perpendicular polarizations at point  $P_2$ ,  $DF_{P_2 P_3}$  is the divergence factor for the path  $P_2 P_3$ ,  $\bar{R}_{P_3}$  are Fresnel reflection coefficients for the two polarizations cases at point  $P_3$ ,  $DF_{P_3 P_4}$  is the divergence factor for the

path  $P_3 P_4$ ,  $\bar{T}_{P_4}$  are Fresnel Transmission Coefficients for the two polarization cases at point  $P_4$  and  $DF_{P_4 O}$  is the divergence factor for the path  $P_4 O$ . The phase at the point  $O$  is:

$$\angle d\bar{E} = \angle \tilde{E}(\bar{k}_{P_1 P_2}) + k_1 \times (|P_1 P_2| + |P_2 P_3| + |P_3 P_4|) + k_2 \times |P_4 O| \quad (7)$$

where  $\angle \tilde{E}(\bar{k}_{P_1 P_2})$  is the phase of the PWS at point  $P_1$ , and  $k_1$  and  $k_2$  are respectively the wavenumbers inside and outside the lens.

#### IV. NUMERICAL RESULTS

In this section we apply the SRT method to extended hemispherical lenses backed with a double-slot antenna of dimensions  $d=0.43\text{mm}$ ,  $l=0.80\text{mm}$ , and  $w=25\mu\text{m}$  (cf. Fig. 1). The frequency is  $f=110\text{GHz}$  and the refractive index of the silicon lens is  $n=3.42$ . We present the radiation pattern of the structure for two different radii:  $R=25\text{mm}$  and  $R=1\text{mm}$ . The extension lengths are chosen so as to make the lens quasi-elliptical: respectively  $E=9.8\text{mm}$  and  $E=0.39\text{mm}$ . Fig. 4 shows the  $E$ -plane radiation patterns of the  $x$ -component of the field, for both configurations.

For  $R=25\text{mm}$ , the lens surface is in the far-field of the planar antenna and the results are compared with previously PO simulated results [1]. The difference between two results is due to the reflection effects inside

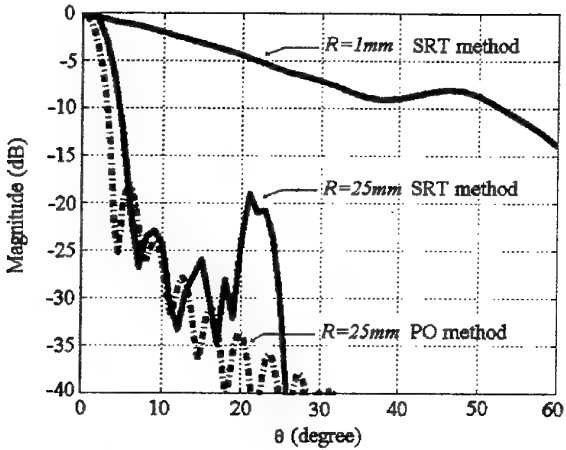


Fig. 4. SRT method simulation for extended hemispherical substrate-lens E-plane radiation patterns for two radii :  $R=1\text{mm}$  and  $R=25\text{mm}$ . The latter is compared with PO method.

the lens which are not taken into account in the PO method. However, in the case of  $R=1\text{mm}$  the lens surface is no longer in the far-field of the planar antenna; we could not compare with other simulated results as the method usually used to model substrate-lens antenna fails in that case.

Fig. 5 and Fig. 6 illustrate the convergence of multiply reflected rays contributions in our method. In Fig. 5 we show the field amplitudes of rays arriving at an observation point situated on the  $z$  axis from a given direction ( $\theta=0.05^\circ, \phi=0^\circ$ ). The reflection order of the rays represents the number of times they have been reflected inside of the lens (from 0 to 50 times in Fig. 5). In Fig. 6 is presented the field at the same observation point, calculated by summation of ray contributions from all possible directions. The field amplitudes obtained are given as a function of the number of internal reflections taken into account. This curve clearly shows that multiply reflected rays contributions must not be neglected : the 4 times reflected rays contribution is even superior to direct rays contribution for the case illustrated here.

## V. CONCLUSION

In this communication we present a new method of modeling substrate-lens radiation patterns. This method is shown to model configurations where the lens surface is not in the far field of the planar antenna, and where internal reflections must be taken into account. This method can be used as a reference where approximate methods are not valid. Numerical results are presented, which allow for a comparison with the usual Physical Optics integration results.

## REFERENCES

[1] V. Popescu, "Modélisation et conception de matrices

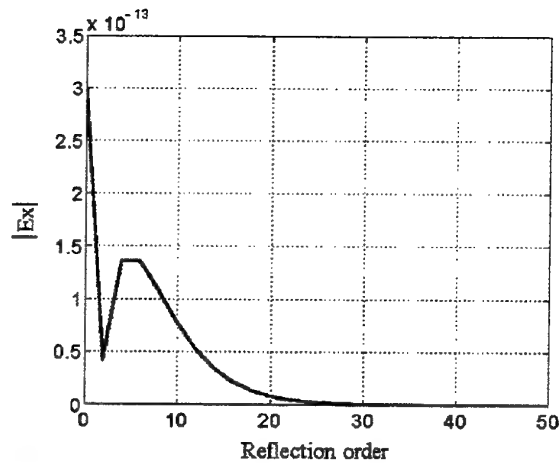


Fig. 5. Differential  $E_x$  amplitudes of single rays all arriving from the same direction ( $\theta=0.05^\circ, \phi=0^\circ$ ) at an observation point situated on the  $z$  axis at a  $z=100\text{mm}$  distance in front of a hemispherical lens ( $R=25\text{mm}$ ) as a function of their reflection order.

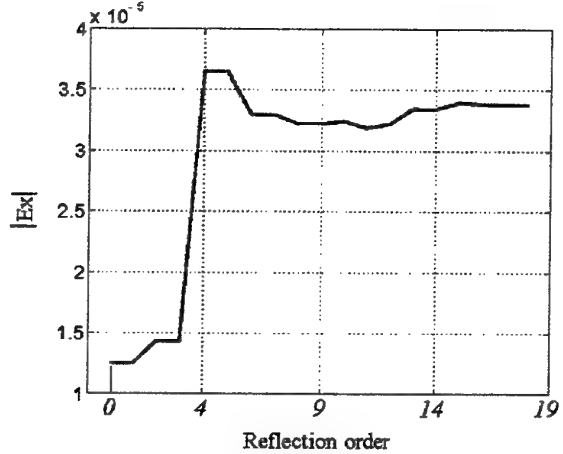


Fig. 6. E-field amplitude calculated by SRT method at the same observation point as in figure 4, and as a function of number of reflection order.

de mélangeurs en structure ouverte destinées à l'imagerie focale millimétrique et submillimétrique, " Ph.D dissertation, Université Paris 6, France, Oct. 1996.

[2] Filipovic D.F., Gearhart S.S., Rebeiz G.M., "Double-slot antennas on extended hemispherical and elliptical silicon dielectric lenses, " *IEEE Trans. MTT*, vol-41, pp. 1738-1749, Oct. 1993.

[3] S. W. Lee, M. S. Sheshadri, V. Jamnejad & R. Mittra, "Reflection at a curved dielectric interface: geometrical optics solution, " *IEEE Trans. MTT*, vol-30, pp. 12-19, Jan. 1982.

[4] G. A. Deschamps, "Ray techniques in electromagnetics, " *Proc. IEEE*, vol-60, pp. 1022-1035, Sept. 1972.

[5] H Ling, R. Chou & S. W. Lee, "Shooting and bouncing rays: calculating the RCS of an arbitrarily shaped cavity " *IEEE Trans. AP*, vol-37, pp. 194-205, Feb. 1989.

# Electronic THz Reflection Spectroscopy for Detecting Energetic Materials

V. Agrawal, T. Bork, S. Kee and D.W. van der Weide, *Member, IEEE*

**Abstract**— We report the first 10-450 GHz single pixel reflection spectra of several energetic materials (explosives). These are measured with an all-electronic reflection spectrometer, and we compare them to those of common objects and human skin to show differences in dielectric contrast. This instrument uses microwave sources to drive picosecond GaAs nonlinear transmission lines and sampling detectors, so it can form the basis of a fully integrated circuit spectroscopic imaging system for screening in security applications.

**Index terms**— reflection spectrometer, electronic terahertz system, nonlinear transmission line, energetic material, explosive

## I. INTRODUCTION

Increasingly sophisticated weapons and explosives require increasingly sophisticated detection technologies. Non-metallic varieties of these threats are especially important because they elude familiar metal-detecting portals, so they have motivated development of a multi-pronged approach to detection, including residue sniffing and computerized tomography. These techniques, however, have significant drawbacks, suffering from invasiveness, slowness, unfamiliarity to the public, and significant potential for false negatives[1].

Threats like these, however, appear to be readily detectable and even identifiable using a broadband of signals in the sub-THz regime (1-500 GHz), based on experiments reported here. Traditional equipment for generating and detecting these frequencies has, however, been difficult, bulky and expensive. The objectives of this work are to develop and apply all-electronic and monolithically integrated technology for generating and detecting these broadband signals to the problem of imaging the reflection spectra of plastic weapons and explosives on human subjects.

Many of the concepts we employ here are being pursued at lower frequencies for target detection at higher resolutions than traditional narrowband radar allows. This

ultrawideband (UWB), carrier-free, impulse, or baseband radar has been rapidly gaining popularity in applications where complex and elusive targets are the norm[2]. UWB radar has benefited from very recent advances in semiconductor technology enabling the production of sub-nanosecond pulses with peak powers of over 1 megawatt but having average powers in the milliwatt regime.

By contrast, the technology we employ—the integrated-circuit nonlinear transmission line (NLTL)—essentially trades power for speed, producing pico- or even sub-picosecond pulses with peak powers less than one watt and average powers in the low microwatt regime. These power levels are non-ionizing and biologically inconsequential, but because we can employ coherent detection, rejecting noise outside the frequencies of interest, we can still measure useful spectra with them.

Baseband pico- and sub-picosecond pulses of freely propagating radiation, usually generated and coherently detected with photoconductive switches and ultrafast lasers[3-5], have been useful for broadband coherent spectroscopy of materials, liquids, and gasses in the THz regime. Such “THz systems” have even been used for what could be called scale-model UWB radar[6]. These highly versatile beams of ultra-short electromagnetic pulses can be treated quasi-optically: They are diffracted and focused with mirrors and lenses, and the resultant effects can be readily observed in the time-domain waveform at the detector. Consequently, such beams are singularly useful for spectroscopy in a difficult-to-access spectral regime, and recent reports of spectroscopic imaging with these optoelectronic systems have generated much interest[7].

These beams of pico- and sub-picosecond pulses have also been generated *without* lasers, using NLTLs with integrated planar antennas[8-10]. Here the burden of complexity and expense is shifted from the laser system onto the circuit design, fabrication technology, and microwave generating equipment needed to realize these all-electronic systems. Photoconductive switches, by contrast, are comparatively easy to make. Usually, however, the ultrafast lasers to drive the photoconductive switches are expensive and bulky, not suited for use in portable or *in-situ* imaging applications where an array might be warranted.

The authors are with the Department of Electrical and Computer Engineering, University of Delaware, Newark, DE.

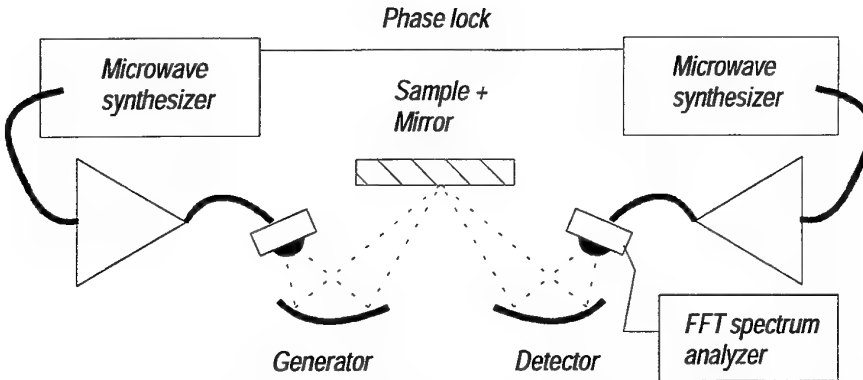


Fig. 1. Single pixel electronic terahertz reflection spectroscopy system. Both generator and detector are focused onto sample with off-axis ellipsoidal mirrors to minimize volume of sample needed to fill the THz beam.

## II. EXPERIMENTAL SETUP

A single-pixel spectroscopic imaging system is illustrated in Fig. 1, which shows the microwave sources, amplifiers and NLTL-based generator and detector, each having a high-resistivity Si substrate lens to help focus and collimate the beam. Both generator and detector are imaged onto a reference mirror using 50-mm off-axis ellipsoidal mirrors, allowing small quantities of energetic material to be fully illuminated. The sampling detector, itself strobed by a NLTL, drives a buffer amplifier and Fast Fourier Transform (FFT) spectrum analyzer to collect background and sample spectra.

### A. Nonlinear transmission lines

Nonlinear transmission lines (NLTLs) are usually realized as integrated circuits on GaAs and consist of series inductors (or sections of high-impedance transmission line) with varactor diodes periodically placed as shunt elements. On the structures used here, a fast ( $\sim 1-2$  ps) voltage step develops from a sinusoidal input because the propagation velocity  $u$  is modulated by the diode capacitance,

$$u(V) = 1/\sqrt{LC(V)}, \text{ where } L \text{ is the inductance and}$$

$C(V)$  the sum of the diode and parasitic capacitance of the line, all per unit length. Limitations of the NLTL arise from its periodic cutoff frequency, waveguide dispersion, interconnect metallization losses, and diode resistive losses. NLTLs are usually pumped by  $\sim 1$  W 1-10 GHz sinusoidal sources, although square-wave generators would ultimately be more efficient. Usually two phase-locked synthesizers are used, one to drive the generator and the other to drive a detector consisting of another NLTL and a diode sampling bridge; this arrangement is analogous to the familiar “pump-probe” techniques used in laser-based spectroscopy.

## III. RESULTS

Like the more common hybrid optoelectronic techniques that use lasers for generating broadband radiation, the NLTLs we use generate and detect broadband spectra. Broadband (as opposed to single-wavelength) imaging has the chief advantage of flexibility: if weapons change composition over the years, a single-wavelength or narrowband source may no longer detect the new composition, but having a broad range of frequencies maximizes the opportunity to detect the new threat’s signature.

One example of this advantage is shown in the data we present here. C-4 is primarily RDX with a plasticizing binder. As shown in Figures 2-4, the broadband reflection spectra out to 450 GHz show clear similarity between C-4 and RDX; both are distinct from HMX, demonstrating specificity in the dielectric response of these targets. The contrast we measure is not fully explained, but probably arises from the granularity of the materials, their dielectric constants and orientation of the sample, as distinct from rotational absorption of chemical bonds.

These spectra each show the average and standard deviation of 8 data sets using 50 harmonics of a 7.75 GHz fundamental with the sample occasionally repositioned to simulate a security screening application in which the target would not be stationary. The presence of standing waves in the highly reflective arrangement resulted in sample-to-background ratios exceeding unity at some frequencies.

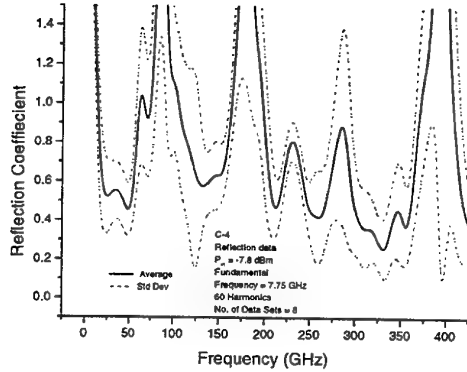


Fig. 2. Reflection spectrum of C-4.

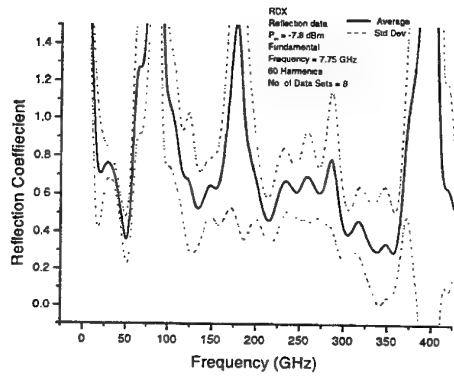


Fig. 3. Reflection spectrum of RDX.

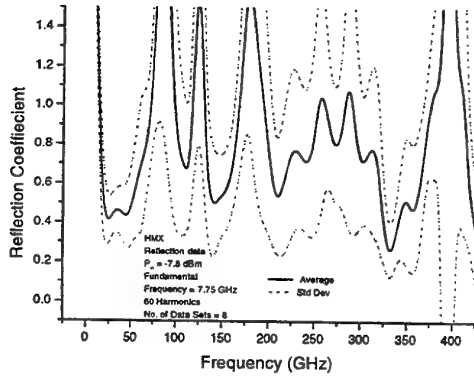


Fig. 4. Reflection spectrum of HMX.

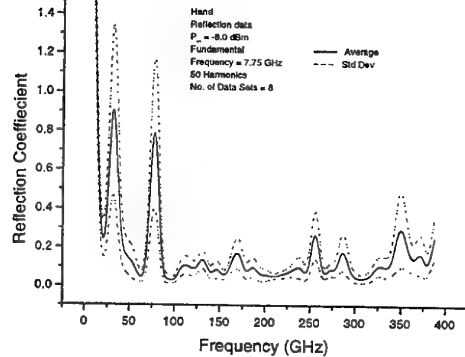


Fig. 5. Reflection spectrum of human hand.

We have measured reflection spectra from several potential threats, such as HMX, RDX, C-4, TNT, naphthalene (similar chemical structure to some explosives), ammonium nitrate solids and slurries, and gasoline, as well as common objects like keys, metals, wallets, credit cards, and notebooks. All show unique and repeatable signatures.

#### IV. CONCLUSIONS

The new information gained from these results can enable progress toward developing multi-pixel arrays of these sources and detectors for a new screening technology. Our current focus is on building inexpensive “single pixel” screening technology by pursuing advances in microfabrication of these devices, integrating more functions on a chip, and reducing the cost of these systems.

Potential advantages stemming from this new approach to screening accrue in combination with neural-network techniques for signature identification. Rapid, millisecond-level screening is also anticipated, due in part to the high repetition rate of the pulses (several GHz) and the availability of wide intermediate-frequency bandwidths in the MHz regime from our new dual-source microwave generator[11]. These advantages in combination with an ability to be integrated into the same or similar-looking security portals as those already familiar to passengers will enhance public acceptance of the new technology.

#### V. ACKNOWLEDGMENT

This work is supported by the Federal Aviation Administration (Dr. W. Makky), DARPA, ONR YIP, NSF PECASE, the University of Delaware Research Foundation, and a Ford Motor Company University Research Award.

## VI. REFERENCES

- [1] P. Mann, "TWA disaster reopens tough security issues," in *Aviation Week & Space Technology*, 1996, pp. 23-27.
- [2] D. Herskovitz, "Wide, Wider, Widest," *Microwave Journal*, vol. 38, pp. 26-40, 1995.
- [3] M. v. Exeter, "Terahertz time-domain spectroscopy of water vapor," *Optics Letters*, vol. 14, pp. 1128-1130, 1989.
- [4] D. Grischkowsky, S. Keiding, M. v. Exeter, and C. Fattinger, "Far-infrared time-domain spectroscopy with terahertz beams of dielectrics and semiconductors," *Journal of the Optical Society of America B*, vol. 7, pp. 2006-2015, 1990.
- [5] M. C. Nuss, K. W. Goossen, J. P. Gordon, P. M. Mankiewich, M. L. O'Malley, and M. Bhusan, "Terahertz time-domain measurement of the conductivity and superconducting band gap in niobium," *Journal of Applied Physics*, vol. 70, pp. 2238-2241, 1991.
- [6] R. A. Cheville and D. Grischkowsky, "Time domain terahertz impulse ranging studies," *Applied Physics Letters*, vol. 67, pp. 1960-1962, 1995.
- [7] B. B. Hu and M. C. Nuss, "Imaging with terahertz waves," *Optics Letters*, vol. 20, pp. 1716-18, 1995.
- [8] D. W. van der Weide, J. S. Bostak, B. A. Auld, and D. M. Bloom, "All-electronic free-space pulse generation and detection," *Electronics Letters*, vol. 27, pp. 1412-1413, 1991.
- [9] Y. Konishi, M. Kamegawa, M. Case, R. Yu, M. J. W. Rodwell, and R. A. York, "Picosecond electrical spectroscopy using monolithic GaAs circuits," *Applied Physics Letters*, vol. 61, pp. 2829-2831, 1992.
- [10] D. W. van der Weide, J. S. Bostak, B. A. Auld, and D. M. Bloom, "All-electronic generation of 880 fs, 3.5 V shockwaves and their application to a 3 THz free-space signal generation system," *Applied Physics Letters*, vol. 62, pp. 22-24, 1993.
- [11] P. Akkarekthalin, S. Kee, and D. W. van der Weide, "Distributed broadband frequency translator," in *1998 IEEE MTT-S International Microwave Symposium Digest*, vol. 3. New York, NY, USA: IEEE, 1998, pp. 1431-1434.

# Imaging of Supercurrent Distribution in YBCO Thin Films Using THz Radiation Excited by Femtosecond Laser Pulses

Masanori Hangyo, Shin-ichi Shikii, Masatsugu Yamashita, Takashi Kondo, Masayoshi Tonouchi, Masahiko Tani, and Kiyomi Sakai

**Abstract**--A new method of imaging supercurrent distribution in YBCO thin films has been proposed and demonstrated by using the THz radiation excited by femtosecond laser pulses. The characteristic distribution of the transport and persistent current in superconducting thin films is obtained and the result is discussed based on the Bean model.

**Index terms**-- high- $T_c$  superconductor, THz radiation, femtosecond laser, supercurrent distribution, critical state model

## I. INTRODUCTION

It is well known that ultrashort electromagnetic pulses (referred to as THz radiation) are radiated into free space by exciting photoconductive switches with femtosecond laser pulses [1], [2]. In a series of papers, we have shown that the THz radiation is also emitted from current biased, magnetic-field applied, and magnetic-flux trapped superconducting YBCO films [3] - [6]. The radiation mechanism is explained in terms of the ultrafast supercurrent modulation by femtosecond laser pulses [7]. At first, the THz radiation was observed for the films fabricated into device structures. However, it is also observed for as-grown superconducting films without device fabrication [8]. The THz radiation is polarized in the direction parallel to the supercurrent direction at the laser spot and its amplitude is proportional to the supercurrent density at the laser spot (the radiation intensity is proportional to the square of the supercurrent density).

In this paper, we propose and demonstrate a new imaging method of the two-dimensional supercurrent distribution in YBCO thin films by scanning the focused femtosecond laser beam and detecting the THz radiation. The experimentally obtained supercurrent distribution under bias current is compared to that expected from the critical state model. The

distribution of a persistent supercurrent flowing in a superconducting thin film loop is also obtained.

## II. EXPERIMENTAL

Figure 1 shows a schematic illustration of the THz radiation from high- $T_c$  superconducting films fabricated into a bow-tie antenna type device. YBCO thin films ( $\sim 100$  nm thick) on MgO substrates are fabricated into device structures using photolithography and wet chemical etching techniques. The samples are mounted on a cold finger of a closed-cycle He refrigerator. The sample stage is specially designed so as to avoid the mechanical vibration of the cold stage of the refrigerator and translated two-dimensionally in the directions perpendicular to the laser beam using a computer-controlled X-Z stage. The femtosecond laser pulses from a mode-locked Ti:sapphire laser ( $\sim 50$  fs time width, 80 MHz repetition rate,  $\sim 790$  nm wavelength) is focused into  $\sim 30$   $\mu$ m in diameter on the sample surface with an objective lens and the THz radiation transmitted through the MgO substrate is collected by an off-axis paraboloidal mirror. The radiation is detected by a low-temperature grown GaAs (LT-GaAs) photoconductive antenna or an InSb hot electron bolometer. The THz radiation amplitude and power are measured by the LT-GaAs detector and InSb bolometer, respectively. The two-dimensional THz

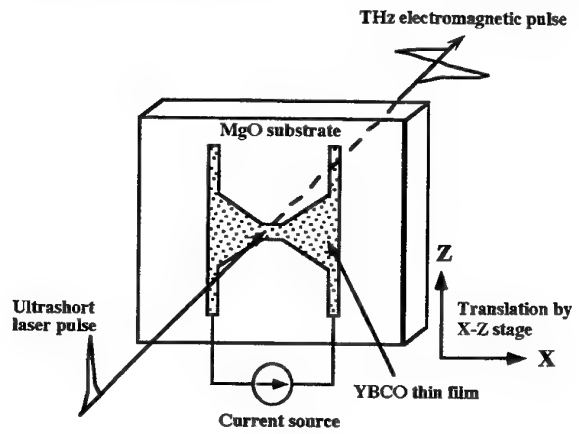


Fig. 1. Schematic illustration of THz radiation from a high- $T_c$  superconducting film.

M. Hangyo, S. Shikii, M. Yamashita, T. Kondo, and M. Tonouchi are with Research Center for Superconducting Materials and Electronics, Osaka University, Osaka 565-0871, Japan.

M. Tani and K. Sakai are with Kansai Advanced Research Center, Communications Research Laboratory, The Ministry of Posts and Communications, Kobe 651-2401, Japan.

M. Tonouchi is also with CREST, Japan Science and Technology Corporation (JST).

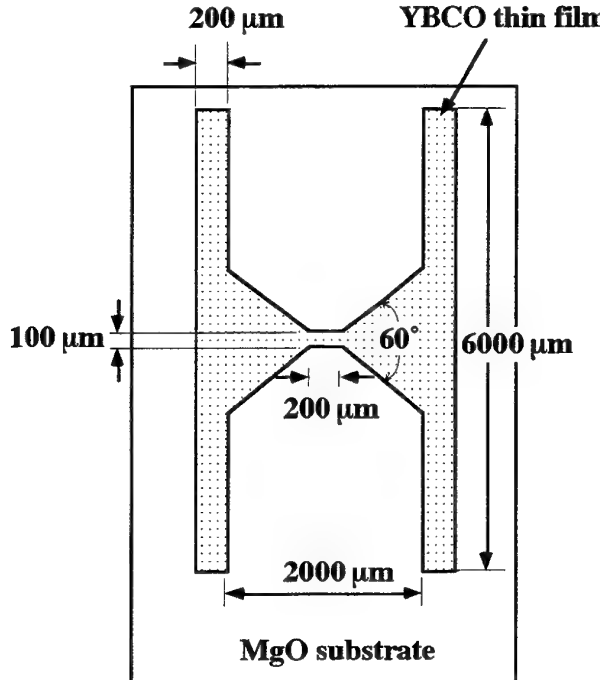


Fig. 2. Schematic structure of a bow-tie antenna type device.

radiation amplitude or intensity is obtained by translating the X-Z stage step by step with measuring the THz radiation excited by the laser pulses.

Figure 2 shows a schematic structure of a YBCO antenna device used for the mapping. It consists of strip lines with a bow-tie antenna at the center.

### III. RESULTS AND DISCUSSION

#### A. Imaging under Bias Current

Figure 3 shows the two-dimensional distribution of the amplitude of the THz radiation measured at 16 K. The pump laser power and bias current are 40 mW and 330 mA, respectively. The sensitivity of the LT-GaAs antenna has a strong dependence on the polarization of the THz radiation. In this case, the direction of the antenna is arranged so that only the polarization component parallel to the X-axis is detected in Fig. 3. It is seen that the THz radiation amplitude is large along the edge of the YBCO film. This result indicates that the supercurrent flows along the edge of the film mainly. When we rotate the detector by 90 degrees to detect the polarization component parallel to the Z-axis, the amplitude becomes large in strip lines which are parallel to the Z-axis. The polarities of the electric fields of the THz radiation from two parallel strip lines are opposite reflecting the opposite transport current directions.

In order to see the supercurrent distribution at the bridge in detail, an MgO hemispherical lens with 3 mm diameter is attached to the back surface of the MgO substrate. This enhances the collection efficiency of the THz radiation around the bridge. The InSb bolometer is used to measure the

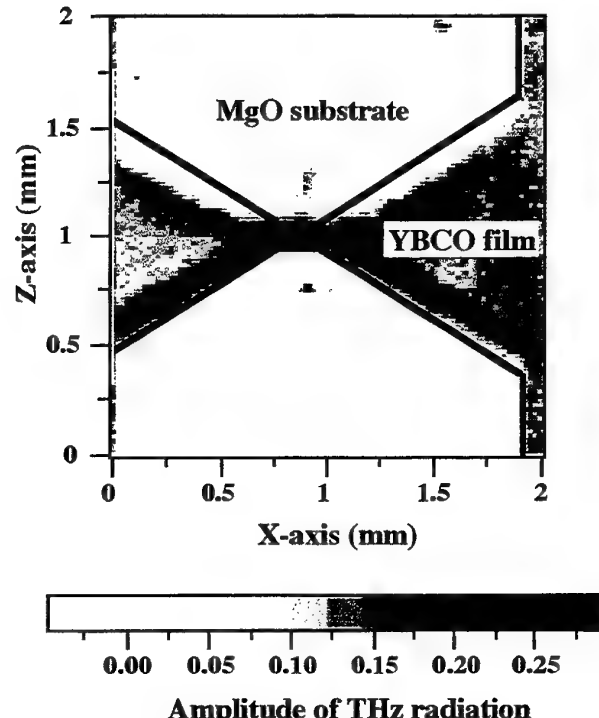


Fig. 3. Two-dimensional distribution of THz radiation amplitude obtained for a bow-tie antenna type device shown in Fig. 2.

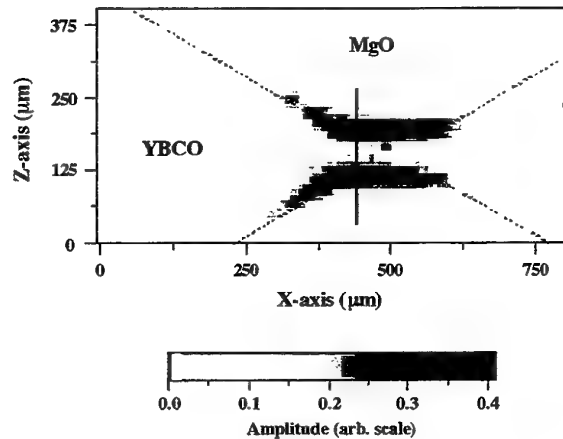


Fig. 4. Two-dimensional distribution of THz radiation amplitude near the bridge.

radiation power. Figure 4 shows a two-dimensional image of the square root of the radiation power, which is proportional to the amplitude, by applying a bias current of 100 mA. The radiation power is large along the edge of the bridge, and this indicates that the transport current flows along the edge mainly in this condition.

Figure 5 (a) shows the cross sectional supercurrent distribution in the bridge along the vertical lines in Fig. 4. We analyzed the supercurrent distribution based on a critical state model by Bean [9]. The critical current of the present sample is 220 mA. Figure 5 (b) shows the supercurrent distribution

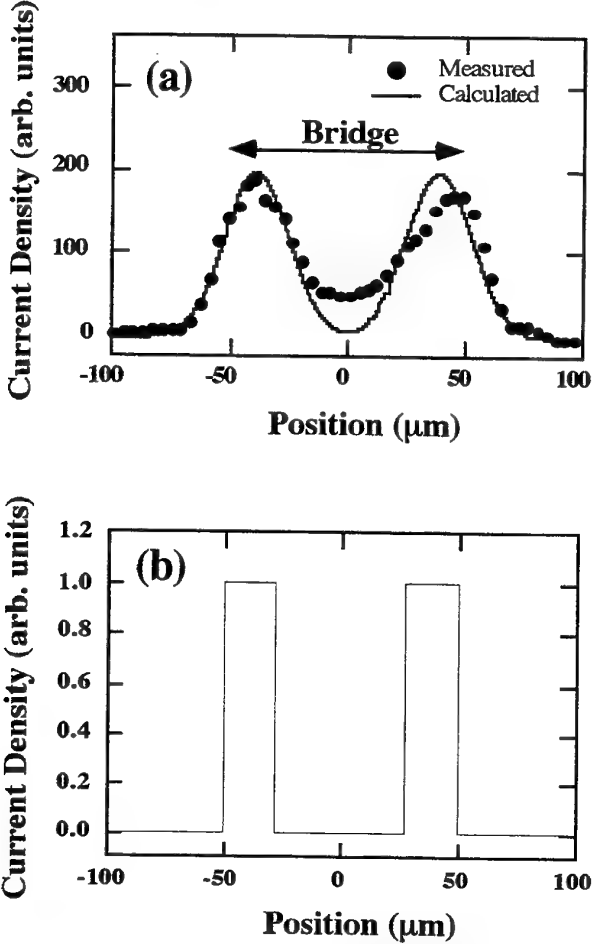


Fig. 5. (a) Cross sectional supercurrent distribution (THz amplitude) along the vertical line shown in Fig. 4. The solid line indicates the convolution between the current distribution based on the Bean model (b) and the laser beam profile.

across the bridge for the bias current of 100 mA according to the Bean model. Since the experimental spatial resolution of the THz mapping is limited by the laser spot size, we take the convolution between the current distribution in Fig. 5 (b) and the laser spot profile assumed as a Gaussian function with a FWHM of 30  $\mu\text{m}$ . The result is shown in Fig. 5 (a). The agreement between the experiment and calculation is good confirming that the supercurrent distribution can be measured by detecting THz radiation excited by femtosecond laser pulses. We observed that the supercurrent distribution progresses into a inner part of the bridge with increasing the bias current which is also in agreement with the critical state model.

#### B. Mapping under Flux-Trapped State

In a previous paper, we have shown that the THz radiation is emitted into free space under external magnetic fields and magnetic-flux trapped states without a bias current [5]. Here, we demonstrate that the persistent current associated with magnetic flux trapped in a superconductor loop can be mapped by using the THz radiation excited by femtosecond laser

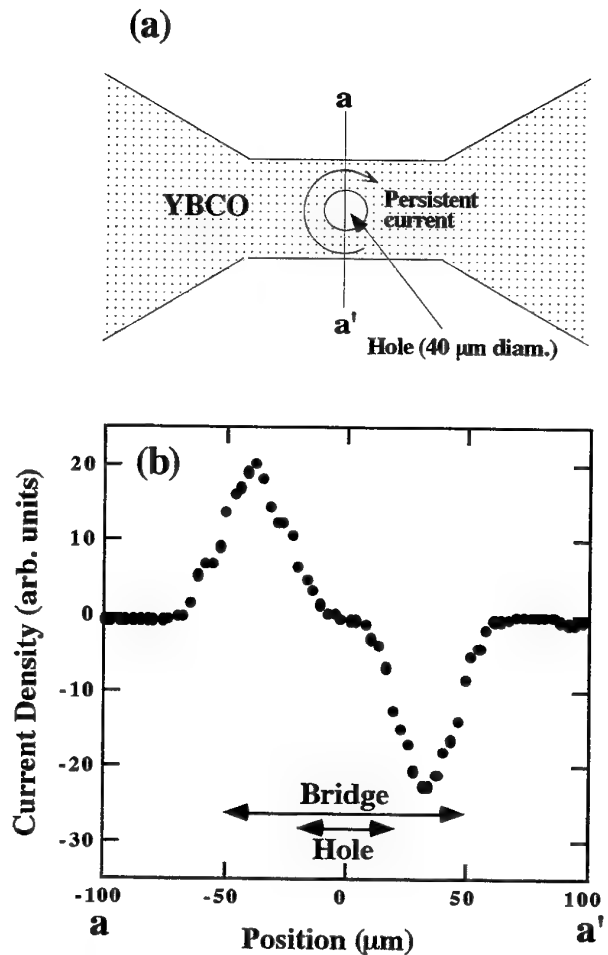


Fig. 6. (a) Schematic structure of a device with a hole to trap magnetic flux and (b) the distribution of the THz radiation amplitude along a-a' shown in (a).

pulses. For trapping magnetic flux, we made a hole 40  $\mu\text{m}$  in diameter in the bridge of the bow-tie antenna type device (see Fig. 2) as shown in Fig. 6 (a). The THz radiation amplitude is measured by the LT-GaAs photoconductive antenna, which detects the polarization component perpendicular to the strip lines (X-axis direction in Fig. 1). In order to trap magnetic flux in the hole, we apply the bias current with irradiating the femtosecond laser pulses at one of the two path of the bridge, and then cut off the bias current [10].

Figure 6 (b) shows the THz radiation amplitude along the a-a' line in Fig. 6 (a). It is seen that the polarity of the electric field of the THz radiation changes with going from a to a'. This means that the direction of the supercurrent is opposite between the upper and lower paths of the bridge in Fig. 6 (a). This fact is understood by considering that the persistent current is circulating around the hole in which the magnetic flux is trapped, and therefore the supercurrent direction is opposite between the upper and lower branches of the bridge. The THz radiation amplitude does not decrease with time indicating that the magnetic flux trapped in the hole does not escape. This property can be used to make a new type of superconducting flux-trap memory [10].

#### IV. SUMMARY

A new method of imaging supercurrent flow in high- $T_c$  superconducting films by measuring the THz radiation excited by femtosecond laser pulses is proposed and demonstrated. The THz radiation amplitude is strong along the edge of the films indicating that the supercurrent flows along the edge of the films. Usually, supercurrent distribution is deduced indirectly from the magnetic field distribution measured by scanning a small Hall sensor or by using a magnetooptic film. The present method is a noncontact method of measuring supercurrent flow directly. The spatial resolution can be increased to  $\sim 1 \mu\text{m}$  by improving focusing optics of the laser beam.

#### Acknowledgments

This work was partly supported by a Grant-in-Aid for Scientific Research from the Ministry of Education, Science, Sports, and Culture, Japan. This work was also partly supported by the public participation program for the promotion of creative info-communications technology R&D of Telecommunications Advancement Organization of Japan (TAO).

#### References

- [1] P. R. Smith, D. H. Auston, and M. C. Nuss, "Subpicosecond photoconducting dipole antennas," *IEEE J. Quantum Electron.*, vol. 24, no. 2, pp. 255-260, 1988.
- [2] D. Grischkowsky, S. Keiding, M. van Exter, and Ch. Fattinger, "Far-infrared time-domain spectroscopy with terahertz beams of dielectrics and semiconductors," *J. Opt. Soc. Amer.*, vol. 7, no. 7, pp. 2006-2015, 1990.
- [3] M. Hangyo, S. Tomozawa, Y. Murakami, M. Tonouchi, M. Tani, Z. Wang, K. Sakai, and S. Nakashima, "Terahertz radiation from superconducting  $\text{YBa}_2\text{Cu}_3\text{O}_{7-\delta}$  thin films excited by femtosecond optical pulses," *Appl. Phys. Lett.*, vol. 69, no. 14, pp. 2122-2124, 1996.
- [4] M. Tonouchi, M. Tani, Z. Wang, K. Sakai, S. Tomozawa, M. Hangyo, Y. Murakami, and S. Nakashima, "Ultrashort electromagnetic pulse radiation from YBCO thin films excited by femtosecond optical pulse," *Jpn. J. Appl. Phys.*, vol. 35, no. 5A, pp. 2624-2632, 1996.
- [5] M. Tonouchi, M. Tani, Z. Wang, K. Sakai, N. Wada, and M. Hangyo, "Novel terahertz radiation from flux-trapped  $\text{YBa}_2\text{Cu}_3\text{O}_{7-\delta}$  thin films excited by femtosecond laser pulses," *Jpn. J. Appl. Phys.*, vol. 36, no. 2A, pp. L93-95, 1997.
- [6] M. Hangyo, N. Wada, M. Tonouchi, M. Tani, and K. Sakai, "Ultrafast optical response and terahertz radiation from high- $T_c$  superconductor," *IEICE Trans. Electron.*, vol. E80-C, no. 10, pp. 1282-1290, 1997.
- [7] M. Tonouchi, M. Tani, Z. Wang, K. Sakai, N. Wada, and M. Hangyo, "Terahertz emission study of femtosecond time-transient nonequilibrium state in optically excited  $\text{YBa}_2\text{Cu}_3\text{O}_{7-\delta}$  thin films," *Jpn. J. Appl. Phys.*, vol. 35, no. 12A, pp. L1578-L1581, 1996.
- [8] S. Shiki, N. Wada, M. Tonouchi, M. Hangyo, M. Tani, and K. Sakai, "Temperature dependence of THz radiation from flux-trapped  $\text{YBa}_2\text{Cu}_3\text{O}_{7-\delta}$  thin films excited by ultrashort optical pulses," *Advances in Superconductivity X*, pp. 1231-1234, Springer, Tokyo, 1998.
- [9] C. P. Bean, "Magnetization of high-field superconductors," *Rev. Mod. Phys.*, vol. 36, no. 1, pp. 31-39, 1964.
- [10] M. Tonouchi, N. Wada, M. Hangyo, M. Tani, and K. Sakai, "Control of magnetic flux in a  $\text{YBa}_2\text{Cu}_3\text{O}_{7-\delta}$  thin film loop using femtosecond laser pulses," *Appl. Phys. Lett.*, vol. 71, No. 16, pp. 2364-2366, 1997.

# Passive and Active Component Design Using PBG

Yongxi Qian, *Member, IEEE*, Roberto Cocciali, *Member, IEEE*, Fei-Ran Yang, and Tatsuo Itoh, *Life Fellow, IEEE*

**Abstract** — Photonic bandgap (PBG) structures offer expansion of the circuit and component design for microwave, millimeter-wave as well as optical applications. This paper presents several recent efforts by the authors' group in conceiving, designing and testing new types of high-frequency circuits, both passive and active, based on the use of PBG structures.

**Index Terms** — PBG, High Q cavity, oscillator, microcavities.

## I. INTRODUCTION

CONVENTIONAL microwave integrated circuits based on planar structures such as microstrip lines and coplanar waveguides have problems when scaled to millimeter and/or submillimeter waves, due to increased metal, dielectric as well as radiation losses at such high frequencies. High Q components are particularly difficult to realize, and for that reason metallic waveguides are used frequently although they are less compatible with modern MMIC technology, especially when one is concerned about convenient and efficient integration with active devices.

In recent years there has been a strong interest worldwide in photonic band-gap (PBG) structures for microwave, millimeter-wave and optical applications. These novel artificial periodic structures show distinctive stopband for the propagation of electromagnetic waves along certain directions over a certain range of frequency [1] [2], thus allowing one to control the behavior of electromagnetic waves with additional dimensions of freedom. The authors have proposed and investigated several planar-type PBG structures, and demonstrated their applications in microwave power amplifier and antenna designs [3-6].

For ultra-high frequency applications in the sub-millimeter-wave and terahertz regions, it might be advantageous to use non-metal structures such as dielectric waveguide and image guide [7]. In this paper we demonstrate several novel components, both passive and active, based on PBG effects in such dielectric-based structures. We will first describe a high Q resonator based on PBG cavity mode in an image guide, as well as a low noise oscillator using this PBG resonator. The second example is a small volume optical cavity, which has great potential for the realization of highly efficient Light Emitting Diodes (LEDs) and low threshold current laser diodes.

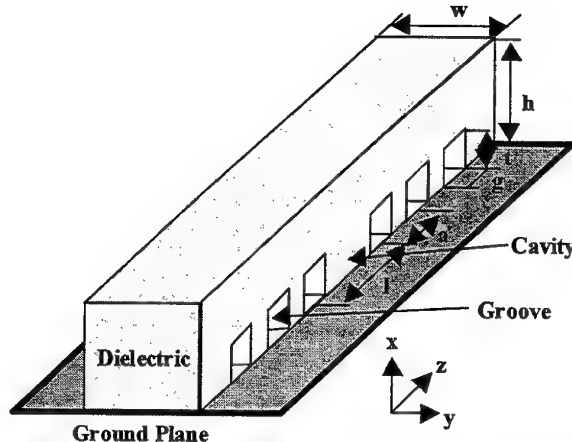


Fig. 1 Schematic of a high Q resonator based on PBG defect-effect in an image guide.

## II. HIGH Q IMAGE GUIDE RESONATOR AND OSCILLATOR

Fig. 1 shows the schematic of a high Q resonator based on the concept of defect mode in PBG structures. A properly designed 1D lattice of grooves, with periodicity  $a$ , would show a stopband for wave propagation along the image guide when the following condition is satisfied:  $\beta a = \pi$ . On the other hand, if a cavity, with length  $l$ , is formed in the middle of the PBG lattice, a sharp, high Q defect mode can be established. This is illustrated by the FDTD simulation results as shown in Fig. 2, which plots the magnetic field intensity profiles in both  $yz$ -cut and  $xz$ -cut of the image guide of Fig. 1. The image guide is excited using a modulated Gaussian pulse, at a location outside the PBG grooves (see Fig. 2). The peak frequency for transmission is found to be 8.255 GHz in this case, which is determined by observing the Fourier spectrum of the field inside the cavity.

To investigate experimentally the characteristics of this high Q resonator, one needs to design a proper coupling scheme to launch and measure the image guide mode. We have designed a novel, efficient transition for this purpose, which is based on a microstrip-fed Yagi-Uda slot array [8]. Fig. 3 (a) shows the image guide PBG resonator as well as the two microstrip-fed Yagi-Uda slot array transitions for S-parameter measurement. The measured transmission coefficient ( $S21$ ), as shown in Fig. 3(b), indicates that a single, high Q cavity mode exists in the 0 - 20 GHz frequency range. The measured peak frequency is 8.276 GHz, which is in excellent agreement with the FDTD

The authors are with the Department of Electrical Engineering, University of California, Los Angeles, CA, 90095, USA.

prediction (0.25 % error). The measured  $Q_u$  is 697, which is reasonably high even though the RT/Duroid 6010 ( $\tan\delta=0.002$ ) used for this experiment is not optimal as a low loss dielectric material for resonators.

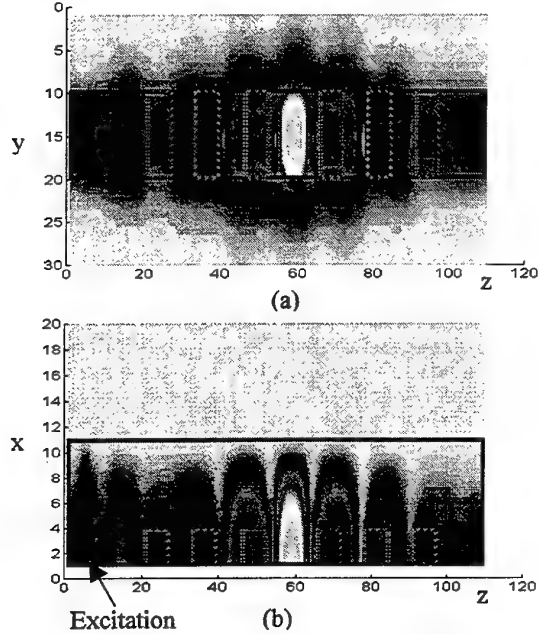


Fig. 2 FDTD simulated magnetic field intensity profile (at 8.255 GHz) in the image guide cavity of Fig. 1, (a) yz-cut and (b) xz-cut. Dimensions are:  $\epsilon_r=10.5$ ,  $h=200$  mil,  $w=300$  mil,  $g=180$  mil,  $a=380$  mil,  $l=570$  mil.

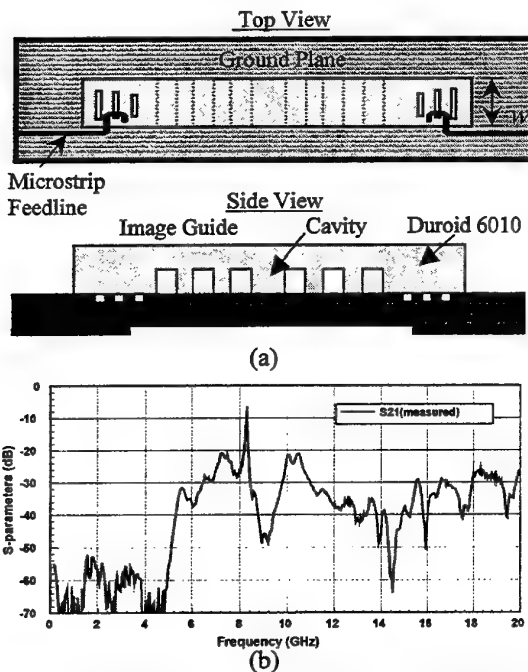


Fig. 3 (a) Schematic of the image guide resonator with microstrip-fed Yagi-Uda slot array transitions, (b) Measured transmission coefficient ( $S21$ ) indicating a high  $Q$  cavity mode at 8.276 GHz.

An instant application of this high  $Q$  resonator is a low noise oscillator design. Fig. 4 (a) shows the schematic of a feedback-type oscillator, which uses two GaAs MMIC gain blocks (HP MGA-64135) to provide the proper amount of signal amplification so that the loop gain satisfies the oscillation condition. The amplifiers are connected by  $50\Omega$  microstrip lines since they are pre-matched. The image guide resonator is placed at the backside of the microstrip substrate similar to that shown in Fig. 3(a). The Yagi-Uda slot array is used both for efficient coupling with the resonator and for extracting the output signal. Fig. 4(b) shows the measured oscillator output in a spectrum analyzer. The output power level is 8.5 dBm after subtracting the coaxial cable loss. A relatively pure spectrum is obtained, with a phase noise level of about -102 dBc/Hz at 100 kHz offset.

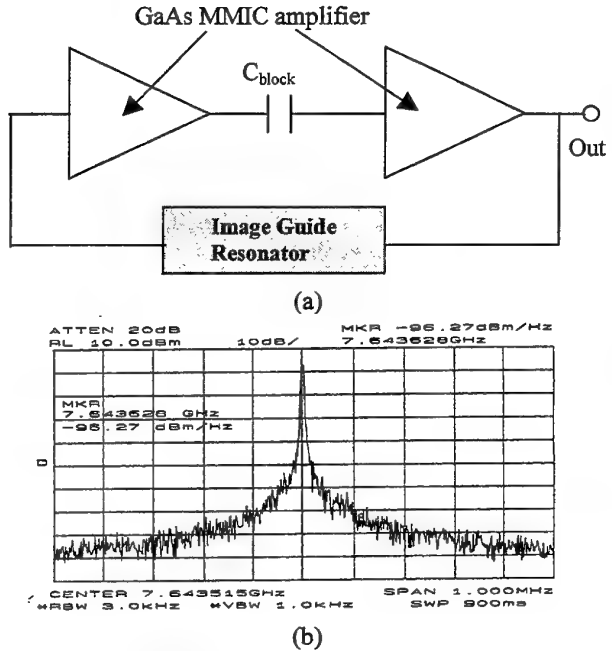


Fig. 4 (a) Schematic of an oscillator using the image guide resonator, (b) Measured spectrum of the oscillator.

### III. MICROCAVITIES FOR SPONTANEOUS EMISSION ENHANCEMENT

PBG-based microcavities have great potential to realize single mode, small volume resonators in the THz frequency range. The use of such cavities to enhance spontaneous emission and realize high efficient LED is an active field of research [9-10]. Fig. 5 shows a small section of a photonic crystal realized by periodically loading with a triangular lattice of holes a slab of light emitter material with high dielectric constant  $\epsilon_r=12$ . The dielectric slab resides on a substrate with a much lower value of dielectric constant, usually glass ( $\epsilon_r=2.25$ ), so that most of the guided modes electromagnetic energy is confined inside the high-dielectric constant slab. The dispersion diagram of the infinitely extending slab can be computed by using the

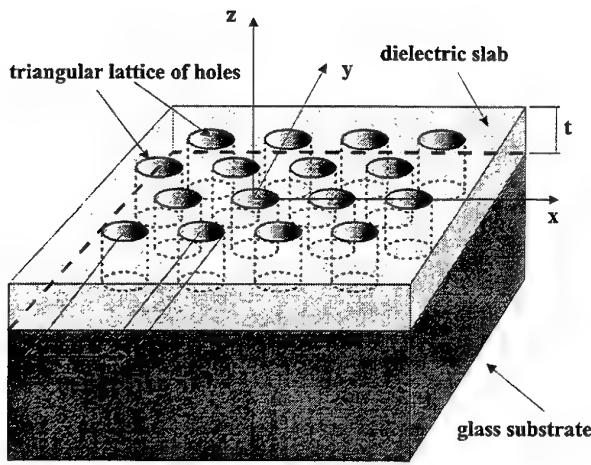


Fig. 5 - Slab of high dielectric constant light emitter material with a triangular array of through holes lying on a low dielectric constant substrate.

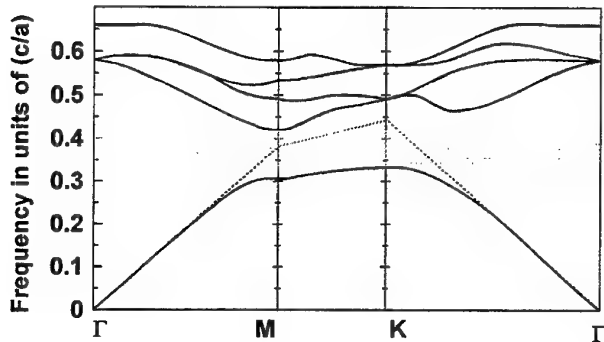


Fig. 6 - Dispersion diagram of TE-like modes of the infinite photonic crystal with a triangular lattice of holes as shown in Fig. 5. To set the horizontal scale,  $\Gamma M = 2\pi/\sqrt{3} a$ .

FDTD to determine the resonant frequencies of a single unit cell of the periodic structure [11]. The computational domain must be truncated using periodic boundary conditions at the lateral walls of the unit cells, and absorbing boundary conditions above and underneath the dielectric slab. Extensive FDTD computations have been carried out considering different values of the ratios  $t/a$  and  $r/a$  expressing the thickness of the dielectric slab and the radius of the holes as a fraction of the periodicity  $a$ . Fig. 6 shows the dispersion diagram of TE-like modes, that is modes with electric field predominantly in the  $xy$ -plane, for the case  $t/a=0.333$  and  $r/a=0.40$ . The dashed lines represent the upper limit to the modes that are confined to the slab and can not leak into the low-dielectric constant substrate. A band-gap for the guided propagation exists in the frequency range from  $0.33c/a$  to  $0.42c/a$ , with  $c$  speed of light in free space. No band-gap has been found for TM-like modes.

Even though a complete band-gap, for both TE-like and TM-like modes, has not been found for this structure, it can be nevertheless employed to realize microcavities by inserting a defect, as previously done for the case of the image guide. Defects realized by either adding or removing an appropriate volume of dielectric material support highly localized electromagnetic modes whose frequency is in the forbidden band-gap of the two-dimensional crystal [9]. The energy of such modes cannot couple to guided modes of the slab, and thus it remains confined inside and around the defect, which acts as a microcavity.

This phenomenon can be exploited to design novel active device such as light emitting diodes. In fact, enhancement of spontaneous emission can be achieved by realizing high electromagnetic energy confinement in the active region of the light emitter material [12]. For this reason, useful defects for this application are those realized by adding material. Three possible configurations, which differ for the position of the defect inside the unit cell, have been studied by using the FDTD technique: material added in the wall between two holes, in the spot between three holes, and in the center of a hole. Fig. 7 shows the resonant frequency and the  $Q$  of the fundamental mode of the microcavity versus the ratio defect volume over volume of a hole, for the case of a defect located at the center of a hole. As the radius of the defect is increased, the resonant frequency of the fundamental mode decrease as expected, and its  $Q$  increases. The third parameter shown in Fig. 7 is the mode effective volume, defined as the total electric energy stored in the microcavity over the maximum electric energy density in the cavity [13]. It represents a figure-of-merit of the energy confinement. For all the three configurations analyzed, there exists an optimum value of the ratio volume of the defect over volume of the holes, for which the effective volume reaches a minimum value (maximum energy confinement). Interestingly enough, the minimum effective volume is about 2, in units of  $(\lambda/2n)^3$ , for all configurations. This value of the effective volume is expected to provide a five-fold spontaneous emission enhancement [13]. Finally, Fig. 8 reports the pattern of the first resonant mode of the microcavity for the value of the defect radius that provides maximum energy confinement.

#### IV. CONCLUSIONS

Photonic band-gap engineering shows great potential for the realization of passive and active components in the terahertz frequency range. In particular, we have investigated novel one- and two-dimensional PBG-based structures that can be used as resonator in the millimeter and sub-millimeter wavelength range. An X-band prototype of the high- $Q$  image guide resonator has been realized, measured, and used for the design of a low noise oscillator.

Active components like light emitting diodes can also greatly benefit from the PBG concept. Extensive FDTD computations have shown the possibility of realizing single mode, small volume resonant cavities at optical frequency, which can potentially lead to the realization of highly efficient light emitting diode.

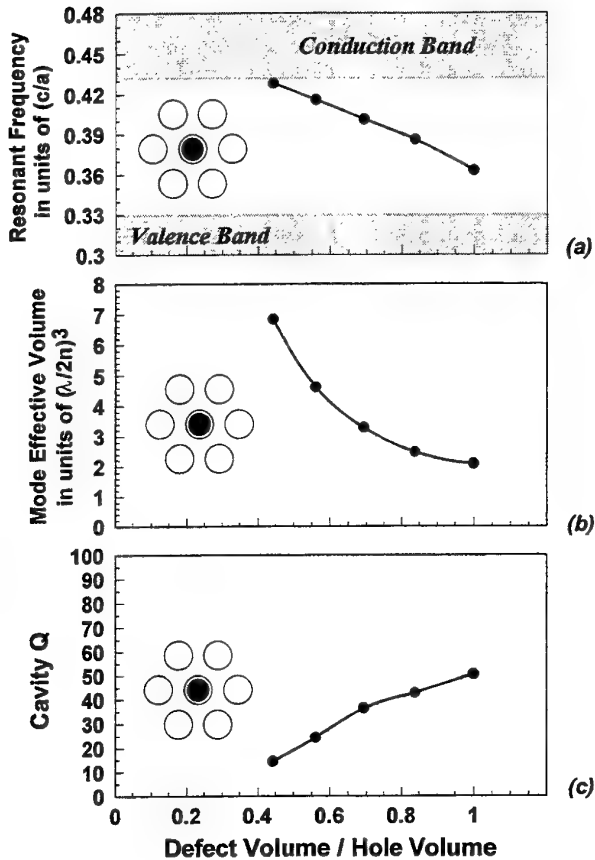


Fig. 7 – Defects located in the center of a hole. (a) Resonant frequency of the mode; (b) Mode effective volume in units of  $(\lambda/2n)^3$ ; (c) Cavity Q-factor.

#### ACKNOWLEDGMENT

This work was supported by US ARO MURI under contract DAAH04-96-1-0005.

#### REFERENCES

- [1] J.D. Joannopoulos, R.D. Meade and J.N. Winn, *Photonic Crystals*, Princeton University Press, 1995.
- [2] E. Yablonovitch, "Inhibited spontaneous emission in solid-state physics and electronics," *Physical Review Lett.*, vol. 58, no. 20, pp. 2059-2062, May 1987.
- [3] Y. Qian, V. Radisic and T. Itoh, "Simulation and experiment of photonic band-gap structures for microstrip circuits," *1997 Asia-Pacific Microwave Conference*, pp. 585-588, Dec. 1997.
- [4] V. Radisic, Y. Qian and T. Itoh, "Broadband power amplifier using dielectric photonic band-gap structure," *IEEE Microwave and Guided Wave Letters*, Vol. 8, pp. 13-14, Jan. 1998.
- [5] V. Radisic, Y. Qian, R. Cocciali and T. Itoh, "Novel 2-D photonic band-gap structure for microstrip lines," *IEEE Microwave and Guided Wave Letters*, Vol. 8, pp. 69-71, Feb. 1998.
- [6] Y. Qian, D. Sievenpiper, V. Radisic, E. Yablonovitch and T. Itoh, "A novel approach for gain and bandwidth enhancement of patch antennas," to be presented at *1998 IEEE RAWCON'98*, Aug. 1998.

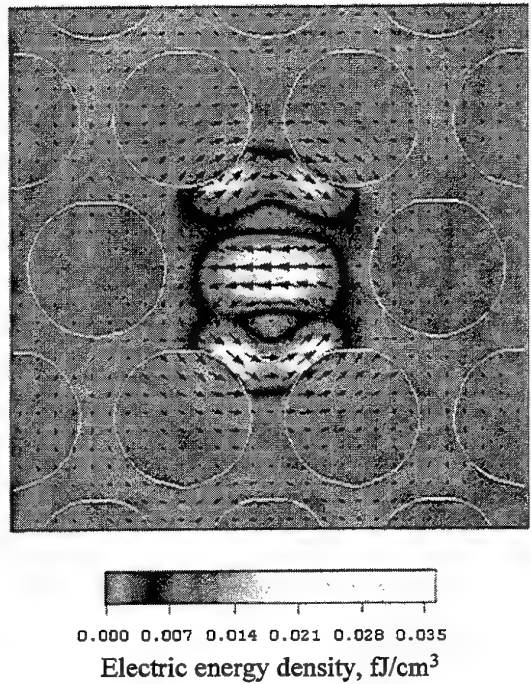


Fig. 8 - Mode pattern of the fundamental mode of the microcavity realized by adding material (Defect). The defect is located in the center of a hole, completely filling it. This configuration provides maximum energy confinement. Energy density distribution in the  $xy$  plane is coded with colors, with in-plane electric field shown as a vector plot.

- [7] T. Itoh and F. Hsu, "Distributed Bragg reflector Gunn oscillators for dielectric millimeter-wave integrated circuits," *IEEE Trans. Microwave Tech.*, vol. MTT-27, pp. 514-518, May 1979.
- [8] F. R. Yang, Y. Qian and T. Itoh, "A novel high-Q image guide resonator using band-gap structures," *1998 IEEE MTT-S Int. Microwave Symp.*, pp. 1803-1806, June 1998.
- [9] E. Yablonovitch, T.J. Gmitter, R.D. Meade, A.M. Rappe, K.D. Brommer, and J.D. Joannopoulos, "Donor and Acceptor modes in photonic band structure," *Physic Review Letters*, vol. 67, no. 24, pp. 3380, June 1991.
- [10] P.R. Villeneuve, S.Fan, and J.D. Joannopoulos, "Microcavities in photonic crystals: mode symmetry, tunability and coupling efficiency," *Physical Review B*, vol. 54, no.11, pp. 7837-7842, Sept. 1996.
- [11] R. Cocciali, T. Itoh, "Surface waves suppression in photonic band-gap substrates," *URSI 98*.
- [12] E.M. Purcell, "Spontaneous emission probabilities at radio frequencies," *Physical Review*, vol. 69, pp. 681, 1946.
- [13] R. Cocciali, M. Boroditsky, K.W. Kim, Y. Rahmat-Samii, E. Yablonovitch, "What is the smallest possible electromagnetic mode volume in a dielectric cavity?," Submitted to *IEE Proceedings, Optoelectronics*.

# Fabrication Technologies for Terahertz Waveguide

Chris M. Mann

**Abstract--**Terahertz waveguide components can now be realised using a variety of methods. The size and geometry of waveguide at terahertz frequencies ideally lends itself to fabrication via a number of micromachining techniques. The use of micromachining allows the realisation of waveguide components that cannot be fabricated via conventional machining at these frequencies. Conventional machining should not, however, be overlooked. Corrugated feedhorns operating at 3THz have been realised using ultra high precision machining techniques. To date it has not been possible to realise the corrugated horn structure via lithographic micromachining.

This paper discusses the relative merits of various fabrication techniques, highlighting any strength or weakness that is relevant to terahertz waveguide fabrication.

**Index Terms--** Terahertz, Waveguide, Micromachining.

## I. INTRODUCTION

A 2.5THz waveguide mixer was first demonstrated in 1996<sup>1,2</sup> at the Rutherford Appleton Laboratory. This work has continued but recently workers at the Jet Propulsion Laboratory (JPL) have also demonstrated a 2.5THz waveguide mixer intended for operation in space aboard NASA's Earth Observation System Microwave Limb Sounder (EOS-MLS)<sup>3</sup>.

Terahertz waveguide devices can therefore now be considered to be a relatively mature technology, however, current devices make use of waveguide cavities which have been fabricated using conventional machining techniques. Thus they are highly expensive and their construction is difficult, limiting their use to applications where cost and complexity are not the driving issues. If terahertz devices are to find more general applications such as industrial processing or covert/medical imaging then new manufacturing techniques must be developed.

## II. MICROMACHINED WAVEGUIDE

### A. Direct Machining

With the use of ultra high precision lathes and milling machines, combined with state of the art metrology it has

been possible to directly machine waveguide circuits that operate at 2.5THz. Needless to say the resulting components are not cheap but they can be relatively plentiful. The dimensions of the waveguide at this frequency are truly miniature being 27x105 $\mu$ m. Specialist techniques have been developed to allow the assembly of the RF circuit. A photograph of a 2.5THz corrugated feedhorn and its radiation pattern are shown in figure 1. For reference, the aperture of the feedhorn is 800 $\mu$ m.

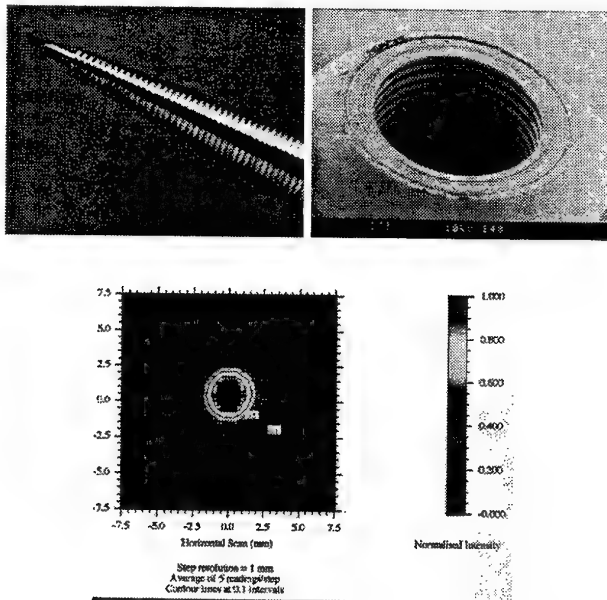


*Fig 1. A 2.5THz corrugated feedhorn mandrel, feedhorn and radiation pattern*

Direct machining still has a number of advantages. From a manufacturing perspective plastic injection molding is a well established technology. In this process the molds are made using conventional machining, the initial cost is high but for large scale production still acceptable. It is likely that conventional machining will be with us for some years to come.

### B. Hollow Pipe Waveguide

The use of micromachining to fabricate waveguide was first demonstrated by workers at the University of Bath<sup>4</sup>. A technique was developed whereby an ultra-thick layer of positive photoresist was patterned using UV lithography and subsequently coated in gold. A schematic of this technique is shown in figure 2. The use of positive

Rutherford Appleton Laboratory, Chilton, Didcot, Oxfordshire, OX11 0QX, The United Kingdom.

photoresist is critical as once the waveguide former has been metallised the resist is then dissolved leaving a hollow pipe. Using this technique it has been possible to directly integrate the active semi conductor device directly into the waveguide. This approach does, however, have a number of hurdles that need to be overcome. The most critical of these is that the process is essentially 2-dimensional. This makes it difficult to incorporate steps in waveguide height or microstrip filter channels (the main circuit architecture that is used to house the various filters used in conventional waveguide devices).

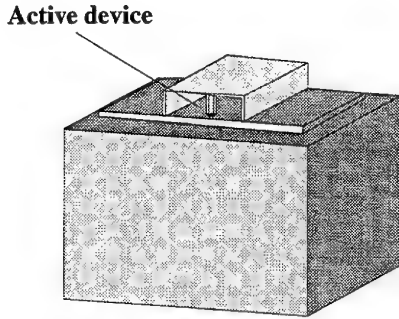


Fig 2. The hollow pipe waveguide approach.

Also, it is not obvious how the traditional horn antenna can be incorporated into this circuit architecture. A flared horn antenna has been incorporated into the design<sup>5</sup>, however, its radiation pattern is far from ideal though it does have the advantage that the beam is elevated upwards from the plane of the substrate.

Finally, there is presently no ultra thick (>200 $\mu$ m) positive resist available. This limits the lowest frequency of operation to around 100GHz before very reduced height waveguide has to be implemented.

### C. Soft X-ray LIGA

Workers at RAL developed a different approach to micromachining terahertz waveguide components. Rather than attempting to completely integrate the active device with the waveguide circuit, the active device was to be integrated separately into a carrier ring and subsequently assembled with the waveguide mount. In order to obtain very vertical sidewalls, use was made of soft (10 $\text{\AA}$ ) X-ray lithography<sup>6</sup>. This has the advantage that the masks required can be relatively thin, only approximately 1 $\mu$ m of gold is required for an exposure of 100 $\mu$ m in depth. This allowed the integration of the masks into the resist itself yielding a 3-dimensional waveguide former. This was subsequently metallised and then removed along with the substrate. The basic concept and process is laid out in figure 3. It is interesting to note that the proposed active device configuration has since been successfully adopted by the workers at JPL for use in their 2.5THz mixer. Soft x-rays are limited to exposure depths of around 100 $\mu$ m limiting its frequency suitability to about 100GHz and

above. In addition, the lithographic process was complex and time consuming

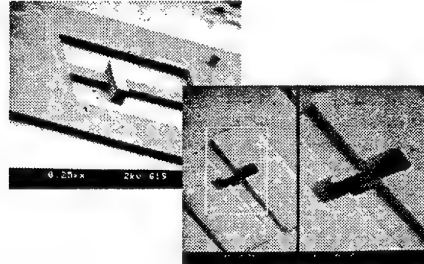
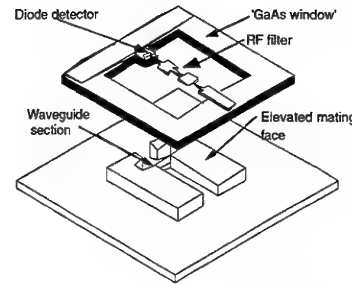


Fig 3. Soft X-ray lithography used to realise complex 3-dimensional 2.5THz waveguide cavities.

### D. Other Exotic Fabrication Techniques

Hard X-ray LIGA (Lithographie Galvanoformung Abformung) allows greater depths to be achieved in positive resist but it is a complex and expensive process. The requirement for thick X-ray masks makes external alignment essential if 3-dimensional structures are to be realised. This has been demonstrated but adds to process complexity. It is able to produce a positive resist waveguide former that has near perfect geometry and surface characteristics. Figure 4 shows an example of X-ray LIGA.

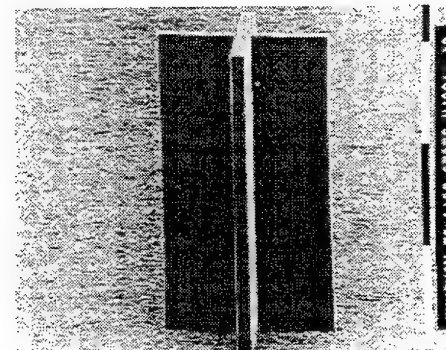


Fig 4. An example of hard X-ray LIGA

Should a requirement for large scale manufacture of terahertz waveguide components emerge then hard X-ray LIGA may be the process of choice.

Other promising fabrication routes are the use of plasma etching techniques. These can be used to etch either a polymer that can be metallised and subsequently removed or etch the structure directly into a substrate such as a silicon

wafer. Inductively Coupled Plasma (ICP) etching systems are able to achieve anisotropic levels in excess of 500. Unlike anisotropic wet etching techniques this technology is not restricted to the natural crystal orientation of the substrate and so can be used to achieve very complex geometry's and vertical walls. The only disadvantage of this technology presently appears to be the cost of the equipment required.

Finally, direct laser machining of corrugated feedhorns into silicon substrates has been demonstrated<sup>7</sup>. This technique has the advantage that true 3-dimensional structure can be realised. This is the only micromachining technique other than direct machining that has been able to demonstrate the fabrication of a corrugated feedhorn at terahertz frequencies. However, this approach requires complex equipment and is comparatively slow.

#### *E. SU-8 and Wet Silicon Processing*

Recently a negative resist has been developed that is ideally suited to the fabrication of terahertz waveguide cavities, SU-8<sup>8</sup>. This resist has caused great excitement in the terahertz community. This can be mainly attributed to the ease with which SU-8 can be patterned to form near perfect waveguide structures. The resist is exposed using 365nm Ultra Violet radiation and is therefore compatible with most conventional lithographic systems. Features as high as 2mm have been demonstrated so in principle it could be used to make full height waveguide below 100GHz. Because the resist is negative, once one image has been exposed into the resist a second layer can then be applied and exposed using a different mask. An example of this is shown below in figure 5. This tallest features are 1mm high.

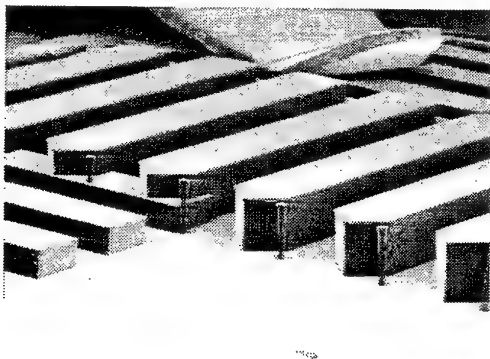


*Fig 5. An example of multilevel SU-8 processing*

In this way it is possible to build up complicated 3-dimensional structures although at present this is limited to vertical or sloping walls. It is therefore possible to create waveguide cavities that contain microstrip filter cavities and waveguide transitions.

A novel technique has been developed that combines SU-8 processing with wet silicon anisotropic etching to form a high performance waveguide horn antenna.

Complete waveguide mixer cavities at 600GHz have been realised using this technique<sup>9,10</sup>. The basic process is shown in figure 6. Basically a <100> oriented silicon wafer has a series of tapered 'V' grooves etched into its surface. The wafer is then planarised using SU-8 and processed. The resulting cavities contain the microstrip filter, fixed position backshort and waveguide to horn transition.

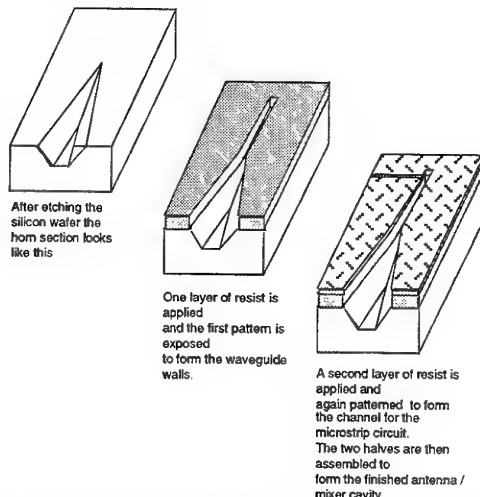


*Fig 7. The composite SU-8/ silicon micromachining technique*

In addition, assembly is greatly simplified by the incorporation of locking alignment pegs and holes. A finished mixer is shown below in figure 8

Whilst SU-8 is extremely easy to process, it is very difficult to remove once exposed. This omits its use as a sacrificial mould.

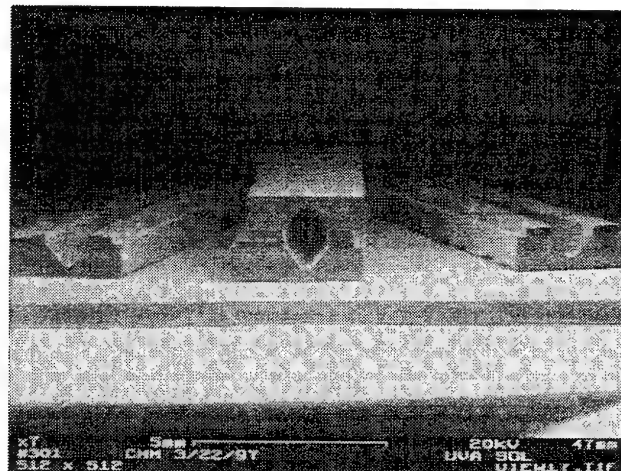


*Fig. 8. An assembled and split micromachining 600GHz mixer cavity*

Its use is therefore limited to the production of cavities into which the active device is later inserted.

RF results for a micromachined mixer fabricated using the SU-8/silicon process are anticipated within the next twelve months. As the design is more or less an exact clone of a successful conventionally machined mixer<sup>11</sup> it is likely that similarly good results will be obtained.

### III. DISCUSSION

There are now a number of very promising techniques available for the micromachining of terahertz waveguide circuits. However, no one single technique offers the perfect solution. For full active device integration a positive or dissolvable resist is required. At present such a resist does not exist. What is required is a positive version of SU-8! All of the elements that make up conventional waveguide devices can be realised using one or more of the above micromachining techniques. These include high performance antennae, microstrip channels, fixed backshorts and waveguide transitions. In addition, elements that are virtually impossible to machine using conventional techniques can be easily produced. Such elements include notch filters and frequency multiplexers which may allow terahertz signal processing.

Coincidentally, there are now very accurate, and just as importantly, fast, software tools available that allow the modeling of such components. This is an important prerequisite for successful implementation of micromachined terahertz waveguide systems.

### IV. CONCLUSIONS

Using a variety of micromachining techniques it has become possible to realise terahertz waveguide circuits. The use of micromachining will allow many more workers to design, build and test terahertz waveguide components. The race is now underway to demonstrate the first fully micromachined RF waveguide system where the active semiconductor device has been directly integrated into the waveguide circuitry via common lithographic processing steps. If successful, it will then become possible to realise more complex device configurations e.g., power combiners, balanced mixer circuitry and potentially, terahertz signal processing.

<sup>3</sup> P. H. Siegel, M. Gaidis, S. Martin, J. Podosek, U Zimmermann, '2.5THz GaAs Monolithic Membrane-Diode Mixer', 9th International Conference on Space THz Technology, Pasadena, CA, March 1998

<sup>4</sup> D.A. Brown, A. S. Treen, N. J. Cronin, *Micromachining of Terahertz Waveguide Components with Integrated Active Devices*, 19th International Conference on Infrared and Millimetre Waves, Sendai, Japan, 1994.

<sup>5</sup> J.W.Digby et al, 'Integrated Micro-Machined Antenna for 200GHz Operation' the IEEE-MTT-S International Microwave Symposium, Colorado, Vol. II, pg. 561, 1997

<sup>6</sup> S. W. Moon, C. M. Mann, B. J. Maddison, I. C. E. Turcu, R. Allot, S. E. Huq, N. Lisi, Terahertz Waveguide Components Fabricated Using a 3D X-ray Microfabrication Technique, Electronic Letters, vol. 32, no. 19, 12 Sept. 1996, pp. 1794-1795.

<sup>7</sup> C. K. Walker et al 'Laser Micromaching of Silicon, A New Technique for Fabricating High Quality Terahertz Waveguide Components' 8th International Symp. on Space THz Technol., Harvard University, March 1997.

<sup>8</sup> K. Y. Lee, N. LaBianca, S. A. Rishton, S. Zolgharnain, J. D. Gelorme, J. Shaw, T. H.-P. Chang, *Micromachining Applications of a High Resolution Ultra thick Photoresist*, J. Vac. SCI. Technol. B 13(6), Nov./Dec. 1995.

<sup>9</sup> T. W. Crowe, P. J. Koh, W. L. Bishop, C. M. Mann, J. L. Hesler, R. M. Weikle, P. A. Wood, D. N. Matheson, *Inexpensive Receiver Components for Millimetre and Submillimetre Wavelengths*, 8th International Symp. on Space THz Technol., Harvard University, March 1997.

<sup>10</sup> C. M. Mann, D. N. Matheson, M. L. Oldfield, P.J.Koh, T.W.Crowe, W.L.Bishop, R.M.Weikle, J. L. Hesler, 'A Simple Micromachining Technique For Millimetre, Submillimetre And Terahertz Waveguide Cavities', the 2nd ESA workshop on Millimetre Wave Technology and Applications, Millilab, Espoo, Finland, 27-29th May, 1998.

<sup>11</sup> J. L. Hesler, W. R. Hall, T. W. Crowe, R. M. Weikle, II, B. S. Deaver, Jr., R. F. Bradley, and S.-K. Pan, *Fixed-Tuned Submillimetre Wavelength Waveguide Mixers Using Planar Schottky Barrier Diodes*, IEEE Trans. Microwave Theory Tech., May 1997.

<sup>1</sup> B. N. Ellison, M.L. Oldfield, D.N. Matheson, B.J. Maddison, C.M. Mann, S. Marazita, T. W. Crowe, P. Maaskant, W. M. Kelly, *First Results for a 2.5 THz Schottky Diode Waveguide Mixer*, 7th International Symposium on Space Terahertz Technology, University of Virginia, March 1996.

<sup>2</sup> B.N.Ellison, M.L.Oldfield, D.N.Matheson, B.J.Maddison, C.M.Mann and A.F.Smith, 'Corrugated Feedhorns at Terahertz Frequencies - Preliminary Results', The Fifth International Symposium on Space Terahertz Technology, Ann Arbor, May 1994.

# Electromagnetic Analysis Of Micromachined Devices

J. Carbonell, J. Danglot, X. Mélique, O. Dupuis, E. Lheurette,  
P. Mounaix, O. Vanbésien, and D. Lippens

**Abstract:-** In this paper, the electromagnetic behaviour of micromachined devices aimed at operating at terahertz frequency is specially addressed. We considered respectively (i) new fabrication techniques for free-standing air-bridged structures for planar device arrays (ii) high-speed low-loss coplanar wave guides deposited on a membrane in GaAs Technology, (iii) metallic/air photonic band gap structures used in filtering and guiding sections (iv) radiating antenna deposited on Low Temperature Grown GaAs used in pulse optical techniques for Terahertz generation.

**Indexing terms** - Micro-machining, EM analysis, Terahertz frequency

## 1. INTRODUCTION

In recent years, micromachining technology has attracted much interest with the prospect of high performance microdevices aimed at operating at terahertz frequency. High-speed transmission lines and high performance patch antennas were fabricated on dielectric membranes [1]. Periodically structured dielectric materials, which exhibit Photonic Band Gaps (PBG's) [2], were micromachined and employed as waveguides, antenna substrates and reflectors. A monolithic integration approach, making used of surface micromachining, is currently used in the fabrication of receivers with Terahertz targeted frequency. Moulded and etched microstructures are now widely used in quasi-optical systems by taking benefit of ultra short optical pulses. In this context, we report here the recent developments carried out at IEMN on the fabrication and the microwave analysis of four types of devices. First of all, we focus our attention about the planar integration of reactive active devices commonly used in multiplier chains. Beyond the search of intrinsic high performance, it is now widely recognised that the diode environment is of major concern. This implies to carefully design the diode embedding in particular the interconnecting elements.

This work was supported by the Centre National de la Recherche Scientifique in the framework of GDR projects 'Photonic crystals and microcavities' and 'Microsystems'.

The authors are with the Institut d'Electronique et de Microélectronique du Nord, U.M.R. C.N.R.S. 9929, Département Hyperfréquences et Semiconducteurs, Université des Sciences et Technologies de Lille, Avenue Poincaré, BP 69, 59652 Villeneuve d'Ascq cedex, France

Resist forming techniques are of great help towards this goal with the successful fabrication of free standing interconnects. Then, we consider the case of coplanar waveguides deposited on a dielectric membrane. In the present work, the novelty stems from the use of GaAs substrates and polyimide films with the proposal of a new tapering section. With respect to PBG's, special attention will be paid to metallic structures which were investigated at millimetre wavelengths. At last, we illustrate the usefulness of microstructuring technologies in quasi-optics techniques.

## 2. INTEGRATION TECHNIQUES

The effort on device fabrication concerns mainly the implementation of technology procedures aimed at planar integrating Heterostructure Barrier Varactors (HBV's). The motivations of such a project are now well known notably the possibility to consider device arrays. The last development carried out in Lille in this field concerns the fabrication of low parasitics HBV in single or multi-device configurations [3]-[6]. Figure 1 shows a Scanning Electron Microphotograph of devices integrated in series by means of air bridge contacting techniques.

The devices were fabricated with typically a set of seven masks including the fabrication of top and side ohmic contacts, posts and airbridges and contacting pads for a subsequent flip-chip technology. For the fabrication of micron scale air bridges which appears as a key stage, we recently developed a pyrolyzation technique in a bi-resist process flow with the aim to achieve a high fabrication yield needed for array implementation. This technique offers two major advantages. First, the resist serves as a temporary mould for the deck formation and second exhibits a convex shape. Generally speaking, the possibility of resist forming techniques can be applied to a variety of microstructures interconnected by free-standing airbridges. The present work was devoted to HBV's. It can be shown however that such a technique can be applied to a large variety of low dimensional devices such as Resonant Tunnelling diodes (RTD's) or Schottky's. It is worth-noting however that for both devices on sub-micron scale, full writing by e-beam of microstructures is often required using a bi-layered technology with T-shaped

metallization using technological procedures very similar to those employed for short gate length transistors.

From the electromagnetic point of view, recent advances in three-dimensional electromagnetic (EM) simulations permit us to model accurately the active device embedded in its environment. For illustration of such a procedure, detailed in reference [6], Figure 2 shows the plot on a Smith chart of the frequency dependence of the reflection coefficient ( $S_{11}$ ) of a dual HBV, measured and calculated respectively. The agreement is good and supports the validity of a top down approach [5].

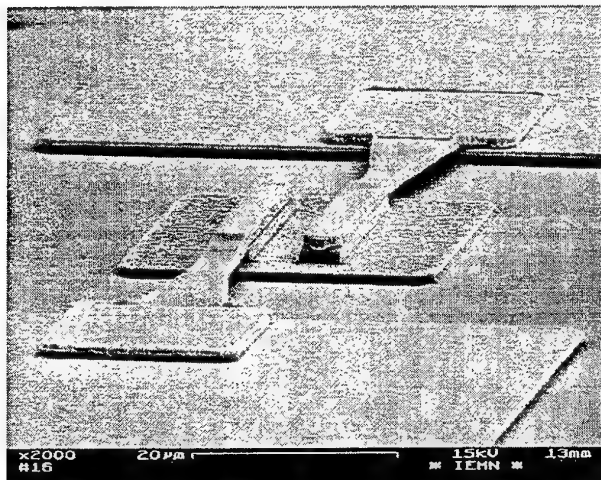


Figure 1: SEM view of planar integrated InGaAs/InAlAs/AlAs HBV's. The blocking barrier use a step-like barrier scheme [4]. Two barriers are integrated in series on the same epitaxy (Dual Barrier varactor). The overall number of single devices is thus 4 with the associated benefit of a high power handling and a low capacitance level [3].

Recently, it was demonstrated that such devices exhibit record performances at millimetre wavelengths [7].

### 3. MICROMACHINED COPLANAR WAVEGUIDES

For the fabrication of micromachined coplanar waveguides, we made use of dielectric membranes deposited on a GaAs substrate with subsequent back-side bulk micromachining. Indeed, since most of solid state devices are now fabricated in III-V material system, it is believed that such a scheme will provide greater functionality. Another novelty of the present work stems from the use of polyimide dielectric film, instead of a conventional  $\text{Si}_3\text{N}_4/\text{SiO}_2$  configuration. It is found that their fabrication is greatly simplified by simple spin coating while maintaining a high etching selectivity and low strain. At last, we proposed a new scheme for the tapering section to perform the transition between free-to-thick- substrate

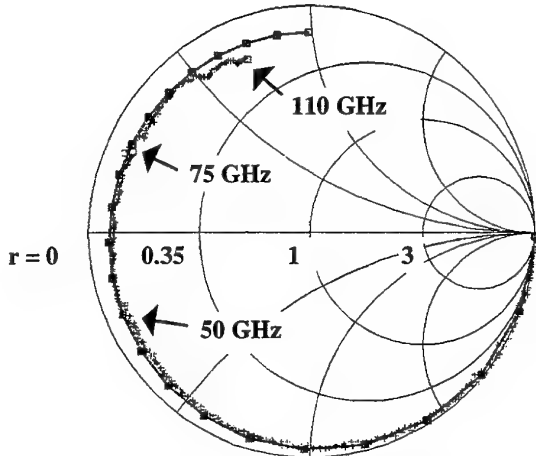


Figure 2: Comparison between the calculated reflection coefficient and the measured data for a dual HBV configuration. The devices are wafer probed by means of a coplanar waveguide scheme. As a consequence the scattering parameter  $S_{11}$  takes the access lines, the interconnecting elements and the active device into account.

regions taking advantage of the anisotropic etching properties [8]. This idea is illustrated in Figure 3 which is a cross section through propagation direction. For designing the taper section, we took benefit of a central parabolic interconnecting region while keeping constant the characteristic impedance. For EM analysis of this transition, we faced the problem of large aspect ratio between the membrane thickness and all other relevant

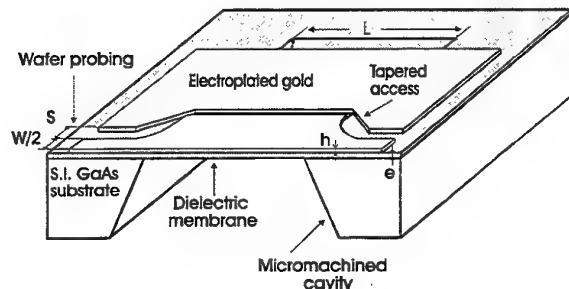


Figure 3: Schematic cross section through the propagation direction of a CPW deposited on a polyimide membrane. In the present work, we took advantage of the tilted etch profile for the fabrication of the taper section.

dimensions (lateral size and etching depth). This condition appears unfavourable to a global analysis. Therefore, we split the structure into two parts (ie) the taper and propagation regions respectively with a full wave 3 D analysis on one hand and a 2D approach on the other hand.

A comparison between calculated and measured  $S_{21}$  data is displayed in Figure 4. Overall, the agreement is good,

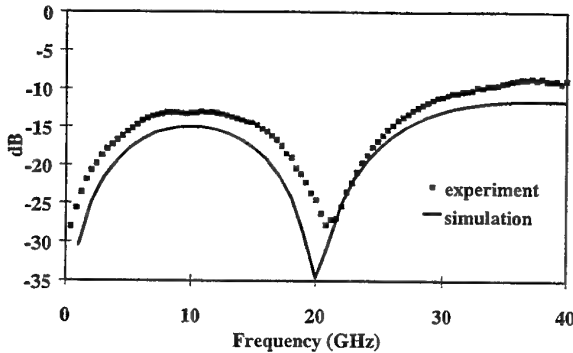


Figure 4: Comparison between modelled and measured data for a constant characteristic impedance taper section for a 3.5 mm long transmission line

despite some uncertainties notably due to mismatch during membrane alignment.

#### 4. METALLIC PHOTONIC BAND GAP

Wire Photonic Band Gap materials, characterised in our laboratory, exhibit a triangular lattice and consist of 1.7 mm diameter metallic wires embedded in air with a filling

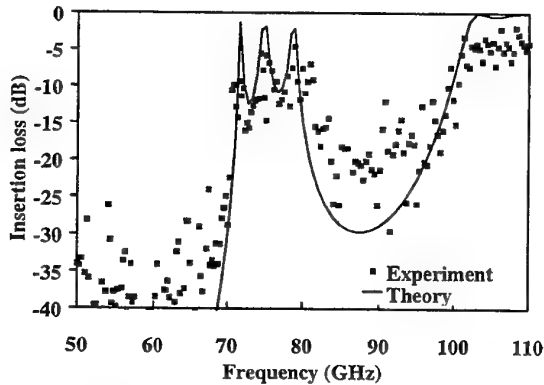


Figure 5: Comparison between calculated (HFSS simulation code) and measured data for a metallic photonic band gap. The lattice of the artificial structure is of diamond-like. The relevant dimensions are 2.69 mm and 4.96 mm respectively. Measurements are carried out in free space by VNA.

factor of 16 %. On such millimetre scale and with an air filled propagation medium, the pass-bands are at millimetre wave lengths (V band and W bands respectively). In that case, accurate Vector Network Analysis (VNA) can be performed by means of conventional HP network analysers with absolute value of the magnitude of  $S_{21}$  obtained by differential measurements. As a matter of illustration of the work conducted at IEMN, Figure 5 shows the frequency variation of measured values of  $S_{21}$  for a four row structure, for a TM electric field polarisation (electric field

parallel to the metallic rods) and a normal incidence. Photonic band gaps are found from dc to  $\sim 70$  GHz and from 80 GHz up to 100 GHz.

Again, a careful analysis of electromagnetic behaviour can be of great help in the understanding of electric field localisation effect [9]. These effects leads to transmission peaks rather than a true miniband and are a direct consequence of a finite superlattice. In Figure 5, we also plotted in solid lines the calculated variation of  $S_{21}$  versus frequency which was computed by means of HFSS<sup>TM</sup> simulation tool. The agreement is relatively good notably for the characteristic frequencies. On this basis, the potential application of such artificial propagation media can be theoretically investigated prior to any technological effort and notably the possibilities afforded when PBG's are employed as guiding structures.

In order to exemplify such a possibility, the electric field magnitude of electric field within a single branch coupling device is plotted in Figure 6. The operating frequency is close to 50 GHz consequently within a forbidden gap. As a consequence, the energy is confined within the guiding section obtained by removing some of the wires leading to a guiding branch width of 3.75 mm.

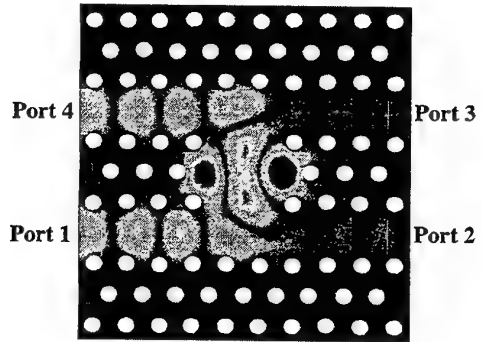


Figure 6: Electric field magnitude at 52.82 GHz for a backward operation of a single branch line coupler.

It can be noted that the operation can be compared to a backward mode with an inversion in the propagation direction. A detailed explanation of process at the origin of this property is beyond the scope of this communication but was found very similar to that involved in coupled quantum wire couplers [10]. In short, the incoming EM energy stream experiences a reflection on the right hand side of the coupling branch and is then driven preferentially towards port 4 rather than port 3. It results from this a great variety of potential applications and perhaps more interestingly the possibility to tune the transmission properties with quantum interference relying devices. Notably it can be shown that alternative approaches to multimode operation are possible by means of multiple-branch-structures. Also, the extension of these ideas into the terahertz frequency band is not unrealistic

taking benefit in particular of micromachining techniques of thick resists of SU-8 type.

## 5. QUASI-OPTICAL SYSTEMS USED FOR TERAHERTZ GENERATION

Low Temperature Grown (LTG) GaAs epilayers were used for implementing the detecting antenna in a pump probe experiment. Unlike GaAs materials grown at a substrate temperature of about 600 °C, LTG GaAs contains a high concentration of deep defects which promotes carrier recombination while maintaining a good crystal quality. Typically, the film consisted of a 10 nm-thick GaAs buffer layer grown at 600°C and a 1μm thick LTG GaAs grown at 200°C under normal As-stabilised conditions. From the crystal mismatch measured by X ray diffraction a concentration of about  $9 \times 10^{19} \text{ cm}^{-3}$  As antisites (As<sub>Ga</sub>) can be measured. On this basis, a rough estimate of carrier life time ( $\tau \sim 200 \text{ fs}$ ) can be calculated.

The pump probe femtosecond experimental set up combines a large-aperture Cr-doped GaAs emitter antenna and a strip-line LTG:GaAs detector antenna [11]. We show in Figure 7 the variation of the detected signal versus delay time. A sharp peak can be seen with a full width at half maximum of 750 fs followed by replicas which result from the reflection of the radiation at the semiconductor-air interface. Fourier transform of a single pulse in order to get the radiated spectrum shows that the maximum amplitude was centered around 140 GHz with a radiated signal up to 1.5 Terahertz. Thinning and microstructuring techniques are of great help for achieving a single pulse operation.

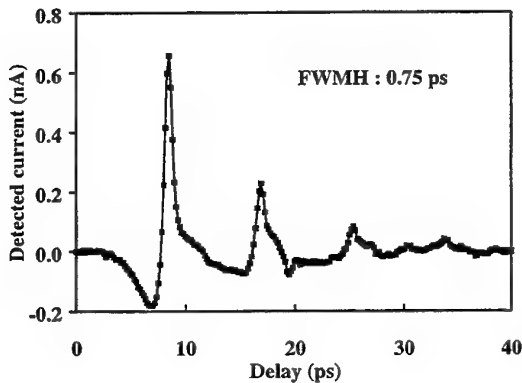


Figure 7: Time response of the radiated electromagnetic field convolved with the transient photoconducting current

## 6. CONCLUSION

In this communication, special attention was paid to the microwave analysis of various micromachined structures

including active and passive Terahertz components. From the view point of fabrication techniques, the ideas are numerous with a frequent use of resist moulding techniques, surface and bulk micromachining, dielectric, semiconductor or metal deposition for fabricating cantilever-type or membrane microstructures. Three dimensional Electromagnetic (EM) and Vector Network Analysis (VNA) are now very efficient for predicting and investigating the rf properties of such microstructures at terahertz frequency. Owing to the joint progresses in technological processes and Computer Aided Design (CAD), it is believed that a reverse engineering approach can be efficiently applied in a research field where a 'cut and try' approach is too risky.

## 7. ACKNOWLEDGEMENTS

The works reported in this communication are partially supported by European Agency (ESA), Centre National d'Etudes Spatiales (CNES) and Centre National de la Recherche Scientifique (CNRS). The pump-probe experiments were carried out at the laboratoire de Physico-Chimie de l'Atmosphère, Université du Littoral, Dunkerque, France. The authors would like to thank E. Delos and S. Lepilliet for technical assistance.

## REFERENCES

- [1] M.T. Weller, L.P.B. Katehi, G. Rebeiz, "High performance microshield line components", *IEEE transactions Microwave Theory and Techniques*, Vol. 43, pp. 534-543, 1995
- [2] See for example Photonic band gap materials edited by C.M. Soukoulis, Kluwer Academic Publishers (1996)
- [3] E. Lheurette et al., "High performance InP-based Heterostructure barrier Varactor in single and stacked configuration", *Electronics letters*, Vol. 32, pp. 1417-1418, 1996
- [4] R. Havart et al. "Step like Heterostructure Barrier Varactor", Accepted for publication in *IEEE Electron Device Letters*
- [5] J. Carbonell, R. Havart, X. Mélique, P. Mounaix, O. Vanbésien, J.M. Goutoule and D. Lippens, "Reverse engineering through Electromagnetic and Harmonic Balance Simulations", accepted to *EuMc*, Amsterdam, October 1998
- [6] X. Mélique et al., "InGaAs/InAlAs/AlAs Heterostructure Barrier Varactors for Harmonic multiplication", to be published in *Microwave and Guided Wave Letters*, Vol. 8, N°7, 1998
- [7] X. Mélique, C. Mann, P. Mounaix, O. Vanbésien, F. Mollot and D. Lippens, "5 mW and 5 % efficiency 216 GHz InP-based Heterostructure Barrier Varactor Tripler", Submitted for publication in *IEEE Microwave and Guided Wave Letters*
- [8] O. Dupuis, J. Carbonell, P. Mounaix, O. Vanbésien and D. Lippens, "High speed low loss micromachined coplanar waveguides in GaAs Technology", accepted to *EuMc*, Amsterdam, October 1998
- [9] J. Carbonell, O. Vanbésien and D. Lippens, "Electric field patterns in finite two-dimensional wire photonic lattices", *Superlattices and Microstructures* Vol. 22, 4, pp.597-605, 1997
- [10] O. Vanbésien and D. Lippens, "Directional coupling in dual-branch-line electron-waveguide junctions", *Phys. Review B*, 52, pp.5144-5153, 1995
- [11] G. Mouret, W. Chen, D. Boucher, R. Bocquet, P. Mounaix, D. Théron and D. Lippens, "High power terahertz radiation from a high repetition rate large aperture photoconducting antenna", *Microwave and Optical Technology Letters*, Vol. 17, pp. 23-27, 1998

# Non-Linear Transmission Lines for Millimeter-Wave Frequency Multiplier Applications

James R.Thorpe Paul Steenson Robert E.Miles

**Abstract**— Novel micromachined waveguides incorporating Heterojunction Barrier Varactors for millimeter-wave applications have been fabricated. Using measured results an accurate Non-Linear Transmission Line (NLTL) model has been developed and utilised to predict the performance of a NLTL frequency tripler using these waveguides and devices for G-Band operation. A port-to-port conversion efficiency for 3<sup>rd</sup> harmonic of better than 1.5 % over a broad frequency range of 264 to 300 GHz for a fundamental power of 20mW has been predicted.

**Keywords**— Non-Linear Transmission Line, Frequency Multiplier, Heterojunction Barrier Varactor, Micromachined Waveguide.

## I. INTRODUCTION

THERE is a need for solid state broad-band sources of power above 100 GHz with applications such as local oscillators for mixers and power sources for quasi-optical, remote sensing and wide-band communication systems. At these frequencies state of the art Gunn diode oscillator - frequency multiplier systems using Schottky diodes [1], Heterostructure Barrier Varactors (HBVs) [2] or Resonant Tunnelling Diodes [3] offer milliwatts of power but with limited bandwidth due to frequency dependent matching at the multiplier stage [4]. Non-Linear Transmission Lines consisting of sections of waveguide periodically loaded with varactors may be operated as very broad-band frequency multipliers. The broad-band nature arises when the NLTL characteristic impedance is equal to that of the driving circuit and load impedance. NLTL triplers utilising Schottky diodes have produced > 15mW of output power between 80 - 108 GHz from a 200mW fundamental [5] demonstrating the suitability of these circuits for broad-band frequency multiplier applications. This paper details the simulated performance of a NLTL frequency tripler for 260-300 GHz operation based upon the measured characteristics of micromachined waveguides [6] integrated with Heterojunction Barrier Varactors (HBVs). A port-to-port conversion efficiency of better than 1.5 % in the frequency range 264 - 300 GHz for 20mW of input power is predicted. For the simulation, an accurate NLTL model has been developed which accounts for loss due to the transmission line and non-linear devices, the factors most detrimental to NLTL performance. This model has shown good agreement with the measured performance of a NLTL doubler operating at 0.1 - 1 GHz. The simulations demonstrate the feasibility of NLTL triplers using micromachined waveguides and HBVs as broad-band multiplied sources at frequencies

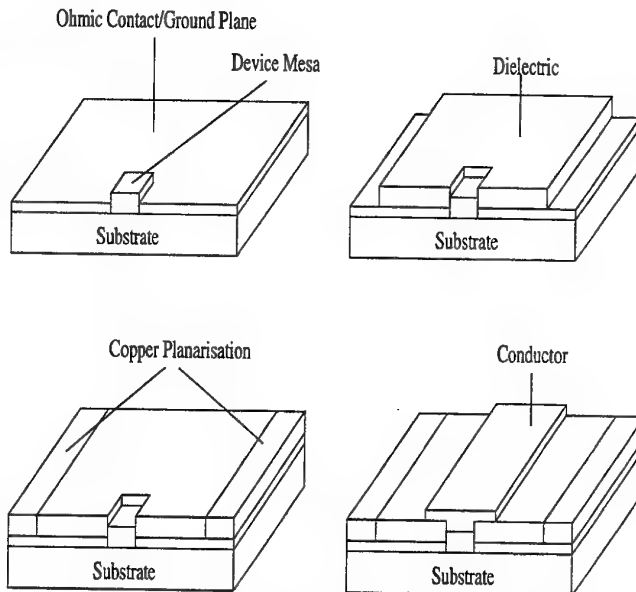


Fig. 1. Fabrication Technique for Micromachined Waveguide

greater than 100 GHz.

## II. MICROMACHINED WAVEGUIDE

For this work a novel micromachined waveguide [6] has been developed for the NLTL sections. This waveguide allows the easy integration of both planar and discrete devices in a wide variety of circuit configurations. The structure lends itself to Terahertz Monolithic Integrated Circuit (TMIC) Technology with interesting possibilities for integration with micromachined structures fabricated using the same ultra-thick photoresist process. Micromachined waveguides [7] and antennas [8] have been demonstrated along with micromechanical tuning elements [9] all of which offer circuit operation in the terahertz regime.

The micromachined waveguide structure supports a quasi-TEM mode of propagation for which a number of accurate circuit models exist [10] [11]. The correlation between these models and the measured performance for our waveguide between 20 - 40 GHz is shown in Figure 2. The propagation of the quasi-TEM mode is reliant upon the signal wavelength being 12.5 % and 25 % of the the conductor width and dielectric thickness respectivly. The fabrication technique for our micromachined waveguide (Figure 1) allows for dielectric thicknesses of between 5  $\mu\text{m}$  and 500  $\mu\text{m}$  with the conductor widths limited by the chosen lithographical method. For this reason the circuit models can be used to simulate micromachined waveguide performance

James R.Thorpe, Paul Steenson and Robert E.Miles are with the Institute of Microwaves and Photonics, Department of Electronic and Electrical Engineering, University of Leeds, Woodhouse Lane, Leeds, LS2 9JT.

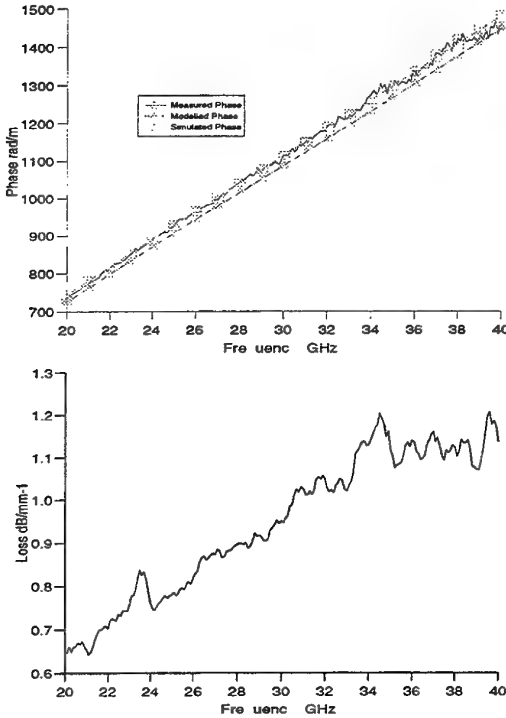


Fig. 2. Performance of Micromachined Waveguide

at terahertz frequencies.

### III. HETEROJUNCTION BARRIER VARACTORS

For this work new 4-stack InGaAs/InAlAs/InGaAs Heterojunction Barrier Varactors (HBVs) on a n+ InP substrate have been fabricated. Three device sizes of 2200  $\mu\text{m}^2$ , 1500  $\mu\text{m}^2$  and 800  $\mu\text{m}^2$  were produced using a self alignment technique. This involved the thermal evaporation of a Ni/AuGe/Ni/Au top ohmic contact to a highly doped InGaAs cap layer and a selective mesa etch using the InP substrate as an etch-stop layer. The bottom ohmic contact, (Ni/AuGe/Ni/Au) was thermally evaporated onto the InP substrate with the mesa etch undercut providing self-alignment prior to a 420 °C anneal in a nitrogen atmosphere. These devices have been integrated successfully into the micromachined waveguide for RF characterisation purposes. The measured capacitance-voltage and current-voltage characteristics for the 800  $\mu\text{m}^2$  device at 10 MHz can be seen in Figure 3.

### IV. NLTL MODEL

The design process for our NLTL is identical to the analysis undertaken for NLTLs which support soliton propagation employing non-linear elements with non-symmetrical capacitance-voltage characteristics about zero bias [5]. In our case we have extended the analysis to include devices with symmetrical capacitance-voltage relationships. A schematic for a single NLTL section is shown in Figure 4(a). The circuit model is shown in Figure 4(b). Here the transmission line sections are represented by an inductance,  $L_l$  with series resistance  $R_l$  representing ohmic losses. The

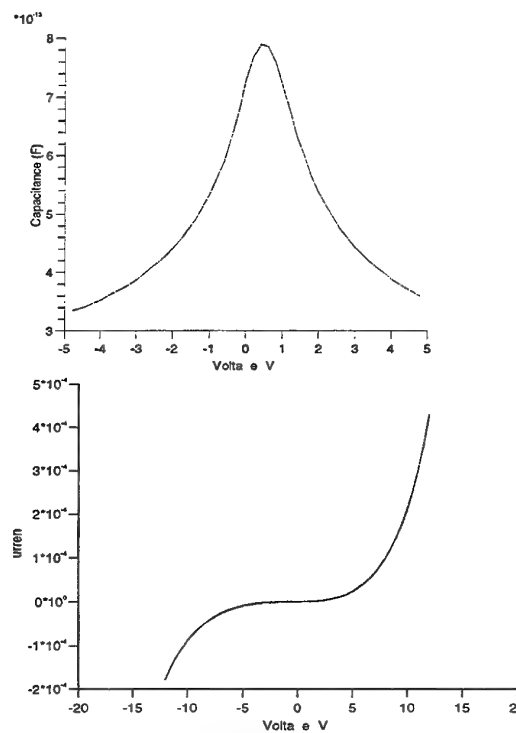


Fig. 3. Measured Capacitance-Voltage (a) and Current-Voltage (b) Characteristics for 800  $\mu\text{m}^2$  4-Stack InGaAs/InAlAs/InGaAs HBVs

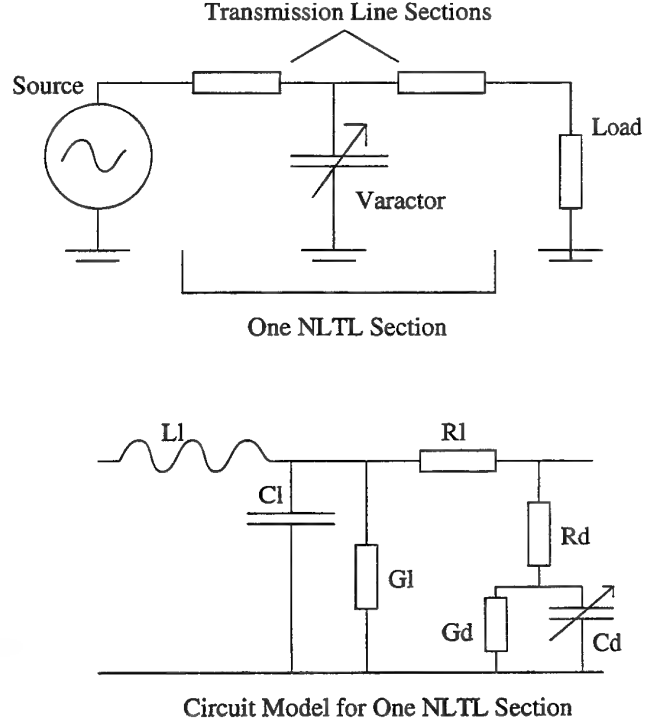


Fig. 4. NLTL Schematic (a) and Circuit (b) Model

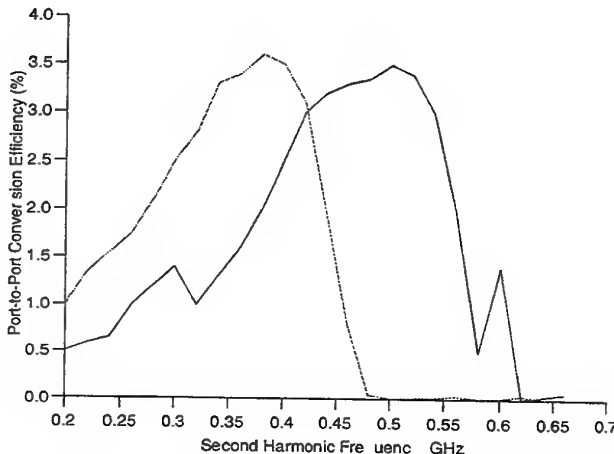


Fig. 5. Modeled (a) and Measured (b) Performance for NLTL Doubler

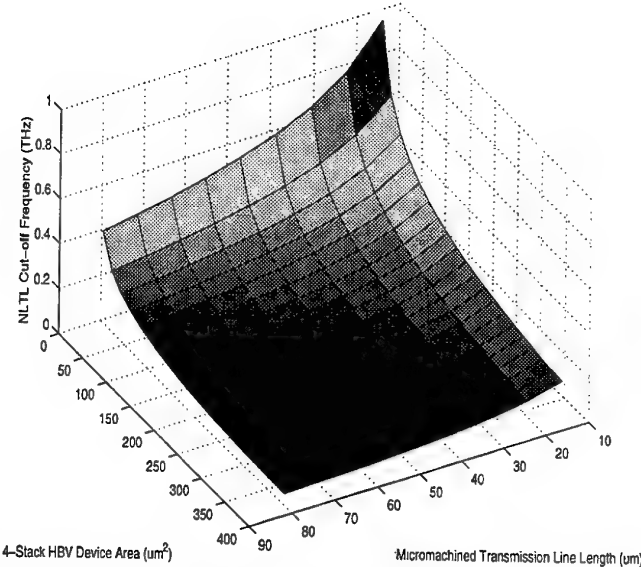


Fig. 6. Cut-off Frequency vs Physical Geometries for HBV Based NLTL Frequency Triplers

capacitance of the transmission line section is represented by  $C_l$  and the dielectric loss by  $G_l$ . The HBV is represented by an ideal non-linear capacitance  $C_d(v)$  and loss elements  $R_d$  and  $G_d$ . This model has been used to simulate the port-to-port conversion efficiency of a NLTL doubler for 0.1 - 1 GHz operation utilising Siemens BB833 varactors on a Duroid<sup>1</sup> 5880 substrate. The Siemens varactor was characterised for non-linearity, series resistance and conductivity using a HP-4145A<sup>2</sup> semiconductor parameter analyser and the results included in the simulation. The results of the simulation can be seen in Figure 5(a). Figure 5(b) shows the measured performance of the NLTL for comparison.

Our NLTL model does not account for the high frequency effects of carrier transport within the HBV heterostructure [12]. These effects cause a deviation from the DC HBV model in Figure 4 at millimeter wave frequencies. Hydrodynamic device simulators [13] have been used to predict these effects and have been integrated with harmonic balance schemes to establish optimised embedding impedances for single diode HBV frequency multipliers [14]. A similar technique would provide improved model accuracy for the optimisation of HBV based NLTL frequency multipliers at millimeter wave frequencies.

## V. MAXIMISING NLTL PERFORMANCE

In the lossless case increased power conversion between the fundamental frequency and generated harmonics for a NLTL frequency multiplier is achieved by increasing the number of sections. A maximum is achieved at half of the *recurrence length* [15]. In a practical situation each NLTL section has associated loss therefore reducing the recurrence length improves conversion efficiency. This is achieved by increasing the magnitude of the non-linearity

per NLTL section with the use of highly non-linear devices. The conversion efficiency of a NLTL frequency multiplier is also maximised by setting the NLTL cut-off frequency ( $f_c$ ) slightly above that of the desired harmonic [16]. The propagation of harmonics above  $f_c$  is prevented and power conversion is concentrated in those harmonics below this value. The value of  $f_c$  also defines the maximum operational frequency.

Figure 6 shows the relationship between  $f_c$  and the physical parameters for our HBVs and micromachined transmission lines. The maximum achievable value of  $f_c$  using these components is largely dependent upon the physical geometries required to realise the devices and waveguide. For NLTLs with high cut-off frequencies HBVs with small zero bias capacitance and hence device area are required. A reduction in device size will cause the value of  $R_d$  to rise reducing the conversion efficiency for the NLTL. A reduction in device area will also limit the extent of the capacitance-voltage non-linearity, having a detrimental effect on the NLTL power handling capability. A positive aspect of reducing the HBV size is to reduce the leakage current through the HBV barrier layers. This will reduce the value of  $G_d$  causing an increase in NLTL conversion efficiency.

## VI. G-BAND NLTL TRIPLEXER SIMULATION

Using our model, simulations for NLTLs employing HBVs which support soliton propagation were undertaken using micromachined transmission line parameters. The design data of Figure 6 was used to select the micromachined transmission line electrical length and HBV zero-bias capacitance for a triplexer with an  $f_c$  of 310 GHz. Accounting for NLTL loss and device non-linearity (section V) it was established that a NLTL with ten sections gave the optimum triplexer performance.

<sup>1</sup>Trade-mark of the Rogers Corporation

<sup>2</sup>Hewlett-Packard Ltd

for growth of the HBV layers and the Royal Society of Engineering for financial assistance during this project.

## REFERENCES

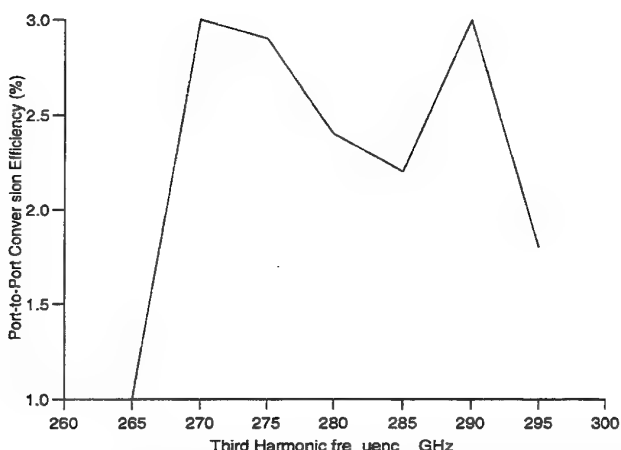


Fig. 7. Simulated Port-to-Port Conversion Efficiency for G-Band NLTL Tripler at 20mW Source Power

The capacitance-voltage relationship for a  $100 \mu\text{m}^2$  HBV was extrapolated from the measured data for the fabricated  $2200 \mu\text{m}^2$   $1500 \mu\text{m}^2$  and  $800 \mu\text{m}^2$  devices. An ohmic contact resistance of  $1 \times 10^{-7} \Omega\text{m}^2$  was assumed so that NLTL performance was not unduly compromised by device loss  $R_d$ . The NLTL design has a  $50 \Omega$  characteristic impedance which alleviates the requirement for frequency selective matching networks when embedding in a  $50 \Omega$  system. Simulated results for the NLTL frequency tripler with an 88 - 100 GHz fundamental (G-Band output) are shown in Figure 7

## VII. CONCLUSION

An accurate model for the simulation of NLTLs has been developed with good agreement found between simulated and measured performance for a NLTL frequency doubler operating at 0.1 - 1 GHz. Novel micromachined waveguides incorporating Heterojunction Barrier Varactors have been fabricated for use in millimeter wave applications. Measured results from these waveguides and devices have been used to simulate the performance of a G-Band NLTL frequency tripler. A port-to-port conversion efficiency of better than 1 % over a broad frequency range of 264 to 300 GHz for a fundamental power of 20 mW has been predicted. These results show the applicability of these circuits as multiplied power sources at frequencies greater than 100 GHz. The use of a micromachined waveguide offers interesting possibilities for the integration of such circuits with micromachined rectangular waveguide, antennas and micromechanical tuning elements for mass produced Terahertz Monolithic Integrated Circuit Applications.

## VIII. ACKNOWLEDGMENTS

The authors would like to acknowledge M.Missous (University of Manchester Institute for Science and Technology)

- [1] J.Thornton C.M.Mann P.de Maagt, "A High Power 270 GHz Frequency Tripler Featuring a Schottky Diode Parallel Pair," *IEEE MTT-Symposium Digest*, vol. 2, pp. 957-958, 1997.
- [2] J.R.Jones W.L.Bishop S.H.Jones G.B.Tait, "Planar Multibarrier 80/240GHz GHz Heterostructure Barrier Varactor Triplers," *IEEE Microwave Theory and Techniques*, vol. 45, no. 4, pp. 512-517, April 1997.
- [3] R.Bouregba D.Lippens L.Palmateer B.Bockenhoff M.Bogey J.L.Destombes A.Lecluse, "Frequency Multiplication using Resonant Tunnelling Diode with Output at Sub-millimetre Wavelengths," *Electronics Letters*, vol. 26, no. 21, pp. 1804-1805, October 1990.
- [4] T.J.Tolmunen A.V.Raisanen A.O.Lehto, "Efficiency Versus Embedding Impedance of Millimeter-Wave Schottky Diode Multipliers," *Proceedings of the SPIE*, vol. 598, pp. 209-216, 1986.
- [5] E.Carman M.Case M.Kamegawa R.Yu K.Giboney M.J.W.Rodwell, "V-Band and W-Band Monolithic Distributed Frequency Multipliers," *IEEE Microwave and Guided Wave Letters*, vol. 2, no. 6, pp. 253-254, June 1992.
- [6] J.R.Thorpe D.P.Steenson R.E.Miles, "High Frequency Transmission Line using Micromachined Polymer Dielectric," *Electronics Letters*, vol. 34, no. 2, pp. 1237-1238, June 1998.
- [7] C.E.Collins R.E.Miles G.M.Parkhurst J.W.Digby H.Kazemi J.M.Chamberlain R.D.Pollard N.J.Cronin S.R.Davies J.W.Davies D.P.Steenson, "Use of Novel Photoresists in the Production of Sub-millimeter Wave Integrated Circuits," *SPIE 4th International Conf. on Millimeter and Submillimeter Waves and Applications - San Diego*, July 1998.
- [8] J.W.Digby C.E.Collins B.M.Towlson L.S.Karatzas G.M.Parkhurst J.M.Chamberlain J.W.Bowen R.D.Pollard R.E.Miles D.P.Steenson D.A.Brown N.J.Cronin, "Integrated Micromachined Antenna for 200 GHz Operation," *IEEE MTT-Symposium Digest*, 1997.
- [9] V.M.Lubcke W.R.McGrath P.A.Stimson D.B.Rutledge, "Performance of Micromechanical Tuning Elements in a 620 GHz Monolithic Integrated Circuit," *Proceedings of the Seventh International Symposium on Space Terahertz Technology*, pp. 220-233, 1994.
- [10] E.Hammerstad O.Jensen, "Accurate Models for Microstrip Computer Aided Design," *IEEE MTT-Symposium Digest*, 1980.
- [11] H.A.Wheeler, "Transmission Line Properties of Parallel Strips Separated by a Dielectric Sheet," *IEEE Microwave Theory and Techniques*, vol. 13, pp. 172-185, 1965.
- [12] E.Kollburg T.L.Tolmunen M.A.Frerk J.R.East, "Current Saturation in Submillimeter Wave Varactors," *IEEE Transactions on Microwave Theory and Techniques*, vol. 40, no. 5, pp. 831-838, May 1992.
- [13] J.R.Jones G.B.Tait S.H.Jones D.S.Katzer, "DC and Large-Signal Time-Dependant Electron Transport in Heterostructure Devices: An Investigation of the Heterostructure Barrier Varactor," *IEEE Transactions on Electron Devices*, vol. 42, no. 8, pp. 1393-1422, August 1995.
- [14] J.R.Jones S.H.Jones G.B.Tait M.F.Zybura, "Heterostructure Barrier Varactor Simulation Using an Integrated Hydrodynamic Device/Harmonic-Balance Circuit Analysis Technique," *IEEE Microwave and Guided Wave Letters*, vol. 4, no. 12, pp. 411-413, December 1994.
- [15] D.Jager, "Soliton Propagation along Periodic-Loaded Transmission Line," *Journal of Applied Physics*, vol. 16, pp. 35-38, 1978.
- [16] M.J.W.Rodwell D.M.Bloom B.A.Auld, "Nonlinear Transmission Line for Picosecond Pulse Compression and Broadband Phase Modulation," *Electronics Letters*, vol. 23, no. 3, pp. 109-110, January 1987.

# Multiplier Technology for Terahertz Applications

Thomas W. Crowe, *Senior Member, IEEE*

**Abstract**—Frequency multipliers based on GaAs diodes remain the most viable option for creating cost efficient and reliable sources of terahertz power. The present status of the diode technology and recent advances in the development of broad band multipliers is reviewed. Additionally, the ongoing efforts to make this technology more cost efficient for a broader range of applications is presented.

**Index terms**—Terahertz, multipliers, varactors.

## I. INTRODUCTION

Terahertz frequencies, defined here as spanning from 100 GHz through 10 THz, offer intrinsic advantages in many scientific and technological applications. Examples include the molecular resonances used to identify environmentally important molecules, the signatures of cosmic gases of interest to radio astronomers, and electron interaction energies important for the studies of quantum solids. At the same time, frequencies higher than microwaves offer many benefits for technology, including wider communication bandwidths, improved spatial directivity and resolution, and system compactness. While the earth's atmosphere is increasingly opaque above 300 GHz, this is not a limitation in short-range radar, is actually desirable for short-range secure communications, and has no affect on satellite-to-satellite or laboratory applications.

These advantages have not been generally realized because of obstacles peculiar to this wavelength range. The most fundamental is the fact that the terahertz band falls in the gap between electronics and photonics. Most of the great successes in electromagnetic engineering have been possible in part because the wavelengths are either much longer than relevant component sizes (DC to microwave) or much smaller (infrared to visible). Neither approximation holds in the terahertz, making

everything from component design through fabrication and testing far more complex. The most important manifestation of these problems is the lack of convenient, tunable solid-state radiation sources analogous to laser diodes in the infrared and transistor oscillators in the microwave. Existing terahertz sources include vacuum tube electronics, very low power solid-state devices, and large laser systems. Though each of these fills an important niche, none fills the role of a practical terahertz source for routine use in a broad range of laboratory environments and commercial applications. This dearth of readily available sources is the most serious single reason this frequency range has remained closed to general use by engineers and scientists.

Most of the pioneering work in the development of terahertz technology has been motivated by the needs of radio astronomers. For example, to perform spectroscopic measurements of terahertz signals from space they have developed highly sensitive heterodyne receivers which require low-noise, frequency pure sources of local oscillator power. Although suitable sources are now available to cover most of this frequency range, these systems continue to use discrete semiconductor devices, many with primitive whisker contacts. Also, design and assembly time remain prohibitive, and repeatability and reliability are inadequate for any but the most rudimentary instruments. NRAO's planned Millimeter Array (MMA) [1] will have some 1000 superconductive mixers and their respective local oscillator (LO) sources, 400 of which will operate above 300 GHz. These must work remotely, with spurious-free response over wide frequency bands and without mechanical adjustments. To meet the demands of the MMA, terahertz technology must be brought to a level of maturity which will result in high component yields and performance close to fundamental limits.

There now exists a range of technologies capable of generating useable amounts of terahertz power. These include low power sources such as quantum

The author is a Research Professor in the Department of Electrical Engineering at the University of Virginia in Charlottesville, VA, 22903.

well oscillators [2,3] and photomixers [4], large laboratory instruments such as molecular gas lasers [5], klystrons and backward-wave oscillators, facility instruments such as free electron lasers, pulsed sources such as p-type germanium lasers [6] and a variety of optically pumped pulse emitters [7] and a host of new and highly speculative electronic and quantum devices. However, none of these yet meets the fundamental criterion of being a useful and reliable source of narrow band, yet broadly tunable cw power which is convenient to operate and maintain, yet compact and inexpensive. The further development of varactor based frequency multipliers, including use of computer based component and circuit design and higher levels of component integration, will allow this goal to be achieved.

## II. GaAs VARACTOR DIODE TECHNOLOGY

Frequency multipliers based on GaAs diodes are a "work-horse" technology for radioastronomy and atmospheric remote sensing applications, particularly when system size and reliability are important. These components have already generated useable power levels to frequencies beyond 1 THz [8] and this technology will surely supply the required LO power for SIS and HEB receivers to at least 2.5 THz. However, for large systems such as the MMA, as well as for routine and cost efficient laboratory systems, this technology must be improved. The cost of these components can be broken into several aspects;

- a) Component design, which often begins nearly from scratch for each new multiplier.
- b) Machining costs for the metal waveguide.
- c) Diode fabrication costs.
- d) Assembly costs, which are exacerbated by the use of discrete diode chips.

There now exist clear paths to reduce each of these costs significantly. First, new computer design tools, including Hewlett-Packard's High Frequency Structure Simulator and Microwave Design System allow most components to be designed fairly accurately and efficiently. Additionally, these tools allow the designer to investigate methods to improve the system bandwidth during the design phase, so that wider band systems without mechanical tuners can now be efficiently developed [9,10]. Achieving full waveguide band multipliers will not only reduce the number of multipliers needed for full spectrum

systems like the MMA, but will also allow the development of convenient laboratory test equipment, such as sweepers and network analyzers.

Machining costs and delays are still a major problem. Even at millimeter wavelengths a typical multiplier block will cost of order \$500 - \$1,000 and take a man-week or so to fabricate, not to mention the typical delay of many months to get time at a commercial machine shop. (This delay is another reason why accurate design tools are so important.) However, recently it has been shown that appropriately designed split-waveguide blocks can be cheaply and efficiently replicated by molding and casting techniques [11]. If this technology is suitably developed for multipliers it should significantly reduce the cost of programs such as the MMA.

Also, micromachining techniques are now being applied to this problem [11,12]. The simultaneous fabrication of dozens or even hundreds of components on a silicon substrate by standard lithographic and etching techniques would drastically reduce costs.

Assuming that suitable multipliers can be efficiently designed and the cost of waveguide manufacture is reduced, the remaining problem will be the time and expense of component assembly. All of the best terahertz multipliers in use today use discrete diode chips that have dimensions on the same order as those of a grain of salt and must be soldered into the circuit with an accuracy of perhaps ten microns. This is a very tedious process at best and is often impossible for all but the most patient and skilled technicians and graduate students. The solution to this problem is to use higher levels of integration so that components such as matching and filtering structures are integrated with the diode during the microfabrication process.

Several groups have now succeeded in fabricating high quality GaAs diodes on quartz substrates [13] with integrated filters, matching circuits and coupling probes [14,15]. Although this technique has so far only been used for mixers, it should be directly transferable to multipliers, provided thermal effects are dealt with effectively. This technique completely eliminates the need to handle and solder very small GaAs chips. In addition to reducing assembly costs this should also increase component uniformity and reliability.

A second method of achieving the desired level of integration is to design and fabricate components directly on semi-insulating GaAs substrates. Although this is a simpler process technology in that the transfer of the processing wafer to quartz is avoided, it requires several important new fabrication processes,

including via hole formation and back side processing. Also, the high dielectric constant of the GaAs will cause circuit design problems which must be resolved. However, none of the issues seems insurmountable, and monolithic GaAs circuits for terahertz applications should prove to be a fruitful area for research.

The overall cost of the GaAs diode chip is typically quite small compared to the cost of a complete multiplier or mixer component, typically of the order of \$200 - \$2,000 depending on frequency and complexity. However, if all other costs are reduced, the chip cost must also be minimized. However, the main driver in chip costs is simply the low volume of chips of each design that are needed. From our experience at UVa, virtually every circuit designer wants to redesign the planar diode chip to suit their specific circuit design. Thus, a completely new fabrication run is required and often the process itself must be altered. As this technology develops, greater volumes should reduce chip prices. Also, as more broadband designs are realized, the same chip will be suitable for many more applications. Finally, if integrated designs are fully developed it should eventually be possible to standardize the process for large wafers and high yield. Thus, as the overall technology is pushed forward it should be possible to reduce the cost of the semiconductor diodes.

### III. SUMMARY

The terahertz region of the electromagnetic spectrum is of great importance for both scientific and technological applications. For the great majority of applications, including radio astronomy and the development of terahertz test equipment, the lack of reliable and cost efficient sources of broadly tunable, cw terahertz power is a major obstacle. Varactor diodes based on GaAs and related compound semiconductors, used in conjunction with solid-state oscillator sources at frequencies near 100 GHz, can fill this need.

The major obstacles include the development of advanced computer co-design tools for devices and circuits, the elimination of traditional machining from the fabrication process, and integration of the diodes and circuit through microfabrication techniques to reduce diode and component assembly costs. The technology now exists to overcome these obstacles. However, these important issues are all closely related and all must be addressed if this technology is to move to the next level. For example, computer based design tools must be accurate enough to allow the

integrated circuits to achieve maximum performance and bandwidth without costly trial and error fabrication and testing. Also, it is likely that only through achieving higher levels of integration can the desired full-waveguide band performance be achieved.

The presentation at the conference will consist of a review of these important issues and a summary of recent and ongoing research at the University of Virginia to resolve these outstanding technological challenges.

### IV. REFERENCES

- [1] J.E. Carlstrom, "The Millimeter Array," Proc. Seventh Intl. Symp. On Space THz Techn., Pp. 17-28, Charlottesville, VA, March 1996.
- [2] B. Jogai, K.L. Wang, K.W. Brown, "Frequency and Power Limit of Quantum Well Oscillators," Appl. Physics Lett., Vol. 48, No. 15, pp. 1003-1005, April 1986.
- [3] T.C.L.G. Sollner, W.D. Goodue, P.E. Tannenwald, C.D. Parker, D.D. Peck, "Resonant Tunneling Through Quantum Wells at Frequencies up to 2.5 THz," Appl. Phys. Lett., Vol. 43, No. 6, pp.588 - 590, Sept. 1983.
- [4] K.A. McIntosh, E.R. Brown, K.B. Nichols, O.B. McMahon, W.F. DiNatale, T.M. Lyszczarz, "Terahertz Photomixing with Diode Lasers in Low-Temperature Grown GaAs," Appl. Phys. Lett, Vol. 67, No. 26, pp. 3844-3846, Dec. 1995.
- [5] Hans-Peter Roeser, "Heterodyne Spectroscopy for Submillimeter and Far-Infrared Wavelengths From 100  $\mu$ m to 500  $\mu$ m," Infrared Physics, Vol. 32, pp. 385-407, 1991.
- [6] E. Bruendermann, A.M. Linhart, H.P. Roeser, O.D. Dubon, W.L. Hansen, E.E. Haller, Appl. Phys. Lett, Vol. 68, p. 1359, 1996.
- [7] B.B. Hu and M.C. Nuss, "Imaging with Terahertz Waves," optics Letters, Vol. 20, No. 16, pp.1716-1719, Aug. 1995.
- [8] R. Zimmermann, T. Rose, T. Crowe and T. Grein, "An All-Solid-State 1 THz Radiometer for Space Applications," Digest Sixth International Symposium on Space THz Technology, Pasadena, March 1995.
- [9] D.W. Porterfield, T.W. Crowe, R.F. Bradley, N.R. Erickson, "A High-Power, Fixed-Tuned, Millimeter-Wave Balanced Frequency Doubler," accepted for publication in IEEE Trans. Microwave Theory and Tech., 1998.
- [10] N.R. Erickson, "Wideband High Efficiency Planar Diode Doubler," Proc.Ninth Intl. Symp. Space THz Techn., pp. 473-480, Pasadena, March 1998.
- [11] T.W. Crowe, P.J. Koh, W.L. Bishop, C.M. Mann, J.L. Hesler, R.M. Weikle, P.A.D. Wood, D. Matheson, "Inexpensive Receiver Components for Millimeter and Submillimeter Wavelengths," Eighth Intl. Symp. Space THz Tech., Cambridge, MA, March 1997.
- [12] C.K. Walker, G. Narayanan, H. Knoepfle, J. Capara, J. Glenn, A. Hungerford, T.M. Bloomstein, S.T. Palmacci, M.B. Stern, J.E. Curtin, "Laser Micromachining of Silicon:

A New Technique for Fabricating High Quality Terahertz Waveguide Components," Proc. Eighth Intl. Symp. Space THz Techn., pp. 358- 376, Cambridge, MA, March 1997.

[13] W.L. Bishop, E.R. Meiberg, R.J. Mattauch and T.W. Crowe, "A Micron Thickness, Planar Schottky Diode Chip for Terahertz Applications with Theoretical Minimum Parasitic Capacitance," The 1990 IEEE MTT-S International Microwave Symposium, Dallas, TX, pp. 1305-1308, May 1990.

[14] I. Mehdi, M. Mazed, R. Dengler, A. Pease, M. Natzic and P.H. Siegel, "Planar GaAs Schottky Diodes integrated with Quartz Substrate Circuitry for Waveguide Subharmonic Mixers at 215 GHz," IEEE-International Microwave Symposium 1994 Digest, pp. 779-782, San Diego, May 1994.

[15] S. Marazita, J. Hesler, R. Feinauegle, W. Bishop, T. Crowe, "Planar Schottky Mixer Development to 1 THz and Beyond," Dig. Ninth Intl. Symposium on Space THz Tech., Pasadena, CA, March 1998.

# Heterostructure Barrier Quantum Well Varactor

V. Duez, X. Mélique, R. Havart, F. Podevin  
P. Mounaix, F. Mollot, O. Vanbésien and D. Lippens

**Abstract-** In this communication, we report on recent developments in multiplier technology using heterostructure barrier varactors. From the epitaxial point of view, the originality stems from a new device configuration based on a quantum-well/barrier scheme. Test samples were fabricated either in GaAs or in InP technology and exhibit significant improvements in terms of capacitance ratio (in excess of 10:1) and capacitance non linearity. On the other hand, we discuss other competing technologies notably planar-doped Heterostructure Barrier Varactors.

**Indexing terms** - heterostructure III-V, Varactor, quantum well, Terahertz

## 1. INTRODUCTION

An Heterostructure Barrier Varactor consists conventionally in a wide band gap semiconductor sandwiched between two narrow gap cladding layers. The heterostructure barrier prevents the conduction while each moderately doped cladding layer can be depleted under reverse and forward bias [1]-[4]. In a first section, we show how the capacitance ratio and subsequently the diode non linearity, of major concern in the frequency capability and conversion efficiency of varactor multipliers, can be significantly improved. To this aim, we took benefit of a new device configuration based on a quantum well-barrier scheme. Recently, we demonstrated the idea in InP technology [5]. In the present communication we are interested in the GaAs-based system with record values in terms of capacitance contrast. In a second stage, we will discuss the choice of a material system and compare the idea developed here to the more conventional  $\delta$ -doping approach.

## 2. DESIGN AND TEST SAMPLE FABRICATION

Figure 1 shows the growth sequence of the fabricated devices. With respect to the generic GaAs/AlAs structure, the AlAs barrier is sandwiched between two quantum wells, formed by the pseudomorphic growth of InGaAs 5nm-thick layers.

The authors are with the Institut d'Electronique et de Micro-électronique du Nord, U.M.R. C.N.R.S. 9929, Quantum device group, Université des Sciences et Technologies de Lille, Avenue Poincaré, BP 69, 59652 Villeneuve d'Ascq Cedex, France

GaAs	$2 \times 10^{18} \text{ cm}^{-3}$	5000 Å
GaAs	$1 \times 10^{17} \text{ cm}^{-3}$	3000 Å
InGaAs	u-d	50 Å
AlAs	u-d	100 Å
InGaAs	u-d	50 Å
GaAs	$1 \times 10^{17} \text{ cm}^{-3}$	3000 Å
GaAs	$2 \times 10^{18} \text{ cm}^{-3}$	1 $\mu\text{m}$
Substrat GaAs SI		

Figure 1 Epitaxial sequence grown by Gas Source Molecular Beam Epitaxy (GSMBE), starting from a semi-insulating GaAs Substrate. The InGaAs with an Indium concentration of 30% layers are grown under pseudomorphic conditions at rather low temperature.

The Indium concentration is 30%. The InGaAs and AlAs layers are undoped (u-d) while the adjacent 300nm-thick GaAs layers are doped to  $1 \times 10^{17} \text{ cm}^{-3}$ . Such a gradient in doping concentration results in a diffusion process. Electrons, in the vicinity of the GaAs/InGaAs heterojunction, experience a real space transfer for occupying the two-dimensional (2D) density of states of the quantum wells. As a consequence under zero-bias conditions, the barrier is sandwiched, in very close proximity, by two highly populated regions while a medium doping level has been preserved in the adjacent layers.

The barrier thickness was chosen equal to 10 nm. This is a trade-off between the blocking capability of the barrier which depends on the ability of electrons to tunnel through it and the targeted capacitance value at zero bias. For the latter, the thinner the barrier, the higher the capacitance. Starting from a Semi-Insulating GaAs substrate, all the epilayers were grown in a Gas Source Molecular Beam Epitaxy (GSMBE) RIBER system.

The test structures consist of mesa-type diodes in a coaxial-like configuration with diameters ranging from 8 to 40  $\mu\text{m}$ . They were fabricated with a standard technology including plasma-assisted reactive ion etching and ohmic contact material metal deposition by means of an electron gun evaporation equipment. Figure 2 shows a Scanning Electron Microphotograph (SEM) of a typical device.

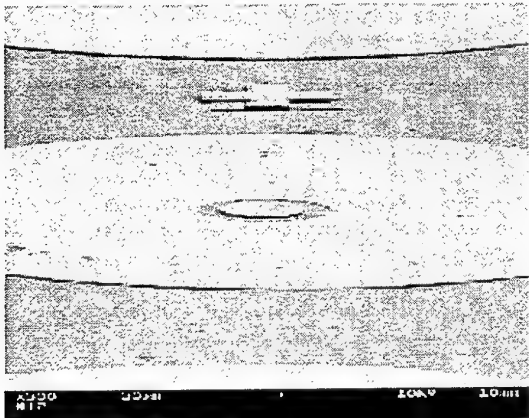


Figure 2 Scanning Electron Microphotograph of a coaxial-type device. The dimensions of contacting pads are compatible with probing techniques so that the devices can be characterised at the wafer level without implying dielectric cross-over or air bridge techniques.

### 3. CAPACITANCE-VOLTAGE CHARACTERISTICS

Figure 3 shows the capacitance-voltage characteristic, measured at room temperature, at a frequency of 8 GHz. The diode diameter is 8  $\mu\text{m}$ . Coplanar probes have been directly positioned onto the central and ring shaped contacts. Despite the simplicity in the characterization method, previous tests have shown that accurate measurements can be performed by this means up to 110 GHz [6]. By this means we have direct information about the intrinsic capacitance and the low frequency series resistance.

Concerning the C-V curve, a high degree of symmetry was found between both bias directions with a zero-bias capacitance of  $\sim 4 \text{ fF}/\mu\text{m}^2$ . Such a symmetry attests of the quality of the samples. Also the fact that we characterise the samples at relatively high frequency permits one to avoid any defect related frequency deviation since the relevant time  $1/f$  ( $f$  is the characterization frequency) are shorter than the corresponding time of expected traps. As a consequence of the high zero-bias value, the capacitance ratio is in excess of 10:1 approximately an improvement of a factor of 2 with respect to the best results published in the literature for conventional HBV structures. More interesting, is the steep decrease in the capacitance values over the voltage range [-2 ; +2 V]. It is believed that this narrowing of the voltage range over which the device is highly non linear is a welcome feature for very high frequency potential application.

### 4 ANALYSIS

In order to analyse the reason of these improvements in the capacitance ratio and subsequently in the non-linearity exhibited by the device, let us consider the schematic of the conduction profile plotted in figure 4 (a) at a bias point very close to the equilibrium condition ( $V=50\text{mV}$ ) and under saturation conditions (b) respectively.

In (a), the electrons are strongly localised within the quantum wells thus forming quasi-degenerate semiconductor regions. As a consequence, the length for electric field screening ( $L_s$ ) is expected to be very short. It is worth-mentioning that much wider  $L_s$  are found for conventional single barrier devices. Indeed in such a case, there is no counterbalance against the repelling effect of the barrier.

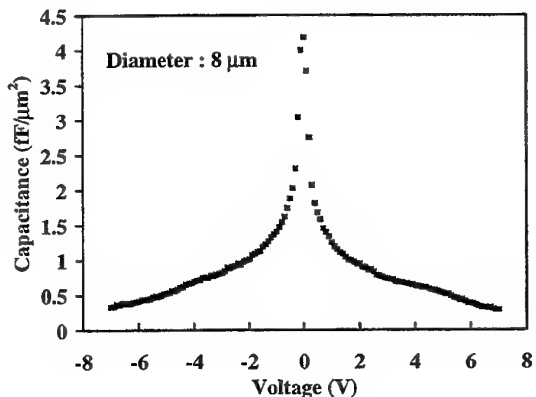


Figure 3: Capacitance voltage characteristic measured at 8 GHz with the rf probes directly positioned onto the pads. The capacitance at zero-bias is in excess of  $4 \text{ fF}/\mu\text{m}^2$  as a consequence of the InGaAs pre-well and post-well which enable a significant charge accumulation at equilibrium

Under bias, the pre-well structure is progressively fed by the adjacent layer which plays the role of a reservoir according to 2D-density of states and Fermi-Dirac statistics. Correlatively, the carriers are escaping from the post-well structure until this quantum well is empty. At this stage, the operation mode should become classical with a full depletion condition of cladding layer reached at approximately 8 V.

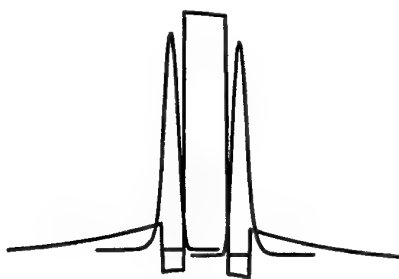


Figure 4 (a): Schematic of conduction profile at voltage  $V=50 \text{ mV}$ . The cladding quantum-wells trap high sheet carrier densities so that the screening lengths are substantially shortened with respect to conventional HBV structures.

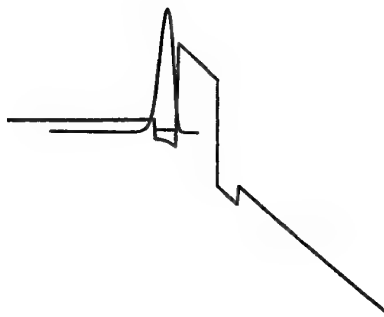


Figure 4 (b) Conduction band profile under full depletion condition

Having this physical interpretation in mind, a rough estimate of the ideal capacitance ratio can be deduced from the relevant lengths using a parallel plate capacitance approximation. At zero bias, the pertinent dimension between the two wave-functions maxima would be  $\sim 20\text{nm}$ . At saturation, the relevant dimension can be compared to the cladding layer thickness namely  $300\text{nm}$ . Under such a crude assumption, the limit value would be 15:1. Correlatively, the non linearity of the devices is drastically enhanced with a steep decrease in the capacitance value at moderate bias voltage and hence pump power when the quantum mode of operation dominates. This improvement in the capacitance -voltage characteristics is particularly important for the applications for which the pump power is limited as it is the case for the second stage in a multiplier chain.

Figure 5 shows the current-voltage characteristics measured at room temperature up to 8 V where a dramatic increase in the current variation versus voltage can be seen. At such relatively high bias voltages, it is reasonable to interpret this breakdown due to impact ionisation in the GaAs moderate doped layer. Otherwise, different conduction regimes are apparent corroborating the previous arguments of various accumulation and depletion modes. Anyway for practical applications, it appears that the device can be driven 'safely' with a peak-to-peak pump voltage between -4 V and +4 V

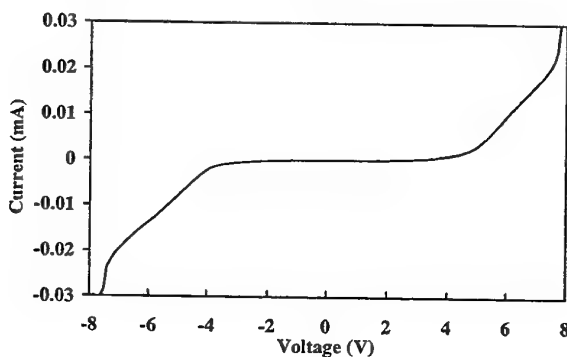


Figure 5: Current-voltage characteristic measured at room temperature under probes. A low conduction regime is preserved for a peak-to-peak voltage of about 8 V. Various conduction modes can also be noted.

## 5. DISCUSSION

Let us now consider the choice of a material system for which this novel idea can be implemented. In fact, there are numerous trade-offs depending on the considered viewpoints, either technological or electrical.

From the technological side, notably for the epitaxial growth, it is obvious that the use of GaAs-based devices appears preferable. In practice, it was found that buried InGaAs pre-well and post-well structures with a 5nm width and an indium concentration of 30 % can be grown by taking care of growth temperature, in order to avoid any dislocations and to preserve a two-dimensional growth.

In contrast, the fabrication of InAs quantum well structures embedded in InGaAs layers lattice-matched to InP, is a formidable task at the required thickness of 5nm. This dimension is imperative for effectively accommodating a quantum level within the wells and hence for trapping electrons. Recently [5], we succeeded the growth of such epilayers provided the buried 5nm-thick InAs wells, over the 2.5nm critical thickness, were grown at low temperature ( $\sim 400^\circ\text{C}$ ) using the surfactant method. Let us recall that a general rule the growth of InP based materials were conducted at  $\sim 520^\circ\text{C}$  for both binary and ternary compounds.

There is also another drawback which results from the use of an Indium Phosphide technology. It is now well known that the growth of thick epilayers, typically several micrometers as it is the case for stacked heterostructure barrier varactor, requires to control carefully the growth conditions. Towards the goal of a large number of devices series integrated on the same wafer, this can be a challenging issue. In our group, in order to preserve the sample quality only two single barriers were stacked on the same epitaxy [3].

From the electrical side however, an InP technology seems more suitable. In fact we demonstrated recently [7] that step-like InAlAs/AlAs barrier schemes can be implemented with very good performances in terms of voltage handling. On the other hand, high quality ohmic contacts can be fabricated taking benefit of low gap material systems and from the possibility to highly dope the structures. In contrast, the blocking capability of bare AlAs heterostructures is relatively poor with respect to InAlAs/InGaAs heterojunctions due to the well known  $\Gamma$ -X mixing effect. On this basis, InP seems more promising for ultra-high frequency whereas GaAs-based devices could be very useful in the lower part of the Terahertz spectrum

Turning now to the choice of a configuration, we demonstrated recently that the concept of a high capacitance ratio can also be implemented by means of planar doping concentrations, in close proximity to the barrier [5]. Basically, this is the same underlying idea namely a modulation of the electron concentration in the cladding layer by means of a High-Low doping profile. Figure 6 shows the comparison between the capacitance-voltage characteristics measured and calculated for a

planar doped structure and a conventional one. For the former we also succeeded to significantly improve the capacitance value at zero bias. However, there exists a large difference between both approaches.

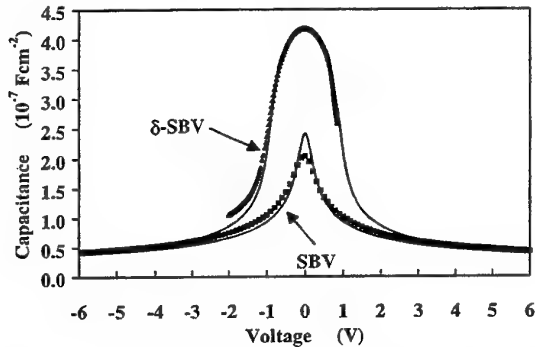


Figure 6: Comparison between the capacitance voltage characteristics of a planar doped HBV ( $\delta$ -SBV) and of a single Barrier varactor (SBV)

In the present work, the buried well are undoped and are formed by *heterojunctions*. In the delta doping case, there is a space charge effect which results in the *electrostatic* formation of adjacent quantum wells. The shape of these wells are highly non symmetric. Figure 7 illustrates the conduction band profile calculated self consistently by taking into account the space charge effect and the electron trapping process. The limit case would be a sheet doping density exactly located at the hetero-interface. It can be demonstrated that such an effect lowers the barrier height with a resulting degradation of the blocking properties of the crystalline barrier.

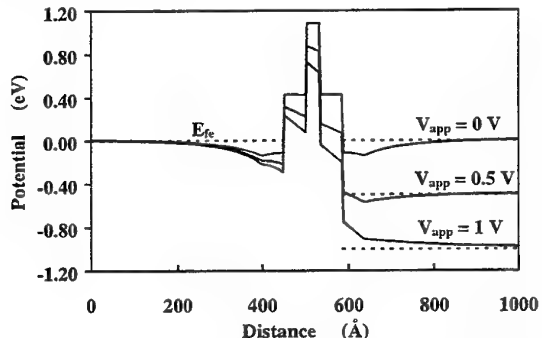


Figure 7 Calculated conduction band profile under various bias conditions for a  $\delta$ -doped HBV.

## 6. CONCLUSION

Significant improvement in the capacitance ratio and in non linear behaviour of diode capacitance have been achieved by making use of band gap engineering via a quantum well barrier scheme. Strained InGaAs layers were deposited by GSMBE forming pre-and post-well structures on each side of the blocking barrier. Under these conditions, the operating mechanisms are dominated at low voltage by carrier dynamics via the quantum well in contrast to the conventional depletion operating mode. This results in a high capacitance level at zero-bias enhancing drastically the capacitance non linearity.

## ACKNOWLEDGEMENTS

This work was partially supported by ESA contract # 9777/92/NL/PB. We would like to thank S. Lepilliet and E. Delos for technical assistance during the rf assessments of the devices.

## REFERENCES

- [1] Krisnamurthi K., Harrison R.G., 'Millimeter-wave frequency tripling using stacked heterostructure-barrier varactor on InP', *IEE Proc. Microw. Antennas Propag.*, 1996, **143**, (4), pp. 272-276
- [2] Rahal A., Bosisio R.G., Rogers, C., Ovey J., Sawan M. and Missous M., 'A W-band medium power multistack Quantum Barrier Varactor Frequency Tripler', *IEEE Microwave and Guided wave Letters*, 1995 , **5**, (11), pp. 368-370
- [3] Lheurette E., Mounaix P., Salzenstein P., Mollot F. and Lippens D., 'High performance InP-based heterostructure barrier varactor in single and stack configuration', *Electronics Letters*, 1996, **32**, (15), pp. 1417-1418
- [4] Jones J.R., Bishop W.L., Jones S. and Tait G.B., 'Planar multibarrier 80/240-GHz Heterostructure Barrier Varactor triplers', *IEEE Transactions on Microwave Theory and Techniques*, 1997, **45**, (4), pp. 512-518
- [5] Lheurette E., Mélique X., Mounaix P., Mollot F., Vanbésien O. and Lippens D. , 'Capacitance engineering for InP-based Heterostructure Barrier Varactor', Accepted for publication in *IEEE Electron Device Letters*
- [6] Mélique X., Carbonell J., Havart R., Mounaix P., Vanbésien O. and Lippens D., 'InGaAs/InAlAs/AlAs Heterostructure Barrier Varactors for harmonics multiplication', *IEEE Microwave and Guided Wave Letters*, 1998, **Vol. 8 N°7**, pp. 254-256
- [7] Havart R. et al. 'Step-like Heterostructure Barrier Varactor', to be published in *IEEE Transactions on Electron Devices*

# Recent Advances in the Performance of InP Gunn Devices for the 100–300-GHz Frequency Range

Heribert Eisele, Anders Rydberg, *Member, IEEE*, George I. Haddad, *Life Fellow, IEEE*

**Abstract**—Improved heat dissipation in InP Gunn devices resulted in RF power levels exceeding 200 mW, 130 mW, 80 mW, and 25 mW at oscillation frequencies of around 103 GHz, 132 GHz, 152 GHz, and 162 GHz, respectively. Corresponding dc-to-RF conversion efficiencies exceeded 2.3% between 102 GHz and 132 GHz. Power combining increased the available RF power levels to more than 300 mW at 106 GHz, around 130 mW at 136 GHz, and more than 125 mW at 152 GHz with corresponding combining efficiencies from 80% to more than 100%. Operation in a second-harmonic mode yielded RF power levels of more than 2 mW around 220 GHz and more than 1 mW around 280 GHz.

**Index Terms**—Gunn devices, millimeter-wave devices, millimeter-wave generation, millimeter-wave oscillators, oscillator noise, phase noise, submillimeter-wave devices, submillimeter-wave generation, submillimeter-wave oscillators.

## I. INTRODUCTION

COMPACT and sensitive submillimeter-wave receivers largely depend on low-noise all-solid-state local oscillators, where a frequency multiplier or a chain of multiplier stages driven with a high-power Gunn device as the fundamental source has been the most common approach [1], [2]. High-power fundamental sources are necessary to provide sufficient local oscillator (LO) power at Terahertz frequencies [2], for example, to pump uncooled Schottky diode mixer subharmonically [3]. As more RF power at higher millimeter- or even submillimeter-wave frequencies becomes available from Gunn devices as the fundamental sources, the number of required multiplier stages and, consequently, the complexity of the LO chain decrease.

Device simulations [4] and preliminary experimental results [5] from devices on integral heat sinks indicated thermal limitations in InP Gunn devices, in particular, at D-band (110–170 GHz) frequencies. Therefore, fabrication technologies based on selective etching were adopted from previously developed processes for GaAs impact avalanche transit-time (IMPATT) [6] and tunnel injection transit-time (TUNNETT) [7] diodes on diamond heat sinks, and resulting InP Gunn devices were mounted on diamond heat sinks in an open package

with reasonably low parasitic elements. This paper describes the RF performance of InP Gunn devices with different doping profiles as single devices in the fundamental mode as well as those employed in power-combining circuits and in circuits for second-harmonic power extraction.

## II. SINGLE-DEVICE PERFORMANCE

Improved fabrication technologies as well as a better understanding of both the physics in transferred-electron devices (TED's) [4], [8], [9] and some of the limitations in InP Gunn devices resulted in the extension of fundamental-mode operation beyond 160 GHz [5], [9]. As shown in Fig. 1, RF power levels exceeding 130 mW around 132 GHz, 80 mW around 152 GHz, and 25 mW around 162 GHz were achieved with devices on diamond heat sinks [9]. Low heat-flow resistances on diamond heat sinks [9] ensure low active-layer temperatures for reliable long-term operation. No signs of appreciable degradation or change in oscillation frequency were observed during continuous-wave (CW) operation for more than 15,000 hours of one device around 131 GHz. At a typical power stability against temperature of better than  $-0.04 \text{ dB}^{\circ}\text{C}$ , the observed fluctuations in the recorded RF power levels of within  $\pm 5\%$  were largely attributed to inevitable changes in the ambient temperature of the laboratory space with the test setup.

As a well-known characteristic of Gunn devices, one device structure can generate RF output power over a wide frequency range. Lowest and highest frequency limits of devices with the graded doping profile [9] have not yet been determined as part of a detailed investigation. Nonetheless, the employed device evaluation procedure [9] typically covers more than one waveguide band. It revealed in some devices that, with the same device in an appropriate cavity and RF circuit, significant RF power levels could be generated easily at any frequency in the range from below 94 GHz to above 155 GHz. An RF power of more than 200 mW was measured with one of these devices in a WR-10 waveguide cavity at an oscillation frequency of 103 GHz.

Material from different epitaxial growth systems, such as, metalorganic chemical vapor deposition (MOCVD) and chemical beam epitaxy (CBE), but also molecular beam epitaxy (MBE), was and is being used with success in the performance studies. As an example, InP Gunn devices with a flat doping profile and from CBE-grown material yielded RF power levels of around 100 mW at oscillation frequencies of around 130 GHz [10].

Heribert Eisele and George I. Haddad are with the Solid-State Electronics Laboratory, Department of Electrical Engineering and Computer Science, University of Michigan, Ann Arbor, MI 48109-2122 USA (e-mail: heribert@engin.umich.edu; gih@eecs.umich.edu)

Anders Rydberg is with the Signal and Systems Group, Department of Material Science, Uppsala University, S-751 21 Uppsala, Sweden (e-mail: Anders.Rydberg@signal.uu.se)

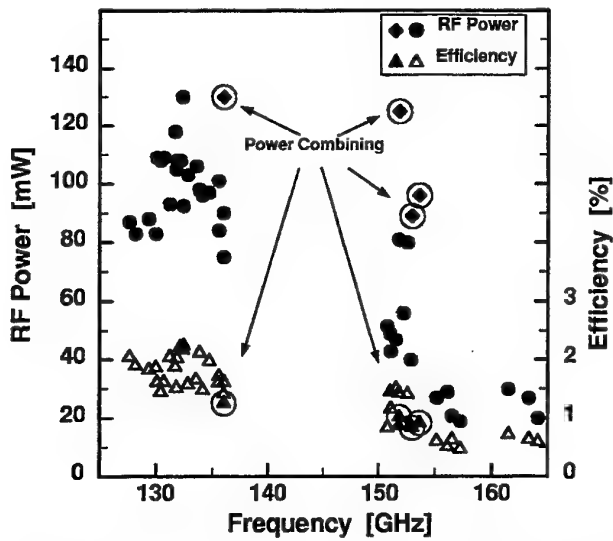


Fig. 1. RF performance of InP Gunn devices on diamond heat sinks at *D*-band frequencies (epitaxial material grown by MOCVD).

Clean spectra were recorded from the vast majority of the Gunn devices tested as free-running oscillators. As an example, an uncorrected phase noise of  $-110$  dBc/Hz was determined at  $500$  kHz off the oscillation frequency of  $103$  GHz and at an RF power of  $180$  mW, which is in line with previously reported values of well below  $-100$  dBc/Hz at *D*-band frequencies [9], [10], [11]. Since the phase noise is at the noise floor of the employed spectrum analyzer with a harmonic mixer, the corrected phase noise is estimated to be well below  $-113$  dBc/Hz.

### III. POWER COMBINING

Power combining of two devices was demonstrated for the first time [12] in the fundamental mode at *D*-band ( $110$ – $170$  GHz) frequencies, but was also shown to result in state-of-the-art RF power levels at *W*-band ( $75$ – $110$  GHz) frequencies. Excellent combining efficiencies from  $80\%$  to more than  $100\%$  were achieved in the simple dual-cavity in-line configuration as illustrated in Fig. 2. Fig. 1 also includes more recent results from additional power-combining experiments. The highest RF power levels to date exceeded  $300$  mW at  $106$  GHz and  $125$  mW at  $152$  GHz and were around  $130$  mW at  $136$  GHz. Recorded spectra were very clean, and phase-noise characteristics were very similar to those reported for single devices in free-running oscillators [9], [10] [11].

### IV. SECOND-HARMONIC POWER EXTRACTION

Millimeter-wave GaAs and InP Gunn devices are also well known for efficient operation in a second-harmonic mode [8], [13]. Very preliminary results up to  $290$  GHz from *D*-band devices on diamond heat sinks were reported [11]. Subsequent experiments yielded RF power levels of  $0.7$  mW at  $269$  GHz,  $1$  mW at  $279$  GHz, and  $1.2$  mW at  $280$  GHz, which were measured with a submillimeter-wave dry calorimeter in a similar configuration with a WR-6 waveguide cavity as before [11].

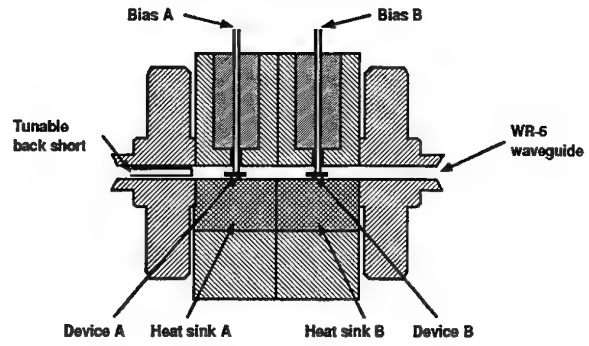


Fig. 2. Schematic of the WR-6 waveguide circuit for InP Gunn device power combining at *D*-band frequencies.

A scaled version of a Carlstrom-type cavity [14] for second-harmonic mode operation in the frequency range  $140$ – $220$  GHz [15], [16] was also employed. Fig. 3 shows a schematic of this waveguide circuit. In this circuit, the coaxial section, which can be tuned with the frequency back short, basically forms a resonant circuit at the fundamental frequency with the device capacitance, the fringe capacitance of the cap on the device, and, if present, the parasitic elements of the device package. Similar to the configuration for extraction around  $280$  GHz [11], the signal at the fundamental frequency cannot propagate in the output waveguide. Therefore, the device is mainly reactively terminated at the fundamental frequency, which causes a large voltage swing in the highly nonlinear device and generation of higher harmonic frequencies [13], [16].

At first, devices on integral heat sinks were evaluated for second-harmonic power extraction in this cavity. These devices were designed for operation at *W*-band frequencies, had flat doping profiles similar to those in [4], and were fabricated from CBE-grown material. RF power levels of more than  $9$  mW at approximately  $150$ – $160$  GHz and more than  $5$  mW around  $170$  GHz were measured and are comparable to values reported previously [15] for devices from MOCVD-grown material [17]. As a result of the resonant cap on top of the device, the cavity also supports fundamental-mode operation above the cut-off frequency of the waveguide. For example, flat-profile devices on integral heat sinks yielded up to  $18$  mW around  $131$  GHz, where low bias voltages and significant frequency tuning with the power back short position indicated fundamental-mode operation.

Subsequently, a *D*-band device on a diamond heat sink was inserted. As expected, operation at higher second-harmonic frequencies was observed. The experiments yielded RF power levels of more than  $2$  mW as measured with the submillimeter-wave dry calorimeter at various frequencies between  $220$  GHz and  $223$  GHz. Tuning of the frequency short appeared to be critical since the devices easily oscillated in the fundamental-mode at numerous *D*-band frequencies around, *e.g.*,  $150$  GHz, but the cavity was not designed for efficient second-harmonic power extraction around, *e.g.*,  $300$  GHz. Furthermore, resulting RF power levels in the fundamental mode turned out to be below the well-established state-of-the-art results from the same batch of InP Gunn devices as shown in Fig. 1, and, in

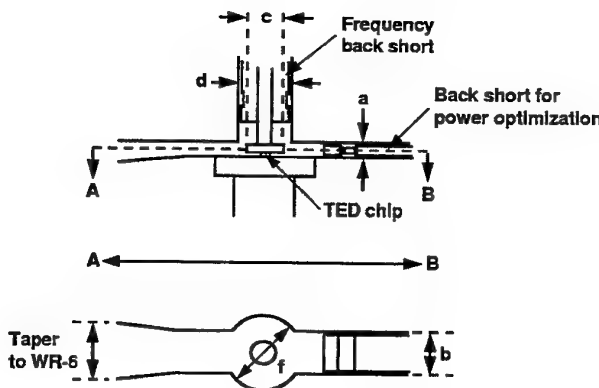


Fig. 3. Schematic of the WR-5/6 waveguide circuit for second-harmonic power extraction, shown for the case of an unpackaged InP Gunn device.

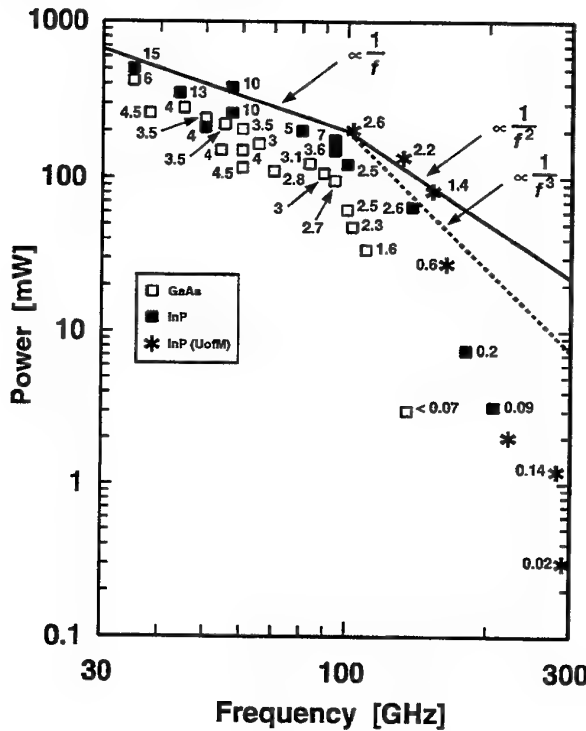


Fig. 4. Published state-of-the art results from GaAs and InP Gunn devices under CW operation in the frequency range of 30–300 GHz. Numbers next to the symbols denote dc-to-RF conversion efficiencies in percent.

fact, fundamental-mode operation was not within the scope of these experiments. Therefore, this mode of operation had to be avoided in this cavity.

## V. CONCLUSION

As can be seen from Fig. 4, the best RF power levels in the 100–300-GHz frequency range are the highest reported to date for any Gunn device. However, the interaction between the circuit and the device, *i.e.*, the impedance levels at the fundamen-

tal and the second-harmonic frequencies, need to be studied in greater detail. This should lead to much improved performance from operation in a second-harmonic mode above 200 GHz.

## ACKNOWLEDGMENT

The authors wish to thank Michael Coulombe from the University of Massachusetts at Lowell for providing the submillimeter-wave dry calorimeter. They are also grateful to T. B. Ramachandran at MDT for providing some of the screw-in packages.

## REFERENCES

- [1] A. V. Räisänen, "Frequency multipliers for millimeter and submillimeter wavelengths," *Proceedings of the IEEE*, vol. 80, pp. 1842–1852, Nov. 1992.
- [2] T. W. Crowe, T. C. Grein, R. Zimmermann, and P. Zimmermann, "Progress toward solid-state local oscillators at 1 THz," *IEEE Microwave Guided Wave Lett.*, vol. 6, pp. 207–208, May 1996.
- [3] I. Mehdi, P. H. Siegel, D. A. Humphrey, T. H. Lee, R. J. Dengler, J. E. Oswald, A. Pease, R. Lin, H. Eisele, R. Zimmermann, and N. Erickson, "An all solid-state 640 GHz subharmonic mixer," *IEEE MTT-S Int. Microwave Symp. Dig.*, Baltimore, MD, June 7–12, 1998, pp. 403–406.
- [4] R. Kamoua, H. Eisele, and G. I. Haddad, "D-band (110–170 GHz) InP Gunn devices," *Solid State Electron.*, vol. 36, pp. 1547–1555, 1993.
- [5] H. Eisele, R. Kamoua, G. I. Haddad, and C. Kidner, "Active two-terminal devices as local oscillators for low-noise receiver systems at submillimeter-wave frequencies," *Arch. Elektrotech.*, vol. 77, pp. 15–19, 1994.
- [6] H. Eisele, "Selective etching technology for 94-GHz GaAs IMPATT diodes on diamond heat sinks," *Solid State Electron.*, vol. 32, pp. 253–257, 1989.
- [7] H. Eisele and G. I. Haddad, "Enhanced performance in GaAs TUNNETT diode oscillators above 100 GHz through diamond heat sinking and power combining," *IEEE Trans. Microwave Theory and Tech.*, vol. 42, pp. 2498–2503, Dec. 1994.
- [8] ———, "Active microwave diodes," in *Modern Semiconductor Device Physics*, S. M. Sze, Ed. New York: Wiley, 1997, ch. 6, pp. 343–407.
- [9] ———, "High-performance InP Gunn devices for fundamental-mode operation in D-band (110–170 GHz)," *IEEE Microwave Guided Wave Lett.*, vol. 5, pp. 385–387, Nov. 1995.
- [10] H. Eisele, G. O. Munns, and G. I. Haddad, "RF performance characteristics of InP millimeter-wave  $n^+ - n^+$  Gunn devices," *IEEE MTT-S Int. Microwave Symp. Dig.*, Denver, CO, June 17–21, 1997, pp. 451–454.
- [11] H. Eisele and G. I. Haddad, "D-band InP Gunn devices with second-harmonic power extraction up to 290 GHz," *Electron. Lett.*, vol. 30, pp. 1950–1951, 1994.
- [12] ———, "Efficient power combining with D-band (110–170 GHz) InP Gunn devices in fundamental-mode operation," *IEEE Microwave Guided Wave Lett.*, vol. 8, pp. 24–26, Jan. 1998.
- [13] L. G. Eddison, "Indium phosphide and gallium arsenide transferred-electron devices," in *Infrared and Millimeter Waves*, Vol. 11, *Millimeter Components and Techniques*, Part III, Academic Press, Orlando, 1984, pp. 1–59.
- [14] J. E. Carlstrom, R. L. Plambeck, and D. D. Thornton, "A continuously tunable 65–115-GHz Gunn oscillator," *IEEE Trans. Microwave Theory Tech.*, vol. 33, pp. 610–619, July 1985.
- [15] A. Rydberg, "High efficiency and output power from second- and third-harmonic millimeter-wave InP-TED oscillators at frequencies above 170 GHz," *IEEE Electron Device Lett.*, vol. 11, pp. 439–441, Oct. 1990.
- [16] ———, "A contribution to the design of wide-band tunable second-harmonic mode millimeter-wave InP-TED oscillators above 110 GHz," *Int. J. Infrared and Millimeter Waves*, vol. 11, pp. 383–404, 1990.
- [17] M. A. di Forte-Poisson, C. Brylinski, G. Colomer, D. Osselin, S. Hersee, J. P. Duchemin, F. Azan, D. Lechevallier, and J. Lacombe, "High-power high-efficiency LP-MOCVD InP Gunn diodes for 94 GHz," *Electron. Lett.*, vol. 20, pp. 1061–1062, 1984.

# Doping-Barrier Varactors for Frequency-multipliers

Markus Krach, Jürgen Freyer, and Manfred Claassen

**Abstract**—The doping-barrier varactor (DBV), proposed as a new device for frequency-multipliers by Freyer and Claassen [1], combines the advantages of varactors with symmetrical capacitance-voltage characteristics with the ability to realise potential barriers, the height of which can be essentially larger as compared to hetero-barrier varactors. The consequence is a higher inset-voltage of current flow from which an increase of input power and higher multiplier efficiencies are expected. The device structure, the numerical simulation as well as first theoretical and experimental results of the DBV are presented in this paper.

## I. INTRODUCTION

Frequency multipliers use non-linear devices to generate harmonics from fundamental oscillators. The Schottky diode is the most commonly applied multiplier device though several novel devices with symmetric capacitance-voltage characteristics like the hetero-barrier varactor [2] show several advantages, e.g. for triplers no bias and no idler circuits are necessary. This leads to simpler rf-circuits and is important if power addition from several sources is aspired. The ratio of maximum to minimum capacitance  $C_{\max}/C_{\min}$  and the inset-voltage of current flow are a measure for the quality of a varactor.

In this paper we present a new type of varactor, the doping-barrier varactor (DBV), which also shows a symmetric capacitance-voltage characteristic. While the barrier height of single-barrier varactors is limited by the maximum conduction band discontinuity, the barrier in the DBV can be essentially higher (for proper design in excess of 1 eV in GaAs).

## II. DEVICE STRUCTURE

The device structure of a DBV is given in Fig. 1. It consists of a  $n^+p^+n^+$  layer sequence embedded in lower doped  $n^-$  material with highly n-doped contact zones.

Width and doping of the  $p^+$ -layer and the two adjacent  $n^+$ -layers are designed such that the depletion layers of both

$p^+n^+$ -junctions merge to one zone which is free of mobile carriers. Under these conditions, the space charge of the ionised doping atoms in the  $n^+p^+n^+$  structure leads to a bump in the conduction band, which represents a potential barrier for the electrons. Since the same bump appears in the valence band, its height must be lower than the band gap, so that the valence band remains sufficiently below the Fermi level to keep the concentration of the holes low.

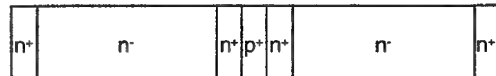


Fig. 1: Schematic layers sequence of the DBV

If a voltage is applied to the DBV, carriers are accumulated in front of the barrier in the  $n^+$ -layer (see Fig. 2) which lower the height of the potential barrier. On the opposite side of the barrier, a depletion layer is created which, due to the relatively low doping concentration of the  $n^-$ -layer, extends widely into this layer. Variations of the voltage change the width of the depletion region thereby forming the desired voltage dependent capacitance of the device. With opposite polarity of the voltage, a mirrored band shape with the same depletion layer width appears leading to a symmetric capacitance-voltage characteristic.

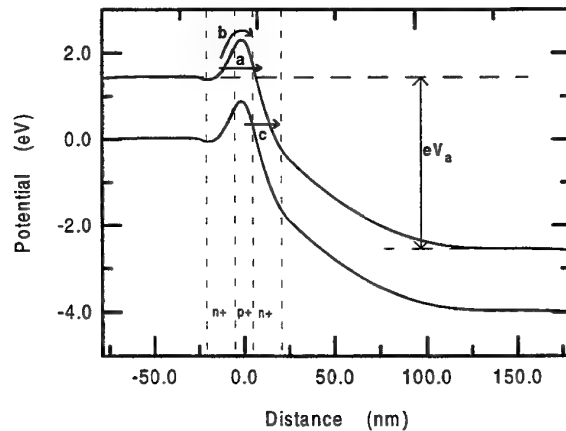


Fig. 2: Schematic energy band diagram of a DBV for applied bias voltage (a) tunnel current through the barrier, b) thermionic emission, c) Zener tunnelling

The authors are with the Lehrstuhl für Allgemeine Elektrotechnik und Angewandte Elektronik, Technische Universität München, D-80290 München, Germany

In Fig. 2 also the different contributions to the conduction current in the DBV are depicted:

- (a) Tunnelling of electrons through the barrier
- (b) Thermionic emission over the barrier
- (c) Band to band tunnelling (Zener tunnelling)

With increasing voltage, the height and width of the barrier is reduced and the probability of the carriers to tunnel through or to overcome the barrier by thermionic emission is increased. For very high voltages and doping concentrations in the inner  $p^+$ - and  $n^+$ -layers, respectively also Zener tunnelling could appear. This would accumulate holes in the  $p^+$ -region and thus has to be avoided.

### III. THEORY

Capacitance-voltage and current-voltage characteristics, necessary for the application of the DBV as millimeter-wave multiplier, are calculated as follows:

For the energy-band diagram in a one-dimensional model of the DBV structure Poisson's equation is solved self-consistently, using Fermi-Dirac distribution function with the following boundary conditions:

1. The semiconductor properties are bulklike.
2. With zero bias, the Fermi level remains constant throughout the entire structure and under applied bias  $V_a$ , the Fermi levels on the left and right hand side of the potential barrier must differ by  $eV_a$ .

The energy-band diagrams for different applied voltages may then be used to calculate the I-V characteristics of the DBV. Thermionic emission of electrons over the barrier and tunnelling of electrons through the barrier is computed using the model of Tsu and Esaki [3] via WKB approximation and the calculation of Zener tunnelling is based upon the generation rate for band to band tunnelling according to Benz et al. [4].

The capacitance versus voltage behaviour of the device is calculated from the change of electric field with applied voltage.

### IV. RESULTS AND DISCUSSION

DBV's with different doping concentrations and width of the inner  $n^+p^+n^+$  layer sequence are investigated. The doping profile must be established such that charge neutrality is obtained within the three barrier layers. Otherwise, for example for too low doping concentration of the  $n^+$ -layers part of the  $n^-$ -layer is already depleted at zero voltage or for too high doping concentration the  $n^-$ -layer will be depleted only for high voltages. To study the influence of the three barrier forming layers on the total varactor performance, doping concentration and width of the  $n^-$ -depletion layers are kept constant ( $N_D = 3 \cdot 10^{17} \text{ cm}^{-3}$ , length = 200 nm). The band edge diagrams of the potential barriers for the investigated structures are given in Fig. 3. The barrier is very steep and thin for high doping concentrations and small widths of the  $p^+$ -layer, respectively the  $n^+$ -layers (A). An

increase of the barrier width for the same height is achieved by a lower  $p^+$ -doping concentration and a wider  $p^+$ -zone (B). If the doping concentration in the  $p^+$ -layer as well in the adjacent  $n^+$ -layers is diminished drastically the barrier height and the slope are reduced (C).

Type	Doping concentration $n^+ / p^+ / n^+ [\text{cm}^{-3}]$	thickness [nm]
A	$5 \cdot 10^{18} / 2 \cdot 10^{19} / 5 \cdot 10^{18}$	20 / 10 / 20
B	$5 \cdot 10^{18} / 5 \cdot 10^{18} / 5 \cdot 10^{18}$	20 / 40 / 20
C	$2 \cdot 10^{18} / 2 \cdot 10^{18} / 2 \cdot 10^{18}$	20 / 40 / 20

Table 1: Doping concentration and layer thickness of the three inner layers of type A, B, and C (Doping concentration of the  $n^-$ -layer:  $3 \cdot 10^{17} \text{ cm}^{-3}$ , length: 200nm)

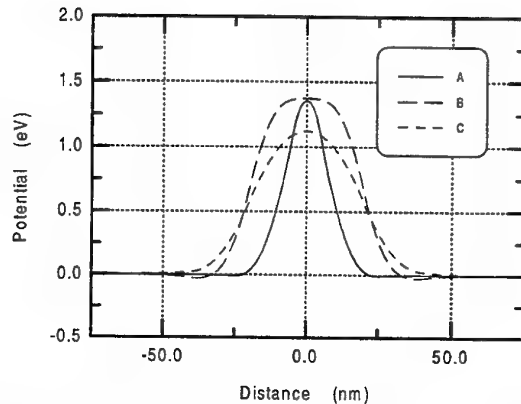


Fig. 3: Energy band structure of the barriers for type A, B, and C of table 1

The ratio  $C_{\max}/C_{\min}$  and the inset of conduction current are important factors for the conversion efficiency and cut-off frequency of a multiplier. Since the maximum capacitance depends on the width of the barrier, a low barrier width is needed for high  $C_{\max}$ . Type A shows the highest maximum capacitance and the highest ratio of  $C_{\max}/C_{\min}$  (see Fig. 4). An increase of the barrier width, realized in structures B and C, lowers the tunnelling current through the barrier but leads to a decrease of the maximum capacitance and therewith of  $C_{\max}/C_{\min}$  (see Fig. 4). First theoretical estimations of the total current show that the portion of the Zener tunnelling current increases with rising steepness of the barrier, i.e. for the device structures of type A and B. The experimental results of the capacitance-voltage and current-voltage characteristics for a DBV of type A are given in Fig. 5. The ratio  $C_{\max}/C_{\min}$  is only 2.5, indicating that the device is not yet optimized. However, even for this device the current-voltage characteristics show an inset voltage of current flow which is about twice that of typical single-barrier varactors at comparable current densities [5].

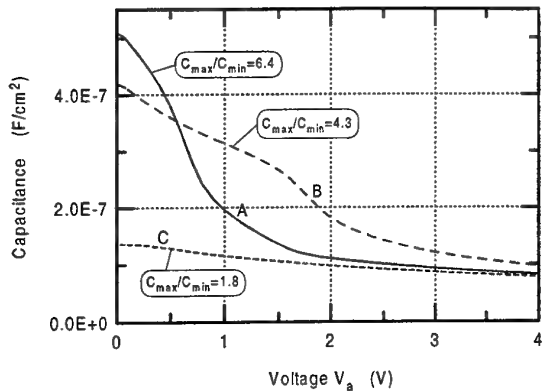


Fig. 4: Capacitance-voltage characteristic of type A, B, and C

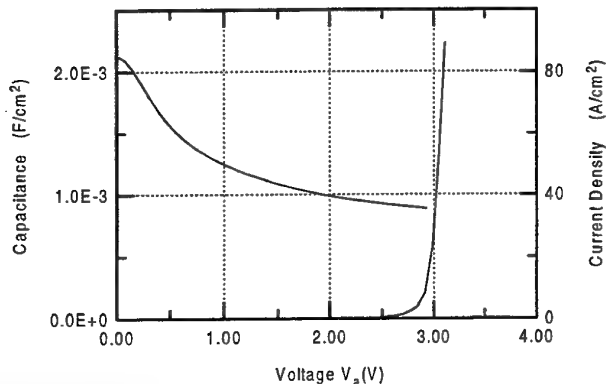


Fig. 5: Experimental capacitance-voltage and current-voltage characteristic of type A

## V. REFERENCES

- [1] J. Freyer and M. Claassen, "New doping-barrier varactor for mm-wave Multiplier Applications", Proceedings of the 22<sup>nd</sup> Workshop on Compound Semiconductor Devices and Integrated Circuits, Zeuthen, Germany, 85 (1998)
- [2] E. Kollberg and A. Rydberg, "Quantum-barrier-varactor diodes for high-efficiency millimetre-wave multipliers", *Electron. Lett.* **25**, 1696 (1989)
- [3] R. Tsu and L. Esaki, "Tunnelling in a finite superlattice", *Appl. Phys. Lett.* **22**, 562 (1973)
- [4] C. Benz, D. Liebig and M. Claassen, "Tunnelling and impact ionization at high electric fields in abrupt GaAs *p-i-n* structures", *J. Appl. Phys.* **81** (7), 3181 (1997)
- [5] D. Choudhury, M. A. Frerking, and Paul D. Batelaan, "A 200 GHz tripler using a single barrier varactor", *IEEE Transactions on Microwave Theory and Techniques*, **41** (4), 594 (1993)

# High Efficiency Frequency Multipliers Using Substrateless Schottky Diodes

Ansgar Simon, Chih-I Lin, Manuel Rodriguez-Gironés, Hans L. Hartnagel,  
Peter Zimmermann, Rüdiger Zimmermann, Ralf Henneberger

**Abstract** -We report on high efficiency frequency multipliers for the frequency range 150 - 500 GHz. These frequency multipliers use the whiskered substrateless Schottkydiode that provides minimum series resistance and improved heat sink capabilities. Recently a doubler efficiency of 40% at 150 GHz and tripler efficiencies of 19% ( $P_{out} = 5.6 \text{ mW}$ ) at 267GHz, 16% ( $P_{out} = 5.5 \text{ mW}$ ) at 300 GHz and 8% ( $P_{out} = 2 \text{ mW}$ ) at 480 GHz are the highest efficiencies that have been achieved.

## I. Introduction

Schottky varactor diodes are the key element for all-solid-state local oscillator sources at frequencies higher than 100 GHz. Although planar diode technology improved substantially, whisker contacted Schottky diodes still provide the highest efficiencies and output powers at frequencies above 300 GHz.

A number of optimisation approaches for whiskered Schottky diodes have improved the performance of multipliers. The traditional chip structure consists of a chip which is typically 100  $\mu\text{m}$  square and 70  $\mu\text{m}$  thick, with ohmic contacts on the back and a honeycomb anode array on top.

The optimisation of a diode covers the following items:

1. Improvement of the chip geometry with respect to power handling capabilities and small parasitics.
2. Improvements of the passivation layer with respect to a high breakdown voltage and good capacitance modulation ratio.
3. Design of the layer structure of the wafer for increased capacitance modulation ratio.

This paper concentrates on the first two optimisation items. The third item is discussed briefly with an example of a special layer structure for a high power frequency doubler.

## II. Device Structure

Fig.1 shows the structure of the substrateless Schottky diode. Substrateless Schottky diodes, proposed in 1995 [1], offer the prospect to increase the power handling capabilities and to receive a minimum series resistance. Compared with the

conventional diode chip the thickness of the  $n^+$ -GaAs substrate is strongly reduced from 100  $\mu\text{m}$  to 2  $\mu\text{m}$ . A 5-10  $\mu\text{m}$  thick Gold disk promotes the mechanical stability of the device and simplifies the handling.

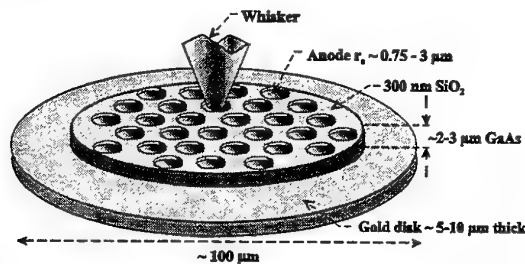


Fig. 1: Structure of the substrateless Schottky diode chip

Due to the reduced geometry, substrateless Schottky diodes offer several advantages compared with a conventional whisker contacted Schottky diodes:

1. Due to minimized dimensions the structure is less affected by the skin effect [2].
2. The  $n^+$ -substrate thickness is reduced to a few microns reducing its contribution to the resistance.
3. Small distance between the active  $n$ -layer and the backside metal provides a good heat sink. Therefore, substrateless Schottky diodes can operate more reliably at high current densities without thermal degradation and the contribution to the system noise is reduced.
4. Reduced semiconductor surface area decreases the leakage current.
5. Reduced device volume allows a better coupling of the input signal into the diode within the waveguide.

Due to these advantages substrateless Schottky diodes give a prospect to attain improved performance of mixers and frequency multipliers in the submillimeterwave regime.

## III. Varactor Optimisation and Results

Important characteristics of a varactor diode are the capacitance modulation ratio  $C_{jo} / C_{min}$ , the breakdown voltage  $U_{br}$  and the series resistance  $R_s$ . Recently new passivation techniques are in use to increase the breakdown voltage and the capacitance modulation ratio for a specific

A. Simon, C.I. Lin, M. Rodriguez-Gironés and H. L. Hartnagel are with the Institut für Hochfrequenztechnik, Merckstr. 25, 64283 Darmstadt  
P. Zimmermann, R. Zimmermann and R. Henneberger are with Radiometer Physics GmbH, Birkenmaarstr. 10, 53340 Meckenheim

doping level. We have established a polyimide passivation technique that leads to an improvement in the breakdown voltage and the capacitance modulation ratio. Fig. 2 gives a comparison of the breakdown voltage of  $\text{SiO}_2$  layers and of the polyimide passivation as a function of the GaAs-doping concentration.

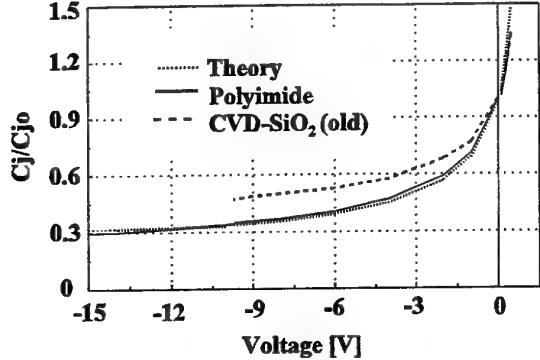


Fig. 2: Capacitance modulation depending on passivation

At the same doping concentration the polyimide passivation offers a 30-50% higher breakdown voltage compared with the best reported values of CVD- $\text{SiO}_2$ . This behavior gives a new flexibility to the design of varactor diodes, i.e. for the same amount of input power higher doping levels are possible. This leads to a smaller series resistance and a reduction of the velocity saturation effect. There are two serious disadvantages of polyimide passivation layers:

1. The adhesion on the GaAs is very poor. This probably can result in reliability problems.
2. There is no anisotropic etching available. The minimum anode diameter is limited.

To overcome these limitations we optimized our CVD-passivation technique. This optimisation is still in progress, but recently we can provide layers with almost the same breakdown voltage ( $U_{br}=14-16\text{V}$  for  $n_{epi}=8 \cdot 10^{16} \text{ cm}^{-3}$ ) as a polyimide passivation and the same reliability as the previously chosen CVD- $\text{SiO}_2$ .

Table 1 : Diode characteristics several substrateless diodes

Device	$N_d$ [cm $^{-3}$ ]	$d_{e-epi}$ [nm]	$d_{anode}$ [ $\mu\text{m}$ ]	$R_s$ [ $\Omega$ ]	$n$	$C_p$ [fF]	$V_{br}$ [V]	$C_p/C_{min}$
SLHA5010	hyperap.	450	6.4	4.5	1.1	50	9	4.1
SLV3518	8E16	560	7	5	1.06	35	18	3.2
SLV2818	8E16	560	6	5	1.06	28	18	3.2
SLV2018	8E16	560	5	5.7	1.03	20	18	3.2
SLV0910	2.6E17	240	3.5	8.3	1.1	9	9	2.2-2.4

Table 1 shows the characteristic parameters of several fabricated devices and table 2 shows the output power and

efficiency that have been achieved with these diodes. Some of these multipliers yielded record output power and efficiency. To our knowledge a tripler efficiency of almost 19% has never been achieved at frequencies close to 300 GHz. With optimised complex doping structures (SLHA5010) we could achieve a very high capacitance modulation ratio. Recently, the doubler efficiency of 40% that has been achieved with this diode is the highest reported value for a single diode multiplier.

Table 2 : Multiplier performances

$V_{in}$ [GHz]	$V_{out}$ [GHz]	Diode	$P_{in}$ [mW]	$P_{out}$ [mW]	Efficiency [%]
75	150	SLHA5010	25	10	40
89	267	SLV2818	30	5.6	18.7
93	279	SLV2018	50	6	12
100	300	SLV2818	35	5.5	15.7
126	378	SLV2818	84	4.1	4.9
160	480	SLV0910	25	2	8
210	630	SLV0910	10	0.7	7

#### IV Conclusion

Schottky barrier varactor diodes have been optimized with respect to applications in the frequency range 150-800 GHz. An improved diode structure and passivation technique leads to a significant performance improvement in the diode characteristics and in various multiplier systems.

#### Acknowledgement

The authors would like to express their acknowledgements to Dr. H. Grothe and Dr. J. Freyer, both from the Technical University of Munich, Germany, for supplying the high-quality epitaxial material.

#### References

1. A. Simon, A. Grüb, M. Rodriguez-Gironés and H. L. Hartnagel, "A Novel Micron-Thick Whisker Contacted Schottky Diode Chip", Sixth Int. Symp. on Space Terahertz Technology, pp 5-12, 1995
2. U. V. Bhapkar, T. W. Crowe, "Analysis of the High Frequency Series Impedance of GaAs Schottky Diodes by a Finite Difference Technique", IEEE Trans. Microwave Theory Tech., Vol. 40, No. 5, pp. 886-894, 1992

# Quantum well intersubband transitions as a source of terahertz radiation

P. Harrison, R. W. Kelsall, P. Kinsler, and K. Donovan

**Abstract**—It is shown that unipolar quantum well systems have potential as sources of terahertz radiation. It is demonstrated that the electronic interactions within these systems must be manipulated in order to favour radiative emission rather than non-radiative loss. Designs are advanced for tunable emitters and optically excited terahertz lasers.

**Keywords**—Terahertz, far-infrared, intersubband, quantum cascade lasers

## I. INTRODUCTION AND THEORY

THE conventional approach to terahertz frequency generation is based on oscillating currents in non-linear electronic devices. In contrast, optical techniques rely on photon emission via electron (or hole) transitions between discrete energy levels. Terahertz photons of frequency 1–10 THz can be produced with energy level separations of between 4 and 41 meV—an energy range which is readily accessible using the confined states in quantum well structures.

### A. Quantum wells and subbands

The confined levels within either the conduction or valence band of a semiconductor heterostructure have one less degree of freedom than bulk, thus giving them a two-dimensional character. Whilst the carriers are confined along one direction ( $z$ -) they are free to move in the other two spatial co-ordinates ( $x$ - and  $y$ -), hence the confined levels are broadened into ‘subbands’—as opposed to the three-dimensional energy ‘bands’ of bulk semiconductors. For an introduction to semiconductor heterostructures, see for example, [1].

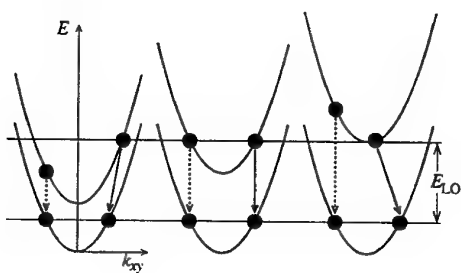


Fig. 1. Energy versus wavevector (momentum) diagrams for radiative (dashed, vertical) and non-radiative (solid, vertical or diagonal) intersubband transitions for energy separations below (left), equal (centre), and above (right) the LO phonon energy

The energy separation of subbands can be easily engineered,

All the authors are members of the Institute of Microwaves and Photonics, School of Electronic and Electrical Engineering, University of Leeds, LS2 9JT, U.K. . E-mail: p.harrison@ee.leeds.ac.uk .

by altering layer thicknesses within the heterostructure, to obtain photon frequencies covering the majority of the infrared spectrum. Helm[2] first observed radiative emission in the mid-infrared and so spurred an enormous interest in ‘intersubband transitions’. Progress in this field has been rapid, with the development of the first intersubband laser in 1994[3] and now even room temperature devices[4]. Note these devices are ‘unipolar’ in that they are only doped with one type of impurity (usually  $n$ -type), as opposed to traditional ‘interband’ bipolar laser diodes which have both  $n$ - and  $p$ -type doping.

The extension of these developments to the far-infrared or terahertz region of the spectrum is non-trivial, in that the much reduced subband separations become of the order of dominant phonons (longitudinal optic (LO) in III-V materials). This causes an increase in the competing non-radiative scattering rates, which can be detrimental to radiative emission. This paper reviews the recent progress in the understanding of these scattering processes and proposes designs for both terahertz lasers and tunable emitters.

### B. Transitions between subbands

Exploiting transitions between subbands (otherwise known as ‘intersubband transitions’) in order to generate radiation requires an understanding of the various competing processes. For example, populating an excited state with a number of electrons (or holes) is sufficient to induce transitions to a lower energy state, as a system will always try to minimise its energy. However only a fraction of those transitions will be radiative, with energy emitted as photons; the majority involve scattering with the lattice, resulting in non-radiative energy, i.e., phonon emission. The strength of a transition is represented by its ‘scattering rate’, which is the number of transitions per unit time, or the reciprocal of the lifetime of an electron (or hole) in an energy level, i.e.,  $1/\tau$ .

## II. INTERSUBBAND SCATTERING AT TERAHERTZ SUBBAND SEPARATIONS

As illustrated in Fig. 1, the subbands due to the in-plane motion of the electrons are parallel and (at low momenta) parabolic, hence a variety of possibilities exist for phonon and photon emission at subband separations of terahertz energies. These are illustrated schematically in Fig. 1. As photons have very little momentum their emission causes a negligible change in the electron momentum and hence the radiative transitions on Fig. 1 (marked by dashed lines) are vertical. The photon does however have a finite energy

$h\nu$  equal to the subband separation  $E_2 - E_1 = \Delta E_{21}$ . If the subband energy separation is equal to the LO phonon energy (other phonon modes do exist, but in this work concentration will be focused on the dominant mode), then the electron can emit a phonon and satisfy the conservation of energy also with a vertical transition, as in the centre diagram. This represents the generation of a low momentum phonon and is the fastest of the three scenarios. On the other hand if the subband separation is less than (left hand diagram) or greater than (right hand diagram) the LO phonon energy then the resulting transition has to be accompanied by a momentum change. This is indicated by the diagonal (solid) lines in Fig. 1; such transitions occur slower than the former case.

#### A. Electron-phonon scattering

For illustrative purposes an infinitely deep single GaAs quantum well is employed, thus exhibiting completely confined wave functions. Such a system is useful as the subband separation  $\Delta E_{21}$  can be varied, by adjusting the quantum well width, without altering the electron wave functions, on which all scattering rates depend. Fig. 2 displays the results of calculations of the electron-LO phonon scattering rate as a function of the subband separation, the computational methods employed have been outlined in earlier works[5].

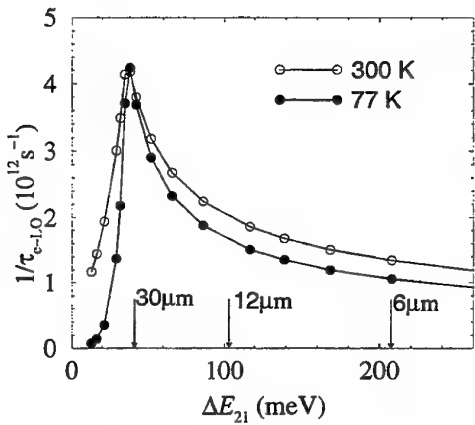


Fig. 2. Electron-LO phonon scattering rate versus energy separation between the lowest two subbands of an infinitely deep GaAs quantum well

The two main features of Fig. 2 are: (i) the scattering rate increases as the subband separation decreases through the mid-infrared (6-12  $\mu\text{m}$ ) before peaking as  $\Delta E_{21}$  equals the LO phonon energy, near the onset of the far-infrared (30  $\mu\text{m}$ ); (ii) below the LO phonon energy the scattering rate is very sensitive to temperature. In terms of competing with an accompanying radiative transition, the former point is a detrimental effect when moving to longer wavelengths; however beyond 30  $\mu\text{m}$  (below the LO phonon energy) this non-radiative mechanism is suppressed, particularly at low temperature.

Fig. 3 displays the origins of this suppression and the temperature sensitivity. At low temperatures the electrons,

described by Fermi-Dirac statistics, occupy all the lowest energy levels. Although an electron in the upper subband near the top of the energy distribution, may have sufficient energy to emit a phonon, the states to which it would scatter are all occupied and hence the transition is prohibited (Pauli exclusion). At higher temperature however, the electrons occupy a broader range of energy states yielding, higher energy electrons in the upper subband and empty states in the lower subband; thus LO phonon emission is possible.

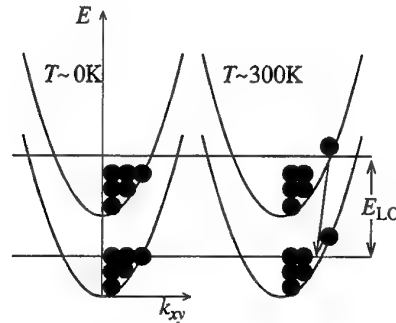


Fig. 3. Prevention of LO phonon emission at low temperatures due to Pauli exclusion, for subband separations less than the LO phonon energy (left), and the activation of such processes due to the thermal broadening of the electron energy distribution at elevated temperatures

#### B. Electron-electron scattering

Electron-phonon scattering is ‘inelastic’ in that the total energy of the electrons is reduced by such an event. Another non-radiative mechanism is electron-electron scattering which is ‘elastic’ in that the total electron energy remains constant.

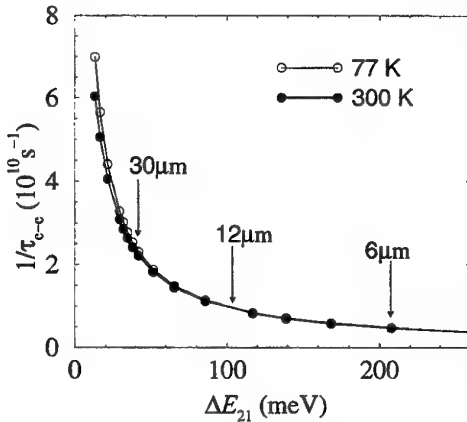


Fig. 4. Electron-electron scattering rate versus energy separation between the lowest two subbands of an infinitely deep GaAs quantum well

Fig. 4 displays the results of calculations of the inter-subband electron-electron scattering rate, again as a function of the subband separation  $\Delta E_{21}$ ; explanation of the computational methods employed is available in an earlier

work[6]. Again it can be seen that this non-radiative rate increases as the energy separation between the subbands is reduced from the mid-infrared to the far-infrared range.

### C. Electron-photon scattering

Finally the remaining scattering rate that is of importance is the electron-photon or radiative scattering rate itself. The two-dimensional form of Smet *et al.*[7] implies that the radiative scattering rate  $\frac{1}{\tau_{\text{rad}}} \propto \Delta E_{21}$ , i.e., the emission of photons becomes less likely, as the subband separation decreases—a detrimental effect.

### D. Summarising

Thus, in summary, the successful design of far-infrared/THz lasers is made difficult by the complex behaviour of the electron scattering rates. In particular, the electron-LO phonon scattering rate has a peak at 30  $\mu\text{m}$ , and a high temperature sensitivity for longer wavelengths. In addition the increase in the non-radiative competing mechanism of electron-electron scattering as well as the decrease in the radiative rate both suggest a reduction in the quantum efficiency of terahertz devices compared to those of the mid-infrared. Despite this, progress has been made in the design of quantum well systems to improve quantum efficiencies, and indeed emission in the terahertz region via intersubband transitions has recently been observed[8].

## III. ENGINEERING THE SCATTERING RATES TO FAVOUR TERAHERTZ EMISSION

### A. Electrically injected emitters

‘Electrically injected’ or ‘electroluminescent’ emitters are devices whose energy input arises from injected electrons (an electric current). A terahertz emitter requires a semiconductor heterostructure in which energy level separations can be produced which are in the range 4–41 meV (1–10 THz).

When an electric field is applied to certain superlattices, the energy states (initially extended over the whole structure) localise. At high enough fields the state can be localised across just one or two wells and from this point onwards its energy is proportional to the field  $F$ . Such a system is known as a Stark Ladder as the energy levels, at any field, are equally spaced. A five well system thus produces 5 states, with the energy separation between the states being proportional to the field. A superlattice in this state offers an ideal opportunity to create a tunable terahertz emitter, in that the emission energy  $\Delta E = E_{n+1} - E_n = eFL$  is of the order of a few tens of meV and is proportional to the field.

The operation of the device is illustrated schematically by Fig. 5. Electrons are injected through an electrical contact from the right at high potential, they then scatter down through the series of discrete energy levels. At each level they can undergo either a non-radiative (electron-LO phonon or electron-electron) or radiative transition. The relative strengths of each are often summarised in terms of the ‘internal quantum efficiency’ which is equal to the

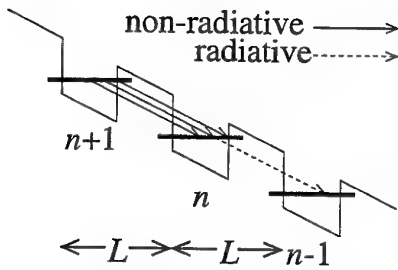


Fig. 5. Electron-phonon (non-radiative) scattering competes with photon emission (radiative scattering) as the electrons ‘cascade’ through the energy level ‘staircase’

fraction of transitions which are radiative. Generally in this type of device this is quite low, peaking at around  $2 \times 10^{-5}$ , at a field of 34  $\text{kVcm}^{-1}$  and at a temperature of 4 K[9]—at which the electron-LO phonon non-radiative scattering is severely suppressed. Such an efficiency means that for every 50,000 electrons in level  $n+1$  only 1 emits a photon when scattering down to level  $n$ . However if the superlattice is fabricated with say 100 periods (quantum wells) then the number of photons generated by 50,000 electrons passing through the complete system is  $100 \times$  as large, giving an internal quantum efficiency of  $2 \times 10^{-3}$ , which although still low, is more promising.

If the superlattice is doped to provide an electron density per unit area of  $N$  in each well at equilibrium operating conditions, then the current density through the device is given by  $J = Ne/\tau$ , where  $\tau$  is the carrier lifetime in any of the levels, i.e.,  $\frac{1}{\tau} = \frac{1}{\tau_{\text{e-e}}} + \frac{1}{\tau_{\text{e-LO}}} + \frac{1}{\tau_{\text{rad}}}$ . Correspondingly the number of photons generated per well equals  $N/\tau_{\text{rad}}$ . With this approach Donovan *et al.*[9] found that a dopant density producing  $10^{11} \text{cm}^{-2}$  in each well produced a current density of  $2.2 \text{kAcm}^{-1}$  at an electric field of 34  $\text{kVcm}^{-1}$ , in turn this device would produce  $2.1 \times 10^{19}$  photons per unit area per unit time per well. For a mesa structure of area  $1 \text{cm}^{-2}$  emitting photons of energy 34 meV, then this implies a peak output power of about 1 mW at a wavelength of 36  $\mu\text{m}$  or 8 THz.

Transitions of this nature have recently been observed[10].

### B. Optically excited systems

If motivated by the desire for lasing from a solid state source, the next stage in the development from an electroluminescent emitter would be an ‘optically excited’ system. This offers the potential of simplifying the design of a lasing structure by removing the necessity to inject electrons through a contact and maintaining a current flow.

Lasing relies upon stimulated emission occurring within an optical cavity, which in turn produces the amplification. In this work attention will be focussed on producing stimulated emission within the active region. A necessary condition for stimulated emission is a population inversion between two energy levels, which in the case of an intersubband system would imply that there must be more electrons in the upper subband than in the lower. To sustain

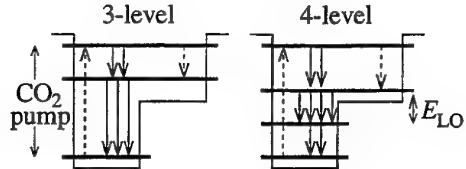


Fig. 6. Three- and four-level optically excited systems based on asymmetric quantum wells

a population inversion at least one other level is required.

Consider first a 3-level system: the rate of change of the population of the second level is given approximately by the rate equation

$$\frac{dn_2}{dt} = \frac{n_3}{\tau_{32}} - \frac{n_2}{\tau_{21}} \quad (1)$$

When the system is at equilibrium, the population of the second level remains constant, hence  $\frac{dn_2}{dt}=0$ . Given this then if  $\tau_{32} > \tau_{21}$  i.e., if the lifetime in the lower state was less than the lifetime of the upper state, then  $n_3 > n_2$ —a population inversion would exist between the third and second levels, thus fulfilling the criteria for stimulated emission.

Berger[11] proposed a 3-subband asymmetric quantum well as a potential design for a terahertz laser, with a population inversion between the third and second subbands. Fig. 6 illustrates the mode of operation. The system is excited by the  $10.6 \mu\text{m}$  line of a  $\text{CO}_2$  laser which excites the reservoir of carriers in the lowest subband to the third subband. Varying the structural parameters of the quantum well allows the excitation criteria to be fulfilled, while at the same time tuning the emission energy  $E_3 - E_2$  across the terahertz region of the spectrum.

Using the methods outlined above, earlier work[5], [6] entailed a study of the scattering rates between the subbands in asymmetric quantum wells. The population ratio  $\tau_{32}/\tau_{21}$  is plotted in Fig. 7 (filled symbols). The main conclusions are: that the population ratios peak around 5-7 THz; they are greater at lower temperatures, and are always less than 1 at 300K. The final point implies that stimulated emission would not be observed at elevated temperatures.

Considering again the criteria for population inversion,  $\tau_{32} > \tau_{21}$ : then if the lifetime of the lower laser level could be reduced, then the population ratio would be improved. The right hand structure of Fig. 6 is an attempt at such a lifetime reduction. An additional fourth subband is introduced beneath the lower laser subband to enhance the scattering out (reduce the lifetime), lasing is now designed to be between the fourth and third subbands. The structural parameters of the asymmetric quantum wells were varied[5] in order to retain the same optical pump energy, but to hold the new subband exactly an LO phonon energy below the lower laser subband, thus maximising the lifetime reduction effect.

Fig. 7 also displays the population ratios for these 4-subband systems (open symbols)[12]. It is apparent that the population ratios are much improved for the higher

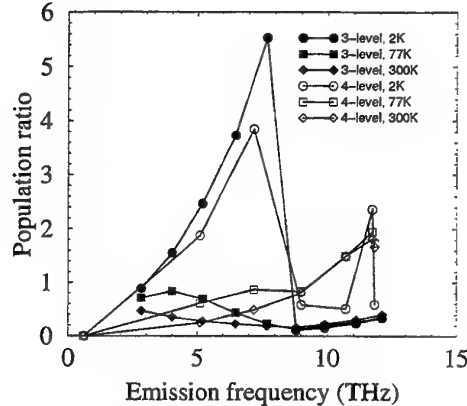


Fig. 7. The population ratio at temperatures of 2, 77, and 300 K for both the 3-level and 4-level systems as a function of emission energy

temperatures and indeed do rise above 1 at the higher terahertz frequencies—thus room temperature stimulated emission is a possibility.

### C. Electrically excited lasers

The final stage of the design of terahertz sources is the electrically injected laser, this is the subject of another work in these proceedings[13].

## IV. CONCLUSION

It has been shown that energy levels of semiconductor quantum well systems can be engineered to provide energy separations in the terahertz region of the spectrum. The potential for emitters and optically excited lasers has been evaluated from the basis of the electron scattering properties. It has been shown that a superlattice could provide tunable emission at around 8 THz albeit at low temperature. Asymmetric quantum wells have been shown to fulfil the electron dynamical criteria to exhibit population inversion at room temperature for emission around 10 THz.

## ACKNOWLEDGMENTS

The authors would like to acknowledge financial support from the School of Electronic and Electrical Engineering, The University of Leeds, and EPSRC (U.K.).

## REFERENCES

- [1] M. J. Kelly, *Low dimensional semiconductors: materials, physics, technology, devices*, Clarendon Press, Oxford, 1995.
- [2] M. Helm, P. England, E. Colas, F. DeRosa, and S. J. Allen, "Intersubband emission from semiconductor superlattices excited by sequential resonant tunneling," *Phys. Rev. Lett.*, vol. 63, pp. 74, 1989.
- [3] J. Faist, F. Capasso, D. L. Sivco, C. Sirtori, A. L. Hutchinson, and A. Y. Cho, "Quantum cascade laser," *Science*, vol. 264, pp. 553, 1994.
- [4] C. Sirtori, J. Faist, F. Capasso, D. L. Sivco, A. L. Hutchinson, and A. Y. Cho, "Mid-infrared (8.5  $\mu\text{m}$ ) semiconductor lasers operating at room temperature," *IEEE Photonics Technology Letters*, vol. 9, pp. 294-296, 1997.
- [5] P. Harrison and R. W. Kelsall, "Population inversion in optically pumped asymmetric quantum well terahertz lasers," *J. Appl. Phys.*, vol. 81, pp. 7135-7140, 1997.

- [6] P. Kinsler, P. Harrison, and R. W. Kelsall, "Pauli exclusion and intersubband electron-electron scattering in asymmetric quantum well structures designed for far-infrared emission," *Phys. Rev. B*, 1998, accepted for publication.
- [7] J. H. Smet, C. G. Fonstad, and Q. Hu, "Intrawell and interwell intersubband transitions in multiple quantum wells for far-infrared sources," *J. Appl. Phys.*, vol. 79, pp. 9305, 1996.
- [8] Bin Xu, Qing Hu, and M.R. Melloch, "Electrically pumped tunable terahertz emitter based on intersubband transition," *Appl. Phys. Lett.*, vol. 71, pp. 440, 1997.
- [9] K. Donovan, P. Harrison, and R. W. Kelsall, "Stark ladders as tunable far-infrared emitters," *J. Appl. Phys.*, 1998, accepted.
- [10] G. Scamarcio, F. Capasso, A. L. Hutchinson, D. L. Sivco, and A. Y. Cho, "Midinfrared emission from coupled wannier-stark ladders in semiconductor superlattices," *Phys. Rev. B*, vol. 57, pp. R6811, 1998.
- [11] V. Berger, "Three-level laser based on intersubband transitions in asymmetric quantum wells: a theoretical study," *Semicond. Sci. Technol.*, vol. 9, pp. 1493, 1994.
- [12] P. Kinsler, P. Harrison, and R. W. Kelsall, "Intersubband terahertz lasers using four-level asymmetric quantum wells," *J. Appl. Phys.*, 1998, submitted.
- [13] K. Donovan, P. Harrison, R. W. Kelsall, and P. Kinsler, "A theoretical study of quantum well terahertz lasers," *1998 IEEE sixth international conference on Terahertz electronics proceedings*, 1998, submitted.

# Quantum Well Structures for THz Bandwidth Near-Infrared Unipolar Semiconductor Lasers

C. Y. L. Cheung, P. Rees and K. A. Shore

**Abstract**—Intersubband semiconductor lasers provide possibilities for obtaining compact laser sources in the mid-infrared (MIR) spectral region. The dynamical behaviour of such lasers is governed by electron lifetimes, which are typically of order 1 ps in coupled quantum well structures. In the present paper, attention is given to the design of a near-infrared unipolar semiconductor laser with a lasing wavelength of 1.55  $\mu\text{m}$ . Calculations have been undertaken of the optical gain spectra of this structure and compared to that of a similar MIR structure. In addition, it has been found that very high direct-current modulation bandwidths would be achievable in these lasers.

**Keywords**—intersubband, near-infrared, unipolar, terahertz bandwidth, semiconductor, quantum wells.

## I. INTRODUCTION

INTERSUBBAND semiconductor lasers have attracted considerable attention following the development by Faist, Capasso *et al* of the so-called Quantum Cascade Lasers which operate in the Mid-Infrared (MIR) [1]. That work gave the first practical demonstration of a long-standing proposal for the utilisation of intersubband transitions to obtain lasing action in semiconductor superlattices [2].

The very considerable progress [3] which has been made in improving the characteristics of unipolar semiconductor lasers has prompted the present authors to undertake work aimed at assessing the expected performance characteristics of intersubband lasers devices including their waveguiding properties [4], and in particular, their anticipated direct current modulation capabilities. In earlier work, use was made of the rate equation model [5,6] to describe the dynamical properties and direct current modulation capability of intersubband lasers. It was observed [7] that since electron lifetimes in intersubband lasers are typically of the same order as the photon lifetime, there is a fine balance between the contributions of the resonance frequency and damping factor in the determination of the maximum modulation frequency in these devices. That work, in particular, indicated that THz modulation bandwidths of intersubband lasers are quite feasible on the basis of the carrier dynamics [8].

In that initial analysis, representative values for carrier lifetimes and interwell tunneling times were utilised. In subsequent work, a self-consistent analysis of the modulation response was performed through a direct calculation of the relevant carrier and tunneling times for a prototype

triple quantum well structure suitable for incorporation in near-infrared intersubband lasers [9].

The present work builds on those foundations to undertake calculations of the optical gain and hence threshold currents for intersubband lasers and hence to examine the feasibility of accessing the predicted THz modulation bandwidth.

## II. OPTICAL GAIN SPECTRA

Starting from the general standard expression for optical gain per metre in a semiconductor [10], we find that

$$g(\hbar\Omega) = \frac{\pi e^2 \hbar}{n \epsilon_0 c m_0^2} \frac{1}{\hbar\Omega} |M_T(E_{21})|^2 \rho_r(E_{21}) \times \int (f_2 - f_1) L(h\nu_0 - E_{21}) dE_{21} \quad (1)$$

where  $|M_T(E_{21})|^2$  is the transition matrix element,  $\rho_r(E_{21})$  is the reduced density of states, and  $L(h\nu_0 - E_{21})$  is the lineshape function. In a QW,  $\rho_r(E_{21}) = \frac{m_r}{\pi \hbar^2 W}$ , where  $W$  is the QW width. The transition matrix element is occasionally written as the dipole moment matrix element  $|z|^2$ , and the relationship between the two is given by  $|M_T(E_{21})|^2 = m_0^2 \Omega^2 |z|^2$ . We will be using the dipole moment matrix element in the equations to follow.

Substituting the above expressions for the density of states and dipole moment matrix element, and using the line shape as proposed in [11,12], we obtain the following expression for the gain:

$$g(\hbar\Omega) = \frac{e^2 |z_{12}|^2 m_r \Omega}{\hbar^2 c n \epsilon_0 L} \int_0^\infty d\epsilon \frac{\hbar \gamma(\epsilon) \cdot [f_2(\epsilon) - f_1(\epsilon)]}{\pi [\hbar\Omega - \hbar\Omega_\epsilon]^2 + [\hbar \gamma(\epsilon)]^2} \quad (2)$$

which is similar to the expression given in [11,12] except that equation (2) above is in mks units and has the reduced effective subband mass,  $m_r$ , where  $\Omega_\epsilon$  the optical transition frequency for the in-plane electron momentum  $\hbar k = \sqrt{2m_2 \epsilon}$ , namely  $\hbar \Omega_\epsilon \equiv \hbar \Omega_0 + \epsilon_2 - \epsilon_1$ , where  $\epsilon_2 \equiv \epsilon$  and  $\epsilon_1 = \hbar^2 k^2 / 2m_1$  are kinetic energies in the upper and lower subbands respectively, characterized by the effective masses  $m_1$  and  $m_2$ , and the distribution functions  $f_1$  and  $f_2$ . Hence the reduced mass,  $m_r = m_1 m_2 / (m_1 + m_2)$ . The function  $\gamma(\epsilon)$  describes the transverse phase relaxation due to intrasubband scattering [11].

In [12], it was assumed that  $\gamma(\epsilon)$  is dominated by the

University of Wales, Bangor, School of Electronic Engineering & Computer Systems, Bangor, LL57 1UT.

E-mail: alan@sees.bangor.ac.uk .

interaction with polar optical phonons, such that

$$\gamma(\epsilon) = \gamma_0 \times \begin{cases} N_{ph} \\ (N_{ph} + 1)\theta(\epsilon - \hbar\omega_{ph}) \end{cases} \quad (3)$$

where the top line describes optical phonon absorption and the bottom line optical phonon emission,  $\gamma_0 = \frac{\pi e^2}{2\hbar} \left( \frac{1}{\kappa_0} - \frac{1}{\kappa_\infty} \right) q_{ph}$ ,  $q_{ph} = \sqrt{2m_e\omega_{ph}/\hbar}$ ,  $N_{ph} = \frac{1}{\exp^{\hbar\omega_{ph}/kT} - 1}$  is the phonon Planck function [11],  $\theta(\epsilon - \hbar\omega_{ph})$  is a step function and  $\hbar\omega_{ph}$  is the optical phonon energy.  $\kappa_0$  and  $\kappa_\infty$  are the low and high frequency dielectric constants respectively.

In Figure 1, results of calculations of optical gain at MIR wavelengths for a single triple quantum well element are shown. It is apparent that a relatively low gain is associated with the relevant intersubband lasing transition. When this is considered together with the relatively large optical losses at MIR wavelengths, it is clear that there is a need to use a multiplication effect where several such elements are included, e.g. in quantum cascade laser structures, in order to achieve and sustain lasing action. In such multi-element structures modulation bandwidths are likely to be compromised by inter-element carrier transport effects which act as intrinsic parasitics [13]. In the next section, results of calculations of optical gain for a NIR structure are presented. It will be seen that a significantly higher gain is achievable at NIR wavelengths in comparison to the MIR.

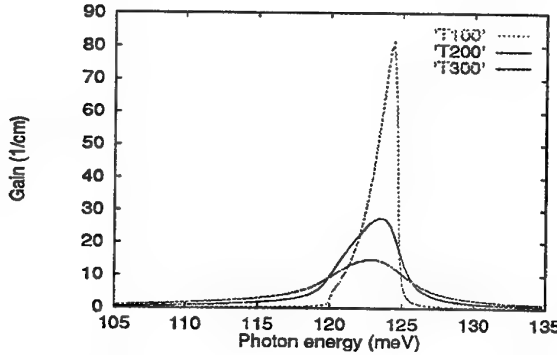


Fig. 1. Optical gain spectra at MIR wavelengths for a single TQW element at temperatures  $T = 100\text{K}-300\text{K}$ .

### III. NIR STRUCTURE

In this work, we utilise a NIR triple quantum well (TQW) structure suitable for intersubband lasing, shown in Figure 2, where the relevant energy levels are indicated with subscripts denoting the quantum well and the superscripts denoting the subband (there is only one subband in  $W_1$  and  $W_3$  and hence the superscripts are omitted). The structure is designed so that at an appropriate bias, its four energy levels are aligned in a manner that causes a transition wavelength of  $1.55\text{ }\mu\text{m}$  to be achieved. At this bias voltage, there also exists an inversion of state lifetimes. An intrawell lasing transition scheme is chosen since, in addition to the larger dipole matrix elements achievable, the

threshold current for intrawell is lower than that for interwell transitions [14]. It is noted that maximising the transition matrix element will also increase the nonradiative decay rate [15,16], but as radiative transitions will similarly increase, tailoring the matrix element for the purpose of reducing nonradiative transitions would appear to be an unnecessary consideration.

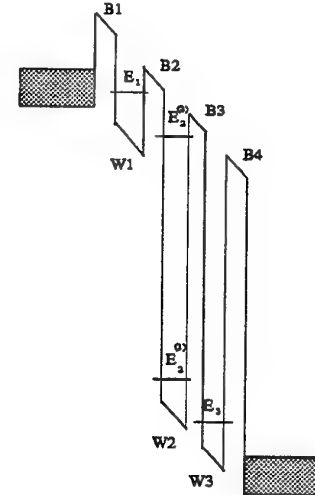


Fig. 2. Schematic conduction band diagram of the coupled well structure, biased to  $550\text{ meV}$ . Well widths are  $W_1=3.10\text{ nm}$ ,  $W_2=3.10\text{ nm}$ , and  $W_3=2.06\text{ nm}$ . Barrier widths are  $B_1=2.00\text{ nm}$ ,  $B_2=3.00\text{ nm}$ ,  $B_3=1.60\text{ nm}$  and  $B_4=1.60\text{ nm}$ . Barrier compositions are AlAs.  $W_1$  is  $\text{Al}_{0.2}\text{Ga}_{0.8}\text{As}$ ,  $W_2$  and  $W_3$  are both  $\text{In}_{0.53}\text{Ga}_{0.47}\text{As}$ .

In contrast to the case of MIR emission, calculations of optical gain at NIR wavelengths, shown in Figure 3, are seen to be significantly higher than at MIR wavelengths. Taken together with the lower optical losses expected in the NIR this strongly suggests that NIR intersubband lasing can be sustained using very few coupled quantum well structures and hence the prospect of THz bandwidth in direct current modulation would appear to be available in such devices.

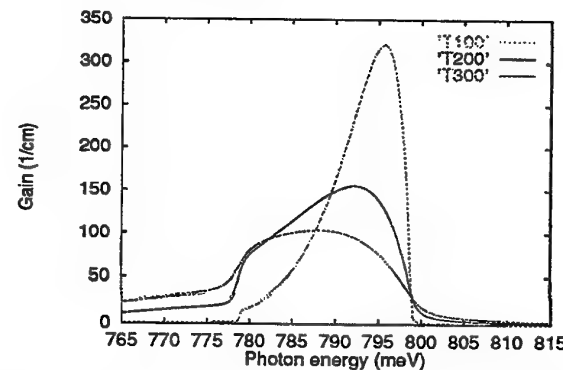


Fig. 3. Optical gain spectra at NIR wavelengths for a single TQW element at temperatures  $T = 100\text{K}-300\text{K}$ .

#### IV. FOUR-LEVEL RATE EQUATIONS AND MODULATION RESPONSE

The population dynamics can be described [5-8] by the rate equations:

$$\frac{dN_1}{dt} = \frac{J}{eL_1} + \frac{L_2}{L_1} \frac{N_2^{(2)}}{\tau_{12}} - \frac{N_1}{\tau_{12}} \quad (4)$$

$$\frac{dN_2^{(2)}}{dt} = \frac{L_1}{L_2} \frac{N_1}{\tau_{12}} - \frac{N_2^{(2)}}{\tau_{12}} - \bar{g}P - \frac{N_2^{(2)}}{\tau_S} \quad (5)$$

$$\frac{dN_2^{(1)}}{dt} = \bar{g}P + \frac{N_2^{(2)}}{\tau_S} + \frac{L_3}{L_2} \frac{N_3}{\tau_{23}} - \frac{N_2^{(1)}}{\tau_{23}} \quad (6)$$

$$\frac{dN_3}{dt} = \frac{L_2}{L_3} \frac{N_2^{(1)}}{\tau_{23}} - \frac{N_3}{\tau_{23}} - \frac{J}{eL_3} \quad (7)$$

$$\frac{dP}{dt} = \bar{g}P - \frac{P}{\tau_T} \quad (8)$$

$$J = \frac{e}{\tau_T} [N_1 L_1 + (N_2^{(2)} + N_2^{(1)}) L_2 + N_3 L_3] \quad (9)$$

where  $J$  is the areal current density,  $P$  the photon density per unit volume, and  $\bar{g} = a(N_2^{(2)} - N_2^{(1)})$ , where  $a$  is the local gain coefficient in units of  $\text{cm}^3\text{s}^{-1}$ .  $\tau_{12}$  and  $\tau_{23}$  are the tunneling times in and out of W2 respectively,  $\tau_T$  is the effective transit time of the carriers through the whole structure, and  $\tau_S$  the intersubband relaxation time.

As is well known, the effect of including the modulation current on the pre-bias current is to produce small variations in the carrier and photon densities relative to their steady state values. The modulation depth can be defined as

$$\eta = \frac{P_{\max} - P_{\min}}{P_{\max}} \quad (10)$$

where  $P_{\max}$  and  $P_{\min}$  are the maximum and minimum variations of the photon density (optical power) with the modulation current respectively.

Due to the picosecond electron lifetimes in these structures it is expected that THz modulation bandwidth should be achievable. Figure 4 below shows the modulation response of the TQW structure of the previous section. The maximum modulation frequency occurs at about 120 GHz for a prebias current five times the threshold value. It is hoped that some improvement may be achieved by further optimisation of the TQW structure, but previous results [7-9] showing the dependence of the modulation bandwidth on the optical output power of the laser (photon density) have indicated that the maximum modulation frequency does not increase monotonically with increasing optical output power. The fact that the carrier lifetimes are of the same order as the photon lifetime, and may even be shorter, indicate that the maximum attainable modulation frequency is essentially determined by the photon lifetime, and that improvements should be obtained by using device design parameters which results in decreased photon lifetime.

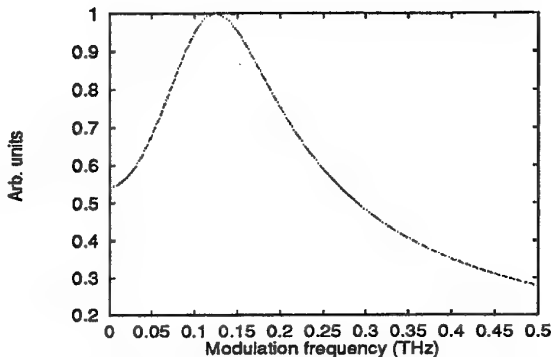


Fig. 4. Modulation response of the NIR structure of Figure 2.

#### ACKNOWLEDGMENTS

CYLC is supported by SEECS, University of Wales, Bangor and by a CVCP ORS award. The work is supported in part by the UK EPSRC under grant GR/K27322.

#### REFERENCES

- [1] J. Faist, F. Capasso *et al*, *Science* **264**, pp. 553-556, 1994.
- [2] R. F. Kazaninov and R. A. Suris, *Sov. Phys. Semiconductor* **5**, pp. 797-800, 1971.
- [3] C. Sirtori, J. Faist *et al*, "Pulsed and continuous-wave operation of long wavelength infrared ( $\lambda = 9.3\mu\text{m}$ ) quantum cascade lasers", *IEEE J. Quant. Electron.* **33**, pp. 89-93, 1997.
- [4] P. S. Spencer, C. Y. L. Cheung and K. A. Shore, "Sensitivity analysis of the optical-waveguide properties of quantum cascade lasers", *IEEE Proc. Optoelectron.* **144** pp. 323-326, 1997.
- [5] W. M. Yee, K. A. Shore and E. Schöll, *Applied Phys. Letts.* **63**, pp. 1089-1091, 1993.
- [6] W. M. Yee and K. A. Shore, *Semicond. Science and Technol.* **9**, pp. 1190-1197, 1994.
- [7] C. Y. L. Cheung, P. S. Spencer and K. A. Shore, *IEEE Proc. Optoelectron.* **144**, pp. 44-47, 1997.
- [8] C. Y. L. Cheung, P. S. Spencer and K. A. Shore, "Analysis of the dynamical properties and modulation response of unipolar semiconductor lasers", *Optical Society of America, CLEO/QELS* Baltimore, Maryland USA, CThS2, May 1997.
- [9] C. Y. L. Cheung and K. A. Shore, "Self-consistent analysis of the dynamical properties and modulation response of unipolar semiconductor lasers", *J. Modern Optics (QE-18 Special Issue)* **45**, pp. 1219-1229, 1998.
- [10] L. A. Coldren and S. W. Corzine, *Diode Lasers and photonic Intergated Circuits*, Chapter 4, John Wiley & Sons, 1995.
- [11] B. Gelmont, V. B. Gorfinkel and S. Luryi, "Theory of spectral lineshape and gain in quantum wells with intersubband transitions", *Appl. Phys. Letts.* **68**, pp. 2171-2173, 1996.
- [12] V. B. Gorfinkel, B. Gelmont and S. Luryi, "Theory of gain spectra for quantum cascade lasers and temperature dependence of their characteristics at low and moderate carrier concentrations", *IEEE J. Quant. Electron.* **32**, pp. 1995-2003, 1996.
- [13] Y. C. A. Wong and K. A. Shore, *J. Modern Optics* **41**, pp. 1271-1277, 1994.
- [14] J. H. Smet, C. G. Fonstad and Q. Hu, "Intrawell and interwell intersubband transitions in multiple quantum wells for far-infrared sources", *J. Appl. Phys.* **79**, pp. 9305-9320, 1996.
- [15] J. Faist, F. Capasso *et al*, "Measurement of the intersubband scattering rate in semiconductor quantum-wells by excited state differential absorption-spectroscopy", *Appl. Phys. Lett.* **63**, pp. 1354-1356, 1993.
- [16] R. Q. Yang "Infrared laser based on intersubband transitions in quantum wells", *Superlattices and Microstructures* **17**, pp. 77-83, 1995.

# An Inter-subband Device with THz Applications

Philip D. Buckle, Philip Dawson, Mark A. Lynch, Chun-Yi Kuo, Mohammed Missous, and William S. Truscott

**Abstract—** Data from optical and electrical measurements on a series of devices based on one design of triple barrier tunnelling structure have been analysed to estimate their behaviour at frequencies over 1 THz. The analysis gives values for the resonantly enhanced admittance, its bandwidth, the bias-frequency relationship and the requirements for a matching circuit to a 50 ohm environment. The results show that one existing structure could be used in oscillators working at 1 THz.

**Index Terms—** resonant tunnelling, triple-barrier devices, inter-subband devices, terahertz oscillators

## I. INTRODUCTION

Quantum mechanical modelling has shown that triple barrier tunnelling structures can act as electrically excited terahertz sources. Terahertz operation is based on an inter-subband resonance and depends on the applied bias producing the correct subband alignment [1]. This paper uses the results of optical and electrical measurements on a series of triple barrier structures to establish the conditions under which a resonant enhancement of the negative conductance should be observed. The data show that many of the necessary criteria for terahertz operation have been met in some of these structures.

## II. STRUCTURES AND DEVICES

The samples were grown in the GaAs/AlGaAs system on semi-insulating GaAs substrates using molecular beam epitaxy in a VG Semicon V90H system. This system gives better than 1% thickness and doping uniformity across 50 mm wafers and a background doping density around  $10^{14}$  cm<sup>-3</sup>. The growth was conducted with a near stoichiometric flux ratio which allowed low growth temperatures (580 – 540 C) and high densities of active silicon n type dopant. A typical structure included the following layers: n<sup>++</sup> bottom contact layer (1  $\mu$ m thick, Si  $3 \times 10^{18}$  cm<sup>-3</sup>), a spacer layer (10 nm, Si  $1 \times 10^{17}$  cm<sup>-3</sup> and 10 nm, undoped), first barrier (4.5 nm, undoped Ga<sub>0.67</sub>Al<sub>0.33</sub>As), first well (6.5 nm, undoped), second barrier (5.4 nm, undoped Ga<sub>0.67</sub>Al<sub>0.33</sub>As), second well (5.4 nm, undoped), third barrier (4.5 nm, undoped Ga<sub>0.67</sub>Al<sub>0.33</sub>As), spacer layer (20 nm, undoped), n

delta doped layer (Si  $1 \times 10^{12}$  cm<sup>-2</sup>), n<sup>++</sup> upper contact (0.5  $\mu$ m, Si  $7 \times 10^{18}$  cm<sup>-3</sup>). A number of parameters were varied, including the aluminium mole fraction in the barriers, but the variable whose effect was most closely studied was the width of the second well which ranged from 6.8 nm to 4.2 nm over a series of 10 samples. Figure 1 shows energies of the quasi-confined levels and the band edge of one of the structures under bias.

Isolated devices were made from all of these structures: the devices were in the form of a double mesa with an active area approximately 80  $\mu$ m square. AuGe/Ni/Au ohmic contacts were made to both the top and bottom contact layers which were exposed on the two mesa steps. The upper contact had an optical window so that optical studies could be conducted in the presence of current flow.

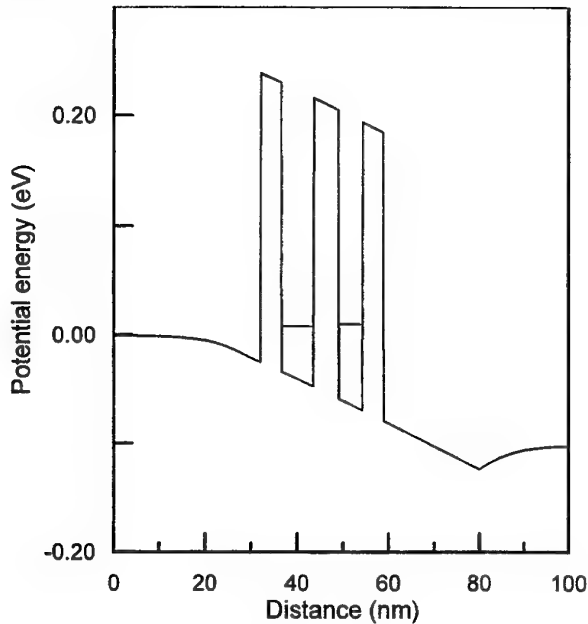


Figure 1: An energy diagram for structure #762 showing the spatial variation of the conduction band edge and the energies of the quasi-confined states at a bias of 0.103 V, just below that which aligns these. At this bias the states are 16 and 18 meV above the conduction band energy in the flat band part of the emitter.

The authors are from the Department of Electrical Engineering and Electronics and the Department of Physics, UMIST (University of Manchester Institute of Science and Technology), P.O. Box 88, Manchester, M60 1QD, U.K.

### III. STRUCTURE CHARACTERISATION

The objective in designing triple barrier structures for terahertz applications is to ensure that, with a bias which lowers the energy of the emitter well quasi-confined state to equal that of the emitter conduction band edge, the energy separation between the two quasi-confined states has the appropriate value for the desired operating frequency. The former condition corresponds to the highest d.c. current density and the latter to the maximum resonant enhancement of the power gain of the device. It follows that the absolute and relative electron confinement energies of the two wells need to be measured if the suitability of any triple barrier structure for a particular terahertz application is to be assessed. In simple quantum well structures, photoluminescence spectroscopy is used to measure the confined electron-hole transition energies allowing the electron confinement energies to be deduced. An intrinsic property of high speed tunnelling structures is that the electron and hole escape times from the quantum wells are very short; these will therefore be a very small fraction of the time taken for radiative electron-hole recombination. It follows that little, if any, intensity can be expected at wavelengths corresponding to the well transitions and none has been observed in our samples. A novel method of photoluminescence excitation spectroscopy, which we have developed, has been used to measure the well transition energies. This technique has been applied to as-grown wafers and yielded good results for all our structures. In it, any optical radiation from the structure at the wavelength for emission from the heavily-doped contact region of the structure is monitored: this region is where holes, optically generated in the wells, will recombine after tunnelling through the barriers. The output of a tunable laser is directed on to the sample (usually cooled to 6 K in most of our experiments) and the wavelength of this light is scanned over the range of the well transitions. Clear signals of an excitonic character have been observed when the incident light has an energy corresponding to any of the lowest electron - heavy hole or electron - light hole transitions in the wells of the sample. We have used the electron confinement energies deduced from these to characterise the samples and to provide rapid feedback to the grower. Figure 2 shows examples of such spectra for a number of our structures. This figure shows two very significant characteristics: first, it is possible to assess the confinement energies and well widths from these spectra, and, second, that the spectra provide a direct confirmation that the energies of the quasi-confined states are well defined in our structures with line widths between 1.0 and 2.0 meV (corresponding to 250 – 350 GHz).

### IV. LEVEL CROSSING EFFECTS

A separation in energy of a few meV between the two quasi-confined states is required for the resonant enhancement of the negative conductance of the devices to occur at terahertz frequencies. It is clearly useful to be able to identify the features that are characteristic of the alignment of these two energies so that the bias can then be

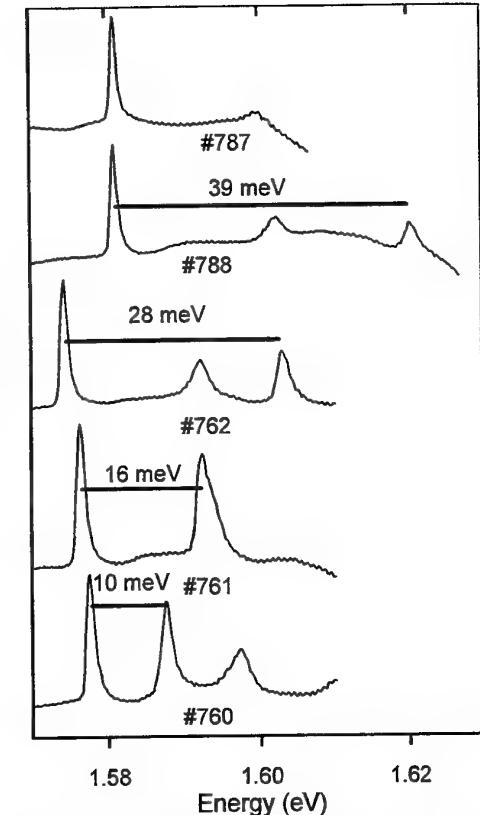


Figure 2: 6 K Photoluminescence excitation spectra from five wafers. The horizontal lines are drawn between the peaks for the electron – heavy hole transitions of the two wells, their length indicates the sum of the electron level splitting and the much smaller heavy hole level splitting. The width of the narrower well in sample #787 was sufficiently small that the absorption was outside the tuning range of the laser. The additional peaks are associated with electron – light hole transitions. The recombination was detected at a wavelength of 816 nm.

adjusted by the appropriate amount to achieve this spacing. Our experimental studies of a series of triple barrier tunnelling structures over the wide range of temperatures 13 K – 300 K, supplemented by numerical calculations based on a physical device model, have established that the current reaches a peak at the bias at which the energies of the states are aligned [2]. This is a direct consequence of the integrated transparency of a triple barrier structure having its maximum value when the energies of the quantum states are aligned. Figure 3 shows the current-voltage characteristics measured on three different structures at a temperature of 80 K. The currents at the biases indicated have the temperature dependence that is predicted for the current at the alignment of the two energies and occurs at a bias that corresponds to the calculated bias for this alignment. It follows that the bias required for the alignment of the energy levels in any structure can be determined if such a feature can be identified. The figure also shows that a structure with a greater difference in the confinement energies of the two wells requires a greater

bias to produce the alignment and gives, for similar emitter well confinement energies, a higher device current at alignment since the energies of the two well states under these conditions are closer to the Fermi level in the emitter. The terahertz negative conductance is a resonant enhancement of the d.c. conductance; it follows that an optimised device will have as large a current density as possible and will therefore operate with a bias as close as possible to that which aligns the emitter well energy with the peak electron density in the emitter. This is the origin of the first structural requirement stated in section III.

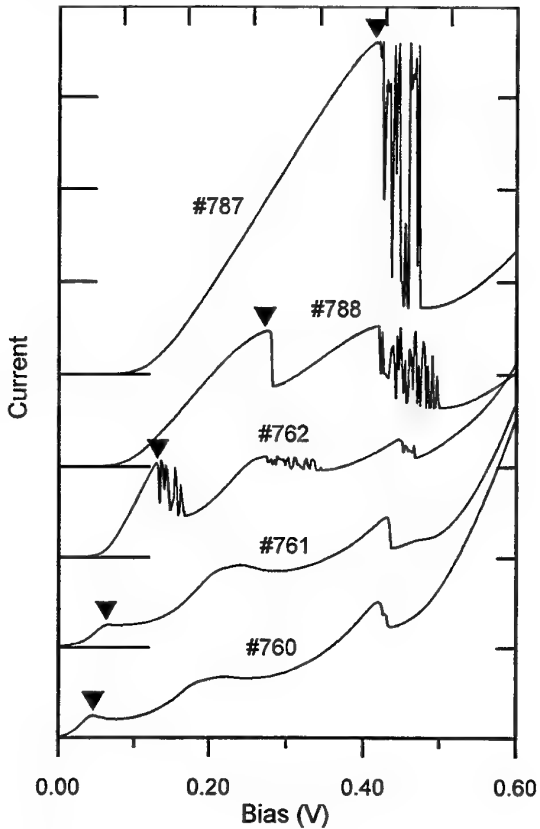


Figure 3: The current voltage characteristics of devices fabricated from five different structures measured at a temperature of 80 K. The peaks indicated by the triangles correspond to the bias at which the energies of the emitter and collector electron states are aligned. The current scale for the three lower curves is 10 mA/division, that for the upper two is 30 mA/division.

Once sufficient bias is applied to a device, an electron current will flow from the emitter to the collector, and any holes generated in the collector, for example by an external light source as in a conventional photoluminescence experiment, would be transported towards the emitter. Under these conditions the quantum wells would have a steady-state population of both electrons and holes, and optical radiation with wavelengths characteristic of the quantum wells should be observable. Such radiation has been studied for our devices for which the upper, collector contact was illuminated by a laser. The variation with bias

of the wavelengths and line shapes give important information about the internal behaviour of the devices [3]. The data shown in figure 4 is the most significant for assessing the terahertz behaviour of these devices. The two curves in the upper part of the figure show the integrated light output characteristic of the emitter and collector wells as a function of bias, whilst the curve in the lower part shows the current-voltage characteristic. The intensity of the output from either well is a function of a number of parameters including the product of the electron and hole densities. The significant feature in this diagram is the abrupt dip at a bias of 0.12 V in the intensity of the light arising from the emitter well. This bias also corresponds to that at which the energies of the two quasi-confined states are aligned. The theoretical model has predicted that the electron density in the emitter well falls when the energies of these two electron states are aligned; we interpret this fall in the intensity of the light as a decrease in the electron density in the emitter well caused by the alignment of the two energies. The significant feature for the prediction of the terahertz behaviour of these devices is the bias range over which the charge decreases: this is shown in detail in the inset of figure 4. The half width in bias of the charge decrease is 16 mV. This is consistent with the observed energy half-widths measured for the two electron states in this sample, namely 1.3 and 2.0 meV, and the measured ratio of 6.0 : 1 between a change in the applied bias and the change in the relative energies of the two well states.

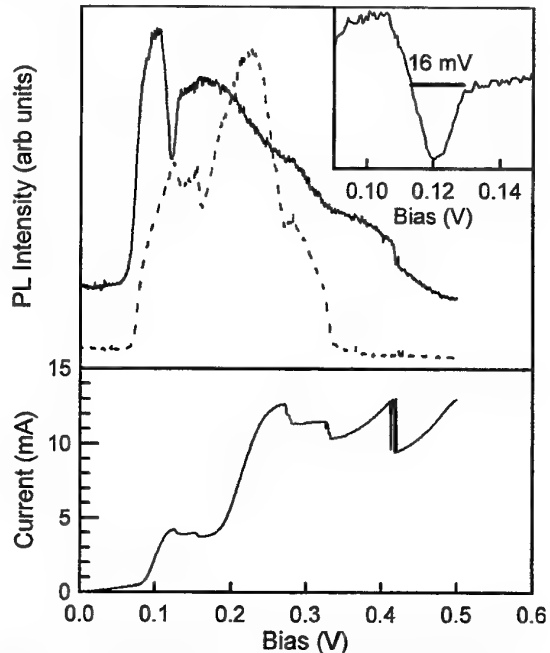


Figure 4: The upper part shows the variation with bias of integrated optical output characteristic of the emitter well (continuous line) and the collector well (dotted line) in a photoluminescence experiment on a single device with structure #762 at 6 K. The lower part shows the current-voltage characteristic of the device measured at the same time. The inset shows in detail the dip in the output from the emitter well around a bias of 0.12 V.

## V. TERAHERTZ BEHAVIOUR

Both the theoretical models of triple barrier devices and the experimental data indicate that the collector current is proportional to the charge density in the collector well and that this charge density is significantly smaller than that in the emitter well except when the two wells are exactly aligned. If an a.c. electric field is applied whose frequency is near to that which corresponds to the difference between the energies of the quasi-confined states of the two wells, then the effect of the electric field will be to drive charge in an oscillatory fashion between the emitter and collector wells. Since the charge density is significantly higher in the emitter well, a relatively small fractional change in this charge will produce a much larger fractional change in the collector well charge and hence a significant change in the collector current. If the frequency corresponds exactly to the energy difference between the two states then the system will be in resonance and the power absorbed from the applied field will be a maximum. Under these conditions, the variation in charge in the collector well, and also the consequent variation in collector current, will be at a maximum; moreover, the current associated with this changing charge will be in phase with the applied field. The charge density in the collector well will therefore lag the electric field by  $90^\circ$  and the time-dependent component of collector current will appear inductive. At frequencies above the resonance, but within its bandwidth, the current associated with the charge oscillating between the wells will lag the applied field; the collector current will therefore have a component that is  $180^\circ$  out of phase with the a.c. bias as well as an inductive part. The maximum in the negative conductance of a triple barrier device will occur at the frequency which exceeds that corresponding to the difference in the two state energies by about half the bandwidth of the inter-state resonance, a condition giving a  $135^\circ$  phase shift between the collector current and the a.c. bias. It should be noted that a quadruple barrier device may have a current  $180^\circ$  out of phase with the a.c. bias at resonance.

In addition to finding the condition for maximum negative conductance, it is necessary to determine the expected magnitude of this conductance, which can be found from the a.c. bias that would give 100% modulation of the collector current in a linear model. The data of figure 4 is most significant in making this estimate. The fall in charge in the emitter well is equivalent to the a.c. resonance for zero frequency and theoretical models show that the conductances for these two cases are comparable. We therefore estimate that, for our structures, an r.m.s bias of 12 mV should modulate the collector current between 200% and 0% of its d.c. value giving an r.m.s. a.c. current of 70% of the static value. The device structure with the highest current density, #787, has a peak current density of over  $1.5 \times 10^3 \text{ A/cm}^2$ ; for this structure the calculated maximum negative conductance is  $5 \times 10^4 \text{ S/cm}^2$ . A negative conductance of  $-0.02 \text{ S}$  required to drive a  $50 \Omega$  system would require a device area of  $40 \mu\text{m}^2$ . The typical depletion length in our structures is 66 nm as determined

from the ratio of the change between different structures in the bias required to align the two energy levels to the change in the zero bias splitting of these levels. The capacitance for a  $40 \mu\text{m}^2$  device with this depletion distance would be 70 fF; such a device would have an impedance at 1 THz of  $2 \Omega$ . The matching circuit for this device would therefore need a Q of 25 in a  $50 \Omega$  environment. The bias at which this resonance would be seen would be about 20 mV below the current peak.

The construction of a matching circuit with a Q of 25 at 1 THz may be beyond current technologies; however, the specific negative conductance is controlled by the current density which is in turn determined by the tunnelling rate through the barriers. The structures for which data have been presented in this paper were designed to meet the requirements for optical measurements. These need reasonable ( $> 0.5 \text{ A}$ ) bias currents for devices with an area comparable to the  $75 \mu\text{m}$  diameter of the image of the illuminating laser. Much greater current densities have been reported for double barrier tunnelling devices fabricated from GaAs with AlAs barriers [4]; it is reasonable to expect that ratios of conductance to capacitance could be achieved which are at least 10 times those reported here. It should be easy to match such devices to a  $50 \Omega$  environment; they therefore have considerable potential as the basis for practical sources of power in the 1 – 3 THz range.

## VI. CONCLUSIONS

Results of measurements on a series of triple barrier devices have been analysed to assess their likely performance at frequencies around 1 THz. There is good experimental evidence that the structures would exhibit a resonantly enhanced negative conductance in this frequency range. It is apparent that one existing structure could be used as a power source if good matching of the structural capacitance could be achieved. Future developments of these devices are likely to improve the ratio of the negative conductance to capacitance; this would allow matching over a broader range of frequencies.

## VII. ACKNOWLEDGMENTS

This work has been supported by the Engineering and Physical Sciences Research Council through grant number GR/J 78013.

- [1] W.S. Truscott, Solid State Electronics, 37 (1994), 1235
- [2] C-Y. Kuo, M.A. Lynch, A.H. Roberts, P.D. Buckle, P. Dawson, M. Missous and W.S. Truscott, to be published in *Physica E* (1998)
- [3] P.D. Buckle, P. Dawson, C-Y. Kuo, A.H. Roberts, W.S. Truscott, M. Lynch and M. Missous, *J. Appl. Phys.* 83 (1998), 882
- [4] L. Yang, D.E. Mars and M.R.T. Tan, *J. Appl. Phys.* 73 (1993) 2540

# Mode locking of far-infrared p-Ge lasers

R. C. Stribbos, A. V. Muravjov, C. J. Fredricksen, W. Trimble, S. H. Withers,  
S. G. Pavlov, V. N. Shastin, and R. E. Peale

**Abstract**— Active mode locking of the THz p-Ge light-to-heavy-hole-band laser is reported yielding 200 ps FIR pulses with a few Watt peak power. It is achieved via radio-frequency (rf) gain modulation at one end of the laser crystal in Voigt configuration. Applying an additional bias voltage at the rf contacts allows to optimize the gain and improve mode locking characteristics. This compensates an intrinsic bias offset caused by charging of the laser crystal due to the asymmetry of (warped-band) hole transport in crossed electric and magnetic fields for the orientation  $B \parallel [112], E \parallel [1\bar{1}0]$  used in our experiments. A transition from single-pulse mode locking to second harmonic mode locking is observed for a crystal with roundtrip frequency equal to the rf frequency, and separation between the two pulses is tuned from zero to half the cavity roundtrip period by changing the external bias to the modulating rf field.

**Keywords**— far infrared, active mode locking, mode-locked lasers, semiconductor lasers, hot hole transport, space charge, p-type germanium

## I. INTRODUCTION

Far-infrared p-Ge ( $N_A \approx 10^{14} \text{ cm}^{-3}$ ) lasers [1] are operated in strong crossed electric and magnetic fields ( $E \approx 0.3 - 3 \text{ kV/cm}$ ,  $B = 0.3 - 3 \text{ T}$ ) at helium temperatures. Their mechanism of stimulated emission (Fig. 1) is based on the largely different motion of light and heavy holes. Heavy holes are repeatedly accelerated up to the optical phonon energy  $E_{\text{op}}$  and scattered back by emitting an optical phonon ( $\tau_0 \approx 0.5 \text{ ps}$ ). Light holes have a much longer lifetime  $\tau_c \approx 10 - 100 \text{ ps}$ , traveling along closed cyclotron orbits below  $E_{\text{op}}$  only interrupted by acoustic phonons and ionized impurities.

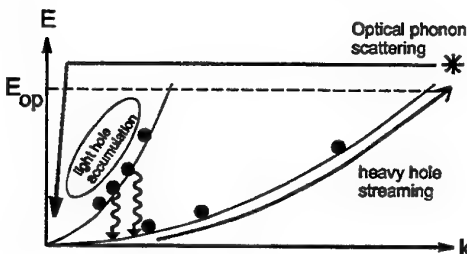


Fig. 1. Pumping mechanism of the p-Ge laser.

Since about 4% of the streaming heavy holes is scattered into the light hole band, lasing can be achieved on either the light-to-heavy-hole transition (inter-valence-band (IVB) laser, 10 W, broadband ( $20 - 30 \text{ cm}^{-1}$ ), tunable between  $50 \text{ cm}^{-1}$  and  $140 \text{ cm}^{-1}$  by changing  $E$  and  $B$ ) or between two light hole Landau levels having a different degree of mixing with the heavy hole band (light-hole-cyclotron-resonance (LHCR) laser, narrowband ( $< 0.1 \text{ cm}^{-1}$ ), 100 mW, magnetically tunable between

$40 \text{ cm}^{-1}$  and  $85 \text{ cm}^{-1}$ ). The lasers are pulsed usually with  $\mu\text{s}$  pulses at a  $1 - 10 \text{ Hz}$  repetition rate, although advanced miniaturization and use of deep acceptors has lead to a duty cycle of 2.5% [2, 3]. Use of permanent magnets [4] and of closed-cycle refrigerators [3] to eliminate liquid cryogens are turning the p-Ge laser into a practical source.

Due to their wide spectrum, the IVB p-Ge lasers are promising for generation of THz pulses on the picosecond timescale with considerable peak power needed for time-resolved (linear and non-linear) THz spectroscopy and other related applications. In Ref. 5 it was proposed to use radio-frequency (rf) gain modulation at one end of laser crystal to induce active mode locking. Monte Carlo simulations showed that a small rf electric field (only a few percent of the main pumping electric field) along the magnetic field can easily modulate the gain by 30-50%. Although the motion of accumulated light holes is magnetically restricted in the transverse plane perpendicular to the magnetic field, they can still move freely along the  $B$ -direction with very high mobility. Consequently, a small longitudinal electric field  $E_L$  is enough to accelerate the light holes beyond the optical phonon energy, and upon emitting an optical phonon they are primarily scattered into the heavy hole band. This strongly reduces the population inversion and the IVB gain. Upon applying a rf  $E_L$  field the gain is maximal at the rf nodes ( $E_L = 0$ ) and minimal at the rf extrema, and thus effectively modulated at twice the rf frequency. When the rf frequency is chosen equal to half the cavity roundtrip frequency ( $v_{\text{rf}} = v_{\text{RT}}/2$ ), only the pulse traveling through the modulator at maximum gain is continually amplified, yielding the typical pulse-train output of a mode-locked laser. This method is attractive because it monolithically integrates a 'cryogenic FIR modulator' and thereby avoids problems encountered when introducing additional elements into the cavity.

Early experimental implementations [6, 7] of this idea yielded indirect indications for mode-locked behavior: upon applying the rf, laser action was prohibited, but lasing reappeared when the rf frequency was equal to half the cavity roundtrip frequency. Recently, active mode locking has been unambiguously demonstrated [8–10] in the time domain, showing a train of 200 ps FIR pulses. Direct evidence of enhanced locking of laser modes in the frequency domain has also been reported [11].

In this paper active mode locking of the p-Ge laser is reported for a 42-mm long crystal ( $v_{\text{rf}} = v_{\text{RT}}/2$ ) and a 84-mm long crystal ( $v_{\text{rf}} = v_{\text{RT}}$ ). Our setup has been designed such that the rf field is superimposed on a variable 'DC' bias level, thereby allowing the modulation to be shifted over the gain-versus- $E_L$  curve. For the short sample, this additional control enables to optimize the gain and improve mode-locking characteristics. For the long sample, the time delay between two pulses traveling through the resonator can be altered from zero to half the cavity roundtrip time by changing the bias level.

R. C. Stribbos, A. V. Muravjov, C. J. Fredricksen, W. Trimble, S. H. Withers, and R. E. Peale are with the Department of Physics, University of Central Florida, Orlando, FL 32816, Phone: 407-823-3076, Fax: 407-823-5112, E-mail: rep@physics.ucf.edu.

S. G. Pavlov and V. N. Shastin are with the Institute for Physics of Microstructures, Russian Academy of Sciences, GSP-105, Nizhny Novgorod 603600, Russia.

## II. EXPERIMENTAL SETUP

Single-crystal, Ga-doped, p-Ge ( $N_A - N_D = 7 \times 10^{13} \text{ cm}^{-3}$ ) was cut into rectangular bars with a cross section of  $5 \times 7 \text{ mm}^2$  and a length of 42.1 and 84.2 mm, respectively. Ohmic contacts were made at the  $5 \times L \text{ mm}^2$  sides by aluminium evaporation, subsequent annealing, and final covering with indium. Crystal ends were polished parallel to each other within 1' accuracy and two external copper mirrors were attached to them via 20  $\mu\text{m}$  teflon film (Fig. 2(c)). Crystals were immersed in liquid helium and magnetic fields up to 1.4 T were applied in Voigt geometry using a room temperature electromagnet. Electric field pulses  $E_{\text{HV}}$  are supplied by a low duty-cycle thyratron pulser. The field orientations were  $E_{\text{HV}} \parallel [1\bar{1}0]$  and  $B \parallel [112]$ . Radiation is conducted out of the top of the cryostat using a brass light pipe sealed with a teflon lens, detected by a fast whisker-contacted Schottky diode (1T17(82), University of Virginia), amplified, and recorded on a transient digitizer (Tektronix SCD5000) with 80 ps resolution. Additional  $\sim 8\text{-mm}$  long contacts (Fig. 2(c)) provide the additional electric field  $E_L \parallel B$  at one end of the crystal. The lengths of the crystals were chosen to have roundtrip frequencies of 904 and 452 MHz, respectively, in order to match the rf frequency band near 452 MHz of relatively cheap ham-radio electronics.

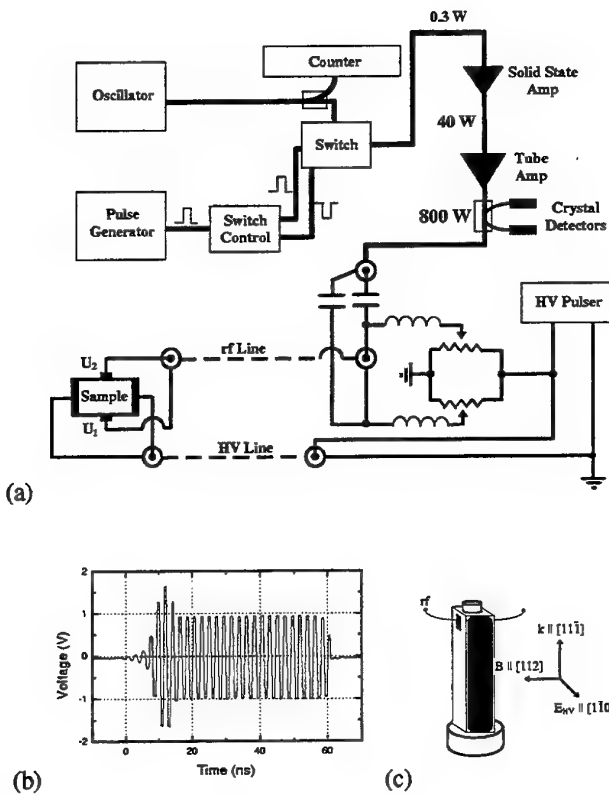


Fig. 2. (a) Rf setup. (b) (Attenuated) output of the pulse-forming rf switch. (c) Laser cavity construction with main high-voltage (HV) contacts, end mirrors, applied fields, and rf contacts at one end.

The rf system shown in Fig. 2(a) produces clean sub- $\mu\text{s}$  pulses (Fig. 2(b)) which just overlap the HV pulses to prevent heating

of the laser crystal by the rf. From the switch, low duty-cycle rf bursts enter a GE MASTR II solid-state power amplifier with gain control to give up to 40 W. This is fed to a Henry Radio Model 2004A tube amplifier to give up to 800 W. Such high rf power is required partly to overcome the unavoidable imperfect match to the low, dynamic impedance of the crystal. The additional bias to the rf signal is supplied by dividing the potentials  $U_1$  and  $U_2$  directly from the main high voltage pulse using two variable resistors.

## III. RESULTS AND DISCUSSION

Fig. 3 shows results of applying rf during the laser pulse. The forward rf power required to extinguish lasing is plotted versus rf frequency in the lower inset. At 452.2 MHz (gain is modulated twice per rf cycle for the 42.1 mm crystal), the laser still operates even when the full available forward rf power is applied, indicating that mode-locking should be occurring [6]. Shifting of the modulation frequency by more than  $\pm 0.5$  MHz blocks the lasing because circulating pulses do not remain in phase with the gain modulation. At resonance, the Schottky diode detector signal plotted in Fig. 3 reveals the mode-locked pulse train. The upper inset shows 150 ps pulses from a different shot. The basic pattern of pronounced, separated pulses is repeatable with relatively minor differences from shot to shot.

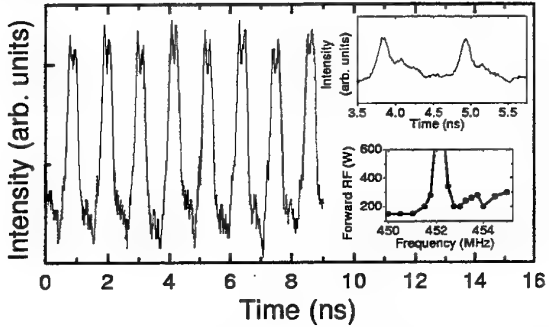


Fig. 3. Actively mode-locked p-Ge laser output. The upper inset shows a different shot with 150 ps pulses. The lower inset shows the rf resonance at half the roundtrip frequency.

It is important to note that for the experiment of Fig. 3, a bias of about 20 V is applied to the rf contacts in addition to the rf power. Changing this bias by more than about 5 V removes the resonance observed in Fig. 3, indicating that for this particular situation mode locking is not possible without the bias.

The significant impact of the bias level to the rf gain modulation field on the output characteristics of active mode-locking is even more evident for the 84.2 mm long sample, which has a cavity roundtrip time of 2.20 ns and hence a roundtrip frequency of 453.6 MHz. A mode-locking resonance is found at 453.8 MHz. The output at resonance is shown in Fig. 4. A train of single pulses occurs with a period equal to the cavity roundtrip time. Upon increasing the external bias, the mode-locked pulses become broader and start to split into two. Further bias increase leads to two separate pulses traveling through the cavity independently (harmonic mode locking).

This behavior is graphically explained in Fig. 5. When the gain is modulated around its maximum (c), two independent

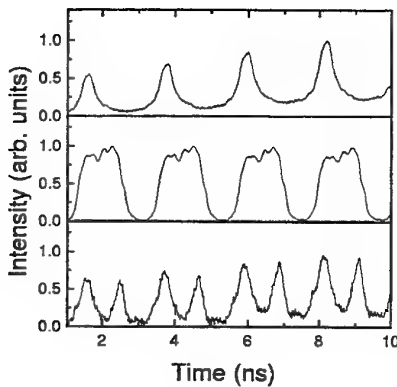


Fig. 4. Mode-locked p-Ge laser pulse structure for the 84.2 mm crystal. External bias added to the rf modulation increases from zero in the three frames from top to bottom.

pulses travel around the cavity separated by half the cavity roundtrip time, since they are synchronized to the nodes of the rf field. Upon shifting the rf offset (b), the two pulses move closer to each-other in order to keep traversing the modulated region at maximum gain. For a certain, sufficiently large offset (a), the two pulses merge completely, and only one pulse is sustained, synchronized to the rf extremum with maximum gain.

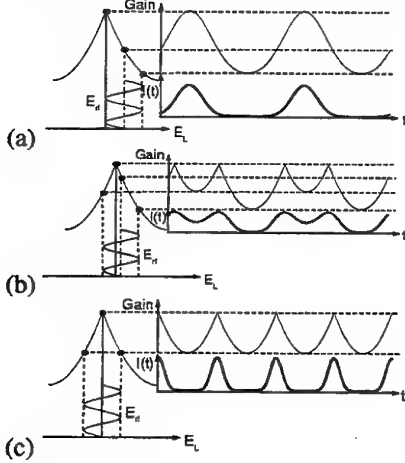


Fig. 5. Explanation of bias effects and pulse-separation control. The left curve plots gain versus external bias. The right curve shows the modulation of the gain versus time, when the rf field is applied at the bias level indicated. The pulse train expected to result is also indicated. The three situations (a) large offset: modulation far from peak of gain-vs.- $E_L$ , (b) small offset: modulation close to peak of gain-vs.- $E_L$  curve, and (c) zero offset: modulation at peak of gain-vs.- $E_L$  curve mimic the experimental results in Fig. 4.

For the 42.1-mm sample, gain modulation at twice the rf frequency is necessary, and rf modulation should be at the peak of the gain-vs.- $E_L$  curve (c). A large offset leads to gain modulation at the applied rf frequency (rather than its second harmonic) at low rf power (a). Circulating pulses would encounter alternatively low and high gain which is unfavorable to mode locking. Even at rf powers sufficient to pass through the gain maximum twice per rf cycle (b), the offset causes broadening of the micropulses and a decrease in their intensity if maximum gain occurs at moments other than the rf zero crossings.

Upon closer examination of these results, however, there ap-

pears to be already an 'intrinsic' offset for both samples when there is no external bias. Without external bias, the output of situation (c) in Fig. 5 is obtained (single pulse mode-locking for the long crystal, and no mode-locking resonance for the short crystal), and an external bias is necessary to (partially) compensate the internal  $E_L$  field and obtain the characteristic output of situations (b) and (a) in Fig. 5 (double pulse mode-locking for the long crystal, and single pulse for the short crystal).

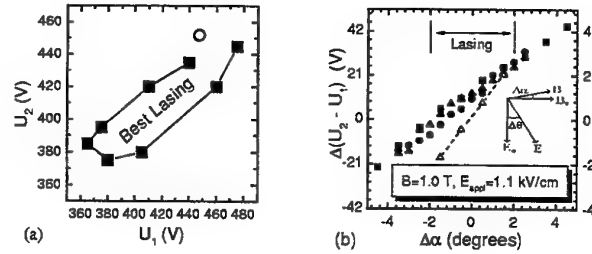


Fig. 6. (a) Lasing domain in  $U_1, U_2$  space. The open circle indicates the operating point without bias circuit. (b) Potential  $U_2 - U_1$  on rf contacts when laser is rotated over an angle  $\Delta\alpha$  around its long axis, thereby introducing a nonorthogonality  $\alpha$  between  $E$  and  $B$ . The point  $\Delta\alpha = 0$  is determined by minimizing the current, and hence  $\Delta\alpha = \alpha$  is assumed. Solid symbols denote the value without bias (different series indicate the error), while open triangles denote the external-bias setting with strongest lasing.

The assumption of an 'intrinsic'  $E_L$  field is confirmed by studying the influence of bias change on pulsed (quasi-CW) operation of the 42-mm laser. Fig. 6(a) shows the region of observed lasing in  $U_2, U_1$  parameter space. The difference  $U_2 - U_1$  is a direct measure of the  $E_L$  field due to charging in the region between the additional contacts, although the zero of this  $E_L$  field might not exactly occur at  $U_2 = U_1$ , since misalignment of the rf contacts will cause an offset. The width of this region confirms the strong dependence of the gain on  $E_L$ : changing  $U_2 - U_1$  over  $\pm 50$  V ( $\Delta E_L \approx \pm 100$  V/cm) from its optimum value brings the laser below threshold. The open circle in Fig. 6(a) indicates the values of  $U_2, U_1$  that the laser establishes by itself without bias. It appears at the border of the lasing region, indicating that there is an intrinsic field  $E_L \neq 0$  which has already significantly reduced the gain. By applying the external bias, this  $E_L$  field can be compensated and the gain in the region between the additional contacts is electrically optimized, yielding longer laser pulses of (somewhat) higher intensity. In Fig. 6(b), both the 'intrinsic' and the gain-optimized values of  $U_2 - U_1$  are plotted upon rotating the laser over an angle  $\Delta\alpha \approx \alpha$  around its long axis. The difference between the two curves ranges from about 35 V/cm for  $\alpha = -2^\circ$  to about zero at  $\alpha = 2^\circ$ .

To start a theoretical discussion of these effects, it is first noted that they can only occur for situations with limited symmetry along the magnetic field, and the field orientation  $E_{\text{HF}} \parallel [1\bar{1}0]$  and  $B \parallel [112]$  used in our (and all previous [6–10]) active-mode-locking experiments indeed lacks a symmetry plane normal to  $B$  in  $k$ -space. For such orientations a significant current  $j_L \parallel B$  might occur even in perfectly crossed  $E$  and  $B$  fields. For streaming holes, this is caused by the highly anisotropic, elongated hole distribution in the anisotropic band (similar to well-known Sasaki-Shibuya effect), while for accumulated holes it results from asymmetry of the accumulation region [12, 13].

The Monte Carlo [12] result in Fig. 7(b) shows that  $j_L$  (normalized by the total current  $j$ ) changes heavily when the E-field is rotated in a plane perpendicular to B. Fig. 7(a) shows the calculated E-field in a cross-section of the 42-mm crystal perpendicular to B. Current saturation is implemented by taking the conductivity  $\sigma_T \propto E^{-f}$ . Near the long ends, the total electric field  $E_{\text{tot}} = (E_{\text{HV}}^2 + E_{\text{Hall}}^2)^{1/2}$  is larger and rotated over an angle  $\phi$  with respect to  $E_{\text{HV}}$  due to the usual Hall effect. Space-charge effects significantly enlarge the affected area. Combining both pictures, one concludes that, due to the inhomogeneity of  $E_{\text{tot}}$ , the  $E_L$  field is relatively small in the central part of the sample, but quite strong in the region between the additional contacts.

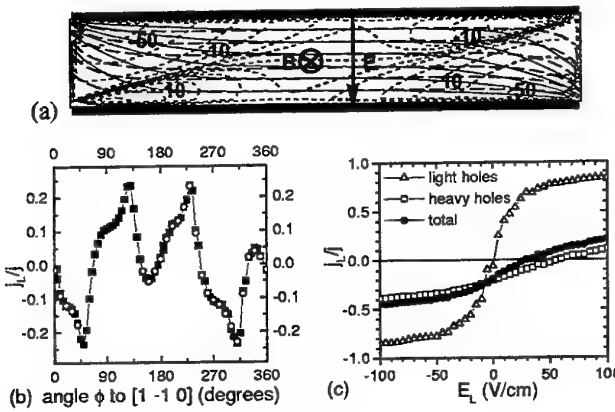


Fig. 7. (a) Equipotential lines (each 100 V) in the sample cross-section perpendicular to the magnetic field for  $f = 0$  (no space-charge, dash-dotted lines) and  $f = 0.7$  (solid lines). The dotted lines indicate contour lines of the space charge (in units of  $\epsilon \times 10^6 \text{ Vm}^{-2}$ ) formed for  $f = 0.7$ . A constant Hall angle ( $\alpha_H = 45^\circ$ ) is assumed. (b)  $j_L/j$  versus the angle  $\phi$  over which E is rotated;  $T = 20 \text{ K}$ ,  $E = 1.35 \text{ kV/cm} \parallel [1\bar{1}0]$  (for  $\phi = 0^\circ$ ),  $B = 1.0 \text{ T} \parallel [112]$ ,  $N_i = 1.3 \times 10^{14} \text{ cm}^{-3}$ ,  $p_0 = 7 \times 10^{13} \text{ cm}^{-3}$ , Brooks-Herring model with self-consistent screening. (c)  $j_L/j$  versus  $E_L$ ,  $T = 20 \text{ K}$ ,  $E = 1.1 \text{ kV/cm}$ ,  $\phi = -45^\circ$ ,  $B = 1.0 \text{ T} \parallel [112]$ .

The theoretical value of the intrinsic offset can be determined by plotting the current  $j_L$  versus the  $E_L$  field along B (Fig. 7(c)). For a rectangular crystal at  $\alpha = 0^\circ$ ,  $j_L$  has to be zero at the sides normal to B, and an internal  $E_L$  field is formed by charging throughout the whole crystal [12] to meet this requirement. The total  $j_L$  is zero for about 30 V/cm in Fig. 7(c), in good agreement with the experimentally observed offset of  $U_2 - U_1 = 15 \text{ V}$  over 5 mm in Fig. 6(b) at  $\Delta\alpha = 0^\circ$ . The intrinsic offset should be zero for  $j_L/j = E_L/E = \sin\alpha$  [12], and in Fig. 7(c) this occurs for  $\alpha \approx 2^\circ$ , again close to the experimental value of  $\alpha$  in Fig. 6(b), for which the curves with and without external bias cross. This is the only value of  $\alpha$  for which no external bias is needed to optimize the gain or move the zero of the rf field to the top of the gain-vs.- $E_L$  curve. Note that this is especially important to achieve active mode locking in short samples, because gain modulation at twice the rf frequency is a prerequisite. Early experiments (with modest rf power and no external bias) indeed reported a rf resonance (like in the lower inset of Fig. 3) only when the crystal was tilted about 2 degrees [6, 7]. Finally, the Monte Carlo simulations also show that the intrinsic offset shifts about 10 V/cm as the crystal is heated from 4.2 K to about 20 K during the macropulse. This leads to pulse broadening when

the gain is modulated at twice the rf frequency, as the situation moves from (a) to (b) in Fig. 5 during the macropulse.

#### IV. CONCLUSIONS

Changing the bias to the rf modulation field of an actively mode-locked p-Ge laser yields precise control of gain modulation characteristics and allows to optimize for shortest pulses or change the time delay between two independent pulses in a laser mode-locked on the second harmonic. In some cases, an external bias is necessary for mode-locking to compensate effects of intrinsic charging of the laser crystal.

#### ACKNOWLEDGMENTS

This work is supported by NSF (ECS-9531933) and AFOSR/BMD (F49620-97-1-0434). Coauthors from IPM thank Russian Foundation for Basic Research (grants 96-02-19275, 96-02-00249 G) for support of this work.

#### REFERENCES

- [1] E. Gornik and A. A. Andronov, Eds., *Opt. Quantum Electron.*, vol. 23, Chapman & Hall, London, 1991, Special Issue FIR Semiconductor Lasers.
- [2] E. Bründermann, A. M. Linhart, L. Reichertz, H. P. Röser, O. D. Dubon, W. L. Hansen, G. Sirmain, and E. E. Haller, "Double acceptor doped Ge: A new medium for intervalence-band lasers," *Appl. Phys. Lett.*, vol. 68, no. 22, pp. 3075-3077, May 1996.
- [3] Erik Bründermann and Hans Peter Röser, "First operation of a far-infrared p-Germanium laser in a standard closed-cycle machine at 15 Kelvin," *Infrared Phys. Technol.*, vol. 38, pp. 201-203, 1997.
- [4] Kijun Park, Robert E. Peale, Henry Weidner, and Jin J. Kim, "Submillimeter p-Ge laser using a Voigt-configured permanent magnet," *IEEE J. Quantum Electron.*, vol. 32, no. 7, pp. 1203-1210, July 1996.
- [5] R. C. Strijbos, J. G. S. Lok, and W. Th. Wenckebach, "A Monte Carlo simulation of mode-locked hot-hole laser operation," *J. Phys. Condens. Matter*, vol. 6, pp. 7461-7468, 1994.
- [6] R. C. Strijbos, J. H. Blok, J. N. Hovenier, R. N. Schouten, W. Th. Wenckebach, A. V. Muravjov, S. G. Pavlov, and V. N. Shastin, "Active mode locking of a p-Ge light-heavy hole band laser by electrically modulating its gain: theory and experiment," In Hess et al. [14], pp. 631-633.
- [7] R. C. Strijbos, A. V. Muravjov, J. H. Blok, J. N. Hovenier, J. G. S. Lok, S. G. Pavlov, R. N. Schouten, V. N. Shastin, and W. Th. Wenckebach, "Electrically controlled gain modulation for active mode locking of far-infrared p-Ge hot hole lasers," in *Conference digest of 15th Int. Semiconductor Laser Conference, Oct. 1996, Haifa, Israel*, 1996, pp. 61-62.
- [8] J. N. Hovenier, A. V. Muravjov, S. G. Pavlov, V. N. Shastin, R. C. Strijbos, and W. Th. Wenckebach, "Active mode locking of a p-Ge hot hole laser," *Appl. Phys. Lett.*, vol. 71, no. 4, pp. 443-445, July 1997.
- [9] J. N. Hovenier, T. O. Klaassen, W. Th. Wenckebach, A. V. Muravjov, S. G. Pavlov, and V. N. Shastin, "Gain of the mode locked p-Ge laser in the low field region," *Appl. Phys. Lett.*, vol. 72, no. 10, pp. 1140-1142, Mar. 1998.
- [10] A. V. Muravjov, R. C. Strijbos, C. J. Fredricksen, H. Weidner, W. Trimble, A. Jamison, S. G. Pavlov, V. N. Shastin, and R. E. Peale, "Mode-locked far-infrared p-Ge laser using an offset rf electric field for gain modulation," in *Proceedings of Workshop on Radiative Processes and Dephasing in Semiconductors, Feb. 1998, Coeur d'Alene, Idaho*, Washington DC, 1998, OSA-TOPS, to be published.
- [11] J. N. Hovenier, A. V. Muravjov, S. G. Pavlov, V. N. Shastin, R. C. Strijbos, and W. Th. Wenckebach, "Active mode locking of a p-Ge hot hole laser," in *Conf. Digest of 22<sup>nd</sup> Int. Conf. on Infrared and MM Waves, July 1997, Wintergreen, Virginia, USA*, Henry P. Freund, Ed., 1997, pp. 217-218.
- [12] R. C. Strijbos, *Hole transport effects in p-Ge lasers*, Ph.D. thesis, Delft University of Technology, 1997.
- [13] R. C. Strijbos, S. I. Schets, and W. Th. Wenckebach, "Appearance of a large 'Hall' current component parallel to B in p-Ge in strong crossed E and B fields," In Hess et al. [14], pp. 469-471.
- [14] Karl Hess, Jean-Pierre Leburton, and Umberto Ravaioli, Eds., *Hot Carriers in Semiconductors*, New York, 1996. Proceedings of HCIS IX, July 31-August 4, 1995, Chicago, Illinois, USA, Plenum Press.

# The *p*-Ge THz laser in low B-field: properties under pulsed and mode locked operation.

J.N. Hovenier, M.C. Diez, T.O. Klaassen, *Member, IEEE*, W.Th. Wenckebach, A.V. Muravjov, S.G. Pavlov and V.N. Shastin.

## Abstract—

A detailed study of the optical output of the *p*-Ge hot hole laser, emitting in the THz range, has been started for (normal) pulsed- as well as for active mode locked operation. Results on wavelength dependent gain and pulse shape for the low magnetic field action range under long pulsed operation are presented. The recently developed technique to achieve active mode locking is described. Results on the shape of the pulses in the small signal gain as well as in the saturated gain regime under mode locked operation are given; FWHM pulse widths of 100 ps have been observed.

**Keywords**—*p*-Ge hot hole laser, THz radiation, mode locking, small signal gain

## I. INTRODUCTION

THE *p*-Ge hot hole laser is as yet the only tunable solid state laser, emitting in the THz range. A well known disadvantage of this source is the need for short pulsed operation, in order to avoid excessive heating of the cryogenically cooled laser crystal [1]. Lately, much effort has been put into the development of techniques to realize *C.W.* operation of this laser, in order to enable the use of this source as local oscillator in THz heterodyne systems [2]. Until now not much work has been performed to employ the possibilities of this laser to create *very short* pulses, that could be of use for time resolved THz experiments.

Some time ago a possible mechanism was discussed to achieve active mode locking of the *p*-Ge laser [3]. Recently we succeeded in the first experimental realization of mode locked operation [4],[5]. Here we present the preliminary results of a more detailed study on wavelength, small signal gain and pulse shape of this pulsed, mode locked, laser. We show that the system is able to produce pulses with a width (FWHM) shorter than 100 ps.

The operation of the *p*-Ge hot hole laser is based on the acceleration of holes in  $\vec{E} \perp \vec{B}$  fields at  $T \leq 20$  K [1]. For the proper ratio of E and B fields,  $E/B \approx 1.3$  kV/cmT, the heavy holes (hh) are accelerated up to high energy, and therefore strongly scattered by optical phonons. A few percent of these hh's are scattered into the light hole band. The light holes do not reach the optical phonon energy, and are thus not scattered, but accumulate on closed trajectories below the optical phonon energy (see fig. 1). The resulting population inversion between the lh-band, which

J.N. Hovenier, M.C. Diez, T.O. Klaassen and W.Th. Wenckebach are with the Department of Applied Physics and DIMES, Delft University of Technology, P.O.Box 5046, 2600 GA Delft, The Netherlands. E-mail (TOK): tjeerd@hfwork1.tn.tudelft.nl

A.V. Muravjov, S.G. Pavlov and V.N. Shastin are with the Institute for Physics of Microstructures, Russian Academy of Sciences, GSP-105, Nizhny Novgorod 603600, Russia.

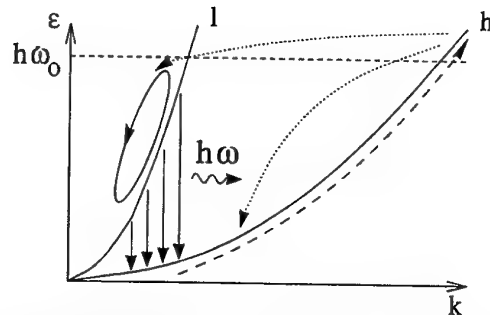


Fig. 1. Mechanism for population inversion : light (l) and heavy (h) hole subbands are shown in an energy-momentum diagram. The pumping cycle is indicated

is split up in discrete Landau levels, and hh-band leads to emission in the (1.5-4.2) THz range. Increase of the amplitude of both E and B field leads to an increase of the laser emission frequency. For proper action,  $\vec{E}$  and  $\vec{B}$  must be accurately perpendicular, as a small component of the electric field  $\parallel \vec{B}$  causes an acceleration of the holes  $\parallel \vec{B}$ , which is not restricted by the action of the Lorentz force. This enables the *light* holes to gain so much energy that they are also scattered by optical phonons, leading to the destruction of the population inversion. Being a disadvantage for normal laser operation, this very effect can be made useful to obtain a modulation of the laser gain. With the application of a periodic electric field  $\parallel \vec{B}$ , the gain reaches a minimum at maximum amplitude of that field, i.e. twice per cycle. By choosing the frequency of such an (rf) field equal to *half* the laser cavity round trip frequency, a modulation of the gain at the round trip frequency is achieved; the essential prerequisite for active mode locking [3].

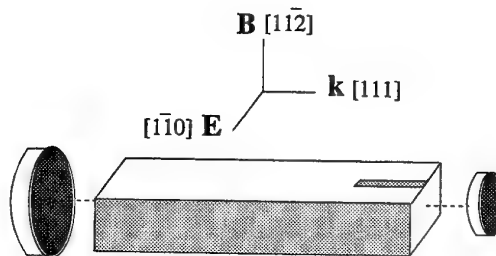


Fig. 2. *p*-Ge laser cavity design

The laser sample used (see fig. 2), the same as in [4], was cut from a single crystal of Ga doped Ge, with  $N_{Ga} = 7.10^{13} \text{ cm}^{-3}$ , in the form of a rectangular parallelepiped of  $5 \times 7 \times 49.46 \text{ mm}$ . The high voltage electric excitation field ( $\vec{E} \parallel [1\bar{1}0]$ ) is applied in pulses of a few  $\mu\text{s}$  long to ohmic contacts covering two opposite lateral surfaces of the sample. The magnetic field ( $\vec{B} \parallel [1\bar{1}2]$ ) is applied perpendicular to the long axis and to  $\vec{E}$  (Voigt configuration). The rf electric field  $\parallel \vec{B}$  for gain modulation is applied in short pulses too, synchronized with the laser excitation, to additional ohmic contacts of  $1 \times 10 \text{ mm}^2$  on the lateral sides of the sample. The frequency is chosen to be 386.1 MHz, equal to half the round trip frequency of 772.2 MHz of the laser cavity. Two gold mirrors, evaporated on quartz substrates and isolated by  $10 \mu\text{m}$  Teflon films are attached to the ends of the sample. The entire system is immersed in liquid helium. At the side of the smaller, 4 mm diameter, mirror, laser radiation is coupled out and detected with fast room temperature GaAs Schottky diode detectors (Faro Technology). The signal is displayed using either a 0.5 GHz bandwidth, 2 GS/s, or a 1 GHz bandwidth, 5 GS/s, oscilloscope to monitor the overall pulse envelope. For a detailed study of the waveform of individual pulses, a 6 GHz bandwidth real time oscilloscope was used. The overall response time of the electronic system was determined to be 100 ps. The laser pulses have also been monitored using a Bismuth micro-bolometer fed by a planar log-periodic antenna on a Si substrate.

## II. PULSED OPERATION

The absence of frequency selective elements in the present cavity, together with the inherently broad band nature of the lh- to hh- hole transition, causes laser action to occur simultaneously at a large number of longitudinal modes. Using a simple blazed reflection grating in combination with a Schottky diode detector, the time- and wavelength resolved optical output of the laser has been studied.

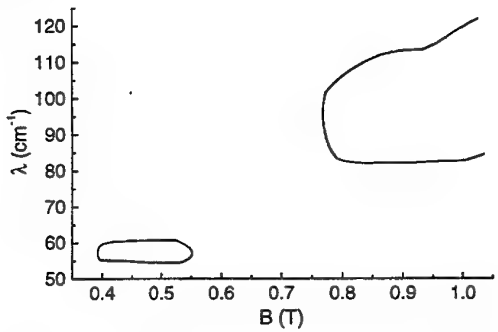


Fig. 3. Frequency band as a function of applied B-field

In fig. 3 the observed frequency band as a function of the applied B-field is shown for normal long-pulsed operation. By increasing the E-field at constant B-field, the intensity of the high energy side of the emission band increases with respect to that of the low energy side. A similar result

has been reported in [6], and was ascribed to the increase of the intensity of spin-flip transitions towards larger E/B ratio. In the low field range and in the lower part of the high field range the radiation is polarized parallel to the magnetic field. For  $B \geq 0.8 \text{ T}$  also a small component  $\parallel \vec{E}$  appears, that increases towards larger E and B fields. In fig. 4 the time dependence of the optical pulse for  $B = 0.5 \text{ T}$  at three different wavelengths is shown, together with the pulse shape of the total optical output, measured using a mirror instead of a grating as reflecting element. The zero of the time scale coincides with the start of the E-field excitation pulse. Simultaneous emission in a broad band occurs, but laser action starts at the short wavelength (high energy) part of the spectrum, and shifts towards longer wavelengths during the optical pulse. Similar effects are observed in the shorter wavelength emission region for  $B \geq 0.75 \text{ T}$  too. The nature of the pulse to pulse intensity variations for the different wavelength regions indicate that this behaviour is not due to the type of optical pumping effects proposed in [7]. These results on the wavelength dependency of the laser action seem to contradict the supposed homogeneous character of the inter valence band transition [8].

From the growth of intensity in the early part of these

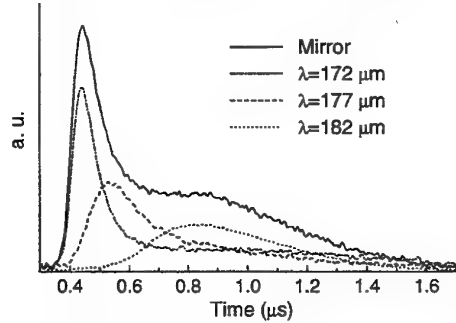


Fig. 4. Time resolved optical output for different wavelengths at  $B=0.5 \text{ T}$

pulses, the wavelength dependent small signal gain  $g(\lambda)$  has been determined to be  $g_{(172)}=0.015 \text{ cm}^{-1}$ ,  $g_{(177)}=0.0026 \text{ cm}^{-1}$  and  $g_{(182)}=0.0021 \text{ cm}^{-1}$ . It must be noted that these values represent the *effective* gain, i.e. the actual (bare) gain reduced by, among others, reflection and outcouple losses. As these losses may well be in the order of  $0.01 \text{ cm}^{-1}$ , the wavelength dependence of the *bare* small signal gain may be not as strong as the above presented values suggest.

We have tested intermediate speed room temperature microbolometers for the detection of these THz pulses, in order to study the possibility to employ these detectors in arrays for simultaneous time- and wavelength resolved experiments. The optical pulse (at  $B = 0.5 \text{ T}$ ) was detected with a  $2 \times 2 \mu\text{m}^2$ , 100 nm thick, Bismuth micro-bolometer in the apex of a planar log periodic antenna fabricated on a 475 nm thick  $\text{SiO}_2$  isolation layer on a Si substrate. Because the light was focussed on the antenna simply using

an  $f/0.6$  lens, instead of a Si hyperhemispherical lens on the substrate, only a small coupling efficiency was realized. Nevertheless, as can be seen in fig. 5, a good signal was obtained, with an estimated thermal relaxation time for the bolometer of 100 ns. This proves the potential applicability of such detectors in intermediate speed pulsed THz experiments.

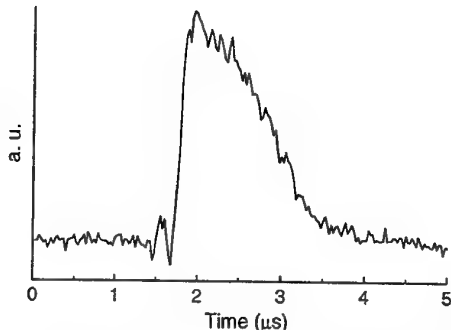


Fig. 5. Antenna-bolometer signal of laser pulse at  $B=0.5$  T

### III. MODE LOCKED OPERATION

With the rf modulation field applied, active mode locking of the laser is achieved [4], [5]. Both in the low and in the high  $B$ -field region the wavelength ranges are slightly smaller and the time delays slightly larger than observed for pulsed operation. This is possibly related to the disturbing effect the rf modulation field has on the start of laser action. We observed that a short rf burst applied *before* the start of the HV excitation, causes an additional delay of normal pulsed laser action. The magnitude of this delay depends on the intensity and duration of the rf burst and on the time interval between the end of the burst and the start of the HV excitation pulse. A simple order of magnitude estimate shows that the observed delay is much too large as to be only the result of local heating effects of the crystal near the rf electrodes. We also found that the precise starting time of the rf pulse appears to be of great importance to obtain optimum mode locked laser action. The origin of these effects is not clear at the moment; possibly, the impact ionization induced by the rf field creates an rf current path that counteracts the later formation of a homogeneous HV current needed to obtain a proper population inversion.

In figs. 6 and 7 the typical time dependent optical output under mode locked conditions, at  $B = 0.5$  T and  $\lambda \approx 172$   $\mu\text{m}$ , is shown. In the early stage of laser action (fig. 6), a regular train of pulses with a 1.3 ns separation, the cavity round trip time, is observed. The increase of intensity of successive pulses reflects the small signal gain of the optical pulse in the cavity per round trip. Also a decrease of pulse width, typical for the build up period of mode locked operation, is observed. The small signal gain is found to be slightly larger than for normal pulsed operation. Because the rf field causes a considerable loss of gain in that part of the crystal which is situated in between the modulation electrodes, clearly the optical pulse must experience a sub-

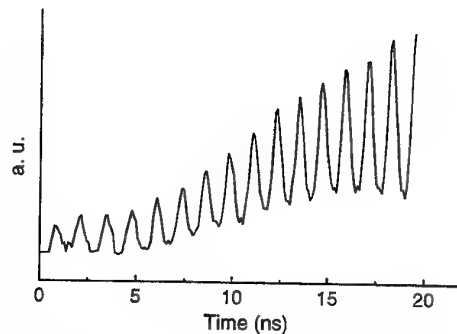


Fig. 6. Single shot laser output in small signal gain region, showing the increase of intensity and decrease of width of the pulse after each successive round trip.

stantial larger gain in the unmodulated part of the crystal than the quasi CW small signal gain discussed before. This suggests that the lifetime of the induced population inversion in that part of the crystal is a non-negligible fraction of the 1.3 ns cavity round trip time.

Under saturated gain conditions, a train of constant amplitude, narrow pulses is observed (see fig. 7). The minimum width of these pulses is found to be about 100 ps FWHM. The electronic risetime of the detection system has been determined to be about 100 ps. It is therefore conceivable that the actual minimum width of the optical pulses may even be shorter. To observe these short pulses properly, also the design of the detector unit becomes very important. The wiggles, visible in fig. 8, are the result of internal reflections in the detector unit, due to a slight impedance mismatch.

Because of the variation of emission wavelengths during the laser action, stationary mode locking at 172  $\mu\text{m}$  is only of short duration: near the end of the emission the pulse train therefore shows irregular behaviour.

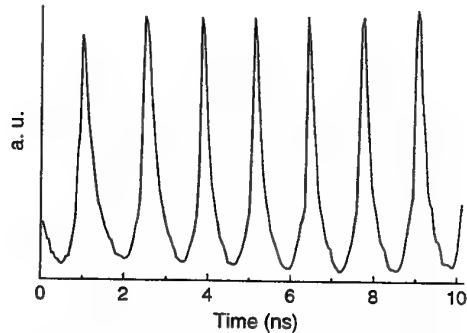


Fig. 7. Pulse train in saturated gain region

Similar as for long pulsed operation, also under active gain modulation, the laser action in the 177-182  $\mu\text{m}$  region is delayed with respect to that in the 172  $\mu\text{m}$  region. The much smaller gain at these wavelengths is probably lowered even more by the disturbing effect of the rf modulation field. No genuine mode locking is observed here, only a low intensity amplitude modulated output is seen, with-

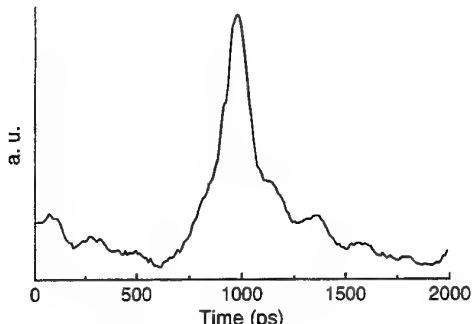


Fig. 8. Shape of micropulse in saturated gain region; the "wiggles" in the tail of the pulse are due to a slight impedance mismatch of the detector.

out the clear mode locking characteristics found at  $172\text{ }\mu\text{m}$ . As the rf modulation apparently diminishes the laser action in the long wavelength region, proper mode locked action at  $172\text{ }\mu\text{m}$  is sustained longer than could be expected from the time resolved experiments under long pulsed operation.

#### IV. ACKNOWLEDGMENT

This work is part of the research program of the European TMR network on THz electronics "INTERACT". The authors thank M.J.W. Vermeulen from the Delft Inter-faculty Reactor Institute for the use of the 6 GHz scope and help with the data acquisition.

#### REFERENCES

- [1] E. Gornik and A. A. Andronov, Eds., *Opt. Quantum Electron.*, vol. 23, Chapman and Hall, London, 1991, Special Issue on Far-infrared Semiconductor Lasers.
- [2] E. Bründermann, A.M. Linhart, H.P. Röser, O.D. Dubon, W.L. Hansen, E.E. Haller, "Miniaturization of p-Ge lasers: Progress toward continuous wave operation", *Appl. Phys. Lett.* vol. 68, pp. 1359- 1361, 1996.
- [3] R.C. Strijbos, J.G.S. Lok, and W.Th. Wenckebach, "A Monte Carlo simulation of mode-locked hot-hole laser operation," *J. Phys. Condens. Matter*, vol. 6, pp. 7461- 7468, 1994.
- [4] J.N. Hovenier, A.V. Murav'ev, S.G. Pavlov, V.N. Shastin, R.C. Strijbos, W.Th. Wenckebach, "Active mode locking of a p-Ge hot hole laser", *Appl. Phys. Lett.* vol. 71, pp. 443-445, 1997.
- [5] J.N. Hovenier, T.O. Klaassen, W.Th. Wenckebach, A.V. Murav'ev, S.G. Pavlov, V.N. Shastin, "Gain of the mode locked p-Ge laser in the low field region", *Appl. Phys. Lett.* vol. 72, pp. 1140-1142, 1998.
- [6] L.A. Reichertz, O.D. Dubon, G. Sirmain, E. Bründermann, W.L. Hansen, D.R. Chamberlain, A.M. Linhart, H.P. Röser, E.E. Haller, "Stimulated far-infrared emission from combined cyclotron resonances in germanium", *Phys. Rev. vol. B* 56, pp. 12069-12072, 1997.
- [7] S.V. Demikhovsky, A.V. Murav'ev, S.G. Pavlov and V.N. Shastin "Stimulated emission using the transitions of shallow acceptor states in germanium", *Semicond. Sci. Technol.* vol. 7, pp. B622-B625, 1992.
- [8] F. Keilmann and R. Till, "Nonlinear far-infrared response of passive and active hole systems in p- Ge," *Semicond. Sci. Technol.*, vol. 7, pp. B633-B635, 1992.



**J. Niels Hovenier** was born in the "Broadcast City" Hilversum, The Netherlands. In 1977 he received a degree in advanced electronic engineering. From 1979 to 1990 he was electronic engineer in the NMR research group at the Physics Department of the University of Leiden. Since 1991 he is opto-electronic engineer at the Physics Department of Delft University of Technology (semiconductors physics group). He was originally involved in far infrared short pulse/high power pilot studies on semiconductor using the Dutch Free Electron Laser FELIX. His present research activities are in mode- locked p-Ge THz lasers and detection of short (ps) THz pulses.



**Tjeerd O. Klaassen** received M.Sc. and Ph.D. degrees in physics, respectively in 1967 and 1973, from the University of Leiden, the Netherlands. As staff member of the Physics Department (Leiden) he was involved in the study of low dimensional magnetic systems using magnetic resonance and relaxation techniques. In 1985 he started in the field of far infrared spectroscopy on impurities in semiconductors. Since 1990 he is with the Department of Applied Physics at Delft University of Technology, involved in (non-) linear far infrared spectroscopy in semiconductors and the development of active (p-Ge laser) and passive (antenna's, transmission lines) components for THz electronics.



**W. Tom Wenckebach**



**Andrej V. Murav'ev**, photograph and biography not available at the time of publication.

**Sergey G. Pavlov**, photograph and biography not available at the time of publication.

# Spatio-temporal Imaging of THz Pulses

Zhiping Jiang, F. G. Sun, and X.-C. Zhang, *Senior Member, IEEE*

**Abstract**— We report the use of an optoelectronic system for the measurement of THz pulses by use of chirped pulse technology. This novel system measures the spatio-temporal distribution of a free-space pulsed radiation with an unprecedented data acquisition rate. Using a linearly-chirped optical probe pulse in free-space for electro-optic measurements, a temporal waveform of a co-propagating terahertz (THz) field is linearly encoded onto the frequency spectrum of the optical probe pulse, and then decoded by dispersing the probe beam from a grating to a detector array. Acquisition of picosecond THz field pulses without using mechanical time-delay devices have been achieved. A single-shot electro-optic measurement of the temporal waveform of a THz pulse has been demonstrated. Unparalleled by other THz sampling techniques, this single-shot method provides what is believed to be the highest possible data-acquisition rate.

**Index terms**— Chirped-pulse technology, Pulsed radiation, THz electro-optic, THz imaging

## I. GENERATION AND DETECTION OF THZ BEAMS

Electro-optic sampling is a powerful technique for the characterization of an electrical waveform such as an electrical signal in an integrated circuit<sup>1,2</sup> or a terahertz (THz) beam in a free-space environment.<sup>3-5</sup> Conventional time domain electro-optic sampling is based on the repetitive property of the signal to be tested. A sequential plot of the signal versus the time delay reassembles the temporal waveform. If the signal to be measured is from a single-event experiment, such as an explosion or breakdown, this technique is clearly not suitable. However, the modulation of the optical probe pulse in this electro-optic sampling technique may provide the means to overcome this shortfall. The temporal modulation can be converted to the wavelength domain by use of free-space wavelength-division multiplexing and demultiplexing. With the introduction of a linearly chirped optical probe beam in the electro-optic sampling experiment,<sup>6,7</sup> it is finally possible to measure a THz pulse with an unprecedented data-acquisition rate, even with single-shot temporal measurement capability.<sup>8-10</sup>

Conventional time-domain optical measurements, such as THz time-domain spectroscopy in pump / probe geometry, use a mechanical translation stage to vary the optical path

between the pump and the probe pulses.<sup>11-14</sup> The intensity or polarization of the optical probe beam, which carries information generated by the pump beam, is repetitively recorded for each sequential time delay. In general, this data acquisition for the temporal scanning measurement is a serial acquisition; the signal is recorded during the probe / pulse sampling through a very small part of the THz waveform (roughly the pulse duration of the optical probe beam). Therefore, the data acquisition rate in this single channel detection is limited to less than 100 Hz for a temporal scan on the order of tens of picoseconds. Clearly, this relatively slow acquisition rate can not meet the requirement for real-time measurements, such as time-domain THz spectroscopy of fast-moving objects or flame analysis. To increase the acquisition rate, parallel data acquisition or multichannel detection is required. One possible method is to extend the novel design from “real time picosecond optical oscilloscopes” for the local-field characterization, to freely propagating THz field applications.<sup>6</sup>

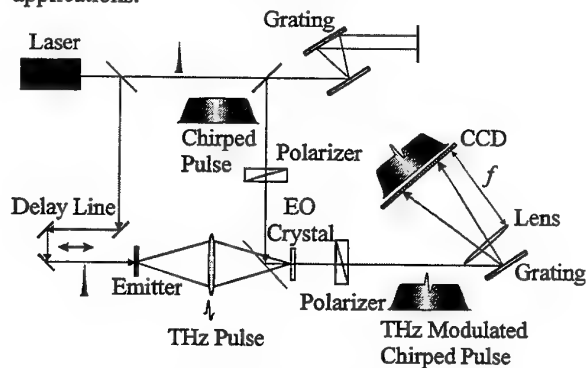


**Fig. 1.** Schematic of experimental setup of electro-optic measurement with a chirped optical probe beam.

Figure 1 schematically illustrates electro-optic sampling with a chirped optical probe beam. A femtosecond laser beam is split into pump and probe beams. The geometry is similar to the conventional free-space electro-optic sampling setup, except for the use of a grating pair for chirping and stretching the optical probe beam, and a grating-lens combination with a detector array for the measurement of the spectral distribution. Due to the negative chirp of the grating (pulse with decreasing frequency versus time), the blue component of the pulse leads the red component. The fixed delay-line is only used for the positioning of the THz pulse, within the duration of

the synchronized probe pulse, (acquisition window) and for temporal calibration.

The pump beam is used to generate a THz beam from an emitter, then focused onto the electro-optic sensor via a polylens. The probe beam is frequency chirped and temporally stretched by a grating pair. When the chirped probe beam and a THz pulse co-propagate in the electro-optic crystal, different portions of the THz pulse, through the Pockels effect, modulate the different wavelength components of the chirped pulse. Therefore, the THz waveform is encoded onto the wavelength spectrum of the probe beam. A spectrometer and a detector array (LDA or CCD) are used to measure the spectral distribution. Figure 2 shows the spectral distributions of the chirped probe pulse measured by the linear diode array (LDA), and the differential spectrum distribution ( $\Delta I$ ). The temporal THz signal can be extracted by measuring the difference between the spectral distributions of the probe pulse with and without THz pulse modulation. This differential distribution reconstructs both the amplitude and phase of the temporal waveform of the THz pulse. The differential spectrum ( $\Delta I$ ) in Fig. 2 shifts horizontally by adjusting the fixed delay line. Moving the fixed delay line is equivalent to placing the terahertz field in a different portion of the probe beam spectrum and it can be used as a marker to calibrate the time scale.

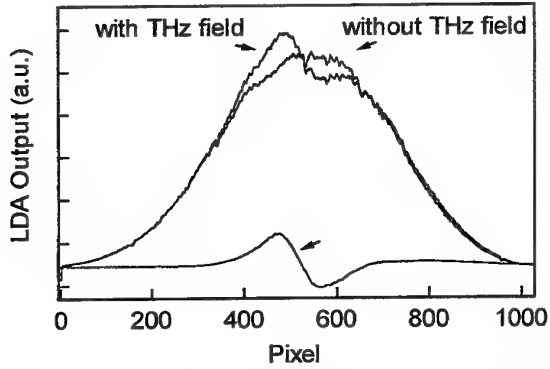


Fig. 2. Spectral distribution of the chirped probe pulse with & without a co-propagating THz field pulse.

Figure 3 shows the normalized differential spectrum distribution ( $\Delta I/I$ ) when adjusting the fixed time delay line at a step of 1.3 ps. The offset of the spectrum is shifted for better display. The noise at the edge pixels comes from the spectrum normalization with a small background. These waveforms shift linearly with the fixed time delay step. The total spectral window (1024 pixels) is equivalent to 44 ps, corresponding to 43 fs/pixel.

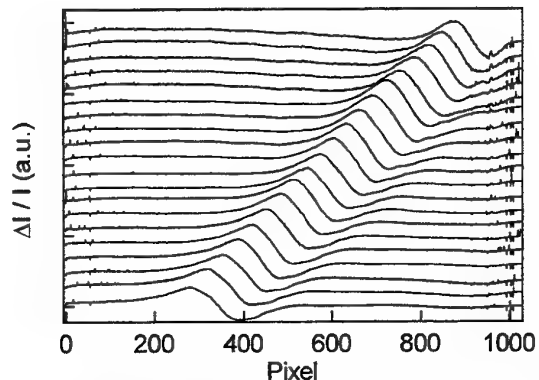


Fig. 3. Normalized differential spectral distribution ( $\Delta I/I$ ) by adjusting the fixed delay line at a step of 1.3 ps.

The electro-optic measurement with a chirped optical probe pulse is capable of a single-shot measurement of a full THz waveform. In this measurement, the repetition rate of the amplified laser was reduced to 10 kHz first, and then it was further reduced to 100 Hz by using an additional optical shutter. A CCD camera (Princeton Instruments, Inc., CCD-1242E) was used to replace the linear diode array. The CCD camera has 1152x1242 pixels and a full well capacity greater than 500,000 electrons. The exposure time of the camera was 10 ms. One shot measurement accepted only one optical probe pulse. We took a single-shot spectrum without the THz field first and saved it as the background, then we took a single-shot spectrum with the THz field and performed a subtraction of the background.

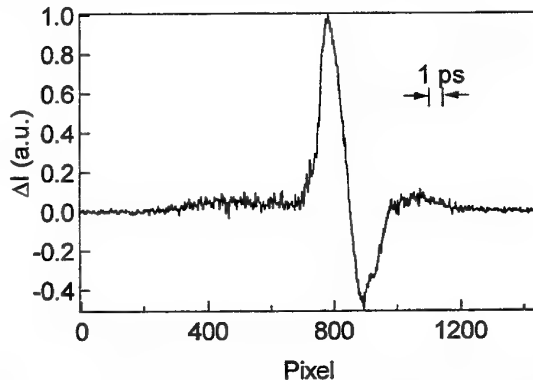


Fig. 4. A single-shot spectral waveform of a THz pulse measured by a chirped optical probe pulse. It reconstructs the temporal waveform of the THz pulse.

Figure 4 plots a single-shot differential spectral distribution waveform of a THz pulse. The single-to-noise ratio (SNR) is better than 60:1. This SNR can be greatly improved by subtracting the S and P components of the single-shot spectrum to reduce the noise, as it is commonly used in the standard differential electro-optic measurements. We expect applications in the measurement of a single event, such as an explosion or breakdown of the electrical field, in dielectrics.

## II. IMAGING OF THZ PULSES

The high data acquisition rate in the chirped pulse measurement makes real-time 1D temporal THz imaging feasible. Here we used a CCD to replace a linear diode array for 1D spatio-temporal imaging. Figures 5 and 6 show the distribution images of THz fields (x position versus time) emitted from dipole and quadrupole emitters, respectively. The measured spatial resolution in the imaging system is better than 1 mm, which is close to diffraction limited resolution in other unchirped THz techniques.

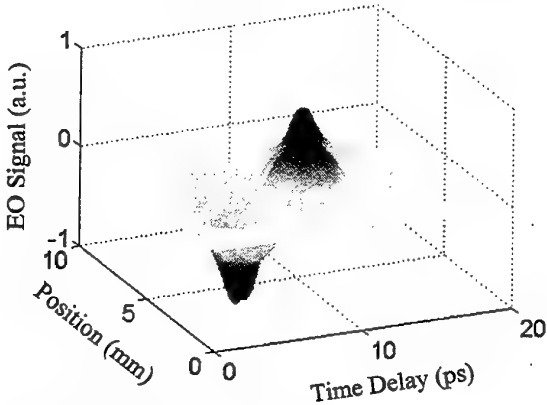


Fig. 5. 1-D THz imaging of a dipole.

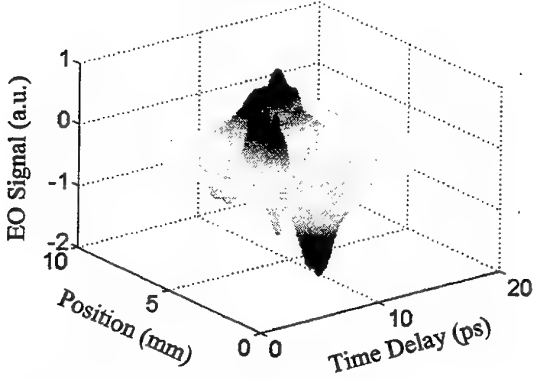


Fig. 6. 1-D THz imaging of a quadrupole.

Figure 6 is a plot of a *single-shot* image from a GaAs photoconductive dipole antenna. This plot contains original data without the signal average and smoothing. The total time for wavelength division multiplexing and demultiplexing is within a few picoseconds. The dipole length is 7 mm, and the bias voltage is 5kV. One-dimensional spatial distribution across the dipole and its temporal THz waveform are obtained simultaneously in a single laser pulse. The size of the spatio-temporal image is 10 mm by 25 ps. In this single-shot measurement the background light per pixel on the CCD camera is  $\sim 200$  counts, whereas that of the modulated probe pulse is  $\sim 50$ . Typical oscillation features and the symmetric spatial distribution of the far-field pattern from a dipole photoconductive emitter are obtained.

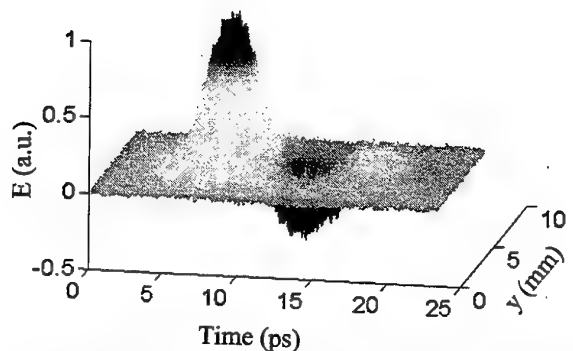


Fig. 7. Single-shot 1-D THz imaging of a dipole field without any signal average. The y-axis corresponds to the spatial position across the dipole emitter.

Figure 8 shows a spatio-temporal image of the THz field from a quadrupole antenna. The size of the spatio-temporal image is 10 mm by 40 ps. The quadrupole has three parallel electrodes separated by 3 mm. The center electrode was biased and the two adjacent electrodes were grounded. The field pattern from two back-to-back dipoles shows opposite polarity depending on the spatial position (y axis). Temporal oscillation from each dipole can be resolved individually. The layered structure in the y-axis direction is due to the optical inhomogeneity of the sensor crystal. A defect point in the ZnTe crystal causes an offset in the field strength of the temporal waveform (E axis in the figure). A high-quality ZnTe crystal with good spatial homogeneity will provide better spatial resolution.

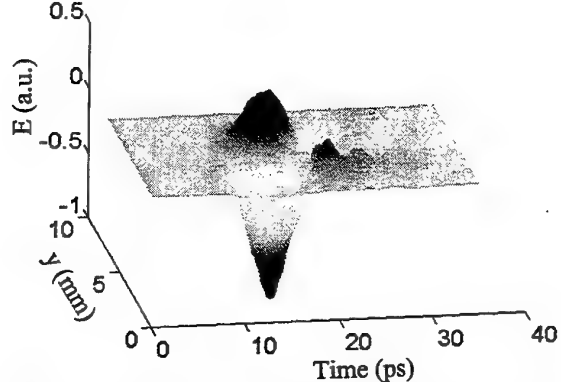


Fig. 8. 1-D THz imaging of a quadrupole field. The y-axis corresponds to the spatial position across the quadrupole emitter.

A CCD camera measures three parameters: x and y positions and amplitude. The chirped-pulse setup applies these three parameters to the measurement of wavelength, spatial position, and amplitude. Since the x position is used for wavelength measurement, the current detection system provides only a 1-D spatial measurement in the y direction. Two dimensional x-y spatial measurements would require four parameters: wavelength, dimensions x and y, and

amplitude. It is possible to construct a single-shot x-y THz field imaging system with a dimension-reduction design.

### III. TEMPORAL RESOLUTION

The advantage of using a chirped optical pulse in electro-optic detection is its superior data-acquisition speed. In a single-shot measurement this speed approaches the fundamental limit. However, the trade-off can be understood from the uncertainty principle. Since the THz pulse within the duration of the synchronized probe-pulse window (acquisition window) modulates only a portion of the probe-pulse spectrum, the limited frequency bandwidth in the modulated spectrum cannot support the required temporal resolution. If the laser pulse is diffraction limited with a simple Gaussian profile of the spectrum, then the limit of the temporal resolution ( $T_{\text{limit}}$ ) in this imaging system is equal to the square root of the product of the original probe-pulse duration ( $T_0$ ) and the chirped-pulse duration ( $T_c$ ):<sup>9</sup>

$$T_{\text{limit}} = \sqrt{T_0 T_c}$$

The existence of the optimal spectral resolution for the spectrometer is well understood according to the time-frequency duality.

The smaller the  $T_c$ , the higher the temporal resolution will be. However,  $T_c$  must be long enough to cover the entire THz waveform. A good compromise might be to allow the  $T_c$  to be twice as large as the THz signal duration. For example, assuming original pulse duration of 100 fs and chirped-pulse duration of 90 ps, the estimated limit of the temporal resolution is 3 ps. In principle, a wider bandwidth can support shorter pulse duration. A white-continuum probe pulse with a higher chirped rate (nanometers per picosecond) should provide better temporal resolution.

### IV. ACKNOWLEDGEMENT

This work was supported by the U.S. Army Research Office and the U.S. National Science Foundation.

### V. REFERENCE

1. B.H. Kolner and D.M. Bloom, *IEEE J. Quantum Electron.*, QE-22, 69 (1986).
2. J.A. Valdmanis and G.A. Mourou, *IEEE J. Quantum Electron.*, QE-22, 79 (1986).
3. Q. Wu and X.-C. Zhang, *Appl. Phys. Lett.*, **67**, 2523 (1995).
4. A. Nahata, D.H. Auston, T.F. Heinz, and C.J. Wu, *Appl. Phys. Lett.*, **68**, 150 (1996).
5. P. U. Jepsen, C. Winnewisser, M. Schall, V. Schyja, S. R. Keiding and H. Helm, *Phys. Rev. E*, **53**, R3052 (1996).
6. J. A. Valdmanis, *Proceeding of Ultrafast Phenomena V*, Springer-Verlag, **82** (1986); *Solid State Technology / Test & Measurement World*, Nov. S40, (1986).
7. Galvanauskas, J.A. Tellefsen, Jr., A. Krotkus, M. Oberg, and B. Broberg, *Appl. Phys. Lett.*, **60**, 145 (1992).
8. Zhiping Jiang and X.-C. Zhang, *Appl. Phys. Lett.*, **72**, 1945 (1998).
9. P.Y. Han, Zhiping Jiang, J.A. Riordan, L. Wang, and X.-C. Zhang, *Proceedings of SPIE*, **3277**, 198 (1998).
10. Zhiping Jiang and X.-C. Zhang, *Opt. Lett.*, **23**, 1114, (1998).
11. For example, see *Ultrashort Laser Pulses and Applications*, Topics in Applied Physics, Springer-Verlag **60**, (1988).
12. P.R. Smith, D.H. Auston, M.C. Nuss, *IEEE J. Quant. Elec.*, **24**, 255 (1988).
13. Ch. Fattiger and D. Grischkowsky, *Appl. Phys. Lett.* **54**, 490 (1989).
14. Q. Wu and X.-C. Zhang, *Appl. Phys. Lett.* **70**, 1784 (1997); **71**, 1285 (1997).

# Tunable THz-wave generation from $\text{LiNbO}_3$ / $\text{MgO}:\text{LiNbO}_3$ optical parametric oscillators

Jun-ichi Shikata, Kodo Kawase, Ken-ichi Karino, and Hiromasa Ito

**Abstract**—Widely tunable coherent terahertz (THz) wave generation from has been successfully demonstrated based on the laser light scattering from the lowest  $A_1$ -symmetry polariton mode of  $\text{LiNbO}_3$ . This method exhibits multiple advantages like wide tunability, coherency, compactness of its system. In this paper, we describe the general performances of this optical parametric oscillator and its application, including the recent study using  $\text{MgO}$  doped  $\text{LiNbO}_3$ .

**Index Terms**—terahertz, tunable, parametric, nonlinear,  $\text{MgO}$  doped  $\text{LiNbO}_3$ , spectroscopy

## I. INTRODUCTION

During the past several years, THz-wave generation and detection have attracted much attention from both fundamental and applied points of view. Most studies have utilized ultrabroad bandwidth characteristics of the mode-locked subpicosecond laser pulses with the sacrifice of the temporal coherence [1,2]. In contrast, we have recently demonstrated a room temperature operated coherent tunable THz-wave generation (frequency: 0.9-2.1 THz, wavelength: 140-310 $\mu\text{m}$ ) from a  $\text{LiNbO}_3$  optical parametric oscillator (OPO) by introducing a novel output coupling method for the THz wave into the system to drastically improve the efficiency [3-6]. In this paper, we describe the characteristics of this THz-wave generator and its application, including the recent studies of the performances using  $\text{MgO}:\text{LiNbO}_3$ .

## II. PRINCIPLE OF OPERATION

This scheme is based on an optical parametric oscillation (OPO) utilizing the infrared and Raman active material, such as  $\text{LiNbO}_3$ ,  $\text{LiTaO}_3$  and so forth. The process involved is the stimulated scattering from the lowest  $A_1$ -symmetry polariton mode [7]. The polariton behaves like a photon in the frequency region far from the resonance, so that a photon at THz frequency ( $\omega_T$ ) and near infrared photon ( $\omega_i$ ) are created parametrically from the input photon ( $\omega_p$ ) according to the energy conservation of  $\omega_p = \omega_T + \omega_i$ , where indices  $p, i, T$  denote pump, idler, THz wave, respectively.

In the scattering process, the momenta of these photons are also conserved (non-collinear phase matching condition) according to  $\mathbf{k}_p = \mathbf{k}_i + \mathbf{k}_T$  (see the inset of Fig.1), which determines the angle-tuning characteristics of the OPO. Continuous and wide tunability is easily obtained by slightly varying the angle between near-infrared pump and idler wavevectors.

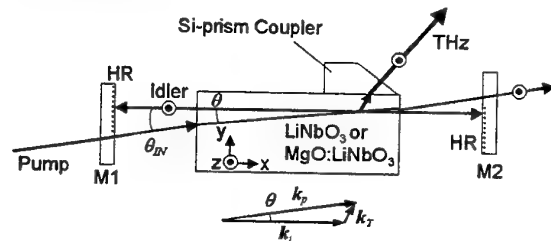


Fig. 1. Experimental cavity arrangement for the THz-wave generation using Si-prism coupler.

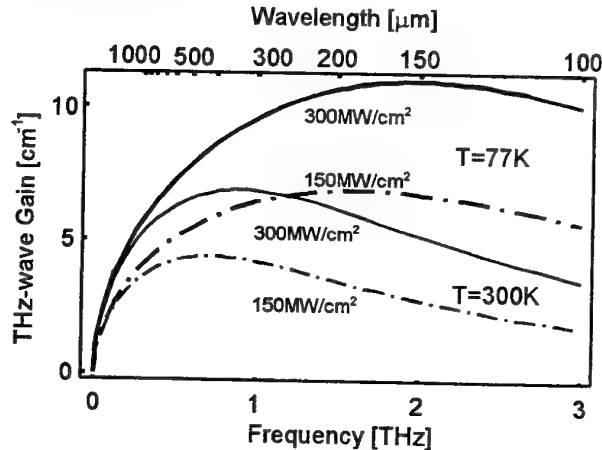


Fig. 2. Calculated parametric gain coefficient for the optical parametric THz-wave generation using  $\text{LiNbO}_3$  crystal pumped at 1.064 $\mu\text{m}$ .

The parametric gain coefficients are derived by considering both parametric and Raman scattering processes. According to the plane wave approach, the expressions are given by [7,8],

$$g_T = g_i \cos \phi = \frac{\alpha_T}{2} \left[ \sqrt{1 + 16 \cos \phi \left( \frac{g_0}{\alpha_T} \right)^2} - 1 \right]$$

J. Shikata, K. Karino, and Hiromasa Ito are with the Research Institute of Electrical Communication, Tohoku University, Sendai 980-8577, Japan.

K. Kawase is with the Department of Applied Physics, Tohoku Gakuin University, Tagajo 985-8537, Japan.

where  $\phi$  denotes the phase-matching angle between the pump and THz wavevectors,  $g_0$  is the parametric gain in the low-loss limit, and  $\alpha_T$  is an absorption coefficient at THz frequency. The calculated results for  $\text{LiNbO}_3$  shown in Fig.2 indicate the order of several  $\text{cm}^{-1}$ 's gain is feasible around the wavelength of 200-300  $\mu\text{m}$ , and cryogenic cooling is effective for highly efficient THz-wave generation due to the reduction of absorption coefficient  $\alpha_T$  [9].

### III. EXPERIMENTS

A schematic diagram of the experimental setup is shown in Fig.1. The pump source was a Q-switched Nd:YAG laser (wavelength: 1.064  $\mu\text{m}$ , pulse width: 30ns) whose polarization was along the z-axis. Mirrors M1, M2 were high-reflection (HR) coated in the half area, and they form an external resonator for the near-infrared idler wave. A 5mm-thick  $\text{LiNbO}_3$  z-plate was cut 70mm long along x-axis. Two end-surfaces in the x-plane were cut parallel, polished and anti-reflection (AR) coated for operation at 1.07  $\mu\text{m}$ . High-resistivity Si ( $\rho > 1000 \Omega \text{ cm}$ ,  $\alpha \approx 0.6 \text{ cm}^{-1}$ ) was chosen for fabricating the prism, and the prism was pressed with the adjustable spring against the y-surface of  $\text{LiNbO}_3$  in order to maximize the coupling efficiency of the THz wave. The whole system including the pump source was constructed in the table-top size. The THz-wave output was detected by a 4K-Si bolometer and its spectrum was measured by a scanning Fabry-Perot etalon consisting of metallic mesh plates.

By varying the incident angle  $\theta_{\text{IN}}$  of pump beam from 1 to 2 deg., the angle  $\theta$  of between the pump and idler inside the crystal was changed from approximately 0.5 to 1 deg. as shown in Fig.3. As the phase matching angle was tuned, the idler and the THz wavelengths varied from 1.068-1.072

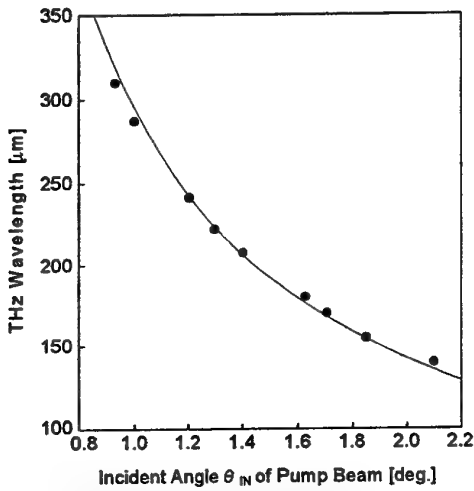


Fig. 3. Tuning characteristics of the THz wave using  $\text{LiNbO}_3$  crystal. The solid curve indicates the calculated tuning curve.

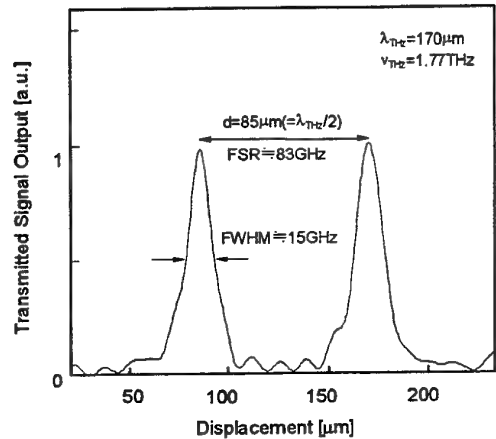


Fig. 4. Spectral measurement of the THz wave using the scanning Fabry-Perot etalon consisting of metallic mesh plates.

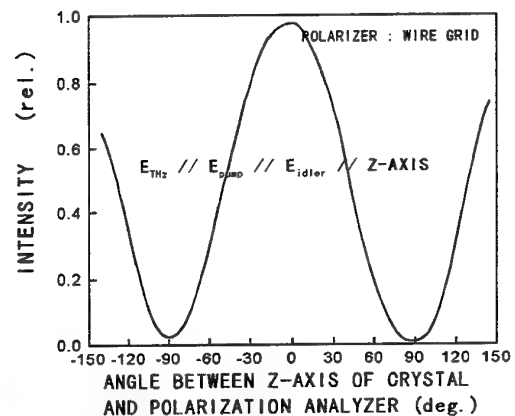


Fig. 5. Measured polarization of the generated THz-wave using a wire grid polarizer.

$\mu\text{m}$  and 290-150  $\mu\text{m}$ , respectively. Due to the ultra low dispersion characteristics of Si at the THz range, as the relation between the refraction interface and phase-matching relation, the radiation angle inside the prism is practically almost constant ( $\sim 0.5$  deg. change for 150-300  $\mu\text{m}$ ), so that the direction of the THz is almost fixed for entire tuning [4]. Fig.4 shows an example of the spectral measurement of THz wave. The displacement of one of the metallic mesh plates corresponds directly to a half of the wavelength. The free spectral range (FSR) of the etalon was about 83GHz, and the linewidth was measured to be  $\leq 15\text{GHz}$ . It is expected that the linewidth will be dramatically narrowed by introducing the quasi-phase-matching method using a domain inverted structure [10] as well as an injection seeding method. The signal output from the Si prism coupler was measured to be more than 10mW and 10 ns (0.1nJ/pulse) with a pump power of 30mJ/pulse. Fig.5 shows the polarization characteristics analyzed by a wire grid polarizer, and it can be seen that the THz-wave was linearly polarized along the z-axis. The observed THz-wave beam had an approximately Gaussian

cross section with  $e^2$  power radius of 5 mm at the distance of 50cm away from the prism.

We have also studied the other nonlinear material which is identified to have much larger photorefractive resistance than that of an undoped  $\text{LiNbO}_3$ , such as  $\text{LiTaO}_3$  or  $\text{MgO:LiNbO}_3$ . Fig.6 shows the dispersion relation of the lowest  $A_1$ -symmetry polariton mode of undoped and 5mol%  $\text{MgO}$  doped  $\text{LiNbO}_3$ , measured by a single-pass Raman scattering experiment. The result shows that there were no significant difference in the angle-tuning characteristics between  $\text{LiNbO}_3$  and  $\text{MgO:LiNbO}_3$  crystals. However, much better performances in the parametric conversion were observed in the  $\text{MgO}$  doped sample. Fig.7 shows the measured output characteristics of the idler wave using  $\text{LiNbO}_3$  or  $\text{MgO:LiNbO}_3$  OPO at a fixed pump energy (38mJ). The latter spectrum exhibits higher conversion efficiency and broader tuning range, and further studies for the mechanism are now in progress.

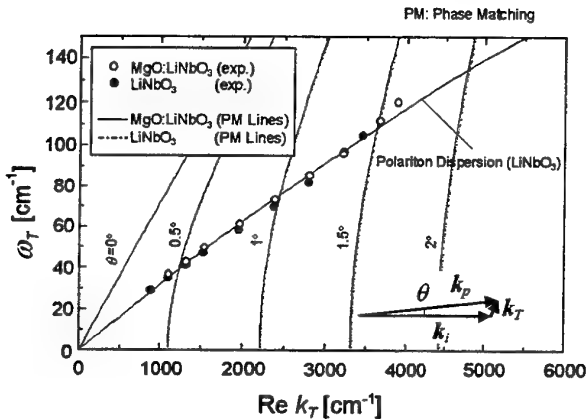


Fig. 6.  $A_1$ -symmetry polariton dispersion of  $\text{LiNbO}_3$  and  $\text{MgO:LiNbO}_3$ , which determines the angle-tuning characteristics of the OPO's.

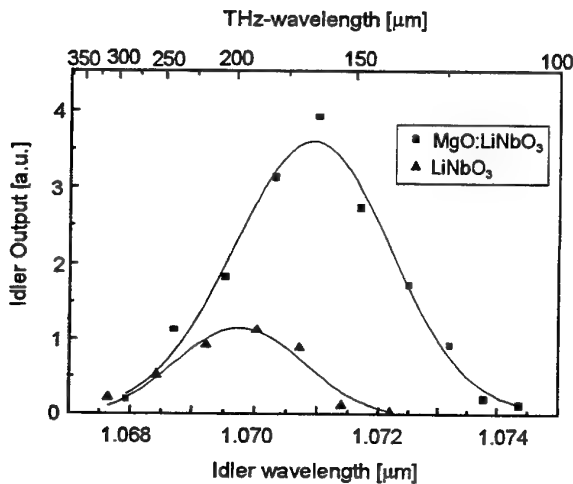


Fig. 7. Measured output characteristics of idler waves using  $\text{LiNbO}_3$  and  $\text{MgO:LiNbO}_3$  OPO's.

#### IV. APPLICATION TO SPECTROSCOPY

A variety of applications using this THz-wave source could be possible. First, we measured the absorption coefficient  $\alpha_T$  in  $\text{LiNbO}_3$  at THz range using this OPO as a coherent tunable source of THz-wave. The dewar containing a  $\text{LiNbO}_3$  crystal was placed on a horizontally sliding stage. As the position of the crystal changes, the propagating length inside the  $\text{LiNbO}_3$  crystal changes, so that the absorption coefficient  $\alpha_T$  could be precisely obtained. Fig.8 shows the measured  $\alpha_T$  in the 1-2 THz region at room temperature and liquid nitrogen temperature. Solid lines indicate the calculated ones from the complex polariton wavectors. The obtained results are in good agreement with the theoretical values.

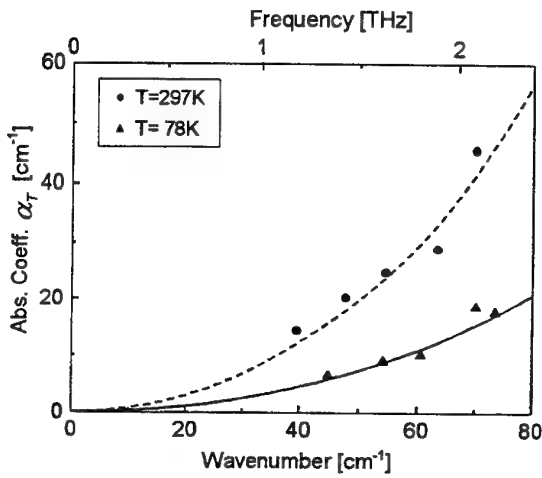


Fig. 8 Measurement of absorption coefficient of  $\text{LiNbO}_3$  utilizing the tunable THz-wave generation from OPO.

An absorption spectrum of water vapor in the air was measured. Using the experimental setup as shown in Fig.9, the THz-wave output from the prism was coupled into a 1 m-long metal hollow tube containing 1 atm-air. The output

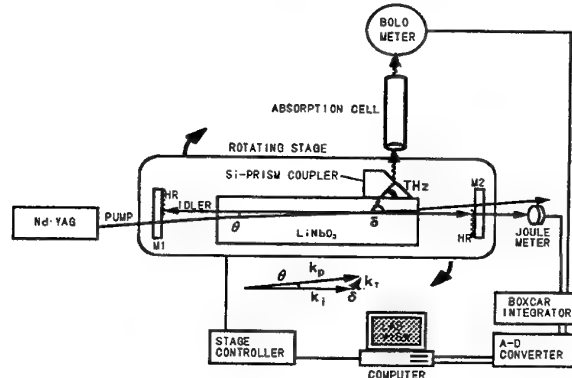


Fig. 9. Experimental setup for the THz-wave radiation utilizing a Si-prism coupler on the y-surface of the  $\text{LiNbO}_3$  crystal.

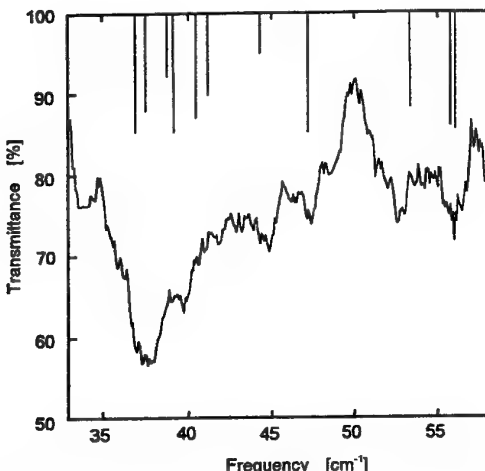


Fig. 10. Atmospheric transmission spectrum obtained by the tunable THz-wave source. THz-wave passed through a 1m-long absorption cell which was filled with 1-atm air.

was measured as a function of the incident angle of the pump beam to the crystal, and the data was calibrated by the background measurement. The measured result is shown in Fig. 10. The spectral resolution is wider than the pressure broadened water absorption linewidth, so that the further spectral narrowing should be necessary. Improved cavity configuration using a grating and/or etalon, as well as the quasi-phase matching scheme are already under our consideration.

## V. CONCULUSION

We have demonstrated efficient THz-wave generation from  $\text{LiNbO}_3$  /  $\text{MgO:LiNbO}_3$  optical parametric oscillators. Measurements on tunability, power, polarization, radiation angle, divergence and absorption have been accomplished, proving this method to be suitable for many application fields. These include spectroscopy, communication, medical and biological applications, THz imaging and so forth. Compared with available sources, the present parametric method has significant advantages such as compactness, wide tunability, and ease of handling. Further study is required for higher efficiency, narrower linewidth and establishing a continuous wave operation utilizing domain inverted structure.

## VI. ACKNOWLEDGEMENT

The authors are greatly indebted to Yamaju Co. for supplying  $\text{MgO:LiNbO}_3$  samples, C. Takyu and T. Shoji of our Institute for their excellent coating and polishing crystals and mirrors. This work has partly been supported by the Grant-in Aid from the Ministry of Education, Science and Culture of Japan, and from the Research Foundation for Opto-Science and Technology.

## REFERENCES

- [1] D. M. Mittleman, R. H. Jacobsen, and M. C. Nuss, "T-ray imaging," *IEEE J. Selected Topics in Quantum Electron.*, vol.2, pp.679-691, 1996.
- [2] Q. Wu, T. D. Hewitt, and X.-C. Zhang, "Two-dimensional electro-optic imaging of terahertz beams," *Appl. Phys. Lett.*, vol. 69, pp.1026-1028, 1996.
- [3] H. Ito, K. Kawase, and J. Shikata, "Widely tunable THz-wave generation by nonlinear optics," *IEICE trans. electron*, vol. E81-C, pp.264-268, 1998.
- [4] K. Kawase, M. Sato, K. Nakamura, T. Taniuchi, and H. Ito, "Unidirectional radiation of widely tunable THz wave using a prism coupler under noncollinear phase matching condition," *Appl. Phys. Lett.* vol. 71, pp.753-755, 1997.
- [5] K. Kawase, M. Sato, T. Taniuchi, and H. Ito, "Coherent tunable THz-wave generation from  $\text{LiNbO}_3$  with monolithic grating coupler," *Appl. Phys. Lett.*, vol. 68, pp.2483-2485, 1996.
- [6] K. Kawase, M. Sato, T. Taniuchi, and H. Ito, "Characteristics of THz-wave radiation using a monolithic grating coupler on a  $\text{LiNbO}_3$  crystal," *Int. J. of Infrared and Millimeter waves*, vol. 17, pp.1839-1850, 1996.
- [7] M. A. Piestrup, R. N. Fleming, and R.H.Pantell, "Continuously tunable submillimeter wave source," *Appl. Phys. Lett.*, vol. 26, pp.418-421, 1975.
- [8] S. S. Sussman, "Tunable light scattering from transverse optical modes in lithium niobate," *Microwave Lab. Report No.1851*, Stanford University, 1970.
- [9] J. Shikata, K. Kawase, M. Sato, T. Taniuchi, and H. Ito, "Cryogenic characteristics of the THz-wave output from  $\text{LiNbO}_3$  optical parametric oscillator," *CLEO '98*, San Francisco, no.CThY2, pp.471-472, May, 1998.
- [10] K. Kawase, and H. Ito, "Submillimeter generation using periodic domain reversal," *Nonlinear Optics*, vol. 7, pp.225-228, 1994.

# Photonic Control of Terahertz Systems

H. Fetterman\*, A. Udupa\*, D. Bhattacharya\*, H. Erlig\*, M. Ali\*, Y. Chang\*  
W. Steier\*\*, L. Dalton\*\*, B. Tsap\*\*\*

semiconductor laser is used in conjunction with a YAG at 1.3  $\mu\text{m}$  to gain sufficient bandwidth.

The use of Optical Control for millimeter wave systems has been extended recently to frequencies well over 100 GHz. New types of optical modulators, detectors and mixers can now be used to make novel systems for the first time operating at submillimeter wavelengths. In addition to the fabrication of the next generation of traveling wave polymer modulators and phototransistors, we have also developed novel approaches to high frequency testing. These involve both high frequency mixing and femtosecond pulse techniques. Applications of this technology to high frequency, electro-optic oscillators and integrated phase conjugation surfaces are now in their initial stages.

Submillimeter, Terahertz, modulators, phototransistors, phase conjugation

## I. INTRODUCTION

NEW ADVANCES HAVE MADE IT POSSIBLE TO MAKE OPTICAL MODULATORS AND PHOTOTRANSISTORS THAT OPERATE AT FREQUENCIES ABOVE 100 GHz. THESE NEW DEVICES ARE BEGINNING TO OPEN UP THE TERAHERTZ SPECTRAL REGION TO NOVEL FORMS OF OPTICALLY CONTROLLED SYSTEMS. IN ADDITION TO THE ACTUAL DEVICES, MAJOR ADVANCES HAVE BEEN DEMONSTRATED IN THE TESTING OF THESE HIGH FREQUENCY SYSTEMS. THIS HAD LED TO A NEW GENERATION OF APPLICATIONS.

## II. MODULATORS

The advances in modulators that we are exploring have involved polymer structures using new types of chromophores. These devices are basically traveling wave structures in which the low dielectric constant of the polymer yields an excellent velocity match between the electric and the optical waves. In figure 1 we show an array of modulators formed on a mylar substrate.

These devices are connected with finline transitions so that they can be coupled to waveguide sources at millimeter wave frequencies. The flexible mylar substrate is low loss and is inserted directly into the guide as shown in figure 2. Using a laser heterodyne technique we are able to measure the frequency response of this system to extremely high frequencies. The actual setup used is shown in figure 3. A

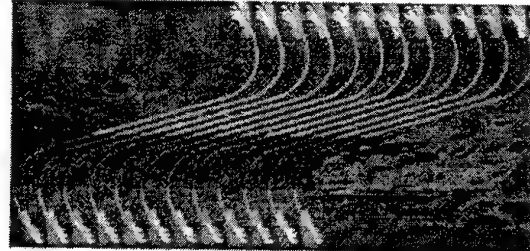


Fig 1. Photograph of the fabricated polymer modulator with integrated finline transitions at both ends of the traveling wave electrode

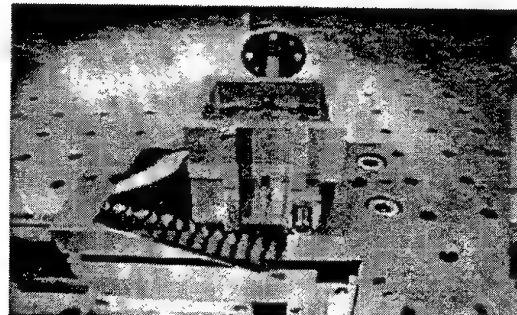


Fig 2. Photograph of the packaged W-band polymer modulator on the Mylar substrate. This shows one of the modulators in the array being fed through the rectangular waveguide

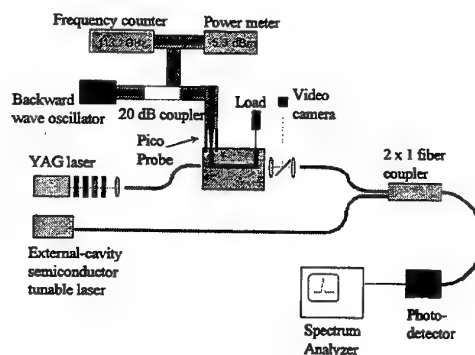


Fig 3. High Frequency Characterization setup

\*University of California at Los Angeles  
\*\* University of Southern California  
\*\*\* Pacific Wave Industries

Using these mixing techniques the response of the device was measured up to 113 GHz [1], and did not show significant roll off as shown in figure 4.

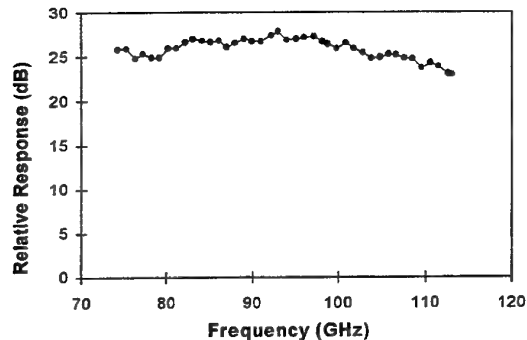
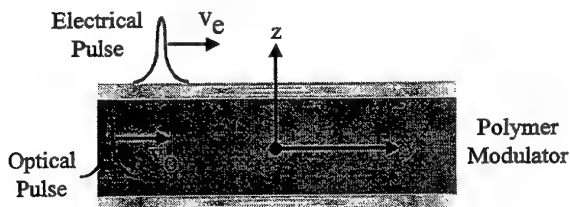


Fig 4. Frequency response of the polymer modulator from 74-113 GHz

This system is now undergoing tests using our Femtosecond pulse techniques such as shown in figure 5. In this system we use a high speed, low temperature GaAs two photon electrooptic switch. The basic system is shown in figure 6.



$$U(\tau) = \int_{-\infty}^{\infty} \int_{-\infty}^{\infty} A I_0(y - v_0(t - \tau)) E_e(y - v_e t) dy dt$$

Fig 5. Time domain characterization of polymer modulator - two pulse approach

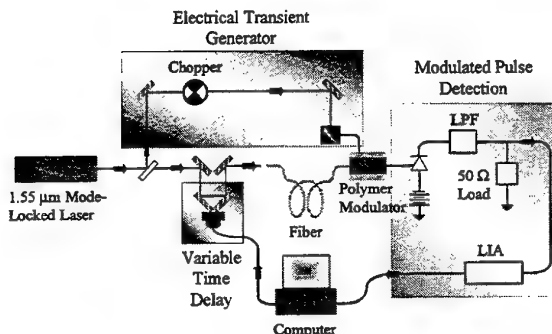


Fig 6. Schematic representation of polymer modulator characterization technique.

### III PHOTOTRANSISTORS

In addition to work on traveling wave modulators we have also looked into high frequency phototransistors using HBT and HEMT structures [2]. One such device is shown in figure 7 uses an HBT device with a polyimide optical guide and a traveling wave configuration. This device can be very fast, and because of it's large volume, capable of handling substantial powers. The results at 60 GHz, shown in figure 8, demonstrates that it can be driven very hard before saturation.

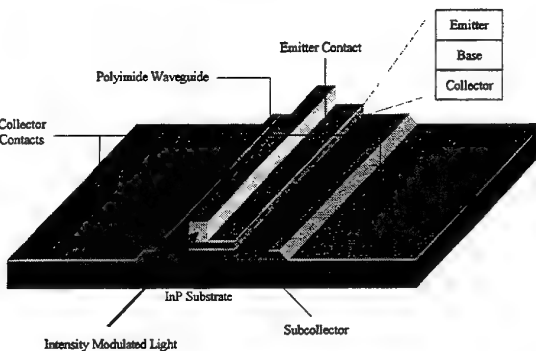


Fig 7. Schematic diagram of the TW-HPT. Polyimide waveguide is defined on top of the active region of an HPT. The HPT's electrodes are coplanar waveguide with a characteristic impedance of  $50 \Omega$

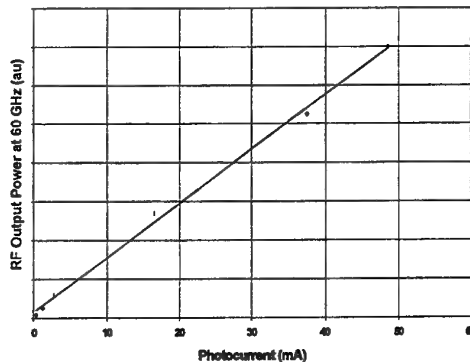


Fig 8. Optical power saturation at 60 GHz for 200  $\mu\text{m}$  long TW-HPT

In another set of experiments we have used a new generation of InP based pseudomorphic HEMTs [3] with special G band probes to mix at 212 GHz. The basic set up for these measurements is shown in figure 9. The actually mixing results are in figure 10 and are being extended to yet higher frequencies with excellent signal to noise ratios.

#### IV. APPLICATIONS

There are many applications for this type of optically controlled high frequency systems. One of the most interesting concepts is the development of a Terahertz oscillator using photonic techniques. We have looked into one such approach using a system pioneered by JPL and shown in figure 11. This system is basically limited by the response of the modulator and the photodetector. In our initial measurements we worked up to 22 GHz to show proof of principle as indicated in figure 12. This work is now being future extended to W band.

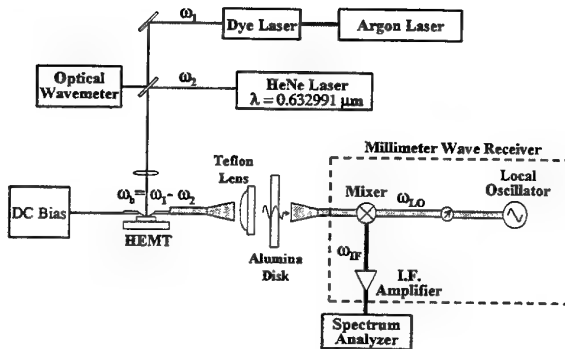


Fig 9. Setup for optical generation of millimeter waves

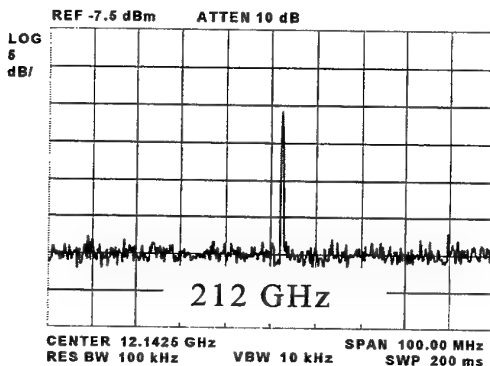


Fig 10. Spectrum analyzer trace of optically generated 212 GHz signal radiated into free space

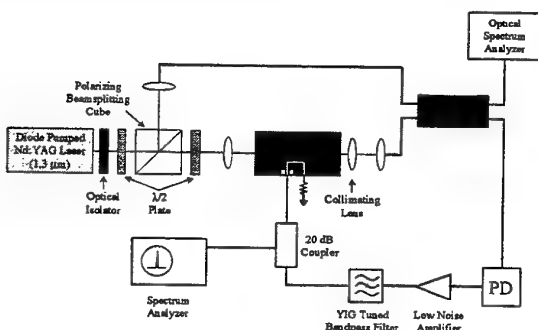


Fig 11. Experimental realization of 22 GHz photonic oscillator

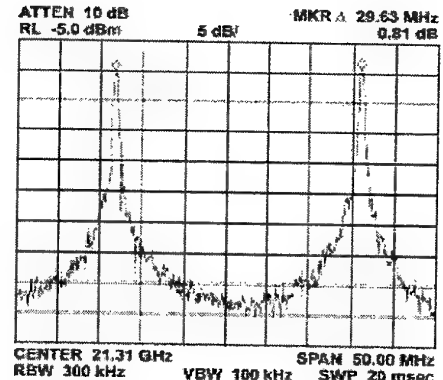
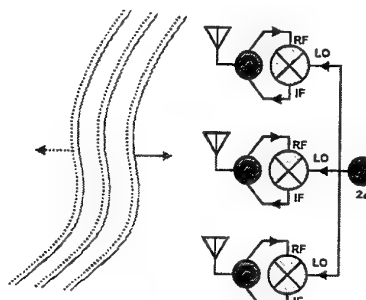


Fig 12. Modes of a 22 GHz photonic oscillator

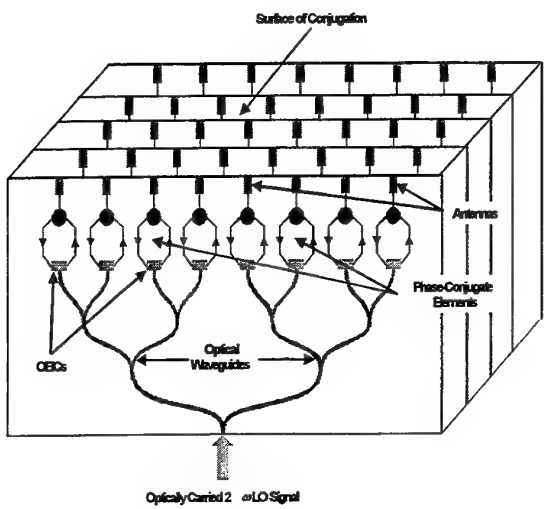
Finally, one of the novel applications at visible frequencies involves the use of nonlinear crystals for phase conjugation. This has been shown to be possible at millimeter wave frequencies using an electronic approach to conjugate the signal at specific antenna elements as shown in figure 13 [4].



$$e^{i(\omega t + \phi_k)} \cdot e^{i2\omega t} \Rightarrow e^{i(2\omega t - \omega t - \phi_k)} = e^{i(\omega t - \phi_k)}$$

Fig 13. Electronic approach of phase conjugation at millimeter wave frequencies

By sampling at sufficiently dense intervals it is possible to conjugate an entire wavefront at submillimeter wavelengths. A prototype array is shown in figure 14 and actually simulates a nonlinear surface. The use of optical connections at these terahertz frequencies is the key enabling technology.



4. Chang, Y.; Fetterman, H.R.; Newberg, I.L.; Panaretos, S.K. "Millimeter-wave phase conjugation using artificial nonlinear surfaces," *Applied Physics Letters*, vol.72, (no.6), 9 Feb. 1998. p.745-7.

**Fig 14.** Prototype array for phase conjugation of an entire wavefront at submillimeter wavelengths.

## V. CONCLUSION

We find that the technology involving lasers has made enormous advances over the last decade. By using this technology we are now capable of making entirely new forms of Terahertz systems. These will include sources and large arrays that are optically controlled. The use of photonics brings an entirely new capability to this area.

## VI. REFERENCES

1. Chen, Datong; Fetterman, H.R.; Chen, Antao; Steier, W.H.; Dalton, L.R.; Wenshen Wang; Yongqiang Shi. "Demonstration of 110 GHz electro-optic polymer modulators," *Applied Physics Letters*, vol.70, (no.25), 23 June 1997. p.3335-7.
2. D. C. Scott, D. P. Prakash, H. Erlig, D. Bhattacharya, M. E. Ali, H. R. Fetterman, and M. Matloubian, "High-Power High-Frequency Traveling-Wave Heterojunction Phototransistors with Integrated Polyimide Waveguide," *Microwave and Guided Wave Letters*, vol. 8, (no. 8), August, 1998, pp. 284-286.
3. Ali, M.E.; Bhattacharya, D.; Fetterman, H.R.; Matloubian, M. "Optical mixing to 211 GHz using 50 nm gate pseudomorphic high electron mobility transistors," *Applied Physics Letters*, vol.72, (no.4, 26 Jan. 1998. p.398-400.
4. Chang, Y.; Fetterman, H.R.; Newberg, I.L.; Panaretos, S.K. "Millimeter-wave phase conjugation using artificial nonlinear surfaces," *Applied Physics Letters*, vol.72, (no.6), 9 Feb. 1998. p.745-7.

# Terahertz frequency regime waveguide photonic microstructures for electro-optic modulation

R.M. De La Rue, M.R.S. Taylor, K. Li\*, M. Sasaki\*, T. Hori\* and M. Izutsu\*

Optoelectronics Research Group, Dept of Electronics and Electrical Engineering, University of Glasgow, Glasgow G12 8QQ, Scotland, U.K.

\*Communications Research Laboratory, Ministry of Posts and Telecommunications, Nukuikitamachi, 4-2-1, Koganei, Tokyo 184-8795, Japan

e-mail: [r.delarue@elec.gla.ac.uk](mailto:r.delarue@elec.gla.ac.uk).

**Index terms** - Terahertz, electrooptic, lithium niobate, integrated optics, photonic microstructures

## I. INTRODUCTION

This paper concerns a novel device concept for electrooptic devices which operate in the millimetre wave to Terahertz frequency regime. More specifically the principles considered are relevant to devices working at centre-frequencies above 100 GHz - in a range extending up to at least 1 THz. There has already been a significant amount of work on photonic bandgap structures for electromagnetic waves in the microwave through to mid-infrared frequency range<sup>1-3</sup> and possibly the earliest clear demonstration of photonic bandgap behaviour<sup>1</sup> was an experiment carried out at microwave frequencies. The presentation will describe operating principles for guided-optical modulator devices which exploit the linear electrooptic (Pockels) effect in the ferroelectric material lithium niobate. Attention is centred on lithium niobate ( $\text{LiNbO}_3$ ) since it is already in use in guided wave electrooptic devices operating at modulation frequencies well into the microwave regime<sup>4,5</sup>. Lithium niobate can also provide the wider range of functions which justifies use of the label 'integrated optics'<sup>6</sup>. The electromagnetic absorption losses of lithium niobate have recently been characterised at frequencies well into the Terahertz regime<sup>7,8</sup>. Under practical operating conditions, the losses are small enough for viable electrooptic devices to be possible at modulation frequencies at least as high as 1 THz.

## II. TERAHERTZ LOSSES AND DIELECTRIC RESONATORS

Above 100 GHz, photonic, electronic and electromagnetic devices which employ metallic electrodes are greatly hampered by conduction losses. One way to overcome this problem is to reduce the device temperature<sup>9,10</sup>. A reduction in temperature, e.g. to 77K, can provide a useful increase in the conductivity of normal metals, but can also provide

further major improvements if suitable superconducting materials are used in the electrodes - at a temperature which is appropriate for the particular superconductor in question. The focus in the present work is on devices which can provide efficient modulation of guided light by coherent Terahertz electromagnetic waves, but which eliminate the usual metallic electrodes. The device is designed to operate over a limited band of modulation frequencies, exploiting resonant electromagnetic structures fabricated directly in the electrooptic material. Performance is ultimately limited by the 'dielectric' losses of the electro-optic material, although scattering losses due to roughness could also be important. By using strong confinement of the modulating electromagnetic waves in a Terahertz image-guide structure, together with a large periodic modulation of the effective guided-mode index, it is possible to produce resonant cavity structures which provide the large electric field strengths required for efficient electrooptic modulation at reasonably modest (Terahertz) r.f. drive-power levels. Because of the scaling of the structure with electromagnetic wavelength, the image-guide based approach used gives greater electromagnetic confinement as frequency increases.

## III. LITHIUM NIOBATE TERAHERTZ IMAGE GUIDE DESIGN

The image guide approach gives strong confinement for the modulating electromagnetic waves, together with a negligible contribution to their propagation losses from the metallic ground plane. The electromagnetic mode solving package, F-wave<sup>11</sup> has been used to design the image guides. Ridge waveguide structures with single transverse mode behaviour for quasi-TM modes have been designed and the dimensions adjusted to produce two radically different guided mode effective indices. The F-wave package allows rapid calculations to be made with both a complex refractive index for the dielectric guide material and a complex refractive index to model the conducting ground-plane. In the Terahertz regime, available data for both dielectric material and metallic conductor properties are somewhat conjectural,

so we have tested the behaviour over a range of plausible parameters. Although the F-wave numerical package is attractive because of its ease of use, understanding gained from earlier work on dielectric-based open waveguides has also been useful.<sup>12</sup>

The cross-section normal to the propagation direction shown in Fig. 1 shows an electric field-strength plot calculated for a single material image guide structure of the 'slab-coupled rib' type, using a refractive index value of 6. This value is an approximation to the square-root of the two distinct relative dielectric constant values of LiNbO<sub>3</sub> which arise because of its anisotropy. The geometry chosen gives sufficient confinement of the mode in the high-index region for the effective guided mode index to be as large as 5. Note also the schematic location of the optical waveguide on the flat face of the structure, immediately adjacent to the metallic ground plane and in a region of maximum electric field. For the present purposes, the waveguide could equally well be formed by either titanium in-diffusion<sup>13</sup> or proton-exchange<sup>14</sup>. In practice, a thin (c. 0.5  $\mu\text{m}$ ) insulating buffer layer would be required to minimise optical frequency propagation losses.

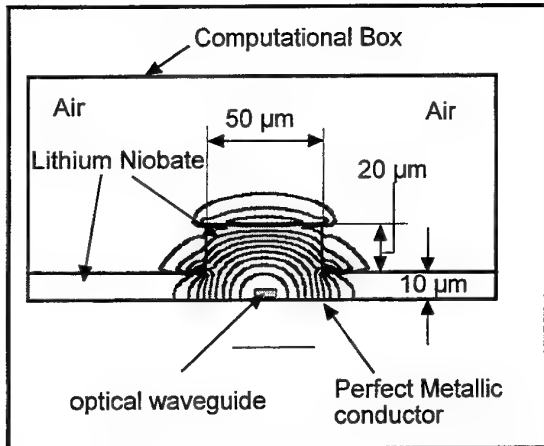


Fig. 1: Field strength plot for high effective index image guide at 1 THz.

Fig. 2 clearly has much less of its modal energy in the high refractive index region and the effective guided mode index is consequently lower at around 2.5. Modest redesigns of the two waveguide cross-sectional geometries can readily give a higher effective index than the structure of Fig. 1 and a lower effective index than the structure of Fig. 2.

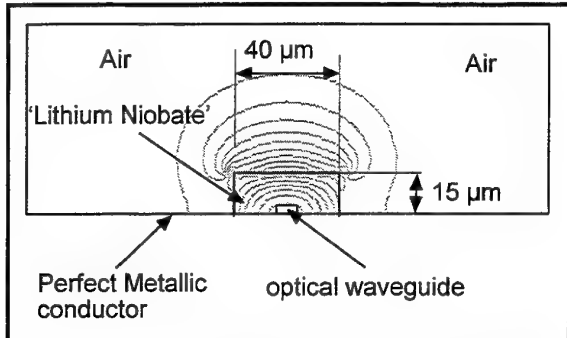


Fig. 2: Field strength plot for low effective index image guide at 1 THz.

#### IV. TERAHERTZ MICROCAVITY DESIGN

The two image guide geometries just considered provide the basis for the design of a Terahertz microcavity structure. The objective is to produce a resonator which delivers a high electric field strength for electrooptic interaction at Q-factor values limited by the unavoidable absorption of the modulator material. The design of the microcavity is based on well-established approaches at optical and lower frequencies. Two distributed Bragg reflector (DBR) mirror stacks are required, with a cavity spacer section between them. Fig. 3 shows schematically several periods of a large index contrast DBR mirror stack realised using the two previous image guide cross-sections.

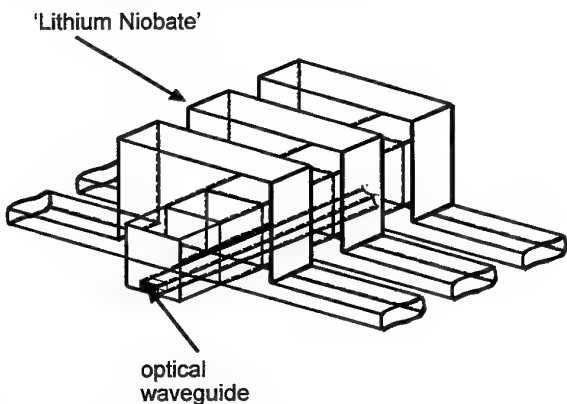


Fig. 3: part of a Terahertz modulator DBR mirror stack, showing alternating cross-sections in each period.

A 10 period DBR stack is approximately 375  $\mu\text{m}$  long at 1 THz, for a structure formed from pairs of the two alternative guide cross-sections. While a design in which the length of each part of a period is  $\lambda/4$  long (as scaled by the appropriate indices) may be considered as typical, the key requirement is that each period be  $\lambda/2$  long for the optical path length. Alternate section lengths within a period could therefore be quite different both physically and optically, as has been used

in some optical waveguide microcavities<sup>15</sup>. Two such DBR mirror stacks with a short spacer section between them can be used to form a cavity with an overall length of less than a millimetre. Simple calculations based on one-dimensional dielectric mirror stacks indicate that six-period DBR mirror stacks are sufficiently reflective to provide a Fabry resonator with an intrinsic Q-factor larger than the upper-limit value (~450) determined by the 1 THz propagation losses in LiNbO<sub>3</sub> at a temperature of 77 K.

## V. TERAHERTZ ELECTROOPTIC MODULATOR

But the device design must also take account of the need to obtain an efficient phase-matched interaction between the optical and Terahertz waves. This both requires a long enough optical path in the region of high Terahertz frequency electric field strength and the use, possibly, of techniques such as (periodic) domain reversal<sup>16,17</sup>. There is also the possibility that the material and waveguide dispersion will be large enough to lead to the conversion of applied phase modulation into amplitude modulation at the device output. Our estimates of the optical frequency dispersion indicate that phase modulation sidebands shifted from an optical carrier by 1 THz will have sufficient velocity differences to produce substantial modulation conversion over propagation distances of the order of 1 mm, i.e. over distances comparable with the envisaged device length.

What optical phase modulation depth is practically possible at 1 THz? Our calculations show that if a resonator Q of 100 and a fully velocity-matched electrooptic interaction only 1 mm long were achieved in the guide structures already calculated, 100 mW of Terahertz guided mode power would be sufficient to produce ~0.4 radian modulation at a free-space optical wavelength of 1  $\mu$ m. This modulation depth should be sufficient to be readily observable when incorporated into a suitably biased interferometric arrangement, e.g. the Mach-Zehnder geometry commonly used in amplitude modulators. A tabulated electrooptic coefficient value of  $r_{33} = 30 \cdot 10^{-12}$  m/V has been used in the above, thus specifying that the guided optical mode electric field polarisation is parallel to the crystal z-axis and normal to the metallic ground plane, i.e. that the optical mode should also have TM polarisation. For TE optical modes, the approximately three times smaller  $r_{13}$  coefficient can be used with the same crystal orientation and a consequent increase in the electromagnetic power required. But, using data from Ito et al, we estimate that the material loss-limited Q-factor value is ~450 at 1 THz and liquid nitrogen (LN) temperature. The power requirement then becomes less

than 50 mW, using  $r_{33}$  for the electrooptic modulation. Much larger Q values become possible at truly cryogenic temperatures, so that really modest drive power levels could then be used. We remark that some possible operating environments could naturally be cryogenic, e.g. in space.

How might a practical modulator be fabricated? One possible approach is to fabricate a suitably shaped tool by precision NC machining or spark erosion and then use ultrasonic machining. Precision diamond sawing could also be useful. Techniques closer to 'conventional' microlithography could also emerge for this task.

## VI. CONCLUSIONS AND FUTURE DEVELOPMENTS

We have found it fruitful to apply photonic bandgap and microcavity concepts in such devices. Multifunction devices in which the local periodicity of the structure determines whether it is a low-loss mirror stack for a Terahertz microcavity or (potentially) an electrooptic beam-steering antenna will be possible. Periodic structures of the same type, but with an increased period length, become receiving/transmitting antennae<sup>18</sup>. It will also be useful to consider other electrooptic materials, in particular the III-V semiconductors, and thus identify alternative materials which combine strong electrooptic effects with low absorption losses at Terahertz frequencies.

## VI. ACKNOWLEDGEMENTS

This work was supported by the COE project at Communications Research Laboratory and one of us (RMD) gratefully acknowledges the personal support provided by the COE project for his extended visit to CRL.

## References

1. E. Yablonovitch, T.J. Gmitter, R.D. Meade, A.M. Rappe, K.D. Brommer and J.D. Joannopoulos, "Donor and acceptor modes in photonic band structure", Phys. Rev. Lett., **67**, pp. 3380-3383, (1991).
2. E. Özbay, E. Michel, G. Tuttle, R. Biswas, M. Sigalas and K.-M. Ho, 'Micromachined millimeter-wave photonic bandgap crystals', Appl. Phys. Lett., **64**, pp. 2059-2061, (1994).
3. E.R. Brown, C.D. Parker and E. Yablonovitch, "Radiation properties of a planar antenna on a photonic-crystal substrate", J. Opt. Soc. Amer., **B10**, pp. 404-407, (1993).
4. M. Izutsu, Y. Yamane and T. Sueta, "Broad-band travelling wave modulator using a LiNbO<sub>3</sub> waveguide", IEEE Jour. Quantum Electronics, QE-13, pp. 287-290, (1977).

5. K. Noguchi, H. Miyazawa and O. Mitomi, "75-GHz Ti:LiNbO<sub>3</sub> modulator", Technical Digest. OFC '94, San Jose, Feb 1994.
6. N.A. Sanford, editor, "Recent advances in lithium niobate optical technology", special issue of IEEE Jour. Quantum Electronics, 33, October (1997).
7. H. Ito, "Widely tunable THz-wave source by means of optical parametric oscillation", International Workshop on Contemporary Photonic Technologies", CPT '98, paper Tb-02-1,pp. 73-76, 12-14th Jan, (1998).
8. J. Shikata, K. Kawase, M. Sato, T. Taniuchi and H. Ito, "Cryogenic characteristics of the output from LiNbO<sub>3</sub> optical parametric oscillator, CLEO '98, San Francisco, USA, paper CThY2, May (1998)
9. M. Sasaki and M. Izutsu, 'On design of high speed light modulator with resonant type electrode", Proc. FST '97, Tsukuba, (1997).
10. M. Sasaki, K. Li and M. Izutsu, "Resonant type electro-optic light modulator with superconductive electrode", submitted conference paper.
11. F-wave IV by M.R.S. Taylor, available on the internet at <http://eeapp.elec.gla.ac.uk/~michaelt/software/fwave/>.
12. A.A. Oliner, S.-T. Peng, T.-I. Hsu and A. Sanchez, "Guidance and leakage properties of a class of open-dielectric wave guides: part II - new physical effects", IEEE Trans Microwave Theory and Techniques, MTT-29, pp. 855-869, (1981).
13. R.J. Esdaile, A.D. McLachlan and R.M. De La Rue, "New Aspects of Titanium diffusion in Lithium Niobate" Technical Digest of Topical Meeting on Integrated and Guided-Wave Optics", Jan. 28-30, 1980, Incline Village, Nevada, pp WB3-1 - 4, pub. by Optical Society of America.
14. A. Loni, R.M. De La Rue and J.M. Winfield, 'Proton-exchanged, lithium niobate planar-optical waveguides: chemical and optical properties and room-temperature hydrogen isotopic exchange', Journal of Applied Physics, 61, pp. 64-67, (1987).
15. T.F. Krauss, B. Vögele, C.R. Stanley and R.M. De La Rue, "Waveguide microcavity based on photonic microstructures", IEEE Photonics Technology Letters, 9, pp.176-178, Feb (1997).
16. R.W. Keys, A. Loni, R.M. De La Rue, C.N. Ironside, J.H. Marsh, B.J. Luff and P.D. Townsend, "Fabrication of domain reversed gratings for SHG in LiNbO<sub>3</sub> by electron beam bombardment", Elect. Lett, 26,pp. 188-189, (1990).
17. F-Z. Guo, C-T. Yu, L. Chen, T. Kobayashi and Y. Chen, "Quasi-velocity-matched electrooptic phase modulator for the synthesis of ultrashort optical pulses", IEEE Jour. Quant. Electron. 33, pp.879-882, (1997).
18. F. Schwering and S.-T. Peng, "Design of dielectric grating antennas for millimetre -wave applications", IEEE Trans. Microwave Theory and Techniques, MTT-31, pp. 199-208, (1983).

# Measurement of Impedance above 110 GHz

Richard J. Collier

**Abstract** - The measurement of impedance above 110 GHz lacks both commercially available measurement equipment and good standard impedances. This paper discusses these problems and goes onto suggest some ways forward for solving them. The paper includes a description of some on-wafer measurements of impedances at 140 GHz and concludes with some recommendations for future research

**Index Terms**—Measurements, Impedance, On-wafer Probes

## I. INTRODUCTION

Measurements of impedance at frequencies above 110 GHz are not straightforward as most commercially available measuring equipment only works up to this frequency. With certain exceptions, measurement systems above 110 GHz have to be individually designed by each research team. No doubt, in the future, when this 'commercial cut-off frequency' is raised this situation will change. This paper will outline some of the features of impedance measurements which are being carried out now despite this lack of 'off the shelf' equipment. The paper will focus on the measurement of on-wafer impedance, which includes many other techniques. However, before that, some discussion of standard impedances will be included as their properties greatly effect the accuracy of many of the measurements.

## II STANDARD IMPEDANCES

The measurement of impedance usually involves the comparison of an unknown impedance with a standard impedance. These standards usually consist of short circuits, open circuits, matched loads and lengths of uniform transmission line. They are constructed to give calculable reflection coefficients. At frequencies above 110 GHz, all of these become much harder to make. For instance, a short circuit consisting of a metal surface perpendicular to the main direction of propagation does not reflect any incident wave perfectly at the surface. The skin effect and the anomalous skin effect cause a phase shift and a reduction in amplitude which is not only frequency dependant but in the case of waveguides is also dependant on the mode characteristics. The problem of short circuits in coplanar waveguide is even more acute, since the conducting plane is not even perpendicular to the main direction of propagation. Here the short circuits cause both radiation and coupling to substrate modes in addition to the

other effects above. Open circuits are equally difficult to make and are often constructed from a short circuit with a quarter wave-length of transmission line. However, since at these frequencies the attenuation of the lines is high, as they do not have simple characteristic impedances or phase constants, so the impedance transformations are complex and certainly not calculable from purely theoretical considerations. The only standard impedance, which is relatively easy to make, is a matched load. Since all transmission lines are attenuating, for example coplanar waveguide attenuation can easily be  $0.5 \text{ dB/mm}^{-1}$ , even a length of line will help to provide a matched load. However, the two resistors at a coplanar waveguide termination do have to be identical otherwise a further complication of mode conversion as well as scattering will occur. Fortunately, in the case of coplanar waveguide the scattering into radiation and substrate modes can enhance the matching properties. Another problem, linked with standards, is the unsatisfactory properties of their connectors. Most connectors have poor insertion loss and repeatability. For instance in metallic waveguide this can be the major source of measurement uncertainty. If coplanar waveguide circuits are going to be probed then the properties of the probe limit the measurement in a similar way to the connectors.

The other problem at these frequencies concerns phase. At these frequencies the phase changes along a line by roughly a degree every micrometre. So if accurate measurements of phase to say 0.1 of a degree are required then all measurements must be stable to 100 nm. Clearly this puts considerable strain on both the mechanical construction and the thermal properties of the materials used in a standard. These thermal properties include not only the coefficient of expansion but also the change of dielectric constant with temperature. This is a particular problem when using a measurement system connected to an impedance via a long length of transmission line—say one metre long. Any flexing or permanent deformation of this line during a measurement will certainly reduce any phase accuracy. It is a feature of the modern calibration procedures that it would not be obvious that the measurements were wrong unless the calibration took place before and after the measurement. Also if metallic waveguide WR29 were used there would be a return loss of nearly 25 dB at 140 GHz which, depending on the sensitivity of the detectors used could seriously limit the range of impedances which could be measured.

What is needed in the future is a set of stable, calculable standards, which can be used to calibrate standards in all currently used transmission lines. Once the standards laboratories have produced these, it should be possible to

The author is at the Electronic Engineering Laboratory, The University of Kent at Canterbury, Kent, U.K.

make accurate impedance measurements like those so easily achieved below 110 GHz with commercial equipment.

### III TRANSMISSION LINES

There are two types of transmission lines used in impedance measurement. The first is usually used to connect the measurement system to the impedance. This may be typically metallic waveguide, coaxial cable or dielectric waveguide. The second is the transmission line connected to the impedance. In the case of integrated circuits this may be coplanar waveguide, microstrip or metallic waveguide. For the first category the ideal properties are accurate manufacture and flexibility combined with low attenuation, dispersion and thermal expansion. Linked with these properties, the transmission lines should also have good connectors. At the moment, the best line is a dielectric waveguide as it has flexibility and low attenuation as well as the possibility of good connectors [1]. The best material for dielectric waveguides is one with a low permittivity and loss tangent. It may be that in the future, like the advent of optical fibres, a specially purified material will be made which has a really low loss tangent. The lowest figure with currently available materials is around  $2 \times 10^{-4}$  which gives an attenuation of less than  $6 \text{ dBm}^{-1}$  at 140 GHz.

Metallic waveguides and coaxial cables have poor connectors and high dispersion and attenuation. The thermal properties for most lines are similar. A typical value for one metre of line at 150 GHz being 20 degrees of electrical phase change for every increase of one degree in temperature.

For the second category, since most of the lengths are less than a millimetre, the accuracy of manufacture is the most important factor. The electrical properties are not the limiting feature, although they will need to be known accurately for calibration and de-embedding.

### IV MEASUREMENT SYSTEMS

The ubiquitous Network Analyser is now so well established below 110 GHz, that it should be available above 110 GHz in the future. The factors, which are preventing this, maybe the quality of available sources, the problems of down-converting these high frequencies below 100 GHz and the availability of high directivity directional couplers. However the size of the market is probably the main cause. With the steady growth of applications above 100 GHz, this may change eventually. In the meantime, there are a variety of techniques available for impedance measurement. These include the sixport reflectometer, the multistate reflectometer and the Millimetre Vector Network Analyser produced by Abmm [2]. The first two can be easily constructed by most laboratories, but do require a stable source and power detectors. The latter is available for measurements from 8 – 1000 GHz and has measurement ports on the end of one metre lengths of coaxial cable. The first two each cost considerably less than the latter. All of the techniques have sources which can be frequency locked to a frequency counter. This enables them to measure high

'Q' factors. One disadvantage of the Millimetre Vector Network Analyser is that a large number of harmonics are entering the device under test. So it is advisable to limit its use to measurements of linear systems. For measurements of on-wafer circuits using probing stations, it is essential that the measurement system is as close as possible to the circuit. The multistate reflectometer has been used for this purpose. It is easily mounted on a probe station and can be connected via a flexible dielectric waveguide to the swept oscillator. This avoids measuring impedances at the end of a long length of line, which is also being moved during measurements. At the University of Kent, a multistate reflectometer has been constructed using dielectric waveguide components [3]. These have included novel directional couplers and programmable phase shifters [4]. The use of dielectric guide has greatly reduced the cost with an enhancement of the electrical properties compared with a metallic waveguide equivalent.

### V COPLANAR WAVEGUIDE PROBES

Coplanar waveguide probes are not available above 120 GHz. The probes all have a coplanar waveguide to coaxial or metallic waveguide transition and have insertion loss of around 1dB rising rapidly with frequency. The University of Kent has developed a novel probe, which use a coplanar to dielectric waveguide transition [5]. The performance of this probe at 140GHz compares well with the performance obtained from commercial probes at 110GHz. One of the problems with probes at high frequencies is that the position on the substrate is far more critical. Since the phase shift change with distance is one degree per micrometre any misalignment between the measurements of standards and unknown impedances can be a major source of phase uncertainty. Also the coupling from the probe to substrate modes is increased at higher frequencies unless the substrate is thinned down. The angle of the probe is also important as well as the configuration of the pads on the substrate. All these probes work very well when the dimension of the pads is much larger than a wavelength. But at 140 GHz the pad size is approaching a tenth of a wavelength and as a result any misalignment of the probe can cause scattering of the input and reflected signal. Clearly circuit designers in the future will have to take into account these pad shapes to minimise these problems.

### VI CONCLUSIONS

This paper has outlined some of the problems ahead for measuring impedances above 110 GHz. It has included a discussion on standard impedances and the need for reliable standards. A brief survey of transmission lines followed with the recommendation that dielectric waveguide be used for transmission over one metre. The various measurement systems were then discussed in conjunction with their use with a probe station. Although, at the moment, measurement activity is small above 110GHz, it is likely to grow in the near future when

hopefully similar equipment to that which exists below 110 GHz will become available.

#### REFERENCES

- [1] R.J.Collier and M.F.D'Souza "Comparison of junctions in both dielectric guides and metallic guides above 75 GHz" *I.E.E. Proceedings-A* vol 139 pp 226-228 September 1992.
- [2] ABmillimetre, 52 Rue Lhomond, 75005, Paris, France.
- [3] I.M.Boese and R.J.Collier "Novel Measurements within 100 - 170 GHz" *26<sup>th</sup> European Microwave Conference - Prague* pp 806 -810 1996.
- [4] R.J.Collier and M.F.D'Souza "Phase Shifter for Dielectric Waveguides" *I.E.E. Proceedings H* pp 202 - 204 April 1992
- [5] I.M.Boese and R.J.Collier "Measurements on Millimetre Wave Circuits at 140 GHz" *I.E.E. Proceedings A* pp 171-176 July 1998

# An Integrated Circuit for Network Analysis within 50-200 GHz

O. Wohlgemuth, B. Agarwal\*, R. Pullela\*, D. Mensa\*, Q. Lee\*, J. Guthrie\*, M. J. W. Rodwell\*,  
R. Reuter, J. Braunstein, M. Schlechtweg, T. Krems, K. Köhler

**Abstract**--This paper presents an integrated circuit, based on nonlinear transmission lines (NLTL), for a vector network analyzer system (VNA) within 50-200 GHz. It is the first integrated circuit containing all elements of a S-Parameter test set: A multiplier to generate the RF signal, directional couplers to separate the incident and reflected waves, and a pair of high speed sampling circuits to convert the signals down to lower frequencies.

## I. INTRODUCTION

Recent progress in III-V devices, especially with InP-based HEMTs and HBTs [1], demand characterization over an extended bandwidth. But commercial broad-band on-wafer S-parameter measurement set-ups are presently limited to 120 GHz bandwidth. We have fabricated an IC for a new measurement system for 50-200 GHz network analysis. NLTLs are used, because they generate high frequency signals in a very wide bandwidth and they can also be used to drive high speed sampling circuits. Among improvements over earlier reported work [2], the present IC uses true directional couplers for high directivity, uses low-order harmonic generation in the stimulus signal generation, and processes the detected (IF) signals directly in the frequency domain, without using time-domain / Fourier transform methods. A high pass-filter at the output of the source frequency multiplier equalizes its output power spectrum, further increasing the signal-to-noise ratio at high frequencies. By mounting buffer amplifiers close to the chip, the IF can be increased to 20 MHz which decreases the phase noise and allows to use the HP8510 directly for IF processing. Together, these improvements substantially increase the system signal-to-noise ratio and directivity. The assembly of the network analyzer (NWA) integrated circuits into

active probes, will allow accurate on-wafer network analysis up to 200 GHz.

## II. DESIGN AND RESULTS

As in earlier work [3], diodes with an exponential doping profile are used for the NLTL. This combines a large capacitance variation and a high breakdown voltage (13 V) with a high large-signal cutoff frequency (2.5 THz).

Fig. 1 shows the block diagram and fig. 2 a microphotograph of the fully integrated circuit. A NLTL used as a frequency multiplier generates the RF stimulus signal. The NLTL was designed for a drive frequency from 34 to 50 GHz, so the second, third and fourth harmonics cover the 68 to 200 GHz bandwidth. Due to lower insertion loss at lower frequencies, the NLTL also operates from 25 to 50 GHz, which increases the bandwidth of the measurement system from 50 to 200 GHz. Fig. 3 shows the output waveform of this NLTL with a fall time of 3.2 ps. The NLTL drives the test port through a directional coupler. The coupler functions as a bias tee, isolating the NLTL frequency multiplier from the DC bias applied to the test port. Further, the coupling increases with frequency, thereby reducing the variation of the DUT drive power with frequency. Two additional couplers are integrated to get the incident and reflected wave and two high speed sampling circuits are used to convert the signals down to 20 MHz IF. The sampling circuits are driven by a second NLTL, operating at half of the frequency of the stimulus NLTL (12.5 to 25 GHz). To reduce reflections from the bias connection, a low pass filter is also integrated on the IC.

The coplanar directional couplers were designed for 10 dB coupling using a 3D simulator [4] to calculate the impedances  $Z_{\text{even}}$  and  $Z_{\text{odd}}$  and the complex propagation constants  $\gamma_{\text{even}}$  and  $\gamma_{\text{odd}}$ . Compared with microstrip couplers, coplanar couplers can easily achieve a high directivity over a wide bandwidth, because the effective dielectric constants of the two modes are nearly the same and almost independent of the fre-

Fraunhofer Institute for Applied Solid State Physics IAF,  
Tullastr. 72, D-79108 Freiburg, Germany,  
Phone: +49 761/5159-538, Fax: +49 761/5159-565,  
Email: olwo@iaf.fhg.de

\* Department of Electrical and Computer Engineering,  
University of California, Santa Barbara, CA 93106,  
Phone: 805-893-3244, Fax: 805-893-3262,  
Email: rodwell@ece.ucsb.edu

quency. To verify the simulation the same coupler was scaled for a center frequency of 90 GHz and measured. Fig 4 shows the directivity and the coupling of the simulation and the measurement. Below 10 GHz signal levels drop below the instrument noise floor, and the isolation cannot be measured accurately. The couplers used in the integrated circuit were scaled for 180 GHz center frequency. To measure the directivity of this coupler, two additional test circuits with a NLTL for the RF source, a second NLTL with a high speed sampler for measuring and the coupler are implemented as test structures on the wafer. In one circuit the coupler can be measured in forward direction, in the other circuit in backward direction. Fig. 5 shows the measured directivity.

The directional couplers at the source frequency multiplier are designed for 6 dB coupling at a center frequency of 200 GHz. This combines relatively high coupling at high frequencies with sufficient attenuation especially at the fundamental frequency.

To characterize the sampling circuit linearity, a test sampling circuit was driven with a single 36 GHz RF input and the output was measured with its harmonics. As the result in fig. 6 shows, the harmonic generation is negligible for input powers below 0 dBm. In the NWA circuit, the measured signals are attenuated by the couplers at least by 10 dB, hence S-parameters of amplifiers with an output power up to 10 dBm can be measured.

One NWA circuit is connected to an on-wafer sampler, so the stimulus signal power at the DUT can be measured. Fig. 7 shows the result, when the multiplier NLTL is driven with 12 dBm input power. The output power varies from -14 to -35 dBm over the 50-200 GHz bandwidth, 5-15 dB lower than simulated. The discrepancy lies in the frequency-dependent attenuation of the sampling circuits, which is approximately 1 dB at lower frequencies and increases up to estimated 10 dB at 200 GHz. In addition in this simulation the couplers could not be simulated with skin-effect losses. At 200 GHz, the stimulus signal power is -35 dBm, which is sufficient for a high signal-to-noise ratio at the IF ports. The stimulus power of -14 dBm can be too high for amplifiers to ensure linearity, so a second IC was fabricated with an additional coupler in the stimulus signal path to attenuate the drive power at lower frequencies. The power at the DUT for this circuit is below -25 dBm for all frequencies.

To measure the directivity of the full integrated circuit, the incident and reflected waves of a NWA circuit with the open test port are compared with the measurement

of a second NWA circuit with a nominal  $50 \Omega$  ( $44 \pm 1.5 \Omega$ ) chip resistor (fig. 8). The directivity is  $> 10$  dB, dropping to  $\sim 7$  dB in a band between 160-190 GHz. In combination with high signal-to-noise ratios, the directivity should be sufficient to permit calibration to 200 GHz.

### III. CONCLUSION

We have demonstrated the first NLTL-based integrated circuit for network analysis within 50-200 GHz which can be used as a S-parameter test set for the HP8510. Packaging these chips into active probes will permit accurate and convenient on-wafer S-parameter measurements and will be performed in the near future at our institute.

### IV. REFERENCES

- [1] R. Pullela, Q. Lee, B. Agarwal, D. Mensa, J. Guthrie, L. Samoska, and M. J. W. Rodwell, "A  $>400$  GHz  $f_{max}$  transferred-substrate HBT integrated circuit technology", Device Research Conf. Tech. Dig. 1997, pp. IIIB-2.
- [2] R. Y. Yu, M. Reddy, J. Pusl, S. T. Allen, M. Case, M. J. W. Rodwell, "Millimeter-wave on-wafer wave form and network measurements using active probes", IEEE Transactions on Microwave Theory and Techniques, vol. 43, no. 4, pp. 721-729, April 1995.
- [3] M. J. W. Rodwell, M. Kamegawa, R. Y. Yu, M. Case, E. Carman, K. S. Giboney, "GaAs nonlinear transmission lines for picosecond pulse generation and millimeter-wave sampling", IEEE Transactions on Microwave Theory and Techniques, vol. 39, no. 7, pp. 1194-1204, April 1991.
- [4] HP85180A High-Frequency Structure Simulator, Hewlett Packard.

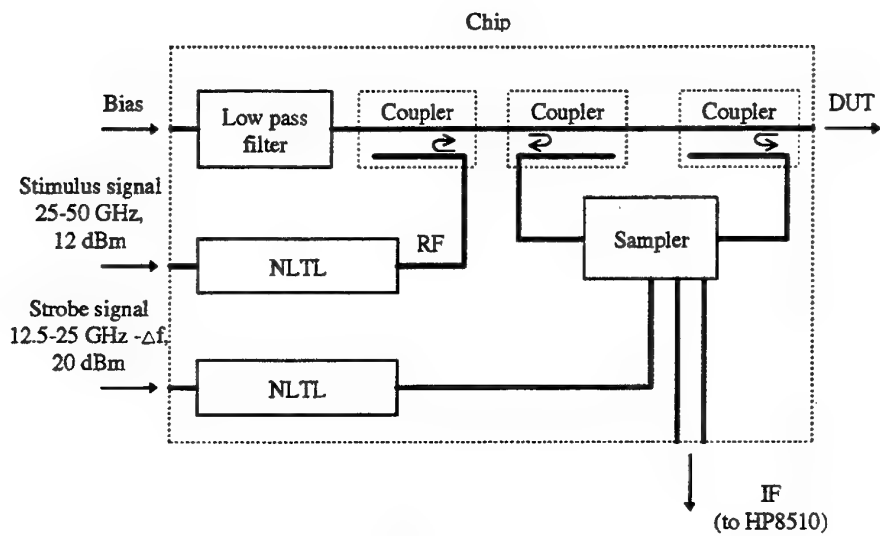


Fig. 1: Block diagram of the chip.

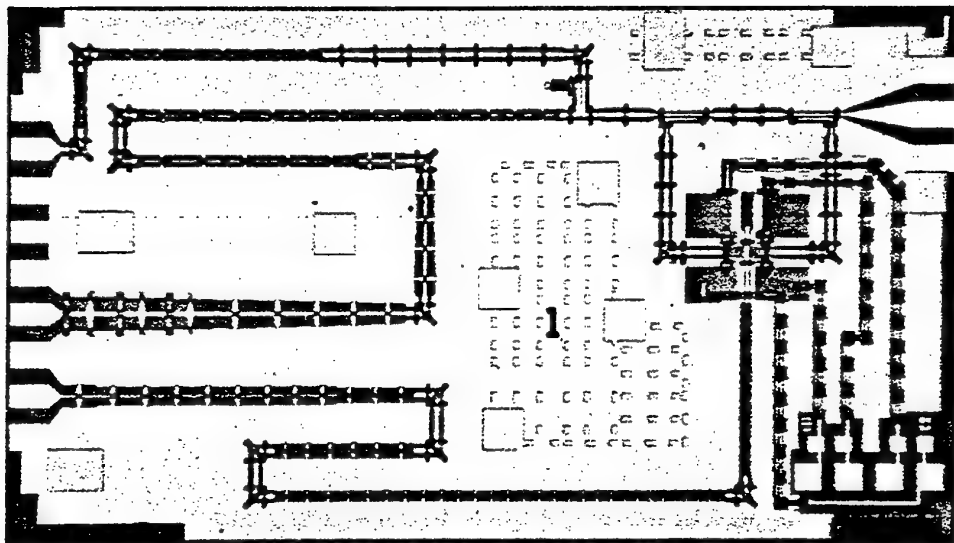


Fig. 2: Microphotograph of the chip. Chip size 3.4 x 2 mm<sup>2</sup>.

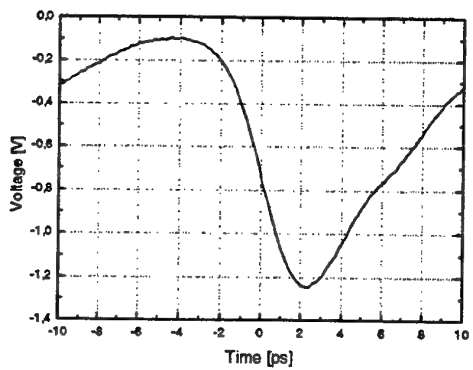


Fig. 3: Measured voltage waveform of the stimulus  
NLTL with 12 dBm input power at 50 GHz, fall  
time  $\sim 3.2$  ps.

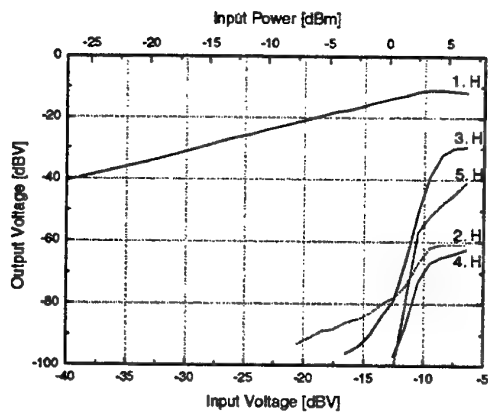


Fig. 6: Nonlinearity of the sampler with a 36 GHz  
input frequency.

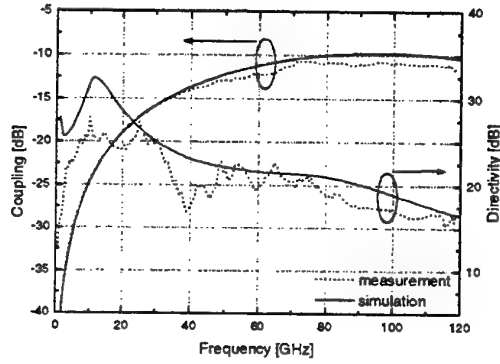


Fig. 4: Simulated and measured coupling and  
directivity of the coupler, designed for 90 GHz center  
frequency.

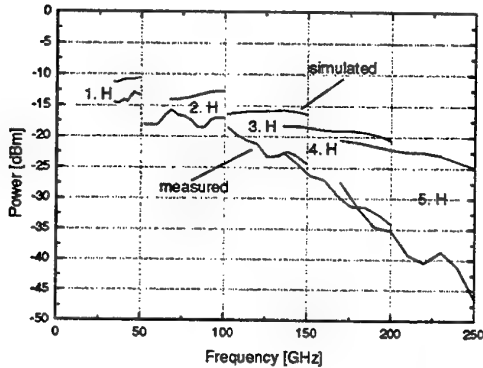


Fig. 7: Simulated and measured power at the DUT.  
The measurement is not corrected for the sampling  
circuit attenuation.

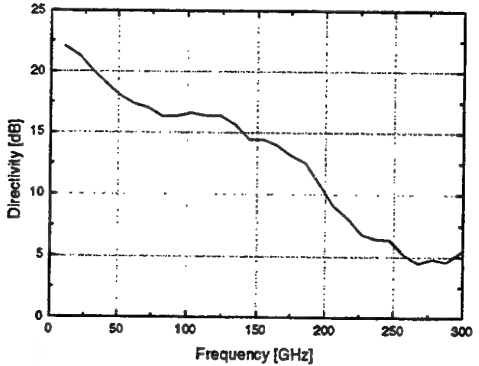


Fig. 5: Measured directivity of the couplers de-  
signed for 180 GHz center frequency.

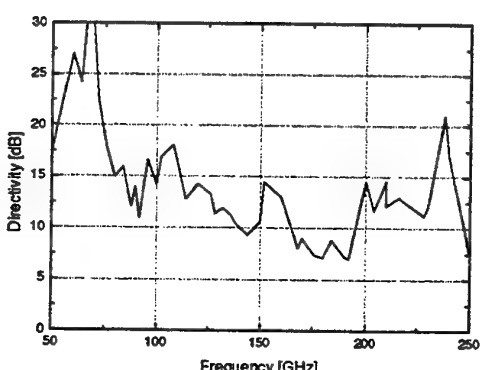


Fig. 8: Measured directivity of the full chip.

# Gas Absorption Spectroscopy with Electronic Terahertz Techniques

D.W. van der Weide, *Member, IEEE*, F. Keilmann, V. Agrawal, and J. Murakowski

**Abstract**—We report the first gas absorption spectra measured with an all-electronic terahertz spectrometer. This instrument uses phase-locked microwave sources to drive GaAs nonlinear transmission lines that produce picosecond pulses, enabling measurement of broadband spectra. By sweeping the fundamental excitation, the spectrometer can also measure single lines with Hertz-level precision, a new mode of operation not readily available with optoelectronic THz techniques. Since this system is based on integrated circuits, it could ultimately function as an inexpensive gas sensing system, e.g. for vehicle emissions.

**Index terms**—spectrometer, electronic terahertz, nonlinear transmission line, gas absorption

## I. INTRODUCTION

There is a strong need for multi-species gas sensing to monitor automotive and factory emissions, particularly in the presence of particulates (e.g. soot from diesels) that scatter near-infrared radiation (NIR) used in current gas sensors.

For wavelengths longer than the NIR, Fourier-transform infrared (FTIR) spectroscopy is the dominant method for measuring multiple gas absorption spectra[1]. While this technique is employed to accurately measure in the millimeter-wave regime with specialized equipment[2], the relative weakness of the black-body source (usually a mercury vapor arc lamp) below  $10 \text{ cm}^{-1}$  (300 GHz) requires prohibitively long scans and averaging times.

In this work we employ a spectroscopic method that is not only compact but also free of the need for a coherent detector so that an incoherent (e.g. photoconductive or bolometric) detection mechanism can be used (Fig. 1). This eliminates the noise inherent in a sampling detector and establishes a baseline for future fully integrated implementations that would use sampling detectors.

## II. EXPERIMENTAL SETUP

In the spectrometer we use here we spatially combine the freely propagating beams from two coherent picosecond pulse generators (which have discrete spectra ranging from  $\sim 6$  to  $> 450 \text{ GHz}$ ), resulting in a compact, reliable, and easy-to-implement micro- and millimeter-wave source for spectroscopy. Because this dual-source interferometer (DSI) modulates each harmonic of one source with a precisely-offset harmonic from the other source—both sources being driven with stable phase-locked synthesizers—the resultant beat frequency can be low enough for detection by a standard composite bolometer[3]. Room-temperature detection possibilities for the DSI include antenna-coupled Schottky diodes, which we have under development.

### A. Spectroscopy using nonlinear transmission lines

To generate the broadband (discrete) spectral energy for this application, we use nonlinear transmission line (NLTL) pulse generators coupled to broadband planar antennas. The GaAs IC NLTLs used in this work consist of series inductors (or sections of high-impedance transmission line) with varactor diodes periodically placed as shunt elements. On this structure at room temperature a fast ( $\sim 1\text{-}2 \text{ ps}$ ) voltage step develops from a sinusoidal input because the propagation velocity  $u$  is modulated by the diode capacitance,  $u(V) = 1/\sqrt{LC(V)}$ , where  $L$  is the line inductance and  $C(V)$  the sum of the diode and parasitic line capacitance[4, 5]. Limitations of the NLTL arise from its periodic cutoff frequency, waveguide dispersion, interconnect metallization losses, and diode resistive losses. Improvements in NLTL design have resulted in sub-picosecond pulses at room temperature[6].

In the dual-source interferometer, the output of each NLTL feeds an integrated bow-tie antenna (Fig. 2) mounted at the focus of a hyperhemispherical high-resistivity silicon lens[7]. These lenses in turn are mounted at the foci of off-axis paraboloidal mirrors. The beams collimated by the mirrors are either transmitted (Source “A”) or reflected (Source “B”) by a wire-grid polarizing beamsplitter. Each beam then contributes equally to the final, linearly-polarized beam by arrangement of a final wire-grid polarizer mounted at  $45^\circ$  to the beamsplitter. Note that, while the prototype

The authors are with the Department of Electrical and Computer Engineering, University of Delaware, Newark, DE. F. Keilmann is with the Max-Planck-Institut für Biochemie, Martinsried, Germany.

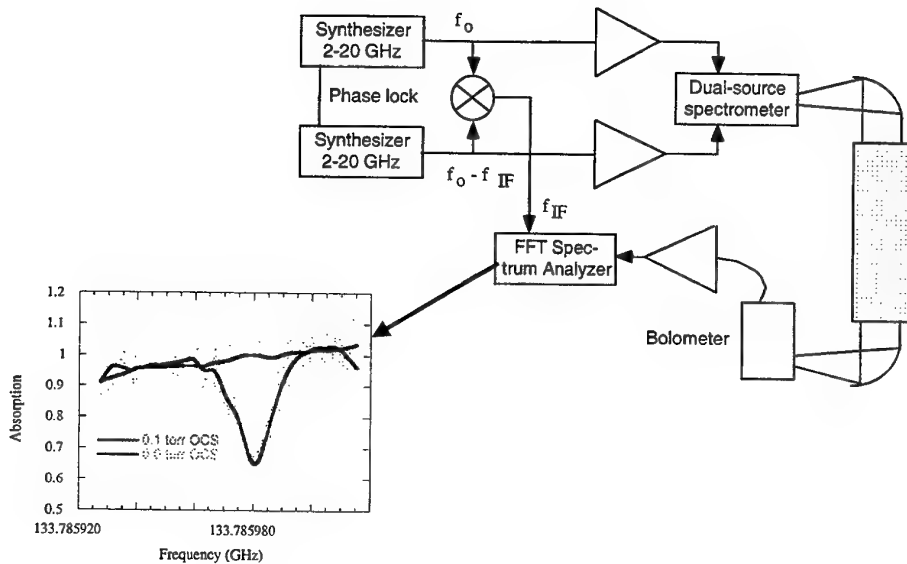


Fig. 1. Dual-source spectrometer system configured for gas absorption measurements. Inset shows raw and smoothed data from 0.1 torr OCS vs. vacuum from a 76 cm long cell, uncorrected for background power slope. Horizontal scale is 20 kHz per large division.

construction is already small (~ 170 mm long, 120 mm wide, and 80 mm high), it would be possible to fabricate two antennas and their circuitry on the same substrate, making the whole system extremely compact[8]. We also note that other workers have described similar ideas using laser-triggered photoconductive switches[9-11], but one advantage of the current system is its all-electronic approach, which offers precise amplitude (0.01 dB) and frequency (1 Hz) control of the fundamental excitation.

offset is used as a trigger for a Fast Fourier Transform (FFT) spectrum analyzer or digital lock-in amplifier. While the synthesizers and broadband power amplifiers used in the present demonstration are expensive, they could be replaced by an inexpensive single source combined with a new NLTL-based frequency translator[12].

### III. RESULTS

As shown in Fig. 1, the DSI can illuminate a single-pass absorption cell using off-axis paraboloidal mirrors to collimate the radiation and collect it for detection by the bolometer. Using a digital lock-in amplifier, we could measure a single harmonic of the DSI, in this case at 133.785980 GHz, the 20<sup>th</sup> harmonic of the fundamental of 6.689299 GHz. To measure the data shown, we used a third synthesizer to provide the 10 MHz timebase for the microwave synthesizers then varied this 10 MHz signal to continuously sweep the harmonics of the DSI. This enabled the extremely narrow linewidth of 0.1 torr OCS to be resolved, with an equivalent  $Q (f_0/\Delta f)$  of  $> 8 \times 10^9$ . We have also measured CO and NH<sub>3</sub> lines using the same method.

By measuring nominally 40 torr OCS absorption in the conventional fixed-fundamental mode (Fig. 3), we observed good correspondence with the predictions of the HITRAN molecular database, though some effects of standing waves were apparent.

Fig. 2. Dual-source interferometer configuration. Each source/antenna combination is at the focus of a paraboloidal mirror and radiates a polarized beam, which is transmitted ("A") or reflected ("B") by the polarizing beamsplitter (PB). The output polarizer (P) selects half the power of each beam. The output waveform is that detected by a bolometer [3].

Each source is fed by a 100-500 mW sinewave generated by one of two microwave synthesizers, both of which share a common 10 MHz timebase. The output of one synthesizer is offset by  $\Delta f \ll f_0$  ( $\Delta f \sim 100$  Hz;  $f_0 = 3-10$  GHz), and this

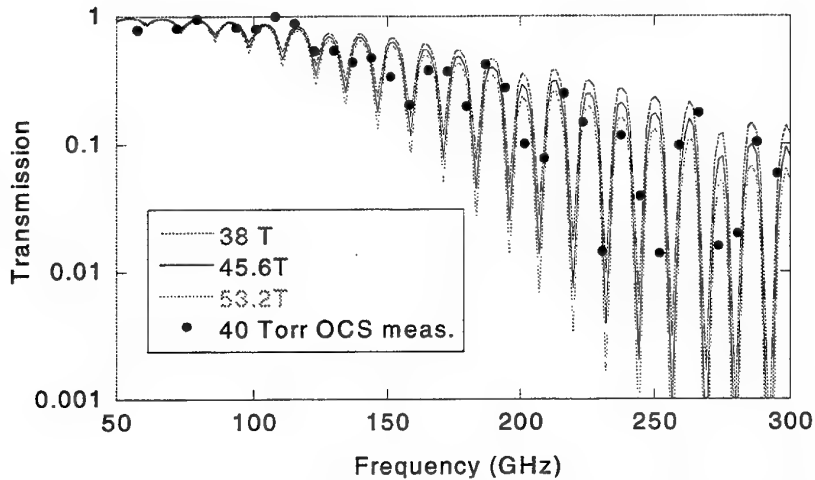


Fig. 3. 40 torr OCS broadband absorption data from a 4 meter cell (points) compared to HITRAN database predictions for 38, 45.6 and 53.2 torr OCS.

#### IV. CONCLUSIONS

We have described and demonstrated a technique for gas absorption spectroscopy using a new all-electronic THz interferometer having no moving parts but rather one whose phase is controlled electronically via a frequency offset between its two identical sources. This enables extremely high quality factor measurements of low-pressure absorption while ensuring absolute accuracy set by phase-locked synthesized sources.

This work lays the foundation for multi-species gas spectroscopy using multiple-resonant cavities and fully integrated THz sources and detectors.

#### V. ACKNOWLEDGMENT

This work is supported by a Ford Motor Company University Research Award, DARPA, ONR YIP, NSF PECASE, and the University of Delaware Research Foundation.

#### VI. REFERENCES

- [1] G. W. Chantry, *Long-wave optics*, vol. 1. London: Academic Press, 1984.
- [2] M. N. Afsar, "Dielectric measurements of millimeter-wave materials," *IEEE Transactions on Microwave Theory and Techniques*, vol. 32, pp. 1598-1609, 1984.
- [3] D. W. van der Weide and F. Keilmann, "Picosecond dual-source interferometer extending Fourier-transform spectrometer to microwave regime," in *1996 IEEE MTT-S International Microwave Symposium Digest*, vol. 3. New York, NY, USA: IEEE, 1996, pp. 1731-1734.
- [4] M. J. W. Rodwell, M. Kamegawa, R. Yu, M. Case, E. Carman, and K. S. Giboney, "GaAs nonlinear transmission lines for picosecond pulse generation and millimeter-wave sampling," *IEEE Transactions on Microwave Theory and Techniques*, vol. 39, pp. 1194-204, 1991.
- [5] M. J. W. Rodwell, S. T. Allen, R. Y. Yu, M. G. Case, U. Bhattacharya, M. Reddy, E. Carman, M. Kamegawa, Y. Konishi, J. Pusl, R. Pullela, and J. Esch, "Active and nonlinear wave propagation devices in ultrafast electronics and optoelectronics," *Proceedings of the IEEE*, vol. 82, pp. 1035-59, 1994.
- [6] D. W. van der Weide, "Delta-doped Schottky diode nonlinear transmission lines for 480-fs, 3.5-V transients," *Applied Physics Letters*, vol. 65, pp. 881-883, 1994.
- [7] D. W. van der Weide, "Planar antennas for all-electronic THz systems," *Journal of the Optical Society of America B*, vol. 11, pp. 2553-2560, 1994.
- [8] D. W. van der Weide and F. Keilmann, "Coherent periodically pulsed radiation spectrometer," United States patent 5,748,309, May 5, 1998.
- [9] B. I. Greene, J. F. Federici, D. R. Dykaar, R. R. Jones, and P. H. Bucksbaum, "Interferometric characterization of 160 fs far-infrared light pulses," *Applied Physics Letters*, vol. 59, pp. 893-895, 1991.
- [10] S. E. Ralph and D. Grischkowsky, "THz spectroscopy and source characterization by optoelectronic interferometry," *Applied Physics Letters*, vol. 60, pp. 1070-1072, 1992.
- [11] C. Karadi, S. Jauhar, L. P. Kouwenhoven, K. Wald, J. Orenstein, and P. L. McEuen, "Dynamic response of a quantum point contact," *Journal of the Optical Society of America B*, vol. 11, pp. 2566-2571, 1994.
- [12] P. Akkaraekthalin, S. Kee, and D. W. van der Weide, "Distributed broadband frequency translator," in *1998 IEEE MTT-S International Microwave Symposium Digest*, vol. 3. New York, NY, USA: IEEE, 1998, pp. 1431-1434.

# QUASI-OPTICS VECTOR MEASUREMENTS OF DIELECTRICS FROM 8 GHz TO THE THz.

P. Goy<sup>1</sup>, S. Caroopen<sup>1</sup>, M. Gross<sup>1</sup>, J. Mallat<sup>2</sup>, J. Tuovinen<sup>2</sup>, F. Mattiocco<sup>3</sup>,

<sup>1</sup>AB Millimètre, 52 rue Lhomond 75005 Paris,

tel: 33 1 47 07 71 00, fax: 33 1 47 07 70 71, abmm001@ibm.net

<sup>2</sup> Millimetre Wave Laboratory of Finland Millilab, ESA external laboratory, Helsinki University of technology, Radio laboratory, PO Box FIN-02015 HUT Finland, juha.mallat@hut.fi

<sup>3</sup> IRAM Domaine universitaire, 300 rue de la piscine, 38406 St Martin d'Hères, mattiocc@iram.fr

## 1. INTRODUCTION.

Dielectrics characterisation is made easier when using vector measurements. These measurements give directly the permittivity, since the phase rotation corresponds to a lengthening of the optical path across the sample. Measurements that are most commonly done are measurements between horns (most of the time by taking advantage of refocusing lenses). The comparison between the detected phase and amplitude with or without the sample gives the permittivity  $\epsilon'$  and the loss  $\tan\delta$ . After filtering using the Fourier transform which operates a time gating, one gets rid of almost all stationary waves effects [1].

In case of samples with very low loss (in practice  $\tan\delta \leq 0.001$ ), this type of simple measurement between horns is not sensitive enough to measure the loss  $\tan\delta$ . One has to make use of the technique of the open Fabry-Pérot cavity, which implies multiplying the number of times that the wave passes through the sample. In comparison with the unloaded cavity, the resonance with the sample is displaced due to the change of the optical path across the sample, and the quality factor Q is damped down due to loss in the sample.

In principle this open cavity measurement method can be performed by using only a scalar detection. Vector detection, however, will be necessary to obtain a first determination of the permittivity  $\epsilon'$  of the sample. In addition, the resonance of the loaded cavity (or even unloaded) may present distorted forms, resulting from the combination of resonant / non resonant contributions (the direct input / output coupling being made easier by the introduction of the sample). The vector analysis (circular shaped resonance in polar plot) allows complete and precise measurement from any form of resonance.

Vector measurements in the range of 8 to 1000 GHz are made possible thanks to the vector network analyser developed since 1989 [2].

To compensate the lack of broadband primary sources, the emitted wave is produced by an harmonic generator (HG). The wave is detected by an harmonic detector (HM). Up to 200 GHz, local oscillators are centimetre sources integrated to the analyser. Whereas

up to the THz, local oscillators are Gunn millimetre sources (centred around 100 GHz).

## 2. MEASUREMENTS BETWEEN HORNS.

The measurement bench consists of two high density polyethylene lenses (HDPE) with no surface coating, focal length  $f = 100$  mm, aperture of 82 mm, and placed at 4f from each other. The HG source is at 2f in front of the first lens and the detector HM is at 2f behind the second lens. The horns used (12 pairs) are corrugated horns in the Q-V-W-D bands (from 30 to 170 GHz), or bimodal (Potter) horns around 190, 285, 380, 475, 570, 665, 760, 855 GHz. The frequency response "in air" of the desired band is recorded at first, then the sample is introduced between the two lenses. The results are tainted with stationary waves effects outside the sample (Fig.1), which are eliminated by time-domain filtering on the FT (Fig.2). The remaining amplitude ondulations (Fig.2) show the stationary waves effects inside the sample, which acts as a Fabry-Pérot resonator (Figs.2-4), except for absorbing samples (Fig.5). Parasitic stationary wave effects are difficult to eliminate in the submillimeter domain (Fig.6).

## 3. CAVITY MEASUREMENTS.

We have used two open Fabry-Pérot cavities, each with a spherical mirror on top, and a plane mirror underneath, providing a horizontal surface on which the sample can be placed.

In the first cavity [3], the geometry is semi-confocal. The distance between mirrors is D, where  $D=150\pm2.5$  mm. D is adjustable by means of a micrometer screw. D is of the order of half the radius of curvature R of the spherical mirror, where  $R=305$  mm. The transverse dimension of the mirrors, made from gold-plated brass, is 65 mm. The input and the output of the microwave are realised by two coupling holes of 1 mm in diameter and 2.5 mm apart, drilled close to the centre of the plane mirror. This tunable cavity offers a maximum quality factor Q (empty cavity) of  $Q=165,000$  around 90 GHz, with  $Q>120,000$  from 80 to 100 GHz, and  $Q>70,000$  from 75 to 110 GHz. The resonance modes are easily identified (Fig.7).

The second cavity [4] has a nearly semi-spherical geometry. The plane mirror is at a fixed

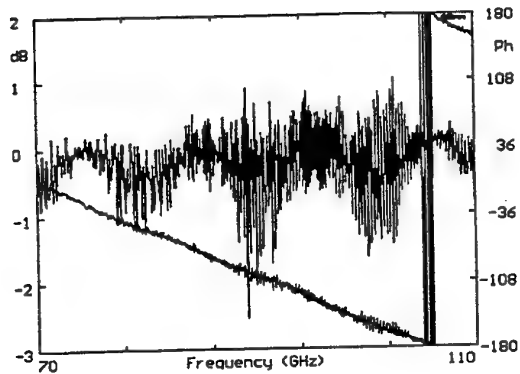


Fig.1. Transmission observed through a 10mm thick Teflon substrate. The descending slope represents the phase. The noisy aspect in the amplitude is due to stationary waves between the horns and the sample.

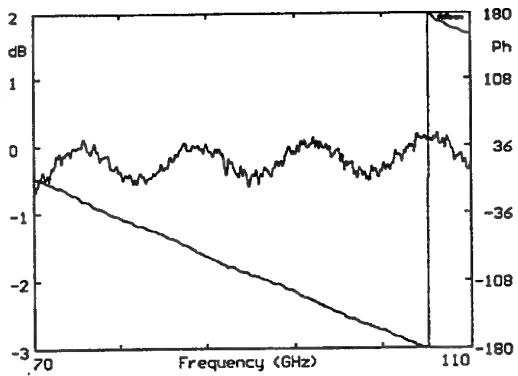


Fig.2. Same as in Fig.1. after filtering the stationary waves effects. The undulations in the amplitude give a period of  $\Delta F = c/2e\sqrt{\epsilon'}$  (where  $e$  is the thickness) in accordance to the observed phase variation:  $\epsilon' = 2.04$ . The losses are too small to be measured.

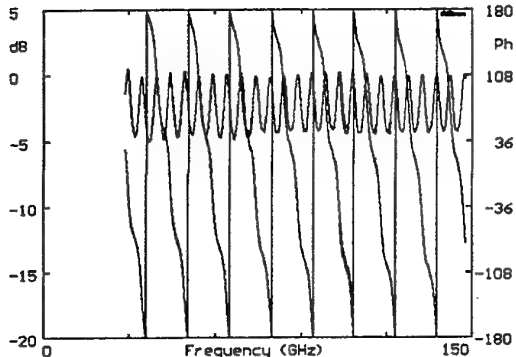


Fig.3. Same as in Fig.2, for a sapphire sample 9.97mm thick and  $\epsilon' = 9.40$ .

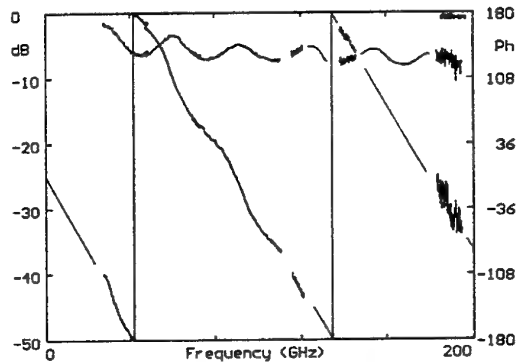


Fig.4. Like in Fig.2, through a 1.52mm thick ceramic substrate of MgO with 5% of SiC. We found  $\epsilon' = 10.4 \pm 0.2$  and a linear decrease of  $\tan\delta$  from 1.1 at 27 GHz to 0.46 at 190 GHz.

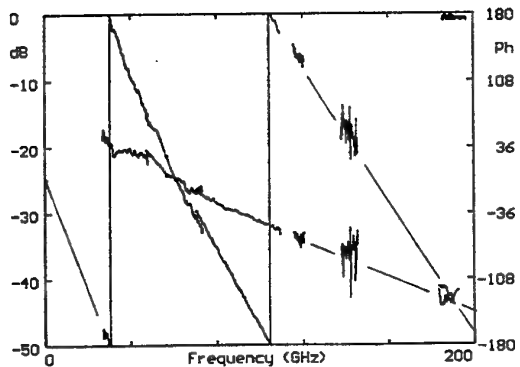


Fig.5 Ceramic AlN+40% SiC,  $e = 1.52$ mm thick. We found that  $\epsilon'$  varies linearly from 19 to 14 when the frequency goes from 28 to 190 GHz, with a decrease in the loss  $\tan\delta$  from 1 to 0.46.

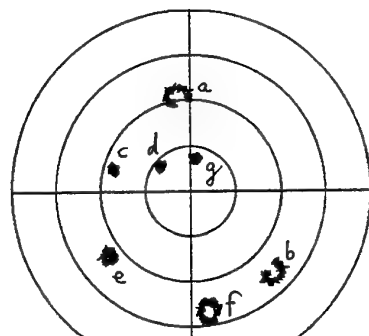


Fig.6. Polar plots of transmission curves from 567.3-568.3 GHz through 15mm in (a) and 10mm in (b) of rexolite with  $\epsilon' = 2.53$ ,  $\tan\delta = 0.0046$ ; 3mm in (c) and 5.75 mm in (d) of plexiglass with  $\epsilon' = 2.60$ ,  $\tan\delta = 0.028$ ; 1.15mm in (e) and 0.93mm in (f) of araldite with  $\epsilon' = 2.90$ ,  $\tan\delta = 0.045$ ; 4.13mm of PVC (Poly-Vinyl Chloride) in (g) with  $\epsilon' = 2.83$ ,  $\tan\delta = 0.041$ .

distance D=143.186 mm from the spherical one. It is close to the center of curvature of the spherical mirror, for which R=149.542 mm. The upper spherical mirror is made from silver coated brass. It includes two coupling holes (for transmission measurements) of 0.8 mm diameter, and 3.5 mm apart, drilled close to the mirror center. The transverse diameter is 180 mm. The lower mirror is made from polished aluminium. It has a diameter of 92 mm. This cavity has the possibility of working in a wide frequency band, from 62 GHz, where Q=138,000, to 310 GHz, where Q=118,000. The quality factor Q is always higher than 110,000, going over 240,000 in the 90-140 GHz band.

Among other advantages (good Q, excellent frequency coverage), the quasi-hemispherical geometry [5] offers a narrow field distribution (waist Wo) located at the center of the plane mirror (Wo=5 mm at 100 GHz). We can therefore characterise samples of small diameters.

The disadvantage of the semi-spherical geometry is that high order modes can be submitted to a negligible diffraction (contrary to the semi-confocal geometry). As a consequence, huge quantities of resonances are observed, in which the identification of the low-order modes to be chosen must be operated carefully with diaphragms (Fig.8).

When varying the frequency, all Fabry-Pérot resonators with fixed distance D between mirrors give periodic resonances, with an interval  $\Delta F$ :

$$\Delta F = c/2D \quad (1),$$

where  $c$  is the speed of light in the medium between mirrors, for instance in air we have measured  $c=2.99711E8$  m/s at 300 GHz. The resonance frequency  $F$  of a plane-spherical open cavity is given by:

$$F = \Delta F [ q + 1 + [ (2p + \ell + 1)/\pi] \cdot \arctan \sqrt{D/(R-D)} ] \quad (2),$$

where  $p, \ell, q$  are indices of the TEM $p$ ,  $\ell, q$  mode. The quantity  $(q+1)$  is the number of half-wavelengths in the resonator. For fundamental Gaussian modes,  $p = \ell = 0$ . In the case of cavity number 1, since  $D \approx R/2$ , Eq.2 gives:

$$F = \Delta F ( q + 1 + 0.25 ) \quad (3),$$

where  $\Delta F$  depends on the the position of the spherical mirror (tunable cavity). In the case of cavity number 2, one has:

$$F = \Delta F ( q + 1 + 0.4339 ) \quad (4),$$

with  $\Delta F = 1046.58$  MHz (non-tunable cavity).

For the best matching of the wave at the surface of the sample, the measurements must be done at frequencies for which the number of half-wavelengths inside the sample is as close as possible to an integer.

The characterisation of a dielectric material will be done at one of these frequencies  $F_s$  with the sample inside the cavity. The loaded quality factor  $Q_s$  will also be measured. Then the sample is removed, without any change of the distance  $D$  between mirrors. The empty cavity gives a resonance frequency  $F_0$  and a quality factor  $Q_0$ . From the four parameters  $F_s, Q_s, F_0, Q_0$  and from the geometry of the cavity and of the sample, one can calculate the permittivity  $\epsilon'$  and the loss  $\tan\delta$  of the sample. For that purpose, there are iterative equations [4] which are part of the software of the vector analyser.

The best measured low-loss material is HDPE (High-Density-Poly-Ethylen) where the results on four samples, from 90 to 310 GHz, are  $\epsilon'=2.323+/-0.016$ ,  $\tan\delta=(2.45+/-0.15)E-4$ . With three samples of Teflon in the 84-94 GHz interval, the results are  $\epsilon'=2.040+/-0.007$ ,  $\tan\delta=(3.1+/-0.3)E-4$ , and, in the interval 251-305 GHz:  $2.033+/-0.01$  (relative decrease of -0.36% on  $\epsilon'$ ), and  $\tan\delta=(4.5+/-0.3)E-4$  (relative increase of 45%). Teflon can be birefringent (Figs.10-12). Rexolite (one sample) gives at 95 GHz:  $\epsilon'=2.535$ ,  $\tan\delta=13.2E-4$ , and at 257 GHz:  $\epsilon'=2.527$ ,  $\tan\delta=27E-4$ .

## REFERENCES.

1. P. Goy, M. Couranjou, M. Gross, JCMM'94, Brest 19-21 octobre 1994.
2. P. Goy, M. Gross, J-M. Raimond, 15th Int. Conf. on IR and mm Waves, Orlando FL, SPIE 1576, 487 (1990), R.E. Temkin Ed.
3. AB MILLIMETRE, model FP-LSC-VEWF.
4. T.M. Hirvonen, P. Vainikainen, A. Lozowski, A. Räisänen, IEEE Transactions on Instrumentation and Measurements, 45, N°4, 780 (1996).
5. R. Heidinger, F. König, 14th Int. Conf. on IR and mm Waves, Würzburg, 2-6 octobre 1989, p.541, M. Von Ortenberg Ed. (1989).

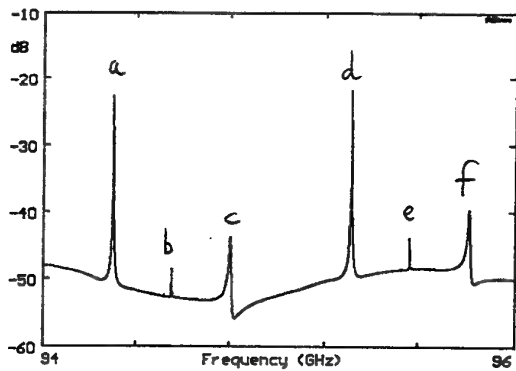


Fig.7 Transmission through the unloaded cavity n°1. The fundamental modes are in a ( $q=93$ ) and d ( $q=94$ ). A few secondary modes are visible:  $l=1$ ,  $p=0$  in (b) and (e);  $l=0$ ,  $p=1$  in (c) and (f) (Eqs2-3).

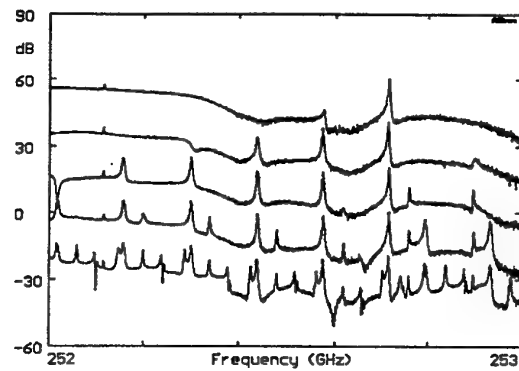


Fig.8. Transmission through the unloaded cavity n°2, without diaphragm (bottom) and with diaphragms of 30, 25, 20 and 16 mm (bottom to the top). The last mode is very clear with a  $q=240$  (Eqs 2-4).

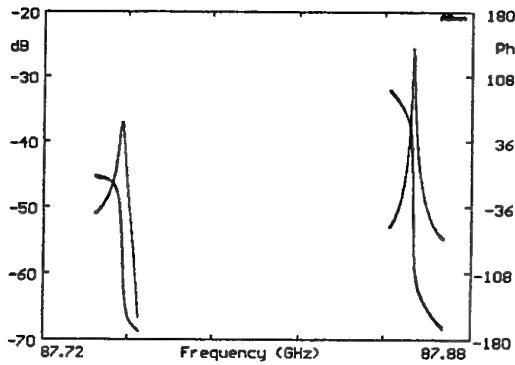


Fig.9. Transmission through the cavity n°1, empty (right) and loaded with a Polyethylen sample, 10.07mm thick (right). Experimental and Lorentzian fits. A shape for the amplitude and Z shape for the phase.

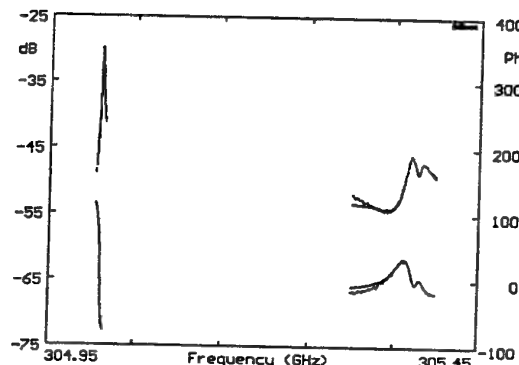


Fig.10. Transmission through the cavity n°2, empty (left) and loaded with a Teflon sample, 9.95mm thick (right). On top, the amplitude curve and below the phase curve. The folded ray shows that Teflon is anisotropic.

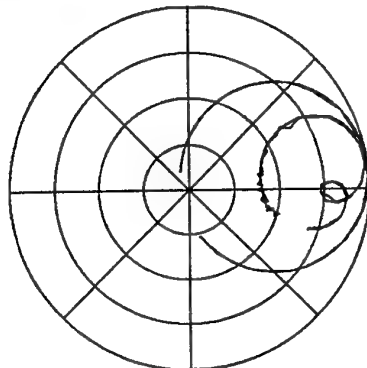


Fig.11. Polar plot of Fig.10, where all amplitudes have been normalised. The simple resonance(Lorentzian) gives a circle as expected, the doubled ray can be fitted by a double Lorentzian. The permittivity gap is narrow:  $\Delta\epsilon' = 2.033$ , i.e  $\Delta\epsilon'/\epsilon' = 0.001$ .

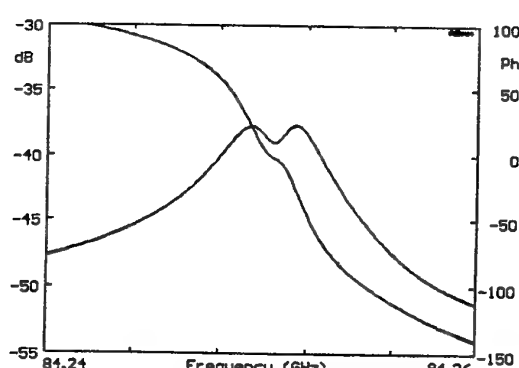


Fig.12. By rotating the Teflon disc on itself, we can find exactly the field polarisation which excites both permittivities, at  $45^\circ$  on the axes of the sample. The experimental curve and the fit of the double Lorentzian are undistinguishable.

# Narrowband Microwave Emission by a Frequency-locked Current Oscillation in a GaAs/AlAs Superlattice

E.Schomburg, M.Haeussler, K.Hofbeck, K.F.Renk, J.M.Chamberlain, D.G.Pavel'ev,  
Yu.Koschurinov, V.Ustinov, A.Zhukov, A.Kovsch, and P.S.Kop'ev

**Abstract**—We report on frequency locking of a self-sustained current oscillation in a GaAs/AlAs wide miniband superlattice oscillator emitting microwave radiation at 23 GHz with a power of about 0.3 mW. The current oscillation was caused by travelling dipole domains and the locking was due to interaction of the domains with an external narrowband high-frequency field. We observed that the linewidth of the frequency-locked oscillation was less than 10 Hz compared to 10<sup>5</sup> Hz for the free oscillator, indicating synchronisation of the dipole domain propagation with the external field.

## I. INTRODUCTION

Recently, it has been observed [1, 2] that doped superlattices with wide minibands show self-sustained current oscillations joint with the emission of microwave radiation in the GHz range. The current through the superlattices was carried by electrons belonging to the energetically lowest conduction miniband. The current-voltage characteristic of the superlattices showed a negative differential conductance produced by a negative differential velocity due to Bragg reflection of the miniband electrons; the effect has been predicted by Esaki and Tsu [3]. The current oscillation in a superlattice was associated with travelling dipole domains caused by instabilities of the space charge in the negative differential velocity region. The occurrence of travelling dipole domains as a consequence of Bragg reflection of miniband electrons was predicted earlier [4].

In this contribution we report on frequency-locking of an oscillator based on current oscillation due to travelling dipole domains in a GaAs/AlAs wide miniband superlattice. The superlattice oscillator was operated at room temperature.

E.Schomburg and J.M.Chamberlain are with the Department of Physics, University of Nottingham, University Park, Nottingham, NG7 2RD, United Kingdom.

M.Haeussler, K.Hofbeck, and K.F.Renk are with the Institut für Angewandte Physik, Universität Regensburg, D-93040 Regensburg, Universitätstr. 31, Germany.

D.G.Pavel'ev and Yu.Koschurinov are with the Department of Radiophysics, Nizhny Novgorod State University, Nizhny Novgorod, Russia.

V.Ustinov, A.Zhukov, A.Kovsch, and P.S.Kop'ev are with the A.F.Ioffe Physico-Technical Institute, St.Petersburg, Russia.

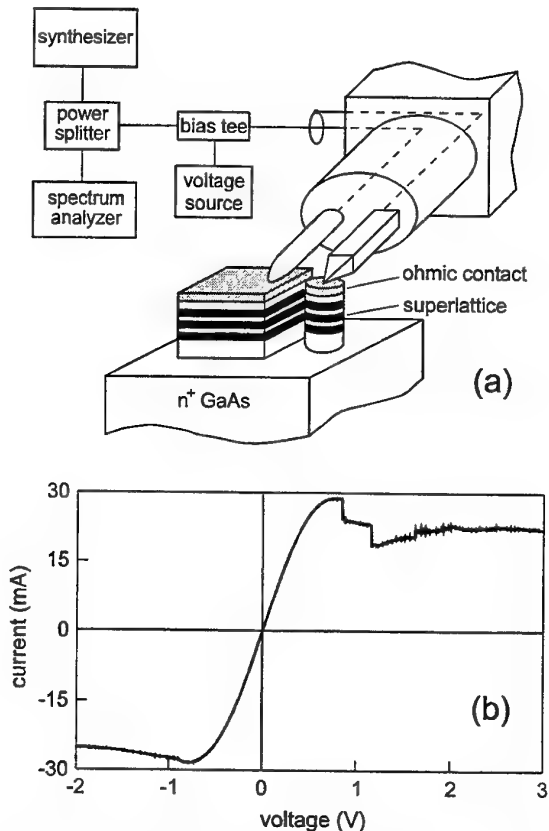


Fig.1. (a) SLED with high-frequency circuit and (b) current-voltage characteristic.

## II. EXPERIMENTAL

The main element of the oscillator was a superlattice electronic device (SLED, Fig.1a) fabricated by use of a superlattice (doping 1.4·10<sup>17</sup> cm<sup>-3</sup>) with 100 periods of 5.1 nm thick GaAs and 0.9 nm thick AlAs layers; the superlattice has been grown by molecular beam epitaxy and had a miniband width of 43 meV. The device consisted of two superlattice mesas with different cross sections (64 μm<sup>2</sup> and 10,000 μm<sup>2</sup>), both covered with ohmic contacts and connected by the n<sup>+</sup> GaAs substrate. The mesa with the smaller cross section acted as an active

element responsible for a non-linear current-voltage characteristic and for the current oscillation. A high-frequency probe needle (picoprobe 67A) connected the SLED to a  $50\Omega$  coaxial cable for transmission of the direct current and high-frequency (HF) current. Direct and HF current were separated from each other by a bias tee. The HF on-wafer probe technique of a superlattice device has been described elsewhere in detail [2]. A power splitter allowed the measurement of the spectrum of the microwave radiation emitted from the active superlattice and coupling of an external microwave field to the SLED. A narrowband synthesiser (Wiltron 69387 A) was used as an external microwave source; this provided radiation within a bandwidth of a few Hz.

### III. RESULTS

The current-voltage characteristic (Fig.1b) of the active superlattice showed a negative differential conductance and was almost antisymmetric up to the voltage, where the negative differential conductance set on. Current jumps in the region of negative differential conductance at positive voltages indicate the occurrence of current oscillations. We attribute the asymmetry of the current-voltage characteristic in the region of negative differential conductance to a geometric asymmetry of the active mesa having a cone-like shape rather than a cylindrical form (due to underetching).

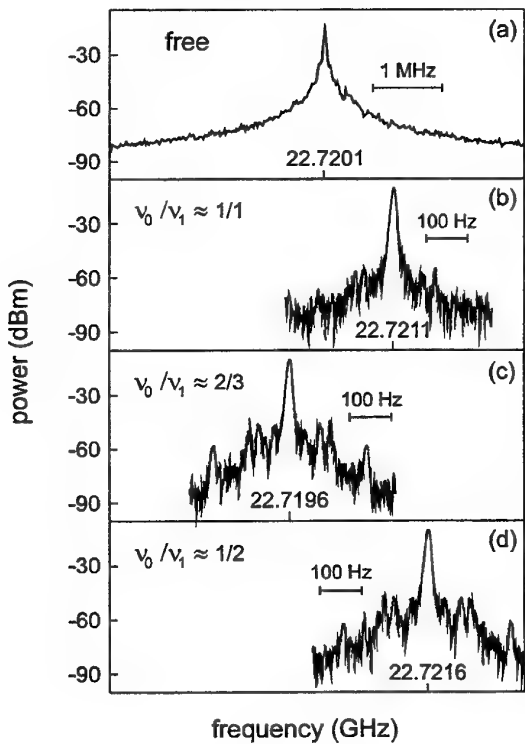


Fig.2. Emission spectrum of the free oscillator (a) with a natural frequency near 22.7201 GHz drawn at a frequency scale of 1 MHz, and of the locked oscillator for different driving frequencies  $v_1 = 22.7211$  GHz (b), 34.0794 GHz (c), and 45.4432 GHz (d) drawn at a frequency scale of 100 Hz. 10 dB loss in the power splitter has to be taken into account.

The superlattice oscillator showed a free self-sustained current oscillation giving rise to microwave radiation at a natural frequency  $v_0$  near 23 GHz with a power of about 0.3 mW and an efficiency of about 1% (Fig.2a). The linewidth at half maximum was about 100 kHz. Applying an external high-frequency field with a driving frequency  $v_1$  near the natural frequency resulted (Fig.2b) in the suppression of the free oscillation and the occurrence of a driven oscillation causing microwave radiation at a driven frequency  $v_0 = v_1$ ; i.e. the oscillator was frequency locked to the external field. Frequency locking was also observed for a driving field with a frequency close to  $3v_0/2$  (Fig.2c) or near  $2v_0$  (Fig.2d). The linewidth (less 10 Hz) of the frequency-locked oscillator was almost the same as that of the driving field. The power of the locked oscillator was almost the same as the power of the free oscillator. The differences in the peak height of the curves of Fig.2 are a consequence of different resolution bandwidths of the spectrum analyser used for the detection of the broad and the narrow lines.

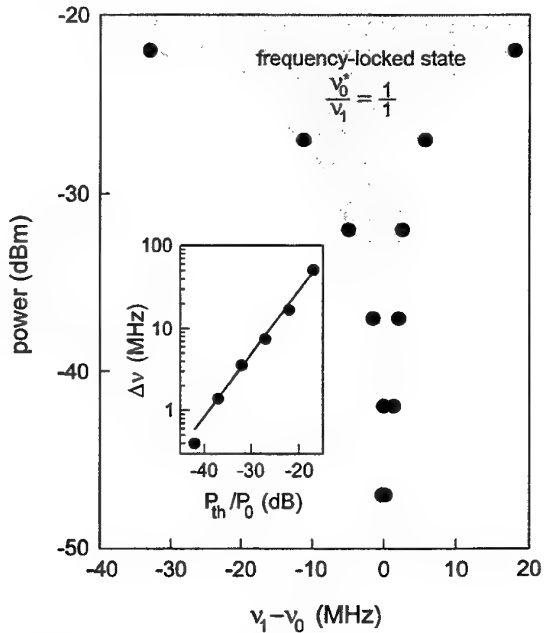


Fig.3. Locking behaviour for a frequency-locked state  $v_0/v_1 = 1/1$ . Points are experimental data of the threshold power and the shadowed region indicates the range of the frequency-locked state. Inset: Locking range as function of locking gain.

By changing the driving frequency, the frequency of the driven oscillator could be adjusted in a certain frequency range (locking range). The locking range of a frequency-locked state strongly depended on the driving power. Fig.3 shows the threshold power  $P_{th}$ , necessary to lock the free oscillator, as function of the frequency distance  $v_1 - v_0$  for the frequency-locked state  $v_0/v_1 = 1/1$ . In the shadowed region of Fig.3 the oscillator was locked, while outside this region the oscillation was disturbed by the driving field and quasiperiodic behaviour occurred. Frequency locking was observed up to a power as low as

30 nW, which was a factor of 10,000 less than the power  $P_0$  of the free oscillator. With increasing power of the external field, the region of frequency locking broadened.

#### IV. DISCUSSION

The free self-sustained current oscillation was caused by travelling dipole domains with a natural frequency related to the ratio  $0.7 v_p/L$ , where  $v_p$  is the peak drift velocity ( $20 \cdot 10^5$  cm/s estimated from the maximum current) and  $L$ , the superlattice length. Our results indicate that the boundary conditions, imposed by the driving field on the domain formation and propagation, result in the locking behaviour of the current oscillation and in line narrowing. We suggest that fluctuations in domain formation and velocity (caused by charge density fluctuations), were responsible for the linewidth of the free oscillator and that a synchronisation of the domain propagation with a driving field resulted in a suppression of the fluctuations and, therefore, in a reduction of the linewidth. We note that a decrease of the oscillator linewidth by injection locking was discussed earlier [5], however, an oscillator with a device having a negative resistance coupled to a RCL circuit has been considered. Experimental evidence for line narrowing by frequency locking was observed for different oscillator types (Gunn and Read diode oscillators [6] and avalanche transit time oscillators [7]). We found (inset of Fig.3) that the locking range  $\Delta v = 2|v_1 - v_0|$  as function of the locking gain (ratio between threshold power  $P_{th}$  and power of free oscillator  $P_0$ ) can be almost described by an square root dependence, which was derived years ago by Adler [8] for an injection locked oscillator with a negative resistance device in a RCL circuit.

Superlattice oscillators emitting narrowband radiation at higher frequencies should be achievable by the

use of superlattices with larger miniband widths. As recently shown, oscillation frequencies at a fundamental harmonic up to 65 GHz [2] or by use of higher harmonics up to 200 GHz [9] can be achieved.

#### V. CONCLUSION

In conclusion, we presented a frequency-locked superlattice oscillator with a simple design that is suitable for generation of ultra-narrowband high-frequency radiation.

#### VI. ACKNOWLEDGEMENT

One of us (E.S.) would like to acknowledge financial support from the European Commission (EC) through the INTERACT Project (FMRXCT 960092). Especially, we would like to thank W.Strasser from the BSW Test Systems & Consulting GmbH for making it possible for us to use the Synthesizer Wiltron 69387 A and his technical assistance.

- [1] K.Hofbeck, J.Grenzer, E.Schomburg, A.A.Ignatov, K.F.Renk, D.G.Pavel'ev, Yu.Koschurinov, B.Melzer, S.Ivanov, S.Schaposchnikov, and P.S.Kop'ev, Phys. Lett. A **218**, 349 (1996).
- [2] E.Schomburg, S.Brandl, K.Hofbeck, T.Bloemeier, J.Grenzer, A.A.Ignatov, K.F.Renk, D.G.Pavel'ev and Yu.Koschurinov, V.Ustinov, A.Zhukov, A.Kovsch, S.Ivanov, and P.S.Kop'ev, Appl. Phys. Lett. **72**, 1498 (1998).
- [3] L.Esaki and R.Tsu, IBM J. Res. Dev. **14**, 61 (1970).
- [4] M.Büttiker and H.Thomas, Phys. Rev. Lett. **38**, 78 (1977).
- [5] K.Kurokawa, IEEE MTT-**16**, 234 (1968).
- [6] J.Josenhans, Proc. IEEE (Lett.) **54**, 1478 (1966).
- [7] J.R.Ashley and F.M.Palka, Proc. IEEE (Lett.) **58**, 155 (1970).
- [8] R.Adler, Proc. IEEE **61**, 1380 (1973); reprinted from Proc. IRE **34**, 351 (1946).
- [9] E.Schomburg, K.Hofbeck, J.Grenzer, T.Bloemeier, A.A.Ignatov, K.F.Renk, D.G.Pavel'ev, Yu.Koschurinov, V.Ustinov, A.Zhukov, S.Ivanov, and P.S.Kop'ev, Appl. Phys. Lett. **71**, 401 (1997).

# Plasma Wave Electronics: Terahertz Sources and Detectors Using Two Dimensional Electronic Fluid in High Electron Mobility Transistors.

M. S. Shur <sup>1</sup>, J.-Q. Lü <sup>1</sup>, and M. I. Dyakonov <sup>2</sup>

**Abstract**— We discuss our recent theoretical and experimental results dealing with plasma waves in High Electron Mobility Transistors (HEMTs) and their applications for sources and detectors operating in millimeter and submillimeter range. Plasma waves in short-channel HEMTs have a resonant response. The HEMTs operating in a plasma wave regime should respond to much higher frequencies than for conventional, transit-time limited devices, since the plasma waves propagate much faster than electrons.

**Index Terms**— Plasma Wave Electronics, High Electron Mobility Transistor, terahertz radiation, detector

## I. INTRODUCTION

Plasma waves in a FET have a linear dispersion law similar to sound waves, and a field effect transistor channel acts as a resonance cavity for plasma waves. A quality factor of such a cavity is on the order of  $Q = sL/\tau$ , where  $s$  is the velocity of the plasma waves,  $L$  is the channel length, and  $\tau = \mu m/e$  is the momentum relaxation time. Here  $m$  is the electron effective mass and  $\mu$  is a low field mobility. In a high mobility, short channel FET, plasma wave instability may occur due to the plasma wave amplification (caused by the wave reflections from the channel boundaries).

$s$  is typically on the order of  $10^8$  cm/s, which is much larger than the electron drift velocity in the two-dimensional electron gas (2DEG) in the FET channel. This is why the propagation of plasma waves can be used for new regimes of FET operation, with a much higher frequency than for conventional, transit-time limited regimes. If plasma oscillations can be excited in a FET by a *dc* current, the FET can be used as an oscillator operating in the terahertz range.<sup>1</sup> Nonlinear properties of the plasma waves can be utilized for terahertz detectors, broad band detectors, mixers, and frequency multipliers.<sup>2,3</sup>

As an example, let us consider an AlGaAs/InGaAs High Electron Mobility Transistor similar to one described in<sup>4</sup>. At 77 K, the momentum relaxation time in 2DEG in InGaAs (where ionized impurity scattering is suppressed) is

$\tau \sim 10^{-11}$  s ( $\tau \sim 3.5 \times 10^{-13}$  s at 300 K). For the electron drift velocity of  $10^7$  cm/s, the electron transit time is  $10^{-11}$  s,  $10^{-12}$  s, and  $3 \times 10^{-13}$  s for a 1- $\mu\text{m}$ , 0.1- $\mu\text{m}$ , and 0.03- $\mu\text{m}$  gate length, respectively. Hence, the electron transit time can definitely be made shorter than the momentum relaxation time at 77 K and perhaps even at 300 K. However, for a typical surface carrier concentration of the 2D electron gas  $n_s = 10^{12}$  cm<sup>-2</sup>, the mean free path for electron-electron collisions is only on the order of the average distance between electrons. The average distance between electrons at this concentration is close to the Bohr radius ( $\sim 100$  Å). Hence, the electron gas is highly non-ideal, and there are a large number of electron-electron collisions during the transit time. Under such conditions, the electrons behave as a fluid moving in the channel without external friction and obeying hydrodynamic equations.

## II. PLASMA WAVE INSTABILITY<sup>1</sup>

Let us first assume that the gate voltage swing is fixed at  $U_0$ , and the channel current is zero. The plasma wave dispersion law,  $k = \pm\omega/s$ , corresponding to the well-known shallow water waves, is readily obtained from the linearized equation of motion and continuity equation. Here  $\omega$  is the frequency,  $k$  is the wave vector and  $s = (eU_0/m)^{1/2}$  is the wave velocity.<sup>5,6</sup>

If the electrons move with a velocity  $v_o$ , the dispersion relation becomes  $k = \omega/(v_o \pm s)$ , which means that the waves are carried along by the flow.

We now consider the situation when the source and drain are connected to a current source and the gate and source are connected to a voltage source,  $V_{gs}$ . The *ac* variation of the electric current at the source side of the channel is possible even for a constant external current since the *ac* current at the source is short circuited to the gate by the *dc* voltage source. These boundary conditions correspond to zero impedance at the source. A study of the temporal behavior of a small fluctuation superimposed on steady uniform flow leads to the following expressions for the real and imaginary parts:  $\omega = \omega' + i\omega''$

$$\omega' = \frac{|s^2 - v_o^2|}{2Ls} \pi m \quad (1)$$

<sup>1</sup> Department of ECSE and CIEEM, Rensselaer Polytechnic Institute, Troy, NY 12180-3590

<sup>2</sup> Université Montpellier 2 - C.N.R.S. UMR3577  
Place E. Bataillon, F-34095 Montpellier, France

$$\omega'' = \frac{s^2 - v_o^2}{2Ls} \ln \left| \frac{s+v_o}{s-v_o} \right| \quad (2)$$

where  $n$  is an odd integer for  $|v_o| < s$  and an even integer for  $|v_o| > s$ . Eq. (2) (see also Fig. 1) shows that for  $s > v_o > 0$ , the steady electron flow is unstable at low electron velocities. The reason for the instability becomes clear if we consider wave reflections from each boundary.

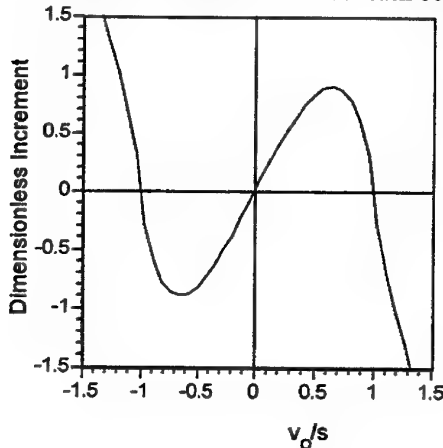


Fig. 1. Dimensionless plasma wave increment,  $2\omega''L/s$ , as a function of Mach number,  $M = v_o/s$ . The steady electron flow is unstable when  $0 < v_o < s$  and  $v_o < -s$ .<sup>1</sup>

The solution of linearized continuity equation and equation of motion shows that the reflection does not change the wave amplitude at  $x = 0$  (where the voltage is fixed), while at  $x = L$  (where the current is fixed), the amplitude ratio of the reflected and oncoming waves is  $(s+v_o)/(s-v_o)$ . Hence, the reflection from the boundary with the fixed current results in the wave amplification for  $v_o < s$ . Let  $\tau = L/(s+v_o) + L/(s-v_o)$  be the time during which the wave travels from the source to the drain and back. During time  $t$ , the wave amplitude grows in  $[(s+v_o)/(s-v_o)]^{t/\tau}$  times since  $t/\tau$  is the number of wave round passages during time  $t$ . Equating  $[(s+v_o)/(s-v_o)]^{t/\tau}$  to  $\exp(\omega''t)$ , we obtain Eq. (2). Thus, the proposed new mechanism of plasma wave generation is based on the amplification of the wave during its reflection from the boundary where the current is kept fixed.

There are two decay mechanisms, which oppose wave growth: external friction related to electron scattering by phonons or impurities, and internal friction caused by the viscosity of the electron fluid. The external friction leads to the addition of the  $-1/(2\tau)$  term to the wave increment. Hence, the wave grows only if the number of scattering events during the transit time is small. The viscosity,  $\nu$ , of the electron fluid causes an additional damping with the decrement of  $\nu k^2$ . Hence, the viscosity is especially effective in damping higher order modes. Comparing  $\omega''$  with  $\nu k^2$  for the first mode, we find that the effect of the viscosity for  $v_o = s$  is small when the Reynolds number  $Re = L v_o / \nu$  is much greater than unity. A very crude estimate

yields  $v \sim 15 \text{ cm}^2/\text{s}$  and  $Re = mv_o L / \hbar \sim 12$  for  $v_o = 10^7 \text{ cm/s}$  and  $L = 0.2 \mu\text{m}$ .

For a sample with  $L = 0.2 \mu\text{m}$  at  $77 \text{ K}$  ( $\tau \sim 10^{-11} \text{ s}$ ), the increment  $v_o/L$  exceeds the decrement  $1/(2\tau)$  caused by the collisions when  $v_o > 10^6 \text{ cm/s}$ . For the same sample, the decrement caused by viscosity,  $\nu(2\pi/L)^2/16$ , is smaller than the increment  $v_o/L$  when  $v_o > \pi^2 \nu / (4L) \sim 1.8 \times 10^6 \text{ cm/s}$ . Hence, the threshold velocity for the instability is well below the peak velocity in GaAs.

Once the electron velocity exceeds the threshold, the plasma waves grow. This growth should lead to oscillations for which the plasma wave amplitude is limited by non-linearity. The amplitude of these non-linear oscillations should be comparable to  $U_o$  if the flow velocity is substantially larger than the threshold value.

The plasma oscillations result in a periodic variation of the channel charge and the mirror image charge in the gate contact, i.e., to the periodic variation of the dipole moment. This variation should lead to electromagnetic radiation. The device length is much smaller than the wavelength of the electromagnetic radiation,  $\lambda_R$ , at the plasma wave frequency. Hence, the ballistic FET should operate as a point or linear source of electromagnetic radiation. Many such devices can be placed into a quasi-optical array for power combining.<sup>7</sup> The maximum radiation intensity is limited by the gate voltage swing. The maximum modulation frequency is still limited by the transit time ( $\sim 2 \text{ ps}$  in our example).

With an exception of a non-resonant FET detector described below, FETs utilizing plasma waves must be short enough so that parameter  $\eta = st/L$  is greater than unity. This corresponds to the condition that can be written as<sup>8</sup>

$$L \ll L_{cr} = \frac{s \mu m}{e} \quad (3)$$

Criterion (3) coincides (within a numerical factor) with the requirement  $\omega_o \tau \gg 1$ . Also, for plasma wave electronics (again, with an exception of the non-resonant FET detectors mentioned above) the frequency of operation has to be much higher than  $\omega_{cr} = 1/\tau$ . Fig. 2 shows the plots of  $L_{cr}$  versus gate bias for different material systems. As can be seen from Figure 2, the required dimensions are well within the range of typical dimensions for deep submicron FETs.

Figure 3 shows the length dependencies of characteristic scales,  $j_o$  and  $U_o$  that correspond to the range of values for currents and voltage, where such an instability should take place<sup>9</sup>.

We chose the mobility values of  $9,000 \text{ cm}^2/\text{V}\cdot\text{s}$ ,  $300,000 \text{ cm}^2/\text{V}\cdot\text{s}$ , and  $3,000,000 \text{ cm}^2/\text{V}\cdot\text{s}$ , which can be achieved in a two-dimensional electron gas (2DEG) in GaAs at  $300 \text{ K}$ ,  $77 \text{ K}$ , and  $4-20 \text{ K}$ , respectively. As can be seen from Fig. 1, sub-0.1 micron dimensions, submicron dimensions, and dimensions on the order of several microns, are required in order to observe the instability in the samples with the lowest, intermediate, and highest values of the electron mobility.

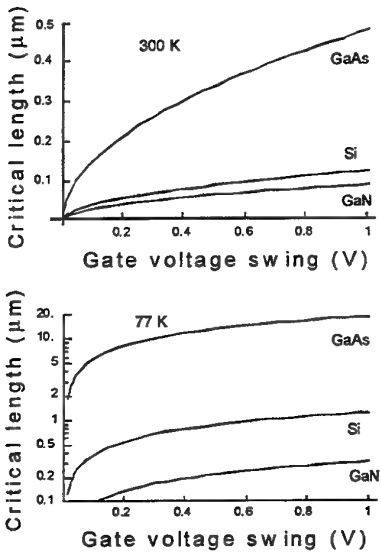
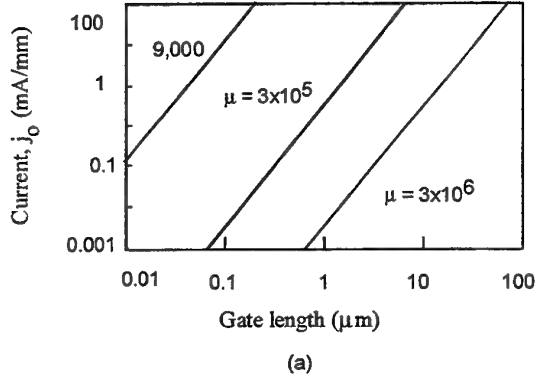
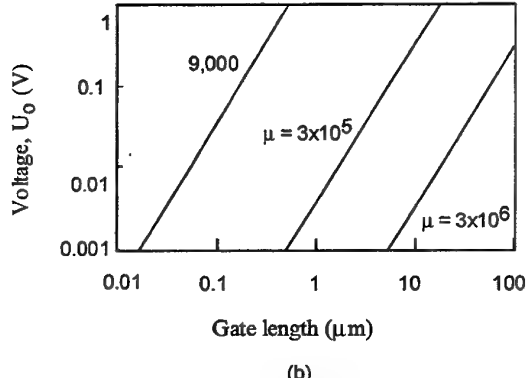


Fig. 2.  $L_{cr}$  versus gate bias for different material systems.<sup>8</sup>



(a)



(b)

Fig. 3.  $j_o$  and  $U_o$  for GaAs for different values of mobility (in  $\text{cm}^2/\text{V}\cdot\text{s}$ ). Numbers near the lines are the values of the low field mobility. Parameters used in the calculation: gate voltage swing,  $U = 0.1 \text{ V}$ , electron effective mass,  $m = 0.063 m_0$ , dielectric permittivity,  $\epsilon = 1.14 \times 10^{-10} \text{ F/m}$ , gate-to-channel separation,  $d = 10^{-8} \text{ m}$ .<sup>9</sup>

There are many unresolved problems that have to be addressed in order to observe this new instability. The role of electron fluid viscosity, the role of boundary conditions

and coupling between electromagnetic radiation and the plasma waves have to be better understood, and integrated antenna structures have to be designed. It is possible that effective coupling will be easier to achieve in periodic structures, such as proposed for an "electronic flute."<sup>7</sup>

### III. PLASMA WAVE DETECTORS

A short channel FET should have a resonance response to electromagnetic radiation at the plasma oscillation frequency. A long channel FET has a non-resonant response to electromagnetic radiation and can be used as a broad band detector for frequencies up to several tens of terahertz. Our estimates show that the sensitivity of the resonant FET detector should exceed the sensitivity of conventional Schottky diode detectors by a factor of  $Q^2$  that is by several orders of magnitude. The sensitivity of the non-resonant, broad band HEMT detector is comparable to the sensitivity of conventional Schottky diode detectors ( $\sim 600 \text{ V/W}$ ).<sup>3,8</sup>

Our recent experimental data (see<sup>10,11,12</sup> and the results below) confirm many features of these theoretical predictions but also pose many questions.

Fig. 4 shows measured and calculated frequency dependencies of the detector responsivity for a GaN Heterostructure FET (HFET) with a cutoff frequency of approximately 2 GHz.

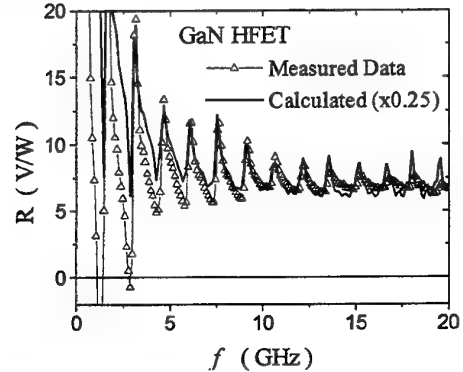


Fig. 4. Measured (symbols) and calculated (solid line) detector responsivity for GaN HFET.  $L = 5 \mu\text{m}$ ,  $V_G = -1 \text{ V}$ , and  $U_T = -2 \text{ V}$ .<sup>11</sup>

The periodic variation of the responsivity with frequency is caused by changes in the transmission line impedance with frequency. As can be seen from the figure, the device operates as broad band non-resonant detector of microwave radiation at frequencies higher than the cutoff frequency and the measured data agree with the theory.

Fig. 5 shows the response of a 0.18-micron AlGaAs/GaAs HEMT detector at 2.5 THz. (The device fabrication and the measurement setup are described in<sup>12</sup>.)

Fig. 6 compares the detector response with the gate current (the drain current is equal to zero). Fig. 7 compares the detector response at 300 K and 77 K.

The gate current is very low, and the gate bias dependence of the detector response cannot be explained by heating. This dependence is consistent with the theoretical predictions (see also<sup>11</sup>).

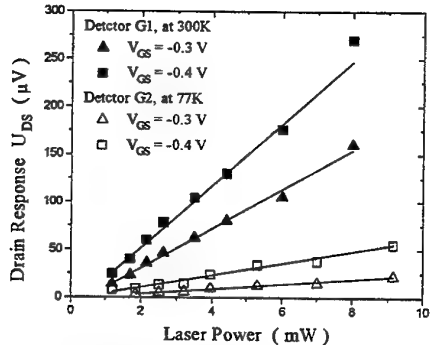


Fig. 5. AlGaAs/GaAs HEMT detector response. HEMT operates as a square-law detector.

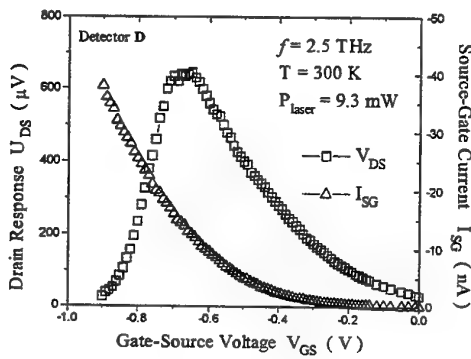


Fig. 6. Detector response at 2.5 THz and gate current.

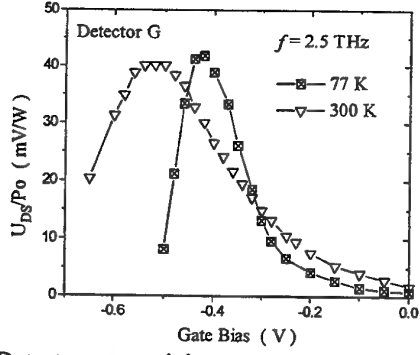


Fig. 7. Detector responsivity at 77 K and 300 K

As expected, the maximum responsivity occurs at the HEMT threshold voltage (around -0.6 V at 300 K), and the responsivity peak shifts with the threshold voltage. However, we do not observe the expected increase in responsivity related to an increase in the mobility at cryogenic temperatures. Possibly, the responsivity is more strongly limited by the viscosity of the electronic fluid, which we might have underestimated. Also, the viscosity is more important at higher harmonics and, as mentioned in<sup>12</sup>, frequency of 2.5 THz corresponds to the third harmonic of the plasma frequency for our devices at approximately 0.3 V gate voltage swing.

Fig. 8 shows the detector response as a function of the angle between the *ac* electric field and the direction from the source to the drain (the electric field is in the device plane). Our theory applies to the case when this angle is

zero. However, the modulation of the electron sheet density also occurs when this angle is 90 degrees, and, hence, the detector should operate for this angle as well.

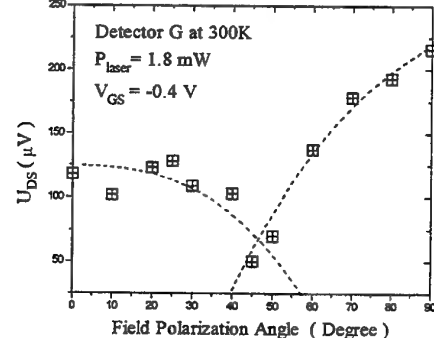


Fig. 8. Polarization dependence of detector responsivity.

#### IV. CONCLUSIONS

We reviewed theoretical predictions for plasma wave generation and excitation in FETs and presented experimental data that show that a FET can operate as detector of electromagnetic radiation in a broad range of frequencies from microwave to terahertz range, including frequencies far exceeding the transistor cutoff frequency.

#### V. ACKNOWLEDGMENT

The US Office of Naval Research (Project Monitor, Dr. John Zolper) and the US Army Research Office (Project Monitor, Dr. Mitra Dutta) have supported this work. We are also grateful to Dr. J. Hesler for his help with the measurements.

#### References

1. M. Dyakonov and M. S. Shur, *Phys. Rev. Lett.*, Vol. 71, No. 15, pp. 2465-2468, Oct. 11 (1993)
2. M. Dyakonov and M. S. Shur, in *Proceedings of 2d ISDRS*, Charlottesville, VA, December, pp. 741-744 (1993)
3. M. I. Dyakonov and M. S. Shur, *IEEE Trans. on Electron Devices*, vol. 43, No. 3, pp. 380-387 (1996)
4. P. C. Chao, M. Shur, R. C. Tiberio, K. H. G. Duh, P. M. Smith, J. M. Ballingall, P. Ho, and A. A. Jabra, *IEEE Trans. Electron Dev.*, ED-36, 461 (1989)
5. A. V. Chaplik, *Zh. Eksp. Teor. Fiz.* 62, 746 (1972) (*Sov. Phys. JETP*, 35, 395, (1972))
6. M. Nakayama, *J. Phys. Soc. Japan*, 36, 393 (1974)
7. M. I. Dyakonov and M. S. Shur, *Appl. Phys. Lett.* Vol. 67 (8), August 21, pp. 1137-1139, 1995
8. M. I. Dyakonov and M. S. Shur, *IEEE Trans. on Electron Devices*, vol. 43, No. 10, pp. 1640-1646, October (1996)
9. M. V. Cheremisin, M. I. Dyakonov, M. S. Shur, and G. Samsonidze, Influence of Electron Scattering on Current Instability in Field Effect Transistor, *Solid State Electronics*, accepted for publication
10. R. Weikle, J.-Q. Lü, M. S. Shur, M. I. Dyakonov, *Electronics Letters*, vol. 32, No. 7, pp. 2148-2149 (1996)
11. J.-Q. Lü, M. S. Shur, R. Weikle, and M. I. Dyakonov, in *Proceedings of Sixteenth Biennial Conference on Advanced Concepts in High Speed Semiconductor Devices and Circuits*, Ithaca, NY, Aug. 4-6 (1997)
12. J.-Q. Lü, M. S. Shur, J. L. Hesler, L. Sun, and R. Weikle, Terahertz Detector Utilizing Two-Dimensional Electronic Fluid, *IEEE Electron Device Letters*, October (1998)

# Excess Noise in Schottky Diodes for THz Applications

G. Rehm, K. Huber, S. Martius

**Abstract**— The precise knowledge of noise contributions from Schottky diodes to mixer performance is essential for the design of heterodyne receivers. This article explains how this noise can be measured over frequency and DC current taking into account receiver mismatch and reflection of noise from the measurement instrument.

**Keywords**— Excess noise, Schottky diodes, Measurement

## I. INTRODUCTION

WITH anode diameters decreasing for higher operation frequencies the current densities in the diode increase rapidly. This results in an additional noise contribution which dominates the overall noise temperature of the diode in certain frequency ranges.

This so called excess noise depends on diode parameters, frequency and DC (bias) current. The origins of excess noise are still uncertain and its prediction is hardly possible. Thus the noise temperature of the diode has to be obtained by measurement under well defined constraints. Only with the current dependent noise temperature in mind a reasonable bias range can be chosen for the mixer design to avoid a diode that could be perfectly matched to the whisker antenna and the IF amplifier but would cause the dominating noise contribution to the system.

## II. THEORY

Earlier publications dealing with this subject have not always taken into account all influences to the noise temperature measurement [6], [9]. These influences include the change of the diode reflection coefficient under bias and the resulting change in delivered noise power to the measurement port, as well as the reaction of the noise power meter to a changing source reflection coefficient. These problems can be solved using a compensation measurement [3] but this technique is hardly applicable to the frequency range in question ( $>1$  GHz).

Figure 1a illustrates the basic measurement setup and the associated variables. With  $T_0$  as the normative temperature (usually 290 K) the measured noise power is equal to:

$$P_N = k_B \cdot \frac{1 - |r_S|^2}{|1 - r_S r_{NPM}|^2} \cdot [T_S + T_{NPM}] \quad (1)$$

$$\text{with } T_{NPM} = T_{min} + T_0 C_N \cdot \frac{|r_s - r_{opt}|^2}{1 - |r_S|^2}$$

All authors are with the Lehrstuhl für Hochfrequenztechnik (LHFT), Universität Erlangen-Nürnberg (UEN), Erlangen, Germany. E-mail: guenther@lhft.e-technik.uni-erlangen.de

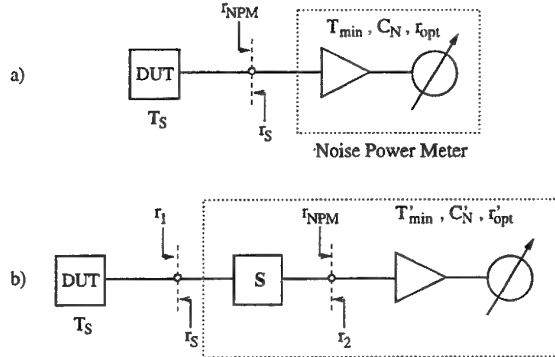


Fig. 1. Schematic measurement setup  
a) basic noise power measurement  
b) modified noise power measurement

As can be seen from equation 1 the contribution of the NPM to the measured noise power is neither negligible nor independent of  $r_S$ . The determination of the parameters  $T_{min}$ ,  $C_N$  and  $r_{opt}$  characterising the NPMs noise performance is difficult. However, with a modified setup featuring an additional passive two port device (including only thermal energy sources) between the DUT and the NPM as shown in figure 1b the NPMs dependence on  $r_S$  can be neglected. The combination of isolator and NPM can be seen as new instrument characterised by  $T'_{min}$ ,  $C'_N$  and  $r'_{opt}$ . In contrast to the original NPM parameters these can be readily obtained by S-parameter measurement of the isolator and a single hot/cold calibration of the new instrument as will be shown in the following. For the diode noise measurement the influence of the required bias-tee can also be included in the S-parameters.

A setup like the modified noise power measurement in figure 1b can be described by

$$T_{sum} = T_{eff,iso} + \frac{T_{NPM}}{G_{av,iso}} \quad (2)$$

where  $T_{eff,iso}$  is the contribution of the isolator and  $T_{NPM}$  of the noise power meter.  $G_{av,iso}$  is the available gain of the isolator and can generally be calculated for any two port device as

$$G_{av} = |s_{21}|^2 \cdot \frac{1 - |r_S|^2}{|1 - r_S s_{12}|^2 \cdot (1 - |r_2|^2)} \quad (3)$$

with  $r_2$  depending on  $r_S$  and  $S$ . However, provided a sufficiently good backward isolation ( $s_{12} \rightarrow 0$ ) it is possible to set  $r_2 = s_{22}$  and  $r_1 = s_{11}$  which makes them independent

of  $r_S$ . Therefore, the practical realisation of  $\mathbf{S}$  will include an isolator. Using equations 1, 2 and 3 we get

$$P_N = kB \cdot |s_{21}|^2 \cdot \left[ (T_S + T_{min,iso}) \cdot \frac{1 - |r_S|^2}{|1 - r_S s_{11}|^2} + T_0 C_{N,iso} \cdot \frac{|r_S - r_{opt,iso}|^2}{|1 - r_S s_{11}|^2} + T_2 \right] \quad (4)$$

$$\text{with } T_2 = \frac{T_{min}(1 - |s_{22}|^2) + T_0 C_N \cdot |s_{22} - r_{opt}|^2}{|s_{21}|^2}$$

where  $T_2$  is the  $r_S$  independent part of the sum. The parameters  $T_{min,iso}$ ,  $C_{N,iso}$  and  $r_{opt,iso}$  can be calculated from  $\mathbf{S}$  and the physical temperature of the isolator  $T_{iso}$  as shown in [2], [4], [5]:

$$C^S = \frac{T_{iso}}{4T_0} \cdot (\mathbf{E} - \mathbf{S}\mathbf{S}^*) \quad (5)$$

$$C_{N,iso} = A + \sqrt{A^2 - B^2} \quad (6)$$

$$r_{opt,iso} = 4 \cdot \frac{(c_{22}^S s_{11} - c_{12}^S s_{21})^*}{C_{N,iso} \cdot |s_{21}|^2} \quad (7)$$

$$T_{min,iso} = 4T_0 \cdot \frac{c_{22}^S}{|s_{21}|^2} - T_0 C_{N,iso} \cdot |r_{opt,iso}|^2 \quad (8)$$

where  $\mathbf{S}^*$  is the complex conjugate transpose of  $\mathbf{S}$  and using the abbreviations

$$A = 2 \cdot \frac{c_{11}^S \cdot |s_{21}|^2 + c_{22}^S (1 + |s_{11}|^2) - 2 \cdot \Re \{ c_{12}^S s_{11}^* s_{21} \}}{|s_{21}|^2}$$

$$B = 4 \cdot \frac{|c_{22}^S s_{11} - c_{12}^S s_{21}|}{|s_{21}|^2}$$

Now  $T_2$  can be obtained from two noise power measurements of a termination at the input at two known temperatures using the Y-factor method. With  $r_S = 0$  equation 4 simplifies to:

$$P_N = kB \cdot |s_{21}|^2 \cdot (T_S + T_{min,iso} + T_0 C_{N,iso} \cdot |r_{opt,iso}|^2 + T_2) \quad (9)$$

$$T_2 = \frac{T_{hot} - Y_2 T_{cold}}{Y_2 - 1} - T_{min,iso} - T_0 C_{N,iso} \cdot |r_{opt,iso}|^2 \quad (10)$$

$$\text{with } Y_2 = \frac{P_{N,hot}}{P_{N,cold}}$$

A comparison between equations 1 and 4 leads to the noise parameters of the modified noise power meter including the isolator.

$$T'_{min} = T_{min,iso} + T_2 \quad (11)$$

$$C'_N = C_{N,iso} \quad (12)$$

$$r'_{opt} = r_{opt,iso} \quad (13)$$

Now noise temperatures of arbitrarily reflecting one port devices can be measured using the Y-factor method.

$$Y = \frac{P_{N,DUT}}{P_N(r_S = 0, T_{ref})} = \frac{\frac{1 - |r_S|^2}{|1 - r_S s_{11}|^2} (T_S + T'_{min} + T_0 C'_N \cdot \frac{|r_S - r'_{opt}|^2}{1 - |r_S|^2})}{T_{ref} + T'_{min} + T_0 C'_N \cdot |r'_{opt}|^2} \quad (14)$$

$$T_S = \frac{Y \cdot (T_{ref} + T'_{min} + T_0 C'_N \cdot |r'_{opt}|^2)}{\frac{1 - |r_S|^2}{|1 - r_S s_{11}|^2}} - T'_{min} - T_0 C'_N \cdot \frac{|r_S - r'_{opt}|^2}{1 - |r_S|^2} \quad (15)$$

### III. MEASUREMENT PROCEDURE

A precise measurement procedure has to obey the following steps, also depicted in figures 2 and 3.

- The reflection coefficient  $r_D$  of the mounted diode has to be measured for the desired frequency and bias current range at a well defined reference plane.
- The S-parameters  $\mathbf{S}$  of the bias-tee/isolator combination have to be acquired for the desired frequency range.
- A noise power meter calibration using a hot and a cold  $50 \Omega$  termination is required.
- Finally, the noise power delivered by the diode under variation of the bias current  $I_{DC}$  is measured at the defined reference plane.

Figure 4 shows a set of measured reflection coefficients at the reference plane of a Schottky diode mounted in a corner cube antenna. As this mixer block contains a matching network the range of  $|r_D|$  varies from 0.05 to 0.95 which gives an idea of the high influence this will have on the noise power delivered to the reference plane. On the other hand, it proves the necessity of a highest possible isolation of the noise power meter input from reflections. Thus, a pair of circulators was used to obtain an isolation of better than 40 dB within the desired frequency range. This also

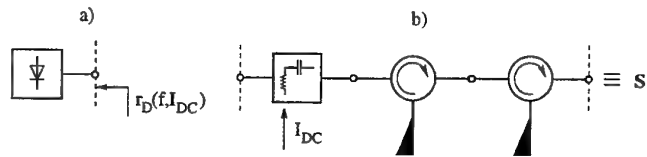


Fig. 2. Network analyser measurements:  
a) diode reflection coefficient  
b) isolator/bias-tee S-parameters

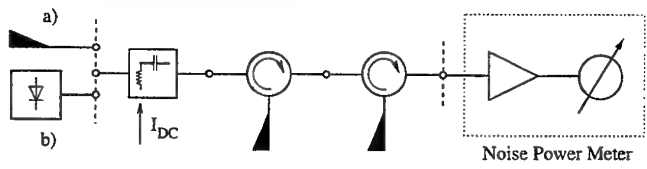


Fig. 3. Noise power measurements:  
a) hot/cold termination  
b) device under test

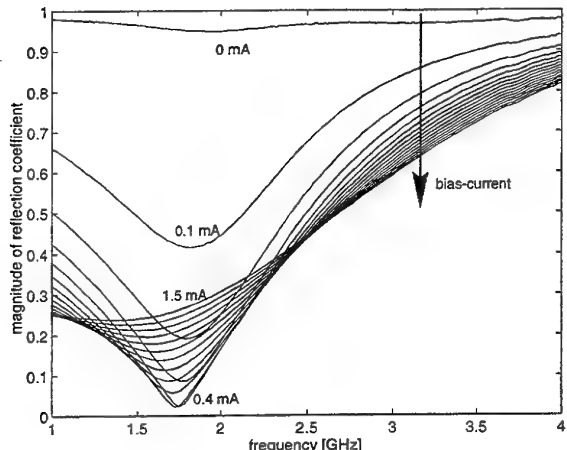


Fig. 4. Reflection coefficients of diode 1 with built in matching circuit

required two separate measurements for 1–2 GHz and 2–4 GHz as the usable bandwidth of the used circulators is limited to one octave.

The S-parameter measurement can easily be done with a good precision and the calculation of the noise parameters from S therefore offers a much better accuracy than any direct measurement of the noise parameters could.

As the noise power measurements of the calibration load and the diode at several bias currents are consecutive, care has to be taken about the stability of the noise power meter. The instruments in use (HP8970B/HP8971C/HP8673G) proved to be sufficiently stable as they showed only a small drift of about 0.1 dB after a 10 hour test run.

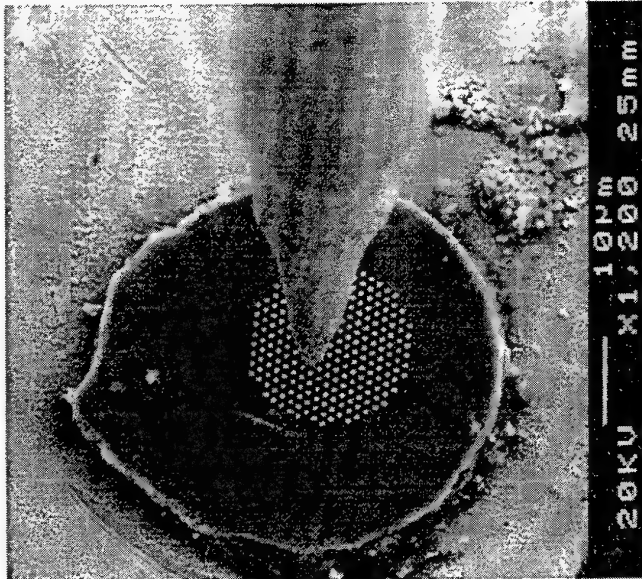


Fig. 5. SEM picture of a substrate-less diode mesa contacted by a 25  $\mu\text{m}$  whisker tip

No.	diameter [ $\mu\text{m}$ ]	$R_S$ [ $\Omega$ ]	$I_S$ [aA]	n	substrate- less
1	0.5	60	6	1.2	yes
2	0.5	45	7	1.2	yes
3	0.5	60	7	1.2	yes
4	0.8	50	500	1.35	no

TABLE I  
PARAMETERS OF THE INVESTIGATED DIODES

#### IV. RESULTS

Several Schottky diodes manufactured by the *TH Darmstadt*[10] have been measured. Their parameters are listed in table I. All diodes have an epi-doping of  $3 \cdot 10^{17} \text{ cm}^{-3}$ . They are mounted in corner-cube antenna blocks and contacted by an etched whisker tip (see figure 5), thus  $R_S$  is the measured series resistance including the whisker.

Figure 6 shows the noise temperatures calculated with equation 15 for the same diode as in figure 4. The strong frequency dependency of the reflection coefficient does not influence the measurements. The printed data is collected at 90 discrete frequencies joined with straight lines. Especially the good match of the two separate frequency ranges (where different isolators were used) joining at 2 GHz proves the high quality of the measurement setup.

In figure 7 the dependency of the noise temperature on the bias current is plotted for all investigated diodes. Though the first three are from the same production cycle, their noise temperatures differ significantly. However, it is remarkable that diode 1 not only shows the highest temperatures for high bias currents but also the lowest temperatures for bias currents less than 0.5 mA. This illustrates the necessity of a precise available noise power measurement prior to selection of the operation conditions.

Finally, figure 8 compares the frequency dependency of the noise temperature for the measured diodes. A fixed bias

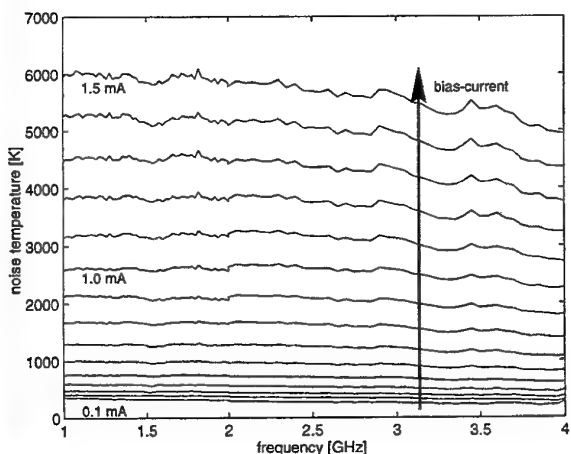


Fig. 6. Noise temperatures of diode 1

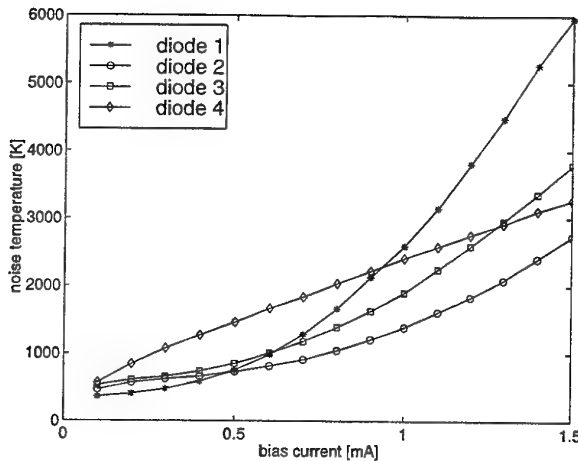


Fig. 7. Noise temperatures at 1 GHz vs. bias current plotted for different diodes

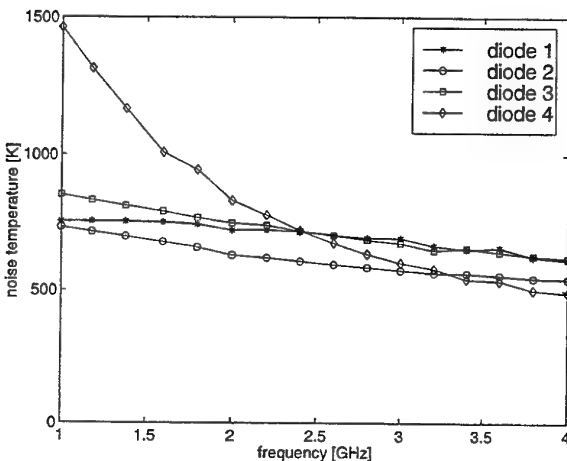


Fig. 8. Noise temperatures at 0.5 mA bias current plotted for different diodes

current of 0.5 mA was chosen as a usual value. Clearly, the sharp drop of excess noise with higher frequencies which has been reported [8] to exist in this frequency range, cannot be observed for the 0.5  $\mu$ m diodes. Only the substrate based 0.8  $\mu$ m diode shows this behaviour.

## V. CONCLUSIONS

A measurement setup and procedure capable of measuring the available noise power of arbitrarily reflecting one port devices has been presented. The calculation of the setup's noise parameters from an S-parameter measurement is key to the high accuracy which can readily be achieved. This setup was used to investigate the noise temperatures of Schottky diodes which are dominated by the current dependent excess noise. Results for the frequency range 1–4 GHz and bias currents up to 1.5 mA are presented and compared for different diodes. Additional measurements for 4–8 GHz and other diodes are currently in work. These results will allow a better optimisation of the mixer operating point and help in choosing the most promising diodes for heterodyne receivers.

## REFERENCES

- [1] H. Bosma, "On the theory of linear noisy systems," *Philips Res. Repts.*, Suppl. Nr. 10, Eindhoven, 1967.
- [2] P. Russer, H. Hillbrand, "Rauschanalyse von linearen Netzerken," *Wissenschaftliche Berichte AEG-Telefunken*, vol. 49, no. 4/5, pp.127-138, 1976.
- [3] M. Spaude, "Ein Impedanzunabhängiges Meßverfahren zur Bestimmung von Zweipol-Rauschtemperaturen im Hochfrequenzbereich," *Dissertation Ruhr-Universität Bochum*, 1984.
- [4] S. Martius, "Netzwerk-CAD mit Streumatrix und Rauschwellen-Korrelations-Matrix," *Nachrichtentechnische Elektronik*, vol. 38, no. 1, pp. 17-18,23,3rd cover page, 1988.
- [5] S. Martius, "Die Messung der Elemente der Rausch-Korrelations-Matrizen  $C^A$ ,  $C^S$  und von  $f_{MIN}$ ,  $\gamma_0$ ,  $C_N$  beim Zweitor," *Frequenz*, vol. 43, no. 4, pp. 115 – 121, 1989.
- [6] N. J. Keen, H. Zirath, "Hot-electron noise generation in gallium-arsenide schottky-barrier diodes," *Electronics Letters*, vol. 19, no. 20, pp. 853 – 854, September 1983.
- [7] G. M. Hegazi, A. Jelenski, K.S. Yngvesson, "Limitations of microwave and millimeter-wave mixers due to excess noise," *IEEE Transactions on Microwave Theory and Techniques*, vol. 33, no. 12, pp. 1404 – 1409, December 1985.
- [8] A. Jelenski, E. L. Kollberg, H. H. G. Zirath, "Broad-band noise mechanisms and noise measurements of metal-semiconductor junctions," *IEEE Transactions on Microwave Theory and Techniques*, vol. 34, no. 11, pp. 1193 – 1201, November 1986.
- [9] S. Palczewski, A. Jelenski, A. Grüb, H. L. Hartnagel, "Noise characterization of schottky barrier diodes for high-frequency mixing applications," *IEEE Microwave and Guided Wave Letters*, vol. 2, no. 11, pp. 442 – 444, November 1992.
- [10] C. I. Lin, A. Simon, H. L. Hartnagel, "Fabrication of substrate-less schottky diodes for the thz applications," in *Proceedings of the 4th International Workshop on Terahertz Electronics*, Erlangen, Germany, September 1996.

# Planar Schottky Diodes for Submillimeter Wave Applications

Chih-I Lin, Ansgar Simon, Manuel Rodriguez-Gironés, Hans Ludwig Hartnagel, *Member, IEEE*,  
Peter Zimmermann, *Member, IEEE*, Rüdiger Zimmermann, Ralf Henneberger

**Abstract**—The main limitation of whisker-contacted diode technology is that no integration is possible. Therefore, the development of competitive planar Schottky barrier diodes has been put forward in the last decade. The quasi-vertical planar Schottky diode was proposed several years ago and the necessary technologies are developed for a reliable fabrication. We show the recent status of this type of planar Schottky diodes. At 200 GHz an output power of 5 mW (12.5 % efficiency) has been achieved with a quasi-vertical planar varactor diode. Recent activities concentrate on anti-parallel Schottky mixer diodes and integration of diodes (0.8  $\mu\text{m}$  anode diameter) with several receiver components. These diodes offer characteristics comparable to substrateless diodes with the same diode parameters.

**Index terms**—Schottky diodes, submillimeter wave technology

## I. INTRODUCTION

GaAs Schottky barrier diodes continue being the key element for mixers and frequency multipliers in the millimeter and submillimeter wavelength because no expensive cryogenic cooling system is required. The main disadvantage of conventional whisker-contacted diodes, that the integration of a whisker-contacted diode with other system components such as antenna and filters is strongly limited, can not be overcome. On the other hand, planar structure with both contact electrodes on the topside of the device offers more flexibility for the integration. The quasi-vertical approach to realize planar diode structure using mesa and high air-bridge technique was suggested in 1993 [1] and the necessary technologies have been already established.

This paper reports the recent developments of the quasi-vertical planar technology and the latest fabricated devices and their characteristics, which include single planar varactor diodes and anti-parallel mixer diodes. Based on the experiences of single devices, integrated mixer structure for

quasi-optic mixing application is initiated. A short description of the new structure will also be presented

## II. DEVICE DESIGN

The Quasi-Vertical planar Schottky Diode (QVD) approach, developed by Technical University Darmstadt, is transferred from the structure of the whisker-contacted substrateless diode [2]. Figure 1 shows sketches of both of the structures.

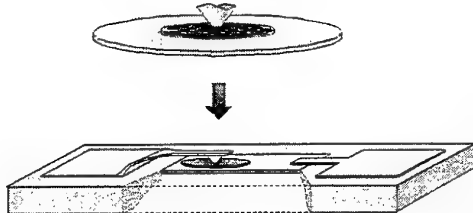


Fig.1: schematic sketch of substrateless Schottky and quasi-vertical planar diode

The substrateless diode has the same geometry as the conventional whisker-contacted diode but with extremely reduced chip size. The thickness of the  $n^+$ -layer of the mesa is chosen for 2  $\mu\text{m}$ , which is comparable to the skin depth of the  $n^+$ -layer at a RF signal frequency up to 300 GHz. Therefore the influence of the skin effect can be eliminated and the high-frequent resistance and inductance can be reduced. The two-micron distance from the backside contact metal to the active  $n$ -layer offers one more effective heat sink beside the whisker. Because of the same symmetrical geometry of these diodes, there is absolutely vertical current flow through the diode and therefore the simulations for the conventional whisker-contacted diodes can be transferred to the QVDs. Many RF measurements for frequency multipliers and mixers using substrateless diodes were done and showed noticeable improvements in the performance [2]. Like the substrateless diodes, the QVDs possess also these geometrical advantages and are expected to be very promising for applications in the THz Regime.

In the design of planar devices, the reduction of the stray capacitance is an important task. The spray capacitance has not only influence on matching and power coupling to the diode, but can also reduce the capacitance modulation of varactor diodes and therefore can reduce the efficiency of

This work was supported by ESA/Estec through Grants 10582/93/NL/NB and 11806/96/NL/CN.

C.I. Lin, A. Simon, M. Rodriguez-Gironés, and H. L. Hartnagel are with the Institut für Hochfrequenztechnik, University of Technology Darmstadt, Merckstr. 25, Darmstadt, Germany.

P. Zimmermann, R. Zimmermann and R. Henneberger are with Radiometer Physics GmbH, Birkenmaarstr. 10, Meckenheim, Germany.

frequency multipliers. Two main contributions to the stray capacitance are the GaAs material beneath the contact pads and the air bridge used for contacting to the Schottky contact. Here we introduce a reduced chip thickness technique to reduce the influence of the GaAs material. An air bridge height of 4  $\mu\text{m}$  over the backside contact (about 2  $\mu\text{m}$  over the mesa) is applied to reduce the stray capacitance of the air bridge. Using finite element analysis, it showed that the stray capacitance doesn't exceed 2fF even with a 4  $\mu\text{m}$  wide air bridge.

### III. SINGLE PLANAR QVD FOR FREQUENCY MULTIPLIERS

For an all-solid-state mixer in THz regime, frequency multipliers are used to generate higher harmonics as LO signal by multiplying the pump signal frequency. Schottky varactor diodes are usually applied in submillimeter frequency multipliers. For the first stage frequency multiplier at about 100GHz, a Gunn-Oscillator is usually as the pump signal, and there is enough power to drive the Schottky diode to work in the full-pumped range. Therefore the current saturation effect has to be taken into account while choosing the material. Considering the relation of the change rate of the depletion layer thickness to the time and the saturation velocity of electron [3] we have chosen a material with a doping level of  $8 \times 10^{16} \text{ cm}^{-3}$  and a thickness of 560 nm for the active n-layer. Using this material we have already gotten many promising RF results in frequency multipliers using substrateless diodes [2].

The amplitude of the RF signal, and the capacitance modulation can be increased if the breakdown voltage increases. Therefore, parallel to the fabrication of QVDs, we have investigated the breakdown voltage in dependence of the passivation. Using Polyimide we have achieved the best breakdown voltage of 16 to 18V, which is 30% more than the value we can get by using PECVD-SiO<sub>2</sub> passivation and more near to the theoretically predicted values [2]. But Polyimide has usually worse adhesion than PECVD-SiO<sub>2</sub>, which may result a long-term reliability problem. Therefore the investigation of the improvement of the passivation is still in progress.

Figure 2 shows a SEM picture of a QVD after soldering onto a microstrip filter for a frequency doubler with an input frequency about 100GHz. The measured DC characteristics, including the series resistance  $R_s=3 \Omega$ , the Ideality factor  $\eta=1.05$  and the breakdown voltage  $V_{bd}=16 \text{ V}$ , are comparable to the substrateless diode with the same material. The measured total capacitance at zero bias is 30fF which includes the stray capacitance of about 7fF. The doubler result, 5mW at 202GHz with an efficiency of 12.5%, is one of the best doubler results in this frequency regime using planar diode technology. The reason for worse efficiency, comparing to the doubler results using whisker-contacted diodes, is possibly due to that the lower capacitance modulation ratio, instead of 3.2, but only 2 because of the stray capacitance.

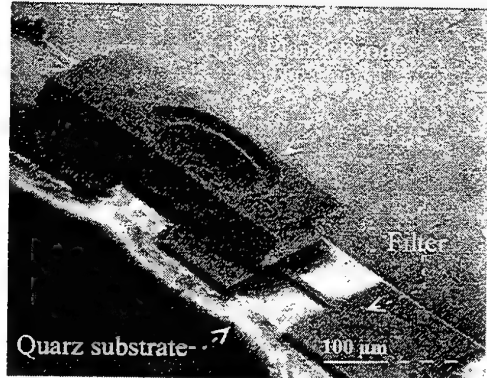


Fig.2: SEM picture of a QVD after soldering onto microstrip filter.

### IV. ANTI-PARALLEL QVD FOR SUBHARMONIC MIXERS

Anti-parallel Schottky diodes are often used in subharmonically pumped mixers because of its symmetrical IV curve. In such mixers the RF-signal has approximately twice the frequency of the LO signal. The advantages of subharmonically pumped mixers are low LO noise, lower LO frequency, easier separation of the RF- and LO-signal and no DC current outside the diodes [4]. Using the planar technology, it is easier to realize anti-parallel Schottky diodes. Usually anti-parallel Schottky diodes are not biased. Therefore, higher LO power requirement is the drawback.

Based on the experiences of QVD, the Anti-Parallel Quasi-Vertical planar Schottky Diode (APQVD) is already developed. Figure 3 shows a SEM picture of an APQVD after separation from the substrate. To notice is that the stray capacitance resulted from the small distance of the two backside contacts is reduced by the only 10  $\mu\text{m}$  thick chip. During the development of the QVDs, it was also noticed that the high air-bridge could be destroyed while the flip-chip soldering of the diode onto the filter structure. In order to avoid such a problem we have introduced two electrolytically plated pillars with a height of 7  $\mu\text{m}$  over the contact pads.

Accurate modeling of the APQVD employed in the mixer is fundamental to design the circuitry in the mixer. The modeling is divided into two parts: modeling of the diode and of the parasitic part around the diode. With the experiences in conventional and substrateless whisker-contacted diodes there was no difficulty to get a proper model of the diode [5, 6]. For the study of the parasitic lump elements of the APQVD, Helsinki University of Technology has used the electromagnetic structure simulator HFSS, whose S-parameter results are fitted with the equivalent circuit and therefore the values of parasitic elements can be evaluated [7].

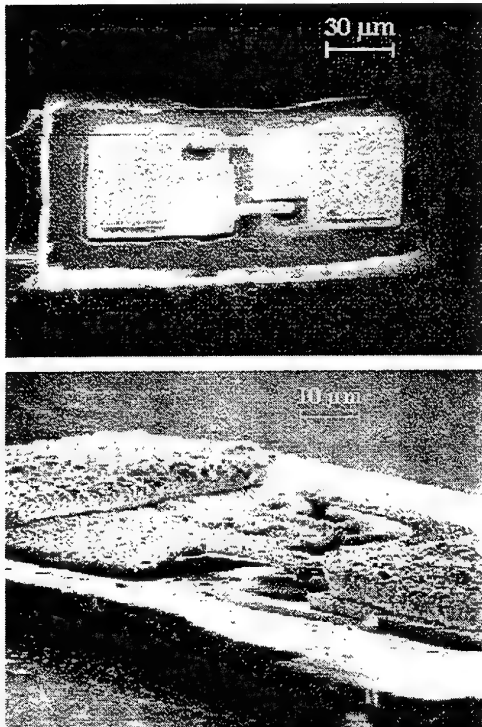
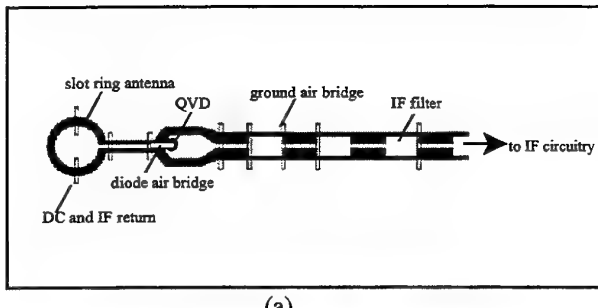


Fig.3: SEM picture of an APQVD after etch separation from the substrate

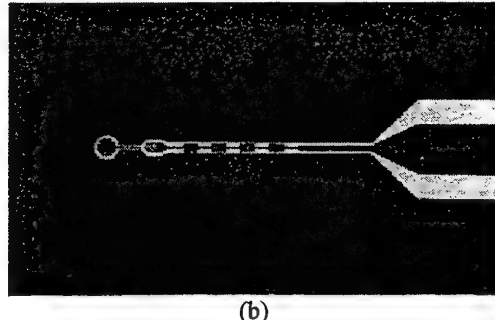
Several batches of APQVDs have been successfully fabricated for 220GHz waveguide subharmonic mixer. By using a material with an active n-layer doping level of  $3 \times 10^{17} \text{ cm}^{-3}$  and a n-layer thickness of 100 nm, the two diodes of an APQVD have typically a very similar IV curve. A series resistance  $R_s=25 \Omega$ , an Ideality factor  $\eta=1.14$  and a breakdown voltage  $V_{bd}=5.4 \text{ V}$  were obtained. Some diodes were delivered to Helsinki University of Technology for RF measurements. After soldering one APQVD onto the microstrip RF filter, the measured diode noise temperature of 350 K / 400 K at 1.4 GHz with a bias current 500  $\mu\text{A}$  shows that this APQVD concept is promising for mixer applications in the submillimeter wavelength regime.

##### V. OUTLOOK TO INTEGRATION

To extend the quasi-vertical planar diode technologies to the full integration of the mixer components, a new ESA/ESTEC activity focusing on an integrated front-end mixer at 650GHz is initiated. This lens-coupled open structure planar mixer includes a planar slot ring antenna feed by coplanar waveguide transmission line, air-bridge connected QVD, IF filter and matching elements, which all are realized on the topside of a semi-insulating GaAs substrate. Figure 4 shows the preliminary design and the technological status before the fabrication of the air bridge to contact the QVD and of the ground air bridges to prevent unwanted modes in the coplanar waveguide transmission line. The used QVD here is chosen with the same material parameters of APQVDs.



(a)



(b)

Fig.4: integrated open structure planar mixer

- (a) schematic sketch
- (b) realized structure

##### VI. CONCLUSION

GaAs Schottky diodes are widely used in frequency multipliers and mixers in the submillimeter wavelength regime. Planar Schottky diodes are developed in the last decade by different research groups to increase the system reliability. Quasi-vertical planar Schottky diode approach, proposed by Technical University Darmstadt, offers an optimized device structure for highest frequency applications. This paper presented the achieved RF results with single quasi-vertical planar Schottky varactor diode for a frequency doubler at 202 GHz and anti-parallel quasi-vertical planar Schottky diode for a subharmonically pumped waveguide mixer at 220GHz.

The demand on all-solid-state high power local oscillators in the submillimeter wave regime requires further optimization of the varactor diode. Therefore the improvement of the breakdown voltage to reach the theoretical value and the optimization of the doping profile to maximize the capacitance modulation is the next goal for planar varactor diode technology. At the same time, with the increasing interest on fully integrated quasi-optical planar mixer systems, we will proceed the further technology development for the integration of the quasi-vertical planar mixer diodes with other system components by using coplanar waveguide and microstrip technique.

## VII. ACKNOWLEDGEMENT

The authors would like to express their acknowledgment to Dr. H. Grothe and Dr. J. Freyer, both from the Technical University of Munich, Germany, for supplying high-quality epitaxial materials.

The research described in this paper was partly sponsored by the European Space Agency, ESA/ESTEC, Noordwijk and the contracts No. 10582/93/NL/NB and No. 11806/96/NL/CL.

## REFERENCES

- [1] A. Simon, A. Grub, V. Krozer, K. Beilenhoff, H. L. Hartnagel, "Planar THz Schottky Diode Based on a Quasi Vertical Diode Structure", *Proc. 4th Int. Symp. Space Terahertz Technol.*, 1993, pp. 392-403.
- [2] C. I. Lin, A. Simon, M. Rodriguez-Gironés, H. L. Hartnagel, P. Zimmermann, R. Zimmermann, "Substrateless Schottky Diodes for THz Applications", *Proc. 8th Int. Symp. on Space Terahertz Technology*, pp. 224-229.
- [3] C. I. Lin, V. Krozer, J. Grajal, A. Simon, H. L. Hartnagel, "Schottky Varactor Diode Optimization for Frequency Multipliers", *Proc. of the Fifth Int. Workshop on Terahertz Electronics*, 1997.
- [4] B. K. Kormanyos *et al.*, "A Planar Wideband 80-200 GHz Subharmonic Receiver", *IEEE Trans. Microwave Theory Tech.*, vol. MTT-41, pp. 1730-1736, 1993.
- [5] T. W. Crowe, "GaAs Schottky Barrier Mixer Diodes For The Frequency Range 1-10 THz", *Int. J. Infrared Millimeter Waves*, vol. 10, pp. 765-777, 1989.
- [6] J. T. Louhi, A. V. Raisanen, "On the Modeling and Optimization of Schottky Varactor Frequency Multipliers at Submillimeter Wavelengths", *IEEE Trans. Microwave Theory Tech.*, vol. MTT-43, pp. 922-926, 1995.
- [7] J. Zhang *et al.*, "Modeling of Quasi-Vertical Planar Anti-Parallel Schottky Diode for Sub-mm-wave Mixers", *Proc. ESA Workshop on Millimetre Wave Technology and Applications*, Noordwijk, Holland, May, 1998.
- [8] J. Mees, *et al.* "Open Structure Integrated Schottky Receiver for Space Applications", *Proc. 20th ESTEC Antenna Workshop on Millimeter Wave Antenna Technology and Antenna Measurements*, ESA/ESTEC, Noordwijk, June, 1997.

# A Planar SIS Mixer for 400–500 GHz

Ralf Nitsch, Karl Jacobs

**Abstract**— We present a new planar SIS mixer for array applications in the 400–500 GHz range. The mixer consists of a double dipole antenna connected to a pair of superconducting tunnel junctions by a novel tuning and matching structure. It is mounted in the focal plane of a silicon parabola collimating the broad double dipole beams into beams with f-numbers of  $\approx 13$ . Four mixers were built in an array configuration on a single substrate and two of them were tested. The receiver DSB noise temperatures are below 300 K in the 456–492 GHz range. The best results are 180 K and 163 K respectively at 473 GHz.

## I. INTRODUCTION

WE present a novel planar SIS mixer for the 400–500 GHz range. The mixer consists of a double dipole antenna connected to a pair of  $1.4 \mu\text{m}^2$  SIS junctions. Four mixers have been arranged in an array configuration and manufactured on a single chip. This chip is mounted in the focal plane of a silicon ( $\epsilon_r = 11.7$ ) filled 24 mm diameter parabolic reflector [3]. About 90 % of the power radiated by the double dipole antennas goes into the dielectric and the reflecting parabola backside collimates the broad double dipole beams into beams with f-numbers of  $\approx 13$ . By placing the mixers offset from the focal point, inclined beams leave the parabola. Fig. 1 shows a sketch of the assembly.

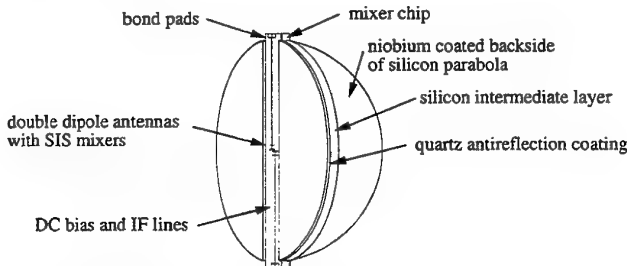


Fig. 1. A sketch of the parabola with the mixer chip and antireflection coating. For clarity, only 2 of the 4 mixers are shown. This sketch is not to scale.

In order to minimize the reflection loss at the interface between the dielectric and free space an antireflection coating is required. This antireflection coating is realized by two  $85 \mu\text{m}$  thick fused quartz plates which are glued onto the parabola at both sides of the mixer substrate. The flat surface is the main advantage of the dielectric filled parabola versus the more common hyperhemispherical substrate lens systems (e.g. [4]) where curved surfaces have to be coated. This is of increasing importance at higher frequencies where thin low loss coatings like crystal quartz are required.

R. Nitsch is with the KOSMA Superconducting Devices and Mixers group, I. Physikalisches Institut der Universität zu Köln, Germany. E-mail: nitsch@ph1.uni-koeln.de .

This paper focuses on the mixer design and measured results of two of the four mixer elements.

## II. ANTENNA AND MIXER CIRCUIT DESIGN

One difficulty in using SIS junctions as submillimeter wave detectors is the high capacitance formed by the junction electrodes and the thin isolation layer. This junction capacitance has to be compensated by inductive components. A simple way to achieve this is the use of two junctions connected by a short transmission line and an antiphase drive of the circuit [5]. Fig. 2 shows the principle.

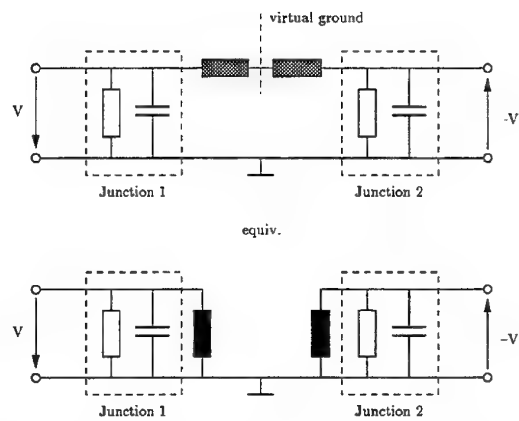


Fig. 2. By driving the circuit in an antiphase manner the node between the two transmission lines (gray coloured) has zero potential with respect to ground. Thus the transmission lines effectively act as two parallel inductors shown in the lower circuit.

The SIS junctions are connected to the dipole antennas by impedance transforming microstrip lines and the so called  $\Gamma$ -match known from radio applications [1]. The  $\Gamma$ -match has three functions: the above mentioned antiphase circuit driving is easily accomplished by connecting the gamma rods to opposite sides of the respective dipole antennas, it is inherently a balun and suited to drive the unbalanced junction circuit, and it has impedance transforming properties. A single  $\Gamma$ -matched dipole antenna has a slightly lop-sided beam pattern but this effect disappears in the double dipole configuration. The RF filter to couple the IF and DC bias is a six element microstrip filter.

Fig. 3 shows a photograph of a manufactured mixer. The thin film capacitors compensate the inductivity produced by the gamma rods and are built by overlaps of the gamma rod ends and the wiring layer. The bends in the circuit allow for optimum transmission line lengths with respect to impedance matching on one hand and an optimum dipole distance for symmetric beam patterns in E- and H-plane on the other hand. At the bottom margin the first RF filter

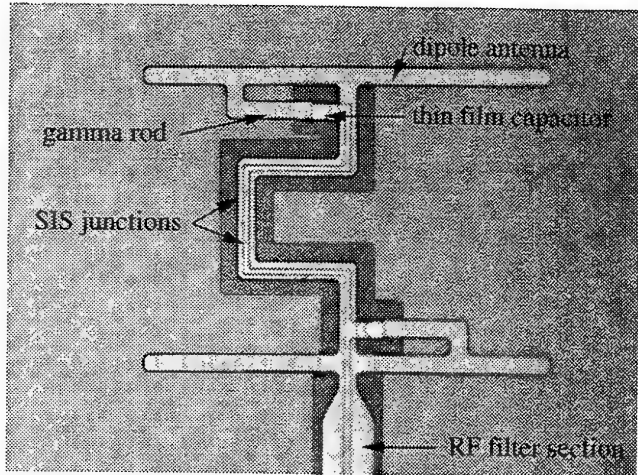


Fig. 3. A photograph of a manufactured mixer. The dipoles are 120  $\mu\text{m}$  long.

section can be seen.

At intermediate frequencies the two junctions are simply connected in parallel except for a negligible phase shift. The IF signal is led through the RF filter to the edge of the parabola by means of a 11.5 mm long and 5  $\mu\text{m}$  wide microstrip line. The IF matching is simplified by the fact, that this transmission line is almost a quarter wavelength long at the 1.5 GHz IF center frequency. The mixer chip is bonded to the IF circuit board just containing 4 open stubs and the microstrip lines to the four SMA type connectors.

The mixer circuit has been analysed and optimized by means of a microwave CAD program [2] whereas the antenna characteristics including the  $\Gamma$ -match on a dielectric half space were determined by scaled model measurements at 0.5 GHz. The superconducting properties of the microstrip transmission lines were taken into account in the circuit analysis.

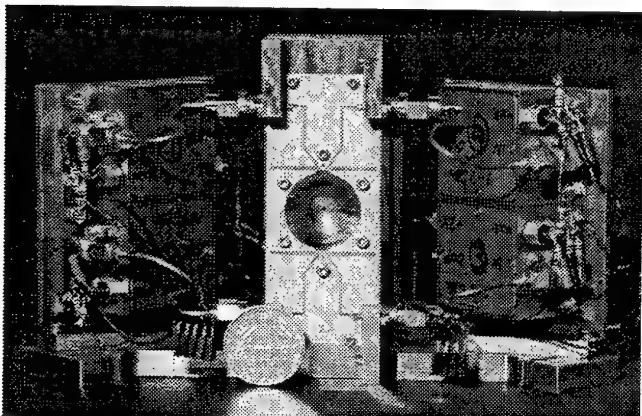


Fig. 4. A photograph of the mixer block. It is surrounded by 4 HEMT amplifiers. In the center of the turned parabola cavity one can see the small diagonal horn for LO injection. The bright area is the IF circuit board. The coin in the foreground is about 23 mm in diameter.

### III. MIXER MANUFACTURING

The silicon chip (approx.  $24 \times 1 \times 0.3 \text{ mm}^3$ ) containing the 4 mixers and the DC-bias/IF-output microstrip lines is glued onto the flat silicon parabola surface. The 0.3 mm thick intermediate layers of silicon and 85  $\mu\text{m}$  thick fused quartz plates are glued onto the parabola at both sides of the mixer substrate. The rear side of the parabola is niobium coated except for a small region around the parabola vertex to allow local oscillator injection via two back to back arranged diagonal horns in the mixer block. This eliminates the need for a signal/LO-diplexer. The niobium coating produces a perfect reflector below the gap frequency of niobium. The parabola is inserted into a copper mixer block and is fixed by means of the IF circuit board covering the mixer block's front side. Fig. 4 shows a photograph of the mixer block.

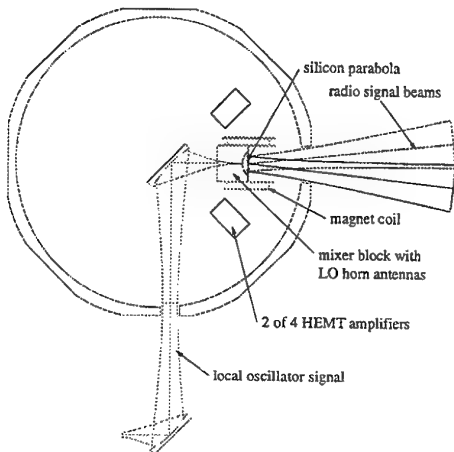


Fig. 5. Sketch of the measurement system.

### IV. RESULTS

Two mixers of the 4 channel array were tested. The LO power is sufficient to pump the mixers although the LO beam is not focussed onto the individual antennas. The DSB system noise temperatures are below 300 K in the range of 456 to 492 GHz. The best results are 180 K (mixer #1) and 163 K (mixer #2) respectively at 472 GHz. Currently beam pattern measurements are under way.

### REFERENCES

- [1] C.A. Balanis: *Antenna Theory - Analysis and Design*, John Wiley & Sons, New York, Chichester, Brisbane, Toronto, Singapore, 1982
- [2] Microwave Harmonica v4.51, Compact Software, Inc., 483 McLean Boulevard, Paterson, NJ 07514, 1994
- [3] P.H. Siegel: *The Dielectric-Filled Parabola: A New Millimeter/Submillimeter Wavelength Receiver/Transmitter Front End*, IEEE Trans. Antennas Propagat., vol. AP-39, no. 1, Jan. 1991, pp. 40-47
- [4] J. Zmuidzinas and H.G. LeDuc: *Quasi-Optical Slot Antenna SIS Mixers*, IEEE Trans. Microwave Theory Tech., vol. 40, no. 9, Sept. 1992, pp. 1797-1804
- [5] J. Zmuidzinas, H.G. LeDuc, J.A. Stern, S.R. Cypher: *Two Junction Tuning Circuit for Submillimeter SIS Mixers*, IEEE Trans. Microwave Theory Tech., vol. MTT-42, no. 4, Apr. 1994, pp. 698-706

# Niobium Nitride Hot-Electron Mixer for THz Frequencies

Yuri Gousev and Håkan Olsson

**Abstract** -- We report on noise temperature measurements for a NbN phonon-cooled hot-electron mixer at radiation frequencies between 0.9 THz and 1.2 THz. Radiation was coupled to the mixer, placed in a vacuum chamber of He cryostat, by means of a planar spiral antenna and a Si immersion lens. A backward-wave oscillator, tunable throughout the spectral range, delivered an output power of few  $\mu$ W that was enough for optimum operation of the mixer. At 4.2 K ambient temperature and 1.025 THz radiation frequency, we obtained a receiver noise temperature of 1550 K despite of using a relatively noisy room-temperature amplifier at the intermediate frequency port. The noise temperature was fairly constant throughout the entire operation range and for intermediate frequencies from 1 GHz to 2 GHz.

**Index terms**-- Hot-electron mixers, THz range receivers, superconducting films, planar antennas.

## I. INTRODUCTION

Astrophysical and stratospherical investigations in the terahertz (THz) frequency range, which are forthcoming events of the next few years, require heterodyne receivers with low-noise mixers. SIS mixers, having lowest noise temperatures up to  $\approx 1$  THz, have a drastic decrease in performance at higher frequencies. Sensitivity of Schottky diode mixers for THz range is limited by high intrinsic noise level in the diode. A superconductive hot-electron mixer (HEM), proposed in [1] and [2], is presently the only alternative to extend heterodyne spectroscopic measurements up to at least 10 THz, possibly over 30 THz. HEMs demonstrate a noise temperature, comparable to that of SIS receivers at 1 THz, and the lowest noise temperatures at higher frequencies [3]. They have also other advantages, like a small required local oscillator (LO) power, a nearly real impedance, and a relatively simple planar technology.

Two different ways to realize a HEM, with cooling of hot electrons via an out-diffusion of carriers from the sensitive element to contact pads [2], or by means of intensive electron-phonon interaction [1], result either in a smaller local oscillator power [3], or in a larger intermediate frequency (IF) bandwidth [4], respectively. Due to the lack of tunable LO sources in the far-infrared

the large IF bandwidth is essentially important for spectroscopic measurements. Though future development of a tunable cw radiation source with a reasonable power at frequencies above 1.5 THz may weaken the latter requirement, IF bandwidth is currently an important issue for the THz mixer.

Large IF signal bandwidths, up to several GHz, of the phonon-cooled HEM have been realized with NbN due to a very short electron-phonon interaction time in this material, which is about 10 ps at 10 K [5]. Even a shorter time has been reported for  $\text{YBa}_2\text{Cu}_3\text{O}_{7-\delta}$  [6], which could result in a high-temperature superconducting THz mixer with large IF bandwidth. Since the effective IF bandwidth of the hot-electron mixer is larger than the conversion gain bandwidth due to decrease of temperature fluctuation noise at high IF [7,4], NbN mixers are supposed to have effective IF bandwidths over 10 GHz.

In this paper we report on first receiver measurements at the Royal Institute of Technology, performed with an NbN phonon-cooled hot-electron mixer. Two devices have been investigated, with different sensitive element volumes and, correspondingly, different optimum LO power. We demonstrate that the receiver noise temperature is fairly constant between 0.9 THz and 1.2 THz throughout the IF measurements range.

## II. EXPERIMENTAL SET-UP

35 Å thick NbN films were deposited on 350  $\mu$ m thick Si substrates by magnetron sputtering of Nb in the atmosphere of Ar and N; a 0.3  $\mu$ m Ti-Au layer was deposited on top. By means of photolithography and ion milling a NbN microbridge and a gold planar logarithmic spiral antenna were formed (Fig. 1). Since NbN films have

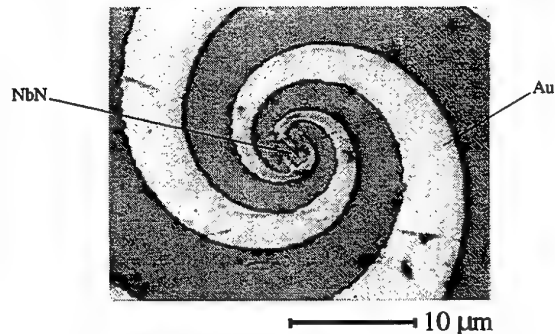


Fig. 1. Inner part of the spiral antenna. NbN film between the antenna arms is transparent and therefore is not visible on the picture.

Manuscript received July 31, 1998. This work was supported by the Swedish Research Council for the Engineering Sciences (TFR) and the Swedish Institute.

The authors are with the Department of Electronics, Royal Institute of Technology, Electrum 229, S-164 40 Stockholm, Sweden.

E-mail: yuri@ele.kth.se

large sheet resistance, the microbridge was shaped in a horse shoe form in order to match the normal state resistance of the device to the radiation resistance of the planar antenna which is  $377[2(\epsilon+1)]^{-0.5} \approx 75 \Omega$  ( $\epsilon = 11.4$  is the dielectric constant of Si). Arms of the planar antenna were connected to a co-planar transmission waveguide [8]. The superconducting transition temperature of NbN film for two devices used in the experiment was 7.5 K (device #1) and 7.9 K (device #2), with a transition width of 1.2 K and 1.1 K, respectively. The normal state resistance, taken at a temperature of 16 K, was  $140 \Omega$  for device #1 and  $320 \Omega$  for device #2.

A Si synthesized elliptical lens with no anti-reflection coating was used to couple radiation to the mixer. A hybrid antenna, consisting of the planar antenna and the immersion lens, had a nearly rotationally symmetrical radiation pattern (Fig. 2) with a main lobe width  $\Theta_A$  of  $1.7^\circ$  at the  $-3 \text{ dB}$  level. The radiation pattern was obtained by measuring a

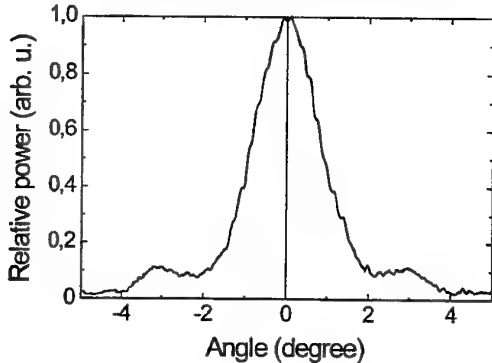


Fig. 2. Radiation pattern of the hybrid antenna at 0.97 THz.

direct detection response of the NbN microbridge to a low power radiation at a frequency of 0.97 THz, produced by a backward-wave oscillator. The effective aperture of the hybrid antenna,  $\approx 100 \text{ mm}^2$ , was about 80 % of the cross-section of the immersion lens, thus approaching a maximum possible value.

Heterodyne measurements were performed with two black body radiation sources; a backward-wave oscillator (BWO), fabricated by ISTOK (Russia), served as a local oscillator at radiation frequencies between 0.9 and 1.2 THz. Maximum total output power, delivered by the BWO, was  $10 \mu\text{W}$  at 0.97 THz. Two black body sources were placed in a vacuum chamber (Fig. 3), connected with a He cryostat, thus eliminating a problem of water vapor absorption in the signal path. One black body was attached to a metal can filled with liquid  $\text{N}_2$  and had a temperature of about 90 K; the can was hanging in the vacuum chamber on a stainless steel tube serving also as a filling path for  $\text{N}_2$ . The other black body was fixed to a wall of the vacuum chamber and had a temperature of 290 K.

A TPX lens, installed instead of one window of the vacuum chamber, was matching the diverging beam of the BWO to the hybrid antenna. A wire grid polarizer served as

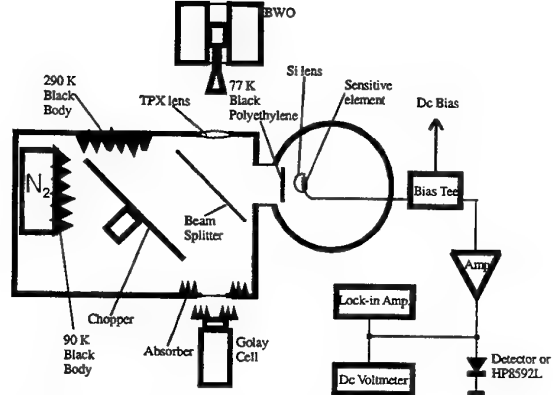


Fig. 3. Block diagram of the experimental set-up.

a beam splitter for device #1; a Mylar beam splitter was used when measuring with device #2. A Golay cell, calibrated with a black body radiation, was set in the LO path to control output power of the BWO. Black polyethylene film, cooled to 77 K, blocked the near-infrared background radiation from the vacuum chamber to eliminate parasitic heating of the mixer. A mechanical chopper with a gold-plated blade switched radiation from the two black bodies. IF signal from the mixer at frequencies between 1 GHz and 2 GHz was amplified by a room temperature amplifier (noise temperature 40 K), then integrated with a diode detector, and recorded by a lock-in amplifier. To measure the IF dependence of the noise temperature, we used an internal detector of HP8592L spectrum analyzer, thus having a possibility to measure the signal at different IF frequencies within the amplifier bandwidth; the resolution bandwidth was set to 3 MHz.

### III. HETERODYNE MEASUREMENTS AND DISCUSSION

Current-voltage (IV) characteristics for both mixers with and without LO power applied are presented in Fig. 4.

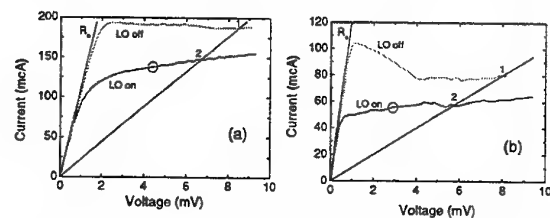


Fig. 4. Voltage-current characteristics for device #1 at an ambient temperature of 3.9 K (a) and device #2 at a temperature of 4.2 K (b). Operation point is marked by a circle.

Dc resistance of both devices increased from a constant value of few  $\Omega$  at bias voltage below 1 mV to about  $30 \Omega$  for device #1 and  $60 \Omega$  for device #2 at a bias of five millivolt. We apply the constant dc resistance at small bias voltage,  $R_s$ , to a dc series resistance of the bias tee ( $3.8 \Omega$ ) and the resistance of the spiral antenna arms. Device #2 demonstrated lower bias currents and higher differential

resistance compared to those of device #1 within the bias voltage interval.

Optimum LO power,  $P_{LO}$ , absorbed by the mixer at a radiation frequency of 0.97 THz, was obtained as a difference between power, dissipated in the mixer at two operation points, 2 and 1, with and without LO applied, respectively. The dc resistance of the mixer at two points and, consequently, the electron temperature, was the same. We extracted the dc power dissipated in the series resistance  $R_s$  when calculating  $P_{LO}$ . Optimum LO power for device #2 (130 nW), was 6 times lower compared to that of device #1 (0.8  $\mu$ W), corresponding to a smaller volume for the device #2. Since the available LO power was limited, we used the wire grid polarizer for heterodyne measurements with device #1, thus providing a larger LO power and having additional losses in the signal path. Besides 3 dB polarization loss in the signal path, the wire grid beam splitter added a resistive loss of 0.5 dB.

Double sideband (DSB) receiver noise temperature for different intermediate frequencies, measured with device #2 at 1.025 THz, is presented in Fig. 5. Though the noise temperature varies within 10 % in the range of our IF amplifier, we could not observe any pronounced IF dependence. Deviations in the noise temperature should be rather explained by the influence of our IF chain.

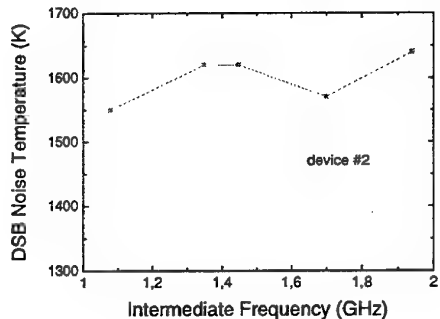


Fig. 5. System noise temperature versus intermediate frequency for device #2.

Noise temperature versus radiation frequency for device #2 is presented in Fig. 6. The noise temperature is fairly constant throughout the operation range. The largest Y-factor, 1.122, and a corresponding noise temperature of 1550 K were obtained at 1.025 THz for an IF of 1.1 GHz. We should point out that all measurements were performed with a room temperature IF amplifier, which contributes about 30 % to the total noise temperature of the receiver. Using a cooled amplifier should result a decrease in noise temperature down to  $\approx 1000$  K.

Device #1 demonstrated a higher noise temperature (Fig. 6). However, unlike device #2, it was used with the wire grid beam splitter, which had much higher losses compared to that of the Mylar beam splitter. Extracting 3.5 dB loss in the grid beam splitter, we obtain a lowest noise temperature of 1170 K at 0.97 THz, which is less than that of device #2 with extracted losses in Mylar. The lower

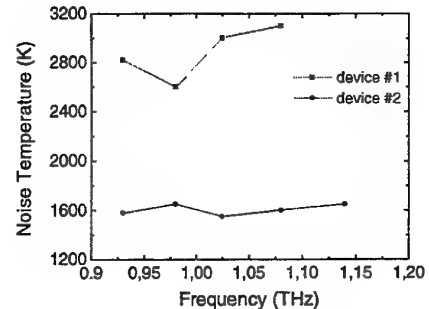


Fig. 5. System noise temperature for different radiation frequencies.

noise temperature of device #1 may be explained by a smaller normal state resistance, resulting in a smaller rf mismatch.

Other rf losses, which contribute to the receiver noise temperature, are listed in Table 1. Extracting reflection loss at the surface of the immersion lens, reflection and transmission loss in the polyethylene filter, and contribution from the IF amplifier, we obtain a 300 K intrinsic noise temperature of the mixer. Better matching a rf and IF impedance would result in even lower noise temperatures.

Element	Loss (dB)	
	Device #1	Device #2
Beam Splitter (wire grid)	3.5	-
Beam Splitter (Mylar)	-	1
Black Polyethylene filter	0.5	0.5
Reflection at Si surface	1.5	1.5
Absorption in Si	0.4	0.4
Rf mismatch	0.4	2.1

Table 1. Rf losses.

The measured low value of the system noise temperature of the NbN phonon-cooled hot-electron mixer and obvious possibilities for further improvement demonstrate the advantages of the mixer at THz frequencies. Comparing our present results with those obtained in the first experiments with phonon-cooled HEM at 2.5 THz [9], where the noise temperature was many times higher, one should find a reasonable explanation for a drastic decrease in sensitivity at the higher frequency. We should mention numerous changes in our present experimental setup, such as better quasi-optical alignment of the system, eliminating the problem of water vapor absorption, and much higher power stability of the BWO compared to that of the FIR gas laser used in [9]. As a one more important factor, we should point out a greatly improved quality of NbN films. We believe there is no physical reason for any deterioration in performance at radiation frequencies up to at least 10 THz.

#### IV. CONCLUSION

We have demonstrated operation of NbN hot-electron mixer in a frequency range between 0.9 THz and 1.2 THz without any deterioration in performance. The measured

DSB receiver noise temperature, about 1550 K, only slightly changes at intermediate frequencies from 1 GHz to 2 GHz, thus proving suitability of phonon-cooled hot-electron mixers for spectroscopic measurements.

#### V. ACKNOWLEDGMENT

We thank G. N. Gol'tsman and B. M. Voronov for fabrication of NbN samples. Yu. Gousev is grateful to KTH staff for technical support.

#### REFERENCES

- [1] E. M. Gershenzon, G. N. Gol'tsman, I. G. Goghidze, Yu. P. Gousev, A. I. Elant'ev, B. S. Karasik, and A. D. Semenov, The mixer for millimeter and submillimeter wavelengths based on electron heating in the resistive state of superconductive films, *Sov. Phys. Superconductivity* **3**(10), pp. 1582-1597 (1990).
- [2] D.E. Prober, Superconducting terahertz mixer using a transition-edge microbolometer, *Appl. Phys. Lett.* **62**(17), pp. 2119-2121 (1993)
- [3] B.S. Karasik, M.C. Gaidis, W.R. McGrath, B. Bumble, and H.G. LeDuc, Low noise in a diffusion-cooled hot-electron mixer at 2.5 THz, *Appl. Phys. Lett.* **71**(11), pp. 1567-1569 (1997).
- [4] H. Ekström, E. Kollberg, P. Yagoubov, G. Goltsman, E. Gershenzon, and S. Yngvesson, Gain and noise bandwidth of NbN hot-electron bolometric mixers, *Appl. Phys. Lett.* **70**(24), pp. 3296-3298 (1997).
- [5] Yu.P. Gousev, G.N. Gol'tsman, A.D. Semenov, E.M. Gershenzon, R.S. Nebosis, M.A. Heusinger, and K.F. Renk, Broadband ultrafast superconducting NbN detector for electromagnetic radiation, *J. Appl. Phys.* **75**(7), pp. 3695-3697 (1994).
- [6] A.D. Semenov, R.S. Nebosis, Yu.P. Gousev, M.A. Heusinger, and K.F. Renk, Analysis of the nonequilibrium photoresponse of superconducting films to pulsed radiation by use of a two-temperature model, *Phys. Rev. B* **52**(1), pp. 581-590 (1995).
- [7] B.S. Karasik and A.I. Elantiev, Noise temperature limit of a superconducting hot-electron bolometer mixer, *Appl. Phys. Lett.* **68**(6), pp. 853-855 (1996).
- [8] Yu.P. Gousev, A.D. Semenov, E.V. Pechen, A.V. Varlashkin, R.S. Nebosis, and K.F. Renk, Coupling of THz radiation to a high-T<sub>c</sub> superconducting hot electron bolometer mixer, *Appl. Phys. Lett.* **69**(5), pp. 691-693 (1996).
- [9] D. Semenov, Yu. P. Gousev, R. S. Nebosis, K. F. Renk, P. Yagoubov, B. M. Voronov, G. N. Gol'tsman, and E. M. Gershenzon. Heterodyne detection of THz radiation with a superconducting hot-electron bolometer mixer. *Appl. Phys. Lett.* **69**(2), pp. 260-262 (1996).

# An Accurate Calculation Method of the Absorbed LO Power in Hot Electron Bolometric Mixers

Harald Merkel, Pavel Yagoubov, Pourya Khosropah, Erik Kollberg

## The authors are with

**Abstract**—Based on a one dimensional heat transport equation for the electrons in a superconducting hot electron bolometer a model for a hot spot mixer is set up. The heating due to a DC bias is limited to the hot spot region where the LO power is absorbed uniformly. This gives rise to a novel measurement method for the absorbed LO power.

## I. INTRODUCTION

Since feasibility of low noise hot-electron bolometric mixers has been proven the focus of interest has moved to optimize the bolometer mixer design and improve and adapt the quasioptics for specific applications. This requires accurate measurement procedures for the absorbed LO power being the key design parameter for antenna matching and optical loss estimation.

The standard "isothermal" method to calculate the absorbed LO power [1] treats the bolometer as a zero dimensional device: Its resistance is described by a single electron temperature which depends on the sum of LO and heating power. Comparing two operating points with the same resistance the total power is identical. The bias power difference in both points yields directly the LO power change. This method gives reasonable results for large bias voltages. In the optimal operating region the so calculated LO power is about a factor 1.5 to 3 smaller compared to calorimetric measurements.

In order to improve the LO power calculation method we treat the bolometer bridge as an one dimensional device which is described by an electron temperature profile. Heating the device with bias power results in the formation and growth of hot spots. The bias power is dissipated in the hot spot where the bridge is in normal state. For operating frequencies above the quasiparticle bandgap the LO power is absorbed uniformly along the whole bridge. So the bias power and LO power heat the bolometer and change the resistance with

different efficiencies. For large bias voltages where the hot spot fills almost the whole bolometer bridge LO and bias power show the same efficiency. Then LO and bias power are directly exchangeable in terms of equal heating and device resistance. Obviously the LO and bias powers are not at all exchangeable for small bias voltages if the hot spot is short. There bias heating is concentrated and a small positive change pushes a comparably large portion of the bridge to normal state. This contrasts LO power which is (for frequencies above the quasiparticle bandgap) uniformly absorbed and yields a comparably small resistance change. This explains why the standard isotherm method yields best results for large bias voltages and why the results are too small for small voltages: There a small bias power difference is sufficient to replace a large LO power leading to identical resistances. It also explains why the discrepancy of absorbed LO power becomes more and more prominent for frequencies above the bandgap: If the LO frequency is below the bandgap only the hot spot plus a small fringe region exhibit a low enough local quasiparticle bandgap to allow LO power absorption. Then LO and bias power dissipation are both localized around the hot spot leading to similar efficiencies. For frequencies above the bandgap LO absorption is uniform and differences in heating efficiencies arise.

The new calculation procedure is carried out as follows:

- Measure two operating points with identical DC resistance and a known LO power ratio and obtain the difference of the DC powers between these points (equivalent to the first step of the traditional "isothermal" method)
- Calculate the conversion function (given below) requiring the hot spot length (obtained from the device resistance) and the thermal healing length (a constant depending on the film properties)
- Convert the DC power difference to a LO power using the power conversion function .

The authors are with the Dept. of Microelectronics , Chalmers Univ. of Technology, Gothenburg , SWEDEN

In the subsequent parts we will shortly summarize the results of an one dimensional thermal model resulting in an expression for the power conversion function and the hot spot length as a function of device resistance and show some calculation examples comparing the hot spot corrected absorbed LO powers with the isothermal approach.

## II. AN ONE DIMENSIONAL HOT SPOT MODEL

It has been recently shown [2] that the resistive properties of HEB in a wide operating region are determined by hot spot formation and growth. In contrast to other phonon cooled HEB models we treat the bolometer as an one-dimensional structure on which a heat conduction equation for the electron temperature  $T$  is set up for a bolometer extending from  $-L$  to  $L$  with a centered hot spot ranging from  $-H$  to  $H$ :

$$\lambda \frac{d^2}{dx^2} T(x) - \sigma [T(x) - T_{bath}] +$$

$$\alpha [P_{RF} + P_{bias} \cdot (u(x+H) - u(x-H))] = 0$$

Ideal thermal coupling of the electrons in the normal conducting pads yields the boundary conditions for the one dimensional heat transport equation:

$$T(-L) = T(+L) = T_{bath}$$

In the above equations  $\lambda$  denotes the thermal conductivity of the electrons,  $\sigma \propto \frac{c_{el}}{\tau_{e \rightarrow ph}}$  the cooling efficiency,  $\alpha$  the heating efficiency.  $P_{RF}$  and  $P_{bias}$  are the RF and bias powers dissipated in the film.  $u(x)$  denotes the Heaviside unit step function. In the following we will use a normalized thermal healing length defined by  $c = \frac{\lambda}{\sigma}$ .

The LO power is absorbed uniformly all over the bolometer strip. Bias power is only dissipated in the hot spot region. The only unknown parameter is the ratio of thermal conductivity and the radiation efficiency referred to as thermal healing length  $\sqrt{c}$ . For a sharp hot spot a closed form solution for the electron temperature is available:

$$T(x) = T_{bath} + \frac{e^{\frac{-H-x}{\sqrt{c}}} \cdot \left( e^{\frac{L+x}{\sqrt{c}}} - 1 \right)}{2 \cdot \left( 1 + e^{\frac{2L}{\sqrt{c}}} \right)} + \left[ \alpha P_{DC} \cdot \left( e^{\frac{2H}{\sqrt{c}}} - 1 \right) \cdot \left( 1 + e^{\frac{L+x}{\sqrt{c}}} \right) + 2 \cdot \alpha P_{LO} \cdot e^{\frac{H}{\sqrt{c}}} \cdot \left( e^{\frac{L}{\sqrt{c}}} - e^{\frac{x}{\sqrt{c}}} \right) \right] + \frac{\alpha P_{DC}}{2} e^{\frac{-H-x}{\sqrt{c}}} \left[ \left( e^{\frac{H}{\sqrt{c}}} - e^{\frac{x}{\sqrt{c}}} \right)^2 \sigma(x-H) - \left( e^{\frac{H+x}{\sqrt{c}} - 1} \right)^2 \sigma(x+H) \right]$$

The hot spot length for a given absorbed bias and LO power is obtained by solving the quartic equation:

$$T(H) = T_c$$

The DC device resistance is proportional to the hot spot length. So knowing the device resistance from measurements the hot spot length is obtained directly circumventing the quite cumbersome procedure to solve the above equation explicitly.

### A. Power conversion function for LO and DC power

The change of the device resistance due to a change in absorbed power becomes then:

$$\frac{\Delta R}{R(T_c)} = \frac{\Delta H}{L} = \frac{\alpha}{L} \cdot \left( \frac{\partial H}{\partial P_{LO}} \Delta P_{LO} + \frac{\partial H}{\partial P_{DC}} \Delta P_{DC} \right)$$

The resistive change may be caused by a change in DC power or in LO power. A change in LO power has therefore to be compensated by a change in DC power for the resistance to remain constant. Measuring a change in DC power between two points with  $\Delta R = 0$  the DC power difference can be converted to a difference in absorbed LO power by the following relation choosing signs properly. Defining a power conversion function  $\chi$  and performing the derivatives one obtains the following relation. It is considerably simplified for small absorbed powers and cold substrates.

$$\begin{aligned} \chi &= \left| \frac{\Delta P_{DC}}{\Delta P_{LO}} \right| = \left| \frac{\frac{\partial H}{\partial P_{LO}}}{\frac{\partial H}{\partial P_{DC}}} \right| = \\ &= \left( e^{\frac{2H}{\sqrt{c}}} + e^{\frac{2L}{\sqrt{c}}} \right) \cdot (T_c - T_{bath}) - \alpha P_{LO} \cdot \left( e^{\frac{H}{\sqrt{c}}} - e^{\frac{L}{\sqrt{c}}} \right)^2 \\ &= \frac{2 \cdot e^{\frac{H+L}{\sqrt{c}}} \cdot (T_c - T_{bath}) + \alpha P_{DC} \cdot \left( e^{\frac{H}{\sqrt{c}}} - e^{\frac{L}{\sqrt{c}}} \right)^2}{e^{\frac{2H}{\sqrt{c}}} + e^{\frac{2L}{\sqrt{c}}}} \\ &\approx \frac{\frac{2H}{\sqrt{c}} + \frac{2L}{\sqrt{c}}}{2 \cdot e^{\frac{H+L}{\sqrt{c}}}} \end{aligned}$$

As a general rule the device resistance reacts more sensitive to DC power than to LO power requiring less DC power to compensate a certain LO power to yield  $\Delta R = 0$ . This results in conversion functions larger than 1. The evaluation of the above conversion function requires an estimate of

the hot spot length and for the thermal healing length.

### B. Length of a hot spot as a function of device resistance

Referring again to the above proportionality chain the proportionality factor between the hot spot length and the device resistance can be expressed by scaling:

Since we assume that the device resistance is caused by a hot spot only the resistance is zero for  $H=0$  and reaches a part  $q$  of its normal resistance if  $H=L$  at  $T_c$ . The factor  $q$  depends on the definition of the critical temperature and  $q \in [0.3 \dots 0.8]$ ,  $R_N$  denotes the normal resistance at about 20K. In the calculations shown below  $q=0.5$  is assumed. Based on these scaling relations the relative hot spot length becomes:

$$\frac{R}{R(T_c)} = \frac{R}{q \cdot R_N} = \frac{H}{L}$$

### C. Estimation of the thermal healing length

The thermal healing length depends on the thermal conductivity and the electron-phonon interaction time. Since the thermal conductivity is not known exactly a reasonable value has been chosen. For all calculations shown below  $\sqrt{c} \approx 10^{-5} \cdot m$  has been assumed.

## III. THE ABSORBED LO POWER CALCULATION PROCEDURE

### A. Intersect two iv curves with a line $R=const$ and calculate DC power difference

On the iv curve pumped with the absorbed LO power to be determined one measured voltage and current in a point of interest  $(u_0, i_0)$ . Results for two devices at two different locations are shown in Table 1. Putting an additional absorber in the LO path (here  $\beta = 0.8 dB$  damping in all measurements) one obtains another pumped iv curve with weaker LO power. Choose then point on this iv curve which exhibits the same resistance as the first point giving  $(u_1, i_1)$ . From these points the difference in DC power is calculated. (For ease of comparison Table 1 indicates the value  $\Delta P = \frac{1}{1-\beta} \Delta P_{DC}$  which is the result of the isothermal approach)

### B. Calculate the conversion function for the chosen resistance

Inserting the device resistance in the hot spot length expression one can evaluate the conversion

function with an appropriate thermal healing length. The value for the conversion function for the given data points are listed as  $\chi$  in the table below. The conversion factors are close to 0dB if the measurement is performed on an almost

normal conducting bolometer with an  $\frac{H}{L} \approx 1$  ("large" measurement) and reaches values up to 40dB for in the limit of small bias voltages.

### C. Convert the DC power difference to a LO power difference

Now the DC power difference from step A is converted to an equivalent LO power difference by multiplication with the power conversion function value from step 2. The so obtained LO power difference equals  $\Delta P_{LO} = (1-\beta) \cdot P_{DC}$ . The absorbed LO power for point 0 is then given by:

$$P_{LO} = \frac{1}{(1-\beta)} \cdot \chi \cdot \Delta P_{DC}$$

The data shown below have been taken from three different devices manufactured at CTH during the last year. Measured iv curve pairs for the isothermal method were already available. The calculation of the local device resistance, the conversion function has been performed in several points for varying bias voltage.

## IV. MINIMAL BIAS POWER TO SUSTAIN A HOT SPOT

The above model is valid under the assumption that a hot spot is present on the bolometer strip. To sustain a hot spot the electron temperature must exceed the critical temperature at least at a single point along the strip. This minimal heating power must be provided by bias or by the LO source. In the framework of this model the electron temperature attains its maximum in the center of the bolometer bridge. According to Ginzburg-Landau's theory of a superconductor the shortest possible hot spot has a length of about twice the correlation length  $\xi$ . Then the bias power needed to sustain a hot spot becomes:

$$P_{DC} = \frac{\frac{1}{\alpha} \cdot (T_c - T_{bath}) \cdot \left( 1 + e^{\frac{2L}{\sqrt{c}}} \right) - P_{LO} \cdot \left( e^{\frac{2\xi}{\sqrt{c}}} - 1 \right)^2}{\left( 1 - e^{\frac{2\xi}{\sqrt{c}}} + e^{\frac{2L}{\sqrt{c}}} - e^{\frac{2L-\xi}{\sqrt{c}}} \right)}$$

For the devices investigated some 10nW are needed to keep the hot spot alive without LO power. Typically LO powers larger than 200nW are needed to generate a stable hot spot without any bias power. So the power levels observed are well in the range where the model is valid.

## V. SUMMARY

Figure 1 shows calculated LO powers using the "traditional" isothermal method exhibiting a substantial drop in LO power at small bias voltages. In Figure 2 results for the absorbed LO power for the same set of devices are shown using the method presented here. The results indicate an almost constant absorbed LO powers as expected from theory and from calorimetric measurements. So the concept of a power conversion function to translate dissipated DC to LO powers based on the physically different action of the both powers yields reliable absorbed LO power data. Furthermore it is solely based on pumped IV curve and  $R(T_c)$  measurements and accurate enough to analyze antenna matching properties of quasioptical bolometric mixers.

## VI. ACKNOWLEDGMENTS

The work presented in this paper has been funded by the European Space Agency under contract #11738/95/NL/MV.

## VII. TABLES AND GRAPHS

device	u0 (mV)	i0(μA)	u1(mV)	i1(μA)
O2, large	2.2	33.0	2.55	38.5
O2, opt.	0.75	23.0	1.05	32.5
N4, large	1.77	49.5	1.82	51.0
N4, opt.	0.59	40.5	0.62	42.5

device	R(Ω)	Pdc1 (nW)	Pdc2 (nW)	χ(1)
O2, large	66.6	72.6	98.1	1.0
O2, opt.	32.6	17.3	34.1	1.5
N4, large	35.7	87.6	92.8	1.0
N4, opt.	14.6	23.9	26.3	1.7

device	PLO isotherm (nW)	PLO hot spot (nW)
O2, large	153.4	153
O2, opt.	101.3	155
N4, large	31.23	31
N4, opt.	14.7	26

Table 1: Measurement results for a large and the optimal bias voltage for two devices

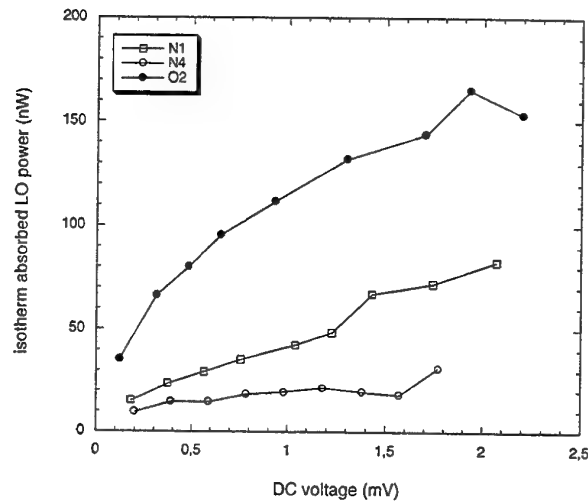


Figure 1: Absorbed LO power obtained with the isothermal method

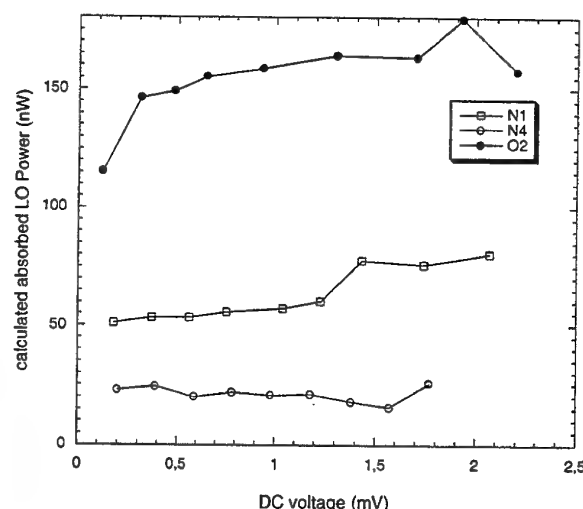


Figure 2: Absorbed LO power obtained with the method presented in this paper

## VIII. REFERENCES

- [1] Hans Ekström, Boris Karasik, Erik Kollberg, "Conversion Gain and Noise of Niobium Superconducting Hot Electron Mixers", IEEE Trans. Microwave Tech. Vol.45 #4, (April 1995) pp.938-946
- [2] Harald F. Merkel, Erik L. Kollberg, K. Sigrid Yngvesson, "A Large Signal Model for Phonon-Cooled Hot Electron Bolometric Mixers for THz Frequency Applications", Proceedings of the 9.th Space Terahertz Symposium, Pasadena, CA (March 1998), in press
- [3] E.M. Gershenson, G.N. Gol'tsman, Y.P. Gousev, A.I. Elant'ev, A.D. Semenov, "Electromagnetic Radiation Mixer Based on Electron Heating in Resistive State of Superconductive Nb and YbaCuO Films", IEEE Trans. Magnetics Vol.27 #2, (March 1991) pp1317-1320

# Performance of NbN phonon-cooled hot-electron bolometric mixer at Terahertz frequencies

P. Yagoubov, M. Krug, H. Merkel, E. Kollberg, *Fellow, IEEE*, J. Schubert, H. -W. Hübers, G. Schwaab, G. Gol'tsman, and E. Gershenzon

**Abstract**—The performance of a NbN based phonon-cooled Hot Electron Bolometric (HEB) quasioptical mixer is investigated in the 0.65-3.12 THz frequency range. The device is made from a 3 nm thick NbN film on high resistivity Si and integrated with a planar spiral antenna on the same substrate. The in-plane dimensions of the bolometer strip are 0.2x2  $\mu$ m. The results of the DSB noise temperature are: 1300 K at 650 GHz, 4700 K at 2.5 THz and 10000 K at 3.12 THz. The RF bandwidth of the receiver is at least 2.5 THz. The amount of LO power absorbed in the bolometer is about 100 nW. The mixer is linear to within 1 dB compression up to the signal level 10 dB below that of the LO. The intrinsic single sideband conversion gain is measured to be -9 dB, the total conversion gain -14 dB.

## I. INTRODUCTION

For detection of THz radiation in radio astronomical applications there is a strong need in low noise broadband receivers. The Nb based SIS mixer is a well established technology in the frequency range from 100 GHz up to 800 GHz, but beyond that frequency, which is the Nb superconducting energy gap frequency, the sensitivity degrades considerably due to the RF losses in the superconductor. Other mixer types, e.g. Schottky diodes, are very noisy and require high local oscillator (LO) power. Due to the few available powerful laser lines in the THz frequency range, this is a very important issue.

The concept of superconducting HEB mixers has been suggested for receivers at submm frequencies in [1]. This mixer technology is already competitive to SIS mixers at frequencies around 1 THz [2-4] and represents a very attractive candidate at higher frequencies. HEB mixer can in principle operate up to at least 100 THz without degradation in performance. An intermediate frequency (IF) bandwidth of several GHz has been achieved for both phonon-cooled [5-7] and diffusion-cooled [8-10] HEB mixers in experiments below 1 THz, the LO power requirement for these mixers is as low as  $\leq$  100 nW. The lowest DSB noise temperatures obtained so far for HEB mixers are: 500 K at 640 GHz, 600 K at 750 GHz, 850 K at 910 GHz, 1250 K at 1.1 THz [2,3] and 2800 K at 1.56 THz

[11] (phonon-cooled NbN HEB); 650 K at 533 GHz [10], 1880 K at 1267 GHz [4] and 3000 K at 2.5 THz [12] (diffusion-cooled Nb HEB). In this paper we present the results of our first measurements of NbN phonon-cooled mixer at frequencies well above 1 THz.

## II. RECEIVER DESIGN

The device is made from a 3 nm NbN film sputtered on high resistivity double side polished silicon substrate. The film is patterned by e-beam lithography to form a 0.2  $\mu$ m long and 2  $\mu$ m wide strip across the center gap of an Au antenna. The details of the fabrication process can be found in [13]. The normal state resistance of the device measured at 20 K is 350 Ohm, the critical current is 230  $\mu$ A. A micrograph of the bolometer integrated with the antenna is shown in Fig. 1. The antenna is an equiangular spiral with a 90° arm width, which yields a self-complementary design. The spiral expansion rate is optimized for smooth and uniform antenna patterns with small variations in beamwidth with frequency and wide bandwidth. Based on previous experiences an expansion rate of 3.2 per turn was chosen for a 1.5 turn antenna. A wide bandwidth is needed at the present stage of the mixer development since it allows to perform mixer measurements and comparison of mixer properties over a wide frequency range. All results presented in this paper were obtained with one device, so the RF bandwidth of the mixer is at least 2.5 THz.

## III. MEASUREMENT SETUPS

For heterodyne measurements we use two different experimental setups. The receiver noise temperature at 0.7 THz and 2.5 THz is measured with the setup shown in Fig. 2. The local oscillator is a FIR laser with an output power of about 1 mW at 2.5 THz which is optically pumped by a CO<sub>2</sub> laser. To prevent back-coupling between the FIR and CO<sub>2</sub> laser cavities and spatial hole burning in the FIR laser, the FIR laser cavity uses a ring laser design. The FIR laser power is coupled out via a 3 mm diameter hole coupler. To be able to monitor its output power, part of the FIR laser beam is coupled onto a pyro detector via a wire grid. A rotatable wire grid was used as an attenuator to adjust the laser power on the device. A Martin Puplett interferometer diplexer based on 10  $\mu$ m thick wire grids couples the signal beam and the local oscillator beam onto

P. Yagoubov, H. Merkel, M. Krug and E. Kollberg are with the Chalmers University of Technology, S-412 96 Gothenburg, Sweden.  
J. Schubert, H.-W. Hübers and G. Schwaab are with the DLR Institute of Space Sensor Technology, D-12489 Berlin, Germany.  
G. Gol'tsman and E. Gershenzon are with the Moscow State Pedagogical University, Moscow 119435, Russia.



Fig. 1. SEM micrograph of the mixer. The  $0.2\text{ }\mu\text{m}$  long and  $2\text{ }\mu\text{m}$  wide NbN bolometer strip is located between the spiral antenna arms.

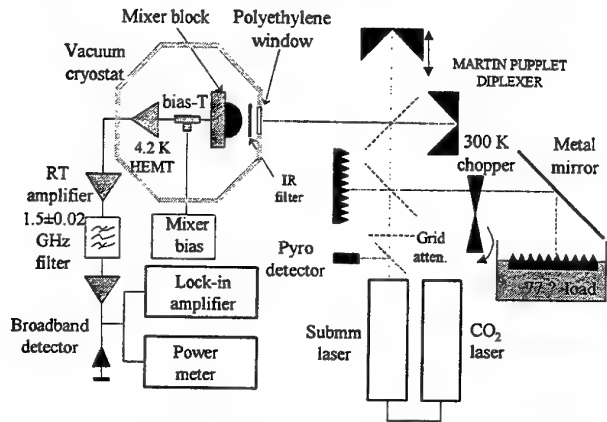


Fig. 2. Schematic of experimental setup for 0.7 and 2.5 THz measurements. For the measurements at 3.1 THz the Martin Pupplet diplexer is replaced by a beamsplitter (not shown in the picture).

the mixer. The FIR power was sufficient to pump the mixer without additional focusing.

For measurements at  $96\text{ }\mu\text{m}$  wavelength a slightly different setup was used. Here, the FIR laser consisted of a high-Q FIR cavity that was transversally excited by the  $\text{CO}_2$  laser. Outcoupling was performed with a movable mirror. Since there is considerable water vapor absorption around 3.1 THz and the diplexer becomes lossy at this frequency, the optical path is shortened and the FIR radiation is coupled onto the mixer by a beamsplitter.

The mixer chip is clamped to a  $12\text{ mm}$  diameter elliptical lens. The mixer block is mounted in a LHe-cooled vacuum cryostat equipped with a  $380\text{ }\mu\text{m}$  Zitex G115 IR radiation filter. The device output is connected through a bias-T to a  $1.3\text{-}1.7\text{ GHz}$  cooled HEMT amplifier with a noise temperature of  $\approx 5\text{ K}$ . The output of the HEMT amplifier is filtered with a  $1.5\pm 0.02\text{ GHz}$  band pass filter, further amplified and detected in a power meter.

The receiver noise temperature at  $650\text{ GHz}$  as well as the linearity of the mixer are measured in another setup shown in Fig. 3. Here one BWO serves as the LO while the second one is used as the signal source. The radiation from the

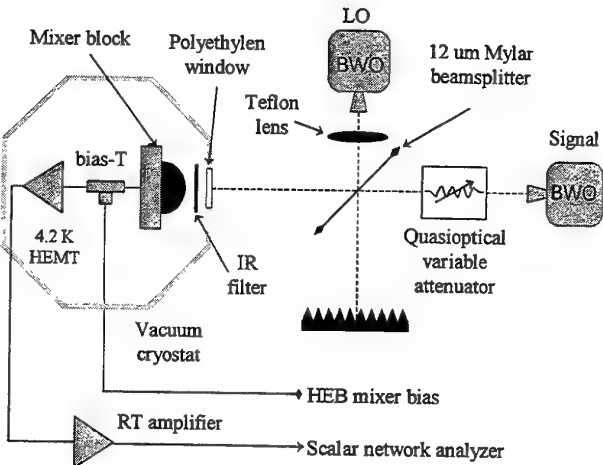


Fig. 3. Schematic of the  $650\text{ GHz}$  measurements setup. The calibrated quasi-optical attenuator allows to vary the signal power and thus measure the  $P_{\text{IF}}$  power vs.  $P_s$ . For the receiver sensitivity measurements the attenuator is removed and the signal BWO is replaced by the hot/cold ( $295/77\text{ K}$ ) loads.

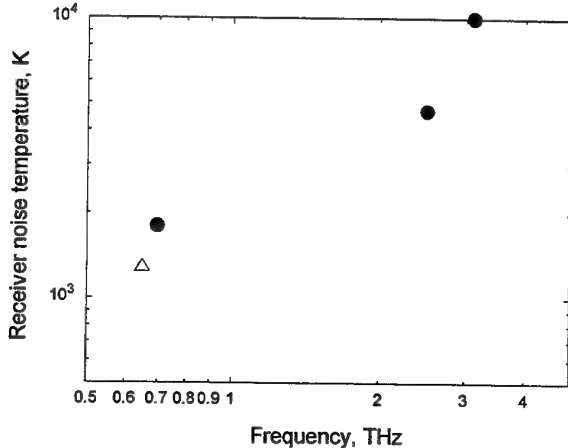


Fig. 4. Receiver noise temperature vs. frequency. The closed circles represent the results obtained in a FIR laser setup. The measurements at  $0.7\text{ THz}$  and  $2.5\text{ THz}$  were performed using a Martin Pupplet diplexer as a beam combiner. Open triangle is the value measured in the BWO setup with a  $12\text{ }\mu\text{m}$  beamsplitter.

LO is focused by a Teflon lens and combined with the signal by a  $12\text{-}\mu\text{m}$ -thick Mylar beamsplitter. The signal power can be varied by means of the quasi-optical attenuator. The attenuator was calibrated beforehand in a linear regime of the mixer. For noise temperature measurements the signal BWO is replaced by hot/cold ( $295/77\text{ K}$ ) loads in the signal path of the receiver. In this setup, the IF signal from the HEMT amplifier is further amplified by a wideband room temperature amplifier and sent to a scalar network analyzer.

#### IV. NOISE TEMPERATURE

The noise temperature is measured using the traditional Y-factor technique. The results of these measurements are plotted in Fig. 4. Here, the closed circles represent the

values obtained in the FIR laser setup. The open triangle shows the value obtained in the BWO setup. The best noise temperature of 1300 K was measured at 650 GHz. This is considerably lower than the value obtained in the FIR laser setup at almost the same frequency, 1800 K at 700 GHz. We believe that this difference is mainly attributed to losses in the diplexer, while the 12  $\mu\text{m}$  beamsplitter almost does not introduce losses. The noise temperature of 4700 K measured at 2.5 THz is already better than the best values obtained with Schottky diode receivers. It can be considerably improved by optimization of the receiver design, mainly by reduction of the optical losses. The rise in noise temperature to 10000 K at 3.12 THz is due to the strong water vapor absorption in the atmosphere. Only this loss is estimated to be 1-2 dB for a distance of 30 cm and 50% humidity, which was the case under our experimental conditions.

## V. LO POWER, LINEARITY AND CONVERSION GAIN

The absorbed LO power is determined using the isothermal method described elsewhere [12,13]. This results in about 100 nW LO power for the mixer presented in this paper.

The results of the IF power measurements vs. signal are plotted in Fig. 5. The 1 dB gain compression point occurs at a signal power which is 10 dB below the LO power. This corresponds to a maximum signal power of 10 nW which can be absorbed in the bolometer.

The numbers on the y-axis are absolute values i.e. obtained by dividing the measured IF power by the known amplification of the IF chain. From this data it is possible to estimate the mixer gain. Taking any point within the linear regime of the mixer, i.e.  $P_{\text{IF}} = -69 \text{ dBm}$ , one can calculate the intrinsic single sideband conversion gain:

$$\eta_{(\text{SSB})\text{int},r} = \frac{P_{\text{IF}}}{P_s}. \quad (1)$$

The signal power in this point,  $P_s = 1 \text{ nW}$ , is obtained from the known value of absorbed LO power, 100 nW, multiplied by the attenuation 20 dB. The result is -9 dB conversion gain. Note that this value does not include optical losses.

The total conversion gain can be derived from the input and output noise temperature measurements:

$$\eta_{(\text{SSB})\text{tot}} = \frac{T_{\text{out}}}{2 \cdot T_{\text{DSB}}}, \quad (2)$$

where  $T_{\text{DSB}} = 1300 \text{ K}$  is the measured at 650 GHz double sideband receiver noise temperature.  $T_{\text{out}} = 100 \text{ K}$  is the output noise temperature which was obtained in the same fashion as in [7]. This gives -14 dB gain. This value contains all losses, including optical losses as well as the mismatch between bolometer and the antenna. Thus, the difference in 5 dB between the measured intrinsic and total conversion gain, attributed to these constituents, sounds quite reasonable.

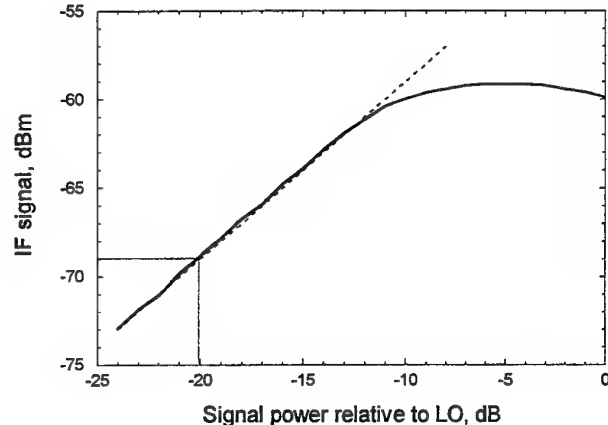


Fig. 5. The IF power vs. signal. The 1 dB saturation occurs at a signal power about 10 dB below LO. This corresponds to 10 nW power which can be dissipated in the bolometer.

## VI. CONCLUSION

We have designed and measured the performance of quasi-optical NbN HEB mixer in the 0.65-3.12 THz frequency range. The receiver has demonstrated low-noise performance, very broad RF bandwidth and large dynamic range. Further optimization of the receiver optics design and disposal of the loss in the signal path due to the water absorption will lead to a considerable improvement of the receiver noise performance beyond 1 THz.

## ACKNOWLEDGEMENT

The authors thank B. Voronov for fabrication of NbN films.

## REFERENCES

- [1] E. M. Gershenson, G. N. Gol'tsman, I. G. Gogidze, A. I. Elant'ev, B. S. Karasik and A. D. Semenov, "Millimeter and submillimeter range mixer based on electronic heating of superconducting films in the resistive state", *Sov. Phys. Superconductivity*, 3, 1582 (1990).
- [2] P. Yagoubov, M. Kroug, H. Merkel, E. Kollberg, G. Gol'tsman, A. Lipatov, S. Svechnikov and E. Gershenson, "Quasi-optical NbN phonon cooled hot electron bolometric mixers with low optimal local oscillator power", *Proc. 9th Int. Symp. on Space Terahertz Technology*, Pasadena, CA, 131 (1998).
- [3] P. Yagoubov, M. Kroug, H. Merkel, E. Kollberg, G. Gol'tsman, S. Svechnikov and E. Gershenson, "Noise temperature and LO power requirement of NbN phonon-cooled hot electron bolometric mixers at Terahertz frequencies", Submitted to *Appl. Phys. Lett.*, 1998.
- [4] A. Skalare, W.R. McGrath, B. Bumble and H. G. LeDuc, "Noise and RF bandwidth measurements of a 1.2 THz HEB heterodyne receiver", *Proc. 8th Int. Symp. on Space Terahertz Technology*, Cambridge, MA, 47, (1997).
- [5] P. Yagoubov, G. Gol'tsman, B. Voronov, L. Seidman, V. Siomash, S. Cherednichenko, and E. Gershenson, "The Bandwidth of HEB Mixers Employing Ultrathin NbN films on Sapphire Substrate", *Proc. 7th Int. Symp. on Space Terahertz Technology*, Charlottesville, VA, 290, (1996).
- [6] S. Cherednichenko, P. Yagoubov, K. Il'in, G. Gol'tsman and E. Gershenson, "Large bandwidth of NbN phonon cooled hot-electron bolometer mixers on sapphire substrates", *Proc. 8th Int. Symp. on Space Terahertz Technology*, Cambridge, MA, 245, (1997).

[7] H. Ekström, E. Kollberg, P. Yagoubov, G. Gol'tsman, E. Gershenzon and S. Yngvesson, "Gain and noise bandwidth of NbN hot-electron bolometric mixers", *Appl. Phys. Lett.* 70, 3296, (1997).

[8] D. Prober, "Superconducting Terahertz Mixer using a Transition Edge microbolometer", *Appl. Phys. Lett.* 62(17), 2119, 26 April 1993.

[9] B.S. Karasik, A. Skalare, W.R. McGrath, B. Bumble, H.G. LeDuc, J.B. Barner, A.W. Kleinsasser, P.J. Burke, R.J. Schoelkopf and D. Prober, "Low noise and wide band hot-electron superconductive mixer for THz frequencies", Presented at the 4<sup>th</sup> Int. Conf. On MM & CMM Waves and Applications, San Diego, 20-23 July 1998.

[10] A. Skalare, W.R. McGrath, B. Bumble, H.G. LeDuc, P.J. Burke, A.A. Verheijen, R.J. Schoelkopf and D. Prober, "Large bandwidth and low noise in a diffusion-cooled hot-electron bolometer mixer", *Appl. Phys. Lett.*, 68, 1558 1996.

[11] E. Gerecht, C.F. Musante, H. Jian, K.S. Yngvesson, J. Dickinson, J. Waldman, P.A. Yagoubov, G.N. Gol'tsman, B.M. Voronov, and E.M. Gershenzon, "Receiver noise measurements up to 1.56 THz for NbN hot electron bolometric mixers", Submitted to *Appl. Phys. Lett.*, 1998.

[12] B. S. Karasik, M. Gaidis, W.R. McGrath, B. Bumble and H. G. LeDuc, "Low noise in a diffusion-cooled hot-electron mixer at 2.5 THz", *Appl. Phys. Lett.* 71, 1567 (1997).

[13] M. Kroug, P. Yagoubov, G. Gol'tsman and E. Kollberg, "NbN quasioptical phonon cooled hot electron bolometric mixers at THz frequencies", *Proc. the 3rd. European Conference on Applied Superconductivity*, Veldhoven, Netherlands, 1997, (Inst. Phys. Conf. Ser. No 158, p.405).

# Tripler Circuit Design with Schottky Varactors

Jesús Grajal, Viktor Krozer, Francisco Maldonado, Emilio González, Chi-I Lin, Hans L. Hartnagel

**Abstract**— We focus on the analysis of the optimum operating conditions for millimeter-wave varactor frequency triplers. This study is based on coupling circuit-oriented analysis with semiconductor simulation. Such an approach enables to concurrently optimize the device electrical and geometrical parameters together with achievable output power, conversion efficiency and the required loads at the specific harmonics. We employ the harmonic-balance method together with a physics-based drift-diffusion numerical device simulator.

**Keywords**— frequency multipliers, Schottky diode modelling, semiconductor simulation, submillimeter-wave multipliers

## I. INTRODUCTION

This paper concentrates on the circuital aspects of frequency triplers designed to operate at millimeter and submillimeter-wave bands. The coupling of physical device modelling for Schottky varactors and a circuit simulator based on the harmonic balance technique allows the global optimization of the circuit characteristics by accounting for the device-circuit interaction. This integrated design philosophy provides another degree of freedom to improve the performance of multipliers and avoids the need of equivalent circuit models.

The 1-D Schottky simulator [1], [2] joins drift-diffusion transport through the semiconductor structure, including impact-ionization, with thermionic and thermionic-field emission currents at the metal-semiconductor contact and heterojunction interfaces. Image force lowering of the metal-semiconductor barrier, tunnelling through the barrier, and a current dependent recombination velocity, which prevents the unphysical effect of carrier accumulation at the interface, are self-consistently implemented into the governing equations.

The influence of bias, input power level, loads at different harmonics, and impact ionization on the efficiency and output power of a  $3 \times 50$  GHz tripler is discussed in detail. This tripler utilizes a Schottky varactor diode D734 from the TU Darmstadt. The diode diameter is  $\phi = 6.7 \mu\text{m}$ , the epi-layer doping is  $N_D = 1 \cdot 10^{17}/\text{cm}^3$  and the epi-layer thickness is  $t_{\text{epi}} = 350 \text{ nm}$ .

The schematic circuit used in these simulations is described in figure 1. Six harmonics are considered in these simulations, and the impedances of the higher harmonics (5th-6th) have been set to  $0.0 \Omega$  for both the resistive and the reactive components. The diode is always matched at

Jesús Grajal, Francisco Maldonado and Emilio González are with the ETSIT, Universidad Politécnica Madrid, Ciudad Universitaria s/n, 28040 Madrid, Spain, email:jesus@gmr.ssr.upm.es

Viktor Krozer is with the Lehrstuhl für Hochfrequenztechnik, TU Chemnitz, Reichenhainerstr. 70, D-09126 Chemnitz, Germany, email:vkrozer@infotech.tu-chemnitz.de

Chi-I Lin and Hans L. Hartnagel are with TU Darmstadt, Merckstr. 25, D-64283, Germany

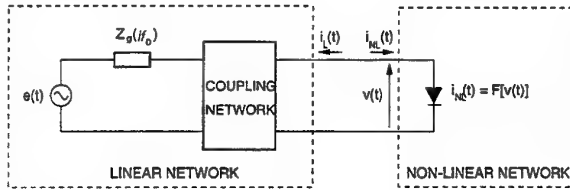


Fig. 1. Coupling Physical Modelling and Harmonic Balance.

the fundamental frequency.

## II. BIAS AND INPUT POWER LEVEL

Maximization of conversion efficiency is obtained by selecting the bias and the input power level in order to provide maximum signal swing between the breakdown voltage  $V_{bd}$  and a forward voltage approaching the barrier height  $\Phi_b$ . If the device is driven harder (mixed varactor-varistor operation), the output power increases but a resistive component of current (forward or reversed) will cause an increase of losses and the decrease in the efficiency. As can be seen in figure 2, the onset of the rectified DC current due to impact ionization for a bias  $V_{bias} = -5 \text{ V}$  coincides with the maximum of the efficiency. It is also clear that the input power level for the maximum of the efficiency,  $P_{av}(f_0) = 10 \text{ dBm}$ , does not coincide with the power level for maximum output power.

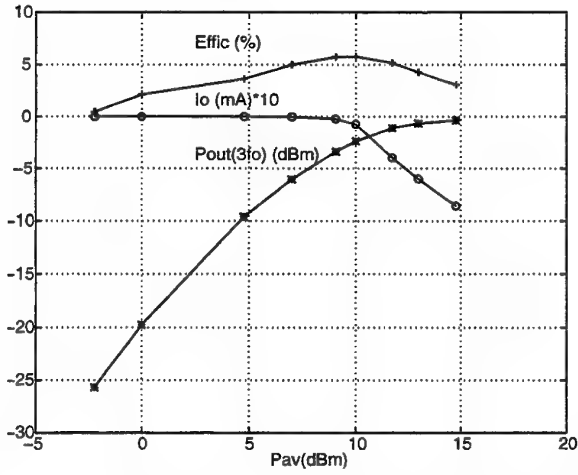


Fig. 2. Conversion efficiency, output power and DC current at  $V_{bias} = -5 \text{ V}$ .

A comparison between the characteristics for  $V_{bias} = -5, -7 \text{ V}$  appears in figure 3. The efficiency is higher for  $V_{bias} = -7 \text{ V}$  because the epi-layer is fully depleted at about  $-7 \text{ V}$ . Therefore, the C-V characteristic is nearly constant for lower voltages (negative semicycles) and this

fact is favourable for the generation of the third harmonic. For  $V_{bias} = -5$  V the third harmonic of the current waveform generated by the negative semicycles of the input signal is out of phase with the third harmonic of the waveform generated by the positive semicycles and thus the efficiency is lower.

For high power levels, the rectification due to breakdown causes the decrease of the efficiency. However, the maximum output power for  $V_{bias} = -7$  V is lower than for  $V_{bias} = -5$  V. The reason is that the onset of avalanche multiplication and the maximum of the efficiency is reached at lower power levels for  $V_{bias} = -7$  V. This reduces the capabilities for maximum power for this bias. If the available power is enough, the optimization for maximum output power must be the main goal. However, at increasing frequencies with limited power for pumping the diode, it is desirable to improve the conversion efficiency.

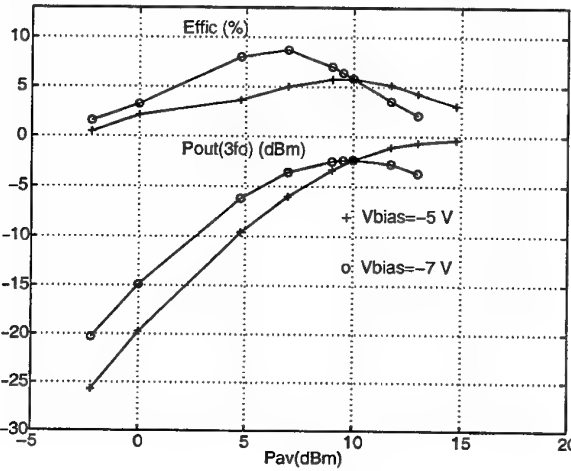


Fig. 3. Conversion efficiency and output power at  $V_{bias} = -5, -7$  V.

Another important point is the matching of the varactor at the fundamental frequency. Figure 4 shows that the quality factor  $Q = \Re\{Z_{in}(f_0)\}/\Re\{Z_{in}(f_0)\} \approx 10 \dots 30$  at low input powers, which means that the matching of the diode is sensitive to changes with power, frequency and bias voltage. For high input power levels the effect of the variation of the input impedances is weak ( $Q \approx 5$ ) due to the fact that the voltage excursion covers the full reverse characteristic of the diode. Our simulations also show a strong increase of the real part of the input impedance at the fundamental frequency  $\Re\{Z_{in}(f_0)\}$  in accordance with [3].

The efficiency for three bias points and an available input power of  $P_{av} = 7$  dBm has been optimized. Table I shows the output power and the loads at the fundamental and third harmonic. The loads at the second and fourth harmonics are shortcircuits.

### III. SENSITIVITY OF TRIPLEX PERFORMANCES TO THE LOADS AT DIFFERENT HARMONICS

Once the optimum conditions for a multiplier are determined, a complete analysis of the sensitivity of these

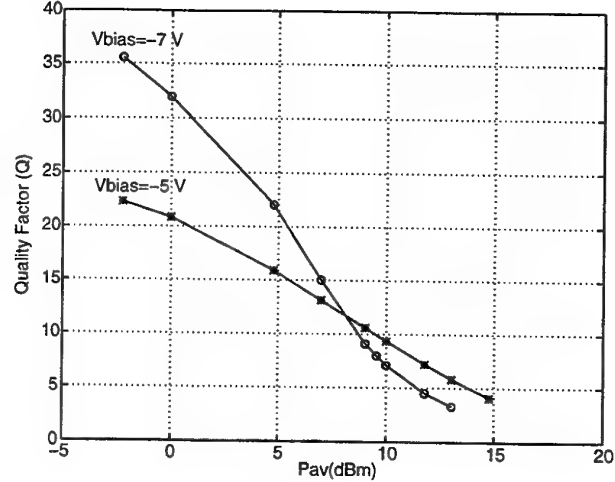


Fig. 4. Quality factor for  $V_{bias} = -5, -7$  V.

TABLE I  
MAXIMUM CONVERSION EFFICIENCY FOR  $P_{av} = 7$  dBm

$V_{bias}$	$\eta$ (%)	$P_o[3f_0]$ (mW)	$Z_g[f_0]$ $\Omega$	$Z_g[3f_0]$ $\Omega$
-3	2.8	0.14	$20.1 + j173.6$	$19 + j70$
-5	5.0	0.25	$16.3 + j213.5$	$17 + j80$
-7	8.7	0.44	$17.2 + j258.2$	$12 + j90$

performances to a change in these conditions is important, not only because of potential instabilities of the bias and impedances in time, but mostly because they change during multiplier tuning or they are difficult to realize. Figure 5 shows the conversion efficiency as a function of the load at the third harmonic  $Z_g(3f_0)$ . Only inductive loads are used in this analysis because the impedance of the diode is capacitive. The loads at the second and fourth harmonics are shortcircuits, the bias voltage is  $V_{bias} = -7$  V, and  $P_{av} = 7$  dBm. The main conclusions are:

- If  $Z_g(3f_0)$  differs from the optimum load  $Z_{g-opt}(3f_0)$ , the efficiency and the output power drop to very low values.
- Decreasing  $\Re\{Z_g(3f_0)\}$  has a stronger effect than increasing it, as is displayed in the contours of the efficiency as a function of the loads at the third harmonic in figure 6.

In frequency triplers, the selection of the impedance at the second harmonic is crucial [4]. The optimum value is a pure reactance that resonates the effective capacitance. This point is clarified with figure 7. The simulations have been performed with  $V_{bias} = -5$  V and  $Z_g(3f_0)$  is the impedance for the maximum of efficiency in table I. It is assumed that the optimum real part of  $Z_g(2f_0)$  and  $Z_g(4f_0)$  should be zero to reduce the power delivered at other harmonics different from the desired harmonic. The results obtained from simulations ( $\eta_{opt} \approx 15\%$ ) suggest that:

- The load at the second harmonic is more important than the treatment of the fourth harmonic. They are independent.
- The resonance for the second harmonic requires inductive loads. Around the maximum of the efficiency, the sensi-

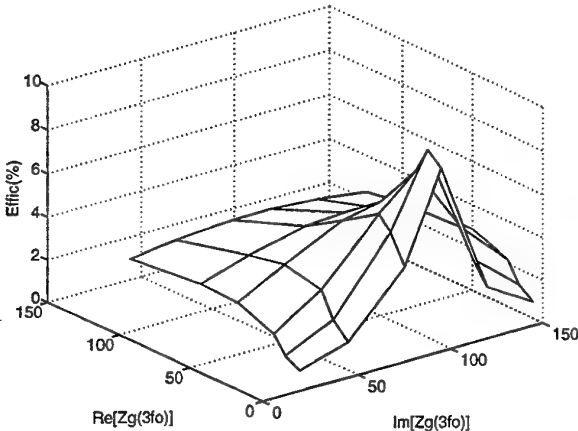


Fig. 5. Sensitivity of the efficiency to the loads at the third harmonic  $Z_g(3f_0)$  for  $V_{bias} = -7$  V.

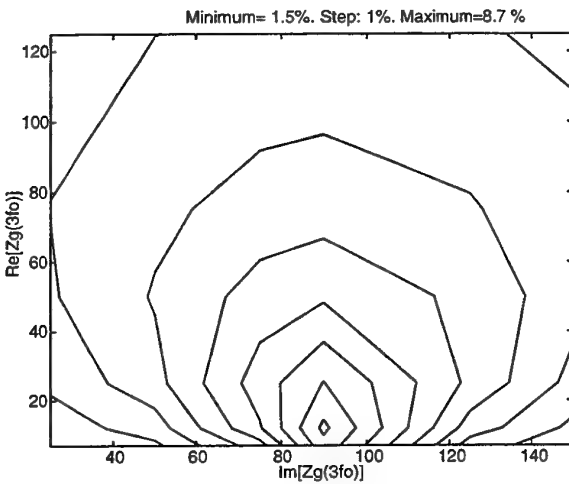


Fig. 6. Contours of the sensitivity of the efficiency to  $Z_g(3f_0)$ .

vity is higher for increasing values of  $Im[Z_g(2f_0)]$ .

- The real part of the varactor input impedance changes sharply with the reactance at the second harmonic, figure 8.
- These performances are independent of the bias and input power.

#### IV. BREAKDOWN CONSIDERATIONS AND DIFFERENT OPERATION REGIMES

An important aspect which has not been studied in depth in the past is that the *RF* breakdown voltage is frequency dependent and can be significantly higher than the *DC* breakdown voltage [5], [6]. If the *DC* avalanche conditions are achieved for only a short period of time, the carriers may not achieve sufficient energy to produce avalanche [6].

The bias point in a varactor frequency multiplier is usually selected for maximum signal swing between breakdown and conduction and, therefore, for maximum capacitance modulation. The measured and simulated breakdown voltage for the diode *D734* is  $BV_{DC} \approx -10$  V. Howe-

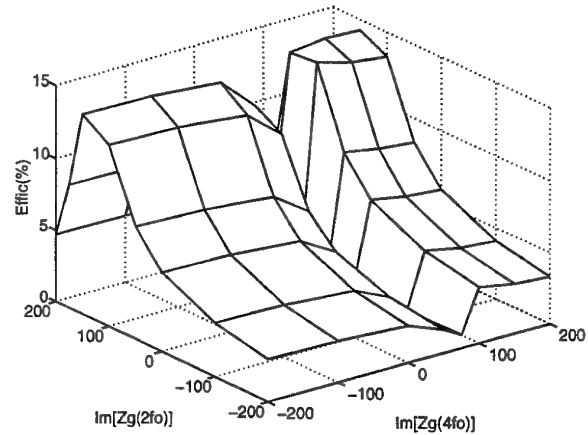


Fig. 7. Sensitivity of the efficiency to the loads  $Z_g(2f_0)$  and  $Z_g(4f_0)$ .  $V_{bias} = -5$  V and  $P_{av} = 7$  dBm.

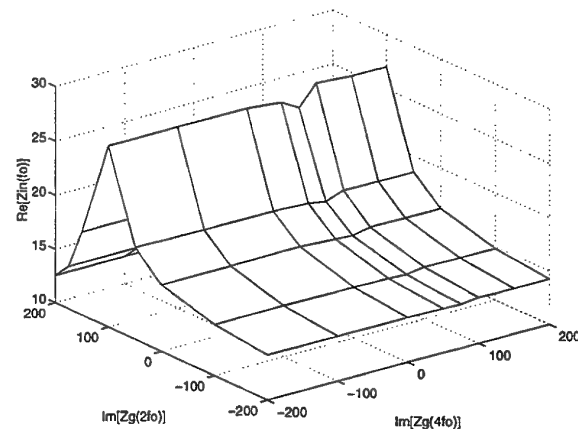


Fig. 8. Sensitivity of input impedance to  $Z_g(2f_0)$  and  $Z_g(4f_0)$ .  $V_{bias} = -5$  V and  $P_{av} = 7$  dBm.

ver, the allowed excursion for the *RF* signal is considerably higher:  $BV_{RF} \approx -15$  V at  $f_0 = 50$  GHz. This can be deduced from figure 9 where the voltage and current waveforms for  $V_{bias} = -7$  V and  $P_{av} = 5, 10, 13$  dBm are displayed. Therefore, the optimum bias point cannot be calculated only from DC considerations.

At low input power levels the operation of a varactor multiplier is mainly determined by the embedding circuit and the choice for the DC operating point of the diode. In contrast, at high power levels the impact ionization in the device is responsible for output power saturation and conversion efficiency decrease, figures 2-3. The embedding circuit exhibits only minor contribution to the overall performance of the multiplier. The highest efficiency of frequency multipliers is obtained in the transition region between low and high power regime [7].

#### V. VALIDATION OF THE SIMULATOR

The utility of the results in this paper are based on the validation of the integrated simulator. We have se-

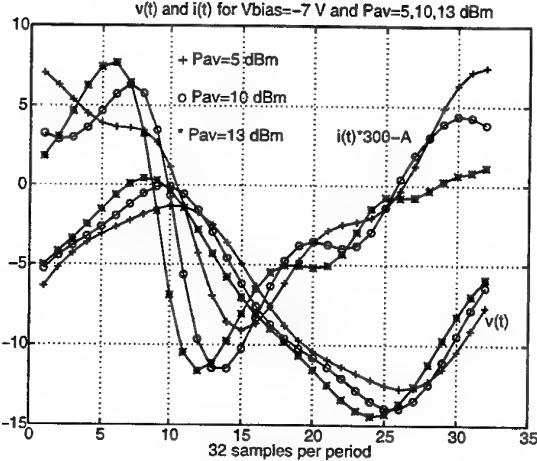


Fig. 9.  $v_D(t)$  and  $i_D(t)$  for  $V_{bias} = -7$  V and  $P_{av} = 5, 10, 13$  dBm.

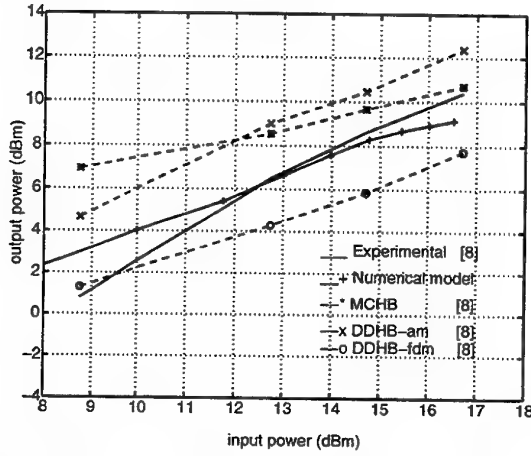


Fig. 10. Validation: a  $2 \times 100$  GHz doubler [8]. The results of the present work are displayed as *Numerical model*.

lected a Schottky varactor frequency multiplier for which measured and simulated data are available. A frequency doubler fabricated with a diode from University of Virginia (*UVA6P4*) working at a fundamental frequency of 100 GHz [8] has been analysed with our simulator and the results are depicted in figure 10 (*Numerical model*: solid line with "+" symbols). The diode parameters were taken from [8], the bias voltage has been set to  $V_{bias} = -10$  V, the loads at harmonic frequencies were set to  $Z_g(nf_0) = (0 + j0) \Omega$  for  $n > 2$ , and the loads at the second harmonic are the optimum ones for the maximization of the output power at each input power, while at the fundamental frequency the diode has been matched. They are compared with measurements (*Experimental*) and with simulated results from other simulators developed at the same University: *DDHB-fdm*, similar to the one developed by the authors with field-dependent mobility coupled with a circuit simulator based on harmonic balance, *MCHB*, a Monte Carlo simulator for the device, *DDHB-am*, similar to *DDHB-fdm* but with the mobility calculated from Monte Carlo simulation. All simulators overestimate the

output power and hence the efficiency of the doubler at power levels  $P_{in} \leq 10$  dBm because of the perfect match of the diode at each power level in contrast to the experimental set-up, where the loads have been optimized for high power levels. Interestingly the Monte-Carlo harmonic-balance code *MCHB* [8] performs worst. Our model performs well for input powers above  $P_{in} \geq 11$  dBm and is able to follow the slope of the measured results. None of the simulations from [8] is able to simulate the correct power slope

## VI. CONCLUSION

The developed device-circuit simulator has proved to be a very useful tool for the optimization of varactor tripler performances by accounting for the device-circuit interaction. It has also allowed to clarify the influence of impact ionization on output power saturation and conversion efficiency decrease at high input power levels.

## ACKNOWLEDGEMENTS

The authors would like to acknowledge the Comunidad Autónoma de Madrid and the European Space Agency for partial financial support of this work.

## REFERENCES

- [1] J. Grajal, V. Krozer, E. González, J. Gismero, F. Maldonado, C.I. Lin, A. Simon, and H. L. Hartnagel. Characterisation of Schottky diode performance by numerical simulation coupled with harmonic balance. In *27th European Microwave Conference*, pages 190-195, Jerusalem, Israel, September 1997.
- [2] J. Grajal, V. Krozer, F. Maldonado, E. González, J. Gismero, C.I. Lin, and H. L. Hartnagel. Optimization of millimeter frequency multipliers by incorporation of numerical modelling into circuit simulators. In *GaAs'98, European Gallium Arsenide and related III-V*, Amsterdam, The Netherlands, 1998. Accepted for publication.
- [3] E. L. Kollberg, T. J. Tolimunen, M. A. Frerking, and J. R. East. Current saturation in submillimeter wave varactors. *IEEE Trans. Microwave Theory and Techniques*, 40(5):831-838, May 1992.
- [4] M. T. Faber, J. Chramiec, and M. E. Adamski, editors. *Microwave and Millimeter-Wave Diode Frequency Multipliers*. Artech House, 1995.
- [5] K. N. Ratnakumar. Avalanche breakdown voltage of a microwave PIN diode. *Solid-State Electronics*, 19:656-657, 1975.
- [6] J. M. Golio. *Microwave MESFETs and HEMTs*. Artech House, 1991.
- [7] J. Grajal, V. Krozer, and F. Maldonado. Modeling and design aspects of millimeter-wave Schottky varactor frequency multipliers. *IEEE Microwave and Guided Wave Letters*, 1998. Submitted.
- [8] R. E Lipsey, S. H. Jones, J. R. Jones, T. W. Crowe, L. F. Horvath, U. V. Bhapkar, and R. J. Mattauch. Monte Carlo Harmonic-Balance and Drift-Diffusion Harmonic-Balance analyses of 100-600 GHz Schottky barrier varactor frequency multipliers. *IEEE Trans. Electron Devices*, 44(11):1843-1849, November 1997.

# Full Wave Modelling of Integrated SubmmW Receivers by Using the FDTD/Lumped Element Method

J. Vazquez, C.G.Parini, P.de Maagt, P.J.B. Clarricoats

**Abstract**--The modeling of integrated receivers requires one to handle the close interaction of non linear detectors and passive elements. Time domain methods such as FDTD can provide full models of these devices. This is demonstrated for a ring slot submmW mixer

**Index Terms**--FDTD, submmw, integrated antennas.

## I. INTRODUCTION

Active integrated antennas are reported to show a better performance than some classical devices, reducing losses, and improving bandwidth, and making the whole system more compacts. At millimetre/submillimetre frequencies the radiating elements are small enough in size (below 1 mm) to be directly constructed upon the semiconductor material, typically in monolithic form. The large amount of free bandwidth and the special propagation properties of millimetre/submillimetre frequency bands, make them suitable for many present and future applications such as the new generation of communication links, Wireless LAN, space scientific and earth observation instruments and automotive collision avoidance radars.

The active antenna with integrated detectors is now probably the most mature of all types of integrated antennas, and several designs have been used as part of scientific instruments as mm-wave cloud radars or plasma diagnostic instruments. Integrated planar devices improve conversion losses and the noise figure of submmW receivers as a consequence of the close interaction between non linear components (detectors or diodes), and passive elements (antennas, filters and transmission lines). The modelling of receivers is most important to obtain reliable designs, but a proper model has to handle both the complex passive structures and the detector features. There is a lack of proper design tools for analysing theoretically these devices. A significant difference between these antennas and traditional feed-horns is that the radiation pattern of the antenna is dependent on the properties of the detector/source, on the way it is mounted in the planar circuit, and on how this circuit is matched to the planar

antenna. Thus to analyse such a structure the active components have to be included within the electromagnetic model.

Most electromagnetic analysis tools cannot handle the non-linear behaviour of the solid-state active devices within the code (e.g. HFSS, ANSOFT). Circuit analysis packages (such as TOUCHSTONE, ENSEMBLE) fare no better as there is no accurate way of modelling the complex electromagnetic propagating and radiating characteristics of these sub structures using equivalent circuits. The Finite Difference Time Domain (FDTD) algorithm is a general method to solve electromagnetic problems, which have been used extensively to model microwave devices. The potential of this method in order to be applied to submmW device modelling has been pointed out by several authors[2][3]. In particular, Finite Difference Time Domain (FDTD) method can model jointly non linear devices and arbitrary 3D passive structures. Schottky diodes and others detecting devices can be included in the FDTD method as non linear differential equations associated to a lumped circuit model. A major objective of this work is to show the ability of FDTD to produce accurate designs of mmW/submmW devices in a general way, including the modelling of non linear devices. In order to achieve this objective a complete FDTD code has been developed under the scope of this work, including all necessary extension and improvements.

The method is demonstrated on the analysis of an annular slot antenna with all the auxiliary elements (feed/bias lines, air bridges), the IF filter and the model of a submmW Schottky diode. Experimental data on the diode is required to estimate the parameters of the non linear lumped circuit model. The results will show radiation patterns of the antenna, currents and field distributions on the structure, impedance analysis, RF isolation at IF port, and conversion loss estimation for the mixer

## II. FDTD/LUMPED ELEMENT MODEL OF SCHOTTKY DIODES

A direct extension of the FDTD method to nonlinear media can be obtained by a straightforward approximation of the partial derivatives of the general Maxwell's equations for non linear media by a central finite difference scheme,

<sup>1</sup>J. Vazquez, C. Parini and P.J.B. Clarricoats are with the Department of Electronic of the Queen Mary and Westfield College, University of London, London E1 4NS.  
P. de Maagt is with the Electromagnetic Division of European Space Agency/ESTEC, Noordwijk, The Netherlands

resulting in a non linear finite difference equations. However, nonlinear FDTD can also be implemented from the classical linear method by means of non linear operator introduced at the equations as some sort of external currents

$$\begin{aligned}\nabla \times \vec{E} &= -\frac{\partial \vec{B}}{\partial t} \\ \nabla \times \vec{H} &= \frac{\partial \vec{D}}{\partial t} + \vec{j}_{ex} + J(\vec{E}, \vec{H}) \\ \vec{B} &= \mu * \vec{H} \quad \vec{D} = \epsilon * \vec{E}\end{aligned}\quad (\text{Eq.1})$$

The electrical field  $E$  and the displacement vector  $D$  are related linearly (the same for  $B$ ,  $H$ ), but the symbol  $J$  describes an operator on the field vectors  $E$ ,  $H$  that can be nonlinear. The nonlinear part is model in this equation as the result of the interaction of a basic linear electromagnetic field with nonlinear induced sources.

A particular case of nonlinear interaction can be approximated from Eq. 1. The nonlinearity is strong but it occurs in regions that are electrically small compared to all the wavelengths in the system (as normally happens for Schottky diodes). In this case the operator  $J$  is approximated by the finite sum of terms of currents produced at discrete space points, which are nonlinearly related to the electromagnetic field at these points.

The approximation to a discrete set of equations can be obtained by using the integral form of the Maxwell equations for elementary unit cell. It is presented here just for one coordinate, but it can be easily extended for the rest of them. The basic FDTD algorithm uses a central difference scheme for the time domain coordinate. However, it can not be done in a straightforward manner for the cells that contains nonlinear current elements.

$$D_z^{n+1}(i, j, k) = D_z^n(i, j, k) + \Delta t \cdot L_h^{h+1/2}(i, j, k) + \sum_l j_z^{n+1/2}(\vec{E}(i_l, j_l, k_l, t)) \quad (\text{Eq.2})$$

This equation can not be solved in an explicit way since  $j_l$  are nonlinear operators on the electrical field that represents the behaviour of the Schottky diode. In general, these operators can be approximated by a discrete scheme, but the equation then becomes a transcendent equation that remains in an implicit form. In most of practical cases the electrical performance of devices can be modelled as a network of of elementary circuits elements. In the case of a Schottky diode the circuit is depicted on fig 1. Voltages and current on the device can be related to the surrounding fields, so a simultaneous solution of the lumped element circuits and Maxwell's equations for the full wave electromagnetic field is possible under a central finite difference scheme.

Each circuit element can be associated to a physical effect. At the same time they can be associated to a mathematical

operation in the equations. For the Schottky diode, the series resistance  $R_s$  is caused by the resistance of the silicon in intrinsic state connecting the junction to the output terminal. The nonlinear capacitance can be considered the sum of two contributions: the junction capacitance due to the deplexion zone free of holes in reverse mode and the diffusion capacitance due to the distribution of electrons into the semiconductor in forward mode.

$$\begin{aligned}C_j(V_d) &= C_j(0) \cdot \left(1 - \frac{V_d}{\Phi_0}\right)^{-m} & V_d < \Phi_0 \\ C_j(V_d) &= \frac{C_j(0)}{ctel} \cdot cte2 + \frac{m \cdot V_d}{\Phi_0} & V_d \geq \Phi_0 \\ C_D(V_d) &= \frac{q}{\eta \cdot k \cdot T} \tau_D \cdot I_0 \cdot e^{q/\eta \cdot k \cdot T \cdot V_d} & (\text{Eq.3})\end{aligned}$$

$C_j$  is the junction capacitance related to the voltage at diode terminals  $V_d$ .  $C_j(0)$  is the zero bias capacitance and  $m$ ,  $ctel$ ,  $cte2$  are suitable constants taking into account the geometry and semiconductor features of the diode.  $C_D$  is the diffusion capacitance highly related to the recombination time  $\tau_D$  of electrons into the semiconductor.  $G(V_d)$  is the classical expression for the conductance of a diode but introducing the parameter  $\eta$  known as the 'ideality factor' to model a real device.

$$G_j(V_d) = I_0 \cdot \left( e^{(q/\eta \cdot k \cdot T) \cdot V_d} - 1 \right) \quad (\text{Eq.4})$$

### III. ANALYSIS OF A SUBMILLIMETRE COPLANAR INTEGRATED RECIEVER

In this paper we consider a submmW integrated antenna and mixer suitable for applications in astronomy (i.e. FIRST/PLANCK) and earth observation (i.e. MASTER). Planar structures are excellent candidates to implement antenna feed & mixer devices for mmW and submmW receivers. Coplanar technology reduces the manufacturing complexity of the antenna since only a single layer is required for the design. These structures can provide compact designs, including in a single device, the detectors, the antenna and all the auxiliary elements such as IF filters, matching and bias lines.

Surface modes can be easily excited in planar printed structures at these frequencies. This problem can be solved by means of a substrate lens with the integrated antenna placed at the lens focus. For this design the local oscillator power will be injected quasi-optically into the detector. The integrated device must include all necessary elements to provide proper matching and DC return lines for the diode and a isolation for the IF port. The radiation pattern of the integrated antenna is required to be rotationally symmetric in order to produce a beam together with the lens of high Gaussian efficiency. However the lens design will not be considered here. Rejection of the image frequency has to be

provided by an external element (i.e. a dichroic plate). The diode has a special base of conductive alloy in order to provide a low series resistance for the junction, this base connects one terminal of the diode to the rest of the circuits. The other diode terminal on top of the diode is connected by an airbridge.

The design is based on an annular slot that produces a highly symmetric pattern at the resonant frequency ( $\lambda=\pi d$  approx.). Most of the energy is radiated inside the dielectric half space rather than the air. The annular slot, which is placed on top of silicon, provides an impedance of 100 ohms at the resonance. This diode can be tuned by the DC bias to match the antenna impedance, but we have also considered the possibility of using a transmission line to match the impedance of the diode. This procedure can improve the conversion loss of the mixer but introduce RF losses in the matching line. In the case showed in the Fig 2, the diode is tuned to a low impedance value (a gross estimate of  $20-j20$  at 650 GHz). The design is completed by adding a IF port connected through a stub to reject the RF in that port.

The FDTD model is based on a grid of  $60 \times 60 \times 120$  cells that represent a  $30 \times 150 \times 300 \mu\text{m}$  box which contains the complete integrated receiver. Parabolic PML boundary conditions have been implemented to eliminate reflections from the boundary of the grid.

The radiation patterns of the integrated antenna inside the lens have been calculated at the central frequency (650GHz). The pattern is reasonably symmetric, but for some misalignment of the E plane. The pattern can be made more symmetrical if the IF stub is slightly shifted. The remaining performance shows a good RF rejection at the IF port (Fig. 5). This clearly demonstrates the point made earlier, that changing the circuit details may change the radiation pattern of an active integrated antenna. Modeling the planar antenna as a passive structure in isolation would lead to erroneous radiation characteristics.

The calculated impedance for the integrated antenna with matching line is shown in the figure 4. As expected, the transmission line adapts the high impedance of the antenna (about 100 ohms) to a low impedance close to the objective ( $25+j30$ ) including the effect of the diode finger. The isolation of the IF port is obtained by the stub which is placed at the center of the annular slot. This stub behaves as an open circuit for the RF and LO and a short circuit for IF. In order to produce a symmetrical pattern the tuning of the stub is shifted to avoid the strong radiation at the resonance, but it provides more than 20dB attenuation for the RF at the IF port

The presentation will include results for the integrated antenna with representative diode characteristics in order to show the performance of the mixer part of the device.

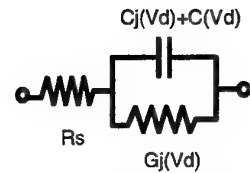


Fig 1 Simple lumped circuit model for the Schottky diode.

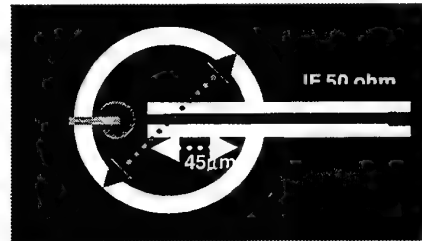
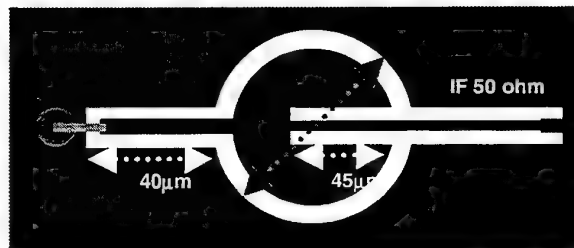


Fig 2. Proposed designs for the integrated receiver. On the left the low diode impedance design with matching line. On the right, design with diode impedance tuned by DC bias to match the antenna.

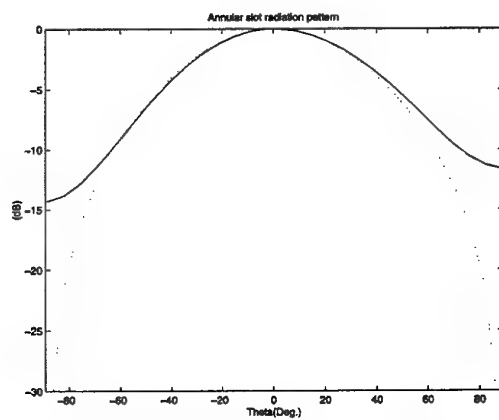


Fig 3. Radiation pattern calculated at 650 GHz (Dashed line: Plane H, Solid line: Plane E).

## V. REFERENCES

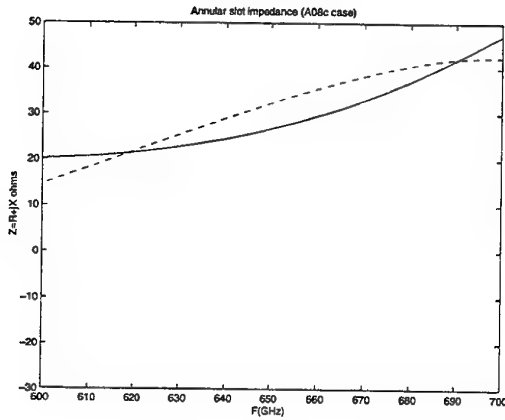


Fig 4. The antenna impedance at diode port can match the low impedance diode (estimated  $20-j20$ ) at 650 GHz using a matching transmission line.

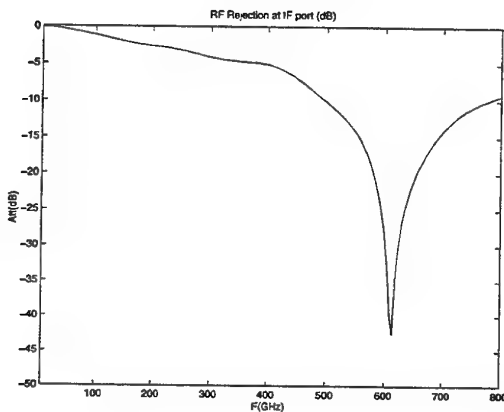


Fig 5. S12 parameter showing the transmission from the RF port to the IF port

## IV. CONCLUSIONS

A coplanar integrated ring slot antenna mixer has been analyzed using an extended FD-TD method. The next stage of this research program is to experimentally verify the FD-TD predictions for this device. On the theoretical side, the extension of the modeling to other active devices (transistors), and the need to be able to handle array-type periodic structures, as well as a single isolated element, in order that devices such as detector arrays (for Imaging) and power combining arrays can be analyzed is currently underway.

- [1] D.Rutledge, D.P. Neikirk, D. P. Kasilingam "Infrared and Millimeter waves". Chapter 1 Integrated circuit antennas. Academic Press 1983.
- [2] S.T.Cheow, T. Itoh "Active and quasi-optical arrays for solid power combining". Chapter 3 active integrated antennas. J.Wiley&Sons 1997.
- [3] P.Ciampolini, P. Mazzanotte, L.Roselli, R. Sorrentino. "Accurate and efficient circuit simulation with lumped element FDTD Technique" IEEE MTT Vol44, Dec 1996.
- [4] G. Rebeiz "Millimeter-Wave and Terahertz Integrated Circuit Antennas". IEEE Proceedings 1992.
- [5] B.Toland, J. Lin, B. Housmand, T. Itoh, "FDTD analysis of an active antenna" IEEE Microwave and guided wave lett. Nov 1994.
- [6] S.Masarweh, T Sherer, S.Yngvesson et al. "Modeling of a Monolithic slot ring quasi optical mixer", IEEE MTT Sep 1994.
- [7] C.E. Tong, R. Blundell. "An Annular Slot Antenna on a Dielectric Half-Space". IEEE APS July 1994.
- [8] A.Taflove. "Computational Electrodynamics: The Finite Difference Time Domain Method". Artech House, 1995.

# Long wavelength infrared streak camera

C. W. Rella, M. Drabbels, and L. D. Noordam\*

**Abstract**--An atomic streak camera has been constructed with a spectral range from 3 – 300 THz and a 2 ps time resolution. Gas-phase Rydberg atoms are used as a infrared sensitive photocathode. Prompt electron emission from the autoionizing Rydberg atoms is obtained when red Stark states are selected.

## 1. Introduction: spectral limitation of streak cameras

The spectral range at which conventional streak camera systems operate is limited by the spectral response of the photocathode used. For most photocathode materials the sensitivity is limited to wavelengths shorter than 1.5  $\mu\text{m}$ . Beyond this wavelength the quantum efficiency of the photocathode becomes negligible. Thus the temporal profile terahertz light pulses can not be measured directly using a conventional streak camera.

We have constructed an atomic streak camera [1-2] in which the photocathode of a conventional streak camera is replaced by a sample of gas phase Rydberg atoms for the conversion from photons to electrons. Due to the low binding energy of the electrons of Rydberg atoms, the IR photon energy is sufficient to photoionize the atoms and create electrons. The combination of a low ionization threshold with the high photoionization cross section makes a Rydberg atom photocathode ideally suited for use in an IR streak camera.

## 2. Infrared streak camera: principle of operation.

The principle of operation of the atomic infrared streak camera is sketched in Fig. 1. Gas phase atoms are excited to a Rydberg state by a UV laser prior to exposure to the IR radiation. The number of photoelectrons, created by the IR photoionization of the Rydberg atoms, is proportional to the instantaneous IR intensity; therefore the temporal profile of the electron pulse mimics the profile of the terahertz radiation. Just as in a conventional streak camera, the electron pulse is accelerated towards a position sensitive detector. The electron pulse passes a set of deflection plates. The electric field of this condenser is ramped in time, causing a time-dependent deflection of the electrons. Hence the electron pulse is streaked over the position sensitive detector, and the profile on the detector is a direct measure of the profile of the terahertz pulse.

## 3. Limitations at long wavelengths

After the initial demonstration of the infrared streak camera at 2.6  $\mu\text{m}$  [1], we investigated the response at longer wavelength. As a IR source the Free Electron Laser FELIX is used (located in Nieuwegein, The Netherlands). The FEL is tunable from 4 to 100  $\mu\text{m}$ , and from the spectral bandwidth the pulse duration is estimated to be about 1 ps. In this particular case the FEL was tuned near

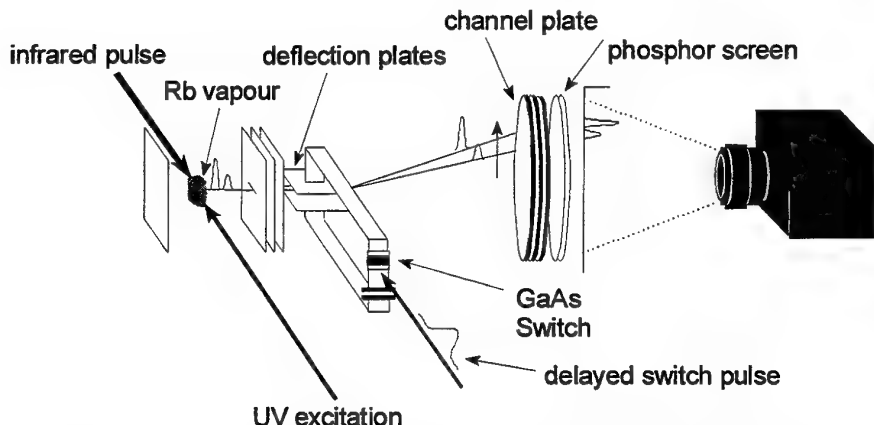


Figure 1: Schematic representation of the atomic streak camera, using gas phase Rydberg atoms to convert infrared photons to electrons.

\* FOM-Institute AMOLF, Kruislaan 407, 1098 SJ Amsterdam, The Netherlands  
E-mail: [rella@amolf.nl](mailto:rella@amolf.nl), ph: +31 (20) 608 13 51, fax: +31 (20) 668 41 06

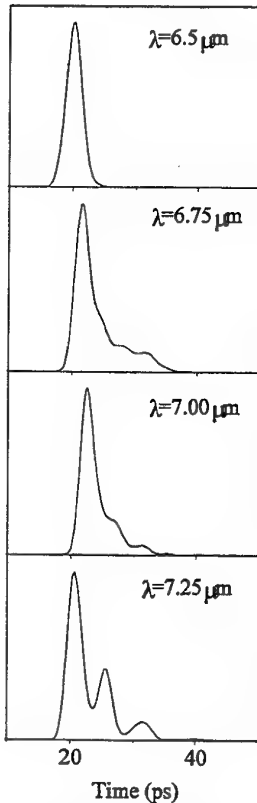


Figure 2: Series of streak camera traces showing delayed ionization of the atom.

$n=11$  rather than  $n=10$ . Moreover in the presence of the electric field each  $n$  state fans out in  $n$  Stark states. Some of these Stark states are better candidates for the IR streak camera than others.

We have investigated the ionization dynamics starting from different Rydberg Stark states as initial state: (1) blue shifted Stark states (the energy of the states increases with increasing field strength, hence the excitation laser has to be blue shifted to stay tuned) and (2) red shifted Stark states. From the results [5] we deduce that the red shifted Stark states with most of the wavefunction located at the down stream end of the potential give the sharpest electron emission peaks and are the states we will use for the streak camera operating at long wavelengths.

7  $\mu\text{m}$  and the initial Rydberg state of potassium was  $n=10$ . The results are shown in Fig. 2. Although the time resolution of the streak camera is excellent at 6.5  $\mu\text{m}$  ( $<3$  ps) the electron emission from the Rydberg atom is no longer prompt at longer wavelengths. For instance at 7.25  $\mu\text{m}$  the excess energy of the electron is so small that the escape time from the atom becomes of the order of 10 ps. The beats in the electron emission are due to angular momentum oscillations of the electron [3, 4] while the electron is still attached to the ionic  $\text{K}^+$  core. Although these quantum beats are certainly interesting from an atomic physics point of view, they are rather disturbing for proper streak camera operation. Thus different initial Rydberg states have to be selected for different spectral regimes. So for  $\lambda=7.25 \mu\text{m}$  we start from

#### 4. Results at 35 and 85 $\mu\text{m}$ .

Selecting a red Stark state as an initial state we tested the streak camera in the far infrared [2]. In Fig. 3 results at 35 and 85  $\mu\text{m}$  are shown. The single shot trace taken at 35  $\mu\text{m}$  shows that even at these long wavelength the streak camera has a time resolution of about 1 ps. The streak trace at 85  $\mu\text{m}$  shows the asymmetric pulse shape of the free electron laser at long wavelengths. Such an exponential growth of the laser intensity was predicted by theory but never directly observed at these wavelengths. Note that the oscillation time of the electromagnetic field at 35  $\mu\text{m}$  is already 0.12 ps and at 85  $\mu\text{m}$  is 0.28 ps!

#### 5. Conclusions

An atomic streak camera has been developed in which the conventional metal photocathode has been replaced with a gas of Rydberg atoms. Using a variety of sources, it has been tested over a broad range of frequencies (3 - 300 THz), and over this range has been shown to respond with ps time response. This device can in principle be operated at even lower frequencies; investigations are currently underway to establish the long wavelength limit of the atomic streak camera. Because of its broad spectral sensitivity, fast time response, and relatively high sensitivity, the atomic streak camera should provide the enabling technology for a range of interesting experiments in the terahertz regime.

**Acknowledgements.** The work described in this article is supported by the Technology Foundation (STW), and the Stichting FOM, which is financially supported by NWO.

#### References

1. M. Drabbels, and L. D. Noordam, Opt. Lett. **22**, 1436 (1997)
2. M. Drabbels, G. M. Lankhuijzen and L. D. Noordam, IEEE-QE (1998)
3. G. M. Lankhuijzen and L. D. Noordam, Phys. Rev. Lett. **76**, 1784 (1996)
4. G. M. Lankhuijzen, F. Robicheaux and L. D. Noordam, PRL **79**, 2427 (1997)
5. G. M. Lankhuijzen, M. Drabbels, F. Robicheaux, and L. D. Noordam, Phys. Rev. A **57**, 440 (1998).

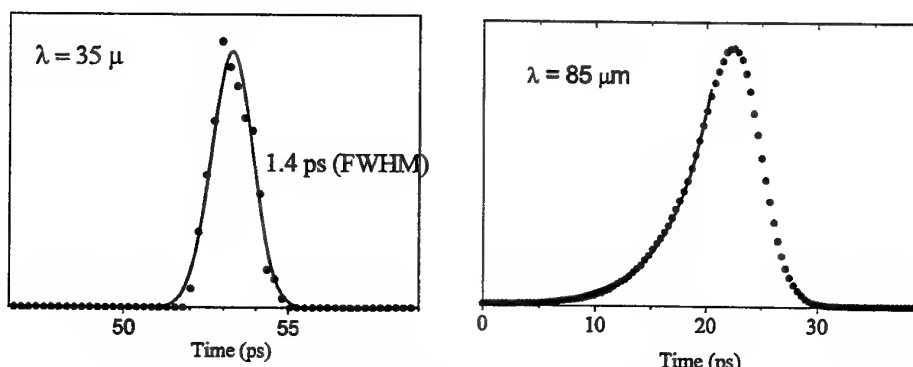


Figure 3: Streak traces at 35 and 85  $\mu\text{m}$ .

# Complex permittivity measurements using a quasi-optical multistate reflectometer

D. Thompson, R.E. Miles and R.D. Pollard

**Abstract**— The complex permittivity of a well established high frequency dielectric has been measured using a quasi-optical multistate reflectometer. The permittivity is determined using two separate methods; one employing waveguide and the other a free-space measurement. The reflectometer is calibrated separately for each technique using free-space and waveguide standards. An analysis of the uncertainties involved in the measurement is given and initial results are presented.

**Keywords**— permittivity measurements, multistate reflectometer

## I. INTRODUCTION

THE importance of accurate measurements in the terahertz region has never been greater. Active device technology is evolving rapidly and terahertz circuits are becoming a reality. Accurate characterisation of these circuits is essential to the iterative process used to refine the understanding of the physics and electromagnetics of the devices in this frequency range. Additionally, the characteristics of the materials used in these circuits must be properly detailed in order to further improve both model and circuit performance. Of particular importance in the design of planar circuits is a knowledge of the substrate dielectric constant.

Measurement technology at terahertz frequencies is constantly under development. One of the aims is to realise a vector network analyser which operates over a sufficiently large bandwidth in the sub-millimetre range. Goy *et al.* [1] have developed a network analyser extension capable of operation up to 1THz. Their design is realised in waveguide and uses multiplied Gunn diode sources and complex mixer circuitry for the detection process. Boese [2] has demonstrated a one-port multistate reflectometer measurement system realised in dielectric waveguide. This arrangement also yields a larger operational bandwidth and has been successful at measuring one-port s-parameters from 110-170GHz.

This paper describes a multistate reflectometer realised with quasi-optical components whereby free-space is the transmission medium. The advantages of such a reflectometer are essentially zero loss, extremely wide operational bandwidth and lower power requirements than a six-port arrangement. Additionally, the reflectometer does not require the use of complex (heterodyning) detection circuitry—phase information is obtained by making a se-

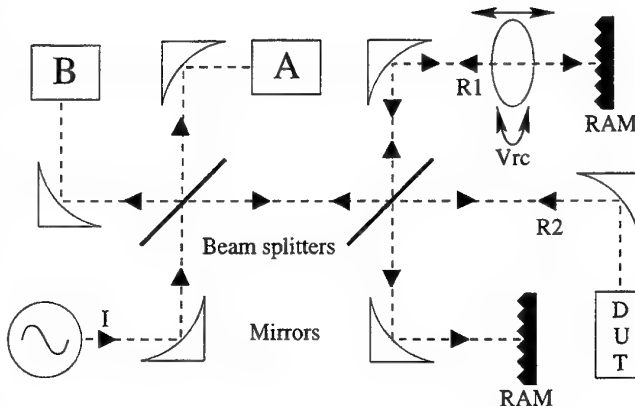


Fig. 1. Quasi-optical reflectometer block diagram

ries of scalar (power) measurements. The circuit configuration is shown in figure 1. The calibration procedure follows the method described in an earlier paper [3] and is performed using both waveguide and free-space standards. The complex permittivity of Rexolite, a well established millimetre-wave material, is then measured. Owing to the dual calibration, the material can be measured when embedded in waveguide or a larger sample can be measured in free-space.

## II. THEORY

There are various methods of determining the complex permittivity of a material. Wide band measurements can be made using the Dispersive Fourier Transform Spectroscopy (DFTS) [4]. Shimabukuro *et al* [5] used a quasi-optical arrangement to determine the dielectric constant and loss tangent of several materials at 94GHz. Here, the complex permittivity is determined by measuring the transmission coefficient for several incident angles of the source signal.

Roberts and von Hippel [6] were early pioneers of dielectric constant measurement. They performed one port reflection coefficient measurements using a standing-wave meter on short circuited material samples in both waveguide and free space. The equation they derived for the dielectric constant was:

$$\frac{\tanh(\gamma_e d)}{\gamma_e d} = \frac{-j}{\beta_e d} \cdot \frac{1 + \Gamma}{1 - \Gamma} \quad (1)$$

where  $d$ , is the length of the sample and  $\Gamma$  is the measured reflection coefficient. The equation is solved for the complex propagation constant  $\gamma_e = \alpha_e + j\beta_e$  of the dielectric in the particular transmission medium. The term

This work was supported by the Engineering and Physical Sciences Research Council of the U.K.

The authors are with the Institute of Microwaves and Photonics, School of Electronic and Electrical Engineering, The University of Leeds, Leeds LS2 9JT. U.K.

$\beta_t = 2\pi/\lambda_t$  is the propagation constant of the transmission media, thus, for waveguide  $\lambda_t = \lambda_g$ , the guide wavelength whereas  $\lambda_t = \lambda_o$ , the free-space wavelength for the quasi-optical measurement. Equation 1 has an infinite number of solutions, thus in practice, two different known lengths of the material must be measured and the resulting equations solved simultaneously in order to determine a value for  $\gamma_\epsilon$  uniquely.

Once  $\gamma_\epsilon$  has been found, the dielectric constant and loss tangent of the material for the waveguide measurement are found from:

$$\epsilon'_r = \left( \frac{\beta_\epsilon^2 - \alpha_\epsilon^2}{\beta_o^2} \right)^2 + \left( \frac{\lambda_o}{2a} \right)^2 \quad (2)$$

$$\tan \delta = \frac{\alpha_\epsilon \beta_\epsilon}{\beta_o^2 \epsilon'_r} \quad (3)$$

while for the free space measurement:

$$\epsilon^* = \frac{-\gamma_\epsilon^2}{\omega^2 \mu_0} \quad (4)$$

which, for a non-magnetic medium becomes [7]:

$$\epsilon'_r = \frac{\beta_\epsilon^2 - \alpha_\epsilon^2}{\beta_o^2} \quad (5)$$

$$\tan \delta = \frac{2\alpha_\epsilon \beta_\epsilon}{\beta_\epsilon^2 - \alpha_\epsilon^2} \quad (6)$$

#### A. Uncertainties

The uncertainty in the final permittivity figure stems from that associated with the reflection coefficient measurement, which in turn is derived from the random fluctuations in measured incident and reflected power. Any uncertainties which arise during the calibration of the reflectometer will also effect the measured result. As mentioned in [3], the four multistate calibration parameters ( $R, S, \alpha$  and  $\beta$ ) are determined by a least-squares algorithm with the known quantities being the measured power ratios and the short circuit standards. The least squares merit function (see for example [8]) for each reflectometer state is thus,

$$\chi^2 = \sum_{i=0}^N \left( \frac{y_i - y(\rho_i, \theta_i; \mathbf{P})}{\sigma_{y_i}} \right)^2 \quad (7)$$

where  $\mathbf{P}$  is a vector of the multistate parameters mentioned above and the  $y_i$ 's are the measured power ratios for each of the  $N$  standards  $pe^{-j\theta_i}$ . The uncertainty of the measured power ratios  $\sigma_{y_i}$  are included in the denominator of the merit function. The aim of the fitting function is to adjust the four components of  $\mathbf{P}$  to obtain a minimum for  $\chi^2$  (ideally zero). At the minimum, the variance of each of the parameters can be computed from the second partial derivatives of the merit function with respect to each of the parameters viz [8]:

$$\sigma^2(\mathbf{P}_j) = [\alpha]_{jj}^{-1} = C_{jj} \quad (8)$$

where  $\alpha$  is the Hessian matrix given by:

$$\alpha_{kl} = \left( \frac{1}{2} \cdot \frac{\partial^2 \chi^2}{\partial P_k \partial P_l} \right)^{-1} \quad (9)$$

To determine the reflection coefficient ( $\rho$  and  $\theta$ ) of the sample, once again a least-squares algorithm with a merit function similar to (7) is used. However, the standard deviation denoted in the merit function must be a combination of the parameter uncertainties and the power measurement uncertainty. The individual parameter uncertainties contribute in different amounts to the overall uncertainty of the measured complex reflection coefficient. The combined uncertainty is found by computing a weighted root-sum-of-squares (RSS) of the individual uncertainties. The weighting factor is the derivative of the minimisation function with respect to the particular parameter, i.e. letting  $f_i = y_i - y(\mathbf{P}; \rho_i, \theta_i)$ :

$$\sigma_{f_i}^2 = \sigma_{y_i}^2 \cdot \left( \frac{\partial f}{\partial y} \right)^2 + \sigma_{P_1}^2 \cdot \left( \frac{\partial f}{\partial P_1} \right)^2 + \dots + \sigma_{P_4}^2 \cdot \left( \frac{\partial f}{\partial P_4} \right)^2 \quad (10)$$

where the  $i$ 's now correspond to the particular state of the instrument rather than a connected standard.

The uncertainty in the complex propagation constant is once again found as a by-product of the least-squares procedure; the merit function of which is based on (1) with  $\Gamma$  being replaced by its constituent magnitude and phase components  $\rho$  and  $\theta$ . As before, the separate uncertainties must be combined in a similar manner to the above prior to the execution of the least-squares routine. The uncertainty in the permittivity is then determined by propagating the uncertainty in the real and imaginary parts of  $\gamma_\epsilon$  through either (2) or (5).

### III. RESULTS

Two sections of waveguide of length 11.96mm and 23.95mm were completely filled with the Rexolite material. It is important that no air gaps exist between the waveguide wall and the material. Collins *et al.* [9] investigated the dependence of the permittivity value with change in the gap dimensions. A 10% error in both  $\epsilon_r$  and  $\tan \delta$  was observed for approximately 4% errors in the ideal size of the dielectric sample. Thus, to eliminate air gaps, an oversized piece of Rexolite was machined and forced into the waveguide. The guide was then machined to the correct length so that the material was flush with the guide aperture. One end of the waveguide was fitted with a short circuit. Equal care must be taken with the free-space measurement; the sample must be oriented normal to the propagation axis of the incoming beam. Any deviation from this would result in an incorrect reflection coefficient measurement and false permittivity results since all of the reflected power would not be directed to the power meters. A test fixture was made to hold the two samples of length 20.03mm and 30.05mm in the correct position. The fixture held the samples at the beam waist of the incident beam to ensure all of the available energy was coupled to the material. A highly polished piece of aluminium was held flush with the rear part of the material to present a short circuit. Figure (2) shows the two test fixture arrangements.

After calibration of the reflectometer at 100GHz, the complex reflection coefficients of the two waveguide sam-

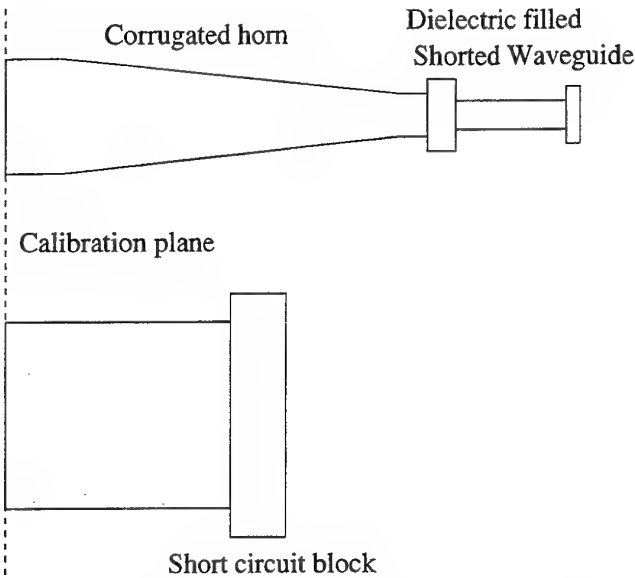


Fig. 2. Arrangement of the waveguide and free-space measurements

ples were measured and the results used to compute the complex permittivity. The uncertainty in the power measurements were obtained by taking 14 readings and finding the mean and standard deviation. The experiment was repeated with the free-space arrangement after calibration using quasi-optical standards. The same method of calibration is employed, using a piece of Radiation-Absorbing-Material (RAM) as the matched load and a highly polished movable metal plate for the sliding short circuit.

The waveguide measurements gave a relative permittivity  $\epsilon'_r = 2.43$  and the loss tangent  $\tan \delta = 0.0011$ . The corresponding uncertainties were  $\pm 0.19$  and  $\pm 0.0009$  respectively. The free-space experiments gave  $\epsilon'_r = 2.46$  and  $\tan \delta = 0.0020$  with an uncertainty of  $\pm 0.05$  and  $\pm 0.0003$ . All uncertainties quoted are for a 95% confidence level. These results, together with results for Rexolite from earlier published papers are shown in Table (I).

TABLE I  
REXOLITE COMPLEX PERMITTIVITY MEASUREMENT RESULTS

Method	Freq.	$\epsilon'_r$	$\pm U_{\epsilon}$	$\tan \delta$	$\pm U_{\tan \delta}$
MSR (wg)	100.0	2.43	0.19	0.0011	0.0009
MSR (fs)	100.0	2.46	0.05	0.0020	0.0003
SWG	94.75	2.41	-	0.0034	-
F-P	94.75	2.56	-	0.0026	-
QO Tx	93.78	2.56	0.005	0.00026	0.00006

In table I MSR refers to the Multistate reflectometer system described here, SWG refers to the shorted waveguide technique, F-P the Fabry-Perot method (both employed by Bridges [10]) and QO Tx denotes the Quasi-optical transmission measurements performed by Shimabukuro [5]. As can be seen, the experimental error associated with the measurements reported in this study are higher than those

reported earlier. This is due ultimately to the poor signal to noise ratio recorded at the power detectors. Improvements could be made by employing more sensitive detectors and/or a more powerful coherent source. However, allowing for these uncertainties, the results obtained agree very well with those reported earlier.

#### IV. CONCLUSION

A multistate reflectometer has been realised using quasi-optical components only. The reflectometer has been calibrated at 100GHz using both waveguide and free-space standards. The complex reflection coefficient of Rexolite has been measured using two separate techniques and the complex permittivity determined from the result. Results of  $\epsilon'_r = 2.43$  and  $\tan \delta = 0.0011$  and  $\epsilon'_r = 2.46$  and  $\tan \delta = 0.002$  for waveguide and free-space measurements respectively were obtained. The results establish the quasi-optical multistate reflectometer as a viable means of making complex permittivity measurements.

#### REFERENCES

- [1] Goy P, Gross M, and Raimond J.M, "8-1000 GHz vector network analyser," *15th Int. Conf. Infrared and Millimeter Waves. Ed. Temkin R.J.*, vol. SPIE 1514, pp. 172-173, 1990.
- [2] Boese I.M and Collier R.J, "Novel measurement system from 110-170 GHz," *IEEE 1st High frequency postgraduate student colloquium. Belfast*, 1995.
- [3] Ide J.P and Oldfield L.C, "The theory and practice of a multistate reflectometer," *RSRE Memo No. 3824*, 1985.
- [4] J. Chamberlain Afsar M.N. and G.W. Chantry, "High precision dielectric measurement on liquids and solids at millimeter and submillimeter wavelengths," *IEEE Transactions on Instrumentation and Measurement*, pp. 290-294, 1976.
- [5] Shimabukuro F.I, Lazar S, Chernick M.R, and Dyson H.B, "A quasi-optical method for measuring the complex permittivity of materials," *IEEE Transactions on Microwave Theory and Techniques*, vol. Vol. 32, no. 7, pp. 659-665, 1984.
- [6] von Hippel A.R, "Dielectrics and waves," *J. Wiley & sons*, 1954.
- [7] Stumper U, "Six-port and four-port reflectometers for complex permittivity measurements at sub-mm wavelengths," *IEEE Transactions on Microwave Theory and Techniques*, vol. vol. 37, pp. 222-228, 1987.
- [8] Bevington P.R, "Data reduction and error analysis for the physical sciences," *New York: McGraw-Hill*, 1969.
- [9] C.E. Collins, R.E. Miles, R.D. Pollard, D.P. Steenson, J.W. Digby, G.M. Parkhurst, J.M. Chamberlain, N.J. Cronin, S.R. Davies, and J.W. Bowen, "Millimetre-wave measurement of the complex dielectric constant of and advanced thick film UV photoresist," *Journal of electronic materials*, vol. Vol. 27, no. 6, pp. 40-42, 1998.
- [10] Bridges W.B, Klein M.B, and Shweig E, "Measurement of the dielectric constant and loss tangent of Thallium Mixed Halide crystals KRS-5 and KRS-6 at 95GHz," *IEEE Transactions on Microwave Theory and Techniques*, vol. Vol. 30, no. 3, pp. 286-292, 1982.

# Dielectric Waveguides at Submillimeter Wavelengths

J. Weinzierl, Ch. Fluhrer, H. Brand

**Abstract**—A flexible waveguide system has been simulated using the field calculation program MAFIA, for the first time realised for frequencies up to 150 GHz and operated in two applications. The flexible waveguide system consists of a rectangular, dielectric fibre made of polyethylene combined with optimised tapers and waveguide adapters, which makes the flexible waveguide easy to use in combination with conventional waveguides.

A minimum attenuation of 4dB/m at 140 GHz has been obtained with the dielectric waveguides, which is about 6dB less than the measured attenuation of D-band waveguides operated at the same frequency. Additionally the phase shift of the flexible waveguides for different bending radii as well as the influence of different tapered fibre terminations was measured and is reported.

**Keywords**—Flexible Waveguide, 150 GHz, Simulation, Measurements

## I. INTRODUCTION

At frequencies of 75 GHz and above only inflexible metallic waveguides or alternatively quasioptical waveguides were used in the past. The frequency range of commercially available, flexible coaxial cables ends at about 40 GHz.

Considering for example field scanning measurement applications or imaging applications in the millimetre wavelength region a flexible waveguide system would significantly improve the design of those setups because only the flexible waveguide together with the field probe has to be moved. Using conventional waveguides for those applications, the whole RF-part of the system has to be moved.

The paper describes the development of a flexible waveguide system for frequencies up to 150 GHz using dielectric waveguides. The realisation of those waveguides is based on simulations using the field calculation program MAFIA, which turned out to be a powerful tool for optimisation of the fibre geometry as well as for the geometry of the waveguide adapters and tapers.

Several measurements of fabricated dielectric waveguides at 75 GHz and 150 GHz were carried out to verify the results obtained from simulation and are presented as well as two application examples using flexible, dielectric waveguides.

## II. NUMERICAL SIMULATION

One of the major criteria for the dielectric waveguides was to get a flexible waveguide system which is compatible to conventional waveguides, that means the flexible waveguide system should use the same standard flanges we

All authors are with the Lehrstuhl für Hochfrequenztechnik (LHFT), Universität Erlangen-Nürnberg (UEN), Erlangen, Germany. E-mail: jochen@lhft.e-technik.uni-erlangen.de

know from rectangular waveguides. So the primary work to do was to develop optimised transitions between metallic waveguides and the flexible, dielectric waveguides. All simulations have been carried out using the field calculation program MAFIA, which is based on the theory of discrete Maxwell grid equations.

Figure 1 exemplarily shows the implementation of the si-

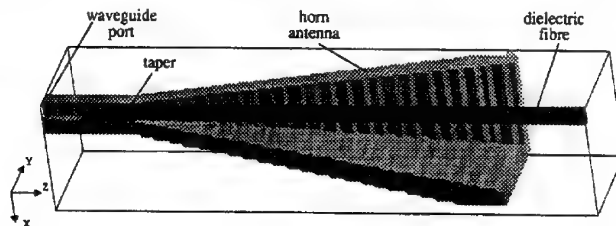


Fig. 1. Implementation of the dielectric waveguide system in MAFIA

mulated waveguide transitions with the dielectric waveguide inside. The transition is formed by a pyramidal horn antenna in which the tapered end of the dielectric waveguide is mounted. The simulation signal is excited in the waveguide port of the horn antenna. Both, single frequency and broadband signal simulations were performed.

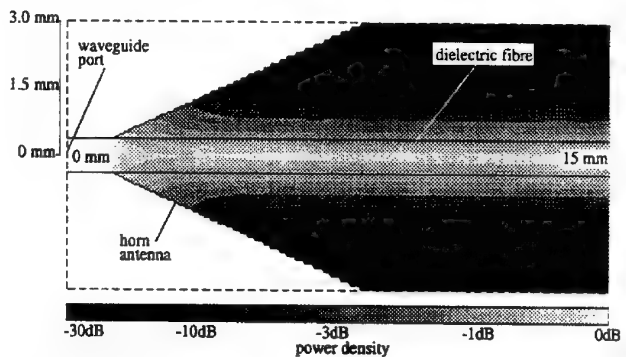


Fig. 2. Signal propagation on a dielectric waveguide: Real part of the Poynting vector

In Figure 2 the result of a single frequency simulation at 150 GHz is presented. By plotting the real part of the Poynting vector the figure shows the signal propagation from the excitation plane in the waveguide port, passing the waveguide transition and propagating along the dielectric fibre. Especially the wave-guiding property of the dielectric fibre can be seen: The major part of the signal is guided within the fibre. Only about 20 percent of the signal power, depending on frequency, material and geometry, is propagating outside the fibre. At a distance of 1.5 mm from the axis the energy density decreases by about 20dB.

Another basic result of the single frequency signal simulations is the influence of the geometry of the pyramidal horn antenna which is shown in Figure 3. Both horn angles

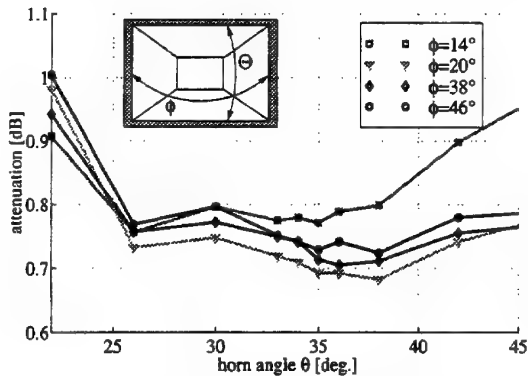


Fig. 3. Influence of horn geometry on transmission characteristics

$\phi$  and  $\Theta$  are varied and their influence on the attenuation of the waveguide system at 150 GHz is calculated. The influence of horn angle  $\phi$  on the waveguide attenuation is rather low for angles higher than 20°, for lower angles  $\phi$  the attenuation increases significantly. The attenuation dependency of angle  $\Theta$  is quite high and shows a local minimum at 38°. One important result from these simulations is, that alternatively for the pyramidal horn antenna a conical horn antenna using the same horn angle  $\Theta$  can be used because of the low influence of horn angle  $\Phi$ , which makes the realisation of the waveguide transitions at 150 GHz a lot easier.

The optimisation of the tapered ends of the dielectric fibre was another important step for the realisation of the dielectric waveguide system. Three different taper configurations shown in Figure 4 were simulated using broadband signal simulation in the frequency range from 135 GHz to 165 GHz. The simulation results of the three different taper configurations are shown in Figure 5. The influence of tapering the ends of the fibre is significant. Both, the tip taper and the dove tail configuration reduce reflection losses by about 0.3 dB to 0.4 dB over the whole frequency range compared to the non tapered end of the dielectric fibre. The difference between the two tapers seems to be rather low as the dove tail taper has better broadband characteristics and the tip taper has little lower attenuation over a wide frequency range.

### III. MEASUREMENTS

For the verification of the obtained simulation results the precise fabrication of the dielectric fibres was necessary. The fibres for 150 GHz operation were cut from bigger fibres, which were extruded from polyethylene granulate, due to the lack of precision of the extruding process for small fibre cross-sections equal to the inner size of D-band waveguides.

Because of the expected field measurement application of the fibres the measurement of the basic transmission properties such as attenuation and dependence on the bending radius as well as the phase shift versus bending radius at



Fig. 4. Simulated taper configurations

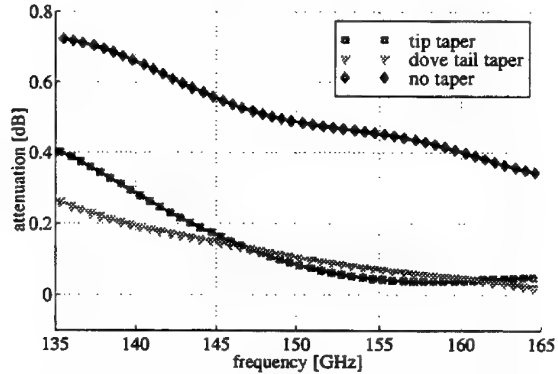


Fig. 5. Transmission characteristics for different tapered ends of the dielectric fibre

150 GHz is of special interest and has been carried out. Figure 6 shows the measured attenuation of the flexible waveguide system compared to standard D-band waveguides at 150 GHz. The dielectric waveguide turned out to

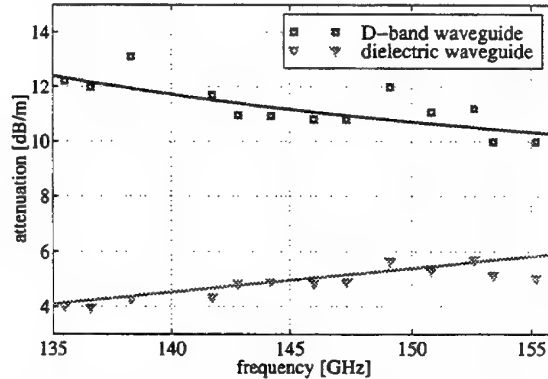


Fig. 6. Measured attenuation of the flexible waveguide system compared to standard D-band waveguides

have between 4dB and 6dB lower attenuation per meter than the D-band waveguides we measured in our laboratories, which makes the dielectric fibre very suitable for these high frequency applications.

Continuing, the fibre characteristics for different bending radii were measured. We got very promising results for the measurement of the additional attenuation by bending the fibre. Up to radii of 3cm no additional transmission losses due to radiation into free space could be measured. Only for smaller radii the additional losses increase up to 2dB for 1cm bending radius, which is the smallest possible fibre radius without damaging the fibre.

The results of measured phase shift versus bending radius is shown in Figure 7. It shows that the phase-shift of the dielectric waveguide has to be put into account for bending radii smaller than 10cm. There is a slight increase of phase-shift for lower frequencies, because the lower the

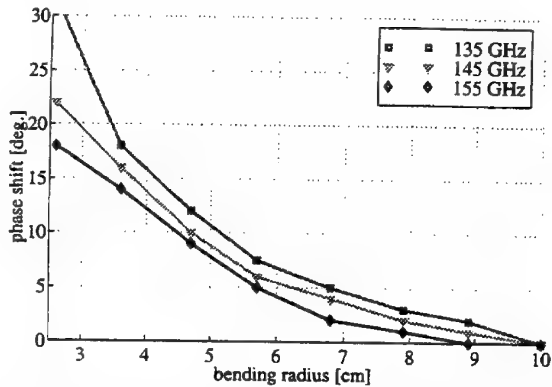


Fig. 7. Phase shift of the dielectric waveguide for different bending radii

frequency the lower the power density in the fibre which increases the influence on the signals phase by bending the fibre. Further measurements have been performed to verify the simulation results for taper configurations and horn antennas. The measurement results for the different taper configurations shown in Figure 4 are presented in Figure 8. In agreement to simulation, the measurement of the non

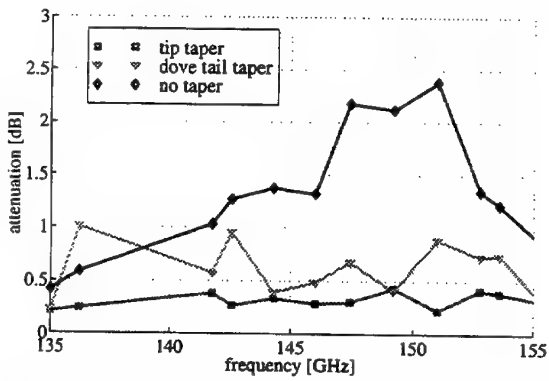


Fig. 8. Measured attenuation of different fibre taper configurations

tapered fibre showed the highest attenuation, which increases up to 2.5dB at 151 GHz. The results for the tip taper and the dove tail taper configuration differ from simulation. The lowest attenuation results were obtained with the tip tapered fibre end over the whole frequency range. The dove tail configuration showed an additional average attenuation of about 1dB compared to the tip taper. This result could not be shown in the simulations and is mostly due to the mechanical instability of the dove tail tapered end of the dielectric fibre which has to be put in the waveguide port of the transition horn antenna. Additionally, it is much more difficult to precisely realise the simulated dove tail tapered end of the fibre than the tip taper which is another reason for the differences between simulation and measurement.

Further measurements concerning the geometry of the waveguide transitions have been carried out to verify the simulation results for the optimised horn antennas. Following the results of measurements of a comparison between a pyramidal horn antenna and a conical horn antenna with the same horn angle  $\Theta = 38^\circ$  (see Figure 3) are shown in Figure

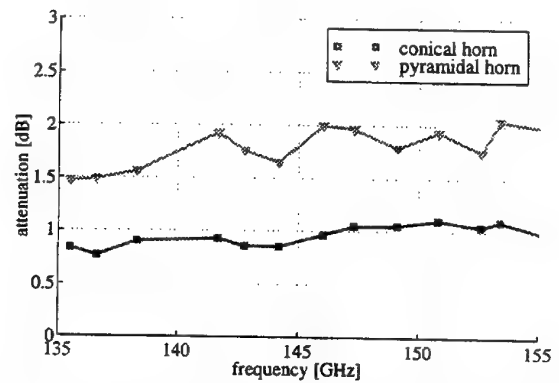


Fig. 9. Measured transmission characteristics of two different waveguide transitions

re 9. Both horn types equally show broadband transmission characteristics, but the conical horn antenna is about 1dB better than the compared pyramidal horn. This difference is mostly due to mechanical tolerances when fabricating the horn. In comparison to the conical horn antenna which was realised by turning on a lathe from one block of brass, the pyramidal horn antenna was made of two symmetrically milled blocks of brass, which were soldered together.

#### IV. APPLICATIONS

The last section of the paper shows two application examples for the flexible, dielectric waveguides: Firstly, a 150 GHz homodyne phase measurement setup for the measurement of phase characteristics of quasi-optical waveguides. Secondly, a transmitter-receiver setup which produces scanned transmission images of dielectric objects at 150 GHz. Figure 10 shows the setup for the homodyne phase measurement system. Both, the scanning and the reference channel of the setup are build up with dielectric waveguides leading to a maximum flexibility of the measurement system.

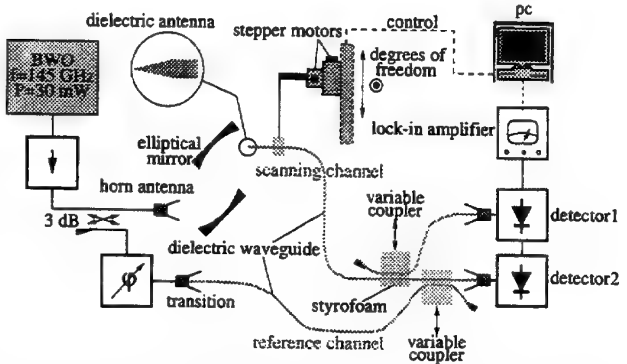


Fig. 10. Homodyne phase measurement setup using dielectric waveguides

Both channels are combined using a coupler, which is realised with dielectric fibres, fixed in a block of styrofoam. The coupling between the fibres can be adjusted by varying the fibre distance. Another identical coupler is used to detect the power density of the measured gaussian beam.

The beam profile is scanned using the tip tapered end of the fibre as antenna leading to a minimum of field distortion in the measurement plane. This dielectric antenna is moved by a numerically controlled stepper motor scanning unit. The signals are detected using lock-in technique to achieve a good signal to noise ratio ( $> 40\text{dB}$ ). Exemplarily first measurement results of this setup are shown in Figure 11. The second presented application example is a 150

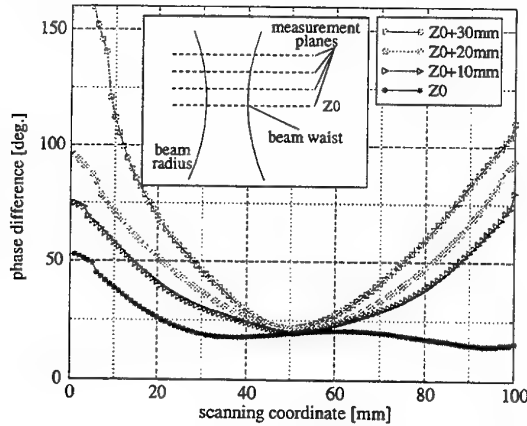


Fig. 11. Measurement results of the homo-dyne phase measurement setup using dielectric waveguides

GHz scanning measurement setup for transmission images of dielectric objects, which is shown in Figure 12. The microwave signal is focused on the device under test (DUT) using a flexible dielectric waveguide. The end of the waveguide is tip-tapered, which forms the transmitter antenna. On the backside of the DUT, the same waveguide configuration acts as a receiver antenna. Both, the transmitter and the receiver antenna are moved in the same way using a numerically controlled stepper motor unit. The signal is detected with a lock-in amplifier for maximum signal to noise ratio. The main advantage of this setup is that the DUT can be fixed because the transmitter and receiver antenna are moved and scan the DUT. So for example objects filled with fluids can be scanned, which is impossible when the DUT has to be moved (e.g. a setup using fixed elliptical mirrors to focus the signal on the DUT) and the setup is fixed. A measurement example is presented in Figure 13. We scanned a bottle made of polyethylene which was filled half with fluid. The fluid level in the bottle can be measured very precise and a small tube inside the bottle can be seen, which cannot be detected using visual techniques for example.

## V. CONCLUSIONS

A flexible waveguide system has been developed, for the first time realised for frequencies up to 150 GHz and operated in two applications. Based on a variety of numerical simulations performed with the field calculation program MAFIA, a flexible waveguide system based on a dielectric fibre made of polyethylene together with optimised waveguide transitions has been realised. The simulation results have been successfully verified by measurements at 150

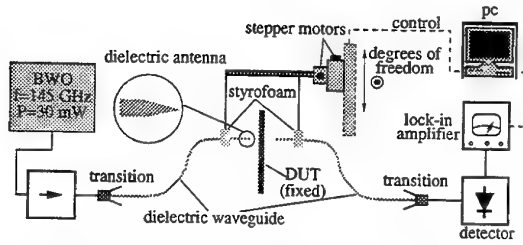


Fig. 12. Transmission images measurement setup using dielectric waveguides

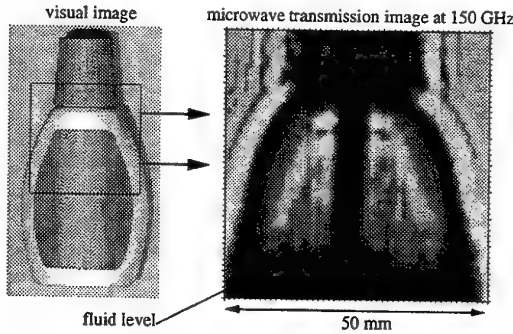


Fig. 13. Transmission images measurement results using dielectric waveguides

GHz. The dielectric waveguide showed up to 6dB lower attenuation compared to measurements with standard D-band waveguides at 150 GHz which makes the developed flexible waveguide system a competitive alternative for the 150 GHz frequency range.

## ACKNOWLEDGEMENTS

The authors would like to thank G. Bauer, L. Höpfel and J. Popp of the mechanical workshop of the "LHFT-UEN" for the fast and precise fabrication of the different waveguide transitions and measurement setup parts. The authors also wish to express their thanks to Dr.-Ing. F. Zahradník of the "UEN-Institute for Material Sciences (Division of Polymeres)" for the useful discussions and the fabrication of the dielectric fibres.

## REFERENCES

- [1] W. Schlosser, "Der rechteckige dielektrische Draht," *Archiv der elektrischen Übertragung*, vol. 7, pp. 403–410, 1964.
- [2] E. A. Marcatili, "Dielectric rectangular waveguide and directional coupler for integrated optics," *The Bell System Technical Journal*, pp. 2071–2102, 1969.
- [3] T. Ramittra, J. Malherbe, "Transition from metal to dielectric waveguides," *Microwave Journal*, pp. 71–74, November 1980.
- [4] R. E. Collin, *Field Theory of Guided Waves*, McGraw Hill, 1960.
- [5] J. Goell, "A circular-harmonic computer analysis of rectangular dielectric waveguides," *The Bell System Technical Journal*, pp. 2133–2160, September 1969.
- [6] J. Heitmann, "Theory and fabrication of dielectric lines and measurements in the frequency range from 26.5ghz to 40ghz," *Nachrichtentechnische Zeitung*, pp. 279–284, 1975.
- [7] J. Howell, P. Toulou, R. Knox, "Radiation losses in curved dielectric image waveguides of rectangular cross section," *Digest of the IEEE International Microwave Symposium-Boulder*, pp. 25–27, 1973.
- [8] D. Marcuse, *Theory of Dielectric Optical Waveguides*, Academic Press, San Diego, 1991.

# The Precision of Quasi-optical Null-Balanced Bridge Techniques for S-parameter Measurement

John W. Bowen and Sillas Hadjiloucas, *Member, IEEE*

**Abstract** — A theoretical analysis of the precision of a quasi-optical null-balanced reflectometer is presented, taking into account quantisation effects, detector noise and source power. A de-embedding technique suitable for micro-machined waveguides is suggested. The resulting error in determining attenuation coefficient and guide wavelength is analysed.

**Index terms** — quasi-optical reflectometer, null-balance, S-parameters, de-embedding errors

## I. INTRODUCTION

At microwave frequencies, measurement of the scattering parameters, attenuation coefficients and characteristic impedances of waveguide components are usually carried out using 4-port or 6-port network analysers [1,2,3]. The measured signals are modified by unwanted but unavoidable, reflections introduced by connection to the test sample, and these have to be removed by calibrating the network analyser with at least three known terminations. Characteristic impedance is conventionally determined with reference to a standard impedance line.

However, as the frequency is increased above 100 GHz, the measurement procedure becomes increasingly difficult. As the waveguide samples become smaller the repeatability of the measurement becomes increasingly dependent on the ability of the user to couple sufficient power to the waveguide ports and to accurately measure the power ratios between the analyser's ports under different calibration conditions. Furthermore, the manufacture of precision reference terminations becomes difficult.

At these higher frequencies, an alternative quasi-optical approach may be used with 3 different waveguide lengths and a polarising Michelson type Dispersive Fourier Transform Spectrometer (DFTS) operated in reflectance mode. In the DFTS technique, time gating is used to separate the individual reflection signatures of the device under test so that the S-parameters can be determined [4]. Although co-averaging of the interferograms can improve on the signal to noise ratio of the individual signatures, there are cases where the mercury-arc lamp has insufficient power and the technique cannot be used. Using a single frequency source alleviates the problems of limited power

output of the source but renders time-gating impossible. A de-embedding technique must be used under these circumstances.

In the following sections we describe a null-balance quasi-optical bridge reflectometer and we analyse the errors involved when balancing it. The errors in the measured amplitude and phase of the reflection signatures propagate in the equations describing the de-embedding procedure and result in errors in the calculated impedance and attenuation of the device under test.

## II. ANALYSIS OF THE NULL-BALANCE REFLECTOMETER

Each element in the optical system shown in Figure 1 can be described by a Jones matrix which relates the polarisation state of the emergent beam to that of the incident beam. Under manual operation, the user iteratively balances the instrument to a null by successive movements of the rotating grid holder and the rotating grid [5].

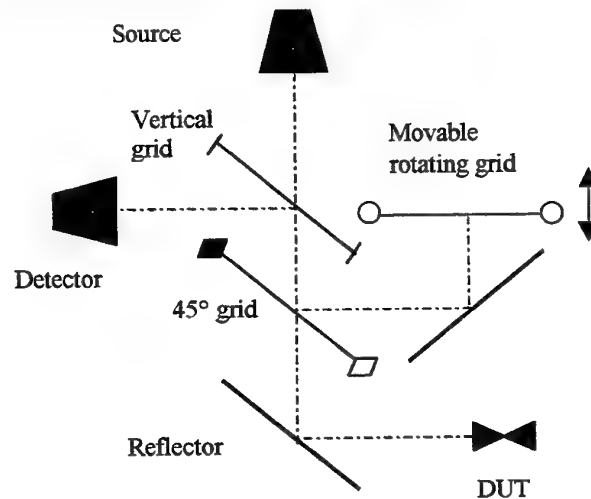


Fig. 1. Null-balance reflectometer configuration

It can be shown that the power  $P$  at the detector is:

$$P = \left| \left( \frac{1+\sin 2\theta}{4} e^{-jkd} - \frac{R}{2} e^{-j\phi} \right) P_0 \right|^2 \quad (1)$$

where  $P_0$  is the modulated source power output,  $\theta$  is the angle of the grid wires to the vertical,  $R$  is the sample

The authors are with the Department of Cybernetics, The University of Reading, P.O. Box 225, Whiteknights, Reading, RG6 6AY, Berkshire, U.K.

reflectance ( $0 < R < 1$ ),  $k$  is the source wavenumber and  $kd$ , and  $\phi$  are the phase delays in the sample and reference arms of the interferometer respectively.

It is found that a null at the detector is obtained when the phase difference between the two paths of the interferometer is zero so that  $R = (1 + \sin 2\theta)/2$ . The reference grid transmits all of the incident polarisation when  $\theta = -45^\circ$  and gives a null when  $\theta = -45^\circ + \gamma$  where  $\gamma$  is half the angle between the adjacent nulls. Thus we find that under balanced conditions  $R = \sin^2 \gamma$ .

In order to further incorporate the source output power in the analysis, the signal to noise ratio at the detector ( $SNR$ ) defined as incident signal power divided by detector noise power, and given from  $SNR = P_0 / NEP\sqrt{B}$  may be used to calculate an error in reflectance  $\sigma_R(R, SNR)$  as a function of sample reflectance and detector  $SNR$  (at a bandwidth  $B$  related to the time constant of the PSD used). This can be directly linked to the measured angle error  $\sigma_\gamma(R, SNR)$  using:

$$\sigma_R(R, SNR) = \left( \frac{\partial R}{\partial \gamma} \right) \sigma_{\gamma_{TOTAL}}(R, SNR) \quad (2)$$

where:

$$\frac{\partial R}{\partial \gamma} = 2\sqrt{R} \cos(\sin^{-1} \sqrt{R}) \quad (3)$$

The  $\sigma_{\gamma_{TOTAL}}(R, SNR)$  term is composed of the following two errors in determining the null position: a) the precision in determining the angle (quantisation error) of the rotating grid  $\sigma_{\gamma_Q}$  and b) the precision in determining the balanced position in  $\theta$  due to the noise equivalent power  $NEP$  of the detector  $\sigma_\gamma(R, SNR)$ . Since these errors are independent, their variances may be added separately [6] and therefore:

$$\sigma_{\gamma_{TOTAL}}(R, SNR) = \sqrt{2\sigma_{\gamma_Q}^2 + \frac{\sigma_\gamma^2(R, SNR)}{2}} \quad (4)$$

the improvement by a  $\sqrt{2}$  factor in the  $\sigma_\gamma(R, SNR)$  term arising because two null measurements are performed during the balancing procedure.

The error  $\sigma_\gamma(R, SNR)$  in the rotating grid angle due to the  $SNR$  when the instrument is assumed to be completely balanced in  $d$  can be calculated from (1) after setting  $kd = \phi$ ,  $P = NEP\sqrt{B}$  and  $\theta = \theta_0 \pm \sigma_\gamma(R, SNR)$ .

Since  $\theta_0 = -\frac{\pi}{4} + \sin^{-1} \sqrt{R}$  it follows that:

$$\begin{aligned} \sigma_\gamma(R, SNR) = & \mp \sin^{-1} \left[ \left( \pm 4\sqrt{P_0^{-1} NEP\sqrt{B}} + 2R - 1 \right) \right] / 2 \\ & + \left[ \mp \pi/2 \pm 2\sin^{-1}(\sqrt{R}) \right] / 2 \end{aligned} \quad (5)$$

where the upper and lower signs are used for reflectances above and below 0.5 respectively.

The theoretical limits to the measurable sample reflectance  $R_{lim}$ , beyond which the nulls become unresolvable, are calculated using (1) after setting  $kd = \phi$ ,  $\theta_{max} = 3\pi/4$  for  $R < 0.5$  and  $\theta_{max} = \pi/4$  for  $R > 0.5$ . It can be shown that:

$$R_{lim} = [1 + \sin(2\theta_{max})]/2 \pm 2\sqrt{P_0^{-1} NEP\sqrt{B}} \quad (6)$$

A similar procedure can be used to calculate the phase errors involved when balancing the reflectometer in  $d$ . Balancing the instrument completely in  $\theta$  with a perfect reflector in the sample arm so that  $R=1$ , it can be shown that the error in  $d$  due to the  $SNR$  of the detector is:

$$\sigma_d(SNR) = \pm \sin^{-1} \left( 1 - 2P_0^{-1} NEP\sqrt{B} \right) \quad (7)$$

The subsequent introduction of a sample with reflectance  $R$  at the sample arm results in a phase delay  $\phi_s$  which is accounted for at the reference arm with a new balanced position  $kd_s = \phi_s$  and a new phase error  $\pm k\delta d_s$  where  $\pm \delta d_s = \sigma_d(R, SNR)$ . Balancing the instrument completely in  $\theta$  so that  $\theta = [\sin^{-1}(1-2R)]/2$  it can be shown that the error in  $d$  due to the  $SNR$  of the detector when a sample is inserted is:

$$\sigma_d(R, SNR) = \pm \sin^{-1} \left( \frac{1 - 2P_0^{-1} NEP\sqrt{B}}{R^2} \right) \quad (8)$$

An error in  $d$  can be directly linked to an error in the measured reflectance  $R$  using:

$$\sigma_\phi(R, SNR) = \left( \frac{\partial \phi}{\partial d} \right) \sigma_{d_{TOTAL}}(R, SNR) \quad (9)$$

where  $\partial \phi / \partial d = k$ . The  $\sigma_{d_{TOTAL}}(R, SNR)$  term is composed of the following two errors in determining the null position: a) the precision in determining the movement (quantisation error) of the micrometer  $\sigma_{d_Q}$  and b) the precision in determining the balanced position in  $d$  due to the  $NEP$  of the detector with and without the sample in position. Since these errors are independent, their variances may be added separately and therefore:

$$\sigma_{d_{TOTAL}}(R, SNR) = \sqrt{2\sigma_{d_Q}^2 + \sigma_d^2(R, SNR) + \sigma_d^2(SNR)} \quad (10)$$

### III. ERRORS RELATED TO THE DE EMBEDDING PROCEDURE

There is currently considerable interest in the development of integrated components based around micro-machined waveguides [7]. While a high repeatability of manufacture

can be achieved, the quasi-optical characterisation of such waveguide components poses its own problems, particularly in the manufacture of terminations other than shorts and lengths of waveguide. The effects of imperfect coupling at integrated feed antennas and optics between the reflectometer and device under test must also be accounted for. Here we present a de-embedding procedure, which may be used to determine the complex propagation constant of the waveguide based on four lengths of waveguide terminated with shorts with nominally identical integrated feed antennas. The reflections from these four test pieces are measured sequentially. It is assumed that the coupling between the reflectometer beam and the feed antenna is the same in all cases.

For a reciprocal 2 port device with scattering matrix  $S$  the measured complex reflectance  $\Gamma_{Si}$  is related to the load reflectance  $\Gamma_{Li}$  by:

$$\Gamma_{Si} = \frac{S_{11} + \Gamma_{Li} (S_{21}^2 - S_{11} S_{22})}{1 - \Gamma_{Li} S_{22}} \quad (11)$$

In Figure 2, the 2-port is identified with a focusing lens, micro-machined antenna and length of micro-machined waveguide. The terminating reflectance  $\Gamma_{Li}$  depends on the complex propagation constant of the waveguide and the length  $l_i$  (Figure 2). It is assumed that the shorts are lossless. The unknown parameters in equation 11 can be found by terminating with four different load reflectances and solving the resulting set of simultaneous equations.

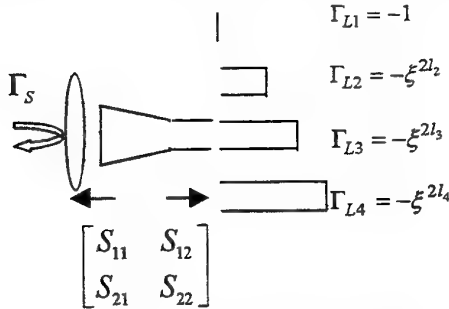


Fig. 2. De-embedding technique using a null-balance reflectometer.

It proves to be mathematically expedient to chose the lengths so that  $l_2 = l_3 / 2 = l_4 / 3$  and to work in length units that make  $l_2 = 1/2$ . The propagation constant  $\xi$  is related to the attenuation  $a$  and guide wavelength  $\lambda_g = 2\pi/k_g$  through:

$$\xi = e^{-a} e^{-jk_g} \quad (12)$$

Taking into account the propagation of errors in amplitude and phase described in (2) and (8) respectively, it is possible to calculate an error term in the measured

complex reflectance  $\sigma_{\Gamma_{Si}}(\sigma_{R_i}, \sigma_{\phi_i})$  for each measurement which is directly related to the de-embedding procedure. Since these errors are independent, their variances may be added separately so that the overall error  $\sigma_{\xi}(\sigma_R, \sigma_{\phi})$  in the de-embedding procedure may be calculated from:

$$\sigma_{\xi} = \sqrt{\sum_{i=1}^4 \left( \frac{\partial \xi}{\partial \Gamma_{Si}} \right)^2 \sigma_{\Gamma_{Si}}^2} \quad (13)$$

where

$$\sigma_{\Gamma_{Si}} = \sigma_{R_i} e^{-j\sigma_{\phi_i}} \quad (14)$$

#### IV. CONCLUSION

We have presented in a systematic manner the errors involved when balancing at a null a quasi-optical reflectometer based on a bridge configuration. We have suggested a de-embedding technique to determine the S-parameters of micro-machined components above 100 GHz from measurements of amplitude and phase alone. Theoretical estimates of the propagation of errors from the reflectometer to the measured attenuation and wave-number will be presented at the conference.

#### REFERENCES

- [1] Engen G.F., 1974. Calibration technique for automated network analysers with application to adapter evaluation. *IEEE Transactions on Microwave Theory and Techniques*, 22, pp. 1255-1260.
- [2] Beatty R.W., Engen G.F., and Anson W.J., 1960. Measurement of reflection and losses of waveguide joints and connectors using microwave reflectometer techniques. *IRE Transactions in Instrumentation*, I-9, pp. 219-226.
- [3] Engen G.F., 1971. An extension to the sliding short method of connector and adapter evaluation. *Journal of Research of the National Bureau of Standards*, 75C, pp. 177-183.
- [4] Bowen J.W., Hadjiloucas S. and Karatzas L.S., (1998). 'Characteristic Impedance measurements of a WR-10 waveguide sample with a Dispersive Fourier Transform Spectrometer' in *Applied Optics and Optoelectronics*, AT Augousti (Ed.) IOP Publications, pp. 181-186.
- [5] A.R. Harvey and J.C.G. Lesurf, 1990. Proc. 15<sup>th</sup> Infrared-millimeter waves Conf., Conf. Digest T.2.8 pp 198-200.
- [6] The expression of Uncertainty and Confidence in Measurement, M3003, NAMAS Report, Ed. 1, Dec. 1997.
- [7] J.W. Bowen, L.S. Karatzas, B.M. Towlson, N.J. Cronin, D.A. Brown, S. Wootton, N. Agbor, J.M. Chamberlain, G.M. Parkhurst, J. Digby, M. Henini, C. Collins, R.D. Pollard, R.E. Miles, D.P. Steenson and D. Thompson, "Micro-machined Integrated Components for Terahertz Frequencies", in Proc. 30th ESLAB Symp. 'Submillimetre and Far-Infrared Space Instrumentation', ESTEC, Noordwijk, The Netherlands, ESA SP-388, pp. 183-186, 1996.

# Design of Air-Filled Rectangular Waveguide Bandpass Filters by DBFILTER code for Terahertz Applications

Djuradj Budimir, *Member IEEE*

**Abstract-** In this paper we describe a CAD of conventional air-filled rectangular waveguide E-plane filter structures for Terahertz applications. The software package DBFILTER has been developed with the specific goal of eliminating all experimental characterizations and manual adjustments required in the final filters. The software package DBFILTER was used for filter synthesis and design, and the one actual filter implementation is presented. The same code can be used for multilayer dielectric or air-filled metal-pipe on wafer rectangular waveguide bandpass filter structures on a GaAs or Silicon substrates with minor modifications

Other techniques such as dielectric-filled metal-pipe rectangular waveguide (see Fig.1a and Fig.2), and micro-machined air-filled rectangular waveguide (see Fig. 1b), have been reported [1-3] as solution.

This paper looks at the design of conventional air-filled rectangular waveguide bandpass filters for terahertz applications. One design example is given, for an arbitrary filter specifications.

## I. INTRODUCTION

The steady growth in commercial interest in millimetre wave and terahertz systems, especially in wireless communications, security and sensor applications, and military and transportation electronics, has provided a significant challenge to conventional microwave circuits and their design methodologies. High performance narrow-band bandpass filters having both a low insertion loss and a high selectivity are important for modern millimetre-wave communication systems. At present most filters at mm-wave and terahertz frequencies are produced in waveguide (air-filled rectangular and nonradiative dielectric) with high associated machining costs.

Conventional waveguide technology is the main filter technology for mm-wave and terahertz frequency range. Eliminating all experimental characterizations and manual adjustments required in the final filters is very important part of filter design. However, due to rectangular waveguide small size, fundamental mode it becomes increasingly difficult to fabricated.

The author is with the Department of Electronic Systems, University of Westminster, London, W1M 8JS, UK.

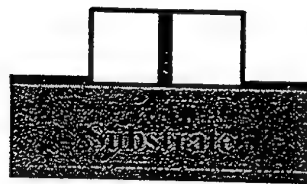
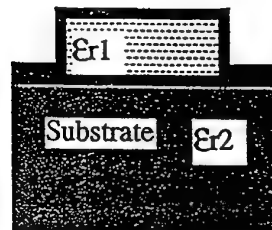


Fig. 1. Transmission line structures commonly used in terahertz filters a) monolithic dielectric-filled metal-pipe rectangular waveguide, b) micro-machined air-filled rectangular waveguide.

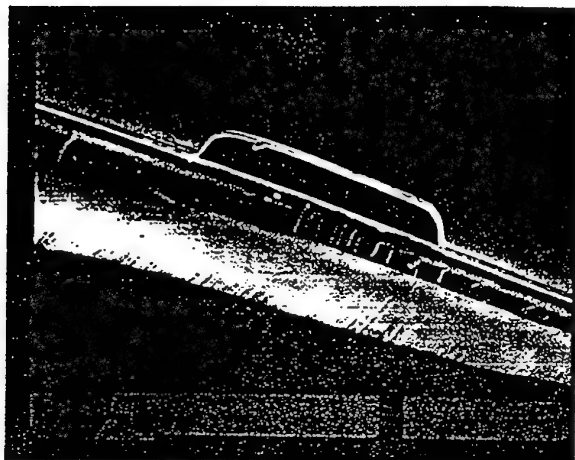


Fig. 2. Photomicrograph of fabricated monolithic air-filled metal-pipe rectangular waveguides (100 x 10 microns).

## II. NUMERICAL RESULTS

The following example illustrates some of the capabilities of the DBFILTER software package. A four resonator J-band conventional air-filled waveguide E-plane bandpass filter with the following specifications has been designed.

Type: Bandpass  
 Waveguide WG139 (WR3): Internal dimension 0.8636-0.4318 mm:  
 Midband frequency: 280 GHz  
 Passband: 270 - 290 GHz  
 Passband flatness better than 0.5dB  
 Passband insertion loss <0.5dB  
 Passband return loss >20dB  
 Metal insert thickness: 0.0050 mm.  
 Filter characteristic: Chebyshev

Figure 3 shows the passband insertion loss calculated using the insert dimensions obtained on convergence by DBFILTER™ software [5]. Mode matching with 30 modes was used throughout the synthesis and the

design. The dimensions of the E-plane insert are given in the same Figure.

Figure 2 shows the transmission line structures commonly used in terahertz filters such as a) dielectric-filled metal-pipe rectangular waveguide, b) micro-machined air-filled rectangular waveguide. The photomicrograph of fabricated air-filled metal-pipe rectangular waveguide (100 x 10 microns) is shown in Figure 3.

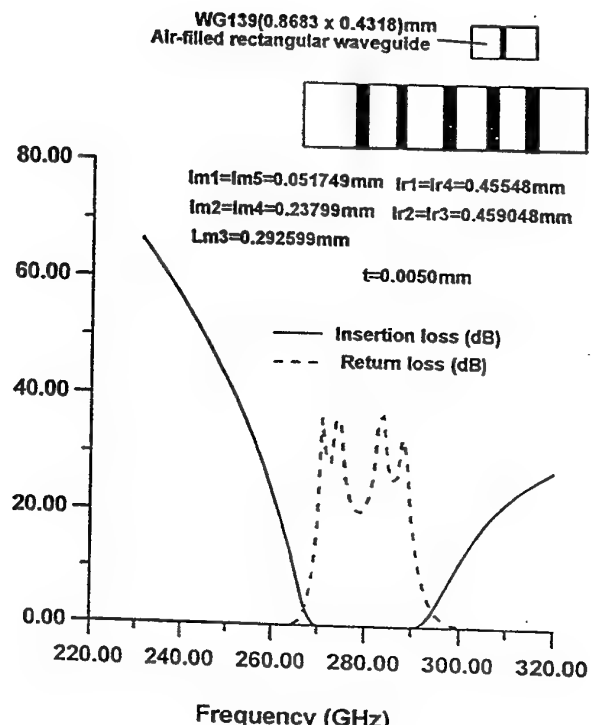


Fig. 3. Calculated insertion loss (solid line) and return loss (dashed line) of the E-plane filter by DBFILTER.

### III. CONCLUSION

The software package DBFILTER was used for filter synthesis and design of a four resonator J-band conventional air-filled waveguide bandpass filter. The same code can be used for multilayer dielectric or air-filled metal-pipe on wafer rectangular waveguide bandpass filter structures on a GaAs or Silicon substrates with minor modifications

### ACKNOWLEDGMENT

The author is grateful to Dr A. A. Rezazadeh and Mr A. H. Khalid at King's College London for assisting in the waveguide fabrication.

### REFERENCES

- [1] S. Lucyszyn, D. Budimir, Q.H.Wang and I.D. Robertson, "Design of Compact Monolithic Dielectric-filled Metal-Pipe Rectangular Waveguide for Millimetre-wave Applications", *IEE Proceedings - Microwave, Antennas and Propagation*, part H, Vol. 143, No.5, October 1996.
- [2] S. Lucyszyn, D. Budimir, and I.D. Robertson, "Design of Low-loss Monolithic Millimetre-wave Filters using Dielectric-filled Metal-pipe Rectangular Waveguides", *ESA/ESTEC Workshop*, November 1995.
- [3] C. E. Collins, J. W. Digby, R. D. Pollard, R. E. Milles, G. M. Parkhurst, J. M. Chamberlain, D. P. Steenson, N. J. Cronin, L. S. Caratzas, and J. W. Bowen, "W-Band Measurements of 100mm Height Micro-machined Air-Filled Rectangular Waveguides", *IEEE MTT-S Digest*, June 1997.
- [4] D. Budimir, "Generalized Filter Design by Computer Optimization", Norwood, MA: Artech House, 1998.
- [5] DBFILTER, "Reference Manual", Version 2.0, Tesla Communications Ltd, London, England, 1997.

# Micro-Machined "Snap-Together" Rectangular Waveguide For Terahertz Circuits

Caroline E. Collins<sup>1,2</sup>, Robert E. Miles<sup>1</sup>, John W. Digby<sup>2</sup>, Geoff M. Parkhurst<sup>2</sup>, Roger D. Pollard<sup>1</sup>, J. Martyn Chamberlain<sup>2</sup> and D. Paul Steenson<sup>1</sup>.

<sup>1</sup>*Institute of Microwaves and Photonics, School of Electronic and Electrical Engineering,  
The University of Leeds, Leeds LS2 9JT, UK.*

<sup>2</sup>*Physics Department, University of Nottingham, Nottingham NG7 2RD, UK.*

**Abstract** - A novel technique for micro-machining terahertz frequency rectangular waveguide components is reported. Known as "T-guide", these precision structures are fabricated in two halves with locating pins on one half and corresponding holes on the other such that they can be snapped together. The resulting waveguides have excellent surface finish, are physically robust and are cheap and easy to manufacture. S-parameter measurements in the frequency range 75 GHz to 110 GHz are reported for the first time for these structures which show that they exhibit lower loss than previously reported micro-machined rectangular waveguides. The "snap together" feature facilitates the incorporation of active devices into these waveguides.

## I. INTRODUCTION

Steady progress in active and passive device technology for the millimetre-wave frequency range is opening up the possibility of a variety of applications such as automotive radar, point-to-point communications, passive imaging, and sensing [1,2]. There is considerable commercial potential in exploiting the large bandwidths available at these high frequencies as soon as a suitable cost-effective technology becomes available [3]. Above 100GHz, standard microwave transmission media such as microstrip and coplanar waveguide become very lossy and hence research is ongoing into alternative technologies [4]. Rectangular waveguide remains popular at these frequencies owing to its low-loss but a major drawback is that it becomes ever more difficult and expensive to manufacture using conventional machining techniques owing to its small size and consequently tight tolerances on dimensions and surface quality.

Techniques have been reported for micro-machining low-cost millimetre and sub-millimetre-wave rectangular waveguides with high dimensional accuracy [5,6]. Well established semiconductor device processing techniques have been used to fabricate a 4 $\mu$ m high rectangular waveguide structure [5] although this did exhibited a loss > 40dB/wavelength at 100 GHz. Micro-machined rectangular waveguides using standard UV photoresist formers have also been reported [6] but,

because of a maximum height limitation of 100  $\mu$ m, (corresponding to 1/13th of full height at 100 GHz) these guides are difficult to couple to standard waveguide with a resulting increase in circuit losses. The LIGA x-ray lithographic process has been used to micro-machine taller, high-aspect-ratio structures [7], but this is both time-consuming and expensive to implement. However, a recently introduced negative photoresist (known as EPON SU-8<sup>TM</sup> [8]) can be used to produce features in excess of 1mm in height with large aspect ratios in a single UV exposure. This paper describes a new technique for the fabrication of micro-machined, rectangular waveguides in two halves using metalised SU-8 photoresist and goes on to present the results of S-parameter measurements on these structures. Greater waveguide heights can be achieved than in [6], reducing attenuation and mismatch loss. Also, the waveguides are physically more robust, thus simplifying the measurement process and increasing the ease-of-handling; they are cheap and easy to make and lend themselves to the accurate manufacture of all kinds of waveguide components at millimetre-wave and terahertz frequencies. The incorporation of locating holes and pins into this new micro-machined waveguide makes it possible to snap the two halves together precisely and repeatably.

## II. WAVEGUIDE FABRICATION

The T-guide fabrication procedure is illustrated in Figure 1. A sacrificial layer of aluminium is first evaporated onto a semiconductor substrate followed by a thick layer of SU-8 photoresist which is spun on top and baked. After the first layer of SU-8 is exposed, a second thick layer is applied, and the whole sample baked again. The second layer is then exposed, carefully lining up the alignment marks on the mask with those already produced in the first exposure. The sample is then given a post-exposure bake and developed. The second resist layer forms the side walls of the waveguide with one piece containing locating pins and the other matching holes to enable the two halves to be snapped together with the edges exactly aligned. Subsequent immersion in potassium hydroxide solution removes the sacrificial aluminium layer, releasing the SU8 waveguide halves.

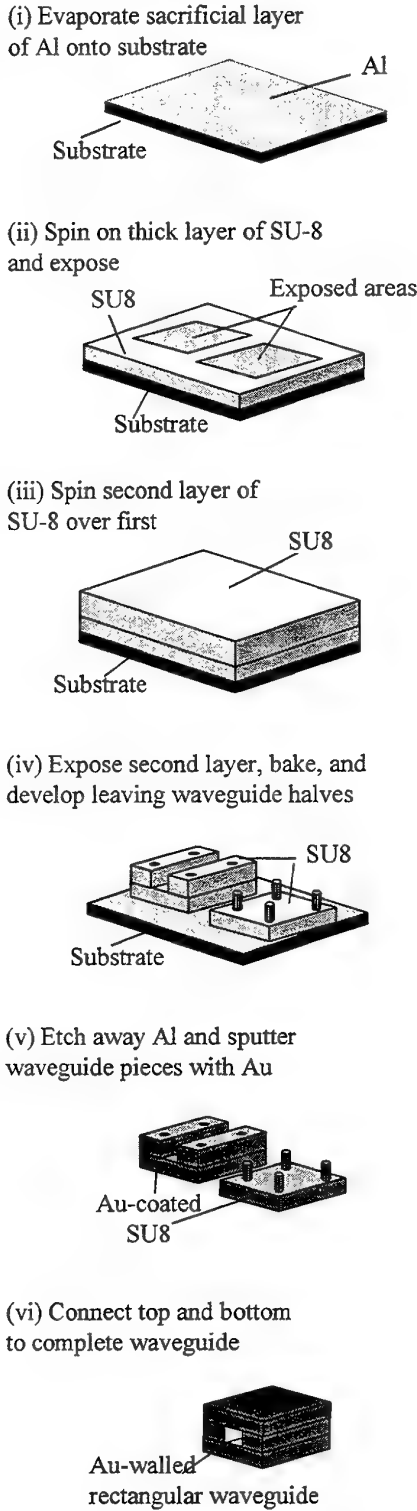


Figure 1. T-guide fabrication, using EPON SU-8™ photoresist

The two halves are sputtered with gold to a thickness of at least 600nm (2 skin depths at W-band) to coat the inside walls. The locating pins are designed slightly smaller than the holes to allow for this thickness of sputtered gold. The final stage in the procedure is to simply snap the two waveguide halves together. Figure 2 shows a photograph of a straight W-band (75 GHz -

110 GHz) waveguide fabricated using this technique before and after snapping together.

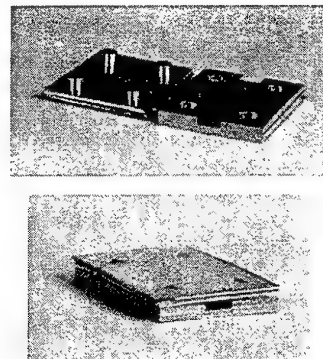


Figure 2. Photograph of a T-guide structure.

The guides were clamped between metal test blocks containing W-band flange detail to enable them to be connected to standard waveguide flanges for electrical characterisation. The lower test block contained a shallow groove into which the SU8 pieces were placed to achieve accurate alignment.

### III. MEASUREMENT TECHNIQUE AND RESULTS

Initial electrical characterisation has been carried out at W-band because of the availability of commercial network analysers at these frequencies. The results presented here are for straight lengths of waveguide, cross-section 2.54mm by approximately 700 $\mu$ m ( $\approx$  half height). A standard TRL calibration was performed at the test ports of a W-band vector network analyser. The micro-machined waveguides were then connected between the test ports as described above and their S-parameters measured. The measurements displayed a periodic ripple caused by multiple reflections between the full to reduced height waveguide junctions. The effect of these reflections was removed by renormalising the measured S-parameters to the characteristic impedance of the micro-machined sample rather than the full height test port impedance. In order to achieve this, the characteristic impedances of the full and reduced height waveguides need to be known and were found from a 3D electromagnetic field simulation of each case. The S-parameters were then renormalised at each measurement point, taking account of the change in waveguide characteristic impedance with frequency.

The renormalised results are shown in Figure 3. The observed loss, attributed mainly to the join between the waveguide halves occurring in the broad wall, is significantly lower than that previously reported for on-chip waveguides [3,4]. The measured sample was several wavelengths long and, as shown in Figure 4, the results actually correspond to an insertion loss of between 0.4dB and 0.8dB per wavelength over most of the measurement frequency range. Whilst this loss may seem high for the W-band waveguide measured here, at

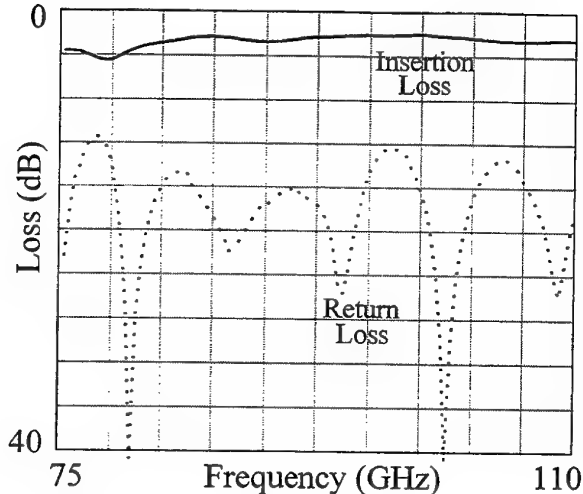


Figure 3. Measured Loss of a T-guide Sample.

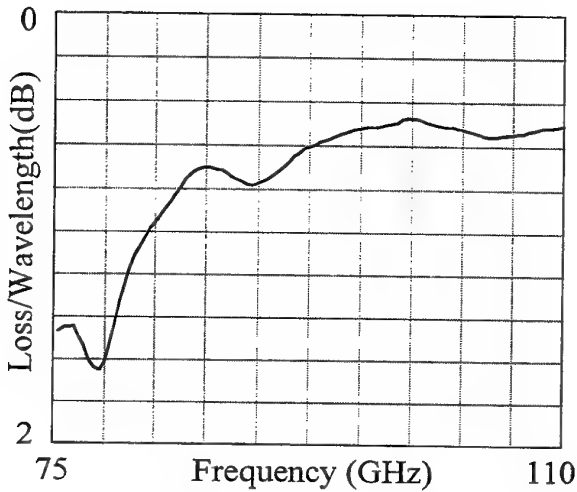


Figure 4. Measured Loss per Wavelength of T-guide.

200 GHz and above, the waveguides could be fabricated in the opposite orientation with a "trough" in both waveguide halves. This would move the join between the two halves to the centre of the broad wall, and hence reduce the electrical losses. In this configuration, waveguide widths up to about 1.4 mm will be possible corresponding to a cut-off frequency in the region of 110 GHz.

#### IV. DISCUSSION AND CONCLUSIONS

A new micro-machined millimetre-wave and terahertz rectangular waveguide technology (known as "T-guides") is reported for the first time. These waveguides are characterised by high dimensional precision and excellent surface quality as a result of the semiconductor device fabrication techniques used in their manufacture. The photoresist used requires only a single UV exposure to form features up to 1mm in height making the new technique simple to implement, robust and cost-

effective. The measured results presented show that the micro-machined waveguides, because of their additional height, achieve much lower loss than previously reported on-chip waveguides [5,6] and do not suffer from the difficulty of coupling into conventionally machined waveguides as they can be bolted directly onto standard flanges. The "snap-together" property means that it easy to mount and demount active devices for terahertz circuit applications. This new technique will be particularly useful at higher frequencies as dimensions become smaller and standard machining becomes very much more difficult.

#### V. ACKOWLEDGEMENTS

This work was carried out with the support of the UK Engineering and Physical Sciences Research Council (EPSRC) as part of the TINTIN program. The authors wish to thank Terry Moseley of the University of Leeds for machining the sample holders, and HP-EEs of for the donation of their high frequency structure simulator software (HFSS).

#### VI. REFERENCES

- [1] L. Raffaelli, "MMW Digital Radio Front Ends: Market, Application, and Technology," *Microwave Journal*, vol. 40, no. 10, pp. 92-96, Oct. 1997.
- [2] T. Ihara and K. Fujimura, "Research and Development Trends of Millimeter-Wave Short-Range Application Systems," *IEICE Transactions on Communications*, vol. E79-B, no. 12, pp. 1741-1753, Dec. 1996.
- [3] J. M. Chamberlain and R. E. Miles (editors), *New Directions in Terahertz Technology*, Kluwer Academic Publishing, Dordrecht, 1997.
- [4] L. P. B. Katehi, "Novel Transmission Lines for the Submillimeter-Wave Region," *Proc. IEEE*, vol. 80, no. 11, pp. 1771-1787, Nov. 1992.
- [5] S. Lucyszyn, Q. H. Wang, and I. D. Robertson, "0.1THz Rectangular Waveguide on GaAs Semi-Insulating Substrate," *Electronics Letters*, vol. 31, no. 9, pp. 721-722, 27th April 1995.
- [6] C. E. Collins, J. W. Digby, R. D. Pollard, R. E. Miles, G. M. Parkhurst, J. M. Chamberlain, D. P. Steenson, N. J. Cronin, L. S. Karatzas and J. W. Bowen, "W-Band Measurements of 100µm Height Micro-Machined Air-Filled Rectangular Waveguides," in *1997 IEEE Int. Micr. Symp. Dig.*, pp. 1439-1442, Denver, CO, June 1997.
- [7] S. W. Moon, C. M. Mann, B. J. Maddison, I. C. E. Turcu, R. Allot, S. E. Huq, and N. Lisi, "Terahertz Waveguide Components Fabricated Using a 3D X-ray Microfabrication Technique," *Electronics Letters*, vol. 32, no. 19, pp. 1794-1795, Sept 12th 1996.
- [8] K. Y. Lee, N. LaBianca, S. A. Rishton, S. Zolgharnain, J. D. Gelorme, J. Shaw, and T. H.-P. Chang, "Micromachining Applications of a High Resolution Ultrathick Photoresist," *J. Vac. Sci. Technol. B*, vol. 13, no. 6, pp. 3012-3016, Nov/Dec 1995.

# Calculation of THz Frequency Conversion by HNDFWM in $\lambda/4$ -Shifted DFB Lasers

Jacques W. D. Chi, *Member, IEEE*, K. Alan Shore, *Senior Member, IEEE*, and Jean Le Bihan, *Senior Member, IEEE*

**Abstract**—We have developed a theoretical model to study the highly nondegenerate four wave mixing in  $\lambda/4$ -Shifted DFB laser diodes. Frequency detuning up to 4THz between the self-generated pump wave and the injected probe wave is envisaged. Wavelength-converted signal can be generated in a comparable bandwidth. Our results are in very good agreement with recent experiment.

**Index terms**—wavelength conversion, DFB laser, wavelength division multiplexing

## I. INTRODUCTION

It has been shown recently that Highly Non-Degenerate Four Wave Mixing (HNDFWM) can be used to achieve efficient THz-range frequency conversion in  $\lambda/4$ -shifted (WQS) distributed feedback lasers (DFB) [1], [2]. In comparison with the use of a Semiconductor Optical Amplifier (SOA) as the mixing medium [3], [4], this approach has important advantages in terms of reductions of electrical current and amplified spontaneous emission noise due to laser action, as well as system simplification arising from the self-generated, dynamical single mode (DSM) pump wave. All these attributes imply significant potential for the use of QWS-DFBs in system applications which exploit wavelength division multiplexing (WDM).

It is appreciated that DFB lasers behave approximately as a SOA for transmitted waves whose frequencies are located outside the DFB stopband, as is the case for HNDFWM with THz-range pump-probe detunings. The SOA-type approach is simple and gives analytical results in some cases [3] but fails to deal with waves whose frequencies are within or near the stopband, and, moreover, cannot study the DFB-reflected waves - which may have severe consequences on system performance. These problems can be resolved using a coupled-wave approach [1] which is used in this paper to study HNDFWM in medium-coupled ( $\kappa L \sim 1$ ) QWS-DFBs. Such lasers give a good compromise in

terms of lasing threshold, gain level, and side-mode suppression ratio [5].

Calculations have been performed using device parameters typical of a quantum-well DFB laser operating at a wavelength  $\lambda=1.55\mu\text{m}$ . It is noted that for small detunings ( $<20\text{GHz}$ ) injection locking and carrier depletion effects may become significant, but these are ignored in the present calculations, and hence results at such small detunings are not considered here.

## II. MODEL

Fig. 1 shows the schematic of the model.

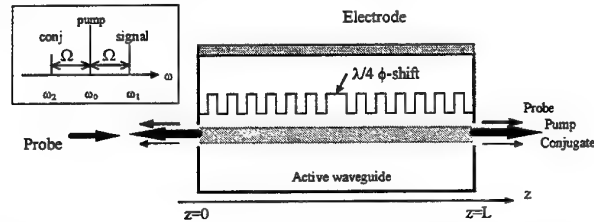


Fig. 1. Schematic of FWM in a QWS-DFB. The facets at  $z=0, L$  are anti-reflection coated (AR). The laser cavity supports the fundamental TE polarised waveguide mode.

The probe (signal) wave at pulsation  $\omega_1$  is injected into the active DFB cavity oscillating at  $\omega_0$ . The conjugate wave at  $\omega_2=2\omega_0-\omega_1$ , which contains the signal information, is then generated by FWM process. The total intracavity field is

$$E(z, t) = \exp(-i\omega t) \sum_{j=0,1,2} \left[ R_j(z) e(i k_B z) + S_j(z) \exp(-i k_B z) \right] + c.c. \quad (1)$$

Here,  $R_j$  and  $S_j$  are the complex envelop functions for the forward (+z) and backward (-z) propagating fields, which are normalised so that  $|E|^2$  gives the wave intensity in  $\text{W/m}^2$ ;  $j=0,1,2$  indicates respectively the self-generated pump, the probe, and the FWM-induced conjugate waves.  $k_B = \pi / \Lambda$  is the Bragg wave number,  $\Lambda$  is the first-order index grating period. Substituting (1) into the scalar wave equation for a DFB waveguide results in the coupled-wave equation [1]

J. Chi and J. Le Bihan are with Laboratoire RESO, Ecole Nationale d'Ingénieur de BREST, C. P. 15, 29608 BREST Cedex, France  
K. A. Shore is with University of Wales, Bangor, School of Electronic Engineering and Computer System, Dean Street, Bangor, Gwynedd LL57 1UT, U.K.

$$\left\{ \begin{array}{l} \frac{dR_j}{dz} = \left[ \frac{i\omega_j^2 \Gamma \chi_j^L}{2k_B c^2} + \frac{i(k_j^2 - k_B^2)}{2k_B} \right] R_j + \left[ \frac{i\kappa k_j}{k_B} \right] S_j \\ \quad + \frac{i\omega_j^2 \Gamma \chi_j^{FWM}}{2k_B c^2 E_0^2} \left[ R_0^2 R_{3-j}^* + 2R_0 S_0 S_{3-j}^* \right] \\ - \frac{dS_j}{dz} = \left[ \frac{i\omega_j^2 \Gamma \chi_j^L}{2k_B c^2} + \frac{i(k_j^2 - k_B^2)}{2k_B} \right] S_j + \left[ \frac{i\kappa k_j}{k_B} \right] R_j \\ \quad + \frac{i\omega_j^2 \Gamma \chi_j^{FWM}}{2k_B c^2 E_0^2} \left[ S_0^2 S_{3-j}^* + 2R_0 S_0 R_{3-j}^* \right] \end{array} \right. \quad (2)$$

Here,  $\Gamma$  is the confinement factor,  $\kappa$  (real) is the DFB coupling coefficient,  $k_j = \bar{n}_j \omega_j / c$  is the wavenumber of the  $j$ th wave in the active region,  $\bar{n}_j$  is the effective mode index given by

$$\bar{n}_{1,2} = \bar{n}_0 \pm \Omega \frac{d\bar{n}}{d\omega} \Big|_{\omega=\omega_0} \quad (3)$$

where  $\bar{n}_0$  is the effective mode index at transparency for  $\lambda=1.55\mu\text{m}$ ,  $d\bar{n}/d\omega$  is the differential index,  $\Omega=\omega_1-\omega_0=\omega_0-\omega_2$  is the detuning between the probe and the pump waves. The nonlinear susceptibilities are given by [3], [7]

$$\chi_{1,2}^L = -\frac{\bar{n}_{1,2} c G_{1,2}}{\omega_{1,2}} (\beta + i) \left( 1 - \frac{|E_0|^2 / I_s}{1 + |E_0|^2 / I_s \mp i\Omega\tau_s} \right) \quad (4)$$

$$\chi_{1,2}^{FWM} = \frac{i\bar{n}_{1,2} c}{\omega_{1,2} (1 + |E_0|^2 / I_s)} \left\{ \frac{g_{cdp} (1 - i\beta)}{1 + |E_0|^2 / I_s \mp i\Omega\tau_s} + \frac{g_{ch} (1 - i\beta_{ch})}{(1 \mp i\Omega\tau_1) (1 \mp i\Omega\tau_2)} + \frac{g_{shb} (1 - i\beta_{shb})}{(1 \mp i\Omega\tau_2)} \right\} \frac{E_0^2}{I_s} \quad (5)$$

Here,  $\beta$  is the linewidth enhancement factor,  $I_s$  is the saturation intensity,  $\tau_s$  is the interband carrier recombination time,  $\tau_1$  and  $\tau_2$  are the characteristic times of the intraband carrier-phonon and carrier-carrier scatterings, respectively;  $\Gamma g_{cdp}$ ,  $\Gamma g_{ch}$  and  $\Gamma g_{shb}$  are the effective gain coefficients for the carrier density pulsation, carrier heating, and spectral-hole burning, respectively;  $\beta_{ch}$  and  $\beta_{shb}$  are the ratios of the real part to the imaginary part of these nonlinear susceptibilities.  $(1 + |E_0|^2 / I_s)$  in the denominator takes into account the effect of gain reduction due to spatial hole burning [3], [6].

The gain spectrum  $g(\Omega)$  is approximated by a parabole :

$$G_{1,2} = \frac{\bar{g}}{1 + |E_0|^2 / I_s} \left( 1 - \frac{(\Omega_0 \pm \Omega)^2}{\Delta\omega_g^2} \right) \quad (6)$$

where  $2\Delta\omega_g$  is the gain bandwidth,  $\Omega_0$  is the frequency mismatch between the lasing wave and the gain peak. With detunings in the range of several THz, This approximation results in reasonable values [2].

The small signal gain  $\bar{g}$  is related to the laser threshold amplitude gain  $\alpha_{th}$  by the gain clamping effect, such that

$$\alpha_{th} L = \frac{\Gamma \bar{g}}{2} \int_0^L \left( 1 + \frac{|E_0(z)|^2}{I_s} \right)^{-1} dz \quad (7)$$

At this point, the boundary conditions must be specified. In order to obtain the best possible SMSR, as well as to eliminate Fabry-Pérot resonance resulting from facet reflections, we choose applying anti-reflection coating at the both facets. The eigenvalue equation for QWS-DFB is then found to be

$$cth\left(\frac{\gamma L}{2}\right) = (\alpha_{th} + \kappa) / \gamma \quad (8)$$

where  $\gamma = \sqrt{\kappa^2 + \alpha_{th}^2}$  is the propagating constant for QWS-DFB. The lasing mode corresponds to that having the lowest  $\alpha_{th}$  from (8). The threshold pump distribution is then given by

$$E_{0,th}(z < \frac{L}{2}) = \frac{\kappa}{\gamma} \sinh(\gamma z) e^{ik_B z} - \left[ \cosh(\gamma z) - \frac{\alpha_{th}}{\gamma} \sinh(\gamma z) \right] \cdot i e^{-ik_B z} \quad (9a)$$

$$E_{0,th}(z > \frac{L}{2}) = \left[ \cosh \gamma(L-z) - \frac{\alpha_{th}}{\gamma} \sinh \gamma(L-z) \right] \cdot i e^{ik_B z} - \frac{\kappa}{\gamma} \sinh \gamma(L-z) e^{-ik_B z} \quad (9b)$$

The pump intensity distribution is then given by  $|E_0|^2 = A(RR^* + SS^*)$ . The constant  $A$  is chosen to give  $|E_0(0)|^2 = I_{out}$ , where  $I_{out}$  is the pump output intensity. Notice that a  $\pi/2$  phase shift is introduced at  $z=L/2$ . This phase shift is also added to the probe and the conjugate waves [1], whose boundary conditions are

$$R_1(0) = A_{inj}, \quad R_2(0) = 0, \quad S_{1,2}(L) = 0$$

The injected probe level  $A_{inj}$  is supposed to be low enough, so that the carrier depletion from probe and FWM can be neglected. The transmission and reflection gains, measured at  $z=L$  and  $z=0$ , respectively, for the probe and conjugate waves, are then defined as

$$T_{1,2} = |R_{1,2}(L)|^2 / |A_{inj}|^2; \quad r_{1,2} = |S_{1,2}(0)|^2 / |A_{inj}|^2$$

$A_{inj}$  here is the field intensity corresponding to the TE waveguide mode. The mode conversion loss from gaussian mode or fiber mode to this waveguide mode must be taken into account when we calculate the injection efficiency.

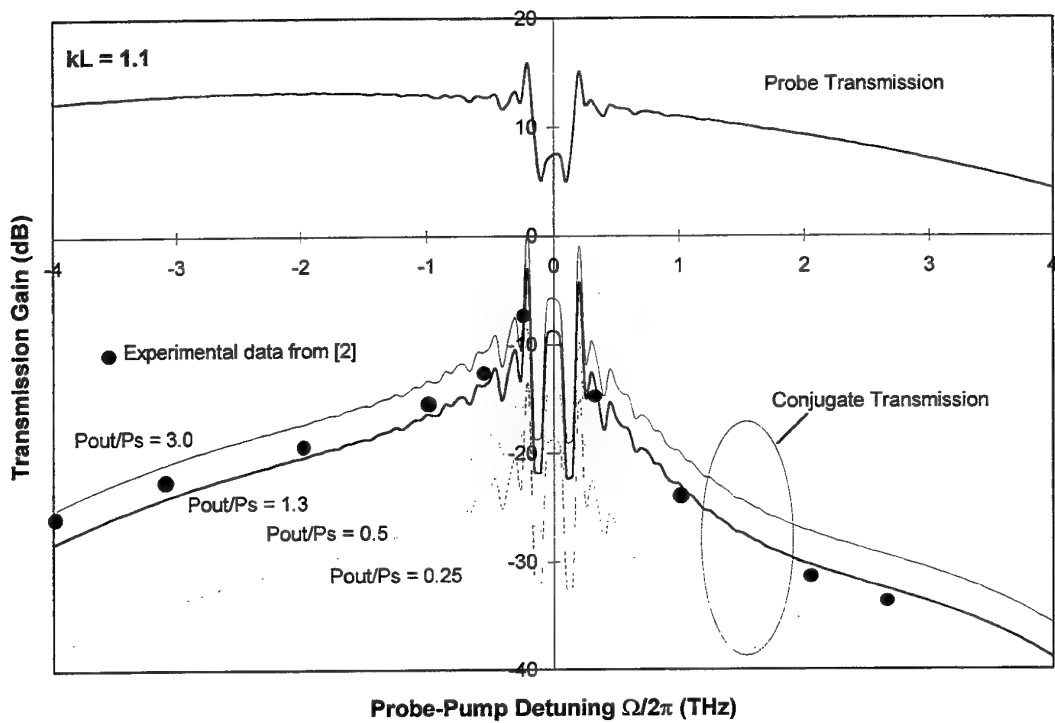


Fig. 2. Probe and conjugate transmission gains, obtained at  $z=L$ , under  $\kappa L=1.1$  with different pump power levels.

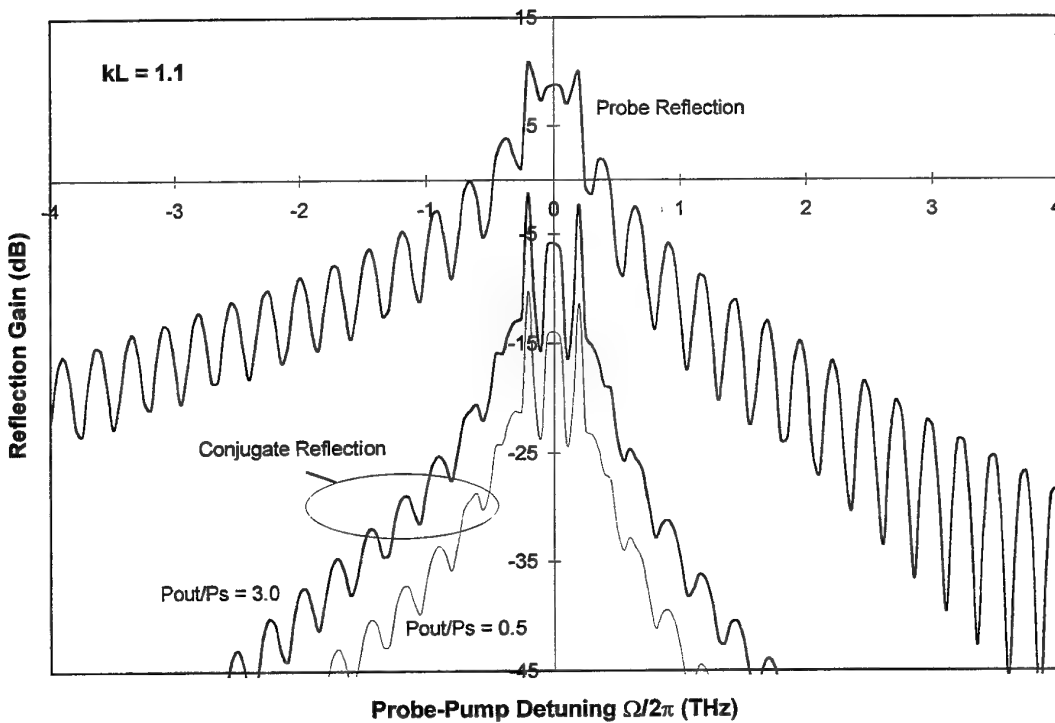


Fig. 3. Probe and conjugate reflection levels at  $z=0$  due to DFB, under  $\kappa L=1.1$  with different pump power levels.

Parameters	Symbol	Value	Unit
CH time	$\tau_1$	400	fs
SHB time	$\tau_2$	20	fs
Effective CDP gain	$\Gamma g_{cdp}$	0.8	$\text{cm}^{-1}$
Effective CH gain	$\Gamma g_{ch}$	0.012	$\text{cm}^{-1}$
Effective SHB gain	$\Gamma g_{shb}$	0.032	$\text{cm}^{-1}$
Imaginary part of CH	$\beta_{ch}$	14	/
Imaginary part of SHB	$\beta_{shb}$	0.6	/

Tab. 1. FWM susceptibility parameters used in the model

In order to compare quantitatively our model with the experimental observations [2], we have adopted the parameters for quantum-well structure, and have used  $\beta=2.5$ ,  $d\bar{n}/d\omega=2.3 \times 10^{-16} \text{ s/rad}$  [7]. Other device parameters are :  $L=300\mu\text{m}$ ,  $\bar{n}_0=3.5$ , saturation power  $P_s=I_sS$ ,  $S$  is the active section and  $I_s=5 \times 10^{10} \text{ Wm}^{-2}$  [3]. A typical value of  $\tau_s=0.5\text{ns}$  is chosen for simplicity, since this parameter has little influence on THz-range FWM. The gain bandwidth  $2\Delta\omega_g/2\pi=15\text{THz}$ , and  $\Omega_0/2\pi=2.2\text{THz}$  [2]. The parameters in (5) are obtained using data-fitting to [2], and their values are listed in Tab.1. These values are in good agreement with those obtained by other groups working on SOA [4], indicating that the basic HNDFWM mechanisms are the same in SOA and in DFB.

### III. RESULTS AND DISCUSSIONS

The model described above is studied numerically using an iterative shooting algorithm [1]. We first used curve-fitting to experimental data [2] with  $\kappa L=1.1$ , while the normalised pump level ( $P_{\text{out}}/P_s$ ) is allowed to change. The result is shown in Fig.2. The best fitting is obtained with the parameter values listed in Tab.1 and  $P_{\text{out}}=1.3P_s$ . Our result is clearly in very good agreement with the experiment.

As expected from gain clamping effect, the probe transmission remains unchanged for different pump powers. Comparing with the experiment [2] and taking into account the effects of mode conversion loss, we calculated that the pump level should be  $P_{\text{out}} \sim 1.7P_s$  (instead of  $1.3P_s$  from Fig. 2) in order to obtain the conjugate level observed in the experiment.

The DFB reflection effects are demonstrated in Fig.3 for different pump powers with  $\kappa L=1.1$ . It is observed that higher gain or higher pump power results in a stronger conjugate reflection, while the reflected probe power keeps unchanged for different pump levels with a given  $\kappa L$ . The undulations in these curves originate from Bragg reflection outside its stop band, and its period is given approximately by  $\Delta\Omega/2\pi = c / (\bar{n}L) \sim 0.28\text{THz}$  with  $L=300\mu\text{m}$ . The reflected probe is almost always higher than or equal to the -20dB level in the detuning range of  $-4\text{THz} \leq \Omega \leq 3\text{THz}$ , while the -20dB bandwidth is  $\sim 0.5\text{THz}$  for the reflected conjugate. It is recalled that these reflected powers are

likely to be re-injected into transmission channels as harmful coherent noises. Their consequences must be considered carefully in WDM system design and other practical applications.

### IV. CONCLUSION

We have studied HNDFWM in QWS-DFB under different operating conditions. Our calculation is in very good agreement with experimental results. Our results may find their applications in WDM systems using QWS-DFB as a wavelength converter.

### REFERENCES

- [1] J. Chi, K. A. Shore, and J. Le Bihan, "Highly non-degenerate four-wave mixing in uniform and  $\lambda/4$  shifted DFB lasers", *IEEE J. Quantum Electron.*, Vol. 33, No. 11, pp. 2011-2020, November 1997
- [2] H. Kuwatsuka, H. Shoji, M. Matsuda, and H. Ishikawa, "Nondegenerate four-wave mixing in a long-cavity  $\lambda/4$ -shifted DFB laser using its lasing beam as pump beams", *IEEE J. Quantum Electron.*, Vol. 33, No. 11, pp. 2002-2010, November 1997
- [3] A. Mecozzi, S. Scotti, A. D'Ottavi, E. Iannone, and P. Spano, "Four-wave mixing in traveling-wave semiconductor amplifiers", *IEEE J. Quantum Electron.*, vol. QE-31, No. 4, pp. 689-699, April 1995
- [4] S. Diez, C. Schmidt, R. Ludwig, H. G. Weber, K. Obermann, S. Kindt, I. Koltchanov, and K. Petermann, "Four-wave mixing in semiconductor optical amplifiers for frequency conversion and fast optical switching", *IEEE J. Selected Topics in Quantum Electronics*, Vol. 3, No. 5, pp. 1131-1145, October 1997
- [5] H. Soda, Y. Kotaki, H. Sudo, H. Ishikawa, S. Yamakoshi, and H. Imai, "Stability in single longitudinal mode operation in GaInAsP/InP phase-adjusted DFB Lasers", *IEEE J. Quantum Electron.*, vol. QE-23, No. 6, pp. 804-814, June 1987
- [6] W. M. Yee and K. A. Shore, "Nearly degenerate four-wave mixing in laser diode with non-uniform longitudinal gain distribution", *J. Opt. Soc. Am. B*, Vol. 11, pp. 1211-1218, 1994
- [7] J. Minch, S. L. Chuang, C. S. Chang, W. Fang, Y. K. Chen, and T. Tanbun-Ek, "Theory and experiment on the amplified spontaneous emission from distributed-feedback lasers", *IEEE J. Quantum Electron.*, Vol. 33, No. 5, pp. 815-823, May 1997

# Multiwave Mixing of Terahertz Detuned Optical Pulses in Semiconductor Optical Amplifiers

J.M.Tang, K.A.Shore

**Abstract**— A new model describing multiwave mixing of terahertz detuned picosecond optical pulses in Semiconductor Optical Amplifiers (SOAs) is presented, by taking into account carrier depletion, carrier heating, spectral hole-burning, two-photon absorption, ultrafast nonlinear refraction and small signal gain differences for different mixing pulses. Special attention is paid to the influence of probe depletion (PD) and cross-gain modulation (XGM) on four-wave mixing (FWM) of optical pulses in SOAs. The effects of PD and XGM become more significant for shorter input pulselength, higher pulse energy and smaller pump-probe frequency detuning. Results indicate that if the effects of PD and XGM are neglected the FWM efficiency can be seriously overestimated.

**Keywords**— Frequency conversion, optical mixing, optical phase conjugate, optical pulses, semiconductor optical amplifiers.

## I. INTRODUCTION

FOUR-Wave Mixing (FWM) has been considered as a useful technique for investigating the physical origin of ultrafast nonlinearities in active semiconductor waveguides, and as a phenomenon having important applications in high-capacity optical communication systems. For practical applications, FWM among ultrashort optical pulses in Semiconductor Optical Amplifiers (SOAs) is of great importance, which has already found applications as a fast AND-gate which is utilized for optical time-division demultiplexing [1-3] and optical sampling [4]. More recently, FWM of short optical pulses has also been used for dispersion compensation in ultra-high bit rate transmission system [5] and wavelength conversion [6].

To investigate FWM characteristics of ultrashort optical pulses in SOAs, several models have been reported [7-9]. Shtaif and Eisenstein's model [7], due to neglect of contribution of ultrafast intraband dynamics on pulse gain saturation, is valid for pulselengths of the order of a few tens of picosecond or longer. Although the model in [8] including the effects of carrier heating and spectral hole-burning processes on the gain saturation can be utilized to describe FWM of subpicosecond optical pulses, the analysis is restricted in validity to the regime of relatively weak pulse energy since it is based on a perturbative theory. Recently, a model developed by Mecozzi and Mørk [9] extends

This work was supported by the EPSRC under Grant GR/L03262, and J.M.Tang is supported by the Professor Wynn Humphrey Davies Scholarship and the School of Electronic Engineering and Computer Systems, University of Wales, Bangor, UK.

The authors are with the University of Wales, Bangor, School of Electronic Engineering and Computer Systems, Bangor, LL57 1UT, U.K. E-mail: alan@sees.bangor.ac.uk

the previous treatments to the case of intense pulses. In such a strong signal case, Probe Depletion (PD) and Cross-Gain Modulation (XGM) will play a role in determining the conjugate pulses. Furthermore, gain saturation and phase change of mixing pulses induced by Two-Photon Absorption (TPA) and Ultrafast Nonlinear Refraction (UNR) should also be incorporated for the case of pulse peak power larger than 1W [10]. However, PD, XGM, TPA and UNR have not been considered in the available theoretical FWM models of optical pulses propagation in SOAs.

By taking into account carrier heating, spectral hole-burning, TPA and UNR, we have obtained a model [10], which is successful in describing the propagation of strong picosecond optical pulses through SOAs. The model is considered to be valid for pulse widths longer than several hundred femtoseconds [10]. In this paper, by incorporating PD and XGM effects a theoretical treatment of FWM of picosecond optical pulses is undertaken on the basis of this model. Attention is focused on the influence of PD and XGM on FWM efficiency. It is emphasized that the XGM considered in this work arises due to two general effects. First of all, the well-known mechanism of carrier depletion [9] is taken into account. In addition, the XGM treated here incorporates interactions which occur between mixing pulses through temporal gain and index gratings induced by beat frequencies between central frequencies of pump and probe/conjugate pulses.

## II. BASIC COUPLED EQUATIONS

Based on the model [10], the basic coupled equations for the complex slowly varying fields  $A_j$  of mixing pulses in unit of  $W^{\frac{1}{2}}$  copropagating along a SOA, can be derived in the following forms

$$\frac{\partial A_0}{\partial z} = \frac{1}{2} \frac{G_0 - \epsilon_2 P_0^2}{1 + \epsilon_1 P_0} A_0 - \frac{i}{2} [\alpha_N G_0 - \alpha_T \frac{\epsilon_1 G_0 P_0 + \epsilon_2 P_0^2}{1 + \epsilon_1 P_0}] A_0 - (\Gamma_2 \beta_2 + i \Gamma_2' \frac{\omega_0}{c} n_2) \frac{1}{\sigma} P_0 A_0 - \frac{1}{2} \alpha_{int} A_0 \quad (1)$$

$$\frac{\partial A_j}{\partial z} = \frac{1}{2} \frac{G_j - \epsilon_2 P_0^2}{1 + \epsilon_1 P_0} A_j - \frac{i}{2} [\alpha_N G_j - \alpha_T \frac{\epsilon_1 G_j P_0 + \epsilon_2 P_0^2}{1 + \epsilon_1 P_0}] A_j - \frac{1}{2} \alpha_{int} A_j - (\Gamma_2 \beta_2 + i \Gamma_2' \frac{\omega_j}{c} n_2) \frac{1}{\sigma} [2 P_0 A_j + A_0^2 A_{3-j}^*] - \frac{1}{2} \eta_{j0} P_0 A_j - \frac{1}{2} \eta_{0,3-j} A_0^2 A_{3-j}^* \quad j = 1, 2 \quad (2)$$

where the gain,  $G_j$ , experienced by the pulses is governed by

$$\frac{\partial G_j}{\partial t} = \frac{G_{sj} - G_j}{\tau_s} - \frac{1}{E_{satj}} \frac{G_0 - \epsilon_2 P_0^2}{1 + \epsilon_1 P_0} P_0 + \Gamma_2 \beta'_j P_0^2 \quad j = 0, 1, 2 \quad (3)$$

The terms with subscript 0,1 and 2 correspond to the pump pulse at central frequency  $\omega_0$ , probe pulse at  $\omega_1$  and conjugate pulse at  $\omega_2$ .  $P_j = |A_j|^2$ .  $\epsilon_1$  (in unit of  $W^{-1}$ ) is the nonlinear gain compression factor due to carrier heating and spectral holeburning [10].  $\epsilon_2$  (in unit of  $m^{-1}W^{-2}$ ) is the nonlinear gain compression factor due to the TPA [10].  $\beta'_j = a_j \beta_2 / [(\hbar \omega_j \sigma)^2 v_g]$ . The effective area of the active region  $\sigma$ , the small signal gain of the SOA  $G_{sj}$  and the gain saturation energy  $E_{satj}$  are defined in their usual forms [11]. Other parameters appearing above are the TPA coefficient  $\beta_2$ ; the nonlinear refractive index coefficient  $n_2$ ; the confinement factors associated with the TPA ( $\Gamma_2$ ) and the UNR ( $\Gamma'_2$ ); the traditional ( $\alpha_N$ ) and the temperature ( $\alpha_T$ ) linewidth enhancement factors; the waveguide loss  $\alpha_{int}$ . All the parameters which are not mentioned explicitly here have their general meanings [11].

In deriving the above equations, both gain dispersion and group-velocity mismatch between the pulses are neglected. The approximation can be easily satisfied in typical FWM conditions of picosecond pulses [8]. Therefore  $t$  denotes the local time in the moving frame with  $v_g$ . The envelopes of pump, probe and conjugate pulses are assumed to be slowly varying in comparison with  $e^{-i\Omega t}$ ,  $\Omega = \omega_1 - \omega_0$  is the frequency detuning. By considering a practical case, in which the pump pulse energy is much larger than that of the probe and conjugate pulses, both interaction terms in (1) and carrier depletion in (3) due to the probe and conjugate pulses can be neglected.

The coupling coefficient  $\eta_{jj'}$  ( $j \neq j'$ ,  $j, j' = 0, 1, 2$ ) can be decomposed into contributions from carrier depletion ( $\eta_{jj'}^{CD}$ ), carrier heating ( $\eta_{jj'}^{CH}$ ) and spectral holeburning ( $\eta_{jj'}^{SHB}$ ), which satisfy

$$\eta_{jj'} = \eta_{jj'}^{CD} + \eta_{jj'}^{CH} + \eta_{jj'}^{SHB} \quad (4)$$

with

$$\eta_{jj'}^{CD} = \frac{a_j \tau_s}{\hbar \omega_j \sigma} \frac{G_{sj} - \epsilon_2 P_j^2}{1 + \epsilon_1 P_j} \frac{1}{(1 - i\alpha_N) \frac{1}{-i(\omega_j - \omega_{j'})\tau_s + 1} \times \frac{1}{-i(\omega_j - \omega_{j'})\tau_1 + 1}} \quad (5)$$

$$\eta_{jj'}^{CH} = \epsilon_T \frac{G_{sj} - \epsilon_2 P_j^2}{1 + \epsilon_1 P_j} \frac{1}{(1 - i\alpha_T) \frac{1}{-i(\omega_j - \omega_{j'})\tau_h + 1} \times \frac{1}{-i(\omega_j - \omega_{j'})\tau_1 + 1}} \quad (6)$$

$$\eta_{jj'}^{SHB} = \epsilon_{SHB} \frac{G_{sj} - \epsilon_2 P_j^2}{1 + \epsilon_1 P_j} \frac{1}{(1 - i\alpha_{SHB}) \frac{1}{-i(\omega_j - \omega_{j'})\tau_1 + 1}} \quad (7)$$

where  $\epsilon_T$  and  $\epsilon_{SHB}$  are the nonlinear gain compression factors due to the carrier heating and spectral holeburning, respectively, and satisfy

$$\epsilon_1 = \epsilon_T + \epsilon_{SHB} \quad (8)$$

$\alpha_{SHB}$  is the linewidth enhancement factor corresponding to spectral holeburning.  $\tau_1$  and  $\tau_h$  are the carrier-carrier scattering time and temperature relaxation time respectively. It should be noted that those expressions used here have similar forms as in Ref.8 except that small signal gain in the corresponding expression of Ref.8 is replaced by  $(G_0 - \epsilon_2 P_0^2) / (1 + \epsilon_1 P_0)$ . The replacement results in a pulse power and longitudinally dependent  $\eta_{jj'}$ , which is necessary if the pump pulse energy is high enough to saturate a SOA significantly.

It can be also seen from the basic equations that the strength of gain (corresponding to the real part of the coupling coefficient) and index (corresponding to the imaginary part of the coupling coefficient) change due to the beat frequency is reduced with decreasing the small signal gain of the SOA. For passive or transparent SOAs, the FWM processes, therefore, rely mainly on the instantaneous effects, such as TPA and UNR, and does not suffer from speed limitations imposed by the carrier modulation time constant or the carrier heating and spectral holeburning time constants. This leads to a symmetric, frequency independent conversion efficiency, assuming phase matching condition is satisfied. The contributions from those instantaneous effects to the FWM process are expressed by using the terms proportional to  $(\Gamma_2 \beta_2 + i\Gamma'_2 \frac{\omega_1}{c} n_2) \frac{1}{\sigma}$  in basic equations.

The terms containing  $P_0 A_j$  (or  $A_0^2 A_j^*$ ),  $j = 1, 2$  in basic equations reflect mixing between the pump at  $\omega_0$  and the signal at  $\omega_j$ , leading to temporal gain and index gratings due to the beat frequency, and the gratings scatter the pump to the frequency  $\omega_j$  (or  $\omega_{-j}$ ). The conjugate pulses are generated through the term proportional to  $A_0^2 A_1^*$ . The terms containing  $P_0 A_j$ ,  $j = 1, 2$  account for XGM, which describes the influence of the pump pulses on the evolution of probe and conjugate pulses through the temporal gratings. The effect of carrier depletion induced by the pump pulse on the changes of gain and index of probe and conjugate pulses are of course included in the analysis. The term proportional to  $A_0^2 A_2^*$  accounts for PD effect, which reflects that the mixing between the pump and conjugate pulses, and also gives rise to the probe pulses. Owing to the much higher peak power in pulse case than that in the CW case, the XGM and PD effects are therefore expected to be very important in governing the FWM conversion efficiency.

In the numerical simulations, a gain model for SOAs presented in Ref.12 is adopted to determine the small signal gains of the different mixing pulses.

### III. NUMERICAL SIMULATIONS

The main parameters used in the calculations are representative for InGaAsP semiconductor material operating at a wavelength of  $\sim 1.55 \mu\text{m}$ . They are:  $L = 200 \mu\text{m}$ ;

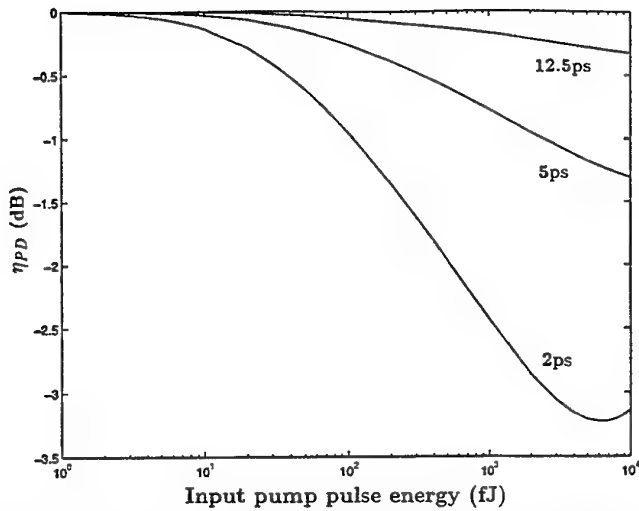


Fig. 1. Calculated dependence of the variation of FWM efficiency induced by probe depletion (PD) effect,  $\eta_{PD}$ , on the input pump pulse energy for different pulse widths.

$\sigma=1.5\mu m^2$ ;  $\Gamma=0.3$ ;  $\Gamma_2=0.5$ ;  $\Gamma'_2=0.28$ ;  $v_g=8.43 \times 10^7 m/s$ ;  $\alpha_{int}=2000 m^{-1}$ ;  $G_{s0}=3.46 \times 10^4 m^{-1}$  (located at the peak of gain spectrum of SOA);  $a_0=3.0 \times 10^{-20} m^2$ ;  $\tau_s=300 ps$ ;  $\epsilon_1=0.2 W^{-1}$ ;  $\epsilon_2=200 m^{-1} W^{-2}$ ;  $\beta_2=37.0 \times 10^{-11} m/W$ ;  $n_2=-3.5 \times 10^{-16} m^2/W$ ;  $\alpha_N=5.0$ ;  $\alpha_T=3.0$ . Other parameters are taken from Refs.8 and 9. The input Gaussian pump and probe pulses have the same pulse width as well as perfect pulse overlap, and in all cases their powers are set in the ratio of 10:1. The properties of the conjugate pulses can be obtained by numerically solving (1)-(3).

The FWM conversion efficiency  $\eta_{FWM}$  is defined as the ratio between the output energy of the conjugate pulse and the input energy of the probe pulse. The calculated behaviours of conjugate pulses agree with the experimental measurements [13-14], and results also show a maximum  $\eta_{FWM}$  value for optimum input pump pulse energy, which is consistent with Ref.9.

To extract the influence of PD and XGM on  $\eta_{FWM}$ , here we define  $\eta_{PD}$  as the difference between  $\eta_{FWM}$  when account is only taken of PD and that when neither PD nor XGM is included. An analogous definition is made for  $\eta_{XGM}$ .  $\eta_{PD}$  and  $\eta_{XGM}$  as functions of input pump pulse energy are shown in Fig.1 and Fig.2, respectively, for different pump pulse widths and a fixed negative frequency detuning, i.e.  $\omega_1 - \omega_0 = -0.5 THz$ . Both  $\eta_{PD}$  and  $\eta_{XGM}$  exhibit strong pulsewidth and pulse energy dependence. With decreasing pulsewidth, the effects of PD and XGM are enhanced considerably. Fig.1 also demonstrates a minimum  $\eta_{PD}$  value (for a pulse width of 2ps), which corresponds to a input pump pulse energy that causes the saturated gain of the SOA to be about zero. For larger pulsewidths a minimum  $\eta_{PD}$  is found at larger pump en-

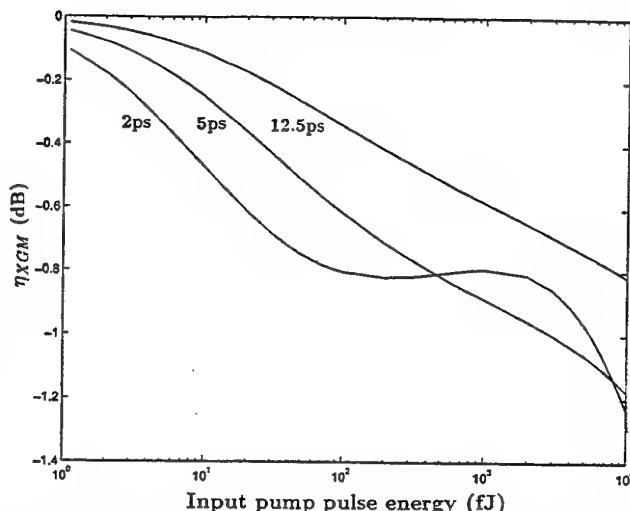


Fig. 2. The change of FWM efficiency induced by cross-gain modulation (XGM) effect,  $\eta_{XGM}$ , versus the input pump pulse energy for different pulse widths.

ergies. In the case of Fig.2, XGM affects  $\eta_{FWM}$  by mainly changing gains of probe and conjugate pulses through the terms proportional to  $P_0 A_j$  ( $j=1,2$ ). XGM leads to a negative (positive) contribution to the gain of the conjugate (probe) pulses since  $Re(\eta_{10})<0$  and  $Re(\eta_{20})>0$  [15]. When the input pump energy is less than the optimum energy ( $\sim 50 fJ$  for 2ps), which corresponds to a maximum  $\eta_{FWM}$ , the gains experienced by mixing pulses are not saturated, resulting in an almost linearly decreasing  $\eta_{XGM}$ , as shown in Fig.2. Increasing the pump power larger than the optimum energy, the decreased conjugate gain and increased probe power due to XGM effect begin to play important roles in determining the conjugate waves, and furthermore, the gains of the SOA are saturated. Therefore, a flatter lineshape is observed. When the peak power of pump pulse is larger than 1W, the TPA and UNR effects become important [10], which strengthen significantly the XGM effect, causing  $\eta_{XGM}$  to decrease sharply.

The detuning dependences of  $\eta_{PD}$  and  $\eta_{XGM}$  for negative and positive frequency detunings are given in Fig.3, where the input pump pulse is fixed at 5ps and 1pJ. For smaller frequency detuning, the effect of PD is shown to be dominant compared with that of XGM, and  $\eta_{PD}$  is remarkably decreased with reduced frequency detuning; while for much larger frequency detuning, the effect of XGM becomes dominant, and the  $\eta_{PD}$  is small enough to be negligible. The crossing point of  $\eta_{PD}$  and  $\eta_{XGM}$  moves to the larger frequency detuning side with decreasing pulsewidth. The above characteristics can be understood by considering Figs.1 and 2.

Fig.3 also demonstrates that  $\eta_{PD}$  is almost symmetric with respect to negative and positive frequency detuning,

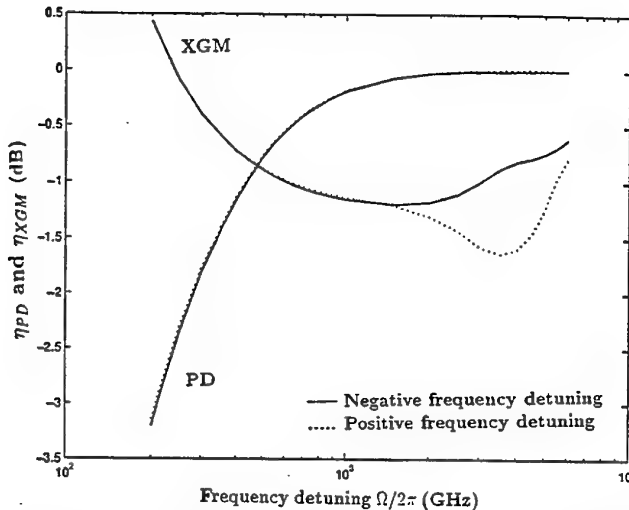


Fig. 3. The variations of FWM efficiency due to probe depletion (PD) and cross-gain modulation (XGM) effects as functions of frequency detuning between probe and pump pulses. Solid (dotted) lines are for negative (positive) frequency detunings.

and that  $\eta_{XGM}$  is asymmetric in larger frequency detuning regime. The symmetry or asymmetry of the FWM efficiency is determined mainly by the phase of the coupling coefficient [15]. The symmetric nature of  $\eta_{PD}$  originates from the symmetry of coupling coefficient in the form of  $\eta_{01}\eta_{02}^*$  which determines the change of the conjugate power induced by PD. The maximum  $\eta_{XGM}$  deviation between negative and positive detunings appears when the frequency detunings are of  $\sim 4$  THz, where the ultrafast intraband processes (especially spectral holeburning that has been considered as the main process to cause the asymmetry of conjugate waves [15]) become dominant compared with carrier depletion process. When the frequency detuning is 1 THz or less,  $\text{Im}(\eta_{10})$  and  $\text{Im}(\eta_{20})$  governing the asymmetry of  $\eta_{XGM}$ , are almost equal and are of opposite signs and thus the  $\eta_{XGM}$  becomes symmetric. When the frequency approaches  $\sim 4$  THz,  $\text{Im}(\eta_{10})$  and  $\text{Im}(\eta_{20})$  have the same sign and therefore an asymmetric  $\eta_{XGM}$  is observed.

#### IV. CONCLUSIONS

In conclusion, the influence of Probe Depletion (PD) and Cross-Gain Modulation (XGM) on Four-Wave Mixing (FWM) efficiency of picosecond optical pulses in SOAs has been investigated numerically. It is shown that the effects of PD and XGM can be significantly enhanced by shorter pulselength, higher pulse energy and smaller pump-probe frequency detuning. The results presented here indicate that if the effects of PD and XGM are neglected the  $\eta_{FWM}$  can be seriously overestimated.

#### REFERENCES

- [1] R.Schnabel, W.Pieper, M.Ehrhardt, M.Eiselt, and H.G.Weber, "Wavelength conversion and switching of high speed data signals using semiconductor laser amplifiers," *Electron. Lett.*, Vol.29, pp.2047-2048, 1993.
- [2] S.Kawanishi and O.Kamatani, "All-optical time division multiplexing using four-wave mixing," *Electron. Lett.*, Vol.30, pp.1697-1698, 1994.
- [3] T.Morioka, H.Takara, S.Kawanishi, K.Uchiyama, and M.Saruwatari, "Polarization-independent all-optical demultiplexing up to 200 Gbit/s using four-wave mixing in a semiconductor laser amplifier," *Electron. Lett.*, Vol.32, pp.840-842, 1996.
- [4] M.Jinno, J.B.Schlager, and D.L.Franzen, "Optical sampling using nondegenerate four-wave mixing in a semiconductor laser amplifier," *Electron. Lett.*, Vol.30, pp.1489-1491, 1994.
- [5] D.D.Marcenac, D.Nesset, A.E.Kelly, and D.Gavrilovic, "40Gbit/s transmission over 103km of NDSF using polarisation independent mid-span spectral inversion by four-wave mixing in a semiconductor optical amplifier," *Electron. Lett.*, Vol.34, pp.100-101, 1998.
- [6] D.Nesset, D.D.Marcenac, P.L.Mason, A.E.Kelly, S.Bouchoule, and E.Lach, "Simultaneous wavelength conversion of two 40Gbit/s channels using four-wave mixing in a semiconductor optical amplifier," *Electron. Lett.*, Vol.34, pp.107-108, 1998.
- [7] M.Shtaif and G.Eisenstein, "Analytical solution of wave mixing between short optical pulses in a semiconductor optical amplifier," *App.Phys.Lett.*, Vol.66, pp.1458-1460, 1995.
- [8] J.Mørk and A.Mecozzi, "Theory of nondegenerate four-wave mixing between pulses in a semiconductor waveguide," *IEEE J.Quantum Electron.*, Vol.33, pp.545-555, 1997.
- [9] A.Mecozzi and J.Mørk, "Saturation effects in nondegenerate four-wave mixing between short optical pulses in semiconductor laser amplifiers," *IEEE J.Select. Topics Quantum Electron.*, Vol.3, pp.1190-1207, 1997.
- [10] M.Tang and K.A.Shore, "Strong picosecond optical pulse propagation in semiconductor optical amplifiers at transparency," *IEEE J.Quantum Electron.*, Vol.34, pp.1263-1269, 1998.
- [11] G.F.Agrawal and N.A.Olsson, "Self-phase modulation and spectral broadening of optical pulses in semiconductor laser amplifiers," *IEEE J.Quantum Electron.*, Vol.25, pp.2297-2306, 1989.
- [12] K.Obermann, S.Kindt, D.Breuer, and K.Petermann, "Performance analysis of wavelength converters based on cross-gain modulation in semiconductor-optical amplifiers," *IEEE J.Lightwave Technol.*, Vol.16, pp.78-85, 1998.
- [13] M.Shtaif, R.Nagar, and G.Eisenstein, "Four-wave mixing among short optical pulses in semiconductor optical amplifiers," *IEEE Photon.Techol.Lett.*, Vol.7, pp.1001-1003, 1995.
- [14] J.Inoue and H.Kawaguchi, "Highly nondegenerate four-wave mixing among subpicosecond optical pulses in a semiconductor optical amplifier," *IEEE Photon.Techol.Lett.*, Vol.10, pp.349-351, 1998.
- [15] A.Uskov, J.Mørk, and J.Mark, "Wave mixing in semiconductor laser amplifiers due to carrier heating and spectral-hole burning," *IEEE J.Quantum Electron.*, Vol.30, pp.1769-1781, 1994.

# Analysis of Terahertz Optical Asymmetric Demultiplexers Subject to Picosecond Control and Signal Optical Pulses

J.M.Tang, K.A.Shore

**Abstract**—A numerical treatment is undertaken to investigate the operating characteristics of TOAD devices subject to frequency detuned signal and control pulses. In comparison with positive detuning, it is shown that negative detuning can greatly enhance the output power in the switched region causing a lower threshold energy, and can decrease the width of the switching window. The results suggests that negative frequency detuning should be adopted for separating pulses by wavelength. This is consistent with available experimental results.

**Keywords**—Terahertz optical asymmetric demultiplexer, Semiconductor optical Amplifiers, Gain saturation, Nonlinear gain compression.

## I. INTRODUCTION

THE optical switch known as the Terahertz Optical Asymmetric Demultiplexers (TOADs) is currently attracting a high degree of interest because of several key developments and new applications in the field of optical data communication and optical parallel data processing [1-2]. The TOAD device is composed of an optical loop mirror, a Semiconductor Optical Amplifier (SOA) placed asymmetrically and an intraloop coupler. A signal pulse enters the loop through port(A) of a coupler and is split into two pulses of equal amplitude and identical phase. These pulses then counter propagate round the loop, and arrive at the SOA at slightly different times. A control pulse is utilized to change the refractive index of the SOA. If an appropriately timed control pulse is used, so that one signal pulse experiences a refractive index difference altered by the control pulse relative to its counter propagating complement, a large phase difference will be induced between the two signal pulses. The two signal pulses will destructively combine at port(A) of the coupler, this results in the majority of the power emerging from the switched port(B). Recently, several theoretical analyses of the operating characteristics of TOADs have been undertaken by taking into account both gain saturation and nonlinear gain compression [4-5]. However, the available analyses were performed for the case of pulses having the same centre frequency. In some experiments, control and signal pulses with different cen-

tre frequency have also been employed [6]. In this paper, the influence of frequency detuning between the signal and control pulses on the operating characteristics of TOAD devices will be examined.

## II. THEORETICAL ANALYSIS

By taking into account carrier heating, spectral hole-burning, two-photon absorption (TPA) and ultrafast nonlinear refraction (UNR), a model has been obtained, which is successful in describing propagation of strong picosecond optical pulses through a SOA in the time and frequency domain [7]. However, there are three trains of optical pulses in a TOAD device: control pulses and counter clockwise signal pulses copropagate, and clockwise signal pulses propagate in the opposite direction. First we deal with the control and the counter clockwise signal pulses. The relation between the counter clockwise and clockwise signal pulses will be discussed later.

We decompose the total counter clockwise electric field into components corresponding to the control pulses at frequency  $\omega_0$ , and the signal pulses at frequency  $\omega_1$

$$A(z, t) = A_0(z, t) + A_1(z, t)e^{-i\Omega t} \quad (1)$$

with

$$\Omega = \omega_1 - \omega_0 \quad (2)$$

where  $A_0(z, t)$  and  $A_1(z, t)$  are the slowly varying envelopes of the control and the signal pulses respectively.  $\Omega$  is the frequency detuning between the signal and control pulses. For typical lengths of the SOA, the relative group delay between the control and signal pulses is much smaller than the picosecond pulse width [8]. Thus we may neglect the group-velocity mismatch. We also shall assume the envelopes of the control and signal pulses to be slowly varying in comparison with  $e^{-i\Omega t}$ . This approximation is consistent with the assumption that the spectra of control and signal can be separated. This leads to different small signal gains for the control and signal pulses [9].

Considering a practical TOAD device, in which the control pulse energy is much larger than that of the signal pulse,

$$|A_0(z, t)|^2 \gg |A_1(z, t)|^2 \quad (3)$$

and inserting the decomposition Eq.(1) into the previous

This work was supported by the EPSRC under Grant GR/L03262, and J.M.Tang is supported by the Professor Wynn Humphrey Davies Scholarship and the School of Electronic Engineering and Computer Systems, University of Wales, Bangor, UK.

The authors are with the University of Wales, Bangor, School of Electronic Engineering and Computer Systems, Bangor, LL57 1UT, U.K. E-mail: alan@sees.bangor.ac.uk

model [7], we have

$$\begin{aligned} \frac{\partial A_j}{\partial z} &= \frac{1}{2} \frac{G_j - \epsilon_2 P_0^2}{1 + \epsilon_1 P_0} A_j - \frac{i}{2} [\alpha_N G_j - \alpha_T \frac{\epsilon_1 G_j P_0 + \epsilon_2 P_0^2}{1 + \epsilon_1 P_0}] \\ &\quad \times A_j - (\Gamma_2 \beta_2 + i \Gamma'_2 \frac{\omega_0}{c} n_2) \frac{1}{\sigma} A_j \sum_j P_j - \frac{1}{2} \alpha_{int} A_j \\ &\quad - \frac{1}{2} \eta_{jj'} P_{j'} A_j \quad (j \neq j') \end{aligned} \quad (4)$$

$$\frac{\partial G_j}{\partial t} = \frac{G_{sj} - G_j}{\tau_s} - \frac{1}{E_{satj}} \frac{G_0 - \epsilon_2 P_0^2}{1 + \epsilon_1 P_0} P_0 + \Gamma_2 \beta'_{2j} P_0^2 \quad (5)$$

where  $j, j' = 0, 1$ . The terms in Eqs.(4) and (5) with subscript 0 or 1 correspond to control or signal pulses.  $t$  denotes the local time in the moving frame with the group-velocity  $v_g$ .  $\epsilon_1$  is the nonlinear gain compression factor due to carrier heating and spectral holeburning [7];  $\epsilon_2$  is the nonlinear gain compression factor due to TPA [7].  $\epsilon_1, \epsilon_2$  are in units of  $W^{-1}$  and  $m^{-1}W^{-2}$  respectively.  $\beta_2$  is the TPA coefficient;  $n_2$  is the nonlinear refractive index coefficient;  $\Gamma_2$  and  $\Gamma'_2$  are the confinement factors associated with the TPA and the UNR respectively;  $\alpha_N$  and  $\alpha_T$  are the traditional and temperature linewidth enhancement factors; The definitions of the small signal gain  $G_{sj}$  and gain saturation energy  $E_{satj}$  have their general forms [7]. Other parameters appearing in the above equations are the group-velocity  $v_g$ , the central frequency of the pulse  $\omega_0$ , the waveguide loss  $\alpha_{int}$ , the carrier lifetime  $\tau_s$ , the differential gain  $a$  and the light velocity in vacuum  $c$ .

The last term in Eq.(4) is added to account for nonlinear interactions between pulses through a temporal grating formed by the control and the signal pulses. The grating scatters the control (signal) to the control (signal) through the terms proportional to  $P_0 A_j, j = 1, 2$ . Since attention is focused on the optical frequencies associated with the signal and control pulses, it is clear that the conjugate optical pulses generated through Four-Wave Mixing (FWM) does not affect the operating characteristics of TOAD. The coupling coefficient  $\eta_{jj'} (j \neq j', j, j' = 0, 1)$  can be decomposed into contributions from carrier depletion (CD), carrier heating (CH), spectral holeburning (SHB) [9]. The real part of  $\eta_{jj'}$  is proportional to the corresponding gain change and the imaginary part is proportional to the corresponding index change. The expressions for the various terms are

$$\eta_{jj'} = \eta_{jj'}^{CD} + \eta_{jj'}^{CH} + \eta_{jj'}^{SHB} \quad (6)$$

with

$$\begin{aligned} \eta_{jj'}^{CD} &= \frac{g_{sj} a_j \tau_s}{\hbar \omega_j \sigma} (1 - i \alpha_N) \frac{1}{-i(\omega_j - \omega_{j'}) \tau_s + 1} \\ &\quad \times \frac{1}{-i(\omega_j - \omega_{j'}) \tau_1 + 1} \end{aligned} \quad (7)$$

$$\begin{aligned} \eta_{jj'}^{CH} &= \epsilon_T g_{sj} (1 - i \alpha_T) \frac{1}{-i(\omega_j - \omega_{j'}) \tau_h + 1} \\ &\quad \times \frac{1}{-i(\omega_j - \omega_{j'}) \tau_1 + 1} \end{aligned} \quad (8)$$

$$\eta_{jj'}^{SHB} = \epsilon_{SHB} g_{sj} (1 - i \alpha_{SHB}) \frac{1}{-i(\omega_j - \omega_{j'}) \tau_1 + 1} \quad (9)$$

where

$$g_{sj} = \frac{G_{sj}}{1 + \frac{P_{sj}}{P_{sj}}}$$

$P_{aj}$  is the average power of the optical beam  $j$  in unit of W.  $P_{sj} = \hbar \omega_j \sigma / (a_j \tau_s)$  is the saturation power of the material relative to wave  $j$ .  $\epsilon_T$  and  $\epsilon_{SHB}$  are the nonlinear gain compression factors due to the carrier heating and spectral holeburning, and satisfy

$$\epsilon_1 = \epsilon_T + \epsilon_{SHB} \quad (10)$$

$\alpha_{SHB}$  is the linewidth enhancement factor corresponding to spectral holeburning.  $\tau_1$  and  $\tau_h$  are the carrier-carrier scattering time and temperature relaxation time respectively. It is also noted that in deriving Eq.(7) the carrier depletion caused by the signal pulses is neglected since the signal pulse energy is extremely small. Therefore, the control pulses are dominant in determining the propagation of signal pulses in the active region of the SOA.

The relation between  $G_{s0}$  and  $G_{s1}$  are determined by the gain model presented in [10]. The properties of the strong control and weak signal pulses can thus be obtained by numerically solving the above basic equations. The dynamic response of the SOA to the control pulses can be expressed by the changes of weak signal pulses [11]

$$T(\tau) = \frac{\int_{-\infty}^{+\infty} |A_1(L, t)|^2 dt}{\int_{-\infty}^{+\infty} |A_1(0, t)|^2 dt} \quad (11)$$

$$\Phi(\tau) = \frac{\int_{-\infty}^{+\infty} \phi_1(L, t) |A_1(L, t)|^2 dt}{\int_{-\infty}^{+\infty} |A_1(L, t)|^2 dt} \quad (12)$$

where  $\tau$  is the time delay between the signal and control pulses.  $L$  is the length of the SOA.  $T(\tau)$  and  $\Phi(\tau)$  relate to the changes of the gain and refractive index of the SOA.

It is assumed that the two weak signal pulses only probe the dynamic changes of the SOA caused by the intense control pulses, and that the control pulse does not induce nonlinearities in other parts of the loop. The gain and refractive index changes sampled by the clockwise signal pulses are thus written as [4-6]

$$T_c(t) = T(t + T_{off}) \quad (13)$$

$$\Phi_c(t) = \Phi(t + T_{off}) \quad (14)$$

where  $T_{off}$  is the time delay between the clockwise and counter clockwise signal pulses, which is determined by the fixed offset  $\Delta x$  from the midpoint of the loop.

Having traversed the loop, the clockwise and counter-clockwise signal pulses are superimposed at the output coupler of the device. The output pulse profiles from ports (A and B) of a TOAD device are described in [4-5]. The operating characteristics of the TOAD device can be obtained by solving the above equations numerically.

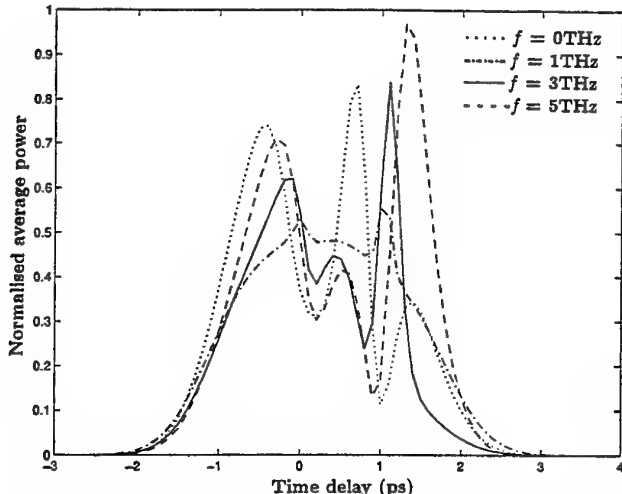


Fig. 1. Normalised average output power from switched port (B) for different positive frequency detunings. Dotted, dash-dotted, solid and dashed lines are for 0THz, 1THz, 3THz and 5THz frequency detunings respectively.

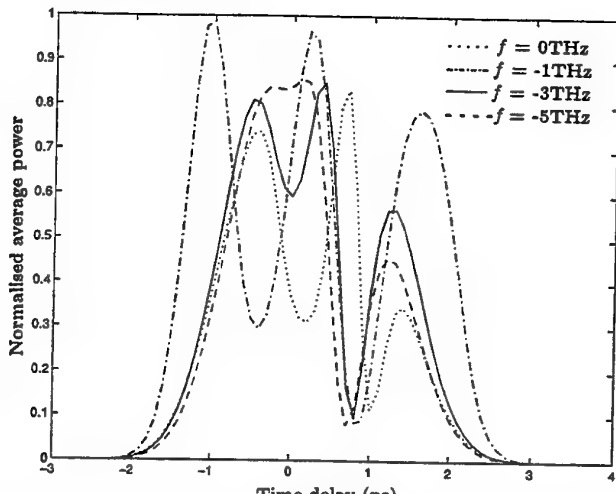


Fig. 2. Normalised average output power from switched port (B) for different negative frequency detunings. Dotted, dash-dotted, solid and dashed lines are for 0THz, -1THz, -3THz and -5THz frequency detunings respectively.

### III. RESULTS

The parameters used in the calculations are representative for InGaAsP semiconductor material operating at a wavelength of approximately  $1.55\mu\text{m}$ , and the values are from Refs.9,11. For simplicity, the central frequency of the control pulses is assumed to be located at the peak of gain spectrum of the SOA.

In the following, calculations are performed for the case where the time delay between the control and counter clockwise signal pulse is varied, and the time delay between the clockwise and counter clockwise signal pulses is fixed. The fixed offset time  $T_{off}$  is determined by the offset distance  $\Delta x$  from the midpoint of the loop, satisfying  $T_{off} = 2\Delta x/v$ ,  $v$  is the velocity of the pulse in the fibre.

For positive ( $\Omega > 0$ ) and negative ( $\Omega < 0$ ) frequency detuning cases, the switching behaviours of TOADs are plotted in Fig.1 and Fig.2, respectively, in which the output power in the switched region for  $\Omega = 0$  is also given. Here the abscissa represents the time delay between the counter clockwise signal pulse and the control pulse, and the ordinate is the average output power from the switched port(B) normalised to the total output power from the device. In obtaining those figures, 1ps Gaussian control and signal pulses with peak powers of 0.5W and  $1 \times 10^{-3}\text{W}$  are employed, and the offset time is fixed at 1ps. In Figs.1 and 2, the switching windows show oscillating output power structures with width longer than 1ps, which is in agreement with the previously published analysis of TOADs [5]. On the other hand, significantly different switching behaviours are demonstrated in those figures for different frequency detunings. For  $\Omega = 1\text{THz}$ , the peaks of oscillating structures are notably damped, resulting in considerably smaller output power than that in the case of  $\Omega = 0$ , while for  $\Omega = -1\text{THz}$ , the oscillating peaks are notably enhanced, producing larger output power in the switched region with

a larger window width, compared with the case of  $\Omega = 0$ . Although the output powers in the switched region in Fig.1 are raised by increasing the value of  $\Omega$ , the values are smaller than the case of  $\Omega = 0$  except for a sharply enhanced peak in the trailing edge of the window. Furthermore, in Fig.1 the widths of the switching windows are considerably broadened for larger  $\Omega$ . However, for the negative frequency detuning cases, as shown in Fig.2, the output power remains larger than the case of  $\Omega = 0$  despite that its value is decreased with the increased  $|\Omega|$ . In particular, the width of the switching window in this case is remarkably reduced by an increase in  $|\Omega|$ . Finally, in Fig.1 larger frequency detuning brings about considerably reduced output power around the centre area of the switching window, causing peaks sharply changed in both leading and trailing window edges, while in Fig.2 larger frequency detuning produces relatively flatter output window profiles.

The above switching behaviours can be explained by using a similar procedure as performed in previous work [4-5]. It should be specially noted that for frequency detuning  $|\Omega| < \sim 1.5\text{THz}$ , the switching characteristics also strongly depend on the interactions between the control and signal pulses, which, however, have been neglected in all previous work.

Using the same parameter values, now taking the frequency detuning to be fixed at  $|\Omega| = 3\text{THz}$ , in Fig.3, the normalised average output powers are plotted as a function of the time delay between the counter clockwise signal and control pulses for different offset times. For larger offset times, nearly square switching windows are observed. Calculations show that the narrow sharp peak in the right hand side can be neglected when the offset time is longer than  $\sim 20\text{ps}$ . Another salient feature is that the output power for the negative frequency detuning case is signifi-

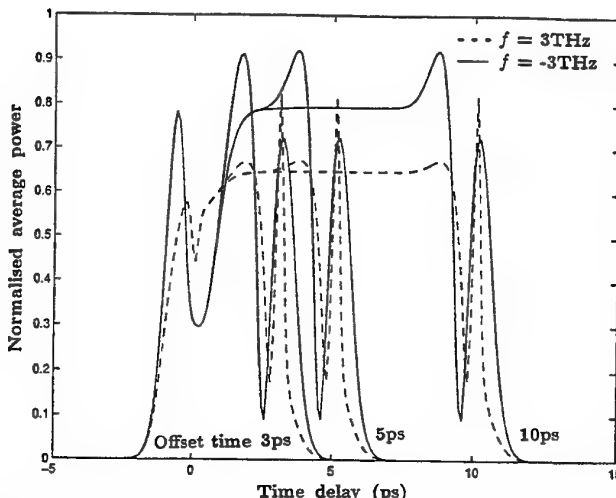


Fig. 3. Normalised average output power from switched port (B) for different fixed offset times and different frequency detunings. The other parameters are the same as Fig.2. Solid (dashed) lines are for -3THz (3THz) frequency detunings respectively.

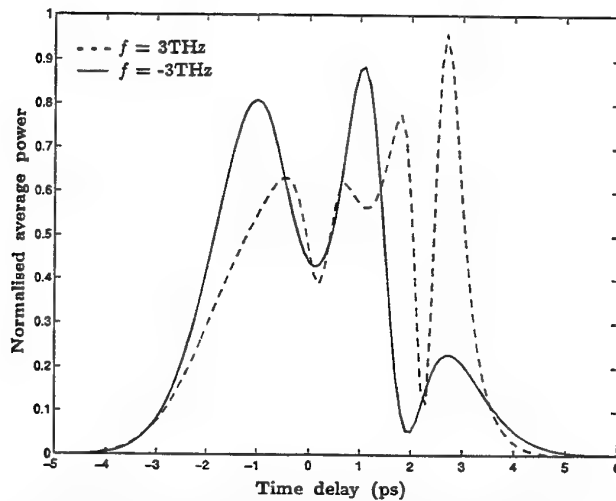


Fig. 4. Normalised average output power from switched port (B) for different frequency detunings between signal and control pulses. Solid (dashed) lines are for -3THz (3THz) frequency detunings respectively.

cantly increased in comparison with the positive case. This indicates that much smaller threshold energy of the device can be obtained by using negative frequency detuning.

Keeping the peak power of 2ps control pulse to be 0.5W, for different frequency detuning  $\Omega = \pm 3\text{THz}$ , the output powers in the switched region are shown in Fig.4, where the offset time is set equal to the control pulse width. In comparison with positive frequency detuning, Fig.4 shows an enhanced output power in the main switched region with relatively reduced window width for the negative detuning case. This results from an enhanced response difference of the SOA between different detuning cases by a relatively stronger control pulse energy.

#### IV. CONCLUSIONS

A numerical treatment has been undertaken to investigate the operating characteristics of TOAD devices for different frequency detunings between the signal and control pulses. In comparison with positive detuning, it is shown that negative detuning can greatly enhance the output power in the switched region causing a lower threshold energy, and can decrease the width of the switching window. From a practical viewpoint, an increase in the operating rate and moves towards of integration of the device will benefit from obtaining a shorter window width with lower threshold energy of TOAD device. Therefore, the results suggests that negative frequency detuning should be adopted for separating pulses by wavelength. This is consistent with available experimental results [6].

#### REFERENCES

- [1] A.D.Ellis, D.A.O.Davies, A.Kelly, and W.A.Pender, "Data driven operation of semiconductor amplifier loop mirror at 40 Gbit/s," *Electron. Lett.*, Vol.31, pp.1245-1247, 1995.
- [2] A.J.Poustie, K.J.Blow, and R.J.Manning, "All-optical regenerative memory for long term data storage," *Opt. Commun.*, Vol.140, pp.184-186, 1997.
- [3] J.F.Sokoloff, P.R.Pruclal, I.Glesk, and M.Kane, "A terahertz optical asymmetric demultiplexer (TOAD)," *IEEE Photon. Technol. Lett.*, Vol.5, pp.787-790, 1993.
- [4] J.M.Tang, P.S.Spencer, and K.A.Shore, "Analysis of the operating characteristic of TOADs utilising gain saturation and nonlinear gain in semiconductor optical amplifiers," *IEE Proc. Optoelectronics* Vol.145, pp.83-87, 1998.
- [5] J.M.Tang, P.S.Spencer, and K.A.Shore, "Influence of fast gain depletion on the dynamic response of TOADs," *IEEE J.Lightwave Technol.*, Vol.16, pp.86-91, 1998.
- [6] R.J.Manning, A.D.Ellis, A.J.Poustie, and K.J.Blow, "Semiconductor laser amplifiers for ultrafast all-optical signal processing," *J.Opt.Soc.Am.B*, Vol.14, pp.3204-3216, 1997.
- [7] J.M.Tang and K.A.Shore, "Strong picosecond optical pulse propagation in semiconductor optical amplifiers at transparency," *IEEE J.Quantum Electron.*, Vol.34, pp.1263-1269, 1998.
- [8] M.Y.Hong, Y.H.Chang, A.Dienes, J.P.Heritage, P.J.Delfyett, S.Djalili, and F.G.Patterson, "Femtosecond self- and cross-phase modulation in semiconductor laser amplifiers," *IEEE J. Selected Topics in Quantum Electron.*, Vol.2, pp.523-539, 1996.
- [9] J.Mørk and A.Mecozzi, "Theory of the ultrafast optical response of active semiconductor waveguide," *J.Opt.Soc.Am.B*, Vol.13, pp.1803-1816, 1996.
- [10] K.Obermann, S. Kindt, D.Breuer, and K.Petermann, "Performance analysis of wavelength converters based on cross-gain modulation in semiconductor-optical amplifiers," *IEEE J. Lightwave Technol.*, Vol.16, pp.78-85, 1998.
- [11] J.Mørk and A.Mecozzi, "Theory of the ultrafast optical response of active semiconductor waveguide," *J.Opt.Soc.Am.B*, Vol.13, pp.1803-1816, 1996.

# A gain switched semiconductor laser pump-probe source

Anthony J. Vickers, Steven B. Alleston, Majid Hassan, Phillippe O. Müller, Didier Erasme

*In this paper we present are latest work on the development of a solid state pump-probe laser. Our initial aim was to develop a system for use in electro-optic sampling but it is clear that there are many sampling techniques that require a pump-probe source. Basic results on the principle of operation will be given as well as a description of the prototype system which has been developed.*

THz, electro-optic sampling, opto-electronics, semiconductor lasers.

## I. INTRODUCTION

As we move into the Tera Era it is important to consider the methods by which one will measure device and circuit responses. Electro-optic sampling of both devices and circuits is now well developed and indeed electro-optic sampling has led directly onto the generation and use of THz beams. Electro-optic sampling and THz spectroscopy requires a short pulse laser source. Most systems operate on a pump/probe sampling method [1-3] and therefore the laser source is required to be split in two. The two separate beams become the pump and probe beams. The pump activates some device or system at a fixed time. The probe beam analyses the response of the system at a variable time delay after the pump. The delay is normally achieved through a mechanically or piezoelectrically driven stage. The net result is that systems are bulky and not readily useful for the future. A few years ago we decided that it would be interesting to investigate the possibility of producing a system based on semiconductor lasers that could provide a complete solid state pump/probe system. We began with a black box approach based on the following diagram.

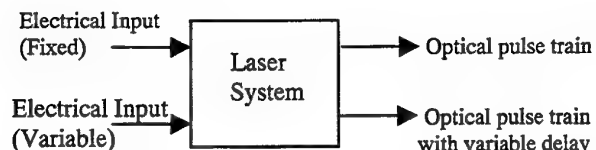


Figure 1: Block Diagram

The authors Vickers, Alleston, and Hassan are associated with the University of Essex, Wivenhoe Park, Colchester, Essex, CO4 3SQ, UK and the authors Müller and Erasme are associated with ENST, 46 Rue Barrault, Paris, Cedex 13, France

Our investigations into a suitable method of achieving the above black box led us to work that had been undertaken on gain switching. When gain switching a laser diode the device is held below threshold with a dc current, and is then excited above by either a short electrical pulse or an RF current. A time lag between the rising edge of the driving signal and the optical pulse is produced. It is known that this is dependent on the level of dc bias below threshold immediately before excitation [4]. This technique of gain switching will in principal work with any semiconductor laser. The movement in time of the laser pulse as the dc bias is altered is accompanied by an alteration in the pulse shape that is not required. In previous work we have shown how it is possible to produce a movement of the pulse without altering the pulse shape by manipulation of the amplitudes of both the dc and the rf components [5]. In this work we show further modeling results and our development of a prototype system.

## II. RESULTS

Our previous work [5] presented the background theoretical model for gain switching and we showed how it is possible to move a pulse whilst maintaining the shape of the pulse. This in essence is the requirement of a solid state pump-probe system. We verified that this was possible using a 1.5 $\mu$ m DFB semiconductor laser. The experimental results are reproduced below.

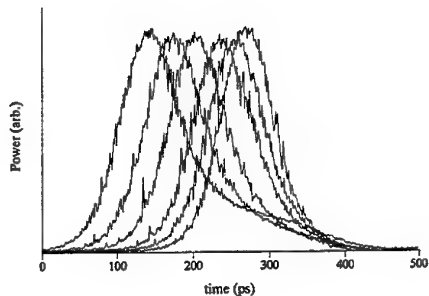


Figure 2: Simulation of the delay

These results were obtained by manipulating the amplitudes of the dc and rf (1GHz) components of the total current applied to the semiconductor laser. When obtained the above results we had no algorithm to work with which would tell us how to manipulate the dc and rf components

in order to achieve a given delay without altering the pulse shape. We have subsequently used our theoretical model to attempt to derive the algorithm. The model uses the same set of rate equations as in our previous work, which are;

$$\frac{dn}{dt} = \frac{i_{d.c.} + i_{r.f.} \sin(2\pi ft)}{eV} - g(n - n_t)s - \frac{n}{\tau_n}$$

$$\frac{ds}{dt} = g\Gamma(n - n_t)s + \Gamma\beta \frac{n}{\tau_n} - \frac{s}{\tau_p}$$

Which relates the electron density,  $n$ , to the photon density,  $s$ . The other symbols represent the dc and rf current components, the modulation frequency,  $f$ , the gain coefficient  $g$ , the electron density at transparency,  $n_t$ , the electron and photon lifetimes,  $\tau_n$  and  $\tau_p$ , the fraction of spontaneous emission coupled into the lasing mode,  $\beta$  and the mode confinement factor,  $\Gamma$ . We have solved these equations for a fixed set of all the variables apart from the dc and rf amplitudes. These two parameters are varied systematically in order to determine a set of results that produce gain switched pulses with the same pulse height and half width. Below we plot the results.

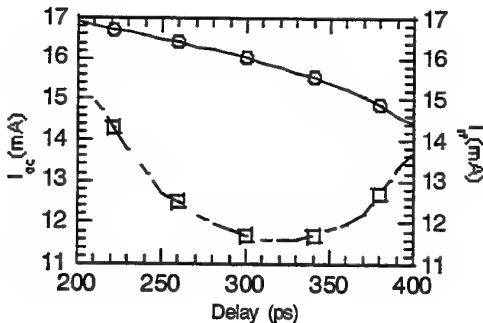


Figure 3: The delay as a function of dc (left scale)/rf(right scale) current components.

This figure predicts the algorithm to produce a gain switched set of pulses that can be delayed by around 200ps. The width of the pulses is determined by the choice of the other parameters. In this case we have chosen typical parameters and our pulse widths are 50ps. The shape of the rf curve in the figure is interesting. As it is roughly parabolic it means that there are a range of rf values for which two dc currents are associated which give different time delays. In other words for a fixed rf amplitude there are two values of dc amplitude which will produce pulses of the same shape but delayed in time with respect to each other.

As a consequence of our initial experimental work and the modeling of the algorithm we have, in collaboration with Cambridge Optical Supplies, developed a prototype system based on two dfb lasers donated by British Telecom (BT). The prototype is shown below.

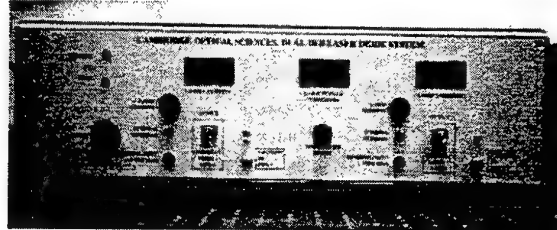


Figure 4: The prototype system

Two dfb lasers are mounted into high frequency headers capable of operating up to 2GHz. The dc is supplied from either an internal or external supply. The rf is supplied externally through SMA connectors. The two lasers are driven separately. The two lasers are mounted on Peltier Coolers and there is a control to adjust the operational temperature of the two lasers. We have undertaken initial trials of the prototype and below we show a trace from a HP54750A oscilloscope showing the output from the two lasers. The outputs from the two lasers are coupled through fibres to two separate New Focus Model 1014 45GHz photodetectors into a two channel HP54752A 50GHz oscilloscope plug-in.

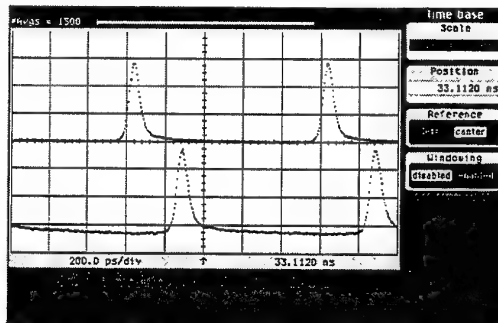


Figure 5: Typical output from the prototype system.

The figure shows the two pulses which are delayed with reference to each other even though the two rf supplies (HP8648C signal generator operating at 1GHz) are phase locked to each other. The pulse widths are around 50ps. This is limited by the available power from the rf supplies. The incorporation of an rf amplifier stage will improve this as will the introduction of a fibre compression stage.

### III. CONCLUSION

In conclusion we have determined the algorithm for producing a delay in a train of gain switched optical pulses without altering the pulse shape. We have built and made simple tests on a proto-type system. All indications are that the prototype is behaving as expected although further more

exhaustive tests are required. We will now proceed to implement rf amplification stages as well as adding a fibre compression stage to the optical output of both lasers.

#### IV. ACKNOWLEDGMENT

Three of us (Vickers and Hassan, and Alleston) would like to thank the EPSRC for financial support. We would also like to thank Cambridge Optical Supplies for the development of the prototype system and BT for the donation of the semiconductor lasers used in the prototype.

#### V. REFERENCES

- [1] D.G. Mclean, M.G. Roe, A.I. D'Souza, and P.E. Wigen, *Appl. Phys. Lett.* **48**(1986)992
- [2] J.A. Valdmanis and G.A. Mourou, *IEEE J. Quantum electron. QE-22*(1996)69
- [3] T.F. Carruthers and J.F. Weller, *Appl. Phys. Lett.* **48**(1986)460
- [4] P.M. Downey, J.E. Bowers, R.S. Tucker, and E. Agyekum, *IEEE J. Quantum Electron.. QE-23*(1987)1039
- [5] A.J. Vickers, S. Alleston, R. Gupta, P.O. Muller, D. Erasme, *Opt. And Quant. Electron* **28**(1996)983-989

# THz Time-Domain Spectroscopy of Electro-Optic Crystals

M. Schall, H. Helm, and S. R. Keiding

**Abstract**—We investigate the optical properties of the nonlinear crystals  $\text{LiNbO}_3$ ,  $\text{LiTaO}_3$ ,  $\text{ZnTe}$  and  $\text{CdTe}$  in the far infrared regime. Using terahertz time-domain spectroscopy (THz-TDS) we have measured the complex frequency response up to 3 THz ( $100 \text{ cm}^{-1}$ ) for these electro-optic crystals with high accuracy ( $<0.5\%$ ). The data are interpreted with a simple Lorentzian oscillator model. Additional absorption features have been found.

**Keywords**— THz-TDS, electro-optic crystal, dielectric function, TO phonon, II-VI compounds

## I. INTRODUCTION

Electro-optic (eo) crystals turned out as suitable candidates for the detection and generation of subpicosecond terahertz (THz) pulses[1]-[3]. Especially detecting high power THz pulses the eo technique shows the best performance and enables 2-dim THz sampling to obtain images[4].

Therefore the knowledge of the optical properties of the electro-optic material in the far infrared (FIR) regime is a prerequisite for an optimal THz-system design[5].

We report an experimental investigation of the dielectric properties of the eo crystals  $\text{LiNbO}_3$ ,  $\text{LiTaO}_3$ ,  $\text{ZnTe}$  and  $\text{CdTe}$  using terahertz time-domain spectroscopy (THz-TDS) in the frequency range between 100 GHz and 3 THz at room temperature[6].

## II. EXPERIMENTAL SETUP

The schematic setup of the THz time-domain spectrometer is illustrated in Fig. 1. Laser pulses of 25 fs duration supplied from a Titan:Sapphire laser at 80 MHz repetition rate are divided into a gate- and a pump beam. The latter is focussed onto an externally biased GaAs chip generating subpicosecond THz pulses[7]. The gate beam is focussed onto a SOS photoconducting dipole antenna, which detects the temporal electric field of the THz pulse[8]. The system is able to generate and to detect FIR radiation in the frequency range between 0.1 THz and 4.5 THz. Horizontally polarized THz radiation is obtained by using a wire grid polarizer (WGP).

The investigated dielectric crystals  $\text{LiNbO}_3$  and  $\text{LiTaO}_3$  are b-cut, i.e. the ordinary and extraordinary axis are lo-

M. Schall is a PhD-student in the Department of Molecular and Optical Physics at the Albert-Ludwigs-Universität, Hermann-Herderstr. 3, D-79104 Freiburg, Germany, FAX: \*\*49-761-203-5955, e-mail: Michael.Schall@physik.uni-freiburg.de, <http://frhewww.physik.uni-freiburg.de>

H. Helm is professor at the Department of Molecular and Optical Physics at the University in Freiburg, Germany, e-mail: Hanspeter.Helm@physik.uni-freiburg.de

S. R. Keiding is a professor in the Department of Chemistry at the University of Aarhus, Langelandsgade 140, 8000 Aarhus C, Denmark, FAX: \*\*45-8619-6199, e-mail: keiding@kemi.aau.dk, <http://kemi.aau.dk/research/femtolab>

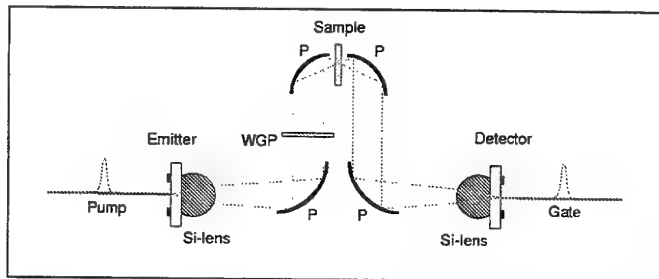


Fig. 1. Experimental setup of the THz spectrometer. (P) paraboloidal mirror, (WGP) wire grid polarizer.

cated in the cutting plane. By aligning the principal axis parallel to the electric field of the THz radiation we measure alternatively the optical properties along both crystal axis.

The II-VI compounds  $\text{ZnTe}$  and  $\text{CdTe}$  have a  $\langle 110 \rangle$  orientation.

The reference pulse and the sample pulse propagated through a 2 mm thick  $\text{ZnTe}$  crystal are presented in Fig. 2(A). The index of refraction and the absorption coefficient of the sample induce a time delay and a change of amplitude in the propagated pulse. The corresponding spectral Fourier components of the two pulses,  $E_{\text{ref}}(\omega)$  and  $E_{\text{sam}}(\omega)$ , are shown in Fig. 2(B).

By taking the ratio of the two complex fourier spectra we determine the frequency dependent index of refraction  $n_{\text{sam}}$ , and the absorption coefficient  $\alpha$  simultaneously:

$$\frac{E_{\text{sam}}(\omega)}{E_{\text{ref}}(\omega)} \propto \exp\left\{i\frac{\omega d}{c}(n_{\text{sam}} - 1)\right\} \exp\{-\alpha d\}. \quad (1)$$

(c: speed of light, d: thickness of the sample)

The accuracy of the measurement is mainly determined by the thickness uncertainty of the samples and is estimated to  $\pm 0.002$  in the absolute value of the index of refraction.

## III. RESULTS AND DISCUSSION

Experimental results for the index of refraction and the absorption coefficient versus the frequency are illustrated in Fig. 3 for  $\text{LiNbO}_3$  and  $\text{ZnTe}$ . In contrast to the isotropic semiconductor  $\text{ZnTe}$ , the dielectric crystal  $\text{LiNbO}_3$  shows a large birefringence in the THz range ( $\Delta n > 1.5$ ).

The simplest approach to represent the results is the Lorentzian single oscillator model. Due to the lowest transverse optical (TO) phonon resonance both the index of refraction and absorption are increasing in frequency. Out of

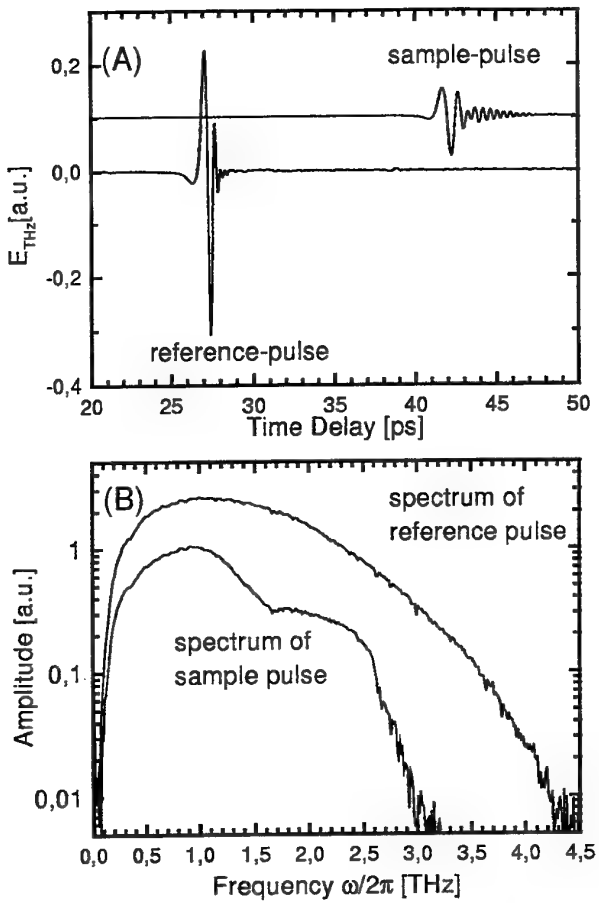


Fig. 2. (A) Reference pulse and sample pulse propagated through a 2 mm thick ZnTe crystal. The sample pulse has an offset for better display. (B) Corresponding Fourier spectra of the two pulses.

the fit we extract the dielectric parameters like the static dielectric constant, the TO resonance frequency and the resonance linewidth. The fits are displayed as solid lines in Fig. 3.

In comparison with the existing literature[9] we found deviations from the ideal Lorentzian absorption profile, which are hints for phonon difference processes occurring below the first lattice resonance[10]. In particular in ZnTe a clear resonance feature at 1.65 THz ( $55 \text{ cm}^{-1}$ ) has been observed.

#### IV. CONCLUSION

We have investigated the dielectric properties of the electro-optic crystals  $\text{LiNbO}_3$ ,  $\text{LiTaO}_3$ , ZnTe and CdTe with the use of THz Time-Domain Spectroscopy. We measured with a high accuracy the frequency dependent index of refraction and absorption coefficient in the far infrared region from 0.1 to 3 THz. The data was fitted by the single oscillator Lorentzian model to extract the dielectric parameters of the lowest TO phonon resonance. We found deviation from the ideal Lorentzian absorption profile, especially

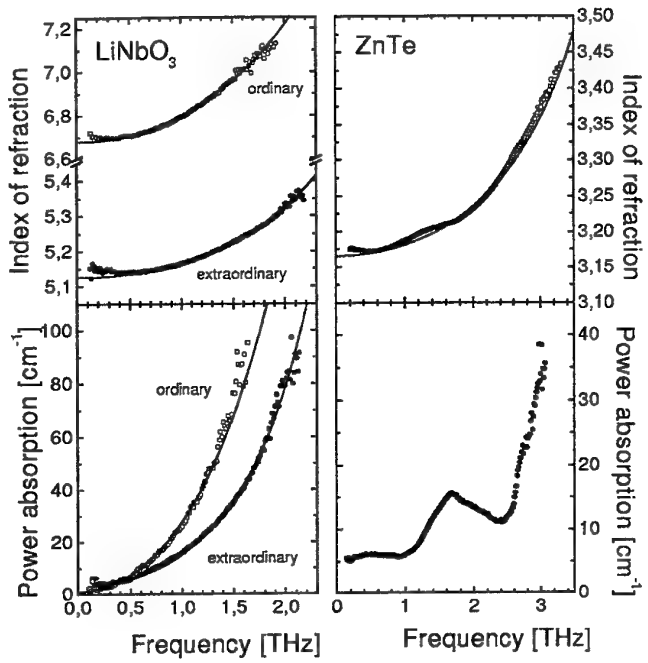


Fig. 3. Index of refraction and absorption coefficient of  $\text{LiNbO}_3$  and ZnTe in the FIR regime obtained by THz-TDS. The Lorentzian fits are represented as solid lines.

in the II-VI compounds, which are most likely higher order phonon processes.

#### REFERENCES

- [1] Q. Wu, and X.-C. Zhang, *Ultrafast electro-optic field sensors*, Appl. Phys. Lett. **68**, (1996)
- [2] P. U. Jepsen, C. Winnewisser, M. Schall, V. Schyja, S. R. Keiding, and H. Helm, *Detection of THz pulses by phase retardation in lithium tantalate*, Phys. Rev. E **53**, (1996)
- [3] A. Nahata, A. S. Weling, and T. F. Heinz, *A wideband coherent terahertz spectroscopy system using optical rectification and electro-optic sampling*, Appl. Phys. Lett. **69**, 2321 (1996)
- [4] Q. Wu, T. D. Hewitt, and X.-C. Zhang, *Two-dimensional electro-optic imaging of THz-beams*, Appl. Phys. Lett. **69**, 1026 (1996)
- [5] C. Winnewisser, P. U. Jepsen, M. Schall, V. Schyja, and H. Helm, *Electro-optic detection of THz radiation in  $\text{LiTaO}_3$ ,  $\text{LiNbO}_3$ , and ZnTe*, Appl. Phys. Lett., **70**, 3069-3071 (1997)
- [6] M. Schall, H. Helm, and S. R. Keiding, *to be published*
- [7] N. Katzenellenbogen, and D. Grischkowsky, *Efficient generation of 380 fs pulses of THz radiation by ultrafast laser pulse excitation of a biased metal-semiconductor interface*, Appl. Phys. Lett. **58**, 222 (1991)
- [8] D. Grischkowsky, S. Keiding, M. van Exter, and C. Fattinger, *Far-infrared time-domain spectroscopy with terahertz beams of dielectrics and semiconductors*, J.Opt.Soc.Am. B **7**, 2006 (1990)
- [9] A. S. Barker Jr., and R. Loudon, *Dielectric Properties and Optical Phonons in  $\text{LiNbO}_3$* , Phys. Rev. **158**, 433 (1967)
- [10] O. M. Stafsudd, F. A. Haak, and K. Radisavljević, *Far-infrared spectrum of Cadmium Telluride*, J.Opt.Soc.Am. **57**, 1475 (1967)

# Frequency-Selective Surfaces analyzed by THz-Time-Domain Spectroscopy

C. Winnewisser, F. Lewen, J. Weinzierl, and H. Helm

**Abstract**—The transmission and phase shift characteristics of dichroic high-pass and cross-shaped grid bandpass filters were measured in the region from 0.1 to 1.5 THz with an electro-optic (eo) sampling THz-Time-Domain Spectrometer. Good agreement with the applied transmission theories [1], [2] is found. In this spectral region, which is difficult to access by conventional means, the knowledge of the frequency response of these frequency-selective surfaces (FSS) is important for applications in frequency mixing and multiplying experiments [3]. Alternatively, FSS's permit temporal shaping of THz pulses for frequency selective ultrafast experiments in the THz range.

**Keywords**— Frequency-selective surfaces, dichroic filter, high-pass filter, bandpass filter, eo-sampling THz-TDS, temporal THz pulse shaping

## I. INTRODUCTION

Dichroic filters and cross-shaped grid bandpass filters are a subgroup of metal mesh filters or so called periodic frequency-selective surfaces [4], which are widely employed as quasi-optical elements in the spectral region from microwaves to the near infrared. FSS's consist of periodically perforated plates, where the shape and arrangement of the apertures on the plate determine the filter transmission characteristic.

## II. EXPERIMENTAL SETUP

The filter transmission characteristics were measured with the eo-sampling THz-Time-Domain Spectrometer presented in Fig. 1. Pulses from a regenerative Ti:sapphire oscillator (Clark-MXR) are divided by a beam-splitter into a probe- and a pump beam. The latter illuminates a GaAs wafer to generate the THz pulse [5]. The THz pulse detection setup, consisting of an eo-crystal between a pair of crossed polarizers, can be referred to as an ultrafast transverse eo-modulator. The eo-detection exploits the linear dependence of the index of refraction on an external electrical field, known as the Pockels effect.

In our case the electrical field of the THz pulse,  $E_{\text{THz}}$ , modifies the optical properties of the eo-crystal, and the

C. Winnewisser is a PhD-student in the Department of Molecular and Optical Physics (<http://frhewww.physik.uni-freiburg.de>) at the Albert-Ludwigs-Universität, Hermann-Herder-Strasse 3, D-79104 Freiburg, Germany. FAX: \*\*49-761-203-5955, e-mail: Carsten.Winnewisser@physik.uni-freiburg.de

F. Lewen is a Postdoc at the I. Physikalisches Institut (<http://www.ph1.uni-koeln.de>) at the Cologne University, Germany. e-mail: Lewen@ph1.uni-koeln.de

J. Weinzierl is a PhD-student at the Laboratory for High Frequency Technology (<http://www.lhft.e-technik.uni-erlangen.de>) at the Erlangen University, Germany. e-mail: Jochen@lhft.e-technik.uni-erlangen.de

H. Helm is a professor, Department of Molecular and Optical Physics at the Freiburg University, Germany. e-mail: Hanspeter.Helm@physik.uni-freiburg.de

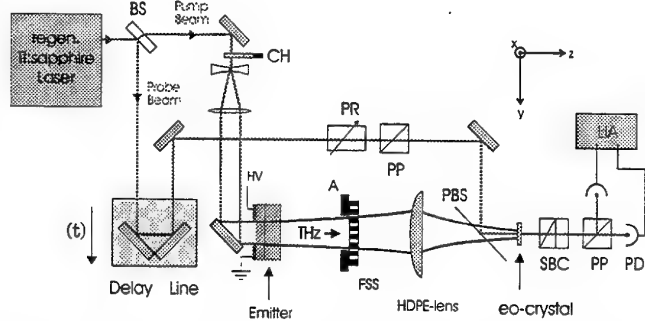


Fig. 1. Experimental setup. BS: beam-splitter; CH: Chopper, chop frequency 130Hz; THz-Emitter: large aperture GaAs chip backed by two GaAs wafers to delay the THz pulse echo [7]; HV: applied high voltage; A: aperture; FSS: frequency-selective surface; PR: polarization rotator; PP: polarizing prisms; PBS: pellicle beam splitter; eo-crystal: ZnTe; SBC: Soleil-Babinet-compensator; PD: balanced photodiodes; LIA: lock-in amplifier.

crystal's index of refraction becomes a linear function of the applied electrical field strength [6]. The THz pulse is recorded with and without the FSS placed in the path of the THz beam.

## III. DICHROIC FILTERS

Our dichroic filters are composed of an equilateral array of hexagonally close packed, circular waveguides, see Fig. 2. The dichroic filters have been scaled down into the submil-

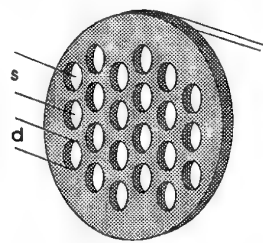


Fig. 2. General design of a dichroic filter.  $s$  represents the spacing between the circular holes,  $d$  is their diameter, and  $l$  is the length of the circular waveguides, which equals the thickness of the plate. The holes are arranged in an hexagonally close packed pattern, which produces a regular, two-dimensional grid structure.

limeter region by the use of a CNC milling machine and they provide a sharp frequency response, which is determined by a specific combination of the plate's geometrical properties: the spacing  $s$  of the circular waveguides, their diameter  $d$ , and their length  $l$ . The general features of these parameters can be summarized as follows [6]: The

cutoff frequency  $\nu_c$  is defined by the hole diameter, which is given for an infinitely long waveguide as  $\nu_c = \frac{1.841c}{\pi d}$ , where  $c$  is the speed of light [8]. The hexagonal hole array of the dichroic filter representing a two-dimensional grating will force electromagnetic (em) waves with frequencies above  $\nu_{\text{diff}} = \frac{2c}{s\sqrt{3}}$  to be diffracted into the first diffraction lobe. The length of the waveguide determines the sharpness of the waveguide and its resonance feature at the peak transmission.

A more detailed description for the transmission of em-waves through a FSS is given by the mode matching theory of Chen [1], which has been successfully applied to different kinds of FSS's in the frequency range between  $40 \text{ cm}^{-1}$  and  $350 \text{ cm}^{-1}$  [9], [10].

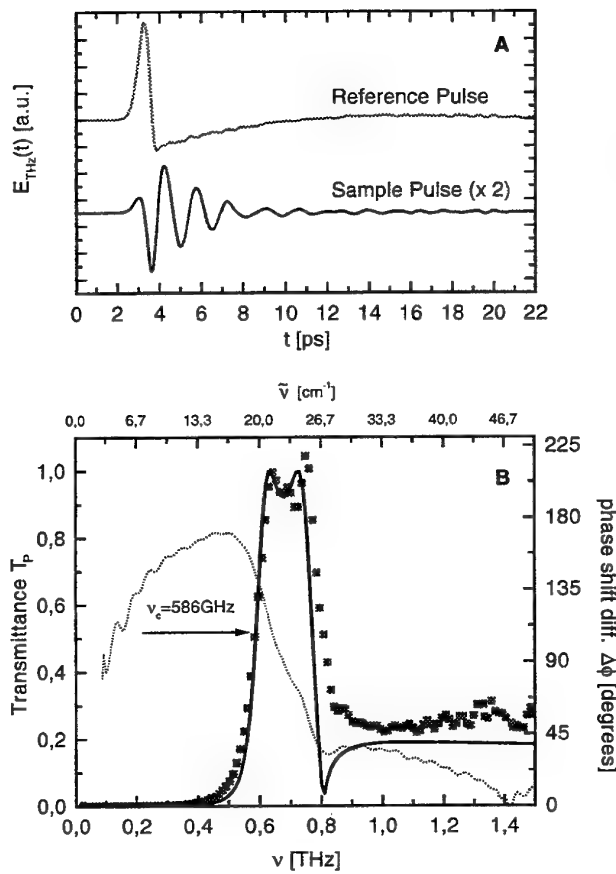


Fig. 3. (A) presents the time domain data of the reference THz pulse (gray line) and sample pulse (black line) of a dichroic filter with a cutoff frequency at 586 GHz. The mechanical parameters of the dichroic filter are  $l = 258 \mu\text{m}$ ,  $d = 300 \mu\text{m}$ , and  $s = 425 \mu\text{m}$ . Part (B) presents the power transmittance  $T_P$  (squares) of the dichroic filter in comparison to the theoretical transmittance characteristic (black line) obtained by Chen's transmission theory [1]. The dotted gray line shows the measured phase shift difference between the reference and sample pulse.

In Fig. 3 (A) the reference THz pulse  $E_{\text{ref}}(t)$  is presented as the gray line. The black line displays the sample pulse,

$E_{\text{sample}}(t)$ , obtained by placing the dichroic filter in the THz beam path. In Fig. 3 (B), the power transmittance  $T_P(\nu)$  is plotted for a dichroic filter with a cutoff frequency at  $\nu_c = 586 \text{ GHz}$ .  $T_P(\nu)$  is obtained by taking the square of the ratio between the Fourier transformed sample and reference data. In Fig. 3 (B) the measured filter transmittance  $T_P(\nu)$  is compared with the theoretical transmittance (black line) obtained from the theory given by Chen [1].

#### IV. BANDPASS-FILTER

In bandpass filters the apertures are usually cross-shaped. These crosses arise from the synthesis of an inductive and a capacitive grid which are well-known from literature [11], [12] and behave like a high-pass and a low-pass, respectively. The bandpass filter curve is deter-

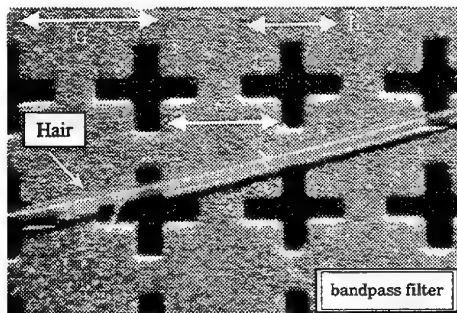


Fig. 4. Microscope image of a galvanized bandpass filter with a resonance frequency at 280 GHz. The parameter set is: mesh period  $G = 810 \mu\text{m}$ , slot length  $L = 570 \mu\text{m}$ , strap width  $C = 650 \mu\text{m}$ , and foil thickness  $t = 10 \mu\text{m}$ .

mined by the choice of the mesh parameters containing the different geometric constants of the mesh period  $G$ , the slot length  $L$ , strap width  $C$ , and the foil thickness  $t$ , see Fig. 4. A numerical field analysis is used to calculate the transmission characteristic of these filters. It is based on a commercial program, called Maxwell's Finite Integration Algorithm (MAFIA) [2]. The experimental and theoretical transmittance of a bandpass filter with a resonance frequency of 280 GHz is displayed in Fig. 5.

#### V. CONCLUSION

We have measured FSS's with an eo-sampling THz-Time-Domain Spectrometer in the FIR spectral region. We show that it is possible to expand the fabrication of purely mechanical dichroic filters into the submillimeter range. The measured transmission characteristics show good agreement with the predictions of the field matching theory of Chen [1]. We anticipate that it will be possible to expand this type of dichroic filter into the visible domain using nanotechnologies.

In the presentation we will discuss filter design criteria and show dichroic filters with cutoff frequencies above 1 THz. Furthermore the application of FSS's as complex temporal shaping elements for THz pulses in frequency selective ultrafast experiments will be discussed. Additional-

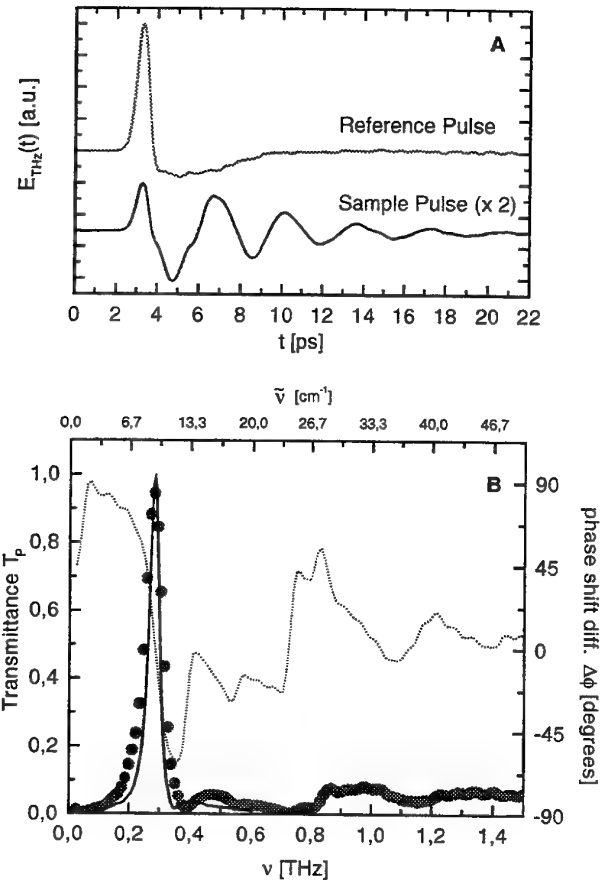


Fig. 5. (A) presents the time domain data of the reference THz pulse (gray line) and sample pulse (black line) of a cross-shape grid bandpassfilter with a resonance frequency at 280 GHz. (B) shows the power transmittance  $T_p$  (squares) of the bandpassfilter in comparison to the theoretical transmittance characteristic (black line) obtained by the MAFIA program. The dotted gray line shows the measured phase shift difference between the reference and sample pulse.

ly we will compare the transmission performance of cascaded dichroic filters with cross shaped grid bandpass filters.

#### REFERENCES

- [1] C.-C. Chen, "Transmission of Microwave Through Perforated Flat Plates of Finite Thickness", *IEEE Trans. Microwave Theory and Techn.*, **MTT-21**, 1 (1973)
- [2] D. Steup and J. Weinzierl, "Resonant THz-Meshes", 4th Int. Terahertz Workshop in Tennenlohe, Germany (1996)
- [3] F. Lewen, S.P. Belov, F. Maiwald, Th. Klaus, and G. Winnewisser, *Z. Naturforschung*, **50a**, 1182, (1995)
- [4] T. Schimert, M. E. Koch, and C.H. Chan, "Analysis of scattering from frequency-selective surfaces in the infrared", *J. Opt. Soc. Am. A* **7**, 1545 (1990)
- [5] J.T. Darrow, X.C. Zhang, D.H. Auston, and J. D. Morse, "Saturation Properties of Large-Aperture Photoconducting Antennas", *IEEE J. Quantum Electron.* **28**, 1607 (1992)
- [6] C. Winnewisser, F. Lewen, and H. Helm, "Transmission characteristics of dichroic filters measured by THz-Time-Domain Spectroscopy", *Appl. Phys. A* **66**, 593 (1998)
- [7] C. Winnewisser, P. Uhd Jepsen, M. Schall, V. Schyja, and H. Helm, "Electro-optic detection of THz radiation in LiTaO<sub>3</sub>, LiNbO<sub>3</sub> and ZnTe", *Appl. Phys. Lett.* **70**, 3069, (1997)
- [8] N. Marcuvitz, *Waveguide Handbook*, McGraw-Hill Book Company, New York (1951)
- [9] M.S. Durchschlag and T.A. Temple, "Far-IR optical properties of freestanding and dielectrically backed metal meshes", *Appl. Opt.* **20**, 1245 (1981)
- [10] H.M. Pickett, J. Farhoomand, and A.E. Chiou, "Performance of metal meshes as a function of incidence angle", *Appl. Opt.* **23**, 4228 (1984)
- [11] R. Ulrich, "Interference filters for the Far Infrared", *Appl. Opt.* **7**, 1987 (1968)
- [12] V.P. Tomaselli, D.C. Edewaard, P. Gillan, and K.D. Möller, "Far-infrared bandpass filters from cross-shaped grids", *Appl. Opt.*, **20**, 1361 (1981)

# Terahertz Operation of GaAs/AlGaAs Metal-Semiconductor-Metal Photodetectors

M. Ryzhii, I. Khmyrova,<sup>†</sup> V. Ryzhii,<sup>†</sup> and M. Willander  
 Chalmers University of Technology and Gothenburg University,  
 Gothenburg, 41296, Sweden  
<sup>†</sup>University of Aizu, Aizu-Wakamatsu, 965-80, Japan  
 (Fax: 81-242 37 2596; E-mail: ryzhii@hotmail.com)

The operation bandwidth of metal-semiconductor-metal (MSM) photodetectors with planar interdigitated Schottky contacts is usually assumed to be limited by the electron and hole transit time effects. This leads to a tendency to reduce the contact spacing to the scale of about few hundredth of micrometer. However, the velocity overshoot effect exhibiting by the photoexcited electrons (holes) can result in marked responsivity of MSM photodetectors with the contact spacing of few tenth of micrometer to optical radiation modulated by terahertz signals.

This paper deals with a Monte Carlo particle study of MSM photodetectors operation in terahertz range of signal frequencies. The obtained numerical results are discussed invoking the developed analytical model of the MSM photodetectors.

We consider planar interdigitated MSM photodetectors made of a thin GaAs absorbing layer on a AlGaAs substrate. The MSM photodetector structure and the geometry of the simulated two-dimensional region are shown in Fig. 1. The thickness of the GaAs layer is assumed to be  $D = 0.2 \mu\text{m}$ .

The Monte Carlo simulator is used to analize the response of the MSM photodetectors at room temperature ( $T = 300 \text{ K}$ ) with different spacing between the Schottky contacts on ultrashort (like  $\delta$ -function) probing optical pulses with different photon energy. The MSM photodetectors with the contact spacing in the range  $W = 0.025\text{--}1.0 \mu\text{m}$  under biasing voltage  $V$  corresponding to the average electric field  $E = V/W = 20\text{--}70 \text{ kV/cm}$  are investigated. The energy of incident photons is assumed to be  $\hbar\Omega = 1.45\text{--}2.0 \text{ eV}$ , so that the initial energy of the photoexcited electrons  $\varepsilon_0 \propto \hbar\Omega - \Delta_g$  ( $\Delta_g$  is the band gap energy) varies in the range 30–580 meV.

The calculated temporal dependences of the photocurrent induced by the photoexcited electrons and holes in the MSM photodetector are subjected to the Fourier transform. The Fourier transform of the transient photocurrent triggered by the optical pulse is

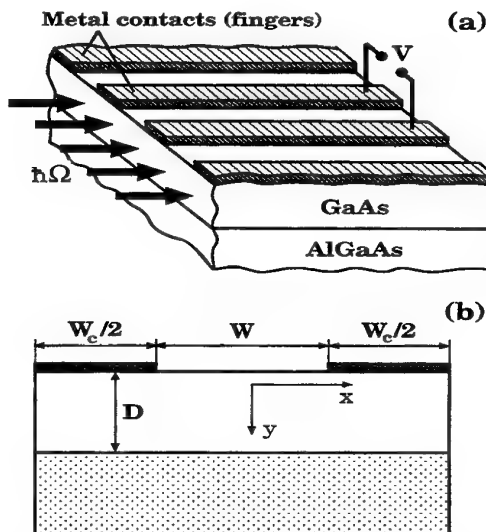


Figure 1: Schematic view of MSM photodetector with lateral light input (a) and structural model used in two-dimensional MC simulation (b).

used for the calculation of the MSM photodetector frequency dependent responsivity. The latter determines the MSM photodetector response to modulated optical signals.

The calculated frequency dependent responsivity for the MSM photodetector with different contact spacing and contact width for the case of average electric field  $E = 50 \text{ kV/cm}$  and the initial energy  $\varepsilon_0 = 80 \text{ meV}$  is shown in Fig. 2. Figure 3 demonstrates the responsivity at signal frequencies  $f = 0.1$  and  $f = 1 \text{ THz}$  as a function of the contact spacing for different  $\varepsilon_0$ . The responsivity versus signal frequency for the MSM photodetector with different spacing-contact widths ratios are seen in Fig. 4.

If the contact spacing decreases beyond  $0.2 \mu\text{m}$  the

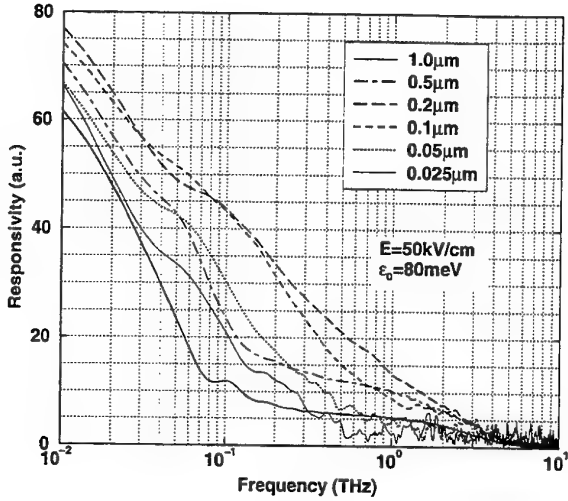


Figure 2: Responsivity as a function of signal frequency for different contact spacing.

responsivity shows a sharp drop. Such a behaviour is associated with the decrease of the electric field in the depth of the absorption layer if  $W < D$ .

The responsivity of the MSM photodetector with the same contact spacing but different contact widths is shown in Fig. 4. It is seen that the reduction of the contact width with fixed contact spacing leads to pronounced deterioration of the responsivity in a wide range of signal frequencies.

The obtained results show that the responsivity of the MSM photodetectors with the contact spacing of about few tenth of micrometer at terahertz signal frequency can be relatively large. The developed analytical device model yields the following formula for the modulus of the frequency dependent responsivity in the terahertz range of signal frequencies

$$\frac{|R(f)|}{R(0)} \simeq 0.55 \frac{\Lambda}{W} \frac{\ln(2W/D)}{1 + 4\pi^2 f^2 \tau^2}.$$

Here  $R(0)$  is the steady-state value of the responsivity,  $\Lambda$  and  $\tau$  are the characteristic length and time of the electron velocity overshoot effect. For GaAs if  $E = 30 - 50$  kV/cm at  $T = 300$  K  $\Lambda \simeq 0.1$   $\mu\text{m}$  and  $\tau \simeq 0.1$  ps. Thus, for  $W = 0.2$   $\mu\text{m}$ ,  $D = 0.2$   $\mu\text{m}$   $|R(f)|/R(0) \simeq 0.2$  if  $f < \frac{1}{2\pi\tau} \simeq 1.5$  THz.

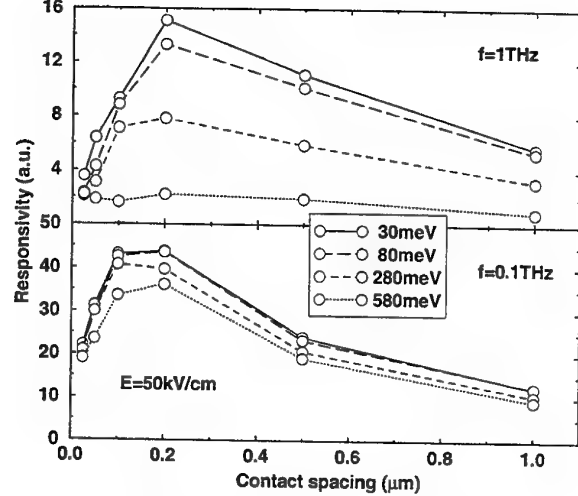


Figure 3: Dependence of the responsivity at  $f = 1$  THz and  $f = 0.1$  THz on contact spacing for different initial energies of the photoelectrons.

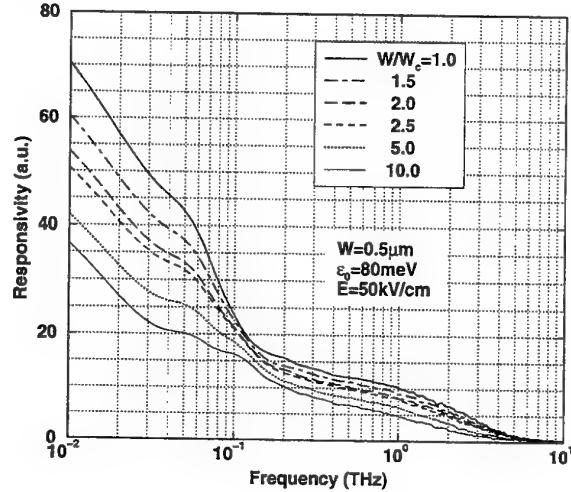


Figure 4: Responsivity versus frequency for MSM photodetectors with different contact spacing - contact width ratios.

# THz-radiation from InAs under Magnetic Field and its Spectrum Control

Hideyuki OHTAKE, Shinji IZUMIDA, Shingo ONO, Zhenlin LIU, and Nobuhiko SARUKURA

**Abstract**— We report significant enhancement of THz-radiation from InAs under magnetic field irradiated with femtosecond pulses. Furthermore, the radiation spectrum is well-controlled by the excitation pulselwidth.

**Keywords**— THz-radiation, chirped pulses, spectrum control.

## I. INTRODUCTION

VARIOUS THz-radiation sources have been intensively studied including photo conductive switches irradiated with ultrashort optical pulses.[1], [2]. For applications to sensing or imaging[3] and time-resolved spectroscopy in the far infrared region, an intense, compact, and simple light source is required. Zhang et al. reported quadratic magnetic field dependence of the laser induced THz-radiation.[4] In this presentation, we report the significant enhancement of THz-radiation power from InAs under magnetic field irradiated with femtosecond optical pulses. The power reaches sub-mW in a 1.7-T magnetic field with 1.5-W excitation power. This is the highest average power ever achieved in THz radiation at around a 100-MHz repetition rate. Furthermore, spectrum of this intense THz-radiation is well-controlled by the width of the excitation pulses.

## II. EXPERIMENTAL SETUP

The experimental setup for the THz-radiation emitter in a magnetic field is shown in Fig. 1. A Ti:sapphire laser delivered 70-fsec pulses at 800 nm with an 80-MHz repetition rate in a 1.5-W average power for the excitation. The sample was non-doped bulk InAs with a (100) surface. The InAs sample itself is highly reflective in the THz region. In this region, the reflectivity of InAs was measured to be approximately 70% for a 45 degree incidence angle. Therefore, the THz radiation was totally generated in the reflection direction. A liquid-helium-cooled InSb bolometer was provided for detection. The InAs sample was placed 45 degrees to the magnetic field, and the excitation laser direction was parallel to the magnetic field. In this geometry, the THz radiation was detected even without the magnetic field, similar to GaAs in [5].

## III. RESULT AND DISCUSSION

In this case, the mechanism of the THz radiation was attributed to the carrier motion in the surface depletion

Hideyuki OHTAKE, Shinji IZUMIDA, Shingo ONO, Zhenlin LIU, and Nobuhiko SARUKURA are with Institute for Molecular Science, 38 Nishigonaka, Myodaiji, Okazaki, 444-8585, Japan. E-mail: otake@ims.ac.jp .

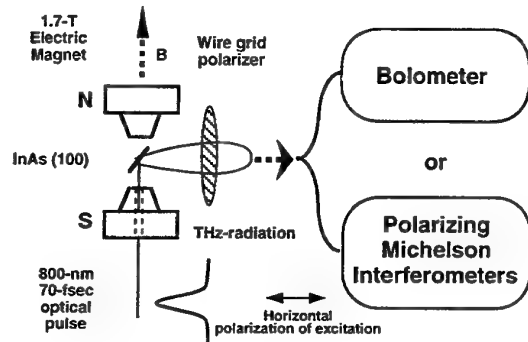


Fig. 1. The experimental setup for THz-radiation emitter in a magnetic field. The sample was non-doped bulk InAs with a (100) surface. A liquid-helium-cooled InSb bolometer with calibrated sensitivity was provided for detection. The maximum field of the electric magnet was 1.7 T, and the magnetic field can also be applied in the opposite direction.

electric field.[6], [7] The excitation power dependence of the THz-radiation power under 1.7-T magnetic field was shown in Fig. 2. The radiation power exhibits almost quadratic excitation power dependence. We have also found that the power of the THz radiation from an InAs sample in a magnetic field is over one order of magnitude higher than that from non-doped GaAs with a (100) surface in the same conditions shown in Fig. 2. The magnetic-field dependence of the THz-radiation power is shown in Fig. 3. The radiation power is quadratically related to the higher magnetic field region as was the case for GaAs.[4]

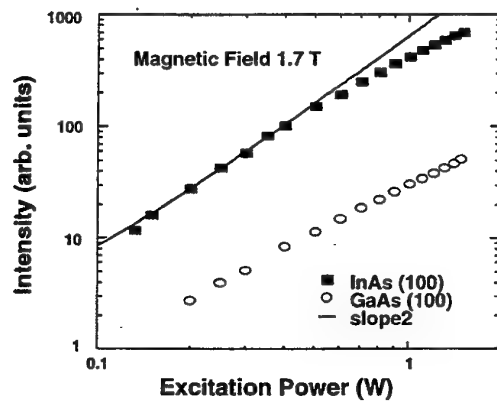


Fig. 2. Excitation-power dependence of THz-radiation power. THz radiation from InAs (circle) increases rapidly as excitation-power increases. THz radiation from GaAs (square) is also shown for comparison. The dotted line indicates slope 2.

Owing to this quadratic magnetic field and excitation

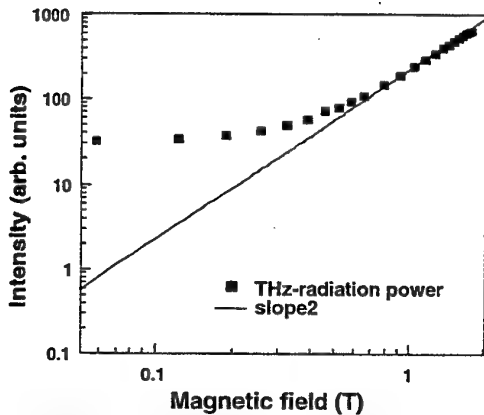


Fig. 3. Magnetic field dependence of THz-radiation power. THz radiation from InAs (solid squares) increases dramatically as magnetic field increases. The solid line indicates slope 2.

power dependence, the total THz-radiation power reaches around  $100 \mu\text{W}$ . The spectra of the horizontal and vertical polarization components of the THz radiation were obtained by a Polarizing Michelson interferometer. The spectral shape for the different magnetic field direction was almost identical. However, the spectral shapes for different polarization components are significantly different as shown in Figs. 4(a) and (b).

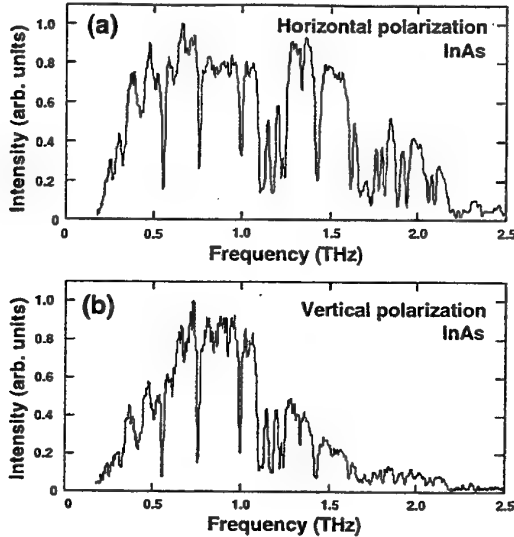


Fig. 4. Spectrum of THz radiation from InAs in a 1.7-T magnetic field obtained by Fourier transformation of the autocorrelation using a Polarizing Michelson interferometer. (a) Horizontal polarization. (b) Vertical polarization. The dips correspond to water vapor absorption.

The higher frequency spectrum is enhanced in horizontal polarization components. For this optical configuration, the ellipticity of the THz radiation was measured for the different magnetic field using a wire-grid polarizer. In the zero field, the radiation was completely polarized parallel to the magnetic field. At around 0.25 T, the radiation

polarization became nearly circular as shown in Fig. 5.

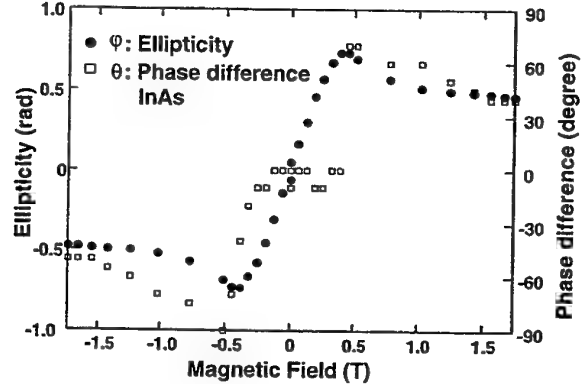


Fig. 5. Ellipticity of THz radiation from InAs. The ellipticity changes dramatically.

This elliptical polarization nature can be attributed to the vertical and horizontal projections of the photo current in semiconductor surface caused by the magnetic field and surface depletion electric field as described in ref. [4]. For the control of this intense THz radiation spectrum, we introduced a high dispersion prism pair to stretch the pulse duration. The pulse duration was changed from 260 to 1100 fsec (FWHM) in autocorrelation. With this stretched pulse for the excitation, we can control center frequency of THz-radiation as shown in Fig. 6.

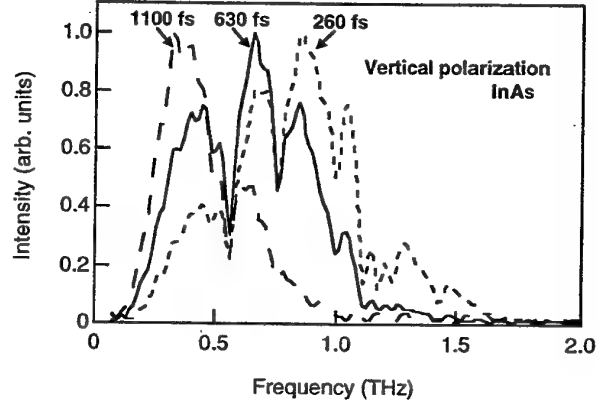


Fig. 6. Spectrum of THz radiation excited with different pulse duration.

#### IV. CONCLUSION

In conclusion, we have demonstrated a new, simple, and intense THz-radiation source just using bulk InAs. An average power of  $100\text{-}\mu\text{W}$  was achieved, owing to the quadratic relationship to the magnetic field and excitation laser power, the high reflectivity of InAs, and smaller effective mass of the electron in InAs. A dramatic change of ellipticity was also observed for different magnetic fields. Furthermore, the radiation spectrum is well-controlled by the excitation pulsewidth. Further increase of magnetic field and excitation power will increase the THz radiation. Development of such simple and intense radiation sources will open up new applications of THz radiation.

## REFERENCES

- [1] For example, D. H. Auston, *Appl. Phys. Lett.*, vol. 45, pp 284, 1984.
- [2] For example, I. Brener, D. Dykaar, A. Frommer, L. N. Pfeiffer, J. Lopata, J. Wynn, K. West, and M. C. Nuss, *Opt. Lett.* vol. 21, pp 1924, 1996.
- [3] D. M. Mittleman, S. Hunsche, L. Boivin, and M. C. Nuss, *Opt. Lett.* vol. 22, pp 904, 1997.
- [4] X. -C. Zhang, Y. Lin, T. D. Hewitt, T. Sangsiri, L. E. Kingsley, and M. Weiner, *Appl. Phys. Lett.* vol. 62, pp 2003, 1993.
- [5] N. Sarukura, Z. Liu, Y. Segawa, S. Koshihara, K. Shimoyama, Y. Kondo, Y. Shibata, T. Takahashi, S. Hasebe, M. Ikezawa, *22nd International Conference on the physics of semiconductors*, pp 1237, 1994
- [6] X. -C. Zhang and D. H. Auston, *J. Appl. Phys.* vol. 71, pp 326, 1992.
- [7] S. L. Chuang, S. Schmitt-Rink, B. I. Greene, P. N. Saeta, and A. J. Levi, *Phys. Rev. Lett.* vol. 68, pp 102, 1992.

# >100 GHz Time Domain Measurement Using Photoconductive Sampling

Jaehoon Lee, Heeseok Lee, Woopoung Kim, Jongjoo Lee, and Joungho Kim

**Abstract**--Photoconductive sampling has been proposed as a potent technique for analyzing high frequency devices and systems, using the photoconductive sampling. The characterization of >100 GHz devices was successfully demonstrated including transmission line, open termination, short termination and filters up to 150 GHz. The induced S-parameter measurements were compared to the FDTD simulation.

**Index terms** measurement, photoconductive sampling

## I. INTRODUCTION

Recently, due to the development of semiconductor design and fabrication technology, the device speed exceeds 100 GHz frequency region. But the measurement bandwidth of the conventional technique is limited by the electrical discontinuity and the associated deembedding process. Therefore new measurement method at the millimeter wave region are proposed, including electro-optic sampling and photoconductive sampling. It is well known that the bandwidth of the electro-optic sampling is higher than that of the photoconductive sampling. On the other hand, the SNR(Signal-to-Noise Ratio) of the electro-optic sampling is smaller than that of the photoconductive sampling. The photoconductive sampling has high bandwidth enough to measure systems or devices at millimeter wave region over 100 GHz. Many papers relating the photoconductive sampling have been reported[1][2]. However, the validity of the measurement was not investigated yet, since no other referable measurement results could be found.

In this paper, we demonstrate the S-parameter measurement of passive devices up to 150 GHz, including transmission line, open/short termination and Low Pass Filters(LPF), and compared them to the FDTD simulation. Due to the advantage of the time domain measurement, 50 ohm termination is not required. Especially, deembedding process was not necessary, using the proposed structure.

## II. BASIC SETUP

The experimental setup of the photoconductive sampling is shown in Fig.1. Fig. 2 shows the layout of the on-wafer measurement structure. It is assumed that there are no reflections from the sampling structure. We used sufficiently long transmission line to neglect the reflections from the end of the transmission line. Thereby, the deembedding process could be removed. Side pumping and probing structure was used. Using this structure, it is possible to measure both one port device and two port device together.

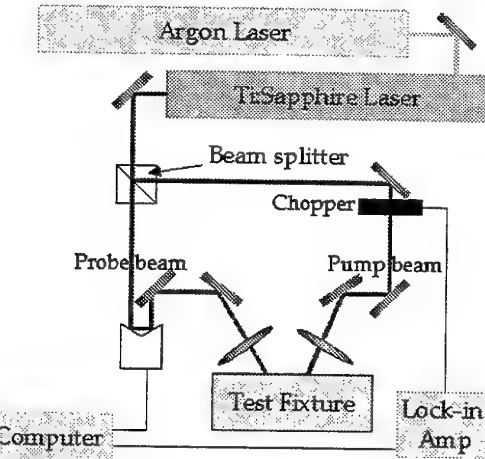


Fig. 1. Experimental setup of the photoconductive sampling.

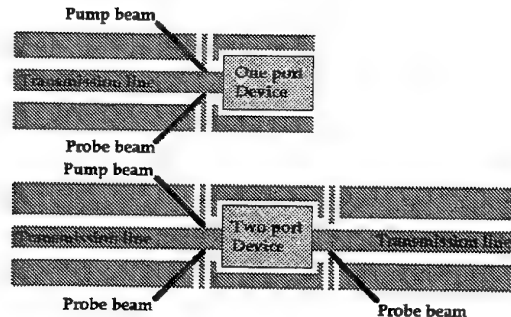


Fig. 2. Layout of the on-wafer measurement.

The authors are with the Department of Electrical Engineering, Korea Advanced Institute of Science and Technology at Kusong, Yusong, Taejon 305-701, Korea.

### III. EXPERIMENTAL RESULTS AND FDTD SIMULATION

#### A. Transmission Line Characterization

Fig. 3 shows the measured waveform of the initial pulse and the transmitted pulse through the 3 mm long CPW transmission line. It is shown that the transmitted pulse is broadened due to the transmission line loss. In the frequency domain, the characteristics of the CPW transmission line exhibits increased attenuation at higher frequency. Also the effective dielectric constant of the CPW is induced up to 100 GHz.

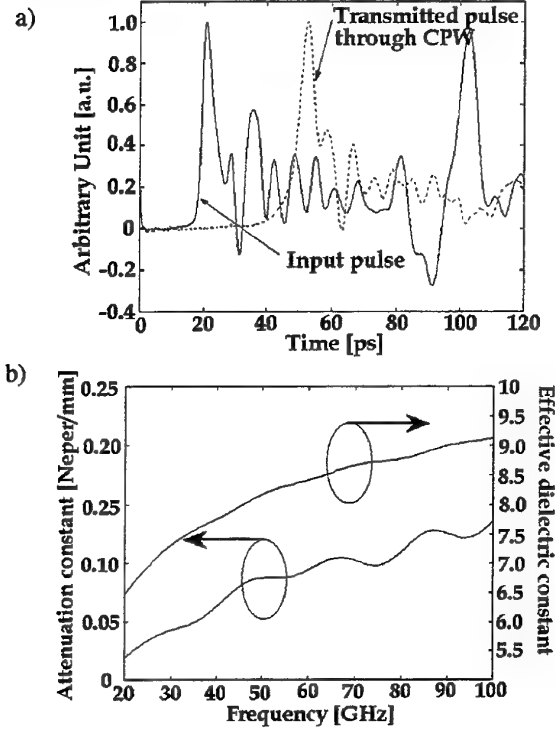


Fig. 3. a) Measurement pulse waveforms of CPW. b) Induced characteristic of CPW.

#### B. Layout of the on-wafer measurement.

Fig. 4 shows the measured and the FDTD pulse waveforms of the open and the short termination. The measured pulses include the input pulse and the reflected pulse from the termination. The reflected pulse from the open termination exhibits a 0 degree phase shift, and that from the short terminations shows a 180 degree phase shift. The discrepancy between the measured pulses and the simulated pulses is caused by the difficulty of current source modeling in the FDTD simulation. However, the peaks are positioned at the same time, ensuring the coincidence of the measurement and the FDTD simulation. In the FDTD simulation, the small pulses between the input pulses and the reflected pulses are resulted from the reflection from the bottom of the LT-GaAs substrate. In

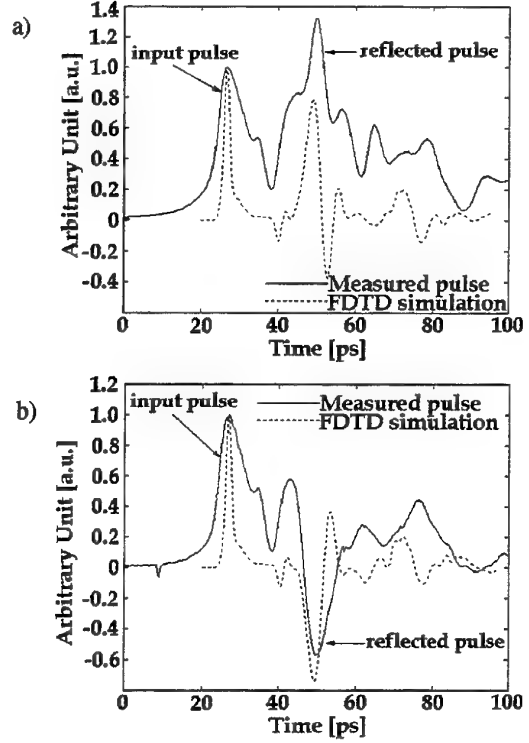


Fig. 4. Measurement and FDTD simulation of input and reflected pulses from the a) open and b) short termination.

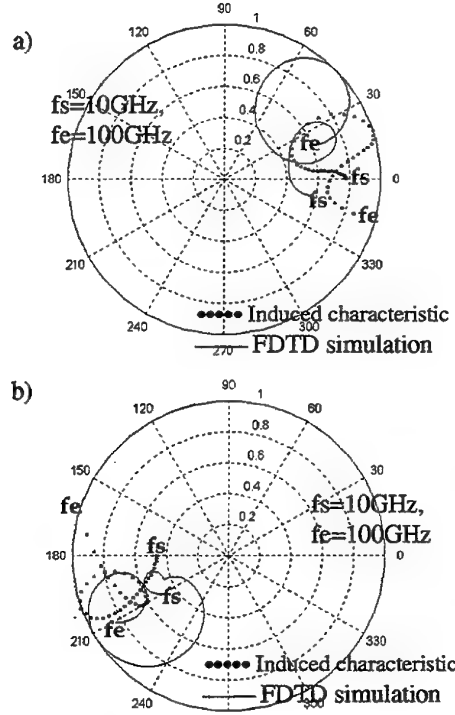


Fig. 5. Induced S-parameters of a) open and b) short termination on smith chart. ( $fs=10GHz$ ,  $fe=100GHz$ )

addition, the induced S-parameters( $S_{11}$ ) of the open and short termination are presented in Fig. 5.

### C. Low Pass Filter

The characterization of the Low-Pass-Filter(LPF) is executed by the same photoconductive sampling procedure without the deembedding process. Fig. 6 shows the concept of this deembeddingless method. With the sufficiently long transmission and same waveguiding structure of an identical length for both transmission line and testing device, the characteristics of the two port devices are obtained without deembedding process.

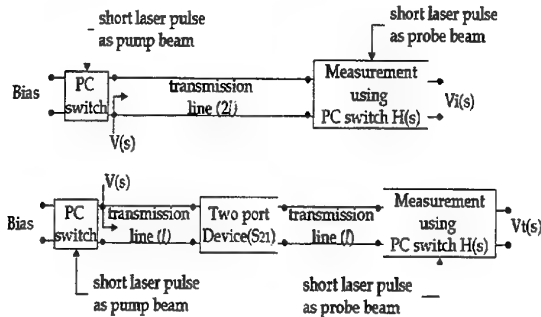


Fig. 6. Concept of the measurement without deembedding process. Both structures have same transmission line structure with an identical length( $2L$ ).

The reflections caused by the discontinuities of the photoconductive sampling structure can cause interference in the measurement time window. Thus, the available time window is determined by the length of transmission lines( $L$ ). In Fig. 6 a), the time delay of the reflection is given by  $4Td_1$  ( $Td_1=L/v_{ph}$ ,  $Td_1$  : the time delay through the transmission line with length  $L$ ,  $L$  : the length of transmission line,  $v_{ph}$  : the phase velocity in the transmission line). In Fig. 5 b), the time delay of the reflection from the two port device is given by  $2Td_1$ . Thus  $vi(t)$  may be expressed as

$$vi(t)=L^{-1}\{Vi(s)\} \quad 0 < t < 4Td_1+2Td_1$$

where  $L^{-1}$  denotes the inverse Laplace transform and  $vi(t)$  is measured waveform through only transmission line. Also  $vt(t)$  may be expressed as

$$vt(t)=L^{-1}\{Vt(s)\} \quad 0 < t < 2Td_1+2Td_1+Td_2$$

where  $Td_2$ : time delay in two port device and  $vt(t)$  is measured waveform through the transmission line and the two port device.

Then,  $Vi(s)$  is the function of the complex frequency variable  $s$ , Laplace transform of initial pump electrical pulse  $V(s)$ , the characteristics of the transmission line, and

the sampling function  $H(s)$ .

$$Vi(s)=V(s) \exp(-sTd_1) \exp(-sTd_1) H(s)$$

Then,  $Vt(s)$  can be expressed as follows with the addition of  $S21$  of the two port device,

$$Vt(s)=V(s) \exp(-sTd_1) S21(s) \exp(-sTd_1) H(s)$$

Referring above two equations, the ratio of  $Vi(s)$  and  $Vt(s)$  will yield the characteristics of the two port device,  $S21(s)$ :

$$S_{21}(s) = \frac{Vt(s)}{Vi(s)}$$

Thus with given signal  $vt(t)$  and  $vi(t)$  from the time domain measurement, the  $S21$  can be simply calculated.

$$S_{21}(w) = \frac{F\{vt(t)\}}{F\{vi(t)\}}$$

As demonstrated above, it is proven that the characteristics of the two port device can be acquired without deembedding process using a suitable time window.

Above procedure has been applied to the characterization of LPF's. Fig. 7 shows Stepped Impedance Low Pass Filters with CPW used in our experiment. Fig. 8 shows the measured response and the induced  $S21$  of the LPF's. The pulse waveform through the LPF's becomes broader than that of the input pulse. Also, it could be seen that the pulse after the 50 GHz LPF is broader than that after the 100 GHz LPF as expected. In addition,  $S21$  and cut-off frequency of the LPF are drawn for each filters in Fig. 8.

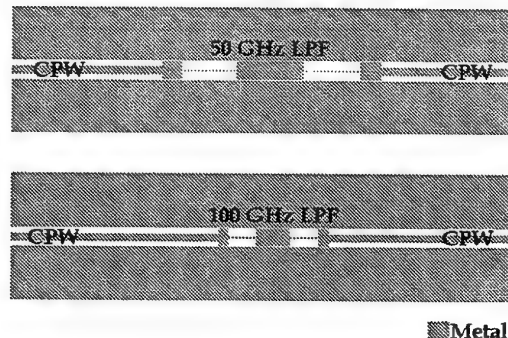


Fig. 7. Stepped Impedance Low Pass Filters with CPW.(a) cutoff frequency=50GHz, (b)cutoff frequency 100GHz).

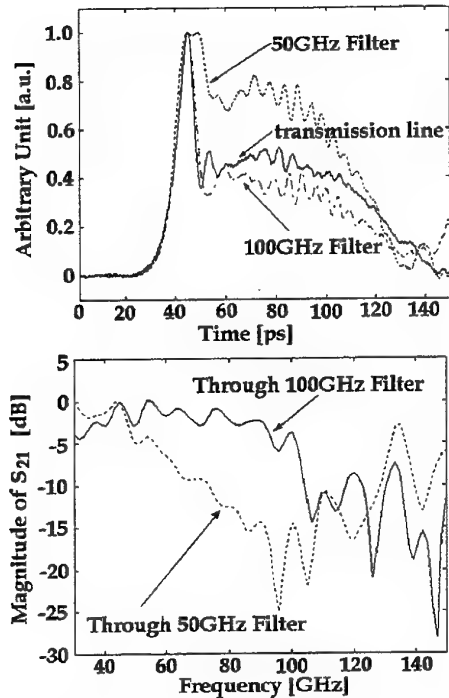


Fig. 8. Measurement of pulse waveforms and induced S-parameters of 50 GHz and 100 GHz Low Pass Filters

#### IV. CONCLUSION

In conclusion, the characterization of >100 GHz devices were demonstrated using the photoconductive pump and probe measurement without accompanying deembedding process. The devices include transmission line, open/short termination and filters. The close agreement of the measurement to the FDTD simulation verifies the reliability and the usefulness of the measurement at the millimeter wave region over 100 GHz.

#### V. REFERENCES

- [1] S.L.Huang, E.A.Chauchard, C.H.Lee, H.A.Hung, T.T.Lee and T.Joseph, IEEE Trans. on Microwave Theory Tech., vol. 40, pp2312-2320, Dec. 1992.
- [2] Christen Rauscher, IEEE Trans. on Microwave Theory Tech., vol. 39, pp1179-1193, July 1991.
- [3] James R. Andrews, Proceedings of the IEEE, vol. 66, No 4, April, 1978.

# Transient Response of Terahertz Emitter using Finite-Difference Time-Domain (FDTD) Method

Heeseok Lee, *Student Member, IEEE*, Jaehoon Lee, and Joungho Kim, *Member, IEEE*

**Abstract**—The transient response and the radiation pattern of the various terahertz dipole antenna were successfully obtained using FDTD method. As a result, a design guideline was presented for the trade-off between the peak height and the 3-dB bandwidth. In addition, the effect of the electrode shape and the laser beam position on the photoconductive switch was investigated.

**Index terms**—terahertz emitter, transient response, FDTD, photoconductive dipole antenna

## I. INTRODUCTION

The efficient generation of high intensity and high bandwidth terahertz radiation using the biased photoconductive antenna has attracted a lot of interest for terahertz spectroscopy[1] and terahertz imaging[2,3]. Photoconductive sampling has been employed to obtain the terahertz waveform from the antenna.

However, more understanding of the antenna geometry effect should be acquired for the optimum design of the emitter and the detector. The effect of the dipole length was investigated by Smith et al.[4], where it was said that the longer dipole antenna produces higher SNR and the shorter dipole detector generates higher bandwidth. Also, the enhancement of the terahertz emitter output was reported by Brener et al.[5], using the electric field singularity in the biased semiconductor. The intensity of the terahertz emitter was enhanced by increasing the static field in the photoconductive gap. However, all this observation was induced from the pump and probe measurement with the different emitter and receiver geometries. In addition, this experiment has required a lot of time and resources.

In this paper, we demonstrate the Finite-Difference Time-Domain (FDTD) Method[6] as an efficient tool to

simulate the transient waveform and the radiation patterns from the terahertz antenna. This simulation method can save the research time and resources a lot. The relation between the antenna geometry to the output waveform and the radiation pattern of the terahertz emitter is reported. Also, the effect of the optical-pulse beam position and the electrode shape is investigated. Finally, a design guideline of the terahertz photoconductive antenna is presented.

## II. TRANSIENT RESPONSE OF TERAHERTZ Emitter USING FDTD

The FDTD method, a full-wave analysis method, is employed to solve 3-dimensional Maxwell's curl equations in time-domain, including the conductive current components. The geometry used in this simulation is shown in Fig.1. First, the transient photocurrent is

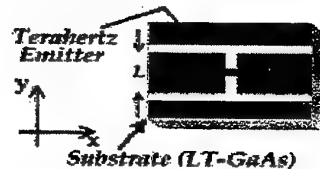


Fig.1. The geometry of the terahertz dipole antenna used in the FDTD calculation

generated when the center ( $5 \mu\text{m} \times 5 \mu\text{m}$  area) of the photoconductive gap is excited by subpicosecond optical pulses. The transient photocurrent is assumed to be a 0.3 ps FWHM Gaussian pulse. The pulse width is determined by the carrier life-time of the LT-GaAs. The static field at the laser beam accelerates the photo-carriers. The static field in the biased antenna can be obtained by solving Laplace's equation. It is believed that the radiated electric field is proportional to the static field at the photoconductive gap in the linear mobility region. The antenna structures are the dipole antenna fed by a coplanar strip line fabricated on an LT-GaAs substrate. The 20- $\mu\text{m}$  width coplanar strip line for dc-bias is assumed to be long enough to neglect the reflections at the end, using Berenger's perfectly matched layer (PML)[7]. Then the transient responses are obtained from the emitters containing various photoconductive gap lengths (H) of the

Department of Electrical Engineering, Korea Advanced Institute of Science and Technology, 373-1 Kusong, Yusong, Taejon 305-701, Korea. (E-mail: heeslee@eeinfo.kaist.ac.kr)

dipole antenna and the spacings ( $L$ ) of the coplanar strip line with 20- $\mu\text{m}$  dipole width.

Fig.2 shows a calculated transient waveform. Also the radiated electric field patterns are illustrated in Fig.3 corresponding to the observation time of (a), (b), (c), and (d) shown in Fig.2.

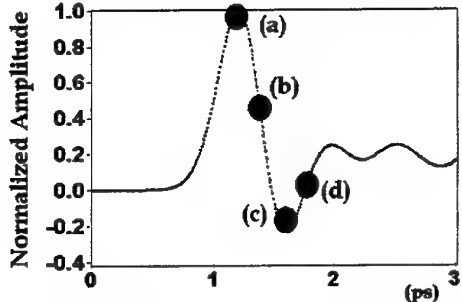


Fig.2. The calculated waveform at 200  $\mu\text{m}$  above the emitter. (a), (b), (c), and (d) indicate the observation time in Fig.3, respectively.

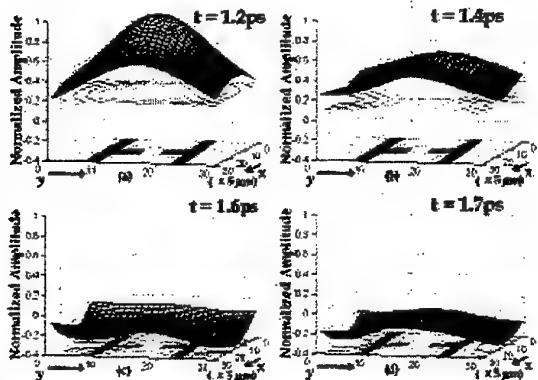


Fig.3. Radiated electric field pattern by FDTD. The observation position is 200  $\mu\text{m}$  above the emitter at 1.2ps(a), 1.4ps(b), 1.6ps(c), and 1.7ps(d) respectively.

In addition, the calculated transient waveforms with the different photoconductive gap length ( $H$ ) are shown in Fig.4. As can be seen from the figure, the transient waveforms exhibit different shape and intensity depending on the antenna geometry. The 3-dB bandwidth and the peak height of the output terahertz waveforms are shown in Fig.5. Below 60- $\mu\text{m}$  photoconductive gap, it is found that the emitted terahertz waveform generates quite different 3-dB bandwidth and peak height depending on the antenna geometry, especially on the photoconductive gap length ( $H$ ). The longer photoconductive gap generates the higher bandwidth. The shorter gap size produces the higher peak height. The shorter spacing between the electrodes induces more current on the antenna electrode, which produces more radiation power. The induced electrode current is delayed by the limited propagation speed, thereby resulting in the lower radiation bandwidth. To design optimum terahertz emitter, the transient response of the antenna as

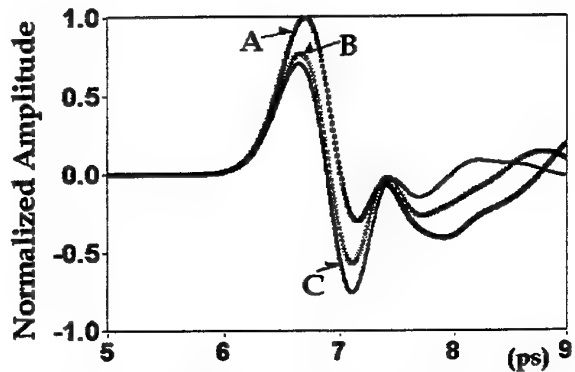


Fig.4. The obtained transient waveforms from the dipole antenna with  $L=105 \mu\text{m}$ ,  $H_A=35 \mu\text{m}$ ,  $H_b=55 \text{ m}$ , and  $H_c=85 \mu\text{m}$  using the FDTD method. The observation point is 300  $\mu\text{m}$  above the dipole antenna inside GaAs substrate.

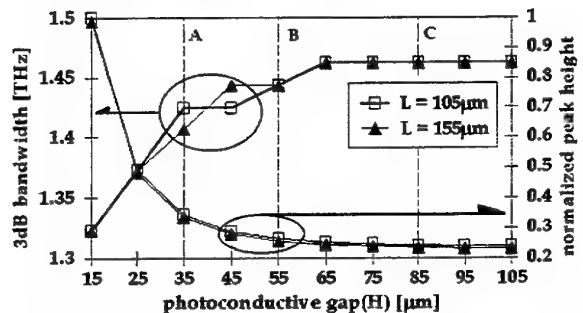


Fig.5. 3-dB bandwidth and peak height for the various geometry of the antenna. The design has to be optimized between the 3-dB bandwidth and the peak height. This figure works as a design guideline. Transient waveform for the case of A, B and C are from those indicated in Fig.4.

well as the method to enhance the static field in the antenna structure, must be known. We found that there is a trade-off between the peak-height and the radiation bandwidth. Fig.5 works as a design guideline.

Also, the dependency of the transient waveform on the laser beam position was examined. Fig.6 presents the effect of the laser beam position between the photoconductive gap. In the simulation, the photoconductive gap ( $H$ ) is assumed 20  $\mu\text{m}$  and the spot-size of the optical illumination is assumed 1  $\mu\text{m} \times 1 \mu\text{m}$ . When the carriers are excited by optical pulse near one of the electrode, more current can be supplied into the antenna, which enhances the output intensity of the emitter. The asymmetric excitation enhances the intensity up to 10 times compared to that of the center-gap excitation, in which the static field is uniform across the gap. The increased radiation intensity can be explained by the static field enhancement caused by the flinging field at the edge of the electrode and by the enhancement of the electrode-current on the antenna. However, the positive electrode effect[8] must include the Schottky barrier change on the metal and semiconductor

interface for complete analysis, which is not considered in the Maxwell's equation.

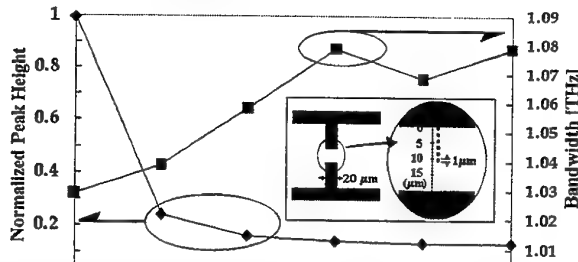


Fig.6 The normalized peak height and bandwidth for the various pumping beam position. The pumping positions are shown in the inset.

The effect of the electrode shape on the transient response was studied using the FDTD. The electrode of sharp shape is believed to enhance the field intensity at the corner of the electrode. The enhancement of the radiation intensity was confirmed using the FDTD. Fig.7 and Fig.8 show the two antenna geometry and the simulated waveforms. The sharp electrode increases the intensity up to 2-times compared to that of the flat electrode. In terms of the dynamic field mechanism, the sharp electrode reduces the impedance mismatch in the photoconductive switch, which acts as triangular tapered lines. The reduction of the impedance mismatch results in the current increase on the electrode. By the help of the static field increase from the electric field singularity[9], the intensity is increased at least 10 times for the sharp electrode compared to that of the flat electrode.

### III. CONCLUSION

In conclusion, this work verifies the usefulness of the FDTD method in the investigation of the geometry effect on the transient terahertz waveform. Also, it is proven that the FDTD method is needed for the design of the optimum terahertz emitter. The output waveforms from the different antenna structure and the optical beam position were calculated by the FDTD method. Additionally, it is found that the radiation pattern, bandwidth, intensity are determined by the electrode shape and the laser beam position. Enormous amount of time and expense can be saved, using the verification based on the FDTD method.

### ACKNOWLEDGEMENT

The authors would like to give thanks to Hyungsoo Kim for calculating the static field in the photoconductive gap. This work was supported by the Research Planning of Future-Oriented Generic Technology of the Ministry of Science and Technology, Korea.

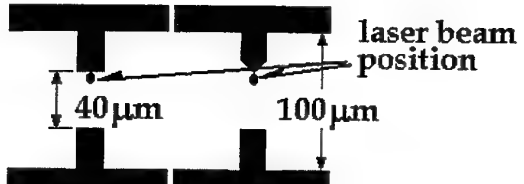


Fig.7 The antenna geometry for comparison of the flat electrode to the sharp electrode. The black dots indicate the laser beam position.

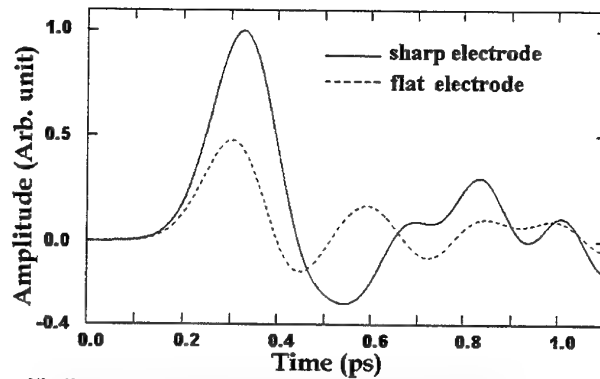


Fig.8 The calculated waveform radiated from a flat electrode and the sharp electrode. The intensity from the sharp electrode is 2-times higher compared to that of the flat electrode.

### REFERENCE

- [1] D.Grischkowsky, S.Keiding, M.Exter, and Ch.Fattinger, J.Opt.Soc.Am.B, 7, 2006 (1990)
- [2] D. M. Mittleman, R. H. Jacobsen, and M. C. Nuss, IEEE J. Select. Quantum Electron. 2, 679 (1996)
- [3] Q. Wu and X. C. Zhang, Appl. Phys. Lett. 71, 1285 (1997)
- [4] P. R. Smith, D. H. Auston, and M. C. Nuss, IEEE J. Quantum Electron, 24, 255 (1988)
- [5] I. Brener, D. Dykaar, A. Frommer, L. N. Pfeiffer, J. Lopata, J. Wynn, K. West, and M. C. Nuss, Opt. Lett. 21, 1924(1996)
- [6] K. S. Yee, IEEE Trans. Antenna Propagat., 14, 302 (1966)
- [7] J. P. Berenger, J. Computational. Phys., 114, 185, (1994)
- [8] D. Krokel, D. Grischkowsky, and M. B. Ketchen, Appl.Phys.Lett. 54, 1046 (1989)

# Terahertz Double-Doppler Wavelength Shifting of Infrared Optical Pulses in Excited Semiconductor Medium

Igor Scherbatko, Alexander Nerukh\*, Member, IEEE, and Stavros Iezekiel\*\*, Member, IEEE

**Abstract--** A time-domain model of an excited semiconductor medium as a moving Bragg grating is used to investigate a double-Doppler wavelength conversion of an infrared ( $\lambda_0 = 15 \mu\text{m}$ ) 0.8 ps optical pulse. In order to investigate ultrafast electromagnetic transients, a time-domain integro-differential equation has been used for simulations. It is shown that the high drift velocity of carriers in InAs semiconductor produces a 10 THz conversion span. The converted pulse width and spectral density depend on contrast of permittivity modulation and have to be as high as possible.

**Index terms--** time-domain, Volterra integro-differential equation, semiconductor, Bragg grating, Doppler wavelength conversion.

## I. INTRODUCTION

All-optical wavelength converters are expected to become key components in future broadband networks. Wavelength division multiplexing (WDM) techniques offer a very effective utilisation of fiber bandwidth directly in the wavelength domain, rather than in the time domain. Several techniques have been proposed to achieve wavelength conversion in fiber-optic links such as direct electro-optic and all-optical wavelength conversions, including cross-gain and cross-phase modulation and also four-wave mixing in semiconductor optical amplifiers. Disadvantages of electro-optic converters include complexity, high power consumption and a cost that rises with bit-rate and with the number of elements. All-optical wavelength converters enable direct translation of the information on the incoming wavelength to a new wavelength without entering the electrical domain [1].

One of the key shortcomings of cross-gain modulation, however, is limited transparency and signal-to-noise deterioration due to a large spontaneous

emission background. Cross-phase modulation suffers from the interferometric nature of such wavelength conversion, which restricts the dynamic range of the input power and adds extra difficulty in controlling input power levels and also has limited transparency [2]. The four-wave mixing scheme in semiconductor amplifiers has low conversion efficiency that decreases rapidly with conversion span.

It is well known that optical and microwave wavelength conversion can be realised by using media with time-varying parameters and the Doppler effect. In [3] it is shown theoretically and experimentally that when a light pulse is incident upon a moving ionization front, the light pulse can be simultaneously upshifted in frequency and compressed in duration. For example, this phenomenon produces intense pulses of 8 mm wavelength radiation by reflecting an incident 3.2 cm microwave pulse off the front of a high-current relativistic electron beam, which plays the role of an overdense plasma.

Application of the Doppler effect in semiconductor optical waveguide is attractive because a moving stepwise ionization front (or excited Bragg grating) can be easily realised by well-known means. For example, an IMPATT diode based on impact ionization in semiconductor layered structures shows appropriate avalanche drift velocity [4]. An external traveling electrical field may be used to excite a moving Bragg grating of carrier density in a semiconductor medium as in GaAs traveling-wave electro-optic modulators and MESFETs.

The evaluation of wavelength shifting by a moving ionization front in a semiconductor medium for a normally incident optical pulse can be made using [3]:

$$f_s / f_0 = (1 + \beta) / (1 - \beta),$$

where  $f_0$  and  $f_s$  are the frequencies of the incident and reflected waves respectively,  $\beta = \frac{V_D}{(c/n)}$  is the ratio between the carrier-plasma drift velocity  $V_D$  and the velocity of light in a medium with refractive index  $n$ . For an optical wavelength of  $\lambda_0 = 1.5 \mu\text{m}$  ( $f_0 = 200$  THz) and InAs semiconductor [4]:  $V_D \approx 1 \times 10^6 \text{ m s}^{-1}$ ,  $n = 3.6$ ,  $\beta \approx 0.012$ . Therefore

The authors are with the \* Techn. Univ. of Radio Electronics, Kharkov, Lenin Av. 14, 310726, Kharkov, Ukraine and \*\* Institute of Microwaves and Photonics, School of Electronic and Electrical Engineering, University of Leeds, Leeds LS2 9JT, UK.

$f_s \approx 1.0243f_0 = 204.9$  THz, that makes up 9.7 THz in absolute value for co- and counter-propagating schemes. This is sufficient wavelength shifting for advanced WDM systems.

## II. THE MODEL OF SEMICONDUCTOR DOUBLE-DOPPLER WAVELENGTH SHIFTER

The moving Bragg grating of a one-dimensional configuration is shown in Fig. 1. Here  $E_0(\tau, \xi)$  is an optical signal that is incident on a semi-infinite dielectric medium with spatial-time varying permittivity:

$$\epsilon(\tau, \xi) = \epsilon \{1 + A \sin[k(\beta\tau + \xi)]\},$$

where  $\tau$  and  $\xi$  are normalised time and spatial coordinates respectively,  $\epsilon$  is the permittivity of the left-side dielectric half-space,  $A$  is the amplitude of the modulation,  $k$  is a scaling factor and  $E_s(\tau, \xi)$  is a scattered electric field (reflected signal).

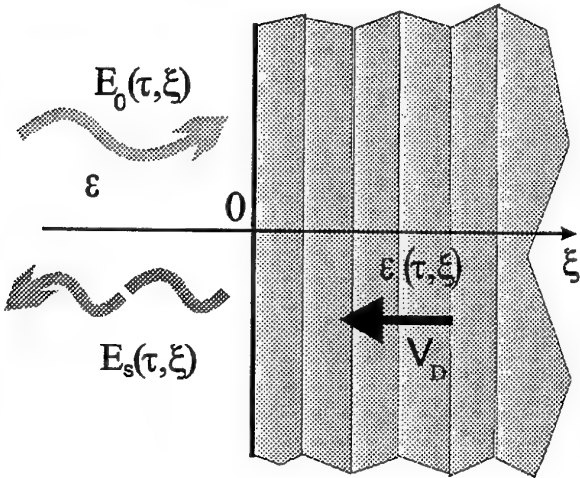


Fig. 1 The model of semiconductor double-Doppler wavelength shifter.

In our case the parameter  $\beta=0.012$  and this denotes the relative velocity of the modulated Bragg grating in the reflected medium. Let the directions of the grating and incident signal be opposing. The parameter  $A$  can be estimated using the relation between refractive index variation  $\Delta n$  in InGaAs semiconductor and the one for permittivity  $\Delta\epsilon$ . This has been done by Visser and Blok [5]:  $\Delta n = 0.1$ , to give  $\frac{\epsilon + \Delta\epsilon}{\epsilon} = \left(\frac{n + \Delta n}{n}\right)^2 \approx 1 + \frac{2\Delta n}{n}$ , or  $\epsilon + \Delta\epsilon \approx \epsilon(1 + \frac{2\Delta n}{n})$ . For this case  $\frac{2\Delta n}{n} \approx 0.05$ , therefore we can put  $A=0.025$ . To solve this transient electromagnetic problem an integro-differential equation approach is used.

## III. THE TIME-DOMAIN INTEGRO-DIFFERENTIAL EQUATION

The time-domain solution of the transient wave propagation problem relies on an integral equation technique which has been used for pulsed EM transient problems recently. The starting point is the integral equation for the electric flux density  $D$  in an active medium:

$$D(\tau, \xi) = D_0(\tau, \xi) - \frac{\partial}{\partial \tau} \int_0^\infty \left\{ \frac{1 - a^2(\tau', \xi)}{2} \right\} \times [D(\tau', \xi + \tau - \tau') + D(\tau', \xi - \tau + \tau')] d\tau' \quad (1)$$

where  $a$  is a parameter which is related to the permittivity  $\epsilon(\tau, \xi)$  as:  $a^2(\tau, \xi) = \epsilon / \epsilon(\tau, \xi)$ . The initial values of permittivity and electrical flux density before parameter changing are  $\epsilon$  and  $D_0(\tau, \xi) = \epsilon E_0(\tau, \xi)$ . For the numerical solution of (1) we assume a uniform grid on the coordinate plane  $(\tau, \xi)$  with equal time  $\Delta\tau$  and spatial  $\Delta\xi$  steps:  $\Delta\tau = \Delta\xi$ . This equality is met with the stability condition for the numerical analysis:  $\Delta x \leq v\Delta t$ , where  $v$  is velocity of light in the medium. The integration paths in equation (1) are then straight diagonal lines, which pass through nodes of the grid. The essence of the proposed methodology is the sequential solution of (1) by marching in time, step by step [6].

## IV. DISCUSSION OF NUMERICAL EXAMPLES

The numerical investigations are carried out for propagation of a square 0.8 ps width TEM optical pulse with  $\lambda_0 = 15 \mu\text{m}$  through the moving Bragg grating. In normalised coordinates the incident signal has the form:

$$E_0(\tau, \xi) = \frac{1}{\pi} \{ \arctan(-50[\tau - \xi - 100]) + \arctan(50[\tau - \xi - 1]) \} \cos\left(\frac{k(\tau - \xi)}{2}\right)$$

Fig. 2 shows the magnitude of the reflected signal versus time for a permittivity modulation coefficient  $A=0.025$ . The resulting backscattered pulse is above 1.2 ps and has a complicated envelope due to the transient-induced time and spatial variation of the medium's parameters. The magnitude spectrum of this solitary optical pulse is shown in Fig. 3. There are several spectral peaks between the main shifted frequency 204.8 THz and the initial one at 200 THz. The efficiency of wavelength conversion is not very high in this case (- 8.5 dB for magnitude).

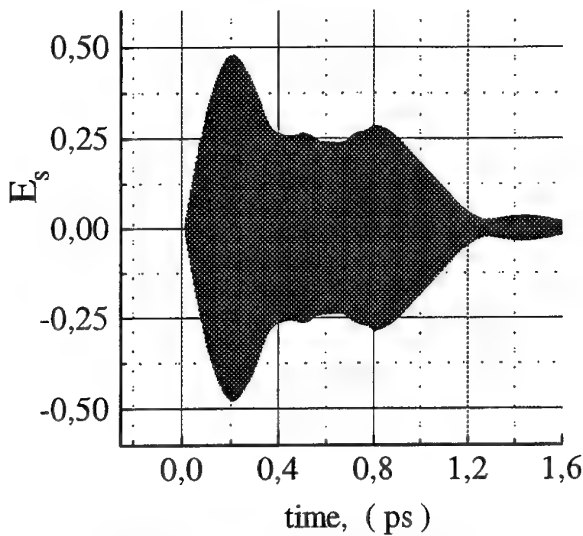


Fig. 2. The magnitude of the reflected signal vs. time for a permittivity modulation coefficient  $A=0.025$ .

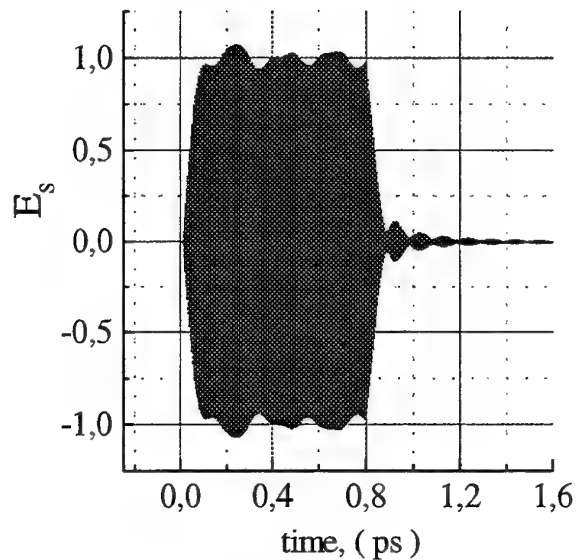


Fig. 4. The magnitude of the reflected signal vs. time for a permittivity modulation coefficient  $A=0.1$ .

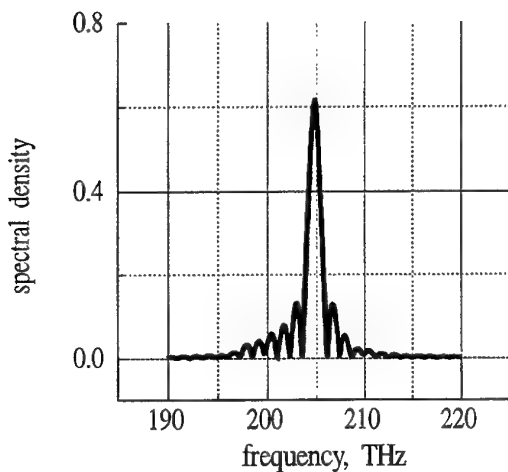


Fig. 3. The spectral density of this solitary optical pulse for a permittivity modulation coefficient  $A=0.025$ .

If we deal with a higher contrast moving Bragg grating we can get better results. For example, if the magnitude of permittivity modulation  $A=0.1$ , the output backscattered pulse has a better shape as shown in Fig. 4. The envelope of this pulse is also modulated at a low frequency, but the damping rate is satisfactory. The spectral density of this pulse is shown in Fig. 5 by a solid line, while the spectrum of the initial optical pulse is shown by dashed line. The converted peak corresponds to 204.8 THz and can be easily selected from the input signal. The conversion efficiency is satisfactory (- 3 dB).

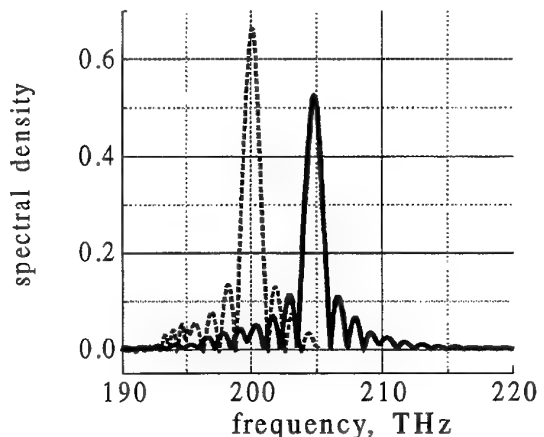


Fig. 5. The spectral density of this solitary optical pulse for a permittivity modulation coefficient  $A=0.025$ .

## V. SUMMARY

We have shown that the traveling Bragg grating of permittivity in a semiconductor medium with high drift carrier velocity can be used to implement double-Doppler wavelength converters. The time-domain model of an excited semiconductor medium is used to investigate a reflection of a  $15 \mu\text{m}$  0.8 ps optical pulse. Investigation of ultrafast electromagnetic transients using the integro-differential equation in time-domain shows that the conversion span in InAs semiconductor can gain 10 THz. The converted pulse width and

spectral density depend on the contrast of permittivity modulation.

#### ACKNOWLEDGMENT

This investigation is being carried out under a Royal Society/NATO postdoctoral fellowship awarded to Dr. Igor Scherbatko for joint research with the Institute of Microwaves and Photonics, School of Electronic and Electrical Engineering University of Leeds.

#### REFERENCES

- [1]. T. Durhuus, B Mikkelsen, C. Joergensen, S. Lykke Danielsen, and K.E. Stubkjaer, "All-Optical Wavelength Conversion by Semiconductor Optical Amplifiers," *J. of Lightwave Technol.*, vol. 14, pp. 942-953, June 1996.
- [2]. S.J.B. Yoo, "Wavelength Conversion Technologies for WDM Network Applications," *J. of Lightwave Technol.*, vol. 14, pp. 955-965 , June 1996.
- [3]. M. Lampe, E. Ott and J.H.Walker, "Interaction of electromagnetic waves with a moving ionization front," *Phys. Fluids* 21(1), Jan. 1978, pp. 42-54.
- [4]. E.R. Brown, J.R. Soderstrom, C.D. Parker, L.J. Mahoney, K.M. Molvar, and T.C. McGill, "Oscillations up to 712 GHz in InGa/AlSb resonant-tunneling diodes," *Appl. Phys. Lett.*, Vol. 58 (20), May 1991, pp.2291-2293.
- [5]. T.D. Visser, H. Blok, and D. Lenstra," Modal Analysis of a Planar Waveguide with Gain and Losses," *IEEE J. of Quantum Electron.*, v.31, pp.1803-1810, Oct. 1995.
- [6]. A.G. Nerukh , I. Scherbatko and O. Rybin, "The Direct Numerical Calculation of an Integral Volterra Equation for an Electromagnetic Signal in a Time- Varying Dissipative Medium,"*J. of Electromagn. Waves and Applications*, V. 12, pp.163-173, 1998.

# Modulated Impurity-Concentration InP-TEDs for Second-Harmonic Oscillators at 260 GHz

Rolf Judaschke and Klaus Schünemann

**Abstract**— InP transferred electron devices of various doping profiles have been theoretically investigated for fundamental- and harmonic-mode operation at frequencies up to 260 GHz. The results are based on an efficient and accurate hydrodynamic simulator which analyzes the device under impressed terminal voltage conditions and in practical oscillator circuits. In comparison with state-of-the-art graded profile diodes, improved performance is demonstrated for modulated impurity-concentration devices for both modes of operation. Especially for power generation above 200 GHz, the proposed modulated impurity concentration diodes are expected to be advantageous in comparison with IMPATT diodes.

**Keywords**— Gunn devices, harmonic-mode operation.

## I. INTRODUCTION

At millimeter-wave frequencies, there is a growing interest in low-noise solid-state oscillators for applications as transmitters in high-resolution radars, local oscillators, and drivers for multipliers. Typical state-of-the-art RF output power levels of different types of oscillators are depicted in Fig. 1. InP Gunn devices operating in the fundamental- and second-harmonic mode have shown to be suitable for the generation of low-noise oscillations at frequencies up to 170 GHz [3], [4]. However, the performance of Gunn oscillators at higher frequencies is still limited (e. g. less than 1 mW beyond 250 GHz [1], [2]). Thus, for power generation at frequencies above 170 GHz in most applications either multipliers or Silicon IMPATT oscillators are used where the latter exhibit poor phase noise characteristics. In this contribution, the performance of InP Gunn devices in both fundamental- and harmonic-mode operation is theoretically investigated. Special emphasis is attached to the influence of different doping profiles as well as the harmonic-mode driving voltage-to-phase relationship on the overall device performance.

## II. ACTIVE DEVICE MODEL

Due to the small characteristic device dimensions, non-stationary transport effects become significant in the millimeter-wave region. Hence, the drift-diffusion equations are often inappropriate and instead, hydrodynamic (HD) models or Monte Carlo (MC) methods are applied. However, the main drawback of the latter methods is their large computational effort. Thus, the hydrodynamic model is a compromise between accuracy and computational efficiency.

In the present work, a hydrodynamic device simulator

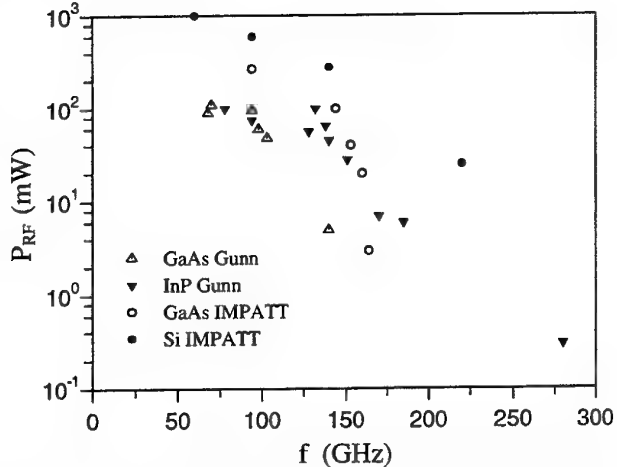


Fig. 1: CW output power of state-of-the-art millimeter-wave solid-state oscillators.

which carefully includes effects of thermal energy as well as diffusive heat flow [5] has been applied. Steady-state transport coefficients have been calculated by a MC code. The solution of the resulting system of partial differential equations is accomplished by a fully implicit, decoupled, yet unconditionally stable finite-difference scheme. Results of the present model closely agree with those of several MC simulations as well as with measured results of Gunn oscillators in the millimeter-wave region. In order to investigate the different device properties, extensive simulations are necessary. These are performed under impressed bias conditions at the device terminal according to

$$V(t) = V_0 + V_1 \sin(2\pi f_1 t) + V_2 \sin(2\pi f_2 t + \varphi).$$

## III. GUNN DEVICES

The individual doping profiles under investigation are shown in Fig. 2. Since the time required for the evolution of the electron charge instability is comparable to the average transit time, Gunn devices for fundamental-mode operation are limited in length to approximately 1  $\mu\text{m}$  which is the common active length of all devices in the present analysis. Furthermore, we assumed a linear increase of the doping density from cathode to anode in order to stimulate the electron charge instability to grow. As a modification of this graded doping profile which has been successfully designed, fabricated, and tested around 130 GHz in [3], a doping notch at the cathode and/or a doping mesa located in the center of the active region have been added. The former creates an above-threshold electrical field near the cathode which insures exclusive nucleation and launching of dipole layers from the cathode, whereas the latter results

R. Judaschke and K. Schünemann are with the Arbeitsbereich Hochfrequenztechnik, Technische Universität Hamburg-Harburg, Wallgraben 55, D-21071 Hamburg, Germany. E-mail: judaschke@tu-harburg.de

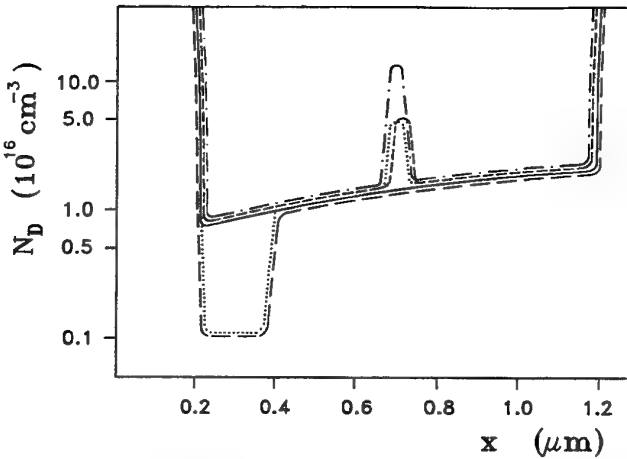


Fig. 2: Doping profiles under investigation: Graded profile (—) [1], cathode notch profile (—), mesa profiles (— · —), (— · — · —), combination of cathode notch and mesa profile (·····).

in a modulation of the strong fundamental current oscillation in order to produce a higher quantity of harmonic output power [6].

The diameter of the different devices is adjusted to result in equal DC-power dissipation of  $P_0 \approx 4.5$  W for given AC-conditions, and the device temperature is assumed to be  $T = 400$  K.

#### IV. RESULTS

For all the doping profiles of Fig. 2, both fundamental- and harmonic-mode simulations have been performed. Fig. 3 shows the RF power generation and device impedance for fundamental-mode operation under impressed terminal voltage conditions. Taking into account the inclusion of series losses, the output power for the graded profile (solid line) is in close agreement with the measured results in [3]. Furthermore, Fig. 3 clearly depicts the increase in RF power for the modified doping profiles which corresponds to an increase in efficiency up to 6 % at 120 GHz. The charge instability evolution over one period of oscillation for the graded profile and mesa profile, respectively, is illustrated in Fig. 4. In comparison, premature instability appearance can be observed for the mesa profile which is advantageous for efficient power generation. For harmonic-mode operation, power extraction at 260 GHz can be expected only in a limited range of the phase angle  $\varphi$ , as is shown in Fig. 5. Thus, a careful adjustment of the load impedance characteristic at both fundamental and harmonic frequency must be fulfilled in practical oscillator circuits. As an additional result, higher harmonic power levels are corresponding with mesa profiles, the harmonic device resistance of which is larger in magnitude in comparison with that of the graded profile. This is an important result since series losses due to bulk resistance and skin effect are responsible for a dramatic degradation of the power generation capability at frequencies above 150 GHz. The charge instability evolution in

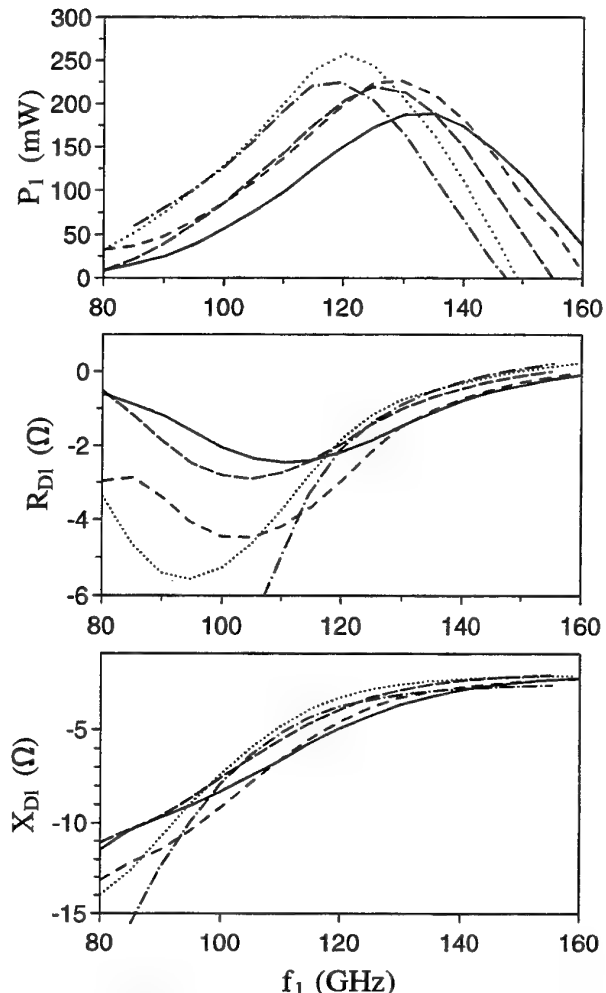


Fig. 3: Fundamental-mode operation,  $V_0 = 4.5$  V,  $V_1 = 2.0$  V, doping profiles as defined in Fig. 2.

Fig. 6 indicates that the dipol layer is modulated as it drifts through the doping mesa. This property confirms the appearance of a higher quantity of harmonic output power. Finally, Fig. 7 compares graded and mesa profile devices as a function of the 2nd-harmonic voltage  $V_2$ .

#### V. CONCLUSIONS

InP Gunn devices of various doping profiles have been theoretically investigated for fundamental- and harmonic-mode operation at frequencies up to 260 GHz. The results are based on an efficient and accurate hydrodynamic simulator which analyzes the device under impressed terminal voltage conditions. In comparison with state-of-the-art graded profile diodes, improved performance is demonstrated for modulated impurity-concentration devices for both modes of operation.

#### ACKNOWLEDGMENT

The authors are indebted to M. Curow for helpful discussions and to D. Liebig for supplying the steady-state transport coefficients.

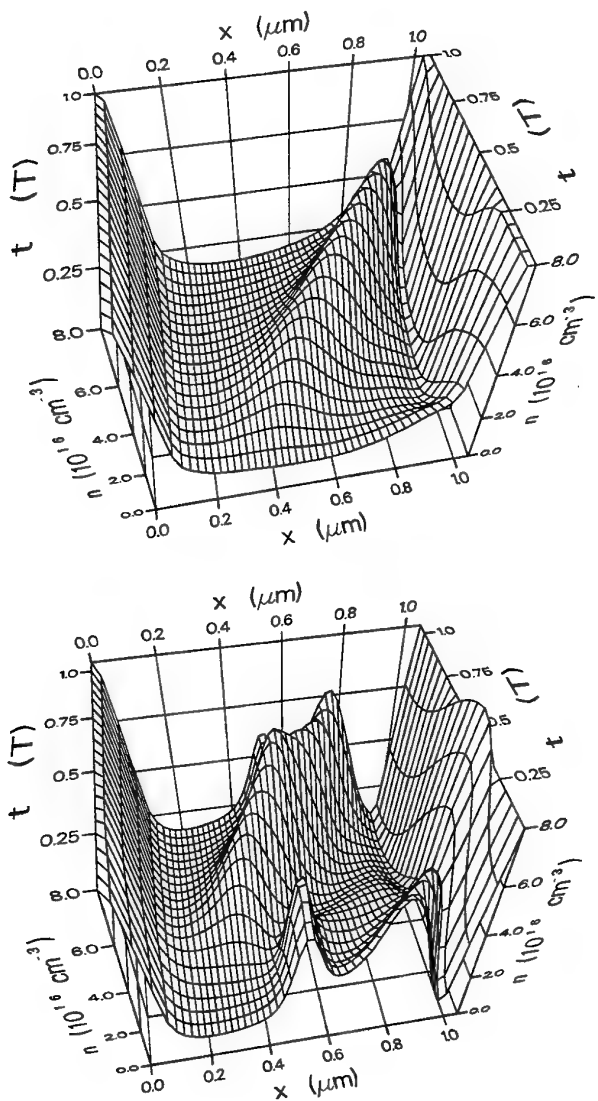


Fig. 4: Electron density evolution over one period for graded profile (— Fig. 2) [1] (upper plot) and mesa profile (--- Fig. 2) (lower plot), fundamental-mode operation,  $V_0 = 4.5$  V,  $V_1 = 2.0$  V.

#### REFERENCES

- [1] H. Eisele, G. I. Haddad, "D-band InP Gunn devices with second-harmonic power extraction up to 290 GHz," *Electronics Letters*, vol. 30, No. 23, Nov. 1994, pp. 1950-1951.
- [2] A. Rydberg, "High Efficiency and Output Power from Second- and Third-Harmonic Millimeter-Wave InP-TED Oscillators at Frequencies above 170 GHz," *IEEE Electron Device Letters*, vol. EDL-11, Oct. 1990, pp. 439-441.
- [3] H. Eisele, G. I. Haddad, "High-Performance InP Gunn Devices for Fundamental-Mode Operation in D-Band (110-170GHz)," *IEEE Microwave and Guided Wave Letters*, vol. 5, Nov. 1995, pp. 385-387.
- [4] J. D. Crowley et al. "140 GHz Indium Phosphide Gunn Diode," *Electronics Letters*, vol. 30, No. 6, Mar. 1994, pp. 499-500.
- [5] M. Curow, "Konsistente Simulation von Millimeterwellen-Oszillatoren mit Gunn-Elementen und IMPATT-Dioden," Ph. D. thesis, Technical University of Hamburg-Harburg, Hamburg, Germany, Mar. 1996.
- [6] S. H. Jones, G. B. Tait, M. Shur, "Modulated-Impurity-Concentration Transferred-Electron Devices Exhibiting Large Harmonic Frequency Content," *Microwave and Optical Technology Letters*, vol. 5, No. 8, Jul. 1992, pp. 354-359.

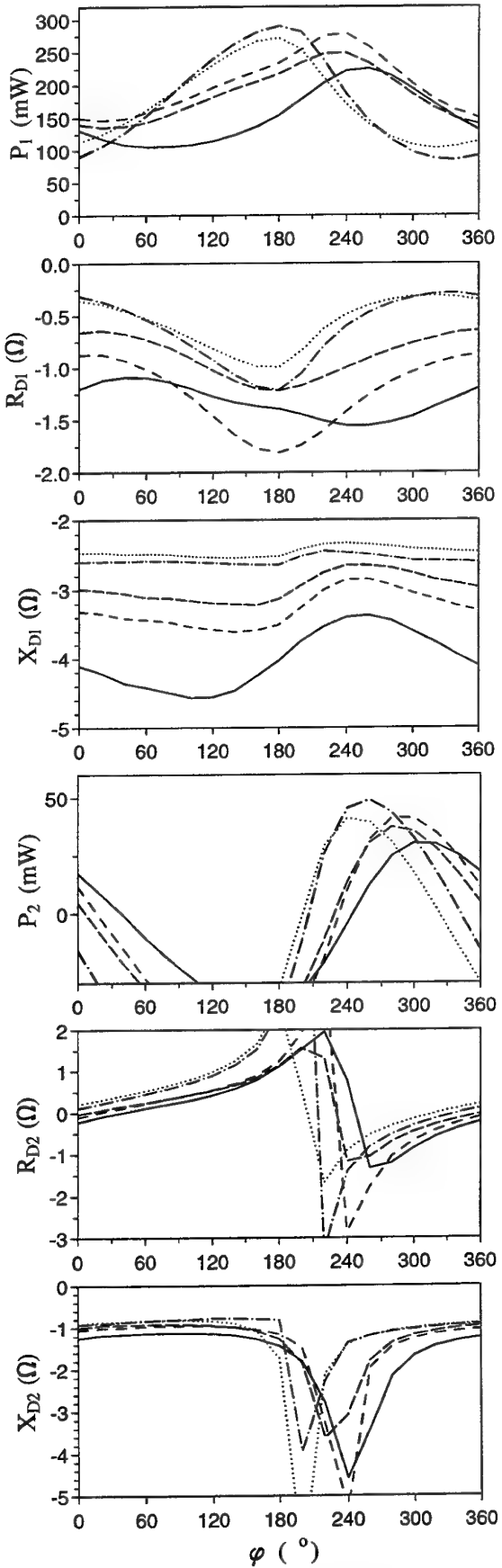


Fig. 5: Harmonic-mode operation  $f = 130/260$  GHz,  $V_0 = 4.5$  V,  $V_1 = 2.0$  V,  $V_2 = 0.5$  V, doping profiles as defined in Fig. 2.

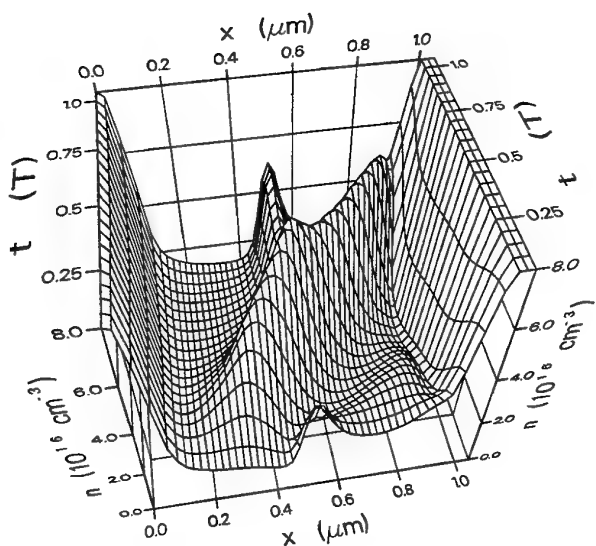


Fig. 6: Electron density evolution over one period for mesa profile (— Fig. 2), harmonic-mode,  $V_0 = 4.5$  V,  $V_1 = 2.0$  V,  $V_2 = 0.5$  V,  $\varphi = 260^\circ$ .

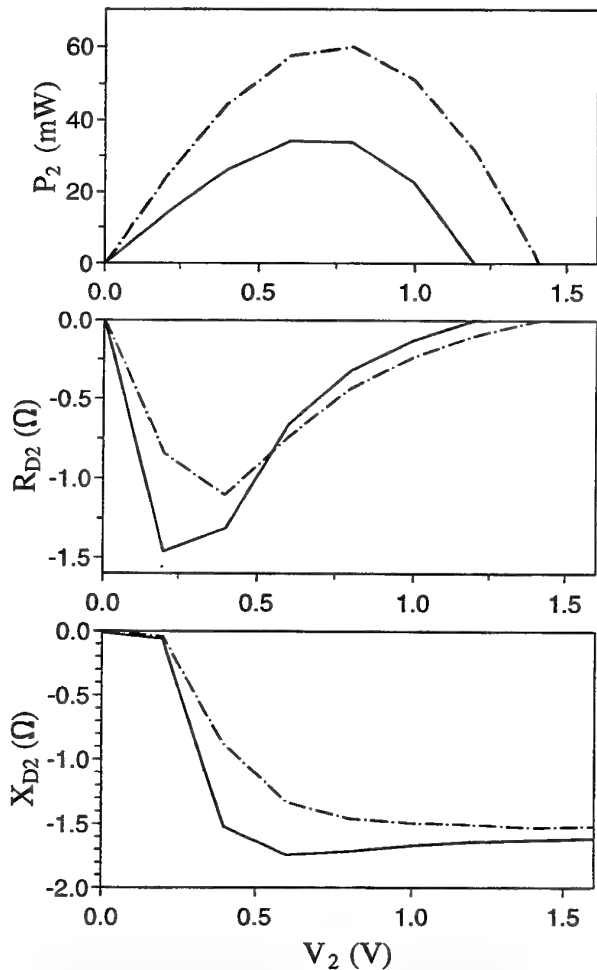


Fig. 7: Harmonic-mode operation  $f = 130/260$  GHz,  $V_0 = 4.5$  V,  $V_1 = 2.0$  V, graded profile (— Fig. 2)  $\varphi = 290^\circ$ , mesa profile (— Fig. 2),  $\varphi = 260^\circ$ .

# Millimetre Wave / Microwave Power Combining from Arrays of Resonant Tunnelling Diodes Defined by *In-situ* Focused Ion Beam Lithography

P. See, C. E. Collins, D. D. Arnone, D. P. Steenson, E. H. Linfield, P. D. Rose, D. A. Ritchie and G. A. C. Jones

**Abstract**—Single and planar arrays of embedded high current density resonant tunnelling diodes (RTDs) with a common emitter and collector electrical connection have been successfully fabricated. This was achieved through a novel technique combining *in-situ*  $\text{Ga}^+$  focused ion beam (FIB) lithography with molecular beam epitaxy (MBE) regrowth. In these devices, the tunnel current path is defined by and confined to regions intentionally left undamaged by the implantation. The ability to fabricate and contact an array of RTDs has a potential impact in realising millimetre wave / microwave power combining applications at terahertz frequencies. Room temperature DC and preliminary *s*-parameter results are presented here for individual and arrays of RTDs produced using this method.

**Index Terms**—resonant tunnelling diodes, arrays, *in-situ* fabrication, focused ion beam lithography, power combining

## I. INTRODUCTION

Double barrier resonant tunnelling diodes (RTDs) have been demonstrated to be the fastest solid state device, operating as a fundamental mode oscillator at 712 GHz, but only emitting modest amounts of millimetre wave / microwave power ( $\sim \mu\text{W}$ ) in the terahertz frequency range [1]. These oscillators are usually very small (sub-10  $\mu\text{m}$  in diameter), non-planar etched pillars ( $\sim 1 \mu\text{m}$  high) so as to minimise capacitance and heating effects. Larger power output (up to 5 mW at 1.18 GHz) has been achieved by combining the power from microscopic arrays of individual devices operating in a single circuit [2]. However, the fabrication of such small area ( $< 100 \mu\text{m}^2$ ) high current density RTDs and electrical connections to each individual pillar-shaped etched mesa is not easy using conventional optical lithographic methods. For example, firstly, the empty regions between each isolated, free-standing structure must be filled with an insulating material. The

deposited insulator is then planarised, ideally levelled with the top surface of the mesa. Often, this is achieved by an ‘etch-back’ technique, leaving the top ohmic contact exposed to allow electrical connections, thus avoiding any need for accurate alignment in the subsequent lithographic stages. The reliability and performance in such an array (as well as the yield) may be very poor because the exposed double barrier tunnel region and the highly  $n^{++}$  doped grown ohmic layer are easily degraded during fabrication.

All these technical difficulties can be minimised, and even avoided, through a combination of *in-situ* focused ion beam (FIB) lithography and molecular beam epitaxy (MBE) regrowth when producing the actual semiconductor wafer itself. The post-growth device fabrication is relatively straightforward and the integrity of the heterojunctions preserved, being embedded and surrounded by highly insulating lattice-matched regions. A significant advantage then occurs since the characteristic resonant tunnelling current is only depended on areas intentionally left undamaged, independent of the large etched mesa, that also provides lower resistance than obtained conventionally. Moreover, this approach allows a common (emitter and collector) bias connection to an array of embedded RTDs with potentially better heat sinking, reliable circuit matching and accurate device modelling. Thus, improved heat dissipation for structures with peak current densities greater than 50  $\text{kA/cm}^2$  can be easily realised by using these microscopic arrays. This is crucial for operation in the terahertz frequency range. Furthermore, this technique offers the possibility of producing planar emission devices that do not rely on separate connections to individual RTDs for coupling radiation out of it. Another advantage is its compatibility with current integrated circuit design rules and geometry.

The overall feasibility of this novel fabrication scheme is investigated here and demonstrated to be successful. Room temperature DC measurements were performed on a single and an array of FIB RTDs with peak current density of  $\sim 5 \text{kA/cm}^2$ . High frequency *s*-parameter characterisation (up to 30 GHz) was carried out on a more suitable higher current density ( $\sim 20 \text{kA/cm}^2$ ) wafer for single embedded RTDs and the preliminary results are reported here.

P. See, E. H. Linfield, P. D. Rose, D. A. Ritchie and G. A. C. Jones are with the Semiconductor Physics Group, Cavendish Laboratory, University of Cambridge, Madingley Road, Cambridge CB3 0HE, UK.

C. E. Collins and D. P. Steenson are with the Institute of Microwaves and Photonics, Department of Electrical and Electronic Engineering, University of Leeds, Leeds LS2 9JT, UK.

D. D. Arnone is with the Toshiba Cambridge Research Centre Ltd., 260 Cambridge Science Park, Milton Road, Cambridge CB4 4WE, UK.

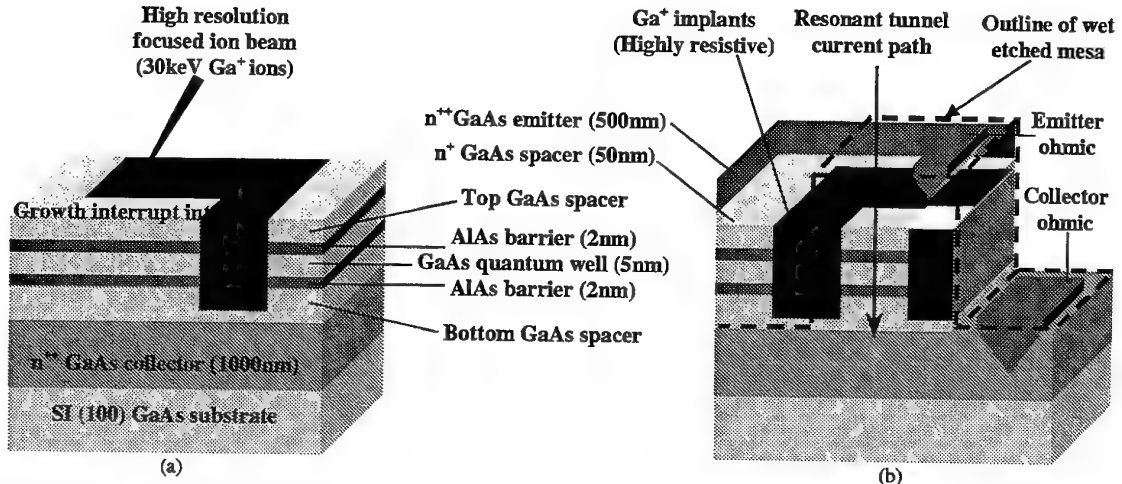


Fig. 1. Schematic cross-section of the FIB RTD (a) during  $\text{Ga}^+$  ion implantation (after the MBE growth interrupt) and (b) after MBE regrowth, including an outline of the large etched mesa, with emitter and collector ohmic contacts. The bottom spacer consists of 100 nm  $n^+$  GaAs followed by 5 nm undoped GaAs, whilst the top is 5 nm undoped GaAs, then 50 nm  $n^+$  GaAs.

## II. GROWTH, FABRICATION AND CHARACTERISATION

High current density double barrier AlAs/GaAs/AlAs RTD semiconductor wafers were produced by MBE growth on a semi-insulating (100) GaAs substrate (Figure 1(a)) [3]. This undoped substrate (as opposed to  $n^+$ ) provided reduced parasitic capacitance, better thermal radiation properties and suited planar device layout (compatible with other integrated circuits). Epitaxial growth commenced with a thick (1  $\mu\text{m}$ ) and highly  $n^{++}$  Si doped (nominally  $\sim 2 \times 10^{18} \text{ cm}^{-3}$ ) GaAs buffer-cum-collector, providing a smooth interface transition from the substrate to the subsequent layers. Following this was a ‘two-layered spacer’ – 100 nm lightly doped ( $\sim 2 \times 10^{16} \text{ cm}^{-3}$ )  $n^+$  GaAs, then a very thin 5 nm undoped GaAs layer. The purpose was to improve the characteristics of the device [4]. Next, double barrier resonant tunnelling junctions were formed and the MBE growth interrupted after 50 nm of the lightly doped  $n^+$  GaAs spacer above it. The wafer was then transferred to a FIB lithography unit via ultra high vacuum interconnected tubes. All chambers in the combined MBE / FIB facility had base pressures  $< 10^{-9} \text{ mbar}$ , thus minimising any possible contamination. Selected areas on the wafer (Figure 1(a)) were targeted with high energy (30 keV) finely focused (resolution  $\sim 0.2 \mu\text{m}$  diameter)  $\text{Ga}^+$  ions (dose  $\sim 5 \times 10^{12} \text{ ions/cm}^2$ ) at normal incidence to the wafer. This room temperature implantation and lateral patterning induced lattice disruption within the crystal, thus rendering the ion irradiated regions highly insulating [5]. These ions penetrate well past the AlAs/GaAs/AlAs double barrier [6], consequently leaving the non-exposed areas to form the intended tunnel junctions in the RTD. After implantation, the wafer was returned to the MBE chamber and another 50 nm  $n^+$  GaAs spacer followed by a low resistance 500 nm  $n^{++}$  GaAs emitter layer regrown over the top of the structure (Figure 1(b)).

Post-growth, standard optical lithography was used to concurrently produce both FIB and control RTDs in five

processing stages. First, the maximum vertical tunnel path was defined by wet chemical etching a mesa structure part-way into the  $n^{++}$  collector. Next layered Ni/AuGe/Ni/Au ohmic metals were evaporated and annealed lightly into the doped emitter and collector. Each device was then further isolated electrically from the others with a deep etch into the undoped GaAs substrate. Finally, insulated areas were formed to prevent any stray interactions between the external contacts leading up to the emitter and collector ohmic metals. These large probe pads were formed by NiCr/Au metallisation. For all the FIB defined RTDs and the ordinary wet etched control devices  $\geq 100 \mu\text{m}^2$ , the emitter contact was sufficiently large to allow four-terminal DC measurements. Two- and four-terminal DC current-voltage ( $I$ - $V$ ) characteristics were measured at room temperature on a pulsed curved tracer by direct probing with sharp gold alloy micro-needles. Preliminary one port (S11) high frequency (45 MHz to 30 GHz)  $s$ -parameter characterisations were performed using a network analyser via co-planar microwave probes on the ‘on-chip’ ground-signal-ground transmission lines leading up to the device. The collector in each device was shorted to the ground lines, providing  $50 \Omega$  impedance-matched termination.

## III. RESULTS AND DISCUSSIONS

Typical  $I$ - $V$  characteristics of an RTD are shown in Figure 2. As the applied bias on the collector becomes more positive (with the emitter earthed), the energy of incident electrons in the doped emitter gradually matches the quasi-bound state within the GaAs quantum well. At this threshold point, a resonant tunnelling current flows and grows with the applied potential until it reaches a maximum value (resonance condition). The current then ceases once this quasi-confined level comes out of alignment with the emitter conduction band (off-resonance state) [7]. Further increase in current beyond this valley is due to non-resonant components (inelastic scattering, thermionic emission, leakage, *etc.*). Oscillations in the negative differential

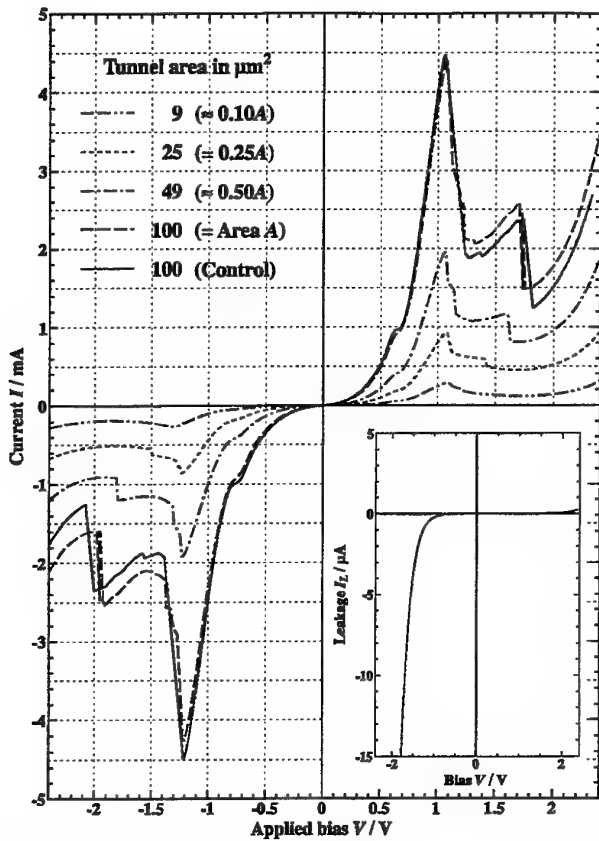


Fig. 2. Room temperature  $I$ - $V$  characteristics of a four-terminal  $100 \mu\text{m}^2$  control RTD (tunnel mesa defined by etching; continuous line) compared to FIB patterned devices (dotted and dashed lines) with different tunnel areas, embedded inside a  $400 \mu\text{m}^2$  etched mesa. (Implant dose  $\sim 5 \times 10^{12} \text{ Ga}^+ \text{ ions}/\text{cm}^2$ ). Devices biased with respect to the collector while the emitter remained grounded. The tunnel area for FIB devices is also expressed as a fraction of  $A$  ( $= 100 \mu\text{m}^2$ ). Inset shows the leakage current (in  $\mu\text{A}$ ) through a totally FIB damaged  $400 \mu\text{m}^2$  mesa within the device bias range.

conductance (NDC) regimes can be attributed to intrinsic bistability and external bias circuit instability [8]. The slight inflexion around  $0.65 \text{ V}$  arose from resonant tunnelling of electrons from the quantised two-dimensional levels formed in the accumulation (light and undoped) layer [9].

Conventionally defined (by wet etching the tunnel mesa) control RTDs showed symmetrical  $I$ - $V$  characteristics around the origin (Figure 2, continuous line) and high peak current density  $J_P$  ( $J_P = 4.5 \text{ kA}/\text{cm}^2$  at an applied potential  $V = 1.05 \text{ V}$ ). There was also a good peak-to-valley current ratio (PVCR = 4) over a wide NDC voltage range  $\Delta V_{\text{NDC}}$  ( $\Delta V_{\text{NDC}} = 0.75 \text{ V}$ ). All these observations indicated that the material quality was not affected by the MBE growth interrupt and transfers for the *in-situ* FIB lithography stage.

Figure 2 also includes the  $I$ - $V$  characteristics (dotted and dashed lines) for FIB patterned RTDs of different tunnel areas (nominally  $9$  to  $100 \mu\text{m}^2$  formed in large etched  $400 \mu\text{m}^2$  mesas). The irradiated regions in these devices were  $\sim 5 \times 10^{12} \text{ Ga}^+ \text{ ions}/\text{cm}^2$ . The peak / valley bias positions ( $1.05$  /  $1.80 \text{ V}$ , respectively) of the FIB RTDs aligned consistently and agree with the control device. Note also the near superposition of traces for the FIB defined and

control RTD with equal tunnelling area ( $100 \mu\text{m}^2$ ). These observations indicated that the ion implants do not adversely affect the energy band profile or the wafer structure.

Leakage current (Figure 2, inset) through a totally implanted  $400 \mu\text{m}^2$  mesa (no intended tunnel path) was negligible ( $< 20 \mu\text{A}$ , highly resistive) in the device operation range, without any signs of isolation breakdown. Since there is no conduction through the FIB implanted sites, this implied that the tunnel current must flow through the regions intentionally left undamaged. By accounting for the FIB defined tunnel area, the peak current density  $J_P$  of, for instance, the  $100 \mu\text{m}^2$  FIB RTD ( $J_P = 4.4 \text{ kA}/\text{cm}^2$ ) was in excellent agreement with the control ( $J_P = 4.5 \text{ kA}/\text{cm}^2$ ). It can also be noted that the peak tunnel current in FIB patterned devices scaled proportionally and consistently as a fraction of the area  $A = 100 \mu\text{m}^2$  (Figure 2). All these characteristics were further observed to be independent of the physical wet etched mesa size (from  $400$  to  $3600 \mu\text{m}^2$ ).

The effects of different  $\text{Ga}^+$  ion doses on the RTD were also investigated [3].  $I$ - $V$  characteristics for devices implanted with low or insufficient number of ions ( $< 5 \times 10^{11} \text{ ions}/\text{cm}^2$ ) were found to be dominated by additional leakage current (especially beyond the valley) through the large etched mesa that contained the embedded RTD. In this case, the tunnel current paths were not totally isolated or properly defined. However, a reduced peak current was observed in samples irradiated with very high dose ( $> 1 \times 10^{13} \text{ ions}/\text{cm}^2$ ). This was attributed to significant lateral ion straggling and depletion effects from the implantation. The induced lateral constriction, which increased with ion dose, effectively reduced the tunnelling area and led to current cut off at a finite geometrical size. For instance, the depletion width for an ion dose of  $\sim 1 \times 10^{13} \text{ ions}/\text{cm}^2$ , was estimated to be  $0.43 \mu\text{m}$ . The optimum  $\text{Ga}^+$  dose for implantation, as used here (with negligible leakage and reliable lateral resolution), was  $\sim 5 \times 10^{12} \text{ ions}/\text{cm}^2$ . Nevertheless, this does depend strongly upon the incident ion energy and position of the growth interrupt.

Preliminary  $s$ -parameter characterisation on devices from a different and more suitable, higher current density wafer ( $J_P \sim 20 \text{ kA}/\text{cm}^2$ ) indicated that the maximum 'cut-off' oscillation frequency for  $25 \mu\text{m}^2$  tunnel area FIB RTDs ( $\sim 18 \text{ GHz}$ , Figure 3(a)) rivalled the conventional wet etched control sample ( $\sim 20 \text{ GHz}$ , Figure 3(b)). Therefore, by implication, the extra shunt capacitance contributed by the large overlaid contact (on the  $400 \mu\text{m}^2$  mesa with the  $25 \mu\text{m}^2$  FIB RTD embedded inside) did not appear to reduce the measured 'cut-off' frequency in this case. More detailed measurements are currently being carried out.

(Here, the maximum 'cut off' frequency is defined as the point where the  $s$ -parameter trace for the device intercepted the unity gain circle on the Smith chart after initial de-embedding, but inclusive of a short transition coplanar waveguide length leading up to the device. Consequently, the actual 'cut-off' frequency is likely to be higher.)

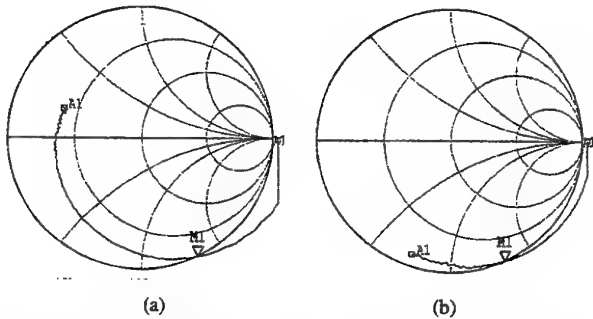


Fig. 3. One port *s*-parameter (S11) characterisation from 45 MHz to 26 GHz of (a) FIB defined RTD ( $25 \mu\text{m}^2$  tunnel area embedded inside a  $400 \mu\text{m}^2$  mesa) and (b) conventional wet etched tunnel mesa RTD ( $25 \mu\text{m}^2$ ). Maximum 'cut-off' frequency marker M1 (a)  $\sim 18$  GHz and (b)  $\sim 20$  GHz. (Device biased in the NDC regime, with the collector shorted to ground line.)

Independent and coherent resonant tunnelling were observed (in DC measurements) through each device (separated by the highly resistive irradiated areas) for arrays of RTDs fabricated using this technique [3]. The total current flowing in an array of FIB RTDs equalled the sum through each individual device. It was also noted that these characteristics were independent of the device configuration and separation in the array, without any detrimental effects from the ion implanted regions. Moreover, the insulating lattice sites should improve thermal dissipation in high current density microscopic arrays, crucial for devices operating at terahertz frequencies. Current summation supports the feasibility of power combining when the circuit is under the correct matched conditions. Further investigations on the interaction between individual RTDs and the optimum device arrangement for maximum power coupling to the external circuit are necessary.

#### IV. CONCLUSIONS

Single and planar arrays of small tunnel area RTDs (down to  $< 10 \mu\text{m}^2$ ) with a common emitter and collector connection have been successfully fabricated using a combined *in-situ*  $\text{Ga}^+$  FIB lithography and MBE regrowth technique. Such structures are often very difficult to achieve with standard optical lithographic methods. The characteristic resonant tunnelling features observed were not affected by the surrounding resistive lattice regions induced by the ion implants. Furthermore, the current was determined to flow solely through the areas intentionally left undamaged, independent of the large wet etched mesa that held the embedded tunnel junctions. Both the DC and AC characteristics of these FIB RTDs were comparable to conventional devices produced by wet etching the tunnel mesa. There were also no excessive parasitic effects from this large mesa at high frequencies. All these observations suggest that the FIB patterned array of RTDs can be adopted to demonstrate power combining applications in the terahertz frequency range. Furthermore, this co-planar fabrication method is suitable and compatible with current microwave and millimetre wave integrated circuits.

#### ACKNOWLEDGEMENT

The authors would like to acknowledge partial funding from the Engineering and Physical Sciences Research Council (UK). E. H. Linfield and D. A. Ritchie acknowledge the support from the Isaac Newton Trust and the Toshiba Cambridge Research Centre respectively.

#### REFERENCES

- [1] E. R. Brown, J. R. Soderström, C. D. Parker, L. J. Mahoney, K. M. Molvar and T. C. McGill, "Oscillations up to 712 GHz in InAs/AlSb resonant tunnelling diodes," *Appl. Phys. Lett.*, vol. 58, pp. 2291-2293, 1991.
- [2] K. D. Stephan, S. C. Wong, E. R. Brown, K. M. Molvar, A. R. Calawa and M. J. Manfra, "5 mW Parallel connected resonant tunnelling diode oscillator," *Electron. Lett.*, vol. 28, pp. 1411-1412, 1992.
- [3] P. See, E. H. Linfield, D. D. Arnone, P. D. Rose, D. A. Ritchie and G. A. C. Jones, "*In-situ*  $\text{Ga}^+$  focused ion beam definition of high current density resonant tunnelling diodes," *J. Vac. Sci. Technol. B*, to be published Nov. / Dec. 1998.
- [4] C. I. Huang, M. J. Paulus, C. A. Bozada, S. C. Dudley, K. R. Evans, C. E. Stutz, R. L. Jones and M. E. Cheney, "AlGaAs/GaAs double barrier diodes with high peak-to-valley current ratio," *Appl. Phys. Lett.*, vol. 51, pp. 121-123, 1987.
- [5] K. Nakamura, T. Nozaki, T. Shiokawa, K. Toyoda and S. Namba, "Formation of high resistance region in GaAs by Ga focused ion beam implantation," *Jpn. J. Appl. Phys.*, vol. 24, L903-904, 1985.
- [6] E. H. Linfield, G. A. C. Jones, D. A. Ritchie and J. H. Thompson, "The fabrication of a back-gated high electron mobility transistor - A novel approach using MBE regrowth on an *in-situ* ion beam patterned epilayer," *Semicond. Sci. Technol.*, vol. 8, pp. 415-422, 1993.
- [7] L. L. Chang, L. Esaki and R. Tsu, "Resonant tunnelling in semiconductor double barriers," *Appl. Phys. Lett.*, vol. 24, pp. 593-595, 1974.
- [8] V. J. Goldman, D. C. Tsui and J. E. Cunningham, "Observation of intrinsic bistability in resonant tunnelling structures," *Phys. Rev. Lett.*, vol. 58, pp. 1256-1259, 1987; T. C. L. G. Sollner, "Comment on 'Observation of intrinsic bistability in resonant tunnelling structures,'" *Phys. Rev. Lett.*, vol. 59, pp. 1622-1623, 1987.
- [9] J. S. Wu, C. Y. Chang, C. P. Lee, K. H. Chang, D. G. Liu and D. C. Liou, "Resonant tunnelling of electrons from quantised levels in the accumulation layer of double barrier heterostructures," *Appl. Phys. Lett.*, vol. 57, pp. 2311-2312, 1990.

# A Theoretical Study of Quantum Well Terahertz Lasers

K. Donovan, P. Harrison, R. W. Kelsall and P. Kinsler

*Abstract*—A theoretical study is made of a GaAs/AlGaAs triple quantum well structure with the aim of developing a three level laser to emit in the terahertz region of the spectrum. The population inversion necessary for laser emission to take place is estimated by calculating the net non-radiative transition rates. It is found that the most effective way of achieving a population inversion is by depopulation to a strongly coupled state. The population inversion can be increased further by decreasing the barrier width between the quantum wells associated with the two lowest energy levels.

**Keywords**— Quantum well, laser, subband, terahertz, population inversion

## I. INTRODUCTION

OPTICAL emission can be generated from unipolar solid state sources by electron transitions between discrete states, or subbands [1]. In a semiconductor quantum well cascade laser, the subbands are localised within quantum wells separated by barriers. Intersubband transitions may be radiative; i.e. result in the emission of a photon, or non-radiative, such as electron-longitudinal optical phonon(e-LO) scattering, or electron-electron (e-e) scattering. The emission frequency of the laser can be manipulated by engineering the energy separation of the subbands.

There have been recent successes in the development of intersubband emitters operating in the mid-infrared (4-12  $\mu\text{m}$ ) region [2]. High power quantum cascade lasers with mW outputs have been reported and output powers as high as 1W have been observed in interminiband superlattice lasers at room temperature [3]. This opens up the possibility of extending the output wavelengths of quantum cascade lasers into the far-infrared or terahertz region of the spectrum (30-300  $\mu\text{m}$  or 1-10 THz). The small energy spacings required for terahertz emission (1-10 THz corresponds to 4-41 meV) can be provided by a compact solid state source based on GaAs technology [4].

The laser structure studied in this work is based on a GaAs/AlGaAs triple quantum well active region. In this structure, the 3 levels shown in Fig. 1 represent quantum confined subbands, one in each well, with the radiative transitions between the second and third subbands.

## II. THEORY

Standard rate equation analysis gives the change in population of level  $|2\rangle$  as the difference between the rate at which it is populated by carriers and the rate at which

K. Donovan, P. Harrison, R. W. Kelsall and P. Kinsler are with the Institute of Microwaves and Photonics, School of Electronic and Electrical Engineering, University of Leeds, LS2 9JT, U.K. Tel: +44 (0)113 233 2043, Fax: +44 (0)113 233 2032. E-mail: phykd@sun.leeds.ac.uk

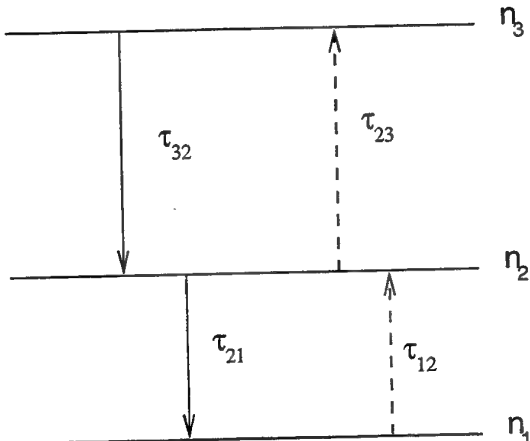


Fig. 1. Schematic diagram of energy levels in a 3-level laser.

they leave, i.e.

$$\frac{dn_2}{dt} = \frac{n_3}{\tau_{32}} - \frac{n_2}{\tau_{21}} \quad (1)$$

where the  $n_i$  are the level populations, and the  $\tau_{ij}$  are the inter-level transition lifetimes.

At equilibrium  $\frac{dn_2}{dt} = 0$ , hence if  $\tau_{32} > \tau_{21}$ , then  $n_3 > n_2$ ; i.e. a population inversion will exist, which is a necessary condition for lasing action. In other words, the lower laser level must be depopulated faster than it is repopulated [5]. A specific range of wavelengths in the 1-10 THz region is required, so this imposes limitations on the intersubband energy separation.

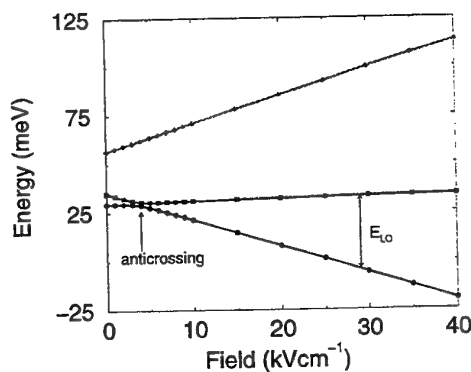


Fig. 2. Subband separation as a function of field.

For intersubband transitions in a quantum well structure, the non-radiative processes are much faster than the

radiative processes, and are therefore the most important in calculations of population inversion. The principal non-radiative transitions are electron-longitudinal optical phonon (e-LO) and electron-electron (e-e) scattering. Depopulation of level  $|2\rangle$  can be achieved in two ways [6]. The first is by resonant LO phonon transitions, where the energy separation between subbands 1 and 2 is engineered to be exactly equal to an LO phonon energy. A second method is to place another energy level in close proximity to the lower laser level, with the similar aim of increasing the transfer rate. One way to engineer this in a semiconductor heterostructure is to make the lower laser level the upper of a pair of subbands at an anticrossing.

The triple quantum well chosen for this work allows both of these methods to be studied at the same time. Three GaAs quantum wells of widths 56.5 Å (left hand well), 96.05 Å (central well) and 84.75 Å (right hand well) were separated by  $\text{Ga}_{0.8}\text{Al}_{0.2}\text{As}$  barriers of width 56.5 Å. The electric field dependence of the 3 confined levels is shown in Fig. 2. The anticrossing between subbands 2 and 1 occurs at a field of 4 kVcm $^{-1}$ , and the subband separation is equal to the GaAs LO phonon energy of 36 meV at a field of 29 kVcm $^{-1}$ . The energy band diagram of the triple quantum well is shown in Fig. 3, along with the wavefunctions at the anticrossing.

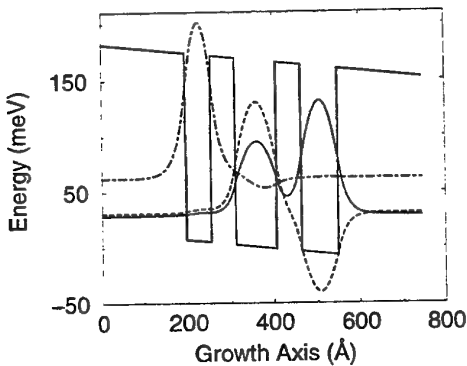


Fig. 3. Schematic diagram of the triple quantum well structure and wavefunctions at the anticrossing: Electric field = 4 kVcm $^{-1}$ .

Non-radiative transition rates were calculated between subbands 3 $\rightarrow$ 2 and 2 $\rightarrow$ 1 at 300K. However, because of the close proximity of subbands 2 and 1, absorption of carriers from 1 to 2 was significant. In fact the transition rate from 1 $\rightarrow$ 2 is about 85% of the emission transition rate from 2 $\rightarrow$ 1. Scattering of electrons from subbands 2 to 3 also takes place, but is not as significant as that from subbands 1 to 2. Nonetheless, an exact solution of the subband populations for this system requires simultaneous solution of the rate equations for all 3 subbands. This solution must be iterated to self-consistency since the subband lifetimes  $\tau_{ij}$  are themselves functions of the subband populations. However, in this work, since we know that the populations in the three subbands of the undoped active region will all be similar, we can obtain an estimate of the population

ratio using the net  $|3\rangle \rightarrow |2\rangle$  and  $|2\rangle \rightarrow |1\rangle$  transition rates:

$$\frac{n_3}{n_2} \sim \frac{\left(\frac{1}{\tau_{21}} - \frac{1}{\tau_{12}}\right)}{\left(\frac{1}{\tau_{32}} - \frac{1}{\tau_{23}}\right)} \quad (2)$$

It must be appreciated that this is no more than a first order approximation, but one which serves the purpose of the present study: i.e., to explore the feasibility of designing quantum cascade structures which can operate as lasers in the THz frequency range. A more sophisticated treatment to follow will include a self-consistent solution of the rate equations.

The barrier width between the central and right hand quantum wells was then reduced in two monolayer intervals from 56.5 Å to a width of 28.25 Å. Non-radiative transition rates were calculated at the anticrossing (which remained close to  $F=4$  kVcm $^{-1}$ ) for six different barrier widths, and the population ratios were determined for each case.

### III. RESULTS AND DISCUSSION

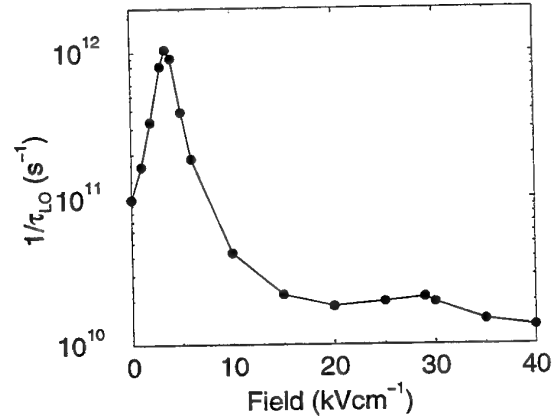


Fig. 4. Electron-LO phonon scattering rate from  $|2\rangle \rightarrow |1\rangle$ .

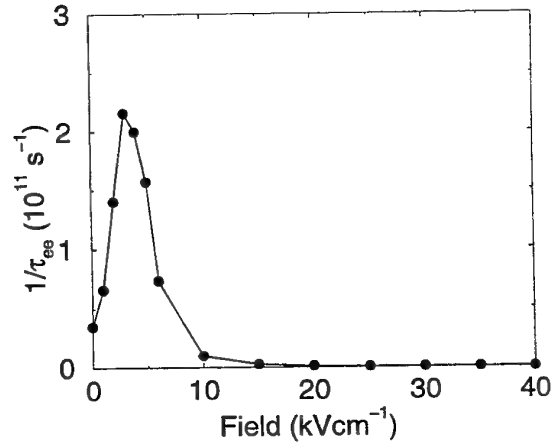


Fig. 5. Electron-electron scattering rate from  $|2\rangle \rightarrow |1\rangle$ .

It can be seen that both the e-LO (Fig. 4) and the e-e (Fig. 5) transition rates peak at the anticrossing, and that

the e-LO rate is a factor of 5 greater than the e-e rate at this field. There is also a small peak in the e-LO emission rate at a field of  $29 \text{ kVcm}^{-1}$ , where resonant LO phonon emission takes place for a subband separation of 36 meV. However, the resonant e-LO emission rate is almost two orders of magnitude less than the e-LO emission rate at the anticrossing.

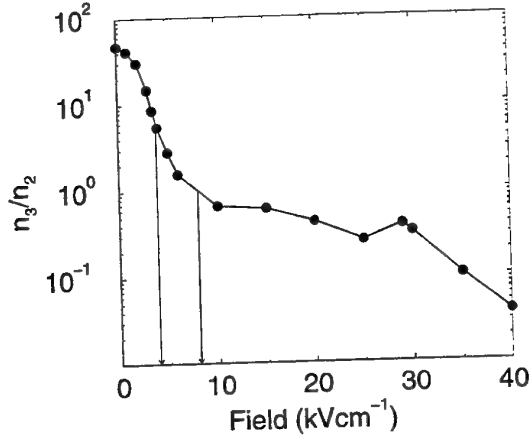


Fig. 6. Population inversion as a function of field. The viable operating range of the device is indicated by the arrows.

Fig. 6 demonstrates that a population inversion  $n_3/n_2 > 1$  can exist at low fields. In addition, Fig. 6 gives the expected operating range of the device; from the subband anticrossing, with  $n_3/n_2 \sim 5$ , to  $F=8 \text{ kVcm}^{-1}$ , where  $n_3/n_2$  falls below 1. Tunable emission is therefore possible from 39-33  $\mu\text{m}$ . At fields below the anticrossing the population ratio is high, but real space ordering of the energy levels prevents optical transitions between subbands 3 and 2 (the wavefunction associated with subband 3 is localised in the left hand well and wavefunction associated with subband 2 is primarily localised in the right hand well; see Fig. 3). Optical transitions can only take place when the wavefunction associated with subband 2 becomes primarily localised in the central well. This occurs at a field of  $4 \text{ kVcm}^{-1}$ .

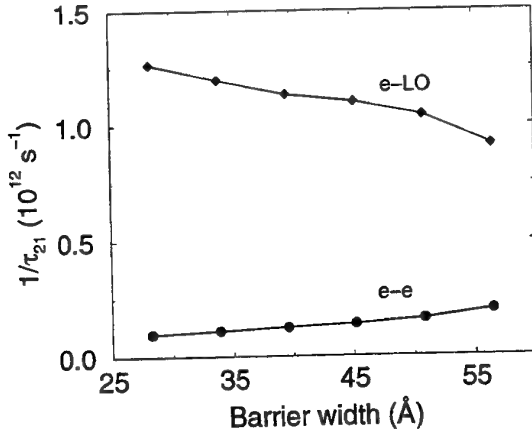


Fig. 7. Electron-LO phonon and electron-electron transition rates as a function of barrier width.

Fig. 7 shows the variation of electron-LO phonon and electron-electron transition rates from subbands 2→1 with the width of the barrier between the central and right hand wells. It can be seen that the e-LO rate decreases as the barrier width is increased, while the e-e rate increases. This behaviour is explained by Fig. 9, which shows the energy difference,  $\Delta E$ , between subbands 1 and 2 versus the barrier width.  $\Delta E$  increases as the barrier width is reduced, so the elastic electron-electron transitions require a larger momentum transfer and are therefore less favourable. Conversely, such a process increases the scattering rate of the inelastic LO phonon emission. This is because a larger proportion of thermally broadened carrier population in subband 2 has sufficient energy to emit an optical phonon [7].

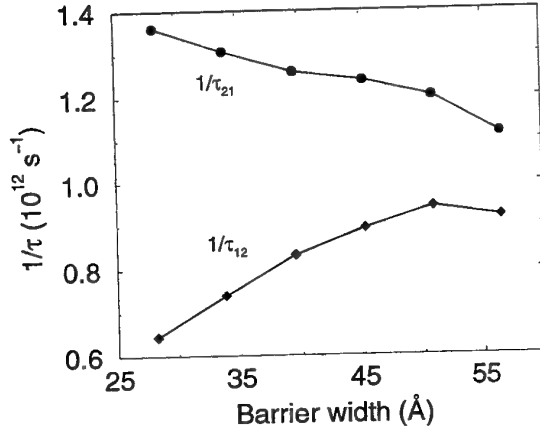


Fig. 8. Transition rates between subbands 1 and 2 as a function of barrier width.

The total transition rates between subbands 1 and 2 are shown in Fig. 8. The 2→1 rate is greater for small barrier widths and decreases as the barrier is widened, whereas the 1→2 rate increases. The former is simply the sum of the rates in Fig. 7 and has been explained. However, for 1→2 transitions both components (e-LO and e-e) increase, due to the smaller momentum changes required.

The result of this structural optimization is that the population ratio increases as the barrier width is reduced, as illustrated in Fig. 10, and that a population inversion of up to 30 can be achieved for a barrier width of 28.25 Å. This is due to the increasing 'net' depopulation rate for subband 2 given by the difference between the curves in Fig. 8.

#### IV. CONCLUSIONS

It has been demonstrated that terahertz emission can be generated by quantum well systems, which provide the required energy level, or subband, separation. A 3 level triple quantum well system has been proposed which could be employed as a possible laser source. Calculation of the electron lifetimes in each level has shown that a population inversion could be engineered in this system. The population inversion can be further increased by reducing the barrier width between the central and right hand quantum wells.

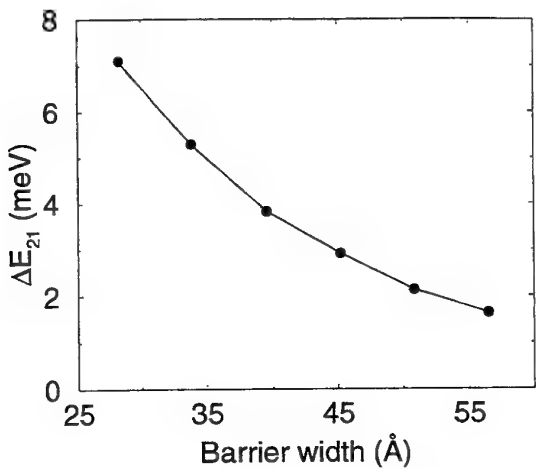


Fig. 9. Energy difference between levels 2 and 1 at the anticrossing, as a function of barrier width.

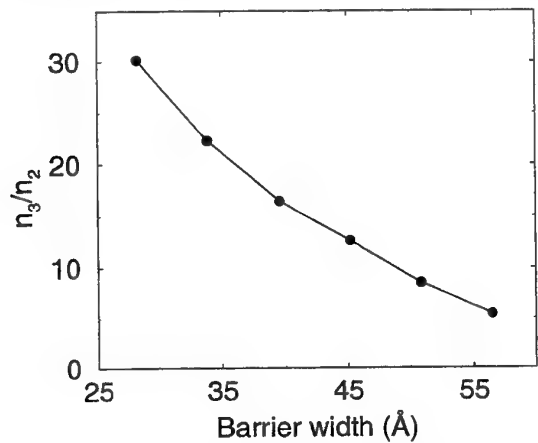


Fig. 10. Population ratio as a function of barrier width.

#### REFERENCES

- [1] J. Faist, F. Capasso, D. L. Sivco, C. Sirtori, A. L. Hutchinson, A. Y. Cho, *Science* **264**, 553 (1994)
- [2] J. Faist, F. Capasso, C. Sirtori, D. I. Sivco, A. L. Hutchinson and A. Cho, *Appl. Phys. Lett.* **67**, 3057 (1995)
- [3] G. Scamarcio, F. Capasso, C. Sirtori, J. Faist, A. L. Hutchinson, D. L. Sivco, and A. Y. Cho, *Science* **276**, 773 (1997)
- [4] P. Harrison, *Semicond. Sci. Technol.* **12**, 1487 (1997)
- [5] K. Donovan, P. Harrison, P. Kinsler and R. W. Kelsall, *Superlatt. Microstruct. to be published*
- [6] P. Harrison and R. W. Kelsall, *Solid State Electronics* **42**, 1449 (1998)
- [7] P. Harrison, R. W. Kelsall, P. Kinsler and K. Donovan, this volume

# THz Emission from Parabolically Graded Quantum Wells in Tilted Magnetic Fields

R. Zobl, M. Fuchshuber, G. Strasser, K. Unterrainer, E. Gornik, K. D. Maranowski, and A. C. Gossard

**Abstract**--We investigate THz emission from electrically excited GaAs quantum structures with parabolic potential shapes under the action of a magnetic field. Coupling of the intersubband plasmon to the cyclotron resonance gives a characteristic mode anticrossing. The magneto dispersion relation for the mode splitting at different tilt angles of the magnetic field is found to be in good agreement with theory.

**Index terms**-- THz emission, parabolic quantum well, magneto-plasmon

## I. INTRODUCTION

The new state of the art in MBE growth technique enabled the fabrication of parabolically graded potential wells based on GaAs/AlGaAs material systems. Parabolic quantum wells (PQWs) with remote doping in the barriers were originally proposed to create the so called jellium, a wide and highly mobile quasi three-dimensional slab of electrons. The completely homogeneous carrier density in this slab is solely determined by the designed curvature of the well.

While sophisticated features predicted for the jellium such as spin density waves and Wigner crystallization so far have not been really attacked, PQWs were thoroughly investigated because of their model character for low dimensional (2D, 1D, 0D) quantum structures, which are often described in terms of parabolic potentials.

PQWs were intensively studied in transmission experiments that soon included magnetoabsorption measurements [2]-[4]. (For a review on PQWs see ref. [1]). Recently, also emission in the FIR from intersubband plasmons in these parabolic quantum wells was reported [5]. This paper extends the emission experiments to measurements of the magnetodispersion for different tilt angles of the magnetic field.

## II. THE GENERALIZED KOHN THEOREM AND MAGNETO-PLASMONS

Parabolic wells absorb and emit FIR radiation only at the bare harmonic oscillator frequency  $\omega_0$  according to eq. (1):

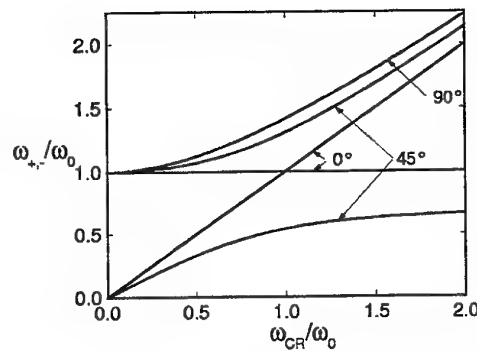


Fig. 1. Calculated resonance positions of the modes  $\omega_+$  and  $\omega_-$  for parabolic potentials in tilted magnetic fields. The mode degeneracy is lifted for a non-zero tilt angle and the anticrossing gap of the coupled harmonic oscillators is a function of this tilt angle only.

$$\omega_0 = \sqrt{\frac{8\Delta}{L^2 m^*}} \quad (1)$$

where  $\Delta$  is the energetic depth of the well,  $L$  is the well width, and  $m^*$  is the effective mass. This is the (generalized) Kohn theorem, originally derived for cyclotron resonance (CR) [6] and later applied to intersubband resonance (ISR) plasmons in PQWs [7], which states that in purely harmonic potentials optical transitions are only related to a center of mass motion of the electrons [8] and are completely independent of electron-electron interactions. The emission frequency, thus, is completely controlled by the grown well curvature. Note from (1) that in PQWs the ISR plasmon coincides with the bulk plasmon.

Resonant coupling of the ISR mode to the CR mode appears when the PQW is subject to tilted magnetic fields, leading to a characteristic anticrossing, which is well known from interacting harmonic oscillators. The problem can be treated analytically [9],[10] and leads to the following expression for the magnetodispersion of the two modes:

$$\omega_{\pm} = \sqrt{\frac{1}{2}(\omega_{CR}^2 + \omega_0^2) \pm \frac{1}{2}\sqrt{\omega_{CR}^4 + \omega_0^4 - 2\omega_{CR}^2\omega_0^2 \cos 2\theta}} \quad (2)$$

where  $\theta$  is the tilt angle of the magnetic field. The dispersion is plotted in Fig. 1 for the three different tilt angles used in our experiments (0°, i.e. Faraday configuration, 90°, i.e. Voigt configuration and an intermediate angle of 45°).

R. Zobl, M. Fuchshuber, G. Strasser, K. Unterrainer, and E. Gornik are with the Institute for Solid State Electronics, Vienna University of Technology, A-1040 Vienna, Austria.

K. D. Maranowski and A. C. Gossard are with the Materials Department, University of California, Santa Barbara, CA 93106, USA.

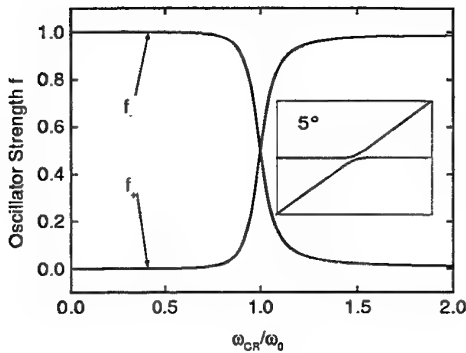


Fig. 2. Calculated oscillator strength for both modes at very small tilt angles (5°, see insert).

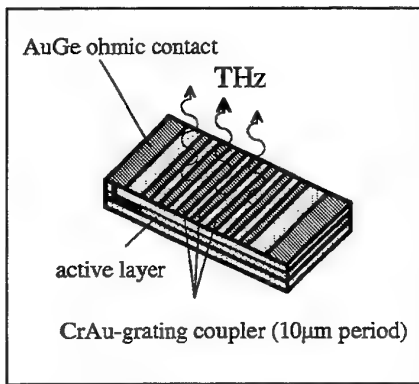


Fig. 3. Device geometry for lateral current injection. The emissive area is approximately 5x5 mm<sup>2</sup>.

Oscillator strengths are also easily calculated. Fig. 2 shows the calculated oscillator strengths for  $\omega_+$  and  $\omega_-$  at small tilt angles. Note from Fig. 1 and Fig. 2, that the overall behaviour of the emission at  $B \neq 0$  for whatever tilt angle is always CR like. Only in the anticrossing region the two modes exchange oscillator strength and coexist at comparable intensities.

### III. SAMPLE DESIGN

Several different samples were grown in the MBE on semiconducting substrates and characterized by van der Pauw measurements as well as FTIR transmission experiments. The two best performing samples (KM210, G318) were chosen for the emission experiments. KM210 has a carrier concentration of  $2.7 \times 10^{11} \text{ cm}^{-2}$  and the mobility is 120 000 cm<sup>2</sup>/Vs. The well is 200 nm wide with a designed oscillator frequency of 1.5 THz. G318 has a carrier concentration of  $2.5 \times 10^{11} \text{ cm}^{-2}$  and a mobility of 40 000 cm<sup>2</sup>/Vs. The well is 76 nm wide for a designed ISR emission at 3 THz. A main difference is that KM210 incorporates vertical sidewalls, whereas the parabolic well of G318 is fully extended to the maximum  $x$  value of 0.3 % Al. Emission experiments on one of the samples (KM210) at zero magnetic field were previously reported in detail [5].

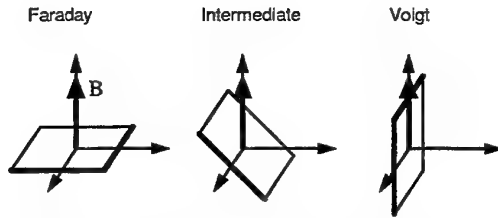


Fig. 5. The three provided orientations of the sample with respect to a magnetic field parallel to the  $z$  direction.

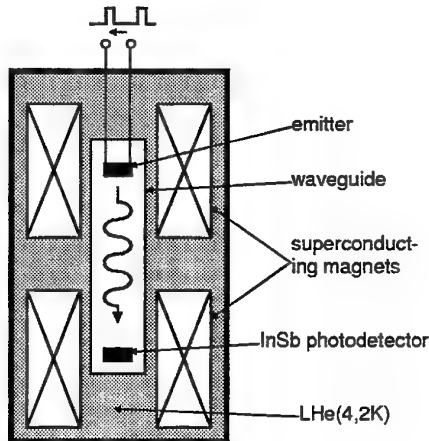


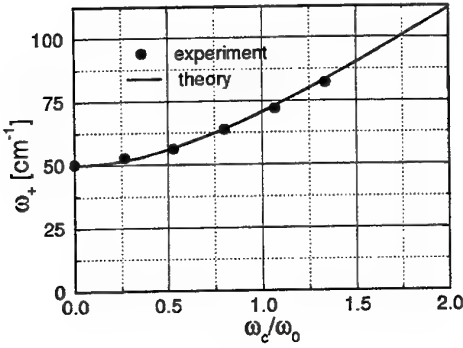
Fig. 4. Experimental setup.

CrAu grating couplers (Fig. 3) are used to couple out the intersubband emission, and two ohmic AuGe channel contacts are annealed for lateral current injection. Different grating periods were found to be without effect on the emission intensity, probably due to the closed cavity in our setup (see sec. IV).

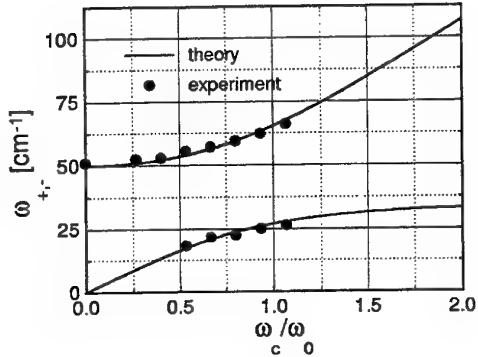
To complete our measurements a set of samples with a semitransparent NiCr layer just underneath the grating couplers was prepared, in order to deplete the well or cause some deformation to its potential shape by applying a gate voltage to the NiCr layer, just as described in [4]. Unfortunately, while this works fine in absorption experiments, no emission was observed, when a semitransparent gate was on top of the samples.

### IV. EXPERIMENTAL SETUP

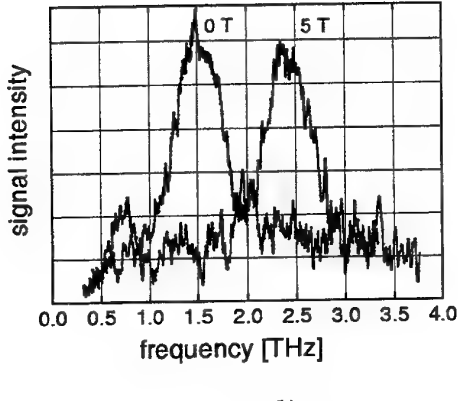
All measurements were performed in a liquid helium cryostat at 4.2 K (Fig. 4). Samples are positioned in the center of a superconducting magnet (5 T maximum). Three tilt angles were provided (Fig. 5). The generated THz radiation is guided to the detector via a polished brass pipe. Both ends of the pipe are closed up with polished brass, thus forming an integrating cavity. An InSb photoconductive detector is used. Tuning of the detector magnetic field tunes the spectral position of its CR absorption giving a spectrally narrow (10 cm<sup>-1</sup>) photocurrent signal from 0.5 THz up to 6 THz.



(a)



(a)



(b)

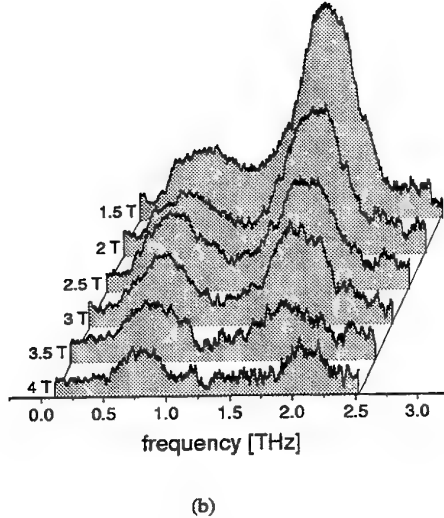
Fig. 6. Magnetodispersion of KM210 in Voigt geometry (a) and spectrum at 0 T and 5 T at the same input power level (b).

Not being limited by slow bolometer response times all samples were driven at repetition rates of more than 20 kHz at duty cycles of 50 %. The amplitude of the applied pulses was varied to give electric fields between 1 V/cm and 30 V/cm, thus covering almost two decades of output signal intensities.

## V. MEASUREMENT RESULTS

Applying magnetic fields at whatever tilt angles suppresses the intersubband emission from both samples even at low field values. Theory predicts the evolution of a strong cyclotron mode instead, which was also confirmed in absorption experiments, [2]-[4]. Therefore, as can also be seen from equation (2) and Fig. 2, strong emission from the  $\omega_+$  branch should be observed.

However, sample KM210 never develops any cyclotron like emission. In this sample compensating for the magnetoresistance with higher voltages to keep input power levels reasonably high irreversibly scatters electrons out of the well (a complete warmup of the sample is needed to recover the original carrier concentration in the well). The loss of carriers, however, gives an additional proof of the Kohn theorem: after one cycle from 0 T to 5 T and back to 0 T, the number of



(b)

Fig. 7. Magnetodispersion of KM210 at intermediate tilt angle (45°),(a), and corresponding spectral emission intensities (b).

electrons in the PQW is considerably reduced without affecting the spectral position of the zero field emission. Intensity, of course, is reduced.

Emission results for KM210, thus, are only obtained at very low input power levels (5 mW) to avoid the escape of electrons, and therefore exhibit very low signal levels. Emission peak positions for all three tilt angles are in good agreement with theory, as seen in Fig. 6(a) and Fig. 7(a). In Voigt configuration there is only the  $\omega_+$  mode, as expected. Its relative peak shift of more than 60 % at 5 T is plotted in Fig. 6(b). Fig. 7(b) shows both modes at the intermediate tilt angle around the isthmus of the anticrossing, where they coexist at comparable intensities, as predicted by the theory.

Results for G318, measured at much higher input power levels (50 mW), are given for Faraday configuration. In contrast to KM210, strong CR emission is found (Fig. 8). At 45° tilt angle the cyclotron like  $\omega_+$  mode still dominates over a much smaller  $\omega_+$  mode up to 5 T (Fig. 9), the minimum gap of

## ACKNOWLEDGMENTS

We acknowledge financial support by the Austrian Science Foundation (FWF, START Y47) and the Gesellschaft fuer Mikroelektronik (GME).

## REFERENCES

- [1] A. Wixforth, M. Kaloudis, C. Rocke, K. Ennslin, M. Sundaram, J. H. English, and A. C. Gossard, "Dynamic response of parabolically confined electron systems", in *Semicond. Sci. Technol.*, vol. 9, pp. 215-240, Mar. 1994.
- [2] K. Karrai, H. D. Drew, M. W. Lee, and M. Shayegan, "Magnetoplasma effects in a quasi-three-dimensional electron gas", in *Phys. Rev. B*, vol. 39, pp. 1426-1429, Jan. 1989.
- [3] K. Karrai, X. Ying, H. D. Drew, and M. Shayegan, "Collective cyclotron resonance in a quasi-three-dimensional electron gas", in *Phys. Rev. B*, vol. 40, pp. 12020-12023, Dec. 1989.
- [4] A. Wixforth, M. Sundaram, K. Ennslin, J. H. English, and A. C. Gossard, "Dimensional resonances in wide parabolic quantum wells", *Phys. Rev. B*, vol. 43, pp. 10000-10003, Apr. 1991.
- [5] K. D. Maranowski, A. C. Gossard, K. Unterrainer, and E. Gornik, "Far-infrared emission from parabolically graded quantum wells", in *Appl. Phys. Lett.*, vol. 69, pp. 3522-3524, Dec. 1996.
- [6] W. Kohn, "Cyclotron resonance and de Haas-van Alphen oscillations of an interacting electron gas", in *Phys. Rev.*, vol. 123, pp. 1242-1244, Aug. 1961.
- [7] L. Brey, N. F. Johnson, and B. I. Halperin, "Optical and magneto-optical absorption in parabolic quantum wells", in *Phys. Rev. B*, vol. 40, pp. 10647-10649, Nov. 1989.
- [8] S. K. Yip, "Magneto-optical absorption by electrons in the presence of parabolic confinement potentials", *Phys. Rev. B*, vol. 43, pp. 1707-1718, Jan. 1991.
- [9] J. C. Maan, "Combined electric and magnetic field effects in semiconductor heterostructures", in *Two Dimensional Systems: Heterostructures and Superlattices*, G. Bauer et al., Eds, Berlin: Springer, pp. 183-191, 1984.
- [10] R. Merlin, "Subband-Landau-level coupling in tilted magnetic fields: exact results for parabolic wells", *Solid State Commun.*, vol. 64, pp. 99-101, 1987.

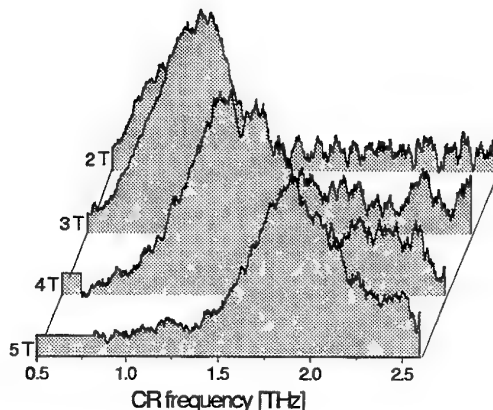


Fig. 8. Pure cyclotron resonance spectra of G318 in Faraday configuration.

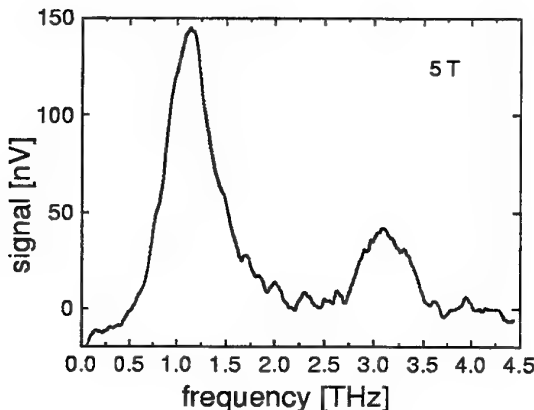


Fig. 9. Spectrum of G318 at 5 T for intermediate tilt angle.

the anticrossing being beyond reach of our setup for this sample.

Under no conditions an escape of carriers from the well was observed when measuring G318. This probably has to be attributed to the fact that G318 in contrast to KM210 has no vertical sidewalls.

## VI. CONCLUSIONS

The magneto dispersion was found in agreement with theory. Strong emission in the cyclotron like regions encourages further experiments in crossed electric and magnetic fields, most interestingly on parabolic p-type quantum wells. Future experiments also should include a determination of the emission strength of the 2D plasmon.

# Large Signal Theory of Plasma Electronics Terahertz Detector.

G. Samsonidze <sup>1</sup>, S. Rudin <sup>2</sup>, and M. S. Shur <sup>3</sup>

**Abstract--**We present the results of the numerical simulation of the terahertz detectors based on High Electron Mobility Transistors (HEMTs). Our results show that the dynamic range of these plasma wave electronics devices is determined by the sheet electron concentration in the channel (in agreement with an analytical theory). As the amplitude of the ac signal applied to the detector increase, the detector responsivity decreases. Also, the fundamental plasma frequency decreases somewhat, and additional responsivity peaks appear at subharmonics of the fundamental frequency in high mobility structures. These results are important for the design of plasma electronics detectors of terahertz radiation.

**Index Terms--**Plasma Wave Electronics, High Electron Mobility Transistor, terahertz radiation, detector

## I. INTRODUCTION

Recent theoretical <sup>1</sup> and experimental results <sup>2</sup> show that terahertz radiation can excite plasma waves in High Electron Mobility Transistors (HEMTs). Hence, HEMTs can be used as resonant plasma wave detectors of terahertz radiation. The sensitivity of such detector has peaks at the plasma frequency and its odd harmonics. The plasma frequency,  $f_p$ , is approximately given by

$$f_p(\text{THz}) = 0.1 U_{gt}^{1/2} (m_e/m)^{1/2} / L,$$

where  $U_{gt}$  is the gate voltage swing in Volts,  $L$  is the gate length in microns,  $m_e$  is the free electron mass, and  $m$  is the electron effective mass. As can be seen from Eq. (1), the resonant HEMT detector can operate in the frequency range from a fraction of a terahertz to ten terahertz or even higher. The detector responsivity is determined by the quality factor  $\omega_p \tau_p$ , where  $\omega_p = 2\pi f_p$  and  $\tau_p$  is the momentum relaxation time. The analytical theory <sup>1</sup> predicts that the responsivity is proportional to  $(\omega_p \tau_p)^2$  and can exceed typical responsivities of Schottky diode detectors by several orders of magnitude. However, the analytical theory is only valid for a small-signal excitation, since it relies on the expansion to the second order of the

basic semiconductor equations. Hence, that theory cannot predict the detector dynamic range, which is determined by the responsivity dependence on the excitation intensity. This characteristic allows us to determine the detector applications. Also, this dependence can be used as a calibration curve in order to estimate the absolute value of the detector responsivity from the measurement data. In this paper, we report on computer simulations of the large-signal detector response. Based on numerical solutions of the basic hydrodynamic equations describing the two-dimensional electronic fluid in a HEMT, we compute the dependencies of the detector responsivity on the excitation level for different gate lengths, electron mobilities, and gate biases. At small excitation levels, the results are in excellent agreement with the analytical theory. At higher excitation levels, the responsivity drops. The shape of the resonant frequency response changes. The deviation from the analytical theory is determined by the ratio  $\Delta n_s / n_s$ , where  $n_s$  is the sheet carrier concentration in the device (which is proportional to the gate voltage swing) and  $\Delta n_s$  is the variation of  $n_s$  induced by the electromagnetic radiation. At very high responsivities, the value of this parameter at which an exact numerical analysis is required might be quite small (just a few percent). The obtained results can be used in order to design both small-signal and large signal HEMT-based detectors of terahertz radiation.

As discussed in <sup>1</sup>, the basic equations describing the two dimensional electronic fluid are the relationship between the surface carrier concentration and gate voltage swing, the equation of motion, and the continuity equation. The surface concentration,  $n_s$  in the FET channel is given by

$$n_s = CU / e \quad (1)$$

where  $C$  is the gate capacitance per unit area,  $U = U_{gc}(x) - U_T$ ,  $U_{gc}(x)$  is the local gate-to-channel voltage. Eq. (1) represents the usual gradual channel approximation, which is valid, when the characteristic scale of the potential variation in the channel is much greater than the gate-to-channel separation,  $d$ .

The equation of motion (the Euler equation) is

$$\frac{\partial v}{\partial t} + v \frac{\partial v}{\partial x} + \frac{e}{m} \frac{\partial U}{\partial x} + \frac{v}{\tau} = 0 \quad (2)$$

<sup>1</sup> Ioffe Physical Technical Institute, St. Petersburg, Russia

<sup>2</sup> U.S. Army Research Laboratory, Adelphi, Maryland

20783

<sup>3</sup> Department of ECSE, Rensselaer Polytechnic Institute, Troy, NY 12180-3590

where  $U$  is the potential in the channel and  $v(x, t)$  is the local electron velocity, and  $m$  is the electron effective mass. (Here we account for electronic collisions with phonons and/or impurities by adding  $v/\tau$  term.) Eq. (2) has to be solved together with the usual continuity equation which (taking Eq. (1) into account) can be written as :

$$\frac{\partial U}{\partial t} + \frac{\partial(Uv)}{\partial x} = 0 \quad (3)$$

For the equivalent circuit shown in Fig. 1, the boundary conditions for the FET channel (for the detector mode of operation) are

$$U = U_0 + U_a \cos \omega t \quad \text{for } x = 0 \quad (4)$$

$$j = vU = 0 \quad \text{for } x = L \quad (5)$$

where  $U_{ac} = U_a \cos(\omega t)$  is the external ac voltage induced across the gate-to-channel capacitance by the incoming electromagnetic wave and  $j$  is the electron current.

The calculations were done for GaAs ( $m = 0.067 m_e$ ), for  $L = 0.1, 0.5, 2.0$ , and  $5.0 \mu\text{m}$  and for the low field electron mobilities of  $0.2, 0.8, 3.0, 6.0, 10.0 \text{ m}^2/\text{V}\cdot\text{s}$ .

Fig. 1 shows a schematic diagram of a HEMT detector. No external bias is applied between the source and drain, and the drain-to-source voltage,  $U_{ds}$ , is induced by the ac signal.

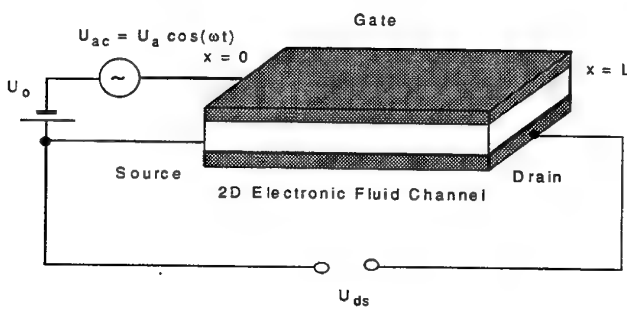


Fig. 1. Schematic diagram of HEMT detector.

Fig. 2 compares the results of the numerical calculations with the predictions of the analytical theory [1].

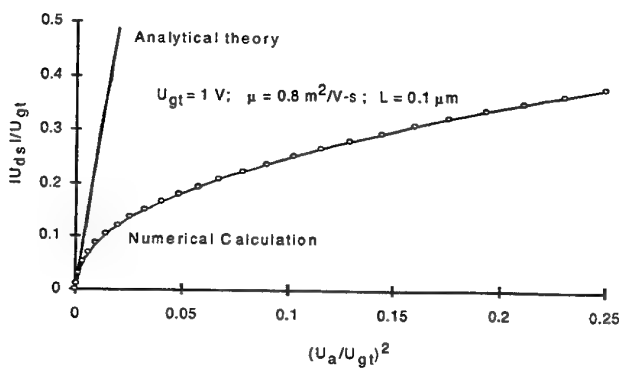


Fig. 2. Comparison of numerical calculations with the analytical theory.  $U_{gt} = U_0 - U_T$ , where  $U_T$  is HEMT threshold voltage.  $\mu$  is the low field mobility.

As can be seen from the figure, the agreement is excellent at small values of the ac signal amplitude,  $U_a$ . However, once  $U_a$  exceeds approximately 10% of  $U_{gt}$ , the detector response,  $U_{ds}$ , becomes a sublinear function of  $U_a^2$ . This corresponds to a dramatic drop in the detector responsivity. Very similar results were obtained for all values of  $L$  and  $m$ . The ratio  $U_a/U_{gt}$  is equal to  $\Delta n_s/n_s$ , where  $n_s$  is the sheet electron concentration in the channel,  $\Delta n_s$  is the amplitude of the variation of  $n_s$  in response to the applied ac signal. Hence, the numerical simulation confirms that the detector dynamic range is determined by the sheet carrier concentration in the channel. As shown in [1], the responsivity decreases with an increase of the gate voltage swing,  $U_{gt}$ . However, our numerical calculations show that the dynamic range increase with an increase of  $U_{gt}$ .

Fig. 3 illustrates the shift of the fundamental frequency of the plasma waves with an increase of the ac signal amplitude.

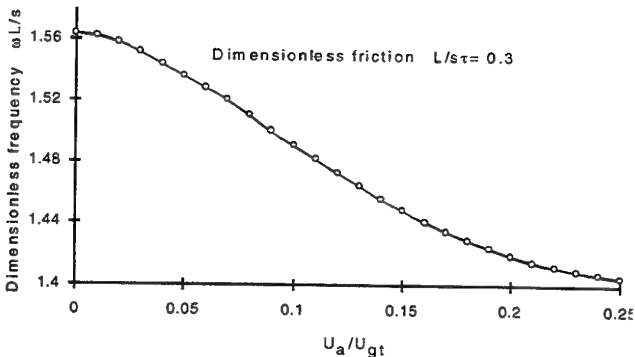


Fig. 3. Plasma frequency versus ac signal amplitude.

At low ac signals ( $U_a/U_{gt} < 0.01$ ), the computed plasma frequency (determined as the frequency corresponding to the peak of the detector responsivity plotted as a function of frequency) is very close to the value predicted by the analytical theory:

$$\omega_p = \pi s/2L$$

where  $s$  is the velocity of the plasma waves. However, this frequency decreases with an increase in the ac signal amplitude.

Fig. 4 shows the computed frequency dependencies of the detector responsivity for the fixed signal amplitude for different values of parameter  $\gamma = L/s\tau$ , where  $\tau$  is the momentum relaxation time. This parameter is the measure of the "friction" of the two-dimensional electron fluid in the HEMT channel. As can be seen from the figure, small additional responsivity peaks (not

predicted by the analytical theory) appear at subharmonics of the fundamental plasma frequency when  $\gamma$  is small.

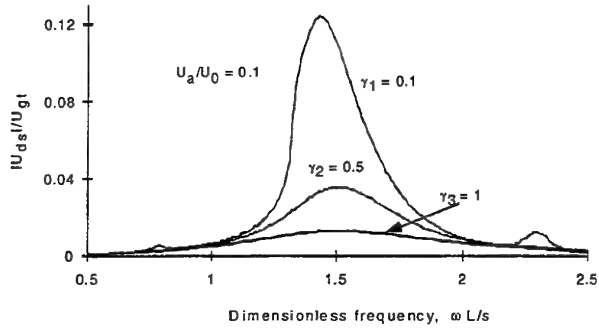


Figure 4. Detector response versus frequency for different values of dimensionless friction parameter,  $\gamma$ .

The deviation from the analytical theory also depends on the dimensionless friction,  $\gamma$  (see Fig. 5)

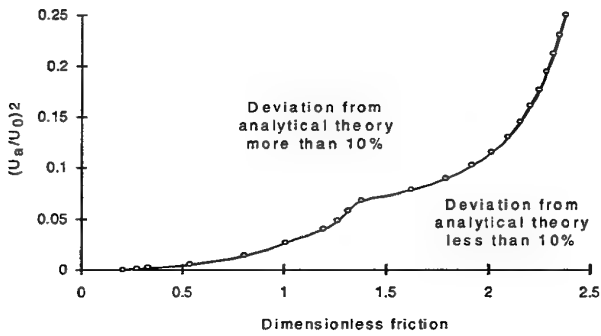


Fig. 5. Comparison between analytical theory [1] and computer simulations. Above the curve, the difference between the analytical theory and computer simulations is larger than 10%. Below the line, this difference is smaller than 10%.

At larger  $\gamma$ , the responsivity is smaller, and, therefore, the variation in the electron sheet density is smaller. Hence, the analytical theory becomes accurate in wider dynamic range.

The analytical theory predicts that the peak responsivity dramatically increases with an increase in the low field mobility. Our numerical simulations show that such an increase is limited to a small signal excitation. This is clearly illustrated by Fig. 6, which shows the computed detector response for the electron mobilities of  $10 \text{ m}^2/\text{V}\cdot\text{s}$ ,  $6 \text{ m}^2/\text{V}\cdot\text{s}$ ,  $3 \text{ m}^2/\text{V}\cdot\text{s}$ ,  $0.8 \text{ m}^2/\text{V}\cdot\text{s}$ , and  $0.2 \text{ m}^2/\text{V}\cdot\text{s}$ . As can be seen from the figure, at large signal amplitude, the effect of the electron mobility is greatly diminished.

Once again, we see dramatic differences between the numerical simulations and the analytical results<sup>1</sup> at very high responsivity values and a good agreement at small responsivity values.

In summary, the analytical theory<sup>1</sup> is in excellent agreement with our computer simulations when the variation of the electron sheet density in the device channel is less than approximately 10% of its dc value. At larger signal levels, we observe dramatic differences, such as a sharp drop in the device responsivity, a noticeable (about 10%) shift of the plasma frequency toward lower frequencies, and the appearance of additional responsivity peaks at the subharmonics of the plasma frequency.

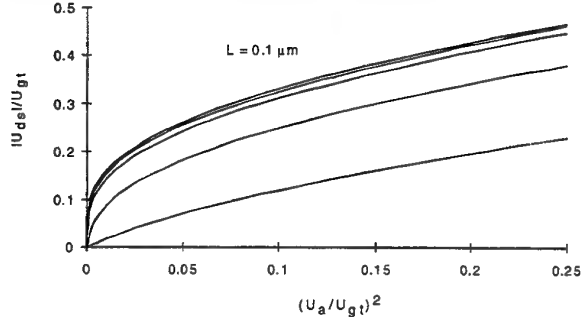


Fig. 6. Detector response versus signal amplitude for different values of low field mobility. The curves (from the top to the bottom) are for the electron mobilities of  $10 \text{ m}^2/\text{V}\cdot\text{s}$ ,  $6 \text{ m}^2/\text{V}\cdot\text{s}$ ,  $3 \text{ m}^2/\text{V}\cdot\text{s}$ ,  $0.8 \text{ m}^2/\text{V}\cdot\text{s}$ , and  $0.2 \text{ m}^2/\text{V}\cdot\text{s}$ , respectively.

Fig. 7 also illustrates this important result. This figure compares the computed detector response as a function of dimensionless friction,  $\gamma$ , with the analytical results (dashed lines) for three values of the ac signal amplitude ( $U_a/U_{gt} = 0.5$  (curves 1),  $U_a/U_{gt} = 0.3$  (curves 2), and  $U_a/U_{gt} = 0.1$  (curves 3)).

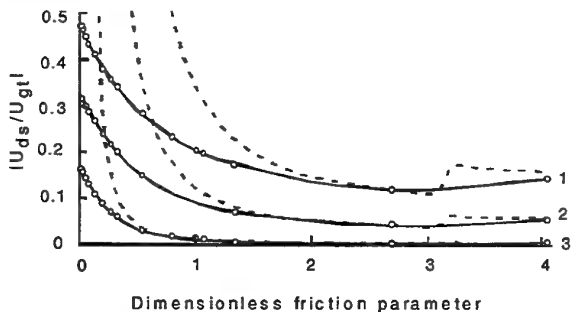


Fig. 7. Comparison of computed detector response as a function of dimensionless friction,  $\gamma$ , with analytical results (dashed lines) for three values of the ac signal amplitude ( $U_a/U_{gt} = 0.5$  (curves 1),  $U_a/U_{gt} = 0.3$  (curves 2), and  $U_a/U_{gt} = 0.1$  (curves 3)).

## References.

- [1] M. Dyakonov and M. Shur, "Detection, Mixing, and Frequency Multiplication of Terahertz Radiation by Two-Dimensional Electron Fluid", *IEEE Trans. Electron Devices*, vol. 43, pp. 380-387 (1996).
- [2] J.-Q. Lü, M. S. Shur, J. L. Hesler, L. Sun, and R. Weikle, "Terahertz Detector Utilizing Two-Dimensional Electronic Fluid," *IEEE Electron Device Letters*, vol. 19, No 7, October (1998)

# Enhanced Harmonic Generation at Terahertz Frequencies with a Two-Frequency Wiggler

Michael G Kong

Department of Electrical Engineering and Electronics, University of Liverpool, Liverpool L69 3GJ, UK

**Abstract**—It is known that a strong harmonic radiation from free electron laser (FEL) devices could lead to a significant reduction in the minimum electron energy required to generate radiation at a given frequency. However practical application of this technique to terahertz FELs has been hampered by the very weak strength of FEL radiation at high harmonics. In this paper, a two-frequency wiggler configuration is considered as a means to enhance the strength of FEL emission at high harmonics. It is shown that by adjusting the nonlinear interference between the two constituent components of the two-frequency wiggler the emission strength around the 10th harmonic can be increased considerably by two orders of magnitude. This characteristics can then be used to reduce the electron energy needed for terahertz radiation from 2.5MeV to below 500keV, thus reducing significantly size and cost of the eventual terahertz FEL system.

## I. INTRODUCTION

The development of terahertz electronics has recently commanded much attention, largely because of its potential to aid significant technological advance in many closely related disciplines such as remote sensing, semiconductor nanostructures, communications, and time-resolved spectroscopy[1]-[4]. One important issue in the field is to develop powerful, coherent, and tunable sources at terahertz frequencies and at present free electron lasers (FELs) are perhaps one of very few such sources. Characteristics commonly associated with free electron lasers are however large size, high cost, and complex designs. Although these characteristics are acceptable for an instrument built on the scale of a national laboratory, they preclude the acquisition of such an instrument by a single university department or research group. As a result, the benefit of the FEL to the progress of terahertz technology is limited. To relieve this limitation, new FEL concepts and interaction mechanisms must be derived so as to reduce its size and cost while maintaining its more desirable features such as tunability, coherence, and large power output.

Many of the FEL's undesirable features stem from the need to employ high energy electron beams which are usually produced by bulky and expensive accelerator systems. This may be illustrated by the dependence of the radiation wavelength,  $\lambda_r$ , upon the period of the wiggler magnet,  $\lambda_w$ , and the electron energy[5]

$$\lambda_r = \frac{\lambda_w}{2\gamma^2} \quad (1)$$

E-mail: [mgk@liv.ac.uk](mailto:mgk@liv.ac.uk) and facsimile: +44 151 794 4540

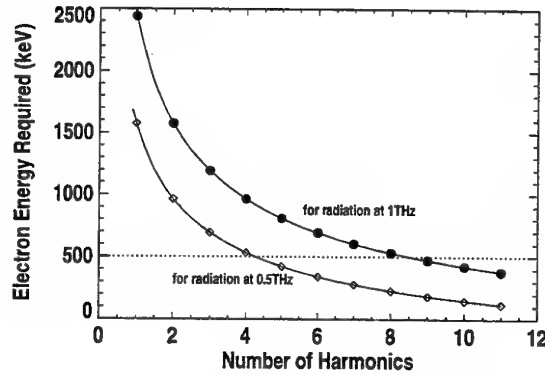


Fig. 1. Reduction in the minimum electron energy required to generate terahertz FEL radiation by operating FEL at harmonics with a single wiggler magnet of  $\lambda_w = 2\text{cm}$ .

where  $\gamma$  is the relativistic factor. Suppose that quasi-optical resonant cavities are used to confine FEL radiation generated at terahertz frequencies. The radiation frequency,  $f$ , can then be calculated from the approximation of  $f = c/\lambda_r$ . We further assume that the permanent magnet technology is employed for wiggler design and construction such that the wiggler field strength can achieve unity at periodicities of a few centimetres. Thus with a standard wiggler magnet with a period of 2cm, radiation at 1THz would require an electron beam of 2.5MeV. With the present accelerator technology, electron beams of 2.5MeV are likely to be produced by either electrostatic accelerators or induction linacs, both of which are of large size and thus high cost[6]. One way to reduce the minimum electron energy required to generate radiation at a given frequency is to operate the FEL at its harmonics and this is best understood by examining the FEL resonant condition[5]

$$\lambda_r = \frac{\lambda_w}{2h\gamma^2} \quad (2)$$

where  $h$  is the number of harmonics. Figure 1 shows that by operating the FEL at its harmonics how the minimum necessary electron energy for generating radiation at terahertz frequencies is reduced when  $\lambda_w = 2\text{cm}$ .

In a conventional FEL system with a planar wiggler magnet, harmonic generation originates from a harmonic oscillation of the axial electron velocity and the emission strength decreases as the harmonic number increases. Thus although significant reduction in electron energy may be achieved by harmonic operation, an effective application of this technique is hampered by the considerably lower radiation strength at high harmonics than that at the funda-

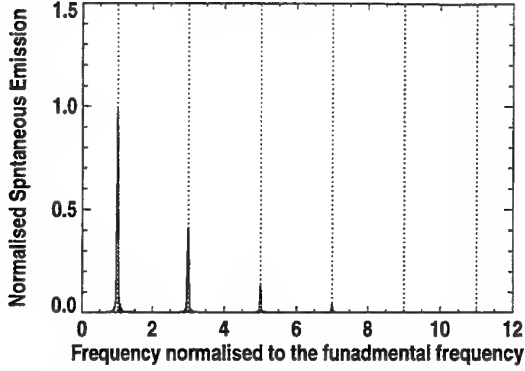


Fig. 2. Spontaneous emission spectrum of a conventional FEL

mental frequency. As a result, the eventual system may operate below the threshold for substantial oscillation at harmonic frequencies. To illustrate this more clearly, we consider the spontaneous emission from a conventional FEL with a planar wiggler. Based on the formulation developed in [5], the FEL spontaneous emission normalised to its peak value at the fundamental frequency is plotted in figure 2 as a function of the radiation frequency. Figure 2 shows that as the harmonic number increases the FEL radiation decreases. In particular, the emission strengths at the 9th and 11th harmonics are 0.97% and 0.23% of that at the fundamental frequency, respectively. Thus for an effective usage of FEL harmonic radiation, its spontaneous emission strength at high harmonics needs to be enhanced considerably.

In this paper, we consider possible enhancement of FEL harmonic generation with a two-frequency wiggler configuration that consists of two conventional wigglers of different periods. Harmonic generation in such an unconventional wiggler configuration is based on a nonlinear interference effect rather than the harmonic oscillation in the axial electron velocity. This work is motivated by recent work on manipulation of FEL gain and spectrum by means of unconventional wiggler configurations[7]-[10].

## II. SPONTANEOUS EMISSION FORMULATION

Consider a magnet system composed of two different conventional planar wigglers of periods  $\lambda_{w1}$  and  $\lambda_{w2}$ , respectively. For the simplicity, we assume that  $\lambda_{w1} > \lambda_{w2}$  and that the on-axis magnetic field of this two-frequency wiggler configuration may be approximated as

$$\vec{B}_w = \hat{y}(B_{w1} \cos k_{w1}z + B_{w2} \cos k_{w2}z) \quad (1)$$

where  $k_{wn} = 2\pi/\lambda_{wn}$  ( $n = 1, 2$ ). Suppose the lengths of the two constituent wigglers are  $L_1 = N_1\lambda_{w1}$  and  $L_2 = N_2\lambda_{w2}$ , respectively. Without violating generality, we assume  $L_2 > L_1$  and  $N_2 = 1 + \text{Int}[L_1/\lambda_{w2}]$ . Therefore eq.(1) is valid for  $0 < z \leq L_1$ , whereas in the small region of  $L_1 < z \leq L_2$  the wiggler field is  $\vec{B}_w = \hat{y}B_{w2} \cos k_{w2}z$ .

Under the perturbation of the alternating magnetic field of eq.(1), an energetic electron beam travelling along the wiggler axis radiates and the induced electromagnetic radi-

ation may be represented by its on-axis electric field component of

$$\vec{E} = \hat{x}E_0 \sin \Phi = \hat{x}E_0 \sin(\omega t - kz + \phi) . \quad (2)$$

The trajectory of an electron beam in the combined field of the wiggler magnet and the induced radiation is in general governed by its equation of motion

$$\frac{d(\gamma m\vec{v})}{dt} = -e(\vec{E} + \vec{v} \times \vec{B}_w) . \quad (3)$$

In the limit of small radiation field, the transverse velocity of an electron entering the two-frequency wiggler along the magnet axis may be easily obtained from eq.(3) as

$$\beta_x = \frac{1}{\gamma} (a_{w1} \sin k_{w1}z + a_{w2} \sin k_{w2}z) \quad (4)$$

where  $a_{wn} = eB_{wn}/mck_{wn}$  is the dimensionless field strength of the  $n$ th constituent wiggler ( $n = 1, 2$ ). Once again with the small radiation field assumption, the electron energy change may be considered to be negligible in the calculation of electron trajectory and as such the axial electron velocity can be derived from  $\beta_0^2 = \beta_x^2 + \beta_z^2$  ( $\beta_0$  being the initial electron velocity) as

$$\beta_z = \left[ 1 - \frac{1 + (a_{w1} \sin k_{w1}z + a_{w2} \sin k_{w2}z)^2}{\gamma^2} \right]^{1/2} . \quad (5)$$

For most short wavelength free electron lasers driven by rf linacs and electron storage rings, the electron energy is highly relativistic[6]. Thus  $\gamma^2 \gg 1$  and the above equation may be approximated as

$$\beta_z \approx 1 - \frac{1}{4\gamma^2} \left\{ (1 + a_{w1}^2 + a_{w2}^2) - a_{w1}^2 \cos 2k_{w1}z - a_{w2}^2 \cos 2k_{w2}z + 2a_{w1}a_{w2} \sin k_{w1}z \sin k_{w2}z \right\} . \quad (6)$$

It is seen that due to the nonlinear dependence of  $\beta_z$  on the field strengths of the two wiggler components in eq.(5) the axial electron velocity contains not only terms due to individual wiggler components,  $a_{wn}^2 \cos 2k_{wn}z$  ( $n = 1, 2$ ), but also their cross term,  $2a_{w1}a_{w2} \sin k_{w1}z \sin k_{w2}z$ . Such a cross term represents a nonlinear interference effect between the two wiggler components on the axial electron velocity. As it will be shown in section III, this nonlinear interference effect plays a very significant role in determining the FEL spectrum and thus the FEL emission at harmonics. Note that the high order terms neglected in deriving eq.(6) contain many other cross terms which have small amplitudes for highly relativistic electron beams.

The energy exchange of an electron with its radiation field is governed by the energy conservation law

$$\frac{d(\gamma mc^2)}{dt} = -e\vec{E} \cdot \vec{v} . \quad (7)$$

Substitution of eq.(2) into the above equation gives

$$\frac{d\gamma}{dt} = - \frac{eE_0}{2\gamma mc} \sum_{n=1}^2 a_{wn} \left[ \cos(\Phi - k_{wn}z) - \cos(\Phi + k_{wn}z) \right] . \quad (8)$$

As illustrated in eq.(8), the axial electron velocity of eq.(6) affects crucially the beam-wave interaction described by eq.(7) via the phase angles of  $\Phi \mp k_{wn}z = \omega t - (k \pm k_{wn})z + \phi$  in which the electron spatial location,  $z$ , needs to be expressed in terms of  $t$ . To this end, the electron average velocity in the axial direction,  $\beta_{z0}c$ , needs to be formulated first. Integration of eq.(6) gives the average axial velocity

$$\beta_{z0} \approx 1 - \frac{1}{2\gamma^2} \left( 1 + \frac{1}{2}a_{w1}^2 + \frac{1}{2}a_{w2}^2 + \xi a_{w1}a_{w2} \right) \quad (9)$$

where

$$\xi = \frac{\sin(2\pi N_1 \lambda_{w1}/\lambda_{w2})}{N_1 \pi (\lambda_{w1}^2/\lambda_{w2}^2 - 1)} . \quad (10)$$

Note that  $\xi = 1$  when  $\lambda_{w1} = \lambda_{w2}$ . However  $\xi \ll 1$  if the two wiggler periods differ from each other appreciably. With  $\beta_{z0}$  formulated in eq.(9), eq.(6) becomes

$$\begin{aligned} \beta_z &= \beta_{z0} + \frac{1}{4\gamma^2} \left[ a_{w1}^2 \cos 2k_{w1}z + a_{w2}^2 \cos 2k_{w2}z \right] \quad (11) \\ &+ \frac{a_{w1}a_{w2}}{2\gamma^2} \left[ \xi + \cos(k_{w1} + k_{w2})z - \cos(k_{w1} - k_{w2})z \right] \end{aligned}$$

If we approximate  $z$  with the nominal electron position  $z_0 = c\beta_{z0}t$  on the right hand side of the above equation, a straightforward integration of  $\beta_z$  in eq.(11) leads to the formulation of the electron spatial location as

$$z = c \int_0^{z_0/\beta_{z0}c} \beta_z(\tau) d\tau = z_0 + \frac{1}{k} \left[ p(z_0) + q(z_0) \right] \quad (12)$$

where

$$p(z_0) = \alpha_0 \sum_{n=1}^2 \frac{a_{wn}^2}{a_{w1}a_{w2}} \frac{\lambda_{wn}}{\lambda_{w1}} \sin 2k_{wn}z_0 \quad (13a)$$

$$\begin{aligned} q(z_0) &= 4\alpha_0 \left[ \xi k_{w1}z_0 + \frac{\sin(k_{w1} + k_{w2})z_0}{1 + \lambda_{w1}/\lambda_{w2}} \right. \\ &\quad \left. - \frac{\sin(k_{w1} - k_{w2})z_0}{1 - \lambda_{w1}/\lambda_{w2}} \right] \quad (13b) \end{aligned}$$

$$\alpha_0 = \frac{ka_{w1}a_{w2}}{8\gamma^2\beta_{z0}k_{w1}} \quad (13c)$$

The terms  $p(z_0)$  and  $q(z_0)$  are related to the nonlinear interference between the two wiggler components of the two frequency wiggler structure, and as it will be shown in section III they affect crucially the FEL spectrum. Using eq.(12), the phase angles in eq.(8) become

$$\begin{aligned} \Phi \mp k_{wn}z &\approx \left[ \frac{\omega}{c\beta_{z0}} - (k \pm k_{wn}) \right] z_0 + \phi - (p(z_0) + q(z_0)) \\ &= \Delta k_n^\pm z_0 + \phi - (p(z_0) + q(z_0)) \quad (14) \end{aligned}$$

where  $\Delta k_n^\pm z = (\omega/(c\beta_{z0}) - (k \pm k_{wn}))z$  and the approximation of  $(k \pm k_{wn})/k \approx 1$  has been assumed.

In eq.(14), all phase angles of relevance to eq.(8) are expressed in terms of the nominal electron position only. This allows eq.(8) to be integrated directly to give the electron energy change over the entire length of the two-frequency

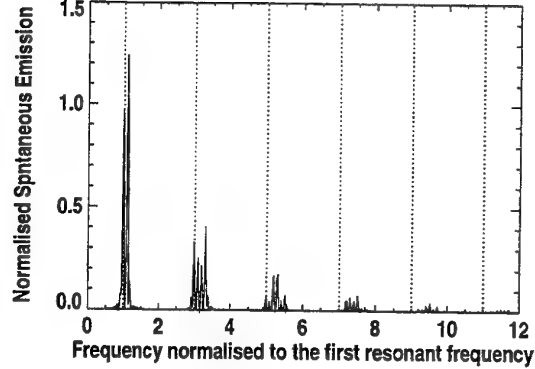


Fig. 3. FEL spontaneous emission in a two-frequency wiggler with  $a_{w1} = a_{w2} = 1$  and  $\lambda_{w1} = 1.1\lambda_{w2}$

wiggler,  $\Delta\gamma$ . According to Maday's theorem on the other hand, the spontaneous emission of the electron beam is proportional to  $\langle (\Delta\gamma)^2 \rangle$  where  $\langle \dots \rangle$  denotes to an average over the initial electron phase. In the SI units, this relationship is given by [11], [12]

$$\frac{d^2W}{d\omega d\Omega} = \frac{m^2 c \omega^2}{8\pi^2 \epsilon_0 E_0^2} \langle (\Delta\gamma)^2 \rangle . \quad (15)$$

The formulation of  $\langle (\Delta\gamma)^2 \rangle$  from eqs.(8) and (14) is rather lengthy but nevertheless straightforward. It can be shown that in the limit of small radiation field the spontaneous emission is given by [12], [13]

$$\frac{d^2W}{d\omega d\Omega} = \frac{a_{w1}^2}{16} \sqrt{\frac{\mu_0}{\epsilon_0}} \left[ \frac{eN_1}{\gamma(1 - \beta_{z0})} \right]^2 \frac{L^2}{L_1^2} S \quad (16)$$

where  $a_{wn} = eB_{wn}/mck_{wn}$  is the dimensionless field strength of the  $n$ th constituent wiggler ( $n = 1, 2$ ) and

$$\begin{aligned} S &= \frac{1}{a_{w1}^2 \omega_{r1}^2} \left\{ \left[ \sum a_{wn} (a_n^+ - a_n^-) \right]^2 \right. \\ &\quad \left. + \left[ \sum a_{wn} (b_n^+ - b_n^-) \right]^2 \right\} \quad (17a) \end{aligned}$$

$$a_n^\pm = \frac{1}{L} \int_0^L \cos(\Delta k_n^\pm z - p(z) - q(z)) dz \quad (17b)$$

$$b_n^\pm = \frac{1}{L} \int_0^L \sin(\Delta k_n^\pm z - p(z) - q(z)) dz \quad (17c)$$

$$\omega_{r1} = \frac{k_{w1}c\beta_{z0}}{(1 - \beta_{z0})} . \quad (17d)$$

The above expressions will be used to explore possible enhancement of harmonic radiation from free electron lasers in the next section.

### III. APPLICATION

To illustrate the characteristics of the two-frequency wiggler configuration, we consider a two-frequency wiggler with  $a_{w1} = a_{w2} = 1$  and  $\lambda_{w1} = 1.1\lambda_{w2}$ . As it is shown in figure 3, the addition of the second wiggler increases appreciably radiation strength at harmonic frequencies. In

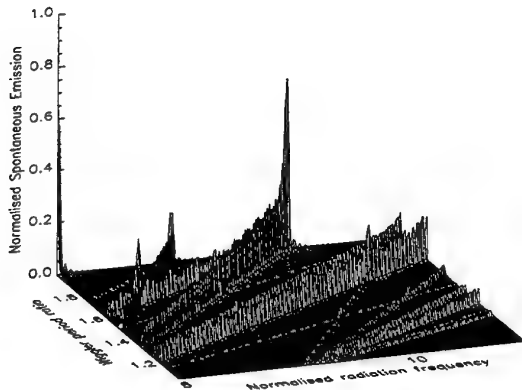


Fig. 4. FEL spontaneous emission in a two-frequency wiggler with  $a_{w1} = a_{w2} = 1$  at different wiggler period ratios

particular, detailed calculation shows that the spontaneous emission at  $\omega = 9.2\omega_{r1}$  is almost twice as much as that in the single wiggler case. This enhancement in spontaneous emission is most probably due to the nonlinear interference between the two constituent wiggler components of the two-frequency wiggler. To further explore this hypothesis, we calculate the spontaneous emission for different values of the wiggler period ratio,  $\lambda_{w1}/\lambda_{w2}$ . As shown in Figure 4, the strength and distribution of the spontaneous emission is indeed strongly dependent upon the periodicities of the two wiggler components and consequently their interference. This finding is consistent with the results of recent work on quasiperiodic wigglers[9], [13]. More importantly, the magnitude of spontaneous emission is increased significantly. In the case of  $\lambda_{w2} = 0.5\lambda_{w1}$ , the value of the spontaneous emission around  $\omega = 10\omega_{r1}$  is now 66% of that of the fundamental spontaneous emission in a conventional FEL. Note that in a conventional FEL with the planar wiggler configuration there is no radiation at even harmonics[5], [6], but its emission strength around the 10th harmonic may be phenomenologically represented by the average of the emission strengths at the 9th and the 11th harmonics. From Figure 1, this representation would give the spontaneous emission at the 10th harmonic a phenomenological value of  $(0.97\% + 0.23\%)/2 = 0.60\%$ . For the FEL with a two-frequency wiggler of  $\lambda_{w2} = 0.5\lambda_{w1}$  in the aforementioned example, its normalised emission strength at the 10th harmonic is 66% as suggested in Figure 4 and this represents an emission strength enhancement of  $66\%/0.60\% = 110$  folds for FEL radiation at frequencies between the 9th and 10th harmonics.

The above example demonstrates that with the two-frequency wiggler configuration the FEL emission at high harmonics can be made sufficiently strong to yield a similar level of power output to that in a conventional FEL operating at the fundamental frequency. This enhancement of harmonic radiation would allow FEL systems with a two-frequency wiggler to be operated at high harmonics while maintaining a level of power output adequate for many practical applications. These findings have significant im-

plication in terms of the characteristics of the eventual FEL system since the electron energy needed to generate FEL radiation at terahertz frequencies can now be realistically reduced at relatively little expense of the resultant radiation strength. For instance, the electron energy for FEL radiation at 1THz can be reduced from 2.5MeV to around 422keV (see Figure 1) when the FEL with a two-frequency wiggler is operated around its 10th harmonic with its radiation strength reduced by only 34% from that at the fundamental frequency.

#### IV. CONCLUSION

A two-frequency wiggler configuration has been considered as a means to enhance the harmonic radiation in free electron laser devices. The spontaneous emission has been formulated, and based on this formulation numerical examples have been used to illustrate the characteristics of two-frequency wiggler based FELs. It has been shown that by adjusting the nonlinear interference between the two constituent wiggler components of a two-frequency wiggler the FEL spontaneous emission can be significantly enhanced at high harmonics. This permits the possibility of achieving an efficient FEL operation at terahertz frequencies with an electron beam energy kept below 500keV. The generation of a strong FEL radiation at terahertz frequencies by low energy electron beams of less than 500keV suggests an interesting prospect of developing and building compact terahertz FELs for use in a university laboratory.

#### REFERENCES

- [1] C. M. Snowden and D. P. Steenson, "Circuits and simulations at 1THz", *Phil. Trans. R. Soc. Lond. A*, vol.354, pp.2435-2446, 1996.
- [2] N. J. Cronin, "Terahertz systems: the demands on devices", *Phil. Trans. R. Soc. Lond. A*, vol.354, pp.2425-2434, 1996.
- [3] S. Zeuner, S. J. Allen, K. D. Maranowski, and A. C. Gossard, "Photon-assisted tunnelling in GaAs/AlGaAs superlattices up to room temperature", *Appl. Phys. Lett*, vol.69, pp.2689-2691, 1996.
- [4] P. L. Marston, "A time-resolved glimpse of the terahertz glory", *Nature*, vol.391, no.6670, pp.841-842, 1998.
- [5] W. B. Colson, "The nonlinear wave equation for higher harmonics in free-electron lasers", *IEEE J. Quan. Electron.*, vol.17, pp.1417-1426, 1981.
- [6] H. P. Freund and T. M. Antonsen, Jr, "Principles of free-electron lasers", Chapman & Hall, London, 1992.
- [7] D. Ircane and P. Bamas, "Two-frequency wiggler for better control of free-electron laser dynamics", *Phys. Rev. Lett.* vol.67, pp.3086-3089, 1991.
- [8] M. G. Kong, *Phys. Rev. E*, "Enhanced optical klystron gain with a multiharmonic wiggler", vol.52, pp.3060-3065, 1995.
- [9] M. Takao, S. Sasaki, and S. Hashimoto, "Spectrum formula of the synchrotron-radiation from a quasi-periodic undulator", *Phys. Rev. E*, vol.52, pp.5454-5459, 1995.
- [10] M. G. Kong, "Mode-selective amplification in a waveguide free electron laser with a two-sectioned wiggler", *IEEE Trans. Plasma Sci.* vol.26, pp.85-91, (1998).
- [11] T. I. Smith, J. M. J. Madey, L. R. Elias, and D. A. G. Deacon, "Reducing the sensitivity of a free-electron laser to electron energy", *J. Appl. Phys.*, vol.50, pp.4580-4583, 1979.
- [12] L. K. Grover and R. H. Pantell, "An upper limit to the gain-energy acceptance produce of the free electron laser", *IEEE J. Quan. Electron.*, vol.22, pp.789-792, 1986.
- [13] M. G. Kong and A. Vourdas, "A new free electron laser interaction mechanism based on a quasiperiodic wiggler", *Proceedings of the 25th IEEE International Conference on Plasma Science*, IEEE Publication 98CH36221, p.195, 1998.

# Standard Design of SMMW Laser Ring Resonators with Optical Pump Beam Guiding

Michael Raum, Klaus Huber

**Abstract**— This article explains the design process for a SMMW ring laser resonator using a single focussing mirror for optical pump beam and SMMW beam guiding. The features of two prototype systems which have been optimized for the 119  $\mu\text{m}$  methanol line are presented. Measurement results concerning output power and beam quality of realized systems are presented.

**Keywords**— SMMW laser, ring resonator, optical pump beam guiding.

## I. INTRODUCTION

THE OH radical is one of the most important radicals involved in stratospheric chemistry. As it is involved in many catalytic cycles, more data on its concentration in the stratosphere will be useful for an improved understanding of the stratospheric chemistry leading to ozone depletion [1].

For its remote sensing, airborne heterodyne receivers sensitive to its emission lines at 2.514 THz are used. The local oscillator for the receivers can be realized by a methanol gas laser running on its 2.523 THz line, which corresponds to a wavelength of  $\lambda_L = 118.8 \mu\text{m}$  in the submillimeter wavelength (SMMW in short) range. The methanol laser is optically pumped by a CO<sub>2</sub> laser on its 9 P 36 line (wavelength  $\lambda_L = 9.695 \mu\text{m}$ ). The heterodyne receiver has to be carried on an airborne platform in order to avoid attenuation of the OH radical signal by the water vapour in the lower atmospheric layers. This requires compactness, efficiency and reliability [2], [3].

The Erlangen Far-Infrared Laser project (ERFILAS in short) deals with the design of SMMW laser heads optimized for the airborne tasks. A ring laser design using quasioptical beam guiding for the pump beam as well as for the SMMW beam guiding has been promoted by our laboratories. Output powers of up to 30 mW for a resonator length of 2 m [4], 19 mW for a resonator length of 1.5 m and 23.4 mW for a redesign of the 2 m resonator [5] at a pump power level of 20 W (minimum pump offset 6 MHz) have already been reported on preceding workshops. The theoretical discussion of the cold resonator will be updated with the newest results. Recent measurement results concerning output power and beam profile will be presented.

## II. OPTICAL PUMP BEAM GUIDING

The ring resonator of the SMMW laser head (perimeter  $L_0$ ) consists of four mirrors as shown in figure 1. It is based on a design by the University of

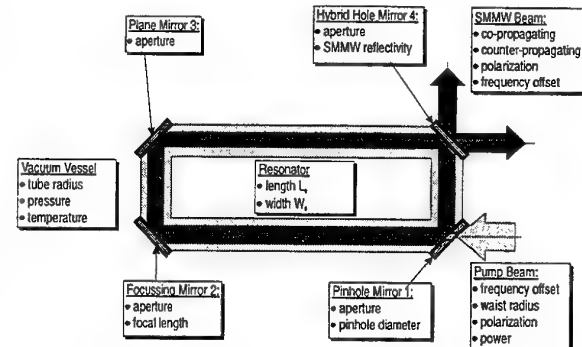


Fig. 1. Geometry of Pump Beam Guiding Ring Resonator

Cologne [6] and has been adapted to the requirements of a 2.523 THz resonator [4].

The pump beam is injected into the SMMW resonator via a pinhole in a plane mirror 1. On its roundtrip through the resonator it passes a focussing mirror 2, a plane mirror 3 and a hybrid hole mirror 4 which perfectly reflect it. After a final reflection on mirror 1 it is ready for another roundtrip. Multiple roundtrips increase the efficiency of the pump process. The SMMW radiation, which can propagate in or against the direction of the pump beam direction (the co- or counterpropagating beam), is coupled out at a hybrid hole mirror 4. The focussing mirror 2 serves for pump beam guiding as well as for SMMW beam guiding.

In the design process of the resonator the constructional parameters of the resonator, i. e. the focal length  $f_B$  of mirror 2, the ring perimeter  $L_0$  of the resonator, the aperture radii of all mirrors  $r_{ap}$  and the pinhole radius  $r_{pin}$  are to be determined.

### A. Determining the g-Parameter

The most important constructional parameters are the focal length  $f_B$  and the ring perimeter of the resonator  $L_0$ . It is useful to introduce the  $g$ -parameter of the resonator

$$g = 1 - \frac{L_0}{2 \cdot f_B} \quad (1)$$

as a characteristic measure for the resonator geometry. In order to maximize the SMMW beam

Michael Raum and Klaus Huber are with the Lehrstuhl für Hochfrequenztechnik (LHFT), University Erlangen-Nürnberg, Germany. E-mail michael@lhft.e-technik.uni-erlangen.de or klaus@lhft.e-technik.uni-erlangen.de

volume, but minimize its spotsizes on the mirrors, a  $g$ -parameter around  $g \approx 0.6$  is adequate [5], [6].

Using ray transfer analysis, it can be shown that not every  $g$ -parameter provides good pump beam guiding. If a  $g$ -parameter obeys the relation

$$g = \cos \left[ \frac{\pi \cdot i}{m + 1} \right] \quad (2)$$

with  $i$  and  $m$  integers, the pump beam is refocussed on the pinhole in roundtrip number  $m+1$ . This leads to a total loss of the remnant pump power. From the viewgraphs given in [7], eleven  $g$ -parameters of resonators providing good pump beam guiding can be derived. They are listed in table I.

TABLE I  
STANDARD RESONATOR G-PARAMETERS

0.53712	0.55104	0.56151	0.57692
0.59679	0.61010	0.63937	0.64799
0.66276	0.67354	0.68524	

### B. SMMW Beam Geometry

With perimeter length  $L_0$  and  $g$ -parameter (i. e. the focal length  $f_B$ ) known, it is possible to completely design the ring resonator. For example, the Rayleigh length of the SMMW beam

$$z_{R,L} = \frac{L_0}{2} \cdot \sqrt{\frac{1+g}{1-g}} \quad (3)$$

which is wavelength independent, its beam waist size

$$w_{0,L} = \sqrt{\frac{z_{R,L} \cdot \lambda_L}{\pi}} \quad (4)$$

and the maximum SMMW beam radius on the focussing mirror within the resonator

$$w_{L,max} = \sqrt{\frac{L_0 \cdot \lambda_L}{\pi}} \cdot \left[ \frac{z_{R,L}}{L_0} + \frac{L_0}{4 \cdot z_{R,L}} \right] \quad (5)$$

can be calculated.

### C. Pump Beam Geometry

The waist radius of the pump beam to be coupled into the resonator is characterized by a pump beam factor  $f_{pb}$  via

$$w_{0,P} = f_{pb} \cdot \sqrt{\frac{z_{R,L} \cdot \lambda_P}{\pi}} \quad (6)$$

and has a maximum spot size of the pump beam

$$w_{P,max} = \frac{1}{f_{pb}} \cdot \sqrt{\frac{L_0 \cdot \lambda_P}{\pi}} \cdot \left[ \frac{z_{R,L}}{L_0} + \frac{L_0}{4 \cdot z_{R,L}} \right] \quad (7)$$

on the focussing mirror. An optimum pump beam factor can be found by compromising between a small

$f_{pb}$  requiring large mirror apertures (see formula (7)) and a large  $f_{pb}$ , increasing the pump beam losses at the necessarily large pinhole (see formula (6)). A closer examination of the pump radiation losses by the pinhole reveals that  $f_{pb} \approx 0.22$  is a good first solution to derive the resonator geometry.

### D. Resonator Geometry

The aperture  $r_{ap}$ , which is the least required for proper SMMW and pump beam guiding, can be determined from the maximum beam sizes on the focussing mirror given by equations (5) and (7) using  $r_{ap} \approx 1.7 \cdot \max\{w_{L,max}, w_{P,max}\}$ . The pinhole serves to inject the pump beam into the resonator. A fraction of 1 % of the pump power is lost when the pinhole radius is chosen to be  $r_{pin} \approx 1.5 \cdot w_{0,P}$ .

Based on the  $g$ -parameters from table I, standard resonator geometries for pump beam guiding resonators can be derived. As the geometry can be expressed by the  $g$ -parameter and the resonator length, names like STD61/2.0 for a resonator with  $g$ -parameter  $g = 0.61$  and a resonator perimeter of  $L_0 = 2$  m are introduced to reference the resonators.

### E. Further Optimization

For the now readily fixed resonator, a further optimization of the injected pump beam geometry is possible. Whereas formula (7) was analytically derived for an endless resonator roundtrip sequence, the attenuated pump beam in reality never reaches the given maximum spot size. Therefore, a further reduction of the pump beam waist size is possible. Depending on the  $g$ -parameter, the pump beam factor can be reduced to  $f_{pb} \approx 0.173 \dots 0.183$ .

## III. TECHNICAL FEATURES

Two SMMW laser heads have been realized in close accordance to the given design process. The first one (ERFILAS-2) was based on a 1.5 m ring resonator perimeter length design with  $g$ -parameter of  $g_2 = 0.55$ , corresponding to a STD55/1.5 standard resonator. The second one (ERFILAS-3) has a ring resonator perimeter of 2 m with a  $g$ -parameter of  $g_3 = 0.61$ , corresponding a STD61/2.0 standard resonator. Figure 2 shows a photograph of the laser

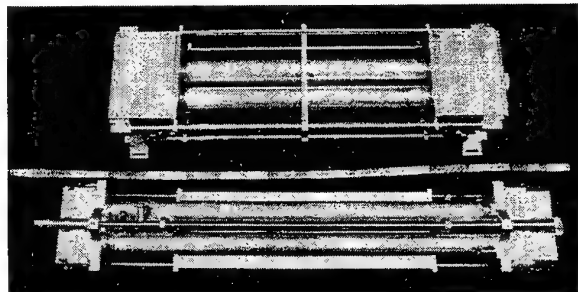


Fig. 2. The ERFILAS-2 (top) and ERFILAS-3 (bottom) SMMW laser heads. The scale applied for length comparison is divided in 10 cm sections.

heads.

The perimeter lengths are thermally stabilized by INVAR-aluminium frames. Two stage tuning units consisting of differential screw and piezoelectric stack are used to provide a tuning range of more than one SMMW wavelength ( $> 119 \mu\text{m}$ ) with an accuracy corresponding to the emission linewidth ( $< 1 \mu\text{m}$ ) [8].

The hybrid hole mirrors consist of a quartz substrate with a pump radiation reflective coating. On the coating, an additional gold layer with an elliptical hole has been applied to form the hybrid hole with an effective diameter of 6 mm. After centering of the hole and applying an antireflection polyethylene coating on their backsides, increased SMMW output power levels were observed.

#### IV. MEASUREMENT RESULTS

##### A. Improvement of Outcouplers

The effects of the mentioned improvements of the hybrid hole mirrors are shown in figure 3 on the example of the strongest mode of ERFILAS-2. The

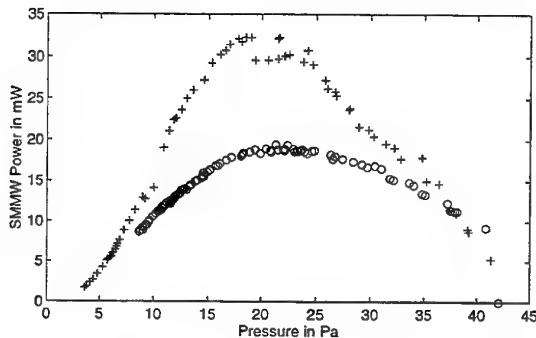


Fig. 3. Pressure scans of the strongest counterpropagating mode of ERFILAS-2 before (circles) and after improvement (crosses) of outcouplers

pump beam has a waist radius of 0.45 mm and provides a pump power of 20 W. A drastical increase in output power from 19 mW to 33 mW can be observed.

##### B. Co- and Counterpropagating SMMW Beam

The measured SMMW laser output powers of ERFILAS-3 on the strongest radial  $\text{TEM}_{00}$  mode are shown in figure 4 for varying pressure. The copropagating SMMW beam provides a much higher output power (up to 48.8 mW) than the counterpropagating one (up to 27.3 mW). This effect is partially a consequence of the dynamical Stark-Effect [9]. Again, an increase of the output power of the counterpropagating beam by the improvement of the outcouplers (former value 23.4 mW [5]) can be noted. The drastical increase from 30 mW in the very first laser design [4] to now 48.8 mW in the copropagating SMMW beam is on the one hand caused by the better outcouplers, on the other hand due to a thickness reduction of the vacuum window from 5 mm to now 1.4 mm. As well, the improved

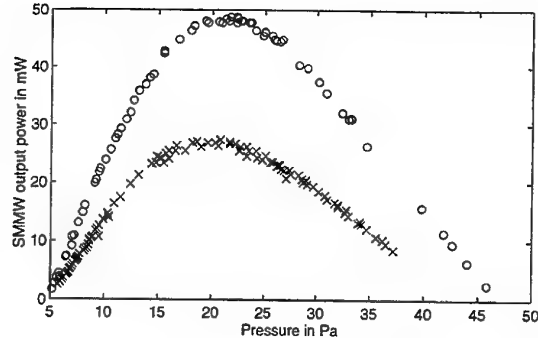


Fig. 4. Pressure scans of the  $\text{TEM}_{00}$  co- and counterpropagating modes of ERFILAS-3 (circles and crosses, respectively)

cooling by the vacuum vessel walls which are closer to the pump and SMMW beam might have a positive effect. The output power of the copropagating beam corresponds to a technical efficiency of up to 6 %.

##### C. Beam Quality

If a critical power is not exceeded, the performance of heterodyne receivers increases with the LO-power coupled into the mixer diode. For an open structure corner cube mixer as used in the OH radiometer, the laser output beam has to be focused to a beam waist of about  $180 \mu\text{m}$  in order to achieve good coupling [10]. Therefore it is extremely important not only to achieve a high output power but also to get this power in a mode which is convenient for focussing by standard elliptical mirrors. Various

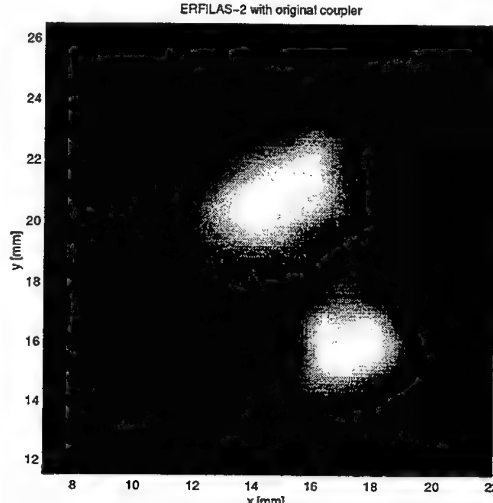


Fig. 5. Mode pattern of the strongest mode of ERFILAS-2 before outcoupler improvements

measurements of beam quality have been carried out with ERFILAS-2 and ERFILAS-3, and beam parameters have been derived. Figure 5 shows the mode pattern of the strongest mode of ERFILAS-2 before the improvements of the hybrid hole mirror. It looks like a rotated  $\text{TEM}_{01}$  mode with two beam maxima of nearly identical intensity. Focussing of this beam by elliptical mirrors would have lead to a

power loss of at least 50 %. After improvement of the outcoupler, the total power has been increased by 12 %, and the beam pattern is a nearly perfect  $TEM_{00}$ . The beam waist has been derived by scanning the beam profile in different distances and fitting the beam waists by an ideal gaussian beam. It turns out that the beam is slightly astigmatic with  $w_{0x} = 2.5$  mm and  $w_{0y} = 2.1$  mm.

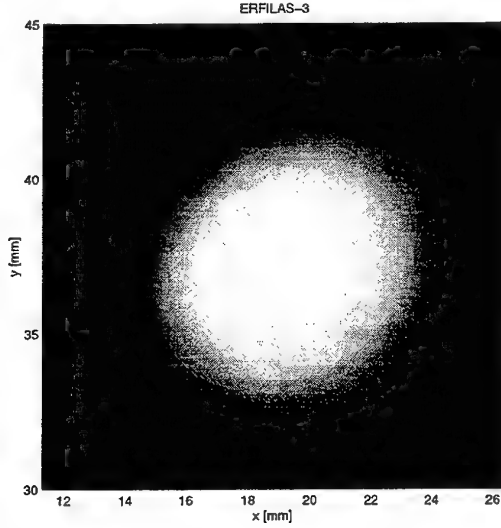


Fig. 6. Mode pattern of the strongest mode of ERFILAS-3 after outcoupler improvements

ERFILAS-3's strongest mode is  $TEM_{00}$  shaped without any measureable astigmatism. Figures 6 and 7 show the beam pattern and its x- and y-cut together with an ideal gaussian fit. The beam waist turns out to be 1.9 mm and is located at the hybrid hole mirror, as is to be expected.

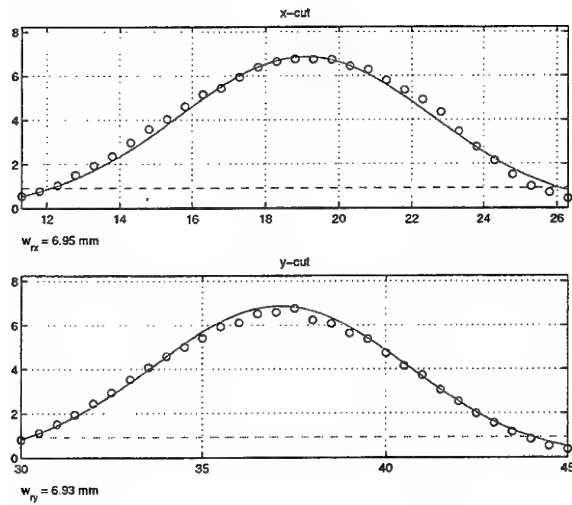


Fig. 7. Beam Pattern of ERFILAS-3 and gaussian fit. The dashed line marks the beam width.

described. In continuation of the work described on earlier workshops of this series, a standard design procedure for SMMW laser ring resonators with optical pump beam guiding has been developed.

The features of two compact system prototypes with 1.5 m and 2.0 m perimeter optimized for the 119  $\mu$ m methanol line have been presented.

Measurements show that output powers of 33 mW in the case of ERFILAS-2 and up to 49 mW in the case of ERFILAS-3 at a pump power level of 20 W can be achieved. The beam of ERFILAS-3 shows a very good quality and is well suited for heterodyne applications.

#### ACKNOWLEDGEMENTS

The authors like to thank Prof. Dr.-Ing. H. Brand for his support of their work. As well, the invaluable help of the staff of the mechanical workshop at the Laboratories for High Frequency Technology, Mr Bauer, Mr Höpfel and Mr Popp, is to be appreciated.

#### REFERENCES

- [1] S. Miller, M. Birk, F. Schreier, and D. Hausmann, "Airborne far-infrared heterodyne remote sensing of stratospheric OH: A feasibility study," *International Journal of Infrared and Millimeter Waves*, vol. 13, no. 9, pp. 1241-1268, 1992.
- [2] G. Chin, "Optically Pumped Submillimeter Gas Lasers and the Prospects for Constructing Space-Qualifiable LO Systems," *International Journal of Infrared and Millimeter Waves*, vol. 8, no. 10, pp. 1219-1234, 1987.
- [3] R. Titz, M. Birk, D. Hausmann, R. Nitsche, F. Schreier, J. Urban, H. Küllman, and H. P. Röser, "Observation of stratospheric OH at 2.5 THz with an airborne heterodyne system," *Infrared Physics and Technology*, vol. 36, pp. 883-891, 1995.
- [4] M. Raum, "2.5 THz Laser with Optical Pump Beam Guiding," in *3rd International Workshop on Terahertz Electronics*, Zermatt 1995.
- [5] M. Raum, "Construction Principles for 2.5 THz Lasers with Optical Pump Beam Guiding," in *5th International Workshop on Terahertz Electronics*, Grenoble 1997.
- [6] E. Michael, J. Stutzki, and D. Hottgenroth, "Ein optisch gepumpter FIR-Ringlaser als offener Resonator mit variabler Auskopplung," *Archiv für Elektrotechnik*, vol. 77, no. 1, pp. 45-50, 1993.
- [7] M. Raum, "Design of a 2.5 THz Submillimeter Wave Laser with Optical Pump Beam Guiding," *International Journal of Infrared and Millimeter Waves*, vol. 16, pp. 2147-2161, 1995.
- [8] M. Raum, "New results on 2.5 THz Laser with Optical Pump Beam Guiding," in *4th International Workshop on Terahertz Electronics* Erlangen 1996.
- [9] R. L. Panock, R. J. Temkin, "Interaction of two laser fields with a three-level molecular system," *IEEE Journal of Quantum Electronics*, QE-13, pp. 425-434, 1977.
- [10] K. Huber, R. Hillermeier, H. Brand, C. I. Lin, A. Simon, M. Rodriguez-Girones, H. L. Hartnagel "2.5 THz Corner Cube Mixer with Substrateless Schottky Diodes," in *Proceedings of the 5th International Workshop on Terahertz Electronics*, Grenoble 1997.

#### V. CONCLUSIONS

The design of SMMW ring lasers using a focussing mirror for optical pump beam guiding has been

# Inversionless amplification of coherent THz radiation

Rainer Martini, Frank Hilbk-Kortenbruck, Peter Haring Bolívar, and Heinrich Kurz

Institut für Halbleitertechnik II, RWTH Aachen, D-52056 Aachen, Germany

An inversion-less amplification of coherent THz emission is achieved by coherent superposition with an electromagnetic background field. This process is applicable to a wide variety of optically impulsively excited THz emitters. The amplification is experimentally demonstrated both in single-pass as well as in resonator configurations. The fundamental limits and prerequisites are discussed, stressing analogies and differences to standard amplification by stimulated emission.

Index Terms—

## I. INTRODUCTION

The time-resolved spectroscopy in the terahertz (THz) region of the electromagnetic spectrum is an important and growing field of research with a wide range of applications. Most THz sources rely on the coherent photoexcitation of charge carrier distributions in diverse semiconductor structures with femtosecond laser pulses. The dominant radiation process is then given by the acceleration of the coherent carrier ensemble, according to Faraday's law of induction. Due to the coherent motion and close spacing of the ensemble of carriers, the coherent electromagnetic THz radiation is emitted in a cooperative manner. Up to now many different kind of broadband [1-3] or tunable emission processes [4-5] have been demonstrated, and the attractive properties of time resolved techniques has raised attractive applications [6]. Nevertheless, a widespread application of the time-resolved technique is hampered above all by the lack of powerful and efficient THz generation processes. One of the main reasons restricting the efficiency of most impulsively excited THz emitters is the fast loss of coherence. Typically the coherence in the emitter system is destroyed by ultrafast scattering processes, restricting the cooperative motion and therefore the coherent emission time  $\tau_{coh}$  to a small fraction of the radiative lifetime  $\tau_{rad}$  [4]. Consequently, only a small portion of the available energy in the system is emitted coherently and the corresponding quantum efficiency  $\eta = \tau_{coh} / \tau_{rad}$  is very low (typically below  $10^{-3}$ ). An efficiency enhancement can be obtained if the emission power is increased so that more energy will be emitted coherently before dephasing occurs. One possibility to accomplish this power increase is the superlinear power dependence on carrier density according to the superradiant characteristics of the cooperative emission process [7]. Such an efficiency enhancement was already shown for the surface-field THz emitter InP [8] and for Bloch oscillations in GaAs / AlGaAs superlattices [9] by increasing the optical excitation intensity. But as excitation density dependent

dephasing and screening effects reduce  $\tau_{coh}$  for high excitation densities only a limited efficiency enhancement can be achieved by this process. In this paper we present a new method to amplify the coherent emission power by phasematched superposition with a coherent background radiation during the emission process. In contrast to former approaches the optical excitation conditions and therefore  $\tau_{coh}$  remains constant during this process, avoiding a saturation of the efficiency enhancement effect. In principle the emission power can thus be enhanced until all available energy is emitted completely during  $\tau_{coh}$ , e.g. the quantum efficiency can be raised to unity. This paper is organized as follows: In the first part, the principle of the amplification process is discussed, stressing analogies and differences to stimulated emission. Afterwards, the proposed properties are confirmed experimentally in a specially designed DFT setup allowing the detailed investigation of the amplification process in a single-pass configuration. The feasibility of repetitive amplification in a ring-resonator is demonstrated afterwards. The paper closes with a brief summary.

## II. PRINCIPLE OF AMPLIFICATION BY PHASEMATCHED SUPERPOSITION

The basic amplification process is based on the superposition of a coherent background radiation during the

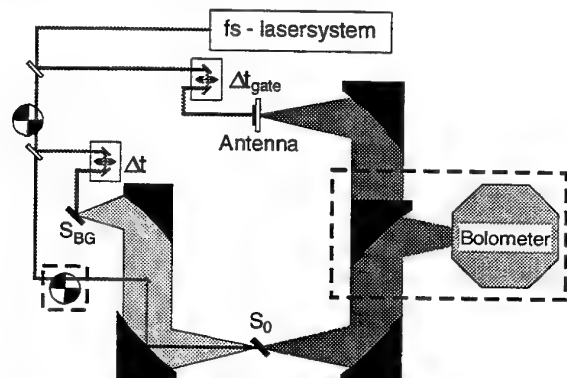


**Fig.1:** Modified diffraction Fourier transformation setup used to study the amplification process. The investigated THz emission is produced from  $S_0$  under irradiation by an independently controlled ( $\Delta t_{gen}$ ) background emitter ( $S_{BG}$ ). The combined electric field is detected and time-resolved with photoconductive antennas. Alternatively a bolometer is used to measure the time-integrated intensity in the same setup (dashed area).

THz emission process. If the propagating direction and the temporal shape of both the background and the newly generated THz fields are chosen identically, the electric field amplitudes will add up. This simple constructive interference already turns out to be an amplification mechanism: As radiation power  $P$  scales quadratically with field amplitude, the constructive interference leads to an overall power increase compared to an uncorrelated emission process. Consequently more energy can be emitted coherently in the short time  $\tau_{coh}$  before dephasing sets in. As a simple example, consider the coherent superposition of a background field (amplitude  $E_{BG}$ ) with a second field (amplitude  $E_0$ ) during its generation process. The field amplitudes add and as result the radiation power is raised by  $\Delta P \sim (E_0 + E_{BG})^2 - (E_0^2 + E_{BG}^2) = 2E_0 E_{BG}$ . As the power of the background radiation is constant, the enhancement  $\Delta P$  has to be attributed to the generation process of the source which is irradiated by the THz background field. The emission power of the second source has been raised by a factor of  $V = 1 + 2E_{BG} / E_0$ . It should be stressed that this amplification process differs from stimulated emission as e.g.  $V$  depends linearly on the background electric field amplitude and not on its power level ( $-E_{BG}^2$ ) as it would for stimulated emission. In the special case of similar amplitudes ( $E_0 \approx E_{BG}$ ) a three times stronger emission is achieved. Obviously a further increase of the background field enhances the amplification factor. A fundamental limit is only achieved when all available energy is emitted during the amplified emission process and the quantum efficiency reaches unity. It is therefore sensible to use this amplification process repetitively in a resonator setup, where the emitted radiation is coupled back and is used as background radiation driving and enhancing the next THz generation process. Each time THz radiation is emitted in phasematched superposition with the backcoupled field the total amplitude of the electric field in the resonator will be raised by the amount of  $E_0$  yielding a quadratic growth of the radiation power. A first estimation of the maximum amplification in a resonator with a round-trip reflectivity  $R$  can thus be estimated by the formula  $(E_0 / (1 - \sqrt{R}))^2$  when stimulated emission and absorption are neglected. Considering typical resonators with  $R \approx 0.9$  as an example, the power of the THz radiation can be amplified by a factor of about 380 by this coherent superposition process. Again significant differences from amplification by stimulated emission can be perceived: in our case, the power level in the resonator scales quadratically with the round-trip number instead of the exponential increase known from stimulated emission. Furthermore coherence between the backcoupled and the newly emitted radiation has to be guaranteed for amplification by coherent superposition, whereas the stimulated emitted radiation is coherent to the 'background' by nature. On the other hand no population inversion is needed for the presented amplification process. As population inversion is extremely difficult to achieve in the THz regime, this fact hence allows to apply this process to much wider group of impulsively photoexcited THz-emitters.

Another point of view shows the amplification character of this process more clearly: the background radiation transmitting the emitter during the synchronously excited THz generation process can be regarded as being amplified as the coherent superposition increases its field amplitude by the amount  $E_0$ .

### III. STUDY OF THE AMPLIFICATION PROCESS

The single-pass amplification process is investigated in a modified diffracting Fourier transform setup [10] using two surface-field THz emitters made from epitaxially grown InGaAs on InP. The samples are excited with 100 fs laser pulses from a commercial Ti:sapphire laser. Figure 1 shows the setup including two complementary detection schemes for time-resolved field and time-integrated power measurements. The optically excited THz emission from the main emitter ( $S_0$ ) is observed under collinear transmission of an identical THz background field produced by a second independently controlled emitter ( $S_{BG}$ ). Tuning their respective generation time delay by  $\Delta t_{gen}$ , the temporal overlap can be adjusted in order to achieve a pure constructive interference. It should be stressed that due to the temporal and spatial separation of the two emitters only the THz generation in the main emitter can be influenced by the background radiation and not vice versa – i.e. the radiated power of the background emitter remains constant. Consequently any power increase has to be attributed exclusively to an amplified THz generation process of the main emitter  $S_0$ .

In the first detection scheme the combined electric field is detected with photoconductive dipole antennas gated by a third optical beam. Tuning the time-delay ( $\Delta t$ ) of the gating pulse enables the time-resolved detection of the electric field amplitude of the combined THz radiation. Fig. 2 shows transients observed for the single (dashed lines) or combined excitation of both emitters for full temporal overlap of the two THz pulses ( $\Delta t_{gen} = 0$  ps). Obviously the electric fields add, as expected for pure constructive

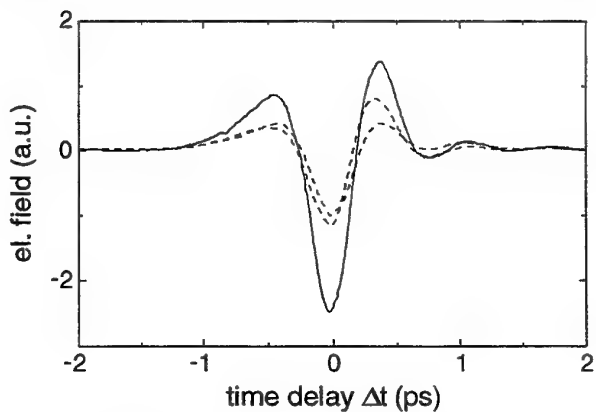


Fig.2 Detected field transients of the THz emission from the background and the main emitter, if only one is excited (dashed lines) and for combined excitation in full temporal overlap (solid curve). The emitted THz fields add up yielding an enhanced radiation power of the irradiated main emitter.

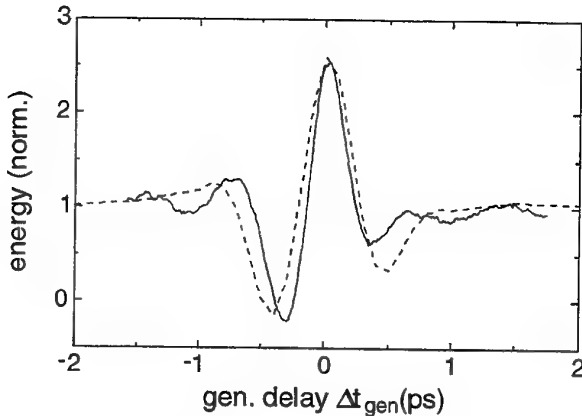


Fig.3 Detected pulse energy of the THz radiation from the main emitter normalized to the emission without the background field. For  $\Delta t_{\text{gen}} = 0$  ps an increase by a factor of 2.7 is observed due to the amplification by the THz background radiation. This is in good agreement with the numerical results shown as dashed curve.

interference. Considering that the power of the combined radiation is proportional to the square of the field amplitude, this already demonstrates an amplification of the emission of the main emitter by a factor of about three, keeping in mind, that the background power remains constant. It should be pointed out, that the temporal shape is not altered yielding two consequences: first, as the excitation density has not changed, the coherent emission time  $\tau_{\text{coh}}$  has remained constant and a true efficiency enhancement is achieved in contrast to an amplification based on superradiance. Second, the broad bandwidth of the THz radiation has not been lowered, proving the ability to amplify extreme broadband radiation. A power FFT performed on the measured signals demonstrates that the original signal bandwidth of 750 GHz (central frequency 1 THz) is only minimally lowered to 730 GHz during the amplification process. Such a broadband amplification could be hardly achieved by stimulated emission due to mode competition effects and the difficulty to achieve gain over such a broad spectral range.

To demonstrate the amplification effect more clearly a bolometer is used to detect the time-integrated emission power of the main emitter, i.e. the emitted energy is measured directly. The dashed area in Fig. 1 marks the modification in the setup needed to detect only the emission from the main emitter ( $S_0$ ) using standard lock-in technique. Fig. 3 shows the observed signal normalized to the unamplified value in dependence of the temporal overlap of the two pulses. For  $\Delta t_{\text{gen}} = 0$  ps an increase of the signal by a factor of 2.7 is observed, corresponding to the coherent field addition already seen in the time-resolved field detection experiment. As only the radiation energy emitted from the main emitter ( $S_0$ ) is detected, this proves directly the amplification of the emission of  $S_0$  by a factor of 2.7. This observation is confirmed by comparison of the detected signal with the one calculated from the cross-

correlation of the time resolved signals, shown in figure 2. The result of this calculation is plotted in figure 3 as a dashed line. The amplitude of the amplification is reproduced well. The slight modification in the signal form is attributed to the restricted bandwidth of the time resolved detection using dipole antennas. In conclusion, this experiment demonstrates, that it is possible to amplify THz radiation by phasematched coherent superposition even over a broad spectral range. This result gains more importance, as this measurement can additionally be interpreted as an analysis of the first round-trip of the amplification in a resonator, indicating its potential as a self-supporting coherent amplification mechanism.

#### IV. RESONATOR CONFIGURATION

We finally demonstrate the feasibility of repetitive amplification by coherent superposition in a resonator setup. In this approach, the resonator couples the emitted radiation back and makes use of it as the background radiation which amplifies the next THz generation process. Fig. 4 shows the ring resonator setup used for our experiment. Gold coated mirrors are used in order to guarantee a high reflectivity of the resonator. The whole system is flushed with nitrogen to reduce the strong water absorption in the 4m resonator pathway. The THz radiation in the resonator is probed and analyzed in a time-resolved extracavity detection scheme using photoconductive dipole antennas. The radiation is extracted using a 10% output coupler. To ensure a phasematched superposition under synchronous pumping, the roundtrip-time of the THz resonator has to be adjusted exactly to the repetition rate  $\tau_{\text{rep}}$  of the optical laser exciting the THz emitter. The detuned situation (not shown) allows nevertheless to detect separately the single round-trips allowing to estimate the losses of the resonator. In our case, about 50% of the amplitude is lost during a roundtrip, which limits the amplification factor in this resonator setup to about seven. Figure 4 shows the detected field transients under resonance

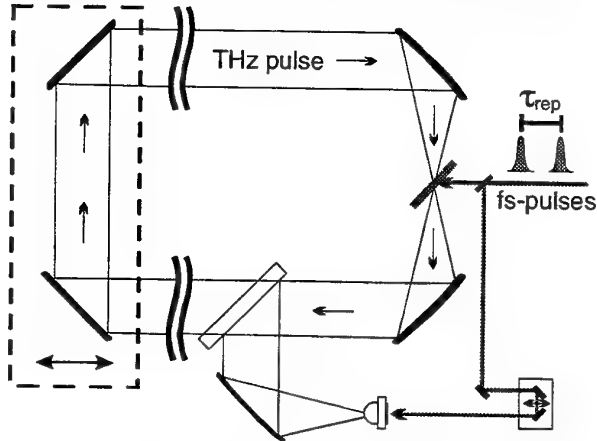


Fig. 4 Ring-resonator setup with extracavity detection to demonstrate the repetitive amplification of THz emission. The round trip time is adjusted to the repetition rate ( $\tau_{\text{rep}}$ ) of the laser to ensure coherent superposition by moving the mirrors in the dashed area.

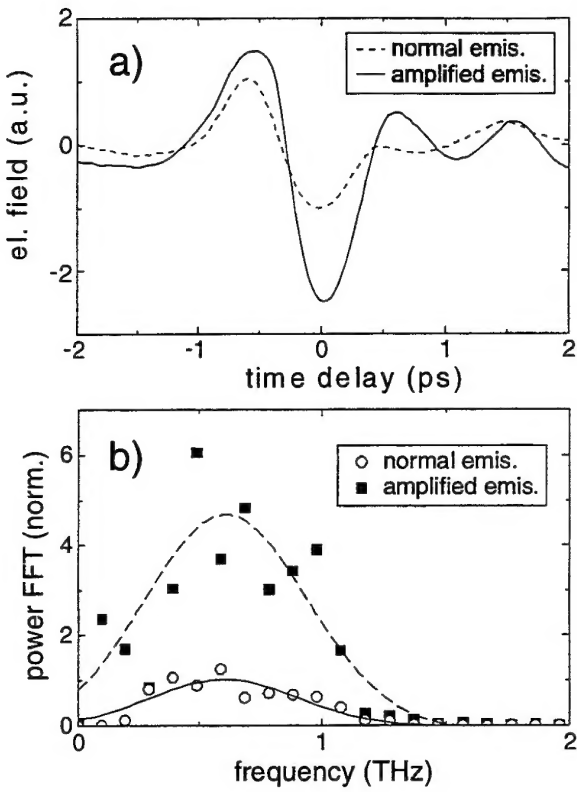


Fig. 5a) Detected electric field amplitude for the direct (dashed curve) and the amplified emission. The amplitude is enhanced by more than a factor of two, yielding a more than sixfold power increase.

b) Corresponding power FFT for the amplified (■) and the normal (○) emission. As guide to the eye a Gauss curvature is fitted to experimental data, showing successful broadband THz amplification with a bandwidth of about 650 GHz (limited by the bandwidth of the original signal) and an average amplification factor of about 5.

for the normal (dashed line) and amplified emission (solid curve). Obviously the field amplitude has increased by more than a factor of two showing a more than sixfold enhancement of the THz radiation power. Currently, the amplification is only limited by the high resonator losses. To estimate the bandwidth of the amplification process the power spectrum is calculated from the observed signals using FFT-procedures. Figure 5 shows the values for the normal (○) and the amplified emission (■). As guide to the eye gauss curves are fitted to the data allowing to estimate the amplification characteristics out of the fitting parameters. The bandwidth of about 600 GHz as well as the central frequency around 600 GHz is not altered by the amplification process. On average, the power of the radiation has been increased by a factor of about 5, whereas peak amplification factors above 6 are reached. Summarizing, the presented analysis demonstrates the possibility for the broadband self-supporting amplification of coherent THz radiation by coherent superposition in a synchronously pumped ring-resonator. Currently the

amplification factor is only limited by the high resonator losses.

## V. CONCLUSIONS

In summary we have presented a new amplification scheme, which can be applied to a wide variety of impulsively optically excited THz emitters. The amplification by coherent superposition is proven first by performing single-pass experiments detecting both time-resolved field amplitudes as well as the time-integrated power corresponding to the emitted THz energy. First experiments of THz amplification in a ring-resonator show a power enhancement of more than a factor of six. These first results demonstrate the feasibility of using this process as an alternative to stimulated emission in order to develop flexible efficient sources of coherent THz radiation. It is important to stress, that this amplification process can be applied to a wider class of emitters, as no population inversion is required.

**Acknowledgements.** The authors would like to thank H.G. Roskos, F. Wolter and C. Schwarz for fruitful discussions and the Bundesministerium für Bildung, Wissenschaft, Forschung und Technologie and the european TMR project *Interact* for financial support.

- [1] P.R. Smith, D.H. Auston, and M.C. Nuss, *IEEE J. Quantum Electron.* **QE-24**, 255 (1988).
- [2] Ch. Fattinger and D. Grischkowsky, *Appl. Phys. Lett.* **54**, 490 (1989).
- [3] X.-C. Zhang, B.B. Hu, J. T. Darrow, and D. H. Auston, *Appl. Phys. Lett.* **55**, 337 (1990).
- [4] H.G. Roskos, M.C. Nuss, J. Shah, K. Leo, and D.A.B. Miller, *Phys. Rev. Lett.* **68**, 2216 (1992).
- [5] C. Waschke, H. G. Roskos, R. Schwedler, K. Leo, H. Kurz, and K. Köhler, *Phys. Rev. Lett.* **70**, 3319 (1993).
- [6] *see for an overview:* M.C. Nuss and J. Orenstein, "THz time-domain spectroscopy" in *Millimeter and Sub—Millimeter Waves*, ed. by G. Gruener (Springer Verlag, Heidelberg, 1998).
- [7] K. Victor, H.G. Roskos, and C. Waschke, *J. Opt. Soc. Am. B* **11**, 2470 (1994).
- [8] B.I. Greene, J.F. Federici, D. R. Dykaar, R.R. Jones, and P.H. Bucksbaum, *Appl. Phys. Lett.* **59**, 893 (1991).
- [9] R. Martini, G. Klose, H.G. Roskos, H. Kurz, H.T. Grahn, and R. Hey, *Phys. Rev. B* **54**, R14325 (1996).
- [10] A. Bonvalet, J. Nagle, V. Berger, A. Migus, J.L. Martin, and M. Joffre, *Phys. Rev. Lett.* **76**, 4392 (1996).

# Receivers for the Sub-Millimeter Array

R. Blundell, C.-Y. E. Tong, S. Paine, C. Papa, J. W. Barrett, R. L. L. Leombruno, R. Kimberk,  
R. W. Wilson and T. R. Hunter

*Harvard-Smithsonian Center for Astrophysics  
60, Garden Street, Cambridge, MA 02138, USA*

**Abstract:** We report here on a 176 – 256 GHz low-noise receiver system recently installed in the first of our Sub-Millimeter Array antennas. The receiver is housed in a cryostat cooled by a closed-cycle helium refrigerator and has a double-side-band receiver noise temperature of about 60 K across the entire input frequency range and an instantaneous bandwidth of 2.5 GHz.

## Introduction

In the frequency range 100 – 1000 GHz superconductor-insulator-superconductor (SIS) mixer receivers are the receivers of choice when low-noise operation, or high sensitivity, is of critical importance. The Sub-Millimeter Array will be the first radio-interferometer to operate at submillimeter wavelengths. It will consist of eight six-meter diameter radio-telescopes, each housing a set of low-noise heterodyne receivers. Since the array is designed to operate in the major atmospheric windows from about 200 GHz to 900 GHz SIS tunnel junction mixer receivers are preferred. Prototype receivers have been laboratory tested, and offer low-noise performance in the frequency ranges: 176 – 256 GHz, 250 – 350 GHz, 400 – 520 GHz, 600 – 720 GHz and 800 – 900 GHz.

## Receiver package

In all cases the mixers used are of the superconductor-insulator-superconductor (SIS) type and are made using niobium tri-layer technology at the Microelectronics Laboratory of the Jet Propulsion Laboratory. The lowest frequency mixer is a lumped element design and is made using optical lithography. The higher frequency mixers are made using electron beam lithography, and above 400 GHz the lowest noise performance is achieved with distributed rather than lumped-element devices. In all cases, the mixer block is made in two parts, a front section which carries the corrugated horn feed and a back piece carries a shorted section of waveguide; the length of which is chosen so as to provide a good match to the SIS mixer element across the input frequency range. For the 176 – 256 GHz mixer, the waveguide dimensions are 1.1 mm wide by 0.27 mm high and the length of the shorted section of waveguide is 0.22 mm. The quartz substrate supporting the SIS mixer element is suspended across the waveguide and is sandwiched between the

front and back sections of the mixer block. A magnetic field can be applied to suppress unwanted Josephson currents via magnetic pole pieces inserted between the front and back sections of the block orthogonal to the axes of the waveguide and the suspended substrate. For completeness, a sketch of the suspended substrate filter and SIS junction design is also shown in the figure. The length of the first section of the low pass filter structure was chosen so as to provide a constant, real impedance to the SIS mixer element across the signal input bandwidth. The thin-film tuning circuit, designed to tune out the parallel plate capacitance of the SIS junction is used to achieve optimum coupling of the signal power to the mixer. Details of this structure can be found elsewhere.

The mixer output is coupled to a low-noise intermediate frequency (IF) amplifier, cooled to about 6 K, via a short section of stainless steel semi-rigid cable and a circulator whose third port is used to couple dc bias to the mixer. Signal input to the mixer is via a thin teflon vacuum window, a series of infra-red blocking filters, and a groove-matched teflon lens cooled to 100 K. Numerous receiver assemblies, or inserts, of this type have been made for the 200, 300 and 600 GHz frequency bands.

## Optical coupling

The optics for the SMA are designed to produce an image of the feed horn aperture at the primary mirror. This configuration maximizes the aperture efficiency, independent of frequency. The signal from the antenna is directed along the elevation axis of the antenna via a flat tertiary mirror and into the receiver cabin via mirror M4 in a bent Nasmyth configuration. Figure 1 shows the general optical scheme. Mirrors M4, M5 and M6 direct the signal towards the receiver steering optics mounted directly above the cryostat. An intermediate image of the feed horn, conveniently placed for receiver noise calibration, is produced between the elliptical mirrors M4 and M5, at this point the optical beam measures only 50 mm across.

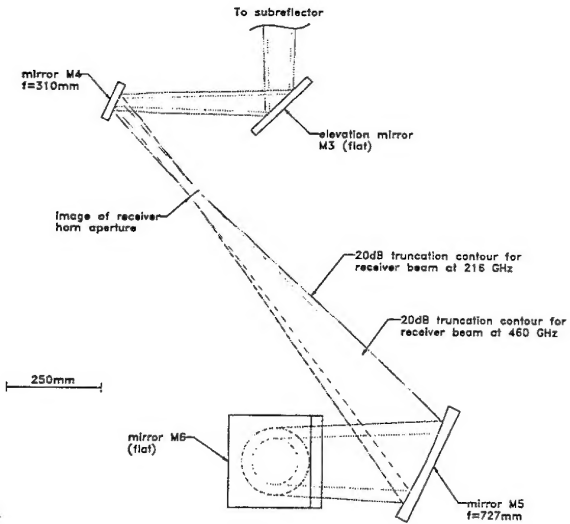


Figure 1: General optical scheme for coupling receivers to the SMA antenna.

A wire grid polarizer is used to separate the signal from the antenna into two polarizations. Referring to figure 2, the reflected signal is then steered by the wire grid polarizer towards one of the four 'low-frequency' receiver positions, the transmitted signal is steered by an additional rotating mirror (not shown) assembly to one of the four 'high frequency' receiver positions. The sets of 'low frequency' receiver optics, up to 400 GHz, use a nickel mesh to combine local oscillator and signal input to the receiver. Since the available local oscillator power is much reduced at high frequencies, the sets of 'high frequency' receiver optics, above 400 GHz, use a Martin Puplett interferometer for LO and signal diplexing.

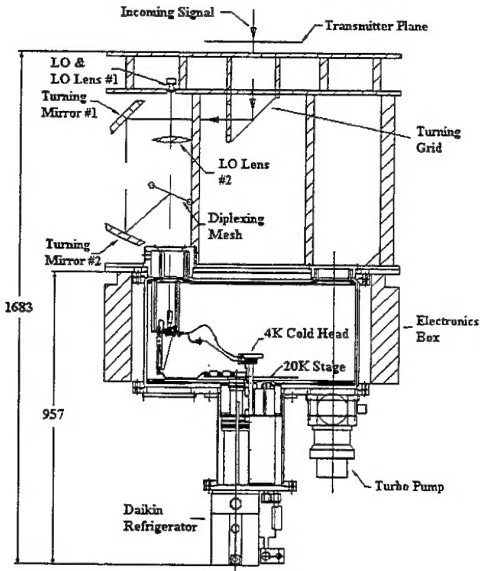


Figure 2: Schematic of the SMA receiver package including optical coupling and cryostat layout.

### Cryostat layout

The cryostat, one per antenna, uses a closed-cycle helium cryocooler to cool the different receivers. It takes less than 24 hours to cool the receiver inserts from room temperature to their operating temperatures, and about 36 hours to warm the system back to room temperature after cooling. A schematic of the cryostat is given in figure 3. In order to provide frequency coverage from about 200 to 900 GHz and provide dual polarization capability at 350 GHz, both requirements of the SMA, up to eight receiver inserts can be cooled. The receiver positions are arranged in a ring on top of the cryostat, every other receiver position is coupled to one of two sets of electronics and second stage IF amplifiers such that combinations of pairs of receivers can be operated at any given time. Individual receiver selection is made by steering the input signal beam, and, at the same time, the IF output of the desired receiver is selected using a cryogenically cooled four-way FET switch.

### Local oscillator

In all cases, the LO is provided by a frequency multiplied Gunn oscillator phase-locked to a 109 MHz reference signal. Each LO chain has a microcontroller board in which fully automatic tuning algorithms reside. Automatic LO tuning and phase locking is achieved with a 99% success rate in about 10 seconds. The power level of the 6 - 8.5 GHz reference signal and the gain of the digital phase-lock loop are immediately adjusted to provide optimum phase noise, determined by a simple bandpass/notch filter combination at the IF. The frequency multiplier backshorts and LO attenuator are adjusted in real time for optimum receiver performance monitoring the total power output of the receiver. Coarse look-up tables for each waveguide device are generated in the laboratory. Receiver tuning, therefore, requires only a commanded mixer-bias voltage and adjustment of the magnetic field to minimize Josephson noise.

### Initial tests

We have tested several receivers in the 200 and 300 GHz frequency bands. A plot of the double-side-band (DSB) receiver noise for a typical receiver built for the 200 GHz frequency band is given below. From the figure, the receiver noise is approximately flat, at 60 K, across the entire operating frequency range. This is somewhat higher than the 40 K we measure in our simple laboratory test set-up. The main reasons for the increased noise are: more room-temperature optical components in front of the receiver, a larger, thicker lens - cooled only to  $\sim 100$  K (in the test system the lens is cooled to about 4 K), and a slight increase in the noise temperature of the production IF amplifier chain. A receiver with similar noise performance has recently been installed in our first SMA antenna for system tests.

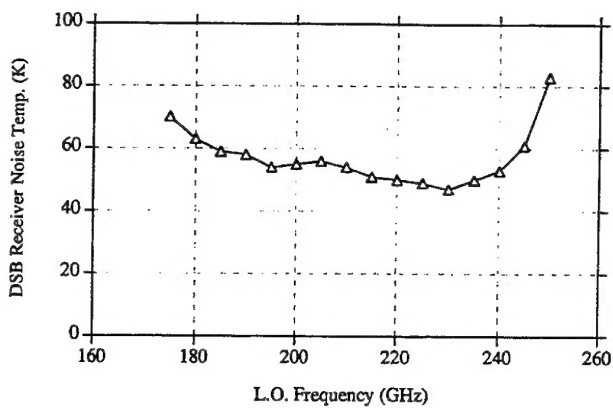


**Figure 3:** Measured DSB receiver noise as a function of Local oscillator frequency

### Summary

We have developed a low-noise heterodyne receiver for operation in the frequency range 176 – 256 GHz. This receiver is part of a much larger system in which up to eight such units can be operated. Initial tests on the full receiver system, coupled to the first SMA antenna, are underway.